Elucidating Mechanisms of Palladium and Iridium Catalysis using *Para*hydrogen

Kate Mary Appleby

PhD

University of York

Chemistry

September 2016

Abstract

This thesis aims to elucidate mechanisms of palladium and iridium catalysis using *para*-H_2. In palladium catalysis, the debate on the nature of the active catalysts tends to focus on homogeneous palladium monomers or heterogeneous palladium nanoparticles; intermediate palladium clusters are repeatedly overlooked. The research herein aims to ascertain the role of such clusters in palladium catalysis. The conversion of palladium monomers to palladium clusters has been investigated. Reactive palladium monomers with the formula $[Pd(OTf)_2(XR_3)_2]$, where X = As or P, and R = aryl or alkyl, have been synthesised. Palladium-catalysed hydrogenation reactions were the focus and the suitability of these monomers for this study was verified by the formation of palladium nanoparticles on addition of hydrogen gas. Nanoparticles were characterised by transmission electron microscopy (TEM). A number of novel monohydride palladium species formed, and were characterised using liquid injection field desorption ionisation mass spectrometry (LIFDI-MS), and nuclear magnetic resonance (NMR) spectroscopy, including *para*-H_2 induced polarisation (PHIP) which is used to enhance NMR signals.

Tri-palladium clusters with the general formula $[Pd_3(XR_3)_4]^{2+}$, were characterised by LIFDI-MS, advanced NMR spectroscopy, and single-crystal x-ray diffraction (XRD). These species are stable. $[Pd_3(PPh_3)_4]^{2+}$ was isolated and found to be an effective catalyst for hydrogenation reactions and mild Suzuki-Miyaura cross-couplings.

PHIP has also been applied in a non-hydrogenative manner using 'signal amplification by reversible exchange' (SABRE). This technique has been used to enhance the ^1H NMR signals corresponding to pyridazine and phthalazine. The formation of SABRE-active iridium complexes with pyridazine and phthalazine and exchange of hydrogen and the *N*-heterocycle at iridium has been investigated. SABRE of the ^1H NMR resonances was optimised. The potential to use drug derivatives of pyridazine and phthalazine as hyperpolarised contrast agents in magnetic resonance imaging (MRI) was verified by successfully hyperpolarising 5-aminophthalazine (an antifungal) and investigating SABRE in biologically-compatible solvents.

List of Contents

List of Figures

List of Tables

Accompanying Material

All characterisation data, including NMR spectra, mass spectra, and elemental analysis, are included in an accompanying electronic appendix on CD. This is attached to the back page of this thesis.

Acknowledgements

I would firstly like to thank my supervisors Professors Simon Duckett and Ian Fairlamb, for their support, patience, and advice throughout my PhD. They have encouraged me to present my research at international conferences and to get involved in many science activities, all of which have been invaluable experience for my future career.

I thank the Duckett and Fairlamb research groups for their enthusiasm and eagerness to help. The away days were incredible – mixing cider with research has fantastic results. I am also thankful for the group meetings, which helped us all gain confidence in presenting our research but also created a comradery, which I will miss. I thank my office mates, especially Pete, Phil, Ryan, Chard, Emma, Rhianna, Amy, Barby, Tom, Alister, Chris, Will, Olga, Robin, Liz, and Dave for keeping me sane whilst also sending me insane. Special thanks also go to George (my bezzie mate).

My research would not have been possible without the help of the technical staff in the department, all of whom I thank. I am especially grateful for the assistance of Karl Heaton in providing me with fantastic mass spectra; Adrian Whitwood, Natalie Pridmore, and Sam Hart for providing amazing crystal structures, Meg Stark for assisting in the collection of incredible TEM images; and Graeme McAllister for providing CHN elemental analysis.

Lastly, but most importantly, I thank my close family and friends who supported my transition from teacher training to PhD, and without whom I would have continued to wonder 'what if…?'. Special thanks go to Victoria, Daniel, and Claire, whose thoughts I cherish. I would like to thank my parents for their encouragement, yet complete lack of interest in my research which gave me a route to escape it. I also thank Jon, my fiancé, for his encouragement in the form of cups of tea, smiles, and hugs.

Declaration

Unless specifically stated and appropriately referenced, the work presented herein is, to the best of her knowledge, the author's original work and has not previously been presented for an award at this, or any other university.

1 Introduction

1.1 Catalytic Species in Palladium Catalysis

The exact nature of the active catalytic species in palladium-catalysed reactions is a matter of significant debate.[1] This is due to the extensive reactivity of intermediate palladium species, which makes identifying key reaction steps challenging, even when using modern analytical techniques. The use of palladium is ubiquitous in the field of catalytic C-C bond formation, which has become prevalent in the academic literature. Early mechanistic hypotheses assumed a homogeneous catalytic cycle, involving one or two palladium atoms, typically with palladium shuttling between the 0 and II oxidation states as shown in Figure 1 for a general carbon coupling reaction.[2-6] Throughout this thesis, Schwartz's definitions of homogeneous and heterogeneous will be used, where a homogeneous catalyst is one with homogeneity in its active sites, whereas a heterogeneous catalyst is one with heterogeneity in its active sites.[7]

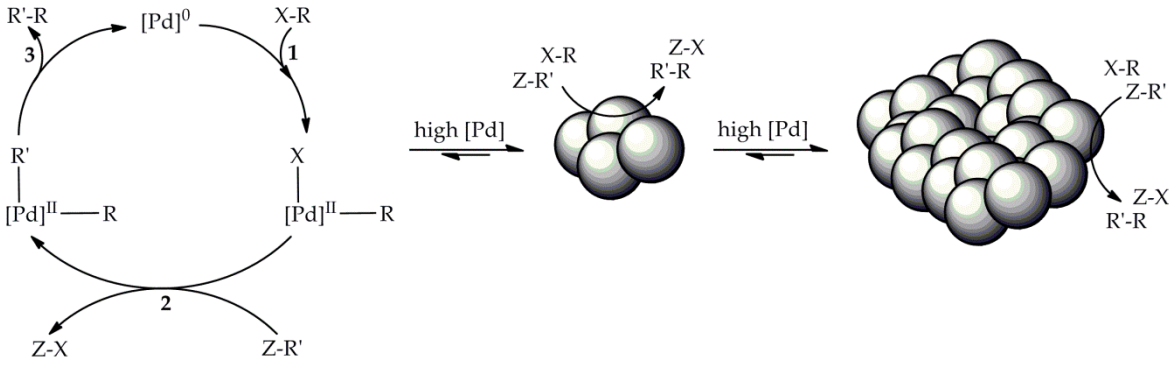

Figure 1: Simplified scheme to show a homogeneous catalytic cycle for a general carbon-coupling reaction, where X is typically a halide or triflate, Z is a metal or pseudo-metal (eg, boron), 1 is oxidative addition, 2 is transmetallation (note – in the Heck reaction this step is alkene insertion),[6] and 3 is reductive elimination. The formation of heterogeneous nanoparticles from the homogeneous molecules via an intermediate cluster phase is also shown.

More recently, heterogeneous palladium-catalysed carbon coupling reactions have been reported whereby catalytically-active palladium nanoparticles form *via* the aggregation of palladium monomers,[8-11] or are synthesised separately and stabilised by

coordinating ligands and polymers prior to their use as catalysts.[12-14] In addition, supported palladium, for example palladium on carbon, also finds use as a carbon-coupling catalyst,[15-17] however leaching of free palladium atoms is reported.[15] It is therefore unclear if catalysis takes place at the surface of the supported palladium or at leached palladium monomers. The homogeneous and heterogeneous dichotomy often leads to these two phases being treated as completely separate, however they are linked by a cluster phase, as shown in Figure 1. There is little reported on the clusters that link homogeneous and heterogeneous catalysis, and this thesis aims to add to this area.

The formation of palladium nanoclusters from a monometallic pre-catalyst is likely to occur during a reaction which requires high temperatures and pressures.[18] Nanoclusters that form in such reactions can diffuse together and coalesce to form bulk metal,[19] which is a thermodynamic minimum. This can be prevented through the use of stabilisers which include anionic ligands such as carboxylates,[20] bulky organic materials such as polyvinylpyrrolidone (PVP),[21] and solvents that possess high dielectric constants such as ionic liquids[22] or dimethylformamide.[23] Anionic ligands stabilise nanoclusters electrostatically, through coulombic repulsion between nanoclusters whereas bulky organic materials stabilise nanoclusters sterically, thereby preventing two nanoclusters from physically touching.[24]

Distinguishing homogeneous from heterogeneous catalysis is difficult and not always conclusive, hence the on-going debate. This issue is not exclusive to carbon-coupling reactions; the mechanisms of many reactions involving palladium catalysts, including hydrogenation reactions, are unclear[24] despite the availability of a wide variety of techniques to probe them. This is due to there being no single definitive technique to decipher the phase of the catalyst, and limited conclusions are gained from these techniques. Furthermore, the nature of the active palladium catalyst can change with subtle changes in reaction conditions for example changes in the solvent or the reactant.[25]

1.1.1 Techniques Used to Distinguish Catalytic Phase

In order to convincingly determine the phase of the active catalyst, a general method has been reported by Finke,[26] and is shown pictorially in Figure 2, however it is

highlighted that this approach is rarely possible as the true catalyst may not be isolable or detectable (step **1.**).

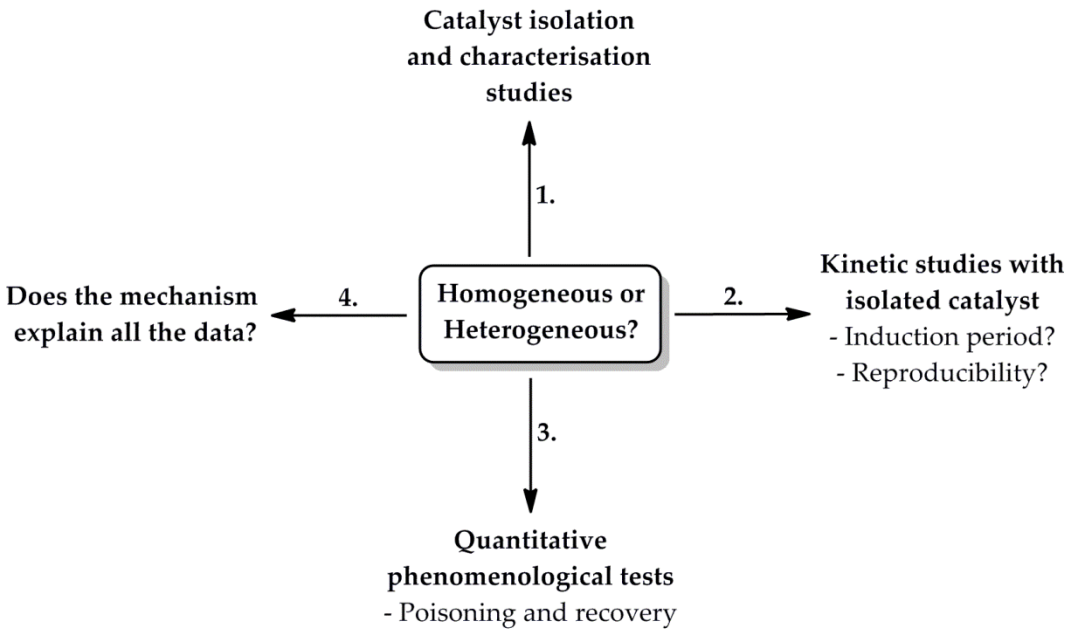

Figure 2: General method to successfully distinguish between a homogeneous and heterogeneous catalyst.

Conventional characterisation techniques can be used to detect active catalytic species, however many are limited by the stability of the catalyst. Unstable catalysts are likely to be present in very low concentrations, and cannot therefore be detected by insensitive techniques, like nuclear magnetic resonance (NMR) spectroscopy. Although conventional NMR spectroscopy is relatively insensitive, this issue can be overcome using hyperpolarisation methods, which are discussed in section 1.2.

1.1.1.1 Electrospray Ionisation Mass Spectrometry

More sensitive techniques include electrospray ionisation mass spectrometry (ESI-MS),[27] which is used to detect ionic species formed in a relatively soft ionisation process. Neutral species must therefore be converted to charged ions, which is commonly achieved by protonation or deprotonation. ESI-MS can be used in the positive-ion or negative-ion mode. Most of the reported uses of ESI-MS to analyse palladium chemistry have employed a positive-ion mode,[28-30] however this can result in the oxidation of palladium(0) to palladium(I). Palladium(I) is likely to have a different reactivity to palladium(0), and should therefore be avoided. For this reason, negative-ion ESI-MS is more appropriate; the reduction of palladium(0) to palladium(−I) is highly unlikely due to the instability of palladium(-I).

The McIndoe group have published many reports on the successful application of time-resolved negative-ion ESI-MS for probing palladium-catalysed reactions, predominantly carbon-coupling reactions.[31-33] Charged ligands, typically phosphonium salts like the monosulfonated triphenylphosphine salt shown in Figure 3, are added to the catalyst species to allow for their detection.[34] Palladium intermediates are detected by their *m*/*z* ratios and their signal intensities are monitored over the reaction time. In addition to typical kinetic traces for starting material and product, kinetic traces for the production and depletion of active catalytic species can be observed and give excellent mechanistic insights. Although ESI is a relatively soft ionisation method, it is often unsuitable for the detection of transition metal complexes with labile ligands or for complexes that do not easily ionise. For these, liquid injection field desorption/ionisation (LIFDI) MS is more appropriate, however this is an insensitive technique.[35]

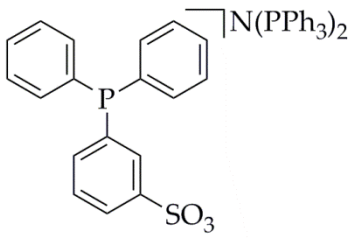

Figure 3: $[N(PPh_3)_2][PPh_2(m\text{-}C_6H_4SO_3)]$.

1.1.1.2 Infrared Spectroscopy

Infrared (IR) spectroscopy is another characterisation technique that has been applied to palladium catalyst studies[36-39] however this suffers from sensitivity and selectivity issues. In order to produce a signal, the bond vibration probed by infrared radiation must induce a change in electric dipole moment.[40] Many bond vibrations are symmetric and therefore IR silent, however they may be observed using Raman spectroscopy if there is a change in polarisability as a result of the vibration.[41]

IR spectroscopy has been widely used to detect reaction intermediates[42,43] however it is commonly used alongside 'reporter' ligands with large oscillator strengths and therefore high IR sensitivities, for example carbonyls or cyano groups.[44] These are introduced to metal complexes of interest so that reaction intermediates that are present in low concentrations can be detected. Gaseous probe molecules, like carbon monoxide, are also used alongside IR spectroscopy to provide information about the surfaces of supported

palladium catalysts.[36-39] The frequencies of the vibrations in the adsorbed gas molecules are characteristic of the catalytic site on which they are bound, for example a signal at 2090 cm^{-1} corresponds to carbon monoxide bound linearly to palladium[36] which is indicative of a low coordinate defect site. The number of active sites on the catalyst surface can be calculated from such data.[36]

1.1.1.3 UV-Vis Spectroscopy

The formation of palladium nanocolloids in chemical reactions can be detected and monitored by UV-vis spectroscopy. Metal nanoparticles and colloids exhibit localised surface plasmon resonances, which correspond to coherent oscillations of the electric field at the particle surface.[45] The colloids will therefore absorb electromagnetic radiation of a frequency that matches the frequency of the plasmon resonance, which is typically in the UV or visible region of the spectrum. Despite unpronounced palladium plasmon resonance bands (due to d-d interband transitions), the high sensitivity of UV-vis spectroscopy allows for the detection of palladium nanocolloids. However, detection of such resonance bands is difficult in the presence of stabilising ligands that absorb light in the same region. This limits the use of UV-vis spectroscopy to identify palladium nanocolloids. In contrast, UV-vis spectroscopy is commonly used to identify gold nanocolloids, which have plasmon resonances with large molar absorption coefficients (~ 10^6 $mol^{-1}dm^3cm^{-1}$).[46]

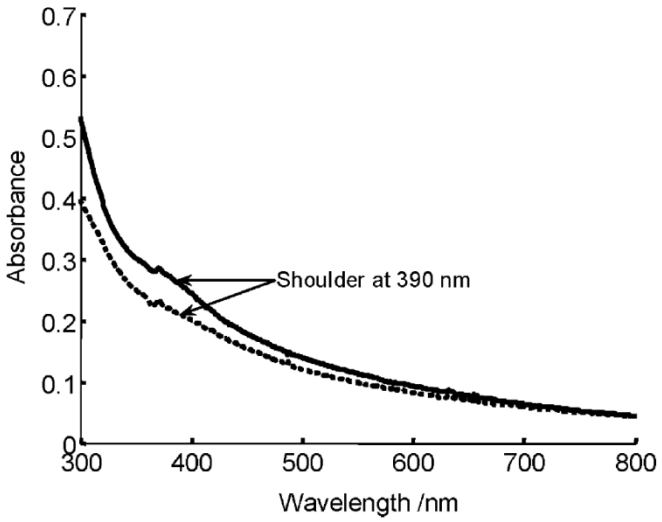

Figure 4: Absorption of two different solutions of palladium clusters prepared from $PdCl_2$. Reproduced from Gaikwad, A. V.; Rothenberg, G. Phys. Chem. Chem. Phys. 2006, 8, 3669 with permission of the PCCP Owner Societies.

An example of a plasmon resonance band corresponding to palladium clusters is given in Figure 4.[47] The plasmon band is sensitive to the size of the palladium clusters, as well as their chemical environment.[48] The Rothenberg and Reetz groups have successfully applied time-resolved UV-vis spectroscopy to monitor the reduction of palladium(II) complexes and the subsequent formation of palladium clusters.[47,49]

1.1.1.4 Transmission Electron Microscopy

The presence of nanoclusters in a reaction mixture can be verified using transmission electron microscopy (TEM), which is a sensitive technique for the detection of nanoclusters that are greater than 1 nm in size.[26,50] A positive TEM result is irrefutable evidence that nanoclusters form either during the reaction, or during TEM sample preparation. The latter can be ruled out through the use of a control sample, in which a stabilising polymer, for example PVP, is added to the sample.[51-53] Stabilising polymers coat nanoclusters, thus influencing their size and shape as they form. Any structural changes during TEM sample preparation are evident by differences in the size and shape of nanoclusters that form with and without the stabilising polymer. The TEM image shown in Figure 5 is of palladium nanoparticles that formed during a C-H functionalisation reaction.[53] PVP was used to stabilise the nanoparticles during TEM sample preparation.

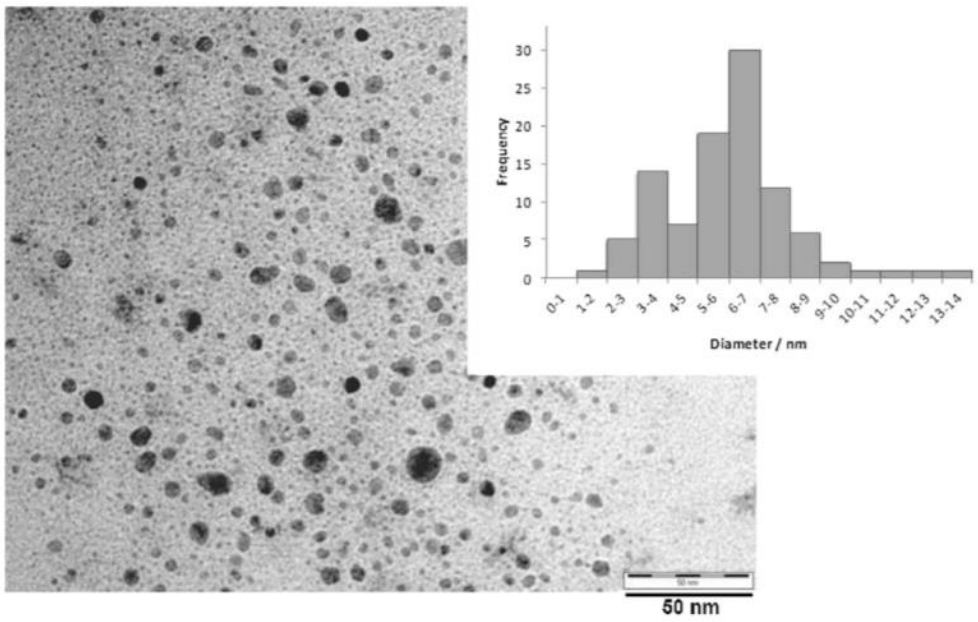

Figure 5: TEM image of nanoparticles that form during C-H bond functionalisation of benzothiazole, with PVP added during TEM preparation. Reprinted from Baumann, C. G.; De Ornellas, S.; Reeds, J. P.; Storr, T. E.; Williams, T. J.; Fairlamb, I. J. S. Tetrahedron 2014, 70, 6174 with permission from Elsevier.

A negative TEM result does not disprove the formation of nanoclusters; nanoclusters that are smaller than 1 nm cannot be detected using TEM and first-row transition metals are often difficult to image due to poor contrast,[54] however this is not an issue with palladium nanoclusters. As a result, TEM is a very useful technique to characterise nanoclusters, but ought to be used alongside other characterisation techniques and kinetic investigations.[26]

1.1.1.5 X-ray Absorption Spectroscopy

One less commonly used, but conclusive technique for the characterisation of palladium nanoparticles during a reaction is x-ray absorption spectroscopy (XAS). The use of this technique was reported by the Fairlamb group for the study of a Suzuki-Miyaura cross-coupling reaction catalysed by PVP-stabilised palladium(0) nanoparticles.[12,13] The oscillations in extended x-ray absorption fine structure (EXAFS) can be assumed to be directly proportional to the local coordination number of the probed palladium atom.[55] The average first-shell palladium coordination number can therefore be calculated from the EXAFS. Time-resolved XAS was used to measure the average first-shell palladium coordination number during the Suzuki-Miyaura cross-coupling reaction, and the results are shown in Figure 6. There was no discernible change in the coordination number throughout the reaction, which suggests that the nanoparticles are very stable under the reaction conditions used and the catalyst is likely to be the heterogeneous palladium nanoparticles.

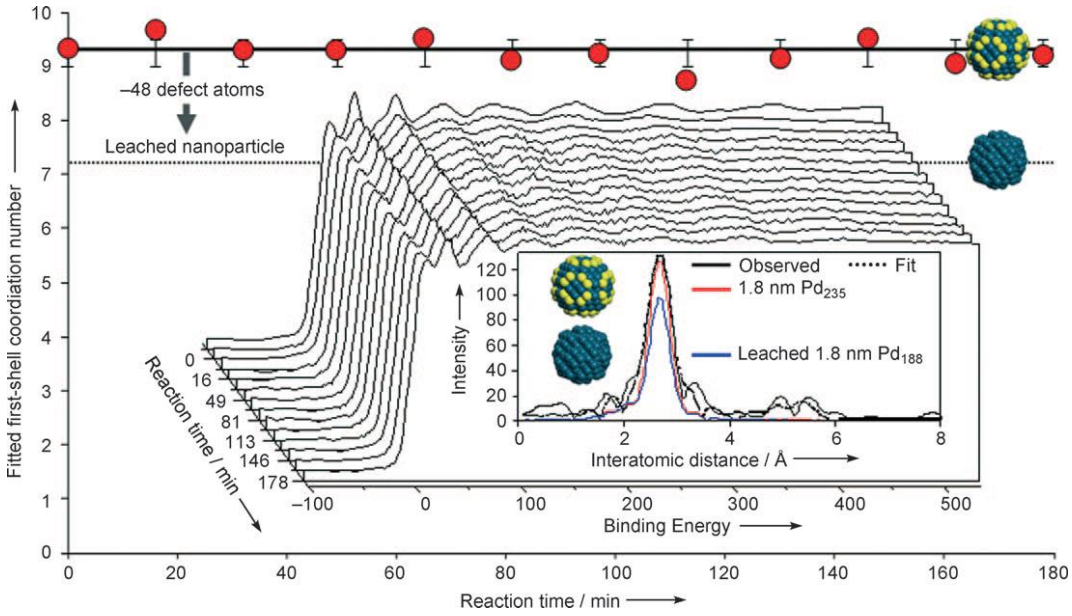

Figure 6: XAS, including EXAFS, spectra of a Suzuki-Miyaura cross-coupling reaction, in which the average local coordination number of the probed palladium atoms does not change. Reproduced from Ellis, P. J.; Fairlamb, I. J. S.; Hackett, S. F. J.; Wilson, K.; Lee, A. F. Angew. Chem. Int. Ed. 2010, 49, 1820 with permission from Wiley.

1.1.1.6 Kinetic Studies

Kinetic studies play a significant role in identifying the true active catalyst in a reaction. Sigmoidal kinetic curves, shown in red, blue, and green, in Figure 7,[56] are typical of heterogeneous reactions, in which the active catalytic species are generated from the metal species supplied. This results in an initial 'lag' time, where very little product is produced due to the need for the catalyst to activate.

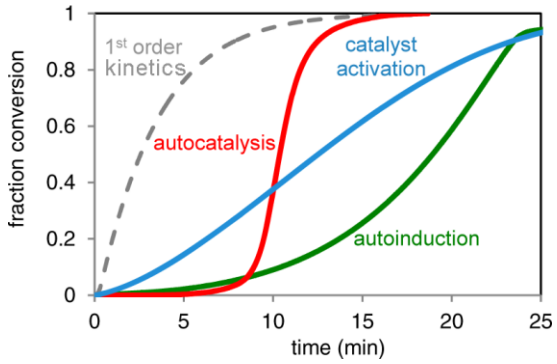

Figure 7: Kinetic profiles of conventional first order kinetics (grey), autocatalysis (red), slow catalyst activation (blue), and autoinduction (green). Reprinted with permission from Mower, M. P.; Blackmond, D. G. J. Am. Chem. Soc. 2015, 137, 2386 copyright 2016 American Chemical Society.

Autocatalysis results in a sigmoidal curve with a large gradient and occurs when a product of the reaction is also a reactant, thus the production of product acts to catalyse

the reaction. An example of this is the Soai reaction,[57] shown in Figure 8 (above, 1), in which a pyrimidyl alcohol reacts with diisopropyl zinc, forming the chiral isopropylzinc alkoxide shown. This species catalyses the enantioselective addition of diisopropyl zinc to a pyrimidyl aldehyde to also form the chiral isopropylzinc alcoxide. This is then hydrolysed to form the enantiomerically pure pyrimidyl alcohol.

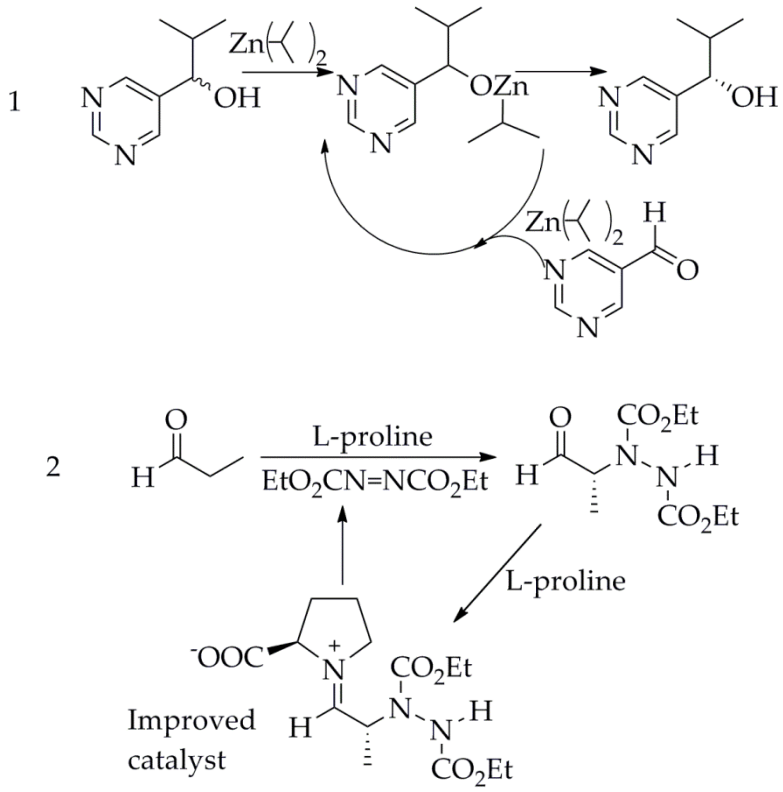

Figure 8: The Soai reaction (above, 1), which is an example of an autocatalytic reaction, and proline-mediated α-amination of propionaldehyde (below, 2), which is an example of an autoinduced reaction.

Autoinduction results in a sigmoidal curve with a gradual incline and occurs when the product formed in a reaction acts to increase the reactivity of the catalyst, but is not directly involved in product production.[58] An example of this is proline-mediated α-amination of propionaldehyde, also shown in Figure 8 (below, 2).[59] In this reaction, L-proline acts as a catalyst, however the amine product formed can react further with the L-proline and form an improved catalyst. As a result, the reaction rate gradually increases during the reaction, until the low concentration of propionaldehyde becomes limiting.

Non-promoted catalyst activation results in a sigmoidal curve that lies between the two extremes of autocatalysis and autoinduction. Evidence for the formation of palladium colloids, either by the observation of palladium black precipitate or by TEM imaging, in addition to the observation of sigmoidal kinetic traces provides a strong case for

heterogeneous catalysis.[60,61] Sigmoidal kinetics are not always observed for reactions that are catalysed heterogeneously because this shape requires specific kinetic behaviour. If the initial nucleation step, shown in Figure 9, in which nanoclusters begin to form proceeds with a rate constant of k_n and is followed by an autocatalytic surface growth step, during which active nanoclusters form rapidly with a rate constant of k_a,[62,63] then k_n must be significantly smaller than k_a, to produce sigmoidal kinetic traces. If, however k_n is a similar value to the rate of catalysis then a sigmoidal trace may not be detected. Furthermore, catalyst deactivation can obscure the kinetic trace.[24]

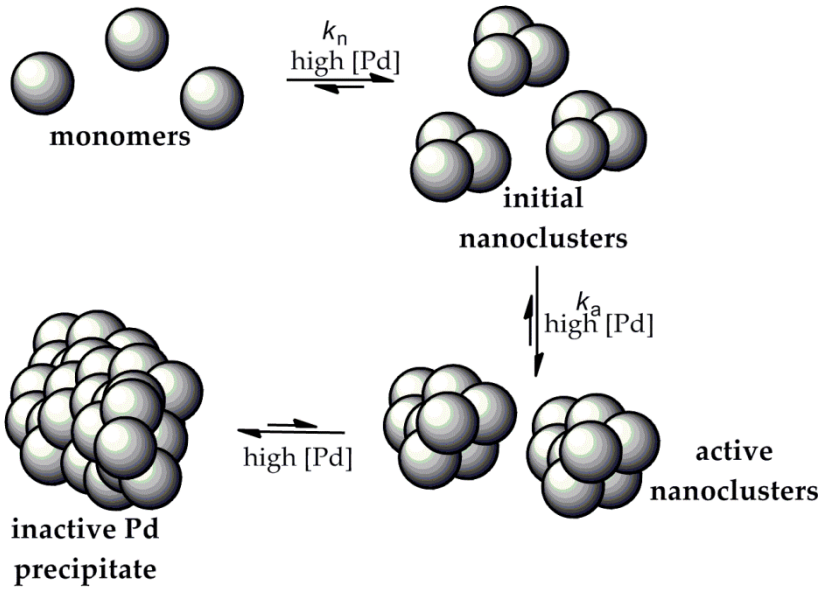

Figure 9: Simplified scheme showing the growth of nanoclusters from monomers, and their aggregation to inactive palladium precipitate.

Additional kinetic evidence, reported to assist in distinguishing the catalytic phase, is found in the influence of the palladium concentration on the reaction rate. If a reaction was truly homogeneous, then an increase in palladium concentration would increase the reaction rate due to the presence of more active catalytic species in solution. In several cases, a different trend is observed, where the turnover frequency (TOF, $mol_{product}\ mol_{Pd}^{-1}\ hr^{-1}$) is found to increase with lower palladium concentrations.[8,9] An example of this, in a Sonogashira cross-coupling reaction,[9] is shown in Figure 10.

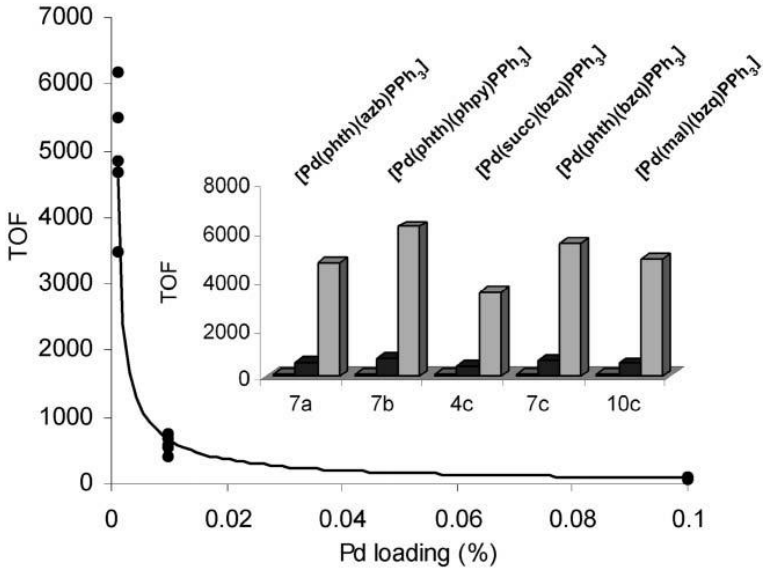

Figure 10: Graph showing an inverse correlation between palladium catalyst loading and TOF in the Sonogashira cross-coupling of 4-bromoacetophenone with phenylacetylene, using the palladacycle pre-catalysts given in the inset. Reproduced from Fairlamb, I. J. S.; Kapdi, A. R.; Lee, A. F.; Sanchez, G.; Lopez, G.; Serrano, J. L.; Garcia, L.; Perez, J.; Perez, E. Dalton Trans. 2004, 3970 with permission of the Royal Society of Chemistry.

The drop in TOF with larger palladium concentrations is attributed to palladium aggregation, and the precipitation of inactive palladium black from the reaction mixture, shown in Figure 9, which may also act as a 'reservoir' of active palladium species. Furthermore, reported increases in TOF with smaller palladium nanoparticle sizes[8,13] suggest that in these cases, catalysis occurs at the low-coordinate vertex and edge atoms on the nanoparticle surfaces – the palladium surface area is larger when smaller nanoparticles are used.

1.1.1.7 Catalyst Poisoning

Mercury is able to poison heterogeneous[1] and homogeneous[25,64,65] metal complexes by forming an amalgam with the metal or adsorbing onto the surface of the metal. Mercury will poison any palladium(0) catalyst that is not protected with strongly bound ligands. As such, it is not a definitive poisoning test, however if the addition of mercury to a reaction mixture does not affect catalysis, then the reaction mechanism is unlikely to involve unprotected palladium(0).[1] If unprotected palladium(0) species are suspected to form from the palladium pre-catalyst, then a control experiment is required to demonstrate that the pre-catalyst does not react with mercury. Characterisation of a heterogeneous palladium(0) amalgam by X-ray photoelectron spectroscopy (XPS),[13] which

analyses the elemental composition at the surface of the amalgam, provides further proof for a heterogeneous palladium(0) catalyst.

Other poisons used to distinguish catalytic phase include carbon disulfide, triphenylphosphine, thiophene, and dibenzo[a,e]cyclooctatetraene (Figure 11),[24] which all bind strongly to metal centres. Dibenzo[a,e]cyclooctatetraene binds to some, but not all, homogeneous catalysts and has little effect on palladium colloids and supported palladium on carbon.[66] It is promoted as a complimentary technique to be used alongside mercury poisoning. The other listed poisons act to inhibit heterogeneous catalysts on addition of less than one equivalent, but inhibit homogeneous catalysts on addition of equimolar or greater amounts.[24] These poisons are, however, limited by the experimental conditions; higher temperatures promote their dissociation from metals. Furthermore, in many palladium-catalysed reactions, multiple palladium species form from the pre-catalyst used, and the amount of each species in solution is unknown, thus the addition of specific equivalents of poisons is impractical. As a result, such poisons are rarely used to distinguish catalytic phase in palladium-catalysed reactions.[1]

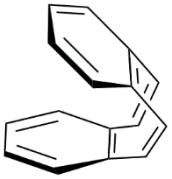

Figure 11: Dibenzo[a,e]cyclooctatetraene.

The Jones group have reported the use of cross-linked poly(vinylpyridine) (Figure 12) – an insoluble solid material that contains many binding sites to extract soluble, unprotected palladium species from a reaction mixture.[67-69] Addition of poly(vinylpyridine) to reactions catalysed by various supported palladium complexes resulted in complete deactivation of the catalyst.[67-69] This suggests that the major active catalysts were leached palladium molecular species, rather than the supported palladium complexes; it is argued that the cross-linked polymer is unlikely to bind to the surface of metal nanoparticles.

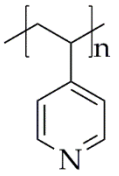

Figure 12: Polyvinylpyridine.

1.1.1.8 Maitlis' Test

In order to distinguish the nature of the true catalyst in a reaction, the catalytic reactivity of a solution can be compared before and after filtering the solution in order to remove any metal particles.[70] The filtrate and the filtered particles can be tested for catalytic activity; a high activity observed in the former is evidence for homogeneous catalysis, and a high activity in the latter is evidence for heterogeneous activity. This is by no means a definitive test; the size of the metal particles extracted depends on the size of the pores in the filter, and most are unable to remove nanoparticles.[24] Furthermore, this test does not account for continued generation of nanoclusters after filtration, thus heterogeneous catalysis cannot be ruled out.[71] Maitlis' filtration has been used extensively to identify leaching of soluble palladium(0) species from supported palladium catalysts. High catalytic activity of the filtrate highlights a catalytic role for such leached palladium species. This has been reported for many different palladium-catalysed reactions, such as Suzuki-Miyaura cross-coupling with palladium perovskites,[72] and Sonogashira cross-coupling with palladium nanoparticles supported on carbon and palladium zeolites.[73,74]

1.1.1.9 Collman's Test

The Collman group devised a method to distinguish homogeneous and heterogeneous catalysts using soluble and cross-linked unsaturated polymers with olefin moieties.[18] In theory, hydrogenation of such polymers will be much slower when using a heterogeneous catalyst with respect to a homogeneous catalyst due to the lack of mobility of the heterogeneous catalyst in the polymer region.[18] This was confirmed by comparing the yield of product and the turnover frequency of hydrogenation reactions with monomeric and polymeric unsaturated substrates. The supported heterogeneous catalysts exhibited much lower activity, and in some cases no activity, when hydrogenating the polymeric substrates with respect to the monomeric substrates whereas the homogeneous catalysts exhibited little difference in activity between monomeric or polymeric substrate hydrogenation.[18] As with Maitlis' test, Collman's test can be used to assess the catalytic

role of leached palladium species from supported catalysts, as leached species increase the rate of polymer hydrogenation.

1.2 Use of NMR to Detect Reaction Intermediates

As mentioned previously, NMR spectroscopy is inherently insensitive[75] and rarely used to detect unstable catalysts that are present in low concentration. NMR probes the nuclear spin states that are created on exposing spin-active nuclei to a homogeneous magnetic field. The magnetic spins of these nuclei align in different orientations with respect to the applied magnetic field (B_0), shown in Figure 13. Those that align with the applied field (α) are slightly more stable than those that align against the applied field (β).

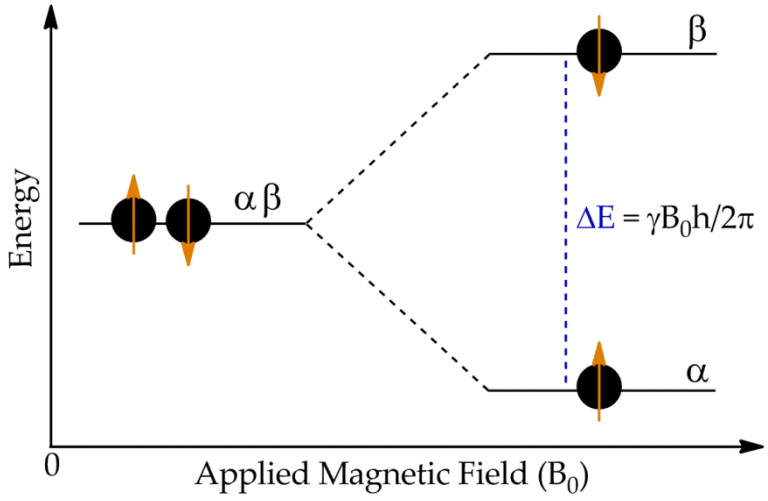

Figure 13: The two spin states – α and β – that are created on exposing a single spin-½ system to a homogeneous magnetic field. An increase in energy difference between the states with an increasing magnetic field strength (the Zeeman effect) is also shown.

The signals observed in NMR spectra are caused by transitions between the spin states, after excitation by a radio wave pulse. Transitions between states only occur when a population difference exists; transitions occur from more populated to less populated levels. Unfortunately, the energy difference between nuclear spin states,[76] given in Figure 13 where γ is the gyromagnetic ratio and h is Planck's constant (6.626×10^{-34} $m^2 Kgs^{-1}$), is very small. For example, proton spin states in a 500 MHz spectrometer have an energy difference of approximately 3.315×10^{-25} J, which equates to radio waves with a wavelength of 0.6 m. The population difference between nuclear spin states can be calculated using the Boltzmann equation,[76] given below, where N_α and N_β are the populations of the α or β

spin state respectively, k_B is the Boltzmann constant (1.381×10^{-23} JK^{-1}), and T is the temperature (K).

$$\frac{N_\alpha}{N_\beta} = exp^{\frac{\Delta E}{k_B T}}$$

When using a 500 MHz spectrometer, $\frac{N_\alpha}{N_\beta}$ is equal to 1.00008, therefore only approximately 1 in every 10^4 nuclear spins is observable. This inherent insensitivity can be improved through the use of stronger magnets but only to a point, beyond which there are physical limits on the field strength.[77] Alternatively, hyperpolarisation methods to increase NMR sensitivity have been reported. These approaches increase the population difference between nuclear spin states, known as polarisation, either using optical pumping, dynamic nuclear polarisation (DNP), or spin isomers.

1.2.1 Optical Pumping

Optical pumping is a technique in which light is used to excite electrons within a system, to produce a large electron spin polarisation. The electron spin polarisation is transferred, *via* spin exchange, to the nuclear spins of NMR-active nuclei of interest.[78] Typically, electron spin polarisation is generated in alkali metal vapours as there is only one valence electron, which simplifies the system.[79] Rubidium vapour is often used for this, as the energy of infrared light required for excitation (794.7 nm) can be provided using titanium sapphire lasers or high power diode lasers.[78]

Circularly polarised light with a spin of +1 is used to excite the electrons in the −1/2 $^2S_{1/2}$ electronic state to the +1/2 $^2P_{3/2}$ electronic state, shown in Figure 14, which then relax into either the −1/2 $^2S_{1/2}$ or the +1/2 $^2S_{1/2}$ electronic states. Any photons emitted in radiative decay are absorbed by a buffer gas (typically nitrogen). Only transitions in which $\Delta S = +1$ are allowed, therefore the electrons in the +1/2 $^2S_{1/2}$ electronic state cannot be excited. Continued excitation of only the −1/2 $^2S_{1/2}$ electronic state leads to a polarisation build-up into the +1/2 $^2S_{1/2}$ electronic state.

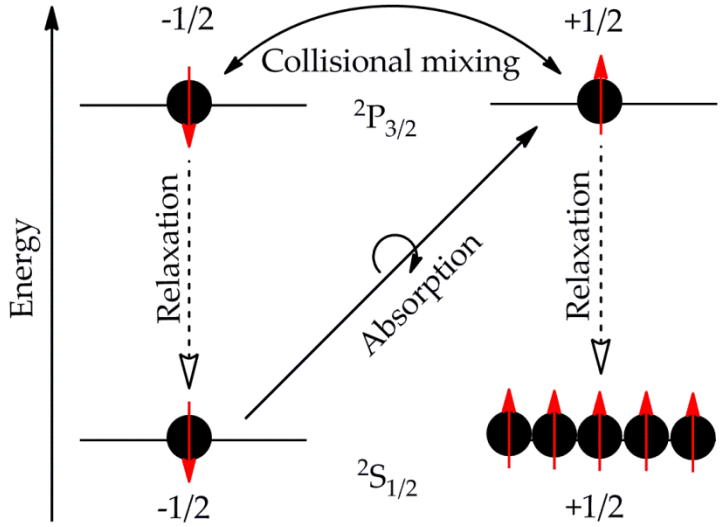

Figure 14: Creation of electronic spin polarisation in the +1/2 $^2S_{1/2}$ electronic state of rubidium atoms, using optical pumping.

Polarisation of the electronic spins can be transferred to the nuclear spins of noble gases. ^{3}He and ^{129}Xe are spin-1/2 nuclei and are typically used in conjunction with polarised rubidium for NMR studies.[80] Polarisation transfers to the noble gas nuclei *via* either binary collisions or the formation of van der Waal complexes. The mechanism of polarisation transfer is complex, and involves a spin-rotation interaction caused by the magnetic fields produced by the colliding nuclei, and an isotropic hyperfine interaction caused by the magnetic field of the noble gas nucleus.[80]

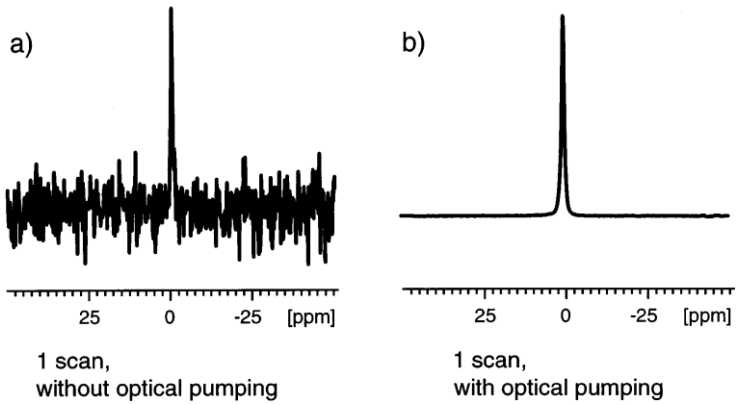

Figure 15: ^{129}Xe NMR spectra of xenon gas a) populated under Boltzmann conditions, and b) polarised via optical pumping. Reprinted from Pietrass, T. Colloids Surf. A. Physicochem. Eng. Asp. 1999, 158, 51 with permission from Elsevier.

The resulting polarised noble gas nuclei exhibit much larger NMR signals with respect to those populated under Boltzmann conditions. This is shown in Figure 15, where optical

pumping has enhanced the ^{129}Xe NMR signal by a factor of 5x10^4.[78] Such polarised noble gases can be used to probe surfaces or porous materials,[81,82] including *in vivo* lung imaging,[83] in conjunction with NMR or magnetic resonance imaging (MRI) spectroscopy.

1.2.2 DNP

As with optical pumping, DNP transfers polarisation from electron spins to nuclear spins. The gyromagnetic ratio of an electron is 660-fold larger than that of a proton (γ_e = 1.76x10^{11}, γ_p = 2.68x10^8).[84] This results in larger energy gaps between electron spin states (approximately 2.19x10^{-22} J at 500 MHz), which require microwave radiation, with a wavelength of approximately 1 mm, for excitation. There is therefore a much larger population difference between electron spin states, with respect to proton spin states, as shown in Figure 16. The theoretical maximum enhancement gained by transferring the Boltzmann spin polarisation from an electron to a proton is 660-fold.[85]

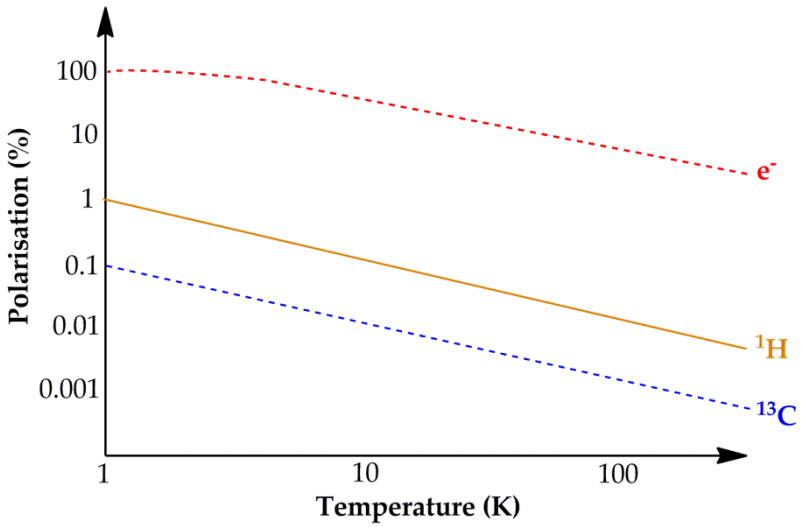

Figure 16: Comparison of the Boltzmann polarisation of an electron, ^{1}H and ^{13}C nucleus as a function of temperature at a magnetic field strength of 9.4 T (500 MHz).

DNP can be conducted on solids or liquids, however most liquids are cryogenically cooled to the solid phase prior to polarisation transfer, and then rapidly dissolved into hot steam before transportation into the NMR spectrometer.[86] To do this, the molecule of interest must be stable to cryogenic cooling (≤ 90 K) however this has been successfully applied to many biological systems including large membrane proteins.[87,88] A solvent mixture of deuterated glycerol, d_2-water, water, the molecule of interest, and a soluble biradical polarising agent, for example TOTAPOL shown in Figure 17, is typically used.[85]

This forms a glass matrix in which the biradical and molecule of interest are evenly distributed.

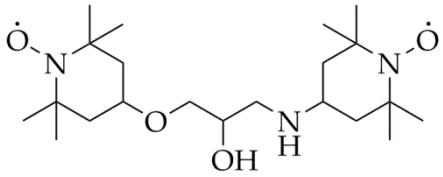

Figure 17: 1-(TEMPO-4-oxy)-3-(TEMPO-4-amino)propan-2-ol (TOTAPOL).

The nuclei and radicals strongly couple, leading to several mechanisms of polarisation transfer from the electron spins to the nuclear spins, on microwave irradiation. These include the solid effect, the cross effect,[89,90] and thermal mixing.[91] The cross effect dominates when using a biradical molecule, as the two radicals are positioned close to one another and couple with each other in addition to a nucleus, leading to the spin system given in Figure 18.[92] Microwave irradiation causes the electron paramagnetic resonance transitions shown in Figure 18, which leads to the NMR transitions shown in blue, resulting in hyperpolarisation of specific nuclear spin states.[93]

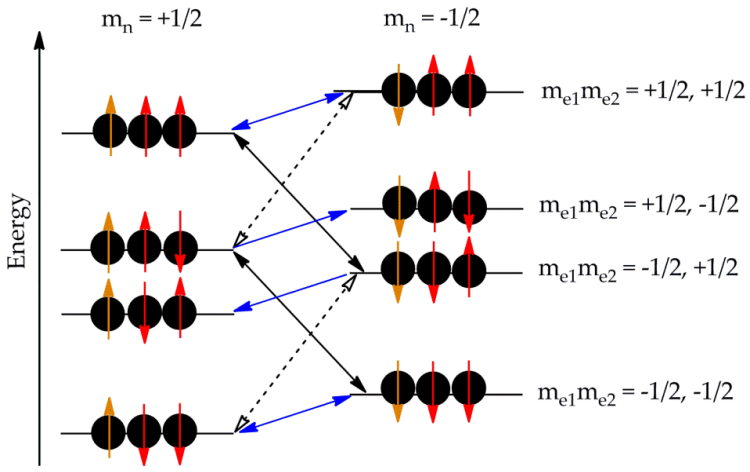

Figure 18: The cross effect mechanism of polarisation transfer from electron spins (m_{e1}/m_{e2}) to nuclear spins (m_n) on irradiation with microwaves. The electron paramagnetic resonance transitions that lead to positive enhancements are given by solid arrows, whereas those that lead to negative enhancements are given by dashed arrows. The NMR transitions are given by blue arrows.

The resulting NMR spectra are enhanced, as shown in Figure 19 for the aluminium environments in mesoporous alumina.[94] In this case, the enhancement value was reported to be 15-fold. This example shows the versatility of DNP – there are few restrictions on

which material can be probed, providing it contains NMR-active nuclei and is not damaged by cryogenic cooling.

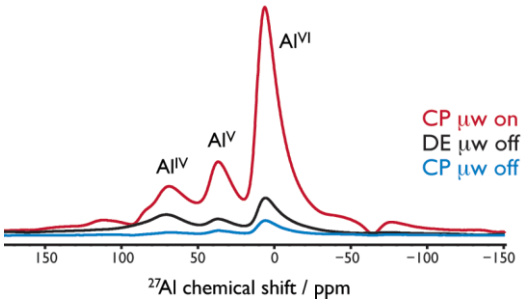

Figure 19: ^{27}Al NMR spectra of different aluminium environments in mesoporous alumina (red) enhanced using DNP with TOTAPOL, (black) without DNP but with magic angle spinning, and (blue) populated under Boltzmann conditions. Reprinted with permission from Lee, D.; Takahashi, H.; Thankamony, A. S. L.; Dacquin, J.-P.; Bardet, M.; Lafon, O.; De Paepe, G. J. Amer. Chem. Soc. 2012, 134, 18491 copyright 2016 American Chemical Society.

1.2.3 Spin Isomers of Hydrogen

A hydrogen molecule consists of two spin-1/2 protons that are covalently bonded *via* favourable bonding interactions between their electrons. When exposed to a homogeneous magnetic field, the two spin-1/2 system shown in Figure 20 is formed. There are four possible spin alignments with the applied field – these are $\alpha\alpha$, $(\alpha\beta+\beta\alpha)/\sqrt{2}$, $(\alpha\beta-\beta\alpha)/\sqrt{2}$, and $\beta\beta$. The $\alpha\alpha$, $(\alpha\beta+\beta\alpha)/\sqrt{2}$, and $\beta\beta$ alignments form a triplet state - this is *ortho*-H_2. The $(\alpha\beta-\beta\alpha)/\sqrt{2}$ alignment lies at a lower energy and forms a singlet state - this is *para*-H_2.[95]

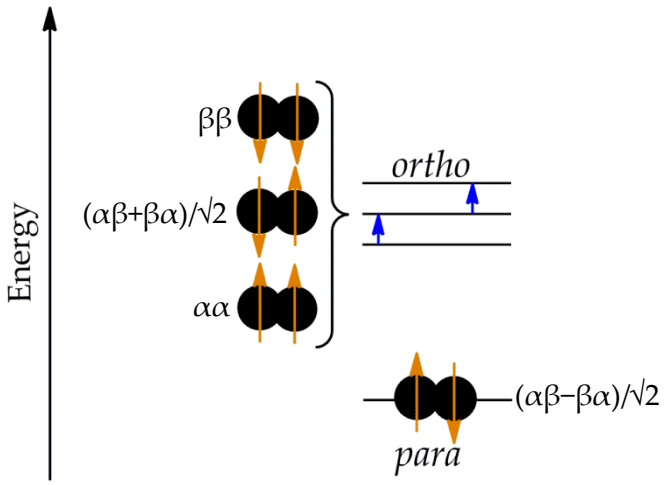

Figure 20: The four possible nuclear spin alignments of the nuclei in a molecule of hydrogen, in an applied homogeneous magnetic field. The spin-allowed NMR transitions are shown as blue arrows.

The ($\alpha\beta$+$\beta\alpha$)/√2 and ($\alpha\beta$-$\beta\alpha$)/√2 states are linear combinations of the antiphase spin alignments, $\alpha\beta$ and $\beta\alpha$ and their derivation is now discussed. In order to distinguish *para*-H_2 from *ortho*-H_2, the total spin angular momentum and the total spin in the z direction can be measured. As shown in Table 1, the total spin angular momentum quantum numbers (S) can be equal to 1 or 0. S = 1 consists of the total spin in the z direction (M_s) values 1, 0 and −1, whereas S = 0 can have only one M_s value of 0.[96]

Taking linear combinations of the individual wavefunctions produces the total wavefunction that gives rise to the measured M_s value. Combining the two spin-½ nuclei in a hydrogen molecule gives the linear combination below, where a^n is the Clebsh-Gordan coefficient.

$$M_s = a^1\alpha\alpha + a^2\alpha\beta + a^3\beta\alpha + a^4\beta\beta$$

In the case of symmetrical spin wavefunctions, S = 1, signs are retained on exchange of the nuclei. The linear combinations $\alpha\alpha$, $\beta\beta$, and ($\alpha\beta$+$\beta\alpha$)/√2, given in Table 1, retain their signs on exchange hence these are the symmetric combinations, which belong to the *ortho* spin isomer. The combination ($\alpha\beta$−$\beta\alpha$)/√2 does not retain its sign on exchange to ($\beta\alpha$−$\alpha\beta$)/√2 hence this is the antisymmetric combination, which belongs to the *para* spin isomer.[96] As S = 0, *para*-H_2 is undetectable in NMR spectroscopy, unless the symmetry of the molecule is broken. *Ortho*-H_2, however, possesses spin angular momentum and the transitions shown as blue arrows in Figure 20 give rise to an NMR signal.

Table 1: Total spin angular momentum (S), total spin in the z-direction (M_s), Clebsch-Gordan coefficients (a^n), and resulting spin wavefunctions (Ψ_s) of the spin states in dihydrogen

S	M_s	a^1	a^2	a^3	a^4	Ψ_s
1	+1	1	0	0	0	**$\alpha\alpha$**
1	0	0	+1/√2	+1/√2	0	**($\alpha\beta$+$\beta\alpha$)/√2**
1	−1	0	0	0	1	**$\beta\beta$**
0	0	0	+1/√2	−1/√2	0	**($\alpha\beta$−$\beta\alpha$)/√2**

1.2.3.1 Generating *Para*-H_2

As mentioned previously and shown in Figure 20, the singlet *para* state lies at a lower energy than the triplet *ortho* state. This is a consequence of the antisymmetric nature of fermionic wavefunctions; hydrogen is a fermionic particle. The total wavefunction (φ_{tot}) can be separated into independent contributions according to the Born-Oppenheimer equation shown below,[96] where φ_{el}, φ_{vib}, φ_{rot}, φ_{trs}, φ_{ns} are the electronic, vibrational, rotational, translational, and nuclear spin contributions, respectively.

$$\varphi_{tot} = \varphi_{el} \times \varphi_{vib} \times \varphi_{rot} \times \varphi_{trs} \times \varphi_{ns}$$

The φ_{el}, φ_{vib}, and φ_{trs} contributions are all symmetric. In *ortho*-H_2, φ_{ns} is symmetric, but is antisymmetric in *para*-H_2. As φ_{tot} must be antisymmetric, φ_{rot} must be antisymmetric in *ortho*-H_2 but symmetric in *para*-H_2. Consequently, the lowest rotational quantum numbers (J) allowed in *ortho*-H_2 and *para*-H_2 are 1 and 0, respectively, which are the lowest odd and even J numbers. *Para*-H_2 is therefore more stable than *ortho*-H_2 because the lowest rotational energy levels (J = 0) can be occupied.

At room temperature, in the absence of an applied magnetic field, hydrogen consists of 75% *ortho*-H_2 and 25% *para*-H_2. These populations are dependent on both the applied magnetic field[97] and the temperature. As *para*-H_2 is the most thermodynamically stable spin isomer, conversion from the *ortho* to the *para* state is promoted at lower temperatures, shown in Figure 21. The conversion process is spin forbidden, and is therefore a very slow process, particularly at the low temperatures at which conversion is favoured. The conversion is a result of the magnetic dipole moment of the nuclei in a hydrogen molecule interacting with the magnetic fields of the neighbouring nuclei.[98] This process can be accelerated with the addition of paramagnetic ions or molecules, which act as catalysts for the conversion. Iron oxide or charcoal are typically used for this purpose.[99] The paramagnetic species induce inhomogeneous magnetic fields at the *ortho*-H_2 molecules, which decouple the parallel spins and reduce the activation energy required to convert the spins.[100] At temperatures of 20 K, *para*-H_2 can be generated with a purity of ~ 99%.[101]

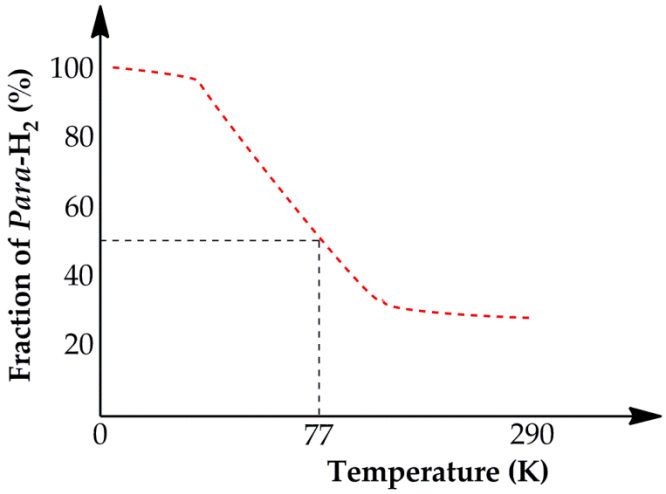

Figure 21: Temperature dependence of the percentage of para-H_2 present in hydrogen gas. Lowering the temperature to 77 K results in 50% para-H_2.

1.2.3.2 NMR Enhancements with *Para*-H_2

Para-H_2 had found use in hydrogenation mechanistic studies when used alongside gas chromatography (Tadros and Vaska)[102], or laser-Raman spectroscopy (Brown and Canning)[103]. The use of *para*-H_2 to increase NMR sensitivity, known as *para*-H_2 induced polarisation (PHIP), was theorised by Weitekamp in 1986,[104] although the effect had been observed prior to this by Eisenberg who had mistakenly attributed it to chemically induced DNP (another polarisation phenomenon).[105] Weitekamp's prediction was verified experimentally in 1987 *via* the *para*-hydrogenation of acrylonitrile to propionitrile, using Wilkinson's catalyst, [$RhCl(PPh_3)_3$].[106]

Para-H_2 is NMR silent as there is no spin angular momentum. To produce an NMR signal, the symmetry of the *para*-H_2 molecule must be broken, therefore it must be transferred to an unsaturated substrate as a pair and give a product which incorporates the hydrogen into two magnetically inequivalent environments.[107] This would suggest that unsymmetrical substrates are required, however, this is often not the case as the binding of symmetrical substrates to the catalyst often breaks the symmetry of the sites into which *para*-H_2 is incorporated. Furthermore, the natural abundance of the spin-1/2 carbon isotope, ^{13}C, is 1.1% and its presence in a small fraction of the substrate molecules results in the magnetic inequivalence of the two sites into which *para*-H_2 can be added, regardless of the symmetry of the substrate.[108]

Simple reaction models to explain the theory behind PHIP and the resulting NMR enhancements are *para*-hydrogenation reactions of unsaturated substrates or metal complexes containing NMR-inactive functional groups. The *para*-hydrogenation of functionalised acrylonitrile to functionalised propionitrile is used as an example, shown in Figure 22, where the R groups are NMR-inactive.[106]

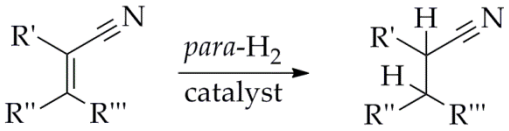

Figure 22: Para-hydrogenation of acrylonitrile, functionalised with NMR-inactive groups, to form propionitrile containing two para-H_2-derived protons.

When this reaction is carried out using normal hydrogen, the spin states, given in Figure 23, are populated under Boltzmann conditions, leading to the transitions shown. Given that in this model the R groups are all inequivalent, the H_2-derived protons in propionitrile are chemically inequivalent. The $\alpha\beta$ and $\beta\alpha$ levels therefore lie at different energies, leading to the four transitions shown in Figure 23, where transitions 1 and 2, and 3 and 4, are of similar energies. The corresponding ^{1}H NMR spectrum is also shown in Figure 23, and contains two doublets.

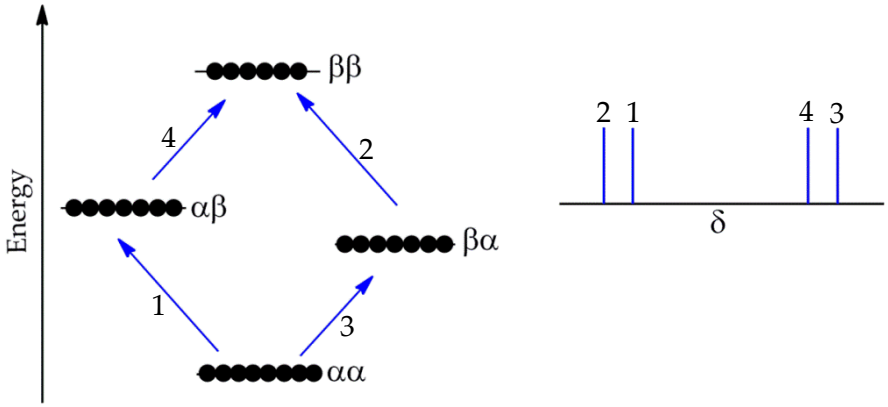

Figure 23: (Left) the four possible nuclear spin alignments of the H_2-derived nuclei in functionalised propionitrile within a homogeneous high magnetic field. The spin-allowed NMR transitions are shown as blue arrows. (Right) the corresponding ^{1}H NMR spectrum.[96]

On replacing normal hydrogen with *para*-H_2, the polarisation from the transferred protons will have the same nuclear spin populations as the *para*-H_2, if *para*-H_2 transfer is fast relative to the relaxation of the protons.[104] Two different phenomena may be observed. *Para*-hydrogenation of the alkene inside the NMR spectrometer is known as

'*para*-H_2 and synthesis allow dramatically enhanced nuclear alignment' (PASADENA).[106] In this case, both the $\alpha\beta$ and $\beta\alpha$ spin states are populated, shown in Figure 24. Theoretically, in the absence of relaxation resulting from molecular tumbling, only the $\alpha\beta$ and $\beta\alpha$ levels are populated and the population difference is far greater than that of the Boltzmann distribution, resulting in large NMR enhancements. The corresponding ^{1}H NMR spectrum is also shown in Figure 24 and contains two antiphase doublets. Transitions 1 and 3 give rise to NMR signals in the opposite phase to transitions 2 and 4 due to their emissive, rather than absorptive, nature. Such antiphase signals are characteristic of PASADENA.

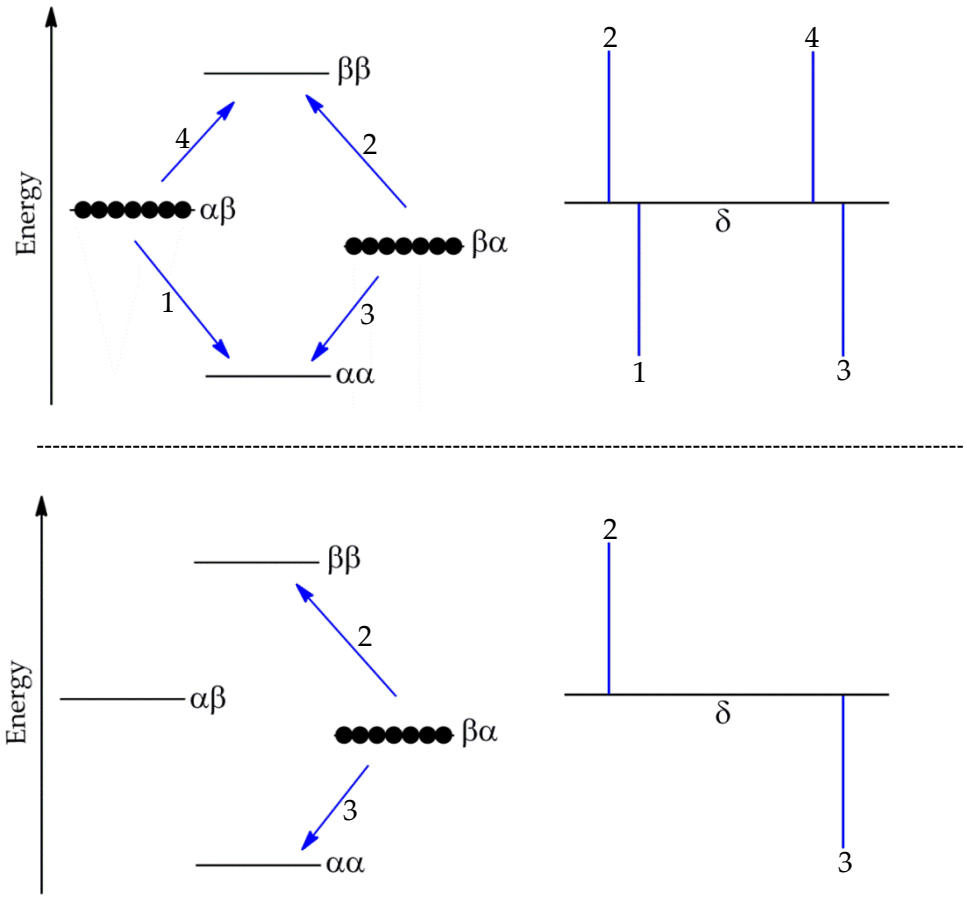

Figure 24: (Above) selective polarisation of the αβ and βα spin states due to PASADENA and the ^{1}H NMR spectrum of the para-H_2-derived nuclei in functionalised propionitrile displaying PASADENA enhancements. (Below) selective polarisation of the βα spin state due to ALTADENA and the ^{1}H NMR spectrum of the para-H_2-derived nuclei in functionalised propionitrile displaying ALTADENA enhancements.

Alternatively, *para*-hydrogenation of the alkene outside of the NMR spectrometer, followed by transfer and detection inside the NMR spectrometer is known as 'adiabatic longitudinal transport after dissociation engenders nuclear alignment' (ALTADENA). In

this case, only the $\beta\alpha$ spin state is populated, shown in Figure 24, resulting in large NMR enhancements of the signals corresponding to transitions 2 and 3. The corresponding ^{1}H NMR spectrum is also shown in Figure 24 and contains two singlets in opposite phases. Again, transition 3 is emissive in nature whereas transition 2 is absorptive. The observation of ALTADENA, rather than PASADENA enhancements is consistent with a faster rate of hydrogenation and a more reactive hydrogenation catalyst.[109]

PASADENA-enhanced ^{1}H NMR spectra of propionitrile, published by Weitekamp in 1987, are compared with spectra collected under Boltzmann conditions in Figure 25. In this case, the spin system is further complicated by coupling between the *para*-H_2-derived protons and the spin-1/2 protons from acrylonitrile however the characteristic antiphase splitting of the ^{1}H NMR signals is unmistakable. Enhancement factors of up to 200-fold were reported.[106]

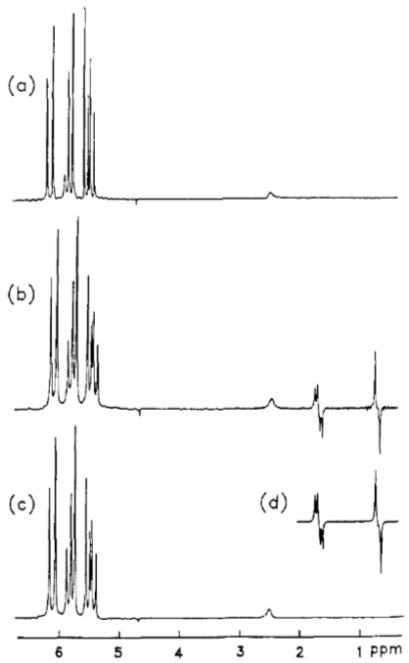

Figure 25: ^{1}H NMR spectra of (a) acrylonitrile signals prior to para-hydrogenation, (b) PASADENA-enhanced signals corresponding to the para-H_2-derived protons in propionitrile, collected immediately after addition of para-H_2, (c) acrylonitrile signals collected after relaxation of PASADENA signals, (d) simulated PASADENA-enhanced signals corresponding to the para-H_2-derived protons in propionitrile. Reprinted with permission from Bowers, C. R.; Weitekamp, D. P. J. Amer. Chem. Soc. 1987, 109, 5541 copyright 2016 American Chemical Society.

The same hydrogenation reaction has also been reported by Bargon in 1990, in which PASADENA-type enhancements of propionitrile were compared using both *para*-enriched

and *ortho*-enriched hydrogen.[110] *Ortho*-H_2 also selectively populates specific spin states, as shown in Figure 26, which leads to population differences that exceed Boltzmann conditions and result in NMR enhancements. As *ortho*-H_2 exists in the three states $\alpha\alpha$, $\beta\beta$, and $(\alpha\beta+\beta\alpha)/\sqrt{2}$, the theoretical maximum NMR enhancements gained using *ortho*-H_2 are 1/3 those gained using *para*-H_2. Furthermore, the enhanced signals from *ortho*-H_2 induced polarisation (OHIP) exhibit the opposite phasing to PHIP signals as the transitions lie in the opposite direction – absorptive PHIP signals are emissive OHIP signals. This theory was supported by the reported OHIP-enhanced NMR signals of propionitrile.[110]

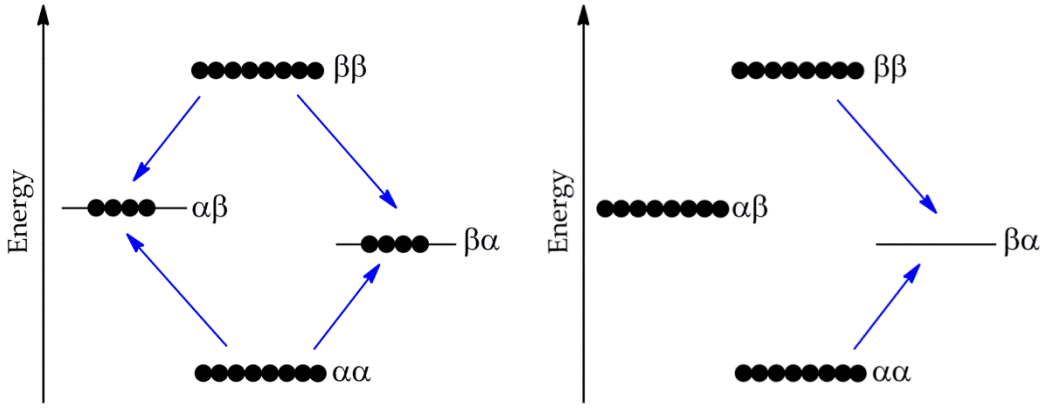

Figure 26: (Left) selective polarisation of the αα, ββ,and half αβ, and βα spin states when using ortho-H_2 to hydrogenate inside the spectrometer in an analogous method to PASADENA. (Right) selective polarisation of the αα, ββ,and αβ spin states when using ortho-H_2 to hydrogenate outside the spectrometer in an analogous method to ALTADENA.

PHIP enhancements are not restricted to ^{1}H nuclei - transfer of PHIP from ^{1}H to hetero-nuclei using 'insensitive nuclei enhanced by polarisation transfer' (INEPT) radio pulse sequences has been reported for ^{13}C, ^{15}N, ^{31}P, ^{195}Pt, ^{103}Rh, and ^{29}Si.[111-113] Polarisation transfer to these hetero-nuclei is particularly useful because of their very low natural abundances. Where it would previously have taken thousands of NMR scans to produce a clear spectrum, it now takes a few hundred, and the expense of enriching the substrate with the desired isotope is no longer present.

1.2.3.3 Elucidating Hydrogenation Mechanisms using PHIP

PHIP has been used to investigate the mechanism of hydrogen transfer in hydrogenation reactions. The observation of PHIP-enhanced NMR signals that correspond to hydrogenated products indicates that hydrogen must add in a pairwise manner. This has been applied to investigations of the $[RuHCl(PPh_3)_3]$ hydrogenation pre-catalyst, which was previously believed to transfer hydrogen atoms from two different hydrogen molecules.[109] *Para*-hydrogenation of d_8-styrene in d_1-chloroform, using this pre-catalyst produces weak PHIP signals, indicating that some of the hydrogen is transferred as a pair to the substrate *via* the $[RuH_2(PPh_3)_3]$ complex.

The reversibility of the oxidative addition of hydrogen to several rhodium hydrogenation pre-catalysts, during the *para*-hydrogenation of phenylacetylene, has also been investigated using PHIP.[114] Both reversible and irreversible hydrogen addition produce PHIP-enhanced ^1H NMR signals, however, reversible hydrogen addition competes with substrate hydrogenation, leading to reductive elimination and relaxation of *para*-H_2 to normal H_2. Reversible hydrogen addition, observed for $[RhCl(PPh_3)_3]$, therefore leads to weaker PHIP NMR enhancements which quickly disappear (within approximately 10 minutes) and do not re-appear on shaking the sample to refresh the *para*-H_2 in solution. Irreversible hydrogen addition, observed for $[Rh(COD)(dppe)]^+$ where dppe is 1,2-bis(diphenylphosphino)ethane, produces stronger PHIP NMR enhancements which decay over a much longer time period (approximately 110 minutes with sample shaking). These observations were supported by previously reported research conducted by Brown and Canning, in which the same complexes were used to hydrogenate cyclohexene with non-equilibrium amounts of *ortho* and *para*-H_2 and the return to equilibrium was measured using laser-Raman Spectroscopy.[103] For these studies, using PHIP NMR spectroscopy rather than Raman spectroscopy is beneficial as the signals are easier to observe and give direct information about the hydrogenation product.

The NMR signal enhancements that result from PHIP have led to the discovery of low-concentration reaction intermediates that are otherwise unobservable under Boltzmann conditions. This has been applied to homogeneous and heterogeneous palladium-catalysed hydrogenation reactions, and several key palladium reaction intermediates have been characterised. Many phosphine-stabilised palladium bis-triflate

pre-catalysts have been reported to *para*-hydrogenate diphenylacetylene and produce PHIP-enhanced intermediates and products. The palladium alkyl species shown in Figure 27 are typically observed by their characteristic PASADENA-enhanced ^{1}H NMR resonances that lie in the range δ 2 to 5.[115] Observation of these species supports a cationic catalytic pathway in which palladium shuttles between the II and IV oxidation states.[116]

Several palladium hydride species have also been reported, and were observed by their diagnostic PASADENA-enhanced hydride NMR signals.[117] These are shown in Figure 28 and include a hydride-bridged di-palladium complex. This suggests a role for both mono-palladium and multi-palladium complexes during hydrogenation reactions and is evidence for heterogeneous catalysis.

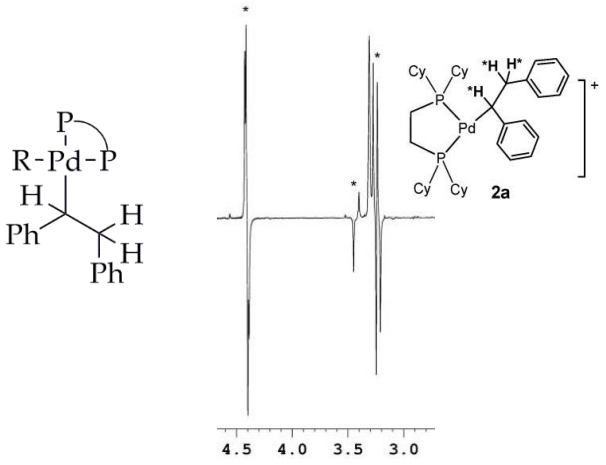

Figure 27: Palladium alkyl intermediate species commonly observed on para-hydrogenating diphenylacetylene with phosphine-stabilised palladium bis-triflate pre-catalysts. R can be triflate, or a π-interaction from the phenyl ring of the bound substrate which leads to a positively charged palladium complex. The ^{1}H NMR spectrum shows the PASADENA signals of complex 2a, reproduced from Lopez-Serrano, J.; Duckett, S. B.; Dunne, J. P.; Godard, C.; Whitwood, A. C. Dalton Trans. 2008, 4270 with permission of the Royal Society of Chemistry.

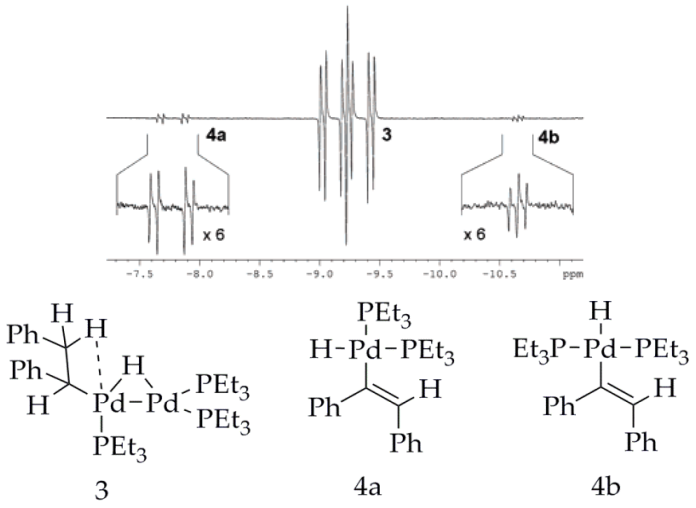

Figure 28: Palladium hydride intermediates detected from their diagnostic antiphase hydride NMR signals, also shown, during the para-hydrogenation of phenylacetylene with $[Pd(OTf)_2(PEt_3)_2]$. Reprinted with permission from Lopez-Serrano, J.; Duckett, S. B.; Lledos, A. J. Amer. Chem. Soc. 2006, 128, 9596 copyright 2016 American Chemical Society.

1.2.3.4 PHIP using Heterogeneous Catalysts

As discussed previously, PHIP is observed if two *para*-H_2 nuclei are transferred pairwise to a reactant, thus retaining their spin correlation, and if the symmetry between the two *para*-H_2 nuclei is broken *via* chemical or magnetic inequivalence.[107] The Horiuti-Polanyi mechanism of hydrogenation at the surface of a heterogeneous metal catalyst[118] is given in Figure 29 for the hydrogenation of ethene. Initially, hydrogen binds to the surface of the metal *via* dissociative chemisorption, which is likely to randomise the hydrogen nuclei.[119] Furthermore, there are two competing pathways, shown in Figure 29, on the route to producing ethane. Hydrogen migration leads to hydrogenation and the formation of the desired product, whereas 'hydrogen scrambling' leads to reformation of the olefin, now with one hydrogen nucleus replaced with another. Dissociative chemisorption of hydrogen followed by 'hydrogen scrambling' is likely to destroy spin correlations and quench *para*-H_2, thus in theory heterogeneous catalysts ought to be unsuitable for PHIP.

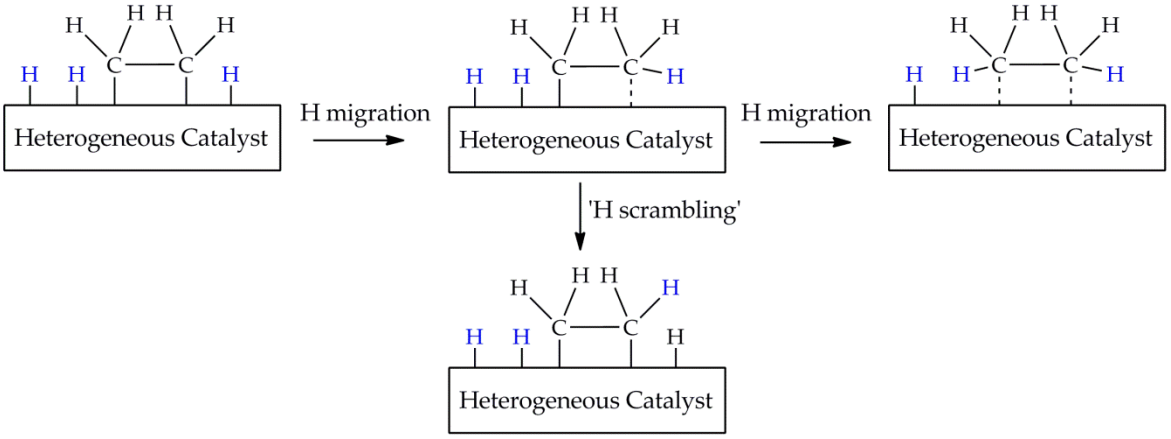

Figure 29: Horiuti-Polanyi mechanism of the hydrogenation of a simple alkene (ethene) at the surface of a heterogeneous catalyst.

A successful heterogeneous PHIP catalyst must hydrogenate predominantly *via* a pairwise transfer of two *para*-H_2 nuclei. The simplest design is therefore an immobilised homogeneous PHIP catalyst, and such catalysts have been reported to be successful.[120,121] Koptyug *et. al.* reported the first heterogeneous PHIP catalyst in 2007,[121] which consisted of Wilkinson's catalyst immobilised on modified silica gel (shown in Figure 30) or polymer beads. These heterogeneous catalysts were used to *para*-hydrogenate styrene in the liquid phase and propylene in the gas phase and generated both PASADENA and ALTADENA ^{1}H NMR signals corresponding to polarised ethylbenzene and propane. Although leaching of the catalyst was observed in the liquid phase, a Maitlis' test confirmed that homogeneous catalysis produced negligible polarisation and heterogeneous catalysis dominated.

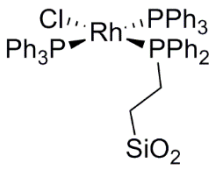

Figure 30: Wilkinson's catalyst immobilised on modified silica gel.

Although the Horiuti-Polanyi mechanism suggests that *para*-hydrogenation at a metal surface is unsuitable for PHIP, several unsaturated substrates have been successfully polarised *via* PHIP using different heterogeneous palladium systems, including nanoparticles and supported catalysts.[122-126] Therefore, with certain heterogeneous palladium catalysts, a pairwise addition of *para*-H_2 to a reactant occurs, and is in competition with the non-pairwise Horiuti-Polanyi mechanism. To promote pairwise

para-H_2 addition, small palladium nanoparticles can be stabilised with capping ligands,[127] for example glutathione (GSH),[128,129] which restrict hydrogen diffusion at the palladium surface, shown in Figure 31, thus spin correlations are retained and pairwise hydrogen addition is more likely.

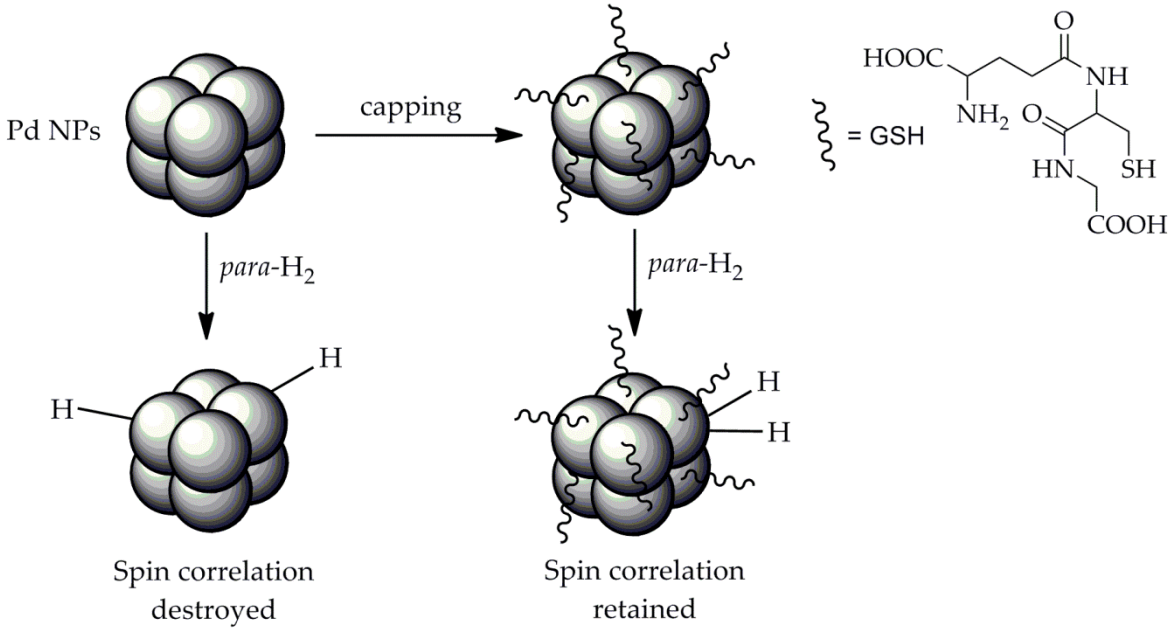

Figure 31: Capping palladium nanoparticles to promote pairwise para-H_2 addition.

The Duckett group have investigated the effect of nanoparticle size on the intensity of the PHIP signals generated on *para*-hydrogenation of methyl propiolate to methyl acrylate shown in Figure 32.[124] In theory, pairwise *para*-H_2 addition should be promoted when using smaller nanoparticles, as reaction sites are more localised,[126] however, the Duckett group found no clear link between nanoparticle size and PHIP intensity. It was concluded that the nature of the metal, nanoparticle dispersion and the nature of the support all influenced the activity of the catalyst and the mechanism of hydrogen addition.

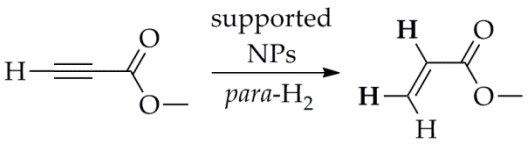

Figure 32: Para-hydrogenation of methyl propiolate to methyl acrylate using supported nanoparticles.[124]

Koptyug's group have investigated the influence of the palladium catalyst support on the mechanism of hydrogen addition to propyne and propene.[125] Interestingly, they found that the palladium support influenced the involvement of a pairwise mechanism; a

titanium dioxide support allowed pairwise *para*-H_2 addition to propene, whereas all other tested supports only allowed non-pairwise addition to propene. The Koptyug group recently reported the successful polarisation of 1-butene, 2-butene, and butane *via para*-hydrogenation of butyne using bulk palladium oxide.[119] PHIP was only observed when using Pd(II) rather than Pd(0); palladium black did not generate any hyperpolarised signals. The involvement of a pairwise hydrogenation mechanism at the surface of bulk palladium oxide is surprising, as one would expect a non-pairwise mechanism to dominate. The authors suggest that there may be reduced hydrogen mobility at the catalyst surface due to strong interactions with the palladium.[119]

Hyperpolarising molecules using heterogeneous, rather than homogeneous catalysts, gives rise to potential biomedical applications. This is due to the ease of catalyst removal which is necessary for *in vivo* studies as a result of the toxicity of such catalysts. Hyperpolarised biologically-compatible molecules, such as ethanol or non-toxic gases, have the potential to be used as sensitive contrast agents in MRI, and have been generated using heterogeneous catalysts.[130-132] In order to be medically useful, polarised contrast agents must transport to the area of interest in the patient prior to detection. This requires polarisation to last several minutes which is possible through the generation of long-lived states.

1.2.3.5 Long-lived States

The use of PHIP to generate hyperpolarised contrast agents for MRI is hindered by short hyperpolarisation lifetimes, which are the result of fast longitudinal relaxation, or small T_1 values associated with the *para*-H_2-derived protons. Such relaxation is caused by several mechanisms, the prevalent being magnetic dipole-dipole interactions between the nuclei of interest and the surrounding spin-active nuclei.[133] This can be reduced through the replacement of the non-*para*-H_2-derived protons with deuterons, and there are several reports of this method being used to successfully lengthen T_1 values.[134,135] The Koptyug group applied this method to produce hyperpolarised d_6-propane *via para*-hydrogenation of d_6-propene using a heterogeneous Rh/TiO_2 solid catalyst, shown in Figure 33.[136] The T_1 values of the *para*-H_2-derived protons increased very little; deuteration proved to have little benefit in prolonging hyperpolarisation in propane. In contrast, accessing long-lived singlet states proved beneficial with an increase in T_{eff} to 6 s.

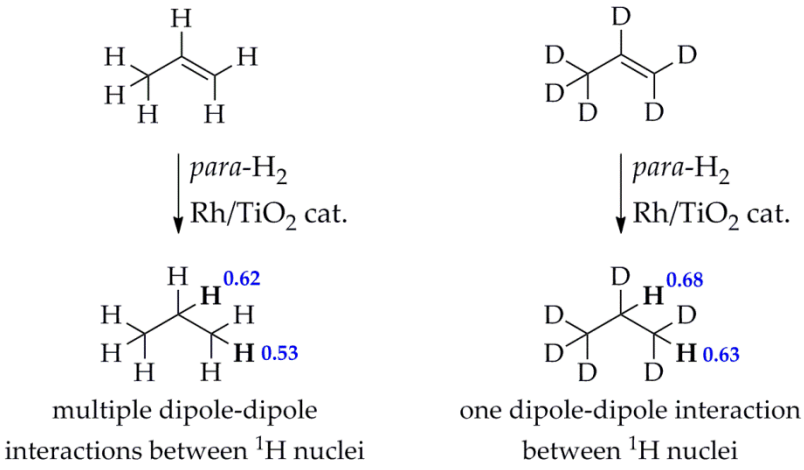

Figure 33: Comparison of the T_1 values (blue) of the para-H_2-derived protons in propane (left) and d_6-propane (right).[136]

Much of the current research into hyperpolarisation focuses on the polarisation of long-lived nuclear spin states, in which polarisation can be stored and 'released' on demand.[137,138] This is achieved through the polarisation of singlet spin states. *Para*-H_2 is an example of such a singlet state, and in the absence of a spin-conversion catalyst it can be stable for several weeks.[137] Singlet states, like those of *para*-H_2, are symmetric and are unperturbed by symmetric relaxation mechanisms, for example intramolecular dipole-dipole relaxation.[139] As a result, the lifetimes of singlet spin states can far exceed the T_1 values of the nuclei. As mentioned when describing *para*-H_2, singlet states have no spin angular momentum and are thus NMR silent. An NMR signal from a polarised singlet state can only be achieved by breaking the symmetry of the singlet state through chemical and/or magnetic inequivalence, causing singlet-triplet mixing.[140]

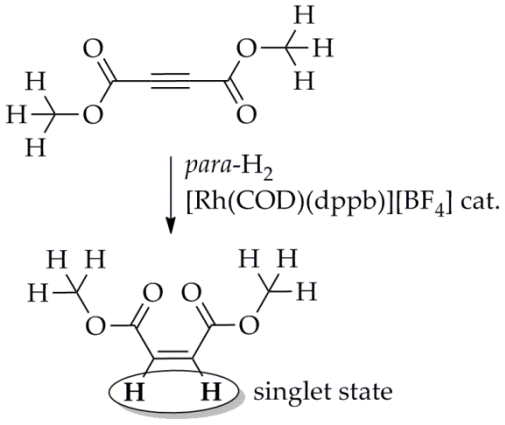

Figure 34: Generation of a hyperpolarised singlet state on dimethyl maleate via para-hydrogenation of dimethyl acetylenedicarboxylate using a Rh catalyst,[141] where dppb is 1,4-Bis-(diphenylphosphino)butane.

In order to form a true singlet state, a molecule must contain a pair of spin-½ nuclei which are positioned away from other nuclear spins to prevent relaxation, and the two nuclei must be magnetically inequivalent so that, at specific applied magnetic fields, the spin state can be probed.[142] Dimethyl maleate is an example of this, generated *via para*-hydrogenation of dimethyl acetylenedicarboxylate, shown in Figure 34.[141] The vinylic protons are magnetically inequivalent due to weak $^{5}J_{HH}$ and $^{6}J_{HH}$ couplings to the methyl protons, and this allows singlet-triplet mixing at specific applied magnetic fields.

Singlet states are populated *via* polarisation transfer, after which polarisation storage and 'release' is typically achieved by simply shuttling the sample between low and high magnetic fields, respectively.[133] It is also possible to store polarisation at high magnetic fields, using a 'spin locking' pulse sequence, in which a radiofrequency is applied to prevent singlet-triplet mixing.[138] The singlet state on dimethyl maleate was investigated by the Spiess group, and a ^{1}H singlet state relaxation time (T_s) of 4 minutes was reported, which is far longer than the T_1 value of just 15 s.[141] This hyperpolarised singlet state was also probed using MRI and several hyperpolarised images were successfully obtained 3 minutes after initial *para*-hydrogenation.[143] The storage of hyperpolarisation through the formation of singlet states is a promising advancement towards the use of PHIP to generate contrast agents for MRI. Long-lived singlet states on heteronuclei, such as ^{13}C, have also been reported,[144] however, accessing long-lived states on ^{1}H nuclei can negate the need for isotopic labelling and reduce costs.

1.2.3.6 Non-hydrogenative PHIP

Signal amplification by reversible exchange (SABRE) is a non-hydrogenative technique which is used to transfer polarisation from *para*-H_2 to a molecule of interest without chemically altering the molecule.[145] This requires a magnetisation transfer catalyst, which is typically an octahedral iridium complex, to which both the molecule of interest and *para*-H_2 are able to reversibly bind. Once bound, the symmetry of the *para*-H_2-derived hydrides is broken by chemical and/or magnetic inequivalence and polarisation transfers from the *para*-H_2 to the substrate at low magnetic fields *via* long-range *J*-coupling.[146] A simplified overview of this is shown in Figure 35.

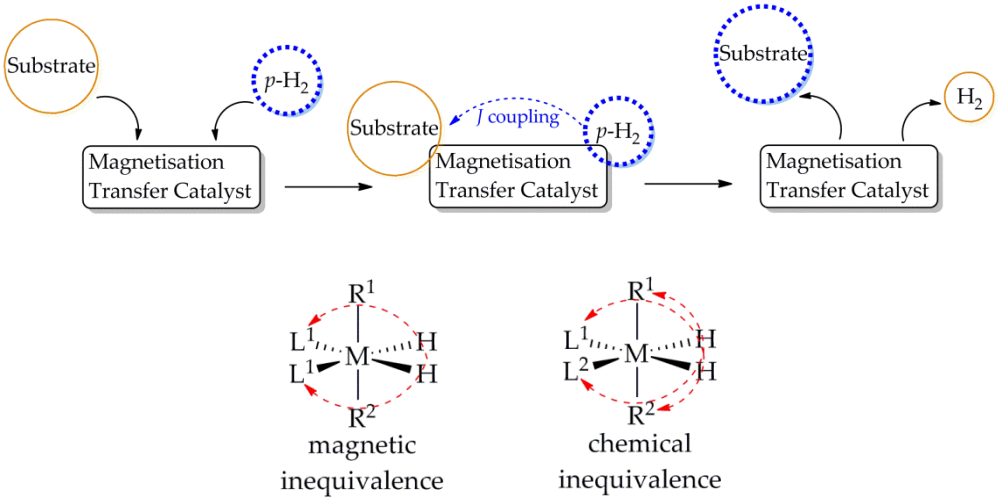

Figure 35: (Above) Schematic showing polarisation (blue) transfer from para-H_2 to a substrate of interest as a result of the SABRE process. (Below) Extent of polarisation transfer across a metal exchange catalyst as a result of magnetic or chemical inequivalence.[147]

When the *para*-H_2-derived hydrides are magnetically inequivalent, polarisation transfers only to the ligands positioned *trans* to them (L^1 in Figure 35), as these molecules exhibit different *J*-couplings to each hydride. The ligands positioned *cis* to the *para*-H_2-derived hydrides (R^1 and R^2) do not receive any polarisation, as they couple to each hydride ligand equally. In contrast, when the *para*-H_2-derived hydrides are chemically inequivalent, polarisation transfers to the ligands positioned both *trans* and *cis* to them (L^1, L^2, R^1 and R^2) as all ligands exhibit different *J*-couplings to each hydride.[147] If an excess of substrate and *para*-H_2 is used, polarisation of the substrate nuclei builds-up over time due to exchange, leading to large NMR signal enhancements.

The SABRE method was discovered by the Duckett group in 2009. Initially, magnetisation transfer complexes based on Crabtree's system, $[Ir(COD)(L)_2]BF_4$,[148] and $[Ir(COD)(L)(MeCN)]BF_4$,[75] where COD is 1,5-cyclooctadiene and L is a phosphine ligand, were used to transfer polarisation from *para*-H_2 to *N*-heterocycles. The SABRE-active complexes, $[Ir(H)_2(L)_2(sub)_2]BF_4$,[148] shown in Figure 36, and/or $[Ir(H)_2(L)(sub)_3]BF_4$,[75] where sub is an appropriate *N*-heterocycle for example pyridine, form on addition of excess hydrogen and substrate. The originally bound COD is hydrogenated to form cyclooctane (COA) which can no longer ligate to the iridium.

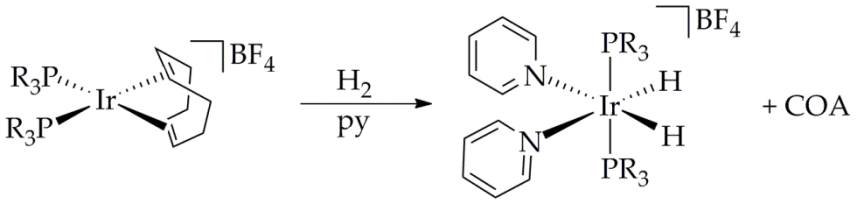

Figure 36: The formation of the active SABRE complex $[Ir(H)_2(PR_3)_2(py)_2]BF_4$ from $[Ir(COD)(PR_3)_2]BF_4$ on addition of hydrogen and excess pyridine (py).

The system was later improved by incorporating bulky N-heterocyclic carbenes (NHCs) into the iridium complexes, which increases the lability of the hydrides and substrates, and reduces the lifetime of the active iridium catalyst that forms.[149] This allows more polarised substrate to build-up in solution over a shorter time period. Typically, [IrCl(COD)(IMes)] is used, where IMes is 1,3-bis(2,4,6-trimethylphenyl)-imidazol-2-ylidene, which forms the SABRE-active $[Ir(H)_2(IMes)(sub)_3]Cl$ complex on addition of excess hydrogen and substrate. This is shown in Figure 37, using pyridine as the example substrate. A comparison of the ^1H NMR signals corresponding to the protons on free pyridine collected under Boltzmann conditions (blue) and the SABRE-enhanced signals (orange) is also shown in Figure 37. There is a clear increase in NMR signal intensity after applying the SABRE technique, with 5500-fold NMR enhancements reported for this system.[150]

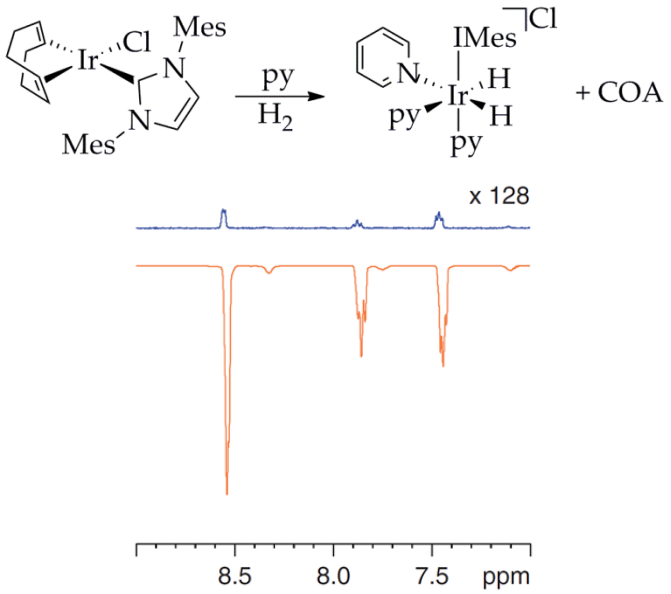

Figure 37: Activation of [IrCl(COD)(IMes)] with an excess of pyridine and hydrogen to form the SABRE-active $[Ir(H)_2(IMes)(py)_3]Cl$ complex (above), and the corresponding ^1H SABRE NMR enhancements of the protons in free pyridine (below) in d_4-methanol. The blue spectrum was collected under Boltzmann conditions and has been magnified 128-fold for clarity. The orange spectrum was collected after introducing para-H_2 into the NMR sample and shaking at low field prior to NMR acquisition. From Adams, R. W.; Aguilar, J. A.; Atkinson, K. D.; Cowley, M. J.; Elliott, P. I. P.; Duckett, S. B.; Green, G. G. R.; Khazal, I. G.; Lopez-Serrano, J.; Williamson, D. C. Science 2009, 323, 1708 with permission from AAAS.

The mechanism of pyridine and hydrogen exchange at iridium, that gives rise to SABRE, has been investigated using a combination of experiment and density functional theory (DFT).[149] It was observed, using exchange spectroscopy (EXSY) NMR measurements, that the pyridine ligand positioned *trans* to the *N*-heterocyclic carbene did not exchange on the NMR timescale, whereas those positioned *trans* to the hydride ligands were observed to exchange. Pyridine exchange was found to be unaffected by a change in pyridine concentration and is therefore dissociative, thus the first step in the exchange mechanism is the loss of a pyridine ligand positioned *trans* to a hydride to form $[Ir(H)_2(IMes)(py)_2]Cl$. This is shown as I_5 in Figure 38.

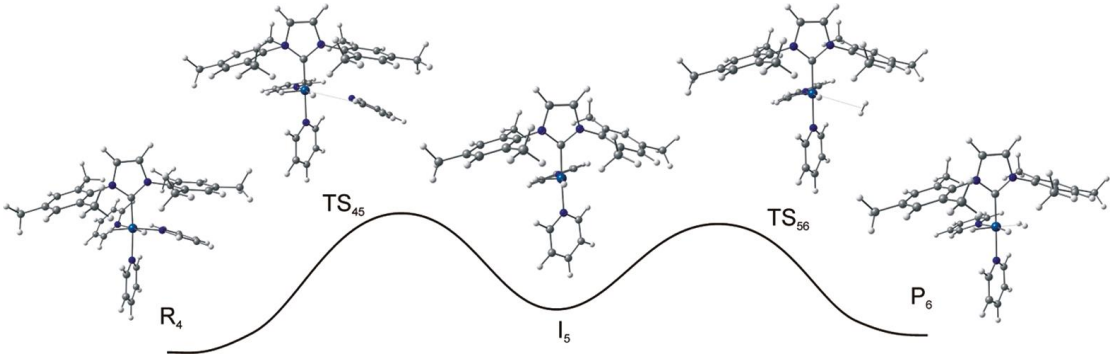

Figure 38: Computed structures and free-energy diagram for pyridine and H_2 exchange in $[Ir(H)_2(IMes)(py)_3]Cl$. Reprinted with permission from Cowley, M. J.; Adams, R. W.; Atkinson, K. D.; Cockett, M. C. R.; Duckett, S. B.; Green, G. G. R.; Lohman, J. A. B.; Kerssebaum, R.; Kilgour, D.; Mewis, R. E. J. Amer. Chem. Soc. 2011, 133, 6134 copyright 2016 American Chemical Society.

Subsequently, a second hydrogen molecule binds to the iridium to form $[Ir(H)_2(\eta^2\text{-}H_2)(IMes)(py)_2]Cl$, shown as P_6 in Figure 38. The first hydrogen molecule can then dissociate and another pyridine molecule can take its place, reforming $[Ir(H)_2(IMes)(py)_3]Cl$ and allowing polarisation to build-up onto free pyridine. Hydrogen exchange rates were observed to increase with hydrogen concentration and decrease with pyridine concentration, which supports the proposed mechanism.[149]

Although an η^2-coordinated dihydrogen iridium intermediate has not been observed by NMR, it is likely to be short-lived and therefore present in very low concentrations. The observed SABRE enhancements of the pyridine resonances provide proof of this; the T_1 values of η^2-coordinated H_2 molecules are typically just tens of milliseconds, rather than classical hydrides which are typically on the second timescale.[151,152] Such fast relaxation of η^2-coordinated H_2 molecules could lead to the relaxation of *para*-H_2 to normal-H_2, resulting in very little signal enhancement if the species were long-lived. This is exemplified by the reported quenching of *para*-H_2 by the long-lived $[(C_5H_3N(CH_2P(^tBu)_2)_2)Ir(H_2)(H)_2]BF_4$ complex shown in Figure 39, which lies in equilibrium with the SABRE-active $[(C_5H_3N(CH_2P(^tBu)_2)_2)Ir(H)_2(py)]BF_4$ complex.[152]

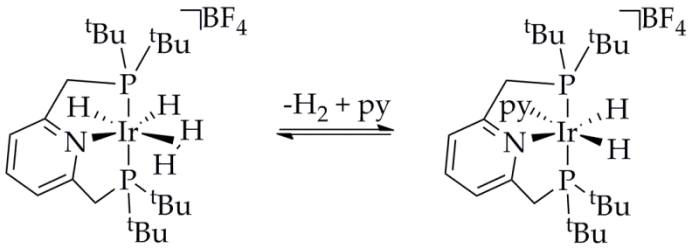

Figure 39: $[(C_5H_3N(CH_2P(^tBu)_2)_2)Ir(H_2)(H)_2]BF_4$ (left) in equilibrium with $[(C_5H_3N(CH_2P(^tBu)_2)_2)Ir(H)_2(py)]BF_4$ (right).

In addition to ^{1}H nuclei, polarisation has been reported to transfer *via* SABRE from *para*-H_2 to hetero-nuclei, including ^{13}C, ^{19}F, ^{15}N, and ^{31}P.[73,153-156] Typically, efficient polarisation transfer to ^{1}H nuclei occurs at low magnetic field, in the range of 50-70 G.[149] At low magnetic fields, chemical shift differences between the *para*-H_2-derived hydrides and substrate protons are smaller due to the Zeeman effect. Optimum polarisation transfer occurs at the magnetic field strength at which the chemical shift differences between the *para*-H_2-derived hydrides and the protons on the substrate ($\Delta\delta_{HH}$ in Figure 40) match the $^2J_{HH}$ scalar coupling between the *para*-H_2-derived hydrides (J_{HH} ~ 5-10 Hz).[146] Transfer to hetero-nuclei requires much smaller magnetic fields (mG)[155,156] due to the larger differences in chemical shifts between the *para*-H_2-derived hydrides and substrate hetero-nuclei.

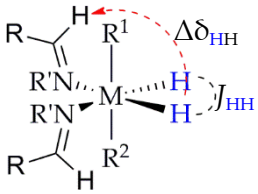

Figure 40: Polarisation transfer is optimised when $\Delta\delta_{HH}$ matches $^2J_{HH}$.

An exciting future application of SABRE is the generation of polarised drug molecules that can be used as hyperpolarised contrast agents in magnetic resonance imaging (MRI). Although the substrates used in SABRE do not undergo hydrogenation, and are therefore not restricted to unsaturated molecules, they are required to reversibly ligate to the polarisation transfer catalyst. Thus far, *N*-heterocycles have proven to exhibit excellent SABRE NMR enhancements, and are present in a variety of different biologically-compatible molecules.[75,157-159]

N-heterocycles promise to be suitable candidates for the generation of polarised contrast agents, however, several hurdles to *in vivo* studies remain. Firstly, the optimisation of SABRE is challenging as many different variables affect the efficiency of polarisation transfer. As SABRE requires substrate and *para*-H_2 exchange at iridium, any variable that affects the rate of exchange will in turn affect polarisation transfer. Previous publications have reported optimum lifetimes of SABRE-active iridium complexes,[150] which depend on the nature of the substrate and the *N*-heterocyclic carbene ligand used. Changes in temperature, iridium concentration, *para*-H_2 concentration, and substrate concentration all affect the rate of ligand exchange and therefore influence the efficiency of polarisation transfer.[145,148-150,160] Additionally, the polarisation transfer time (PTT), during which polarisation transfers from *para*-H_2 to the substrate at low field, and the polarisation transfer field (PTF, referring to the magnetic field) also have an effect on the efficiency of polarisation transfer.[150,153,157]

Another challenge in the use of SABRE to produce hyperpolarised contrast agents is the need to use biologically-compatible solvents. Typically, SABRE is carried out in d_4-methanol, however, this is not biologically-compatible, therefore alternative solvents are required. Although water is an obvious solvent choice, SABRE has not yet been shown to work effectively in this solvent.[161,162] The use of ethanol, followed by dilution with water has been successful.[161-163]

In order to be medically useful, after injection the polarised contrast agents must transport to the area of interest in the patient prior to detection which requires the polarisation to last several minutes. The T_1 values of polarised nuclei are dramatically shortened in the presence of the magnetisation transfer catalyst due to exchange at iridium.[163] In order to lengthen the polarisation lifetime, the T_1 values of substrate nuclei can be lengthened by deactivating the magnetisation transfer catalyst. This has recently been successfully achieved by the Duckett group, using 1,10-phenanthroline.[164] This bidentate *N*-heterocycle irreversibly binds to the iridium exchange catalyst, shown in Figure 41, by displacing the two substrate ligands that are positioned *trans* to the hydride ligands. The polarised substrate can no longer exchange at iridium, which for pyridine and nicotinamide resulted in approximately 5-fold increased T_1 values and polarisation that lasted up to three minutes.[164]

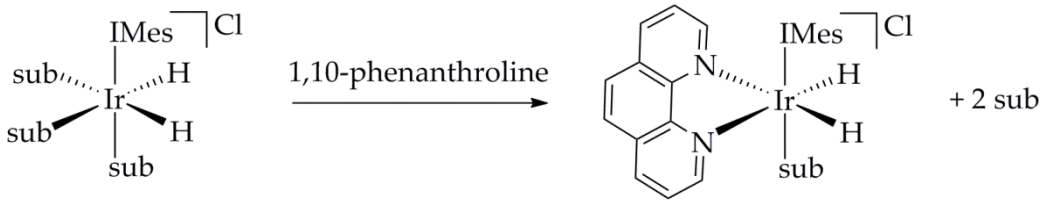

Figure 41: Deactivation of $[Ir(H)_2(IMes)(sub)_3]Cl$ with 1,10-phenanthroline. Sub is pyridine or nicotinamide.

SABRE has a high potential to create hyperpolarised contrast agents for use in *in vivo* MRI. If successful, it would lead to the acquisition of better resolved MR images in less time, using relatively inexpensive techniques and biologically-inert chemicals.[164] This would be a marked improvement on the use of DNP, which requires expensive, specialised equipment and much longer sample preparation times.

1.3 Summary

In order to distinguish the phase of a palladium-catalysed reaction, whether it is homogeneous or heterogeneous, the active catalytic species must be identified. A range of different techniques are available for the detection and characterisation of palladium catalysts, including those present in very low concentrations. ESI-MS, IR spectroscopy, UV-vis spectroscopy, TEM imaging, and EXAFS spectroscopy have proven to be exceptionally useful in detecting and characterising the active palladium catalysts present in reaction solutions, with the latter two techniques used predominantly to detect any nanoclusters that form.

NMR spectroscopy, combined with hyperpolarisation methods, is now a viable spectroscopic technique for the detection of low-concentration palladium intermediates. PHIP, in particular, has been used to investigate low-concentration palladium species that form as intermediates during the *para*-hydrogenation of unsaturated substrates. The relatively new technique, SABRE, is also becoming a useful hyperpolarisation method, which has the potential to generate hyperpolarised contrast agents for MRI.

Once plausible palladium catalytic species have been identified, their catalytic activity must be investigated. Kinetic traces are useful in determining whether the identified catalysts are active as found, or are in fact pre-catalysts that require activation prior to catalysis. The former case gives rise to typical 1st order kinetic traces, whereas the latter

gives rise to sigmoidal traces which are often suggestive of heterogeneous catalysis. Catalyst poisoning and filtration studies can also be very useful in determining catalytic phase but are often conducted alongside kinetic studies due to their frequently inconclusive results. It is important to note that no single technique can distinguish the phase of a palladium-catalysed reaction, however, a combination of spectroscopic techniques with kinetic data and phenomenological tests that all point to one phase produces a strong argument. The Finke group has reported many catalytic studies proving that catalysts originally thought to be homogeneous were in fact heterogeneous, outlining the necessity for thorough experimentation prior to assigning a phase.[24,64,165,166]

1.4 Thesis Aims

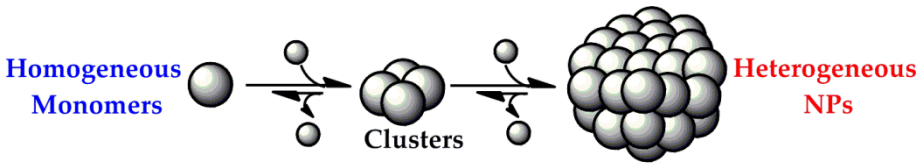

Figure 42: Scheme to illustrate the equilibria between the palladium monomers, clusters, and nanoparticles in solution during palladium catalysis.

The research detailed in this thesis aimed to contribute to the debate on the nature of the active catalytic species present in palladium-catalysed reactions, with a focus on exploring the palladium cluster phase, which lies intermediate between the homogeneous and heterogeneous phases (Figure 42). This was achieved through the completion of the objectives given below.

- To synthesise phosphine or arsine-stabilised palladium bis-triflate complexes, which are the monomers of interest, and to verify the formation of nanoparticles from these monomers on addition of hydrogen (Chapter 4).
- To identify and characterise palladium intermediates, including clusters that form en-route to nanoparticles, using advanced NMR techniques (Chapter 5).
- To examine the reactivity of isolated clusters, including photochemistry, *para*-hydrogenation reactions, and carbon-coupling reactions, and assess the nature of the catalytic phase (Chapter 6).

In addition to the use of PHIP to investigate palladium catalysis, the SABRE technique was explored with a view to generating contrast agents for MRI. This was achieved through the completion of the objectives given below.

- To form an active SABRE catalyst to hyperpolarise the two *N*-heterocycles pyridazine and phthalazine, which are common drug motifs. To investigate the mechanism of *N*-heterocycle and hydrogen exchange at the iridium centre (Chapter 2).
- To optimise SABRE of pyridazine and phthalazine and progress towards imaging applications (Chapter 3).

A summary of the research detailed in Chapters 2-6 is given in Chapter 7, alongside the potential for future study.

2 SABRE of Pyridazine and Phthalazine

SABRE is a method of transferring polarisation from *para*-H_2 to a substrate without chemically altering the substrate.[148] Polarised biological molecules have the potential to be used as non-toxic MRI contrast agents. These could be used alongside the gadolinium-based agents that are currently used, which have been linked to nephrogenic systemic fibrosis in patients with renal dysfunction. In these patients, the gadolinium is not efficiently excreted from the body, and deposition of free gadolinium causes fibrous connective tissue to form.[167] As a result, gadolinium-based contrast agents are not suitable for patients with renal dysfunction, and replacement contrast agents are required.

2.1 Introduction to SABRE-active Complexes

Initially, SABRE was carried out using complexes based on Crabtree's system, $[Ir(COD)(L)_2]BF_4$,[148] and $[Ir(COD)(L)(MeCN)]BF_4$,[75,145] where L is a phosphine ligand. The SABRE-active complexes, $[Ir(H)_2(L)_2(sub)_2]BF_4$,[148] and/or $[Ir(H)_2(L)(sub)_3]BF_4$,[75,145,148] where sub is substrate, form on addition of excess hydrogen and substrate. The system was later improved by incorporating bulky *N*-heterocyclic carbenes (NHCs) into the iridium complexes. The stronger σ-electron donation from the NHC ligands, in comparison to the phosphines, and weaker π-acceptance[168] (Figure 43) increases the lability of the hydrides and substrates, and reduces the lifetime of the active iridium catalyst that forms.[149] Hyperpolarised substrate builds up more quickly, in solution, leading to improved enhancement factors.

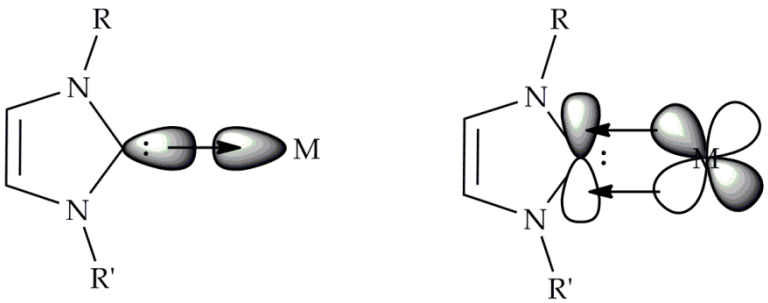

Figure 43: Strong σ-donation from an NHC to a metal (left), and weak π-back donation from a metal to an NHC (right).

Typically, SABRE is carried out using the [IrCl(COD)(IMes)] pre-catalyst shown in Figure 44.[150] This is a 16-electron Ir(I) complex, with a bulky 1,3-bis(2,4,6-

trimethylphenyl)-imidazol-2-ylidene (IMes) NHC. On addition of hydrogen and substrate, the COD is hydrogenated to COA, and no longer ligates. The 18-electron Ir(III) complex, also shown in Figure 44, commonly forms, which undergoes exchange with free substrate and hydrogen in solution. On replacement of hydrogen with *para*-H_2, polarisation spontaneously transfers from the *para*-H_2-derived hydrides to the substrate molecules *via J*-coupling.

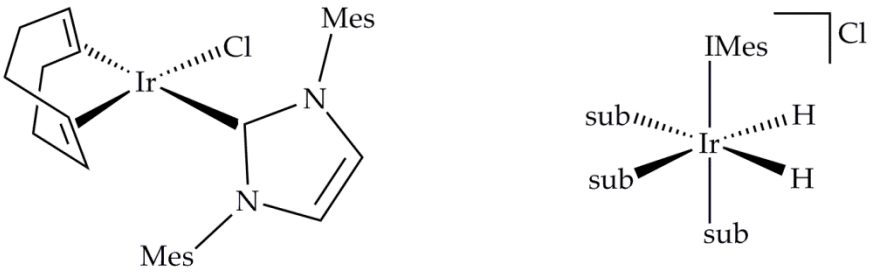

Figure 44: The commonly used SABRE pre-catalyst [IrCl(COD)(IMes)] (left) and the active catalyst that forms from it on addition of an excess of H_2 and substrate (right, where sub = substrate).

2.2 Substrates of Interest

SABRE was first observed in pyridine, which reversibly coordinates to iridium complexes through donation of the lone pair of electrons on the nitrogen atom.[148] Interest now lies in polarising substrates that are biologically-relevant, for their utilisation as MRI contrast agents. Herein, pyridazine and phthalazine, shown in Figure 45, are the substrates of interest, as they are found as moieties in a number of drug molecules, including hydrazinophthalazines, which are used to treat high blood pressure.[169] Pyridazine and phthalazine derivatives also have antifungal,[170] anti-HIV,[171] and anti-cancer[172,173] properties.

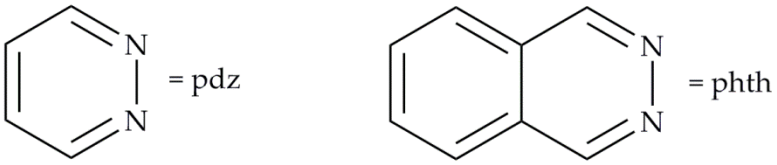

Figure 45: Substrates of interest: pyridazine (pdz, left), and phthalazine (phth, right).

As with pyridine, pyridazine and phthalazine can coordinate to iridium *via* donation of the lone pair of electrons on the nitrogen atom, however there are now two contiguous nitrogen donor atoms, which leads to the possibility of ligation through one[174-179] or both[180]

of them. Furthermore, exchange of pyridazine and phthalazine with iridium is complicated by the possibility of a 1,2-metallotropic shift of the ligated nitrogen, whereby the contiguous nitrogen donor atoms shift position (Figure 46). This was first observed in several ruthenium porphine complexes, containing axially-bound methylated pyridazine ligands.[175] More recently, a number of reports have focussed on the 1,2-metallotropic shifts of pyridazine and phthalazine-type ligands in octahedral complexes containing chromium,[177] platinum,[174,178,180] and rhenium.[179] In these reports, the mechanism of the 1,2-metallotropic shift is considered to be haptotropic in nature (Figure 46), however, a theoretical study on azine shifts in octahedral complexes of chromium, manganese, iron, and cobalt, predicts that a dissociative mechanism is more probable as the transition metal becomes more electron-rich, or the ligand *trans* to the coordination site becomes more electron-donating.[181] A haptotropic shift can occur *via* the formation of either two sigma interactions (shown in Figure 46),[182,183] or a pi interaction between the iridium and the nitrogen donor atoms. The latter requires the *N*-heterocycle to shift out of plane to allow for p orbital overlap and is uncommon in the literature.

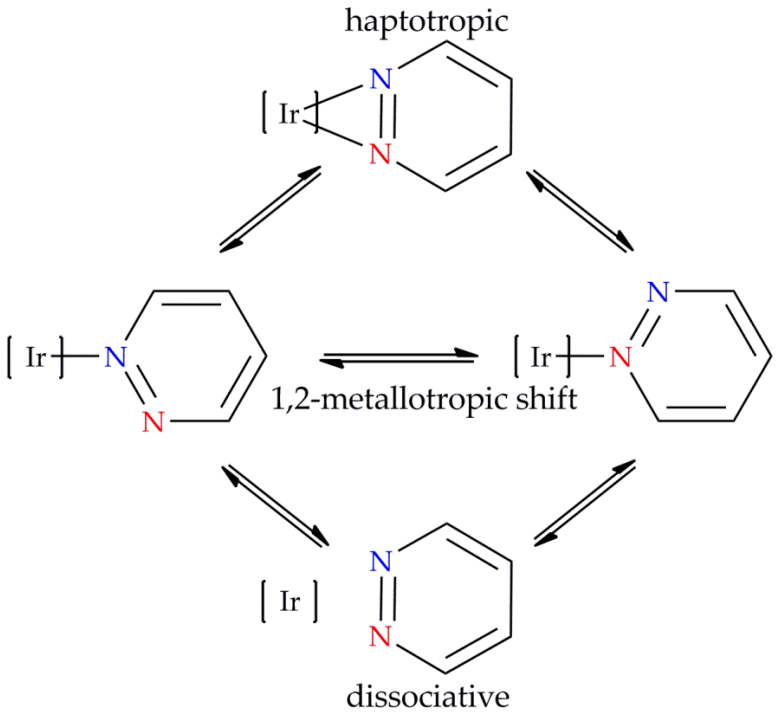

Figure 46: Possible mechanisms of the 1,2-metallotropic shift exhibited by pyridazine and phthalazine (pyridazine is shown as the example).

2.3 Synthesis of a SABRE-active Catalyst

2.3.1 Formation of [Ir(COD)(IMes)(sub)]Cl

The catalyst precursor, [IrCl(COD)(IMes)] was synthesised according to published procedures.[184-187] Dissolution of this complex into d_4-methanol gives a bright yellow solution. Addition of excess pyridazine or phthalazine, results in an immediate colour change to bright orange, due to the formation of [Ir(COD)(IMes)(pdz)]Cl or [Ir(COD)(IMes)(phth)]Cl, where the chloride ligand has been displaced by the *N*-heterocycle, with the chloride now acting as a counterion (Figure 47).

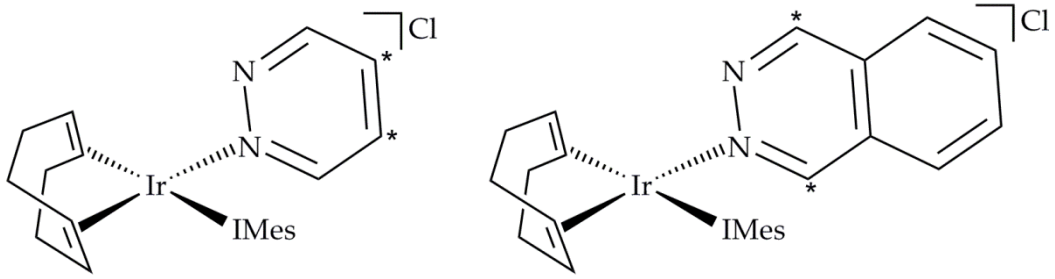

Figure 47: [Ir(COD)(IMes)(pdz)]Cl (left) and [Ir(COD)(IMes)(phth)]Cl (right). Proton resonances used to follow 1,2-metallotropic shifts are marked*.

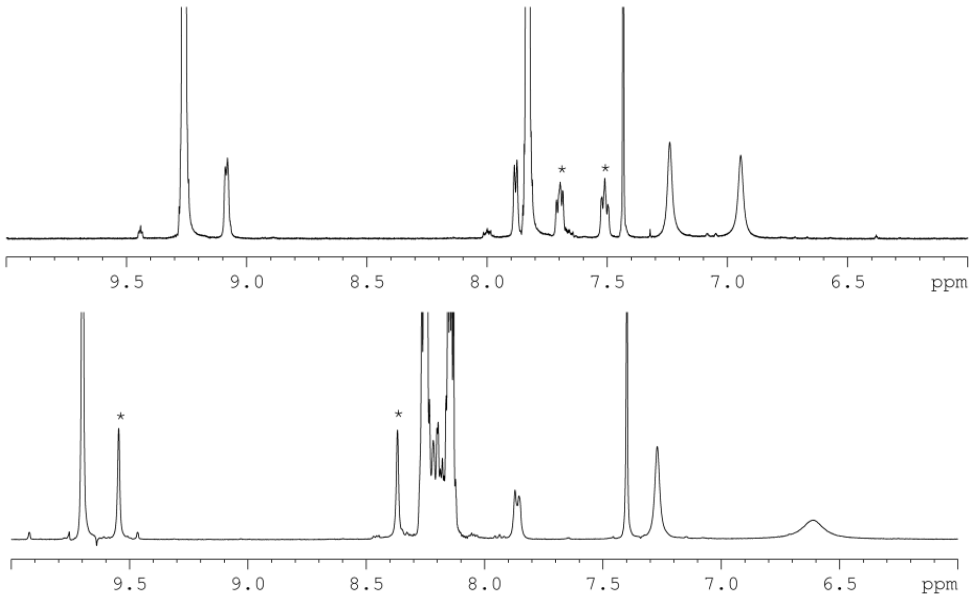

Figure 48: Aromatic region of the ^{1}H NMR spectrum of [Ir(COD)(IMes)(pdz)]Cl (above, free pdz signals are at δ 9.27 and 7.85), and [Ir(COD)(IMes)(phth)]Cl (below, free phth signals are at δ 9.71, 8.26 and 8.15), at 253 K. Signals used to quantify shifts are marked*.

These are 16-electron Ir(I) complexes. Their ^{1}H NMR signals are broad at room temperature, which suggests a level of fluxionality. The ^{1}H NMR spectra are resolved on cooling the samples to 253 K (Figure 48). Line-shape analysis is used to calculate rates from NMR spectra in which the NMR signals move to a point of coalescence.[188] Slower dynamic processes are monitored by EXSY methods. At the low temperatures required to resolve the ^{1}H NMR spectra of [Ir(COD)(IMes)(sub)]Cl, the dynamic processes were too slow to observe any line-shape coalescence. The fluxionality of these complexes was therefore explored using 2-D NOESY with mixing times that were incremented from 0.1 to 1 s. Exchange is observed as cross peaks in the opposite phase to nOe cross peaks.[189]

No exchange could be observed between the bound and free *N*-heterocycles on the NMR timescale. The protons that had been chemically equivalent on the free *N*-heterocycle, become inequivalent on the bound *N*-heterocycle. These protons were observed to exchange due to intramolecular 1,2-metallotropic shifting of the bound *N*-heterocycle. This is a haptoptropic shift, which occurs *via* η^2-coordination of the N=N bond,[175] as shown in Figure 46, rather than by dissociation of the *N*-heterocycle which would lead to the formation of the 14-electron [Ir(COD)(IMes)]Cl complex, and exchange with free *N*-heterocycles. The haptotropic shift is likely to proceed *via* a trigonal bipyramidal transition state, rather than a Berry-pseudorotation, in accordance with molecular orbital studies by Alvarez *et. al.*[181]

The rates of the 1,2-metallotropic shift were quantified by examining the exchange of the IrNCHC**H** (δ 7.69) and IrNNCHC**H** (δ 7.51) protons in [Ir(COD)(IMes)(pdz)]Cl, and the IrNC**H** (δ 9.55) and IrNNC**H** (δ 8.37) protons in [Ir(COD)(IMes)(phth)]Cl (shown in Figure 47 and Figure 48). 1-D slices were taken from the 2-D NOESY spectra, and the integrals of the diagonals and cross peaks were compared. Integral ratios of the observed peaks were converted into the percentage abundance of each species, which was plotted against the mixing time. Rate constants were determined by fitting first order relationships to these data according to the formulae below, where $[A]$ is the integral of the diagonal peak, $[B]$ is the integral of the cross peak, and k_{AB} is the rate constant of the 1,2-metallotropic shift. This is explained in detail in Appendix A, section A.1.1.

$$[A]_{t+\delta t} = [A]_t - k_{AB}[A]_t\delta t + k_{BA}[B]_t\delta t$$

$$[B]_{t+\delta t} = [B]_t + k_{AB}[A]_t\delta t - k_{BA}[B]_t\delta t$$

An example plot is shown in Figure 49. In order to calculate the activation parameters, the rates were obtained at the different temperatures given in Table 2. The NMR sample temperature readings were compared to those calculated from the chemical shift differences between the CH_3 and OH methanol signals[190] and were found to be accurate within ± 0.5 K. The errors in the observed rate constants were calculated using the Jack-knife method, which is explained in detail in Appendix A, section A.1.2.[191] Rate constants of the 1,2-metallotropic shift of the *N*-heterocycle are higher in [Ir(COD)(IMes)(phth)]Cl than in [Ir(COD)(IMes)(pdz)]Cl, which suggests a smaller energy barrier to shifting of bound phthalazine rather than pyridazine.

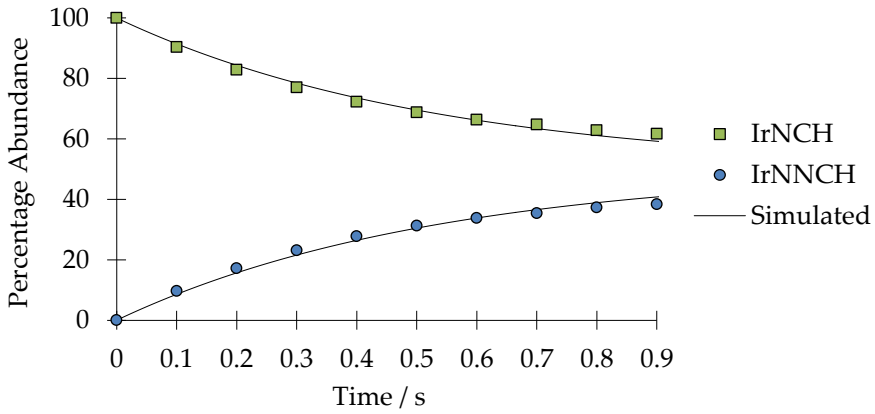

Figure 49: Graph to show the transfer of polarisation from IrNCH to IrNNCH in the bound phthalazine of [Ir(COD)(IMes)(phth)]Cl, as a result of a haptotropic shift, at 235 K.

Table 2: Rate constants calculated for the haptotropic shift of the bound N-heterocycle in [Ir(COD)(IMes)(sub)]Cl, from 235-260 K, each determined from a single analysis.

Temperature (K)	**Rate constants of 1,2-metallotropic shift (s^{-1})**	
	[Ir(COD)(IMes)(pdz)]Cl	**[Ir(COD)(IMes)(phth)]Cl**
235	-	0.923 ± 0.001
240	0.729 ± 0.001	1.873 ± 0.003
245	1.501 ± 0.003	3.955 ± 0.003
250	3.155 ± 0.002	7.318 ± 0.004
255	5.80 ± 0.01	13.426 ± 0.004
260	12.74 ± 0.02	-

The activation parameters for the 1,2-metallotropic shifts were calculated from Eyring plots, using the Eyring equation given, where *k* is the rate constant of the 1,2-

metallotropic shift (s^{-1}), k_B is the Boltzmann constant (1.381×10^{-23} JK^{-1}), R is the gas constant (8.314 $JK^{-1}mol^{-1}$), and T is temperature (K).

$$ln\frac{k}{T} = \frac{-\Delta H^{\ddagger}}{RT} + ln\frac{k_B}{h} + \frac{\Delta S^{\ddagger}}{R}$$

In this process, when at the transition state, there is an approximately equal probability of the substrate shifting, or returning back to its original position. For this reason, $ln\frac{2k}{T}$ was used in place of $ln\frac{k}{T}$, given in the Eyring equation. An example plot is shown in Figure 50. The gradient and intercept were found using the linear regression option in Excel's 'Analysis Toolpak', and the enthalpy and entropy of activation were calculated from these values. The errors in the enthalpy and entropy of activation were calculated using the Jack-knife method.[191] The Gibb's free energy of activation ($\Delta G^{\ddagger}$) could then be calculated using the formula shown below, and the error in the value calculated according to propagation of errors, see Appendix A section A.1.4.

$$\Delta G^{\ddagger} = \Delta H^{\ddagger} - T\Delta S^{\ddagger}$$

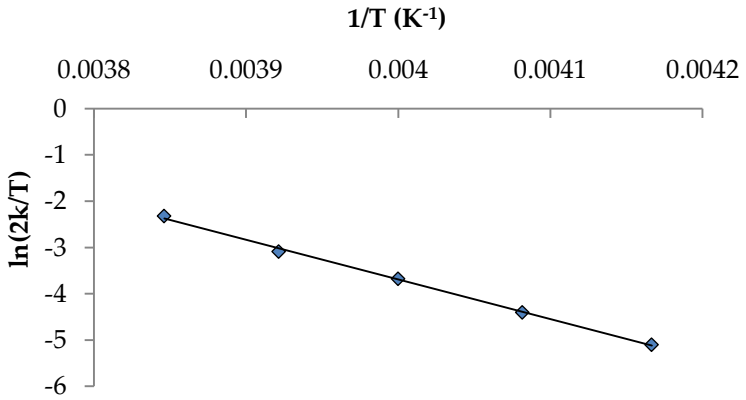

Figure 50: Eyring plot to calculate the activation parameters of the 1,2-metallotropic shift of the bound pyridazine in [Ir(COD)(IMes)(pdz)]Cl.

Table 3: Activation parameters for the haptotropic shift of the bound N-heterocycle in [Ir(COD)(IMes)(sub)]Cl.

Complex	$\Delta H^{\ddagger}$ (kJ mol^{-1})	$\Delta S^{\ddagger}$ (J mol^{-1} K^{-1})	$\Delta G^{\ddagger}_{(300K)}$ (kJ mol^{-1})
[Ir(COD)(IMes)(pdz)]Cl	71.3 ± 0.3	57 ± 1	54.2 ± 0.4
[Ir(COD)(IMes)(phth)]Cl	66.0 ± 0.1	43.0 ± 0.6	53.1 ± 0.2

The activation parameters calculated for the 1,2-metallotropic shifting of the bound *N*-heterocycles in [Ir(COD)(IMes)(sub)]Cl are shown in Table 3. The enthalpy of activation is larger for the shifting of pyridazine rather than phthalazine, suggesting that the Ir-pdz bond is stronger than the Ir-phth bond, and more energy is required to manipulate it. The literature p*K*a values for protonated pyridazine and phthalazine are 2.33 and 3.50, respectively.[192] Phthalazine is the stronger base, yet less energy is required to manipulate the Ir-phth bond. The lower stability of the Ir-phth bond in the ground state presumably leads to a longer bond, and smaller enthalpy of activation. A longer bond also leads to a more disordered ground state, which accounts for the smaller entropy of activation of the 1,2-metallotropic shift in [Ir(COD)(IMes)(phth)]Cl. According to Casarini *et al*, conformational processes with $\Delta S^{\ddagger}$ values that are significantly different from zero are likely to reflect inaccuracies in data measurements, thus few conclusions ought to be drawn from such $\Delta S^{\ddagger}$ values.[193] Overall, the Gibb's free energy of activation for the 1,2-metallotropic shift is larger for the [Ir(COD)(IMes)(pdz)]Cl complex.

2.3.2 Formation of $[Ir(H)_2(COD)(IMes)(sub)]Cl$

A SABRE-active catalyst must exchange with *para*-H_2, hence an iridium hydride complex is required. Addition of hydrogen gas (3 bar) to cold (~ 240 K) d_4-methanol solutions of [Ir(COD)(IMes)(sub)]Cl, with an excess of substrate, resulted in an immediate colour change from bright orange to colourless, due to the formation of $[Ir(H)_2(COD)(IMes)(sub)]Cl$. ^{1}H NMR spectra of $[Ir(H)_2(COD)(IMes)(pdz)]Cl$ contain diagnostic doublets at δ −13.84 and −17.69 which couple to one another and correspond to two chemically inequivalent hydride ligands (Figure 51). Similarly, ^{1}H NMR spectra of $[Ir(H)_2(COD)(IMes)(phth)]Cl$ contain doublets at δ −13.87 and −17.55 which also correspond to two chemically inequivalent hydride ligands (Figure 51).

As the hydrides are chemically and magnetically inequivalent, the iridium complexes could adopt one of two possible geometries, shown for pyridazine in Figure 52. In the first (a), one hydride is positioned *trans* to the bound COD and the other lies *trans* to the *N*-heterocycle. In the second (b), one hydride is positioned *trans* to the bound COD and the other lies *trans* to IMes.

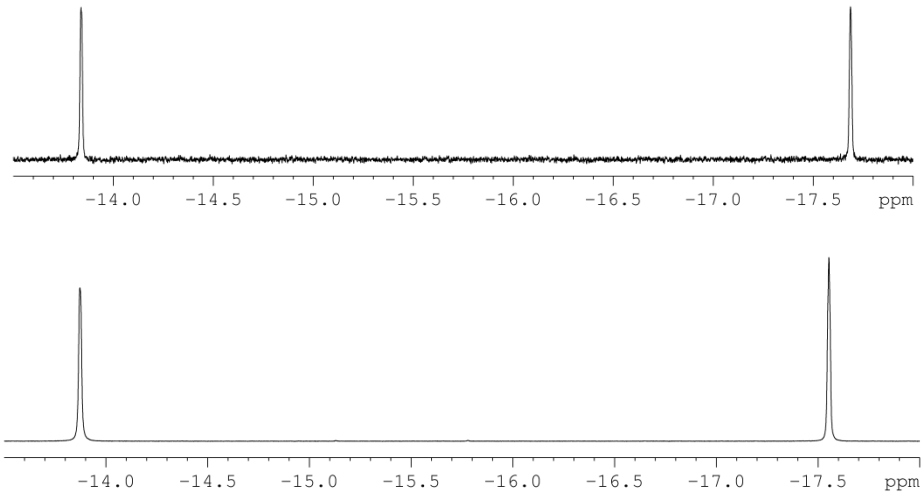

Figure 51: Hydride region of ^{1}H NMR spectra corresponding to [Ir(H)$_2$(COD)(IMes)(pdz)]Cl (above) and [Ir(H)$_2$(COD)(IMes)(phth)]Cl (below), at 240 K.

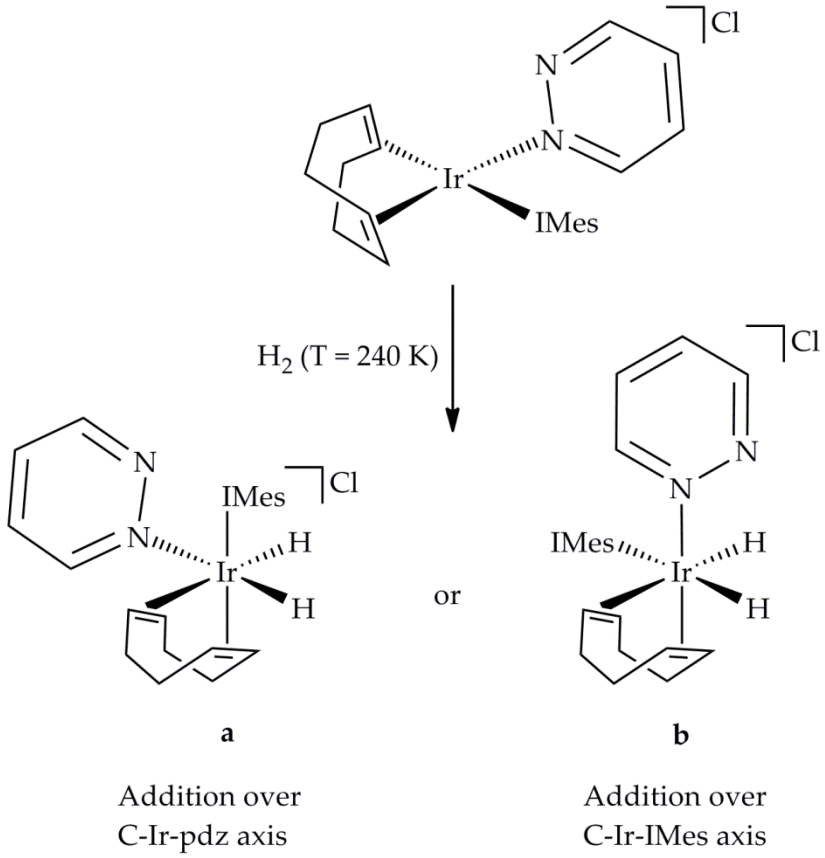

Figure 52: The two possible geometric isomers of [Ir(H)$_2$(COD)(IMes)(pdz)]Cl that can form on addition of H$_2$ to [Ir(COD)(IMes)(pdz)]Cl.

On changing the *N*-heterocycle from pyridazine to phthalazine, the hydride signals at higher field have a difference of only 0.03 ppm, whilst those at lower field have a difference of −0.14 ppm. This suggests that the hydrides at lower field lie *trans* to the *N*-heterocycle (supporting geometry **a**) and are therefore more strongly affected by a change

in *N*-heterocycle. ^{15}N-optimised HMQC spectra of [Ir(H)$_2$(COD)(IMes)(pdz)]Cl and [Ir(H)$_2$(COD)(IMes)(phth)]Cl contain cross peaks between the respective hydride signals (δ −17.69, and δ −17.55) , and ^{15}N signals in bound pyridazine or phthalazine (δ 294.3 or δ 266.6). This further supports the hydrides at lower field being positioned *trans* to the *N*-heterocycle. Furthermore, cross peaks between the hydride signals at higher field (δ −13.84, and −13.87) and two bound COD signals (δ 5.03 and 4.45, δ 5.23 and 4.34) are visible in COSY NMR spectra, hence geometry **a** must form. Signals corresponding to complexes in geometry **b** are not observed in any NMR spectra. The C-Ir-pdz axis must be the most electron-rich and therefore most able to promote hydrogen addition across it.[194,195] Both [Ir(H)$_2$(COD)(IMes)(sub)]Cl complexes have been fully characterised by NMR. These data can be found in the Experimental, section E.3.3.

On degassing the d_4-methanol solutions of [Ir(H)$_2$(COD)(IMes)(sub)]Cl containing an excess of substrate and hydrogen, the solutions changed colour from colourless, back to bright orange. Subsequent ^{1}H NMR spectra no longer contained any signals in the hydride region, and the signals corresponding to [Ir(COD)(IMes)(sub)]Cl were present once more. Oxidative addition of hydrogen to these iridium (I) complexes is clearly reversible. Similar reversible hydrogen addition to an iridium (I) complex has been published by Searles *et. al.*; an iridium pyridylpyrrolide COD complex was reversibly oxidised by hydrogen.[196]

2.3.3 Addition of *Para*-H$_2$ to [Ir(COD)(IMes)(sub)]Cl

The reversibility of the oxidative addition of hydrogen to [Ir(COD)(IMes)(sub)]Cl, and the immediate formation of [Ir(H)$_2$(COD)(IMes)(sub)]Cl, implied that PHIP could be employed to observe enhanced hydride NMR resonances. *Para*-H$_2$ (3 bar) was added to the d_4-methanol solutions of [Ir(COD)(IMes)(sub)]Cl, which contained an excess of substrate. The sample was shaken at 65 G for 10 seconds, and a ^{1}H NMR spectrum was immediately acquired. Dramatic PHIP-enhancements of the hydride signals were indeed observed, and are shown for [Ir(H)$_2$(COD)(IMes)(pdz)]Cl in Figure 53.

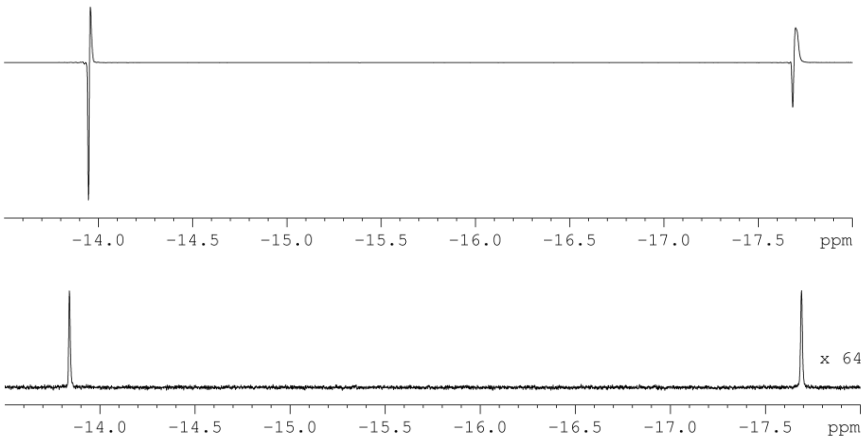

Figure 53: Hydride regions of ^{1}H NMR spectra of [Ir(H)$_2$(COD)(IMes)(pdz)]Cl, comparing PHIP-enhanced hydride signals (above) to thermal hydride signals (below, magnified 64-fold).

The hydride signals at higher field (δ −13.84, and −13.87), which correspond to the hydrides that lie *trans* to the COD, are sharper than those at lower field (δ −17.69, and δ −17.55), which correspond to the hydrides that lie *trans* to the *N*-heterocycle. Furthermore, the enhancement factors of the sharper hydride signals are greater than those of the broader signals, given in Table 4. The enhanced NMR signals do not resemble typical in-phase/antiphase PASADENA signals. The up-field signals have more in-phase character than the down-field signals, suggesting that there is an overlap of both PASADENA and ALTADENA signals here. When the signal magnitudes are analysed, in order to calculate their enhancement factors, the more extensive overlapping of broader peaks will cancel more of the NMR signal. This accounts for the apparent smaller enhancements observed for the broader hydride signals.

NMR line widths are dependent on the T_2 (transverse relaxation time) and the T_1 (longitudinal relaxation time) values of the state that is probed, as well as any dynamic effects and additional unobservable couplings.

Table 4: Enhancement factors of the PHIP-enhanced ^{1}H NMR hydride signals in [Ir(H)$_2$(COD)(pdz)]Cl, and [Ir(H)$_2$(COD)(phth)]Cl.

Complex	**Enhancement factors**		
	C-Ir-**H**	N-Ir-**H**	Total
[Ir(H)$_2$(COD)(IMes)(pdz)]Cl	90	70	160
[Ir(H)$_2$(COD)(IMes)(phth)]Cl	50	40	90

The T_1 values of each hydride signal in the two complexes were investigated using inversion recovery experiments, in which the magnetisation aligned in the Z-direction is inverted to the –Z direction using a 180 ° pulse (Figure 54). The magnetisation is then allowed to relax for a set time, τ, after which it is aligned into the Y-direction using a 90 ° pulse and detected. The intensity of magnetisation is collected at different delay times (τ), and plotted. An example plot is shown in Figure 55.

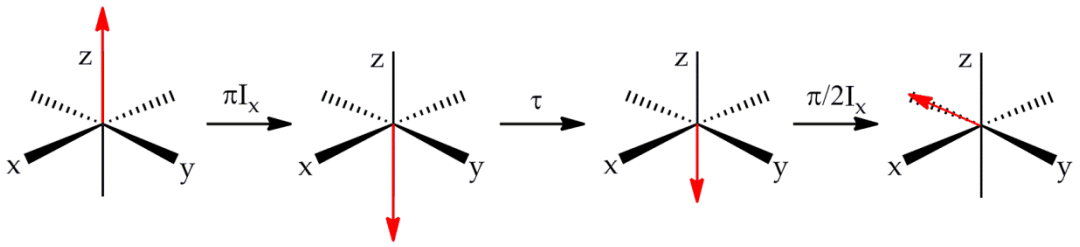

Figure 54: Vector diagram to show the transfer of magnetisation in an inversion recovery experiment.

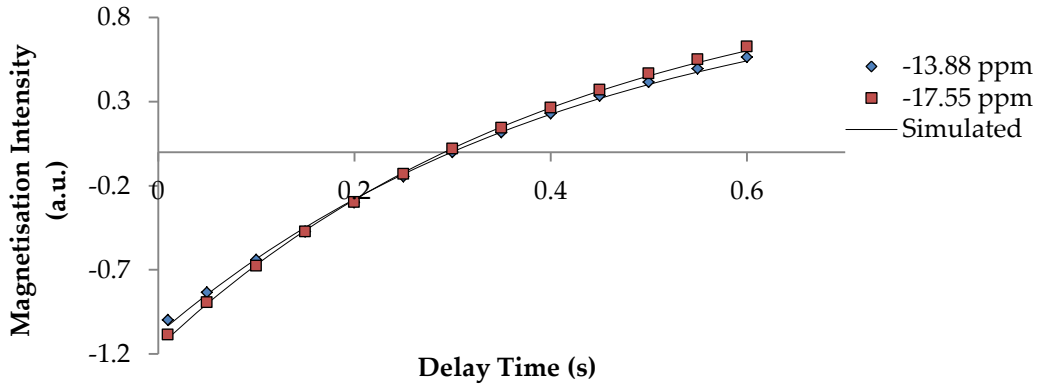

Figure 55: Graph to show the change in magnetisation intensity, with respect to the intensity when τ = 0.001 s, as a function of the delay time (τ) in an inversion recovery experiment used to calculate the T_1 of the hydride NMR signals in [Ir(H)$_2$(COD)(IMes)(phth)]Cl.

The T_1 values were calculated by fitting the experimental data to the formula given below, where τ is the delay time (s), M_τ is the magnetisation intensity after a delay time τ, and M_0 is the magnetisation intensity when τ = 0. The calculated T_1 values are given in Table 5 and are typical of classical iridium hydrides.[197] The associated errors were calculated using the Jack-knife method.

$$M_\tau = M_0[1 - 2exp^{\frac{-\tau}{T_1}}]$$

The hydride signals at higher field have a slightly longer longitudinal relaxation time, which contradicts their broader line widths. The values, however, do not differ

significantly from those for the hydride signals at lower field. The difference in line shape cannot, therefore, be attributed to relaxation effects. It is probable that the hydrides that lie *trans* to the *N*-heterocycle give a broader signal due to the 1,2-metallotropic shifting of the *N*-heterocycle, which results in a change in the chemical environment of the hydride.

Table 5: Longitudinal relaxation time of the hydride ^{1}H NMR signals in [Ir(COD)(H)$_2$(pdz)]Cl, and [Ir(COD)(H)$_2$(phth)]Cl.

Complex	Signal (δ)	T_1 (s)
[Ir(COD)(H)$_2$(IMes)(pdz)]Cl	−13.84	0.4252 ± 0.0008
	−17.69	0.412 ± 0.001
[Ir(COD)(H)$_2$(IMes)(phth)]Cl	−13.87	0.4309 ± 0.0002
	−17.55	0.4202 ± 0.0002

In addition to the hydride signal enhancements, which result from PHIP, polarisation is observed to transfer into the aromatic and vinyl regions of the ^{1}H NMR spectrum, shown for [Ir(COD)(H)$_2$(IMes)(pdz)]Cl in Figure 56. This confirms the presence of *J*-coupling between the hydrides and the polarised ligands. Polarised signals between δ 4.3 and 5.4 correspond to the vinylic protons of the bound COD that are positioned both *trans* and *cis* to the hydrides. The emissive nature of the polarised COD signals suggests that polarisation results from a SABRE-like transfer. There is no evidence of any free COD, cyclooctene (COE) or COA signals, and corresponding EXSY spectra prove that the bound COD is not able to reversibly accept a hydride ligand, which has been observed in related iridium complexes.[198] This is therefore a non-hydrogenative effect, whereby polarization has transferred from the *para*-H_2-derived hydrides to the vinylic protons of bound COD at low magnetic field, *via J*-coupling.

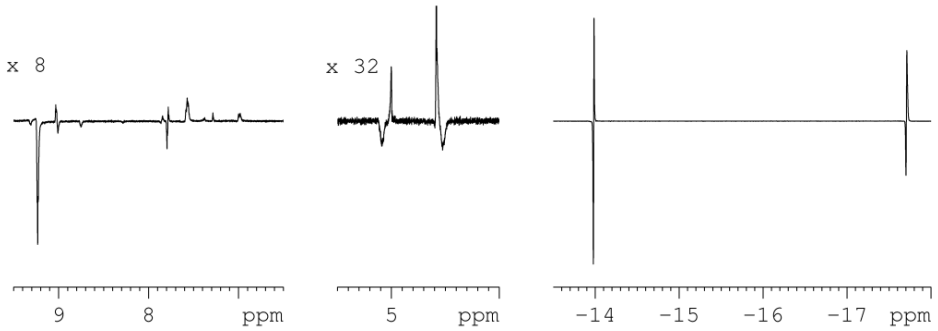

Figure 56: ^{1}H NMR spectra showing PHIP of some of the proton signals in [Ir(H)$_2$(COD)(IMes)(pdz)]Cl; SABRE of protons in free and bound pyridazine (left, magnified 8-fold), PHIP of vinylic protons in bound COD (middle, magnified 32-fold), PHIP of hydrides (right).

Polarised signals observed between δ 7.7 and 9.8 correspond to protons on either bound pyridazine or phthalazine molecules that lie *trans* to the hydride ligands, or free pyridazine or phthalazine molecules. Polarisation of the free substrate must be the result of SABRE, and this verifies that there is exchange between bound and free substrate when the sample is shaken outside the spectrometer.

The [Ir(H)$_2$(COD)(IMes)(sub)]Cl complexes are SABRE-active, however, they are not stable at temperatures above 250 K and are therefore unsuitable for MRI applications.

2.3.4 Formation of [Ir(H)$_2$(IMes)(sub)$_3$]Cl

Warming d_4-methanol solutions of [Ir(H)$_2$(COD)(IMes)(sub)]Cl, with an excess of substrate and hydrogen, to 298 K for approximately one hour, resulted in a change in colour from colourless to bright yellow due to the formation of [Ir(H)$_2$(IMes)(sub)$_3$]Cl, shown in Figure 57. The [Ir(H)$_2$(COD)(IMes)(sub)]Cl complexes are not stable at temperatures above 250 K, as hydrogenation of COD to COA occurs (COE signals are not observed in ^{1}H NMR spectra). The two vacant sites at iridium, created by the hydrogenation of bound COD, become occupied by a further two substrate molecules. The use of a bulkier *N*-heterocycle, for example quinazoline, can result in only one additional substrate molecule occupying one of the vacant sites, with the other site becoming occupied by a solvent molecule, thus forming [Ir(H)$_2$(IMes)(sub)$_2$(sol)]Cl.

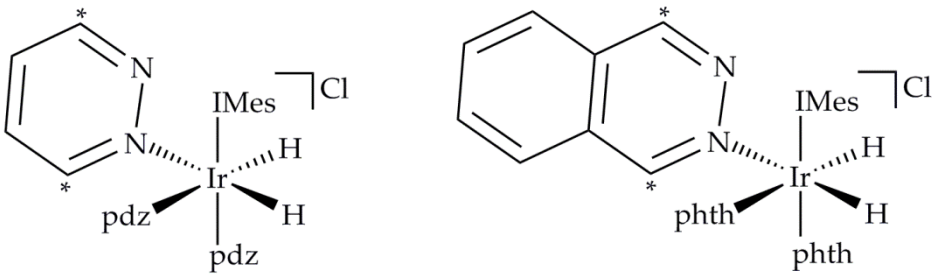

Figure 57: [Ir(H)$_2$(IMes)(pdz)$_3$]Cl (left), and [Ir(H)$_2$(IMes)(phth)$_3$]Cl (right). The proton resonances used to quantify exchange are marked *.

This is not the case with either pyridazine or phthalazine, where a clean transformation to [Ir(H)$_2$(IMes)(sub)$_3$]Cl is confirmed by a single diagnostic singlet resonance in the hydride region of the ^{1}H NMR spectra (Figure 58); the hydride ligands are chemically equivalent. The two equatorial *N*-heterocycles that lie *trans* to the hydride ligands are also chemically equivalent, whereas the axial *N*-heterocycle which lies *trans* to the carbene is distinct. Furthermore, on binding to iridium, the symmetry of the *N*-heterocycle is lost, resulting in complicated ^{1}H NMR signals for the protons of the bound *N*-heterocycles.

The four doublets in the ^{1}H NMR spectrum of [Ir(H)$_2$(IMes)(pdz)$_3$]Cl, at δ 9.62, 9.31, 8.75 and 8.29 have respective integral ratios of 1:2:2:1, and correspond to bound NC**H** environments; one axial at δ 9.62 and 8.29, and two equatorial at δ 9.31 and 8.75. The three multiplets at δ 7.62, 7.48 and 7.40 have respective integral ratios of 2:1:3 (that at δ 7.40 consists of two overlapping peaks). These correspond to the bound NCHC**H** environments; one axial at δ 7.48 and 7.40, and two equatorial at δ 7.62 and 7.40. The axial and equatorial arrangements of the three pyridazine ligands at iridium were further confirmed by nOe measurements. These revealed that both the equatorial IrNC**H** and IrNNC**H** environments interact with methyl protons of the mesityl rings in IMes that resonate at δ 2.22 and 2.04 which confirms that the equatorial pyridazine ligands lie in close proximity to the IMes ligand.

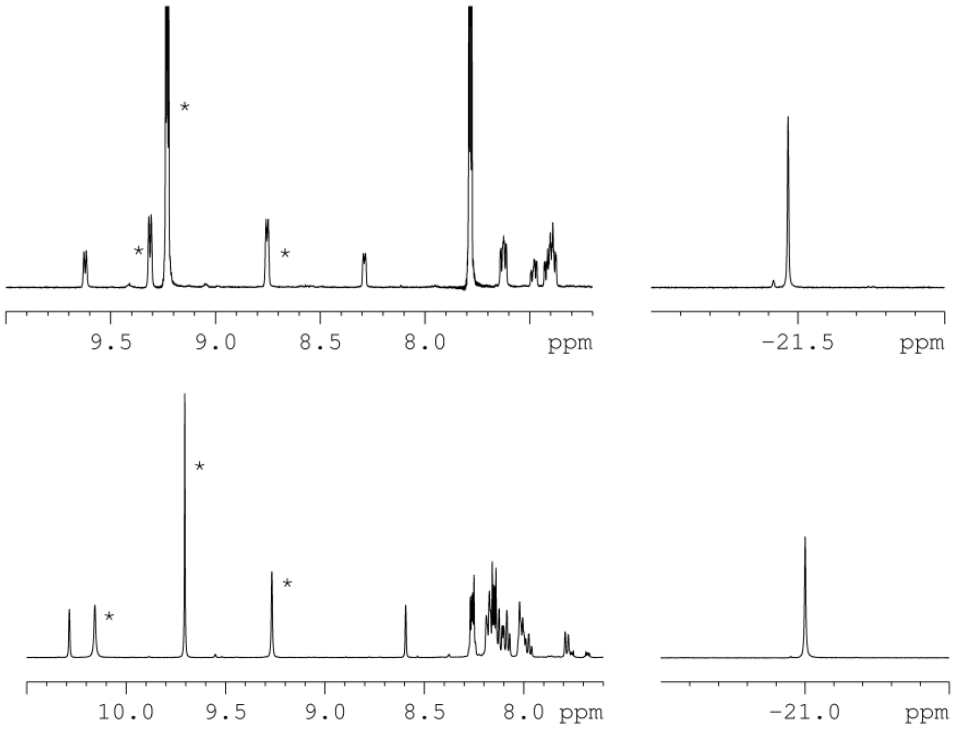

Figure 58: Aromatic and hydride regions of the ^{1}H NMR spectra of [Ir(H)$_2$(IMes)(pdz)$_3$]Cl (above, free pdz signals are at δ 9.23 and 7.78), and [Ir(H)$_2$(IMes)(phth)$_3$]Cl (below, free phth signals are at δ 9.63, 8.26 and 8.15). Signals used to quantify exchange are marked *.

The four singlets in the ^{1}H NMR spectrum of [Ir(H)$_2$(IMes)(phth)$_3$]Cl, at δ 10.28, 10.16, 9.27 and 8.60, have respective integral ratios of 1:2:2:1 and correspond to bound NC**H** environments; one axial at δ 10.28 and 8.60, and two equatorial at δ 10.16 and 9.27. The multiplets at δ 8.05, 7.91 and 7.78 correspond to the bound NCHCC**H**C**H** environments. The integral ratios cannot, however, be compared due to peak overlap with free phthalazine at δ 8.15. As before, the axial and equatorial arrangements of the three phthalazine ligands at iridium were further confirmed by nOe measurements which revealed that the equatorial IrNC**H** and IrNNC**H** environments interact with methyl protons of the mesityl rings in IMes that resonate at δ 2.07 and 1.92. This confirms that the equatorial phthalazine ligands lie in close proximity to the IMes ligand. Full NMR characterisation of both [Ir(H)$_2$(IMes)(sub)$_3$]Cl complexes is given in the Experimental, section E.3.3.

In order for SABRE of pyridazine and phthalazine to operate, the reversible binding of the *N*-heterocycle and hydrogen is necessary. A series of 1-D EXSY measurements were used to probe exchange in [Ir(H)$_2$(IMes)(pdz)$_3$]Cl and [Ir(H)$_2$(IMes)(phth)$_3$]Cl, and both ligand exchange and hydrogen loss pathways were observed. These processes were too

slow below 280 K to be detected. The upper limit of the measurements is 325 K, which is 12 degrees below the boiling point of the methanol solvent. At this temperature, the exchange rates were too slow to observe any dynamic effects through a change in NMR spectral line-shape.

In the first EXSY experiments, NMR signals corresponding to the NC**H** environment of the axial *N*-heterocyclic ligands in $[Ir(H)_2(IMes)(pdz)_3]Cl$ (δ 9.62 and 8.29) and $[Ir(H)_2(IMes)(phth)_3]Cl$ (δ 10.28 and 8.60) were probed at temperatures up to 320 K with mixing times up to 1 s. No magnetization transfer was observed from these sites, and only the irradiated peaks appeared in the spectra. This suggests that the axial ligands remain bound to the iridium on the NMR timescale. In contrast, when the equatorial *N*-heterocyclic ligands of $[Ir(H)_2(IMes)(pdz)_3]Cl$ and $[Ir(H)_2(IMes)(phth)_3]Cl$ were probed, both ligand exchange with the free substrate, and 1,2-metallotropic shifting of the equatorial ligand's bound nitrogen was observed. Such exchange pathways have been observed in related systems.[174-180]

The rate constants for substrate dissociation, and 1,2-metallotropic shifting were calculated at different temperatures by collecting EXSY spectra, after specified mixing times (typically from 0.1 to 1.0 s). The peak at δ 8.75, corresponding to the IrNNC**H** protons of equatorial pyridazine, was selectively irradiated. Exchange into free pyridazine and shifting into bound pyridazine was measured. An EXSY spectrum showing exchange of the equatorial pyridazine ligands in $[Ir(H)_2(IMes)(pdz)_3]Cl$ is shown in Figure 59, with a simplified schematic of the exchange process given in Figure 60. In addition, when the hydride signal of $[Ir(H)_2(IMes)(pdz)_3]Cl$ at δ −21.47 was selectively irradiated, exchange into the signal for dihydrogen at δ 4.58 was observed. Similarly, when $[Ir(H)_2(IMes)(phth)_3]Cl$ was examined, the peak at δ 9.27, which corresponds to equatorial phthalazine protons IrNNC**H**, was probed. Both ligand dissociation and shifting of the phthalazine binding site were evident, as was hydrogen loss on examining the hydride signal of $[Ir(\mathbf{H})_2(IMes)(phth)_3]Cl$.

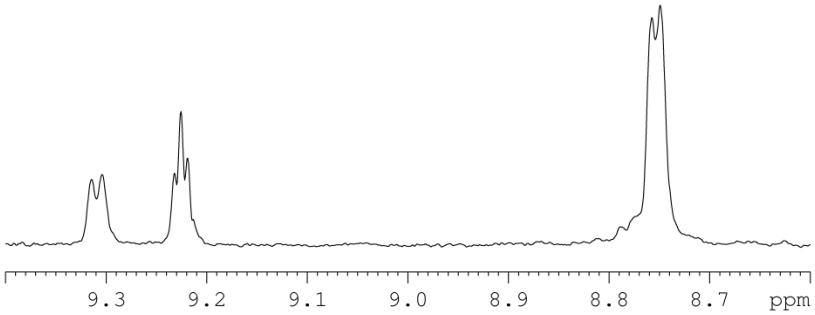

Figure 59: EXSY spectrum acquired with a mixing time of 0.3 s, after irradiating the equatorial IrNNCH signal at δ 8.75 at 300 K.

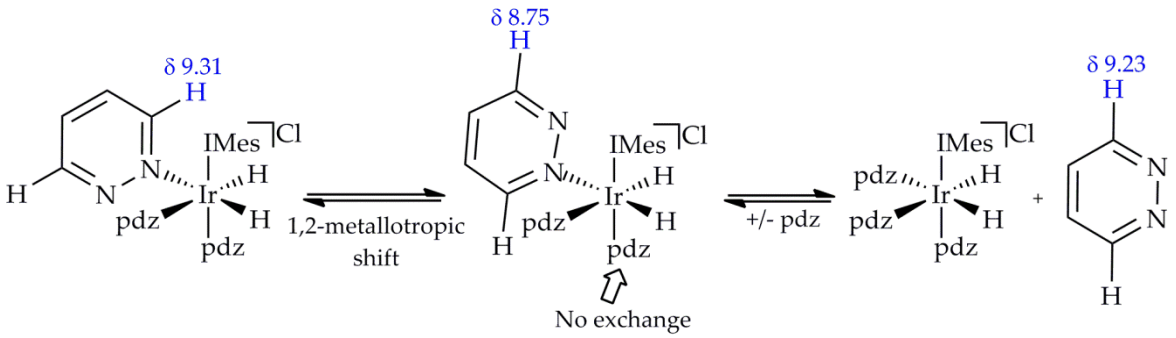

Figure 60: Simplified schematic of the exchange processes possible at the equatorially-bound pyridazine in $[Ir(H)_2(IMes)(pdz)_3]Cl$.

Ratios of the integrals of the observed peaks were converted into the percentage abundance of each species, which was plotted against the mixing time. Fitting the data for exchange of the *N*-heterocycle was challenging, as an equation that accurately described the transfer of magnetic polarisation from the irradiated bound species to the free and shifted species *via* exchange was required. Eleven different polarised species, including unobservable intermediates, can form due to *N*-heterocycle exchange, and these are discussed in Appendix A section A.1.6, in addition to the formulae that were used to model their formation and depletion. Despite some papers reporting a dissociative 1,2-metallotropic shift mechanism of pyridazine-like *N*-heterocycles, our exchange data would only fit to a model in which the 1,2-metallotropic shift is assumed to be haptotropic in nature. An example plot is shown in Figure 61. The errors associated with each rate were calculated using the Jack-knife procedure.[191]

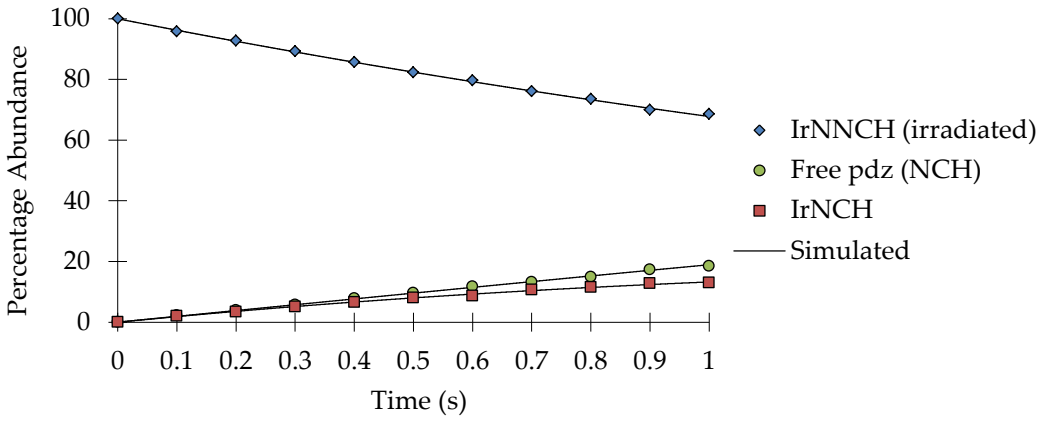

Figure 61: Graph to show the transfer of polarisation from IrNNCH to IrNCH in the bound pdz of $[Ir(H)_2(IMes)(pdz)_3]Cl$ as a result of a haptotropic shift, and from IrNNCH to NCH in free pdz as a result of dissociation, at 290 K.

In order to calculate the activation parameters of the different exchange processes, the rate constants of substrate dissociation and shifting, as well as hydrogen dissociation, were calculated at the different temperatures given in Table 6. Eyring-Polanyi plots, given in Appendix A, were then used to calculate the enthalpy and entropy of activation ($\Delta H^{\ddagger}$ and $\Delta S^{\ddagger}$ respectively), from which the Gibb's free energy of activation ($\Delta G^{\ddagger}$) was calculated. The activation parameters for the exchange processes in $[Ir(H)_2(IMes)(sub)_3]Cl$ are given in Table 7.

The $\Delta H^{\ddagger}$ values reflect the Ir-N bond energies. In both complexes, the enthalpy change on reaching the transition states for the haptotropic shift is lower than that of dissociation, which suggests that less energy is required to 'shift' the Ir-N bond, rather than formally break it. Phthalazine has a weaker Ir-N bond and smaller $\Delta H^{\ddagger}$ term. Consequently, the Ir-N bond is longer and the gain in entropic freedom on reaching the transition state for both phthalazine dissociation and shifting is less. The two effects act to compensate each other and their $\Delta G^{\ddagger}_{300\,K}$ values are similar. This is particularly noticeable in the haptotropic shift, where the $\Delta H^{\ddagger}$ and $\Delta S^{\ddagger}$ terms for phthalazine are lower by 16.2 kJ mol^{-1} and 55 J K^{-1} mol^{-1} respectively. A similar effect is also observed for the rupture of the Ir-H bonds; the $\Delta G^{\ddagger}_{300\,K}$ values are similar for both complexes.

Table 6: Rate constants of N-heterocycle dissociation and haptotropic shifting, as well as hydrogen dissociation in $[Ir(H)_2(IMes)(sub)_3]Cl$, from 280 – 325 K, each determined from a single analysis.

Temperature (K)	Rate of *N*-heterocycle dissociation (s^{-1})		Rate of H_2 dissociation (s^{-1})		Rate of *N*-heterocycle haptotropic shift (s^{-1})	
	$[Ir(H)_2(IMes)(pdz)_3]$	**$[Ir(H)_2(IMes)(phth)_3]$**	**$[Ir(H)_2(IMes)(pdz)_3]$**	**$[Ir(H)_2(IMes)(phth)_3]$**	**$[Ir(H)_2(IMes)(pdz)_3]$**	**$[Ir(H)_2(IMes)(phth)_3]$**
280	0.0454 ± 0.0002	0.0603 ± 0.0003	0.091 ± 0.005	0.094 ± 0.005	0.0376 ± 0.0001	0.0326 ± 0.0002
285	0.0986 ± 0.0001	0.1153 ± 0.0003	0.183 ± 0.003	0.169 ± 0.005	0.0942 ± 0.0002	0.0697 ± 0.0004
290	0.1926 ± 0.0002	0.2110 ± 0.0003	0.347 ± 0.008	0.33 ± 0.01	0.1925 ± 0.0003	0.1419 ± 0.0005
295	0.3611 ± 0.0008	0.382 ± 0.001	0.70 ± 0.02	0.59 ± 0.08	0.4078 ± 0.0008	0.3212 ± 0.0008
300/301	0.642 ± 0.003	0.663 ± 0.003	1.46 ± 0.01	1.12 ± 0.03	0.819 ± 0.02	0.673 ± 0.002
305	1.073 ± 0.006	1.085 ± 0.005	2.83 ± 0.06	1.69 ± 0.05	1.203 ± 0.005	1.103 ± 0.003
310	1.61 ± 0.02	1.69 ± 0.02	5.1 ± 0.1	3.11 ± 0.08	1.84 ± 0.04	1.98 ± 0.01
315	4.81 ± 0.01	3.03 ± 0.02	-	5.4 ± 0.1	5.01 ± 0.03	3.43 ± 0.02
320	8.93 ± 0.03	4.69 ± 0.03	-	9.3 ± 0.1	9.36 ± 0.04	5.69 ± 0.03
325	-	7.57 ± 0.03	-	16.0 ± 0.5	-	8.22 ± 0.05

Table 7: Activation parameters for the dissociation of hydrogen, and dissociation and haptotropic shifting of the equatorially-bound N-heterocycles in $[Ir(COD)(IMes)(sub)]Cl$.

Process	**$\Delta H^{\ddagger}$ (kJ mol^{-1})**		**$\Delta S^{\ddagger}$ (J K^{-1} mol^{-1})**		**$\Delta G^{\ddagger}_{(300\ K)}$ (kJ mol^{-1})**	
Complex	**$[Ir(H)_2(IMes)(pdz)_3]$**	**$[Ir(H)_2(IMes)(phth)_3]$**	**$[Ir(H)_2(IMes)(pdz)_3]$**	**$[Ir(H)_2(IMes)(phth)_3]$**	**$[Ir(H)_2(IMes)(pdz)_3]$**	**$[Ir(H)_2(IMes)(phth)_3]$**
Sub. Dissociation	97.9 ± 0.3	92.0 ± 0.3	85 ± 1	62 ± 1	72.5 ± 0.3	73.3 ± 0.3
Haptotropic shift	94.3 ± 0.4	78.13 ± 0.06	72 ± 1	17.4 ± 0.2	72.6 ± 0.3	72.93 ± 0.06
H_2 loss	95.6 ± 0.2	83.6 ± 0.1	82.4 ± 0.8	39.8 ± 0.4	70.9 ± 0.3	71.6 ± 0.2

Literature $\Delta G^{\ddagger}_{300\,K}$ values for 1,2-metallotropic shifting of pyridazine and phthalazine-type ligands in different octahedral complexes vary substantially from 56-93 KJ mol^{-1}.[174,177-180] Although the $\Delta G^{\ddagger}_{300\,K}$ values for the shifting of pyridazine and phthalazine in $[Ir(H)_2(IMes)(sub)_3]Cl$ lie within the literature range, a direct comparison with literature values cannot be made due to the sensitivity of $\Delta G^{\ddagger}_{300\,K}$ to the metal and the ligand environment. To the best of our knowledge, there are no other examples of the haptotropic shifting of pyridazine and phthalazine ligands in iridium complexes.

2.3.5 Mechanism of Exchange in $[Ir(H)_2(IMes)(sub)_3]Cl$

To elucidate the mechanism of exchange, the influence of the substrate concentration and hydrogen pressure on the rate of exchange was investigated. In the first mechanistic study, the aforementioned rate constants were examined at a constant temperature (298 K), iridium concentration (5.2 mM), and free substrate concentration (8.4 mM), with varying pressures of hydrogen. The effect of hydrogen pressure on exchange in $[Ir(H)_2(IMes)(pdz)_3]Cl$ is shown in Figure 62. The corresponding rate data is given in Appendix A, section A.1.9.

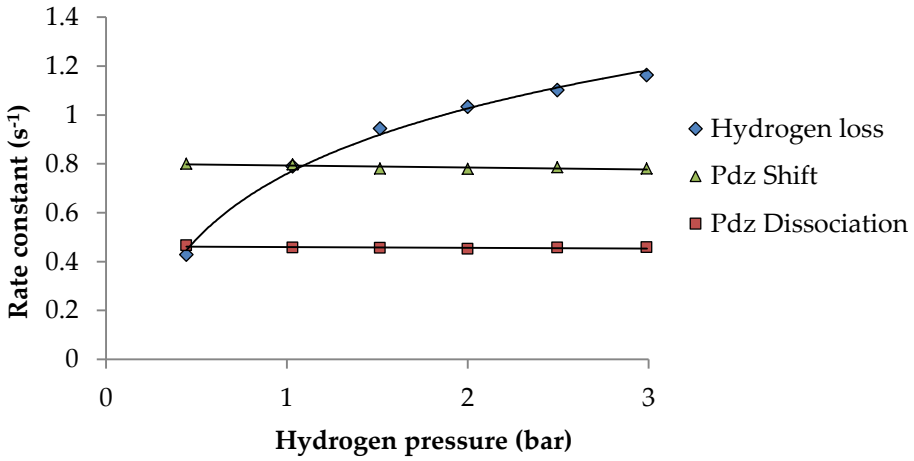

Figure 62: Graph to show the effect of hydrogen pressure on exchange rate constants in $[Ir(H)_2(IMes)(pdz)_3]Cl$.

Table 8: Concentrations of hydrogen gas in methanol, at the experimental pressures of hydrogen shown, at a constant temperature of 298 K.

H_2 pressure (bar)	Concentration of H_2 (mM)
0.445	1.47 ± 0.06
1.032	3.4 ± 0.1
1.515	5.0 ± 0.2
2.000	6.6 ± 0.3
2.495	8.2 ± 0.3
2.990	9.9 ± 0.4

The concentrations of hydrogen gas dissolved in methanol at the pressures studied are given in Table 8. These were calculated using the literature values published by Krüger *et al*.[199] A study by Michels *et. al.* demonstrated that the solubility of hydrogen increases linearly with pressure, in the regime used,[200] and therefore the concentrations can simply be scaled according to the pressure used.

At the lower hydrogen pressures used, the concentration of hydrogen in solution is less than the concentration of iridium, which is limiting the formation of $[Ir(H)_2(IMes)(sub)_3]Cl$, and therefore inhibiting the observed rate of hydrogen loss from this complex. As expected, an increase in the hydrogen pressure results in an increased rate of hydrogen dissociation; a higher concentration of hydrogen in solution promotes formation of $[Ir(H)_2(IMes)(sub)_3]Cl$, which in turn promotes hydrogen dissociation. As the hydrogen concentration in solution increases beyond the concentration of iridium (> 1.5 bar of hydrogen), the rate of hydrogen loss plateaus; the concentration of hydrogen is no longer the limiting factor in hydrogen loss. Interestingly, dissociation and haptotropic shifting of the *N*-heterocycle are entirely independent of the hydrogen pressure, which suggests that they are independent of hydrogen exchange.

In the second mechanistic study, the rate constants were examined at a constant temperature (285 K), iridium concentration (5.2 mM), and hydrogen pressure (3 bar), with varying concentrations of substrate. The corresponding rate data is given in Appendix A, section A.1.10. The effect of substrate concentration on exchange in $[Ir(H)_2(IMes)(pdz)_3]Cl$ is shown in Figure 63. The correlations are mirrored in $[Ir(H)_2(IMes)(phth)_3]Cl$.

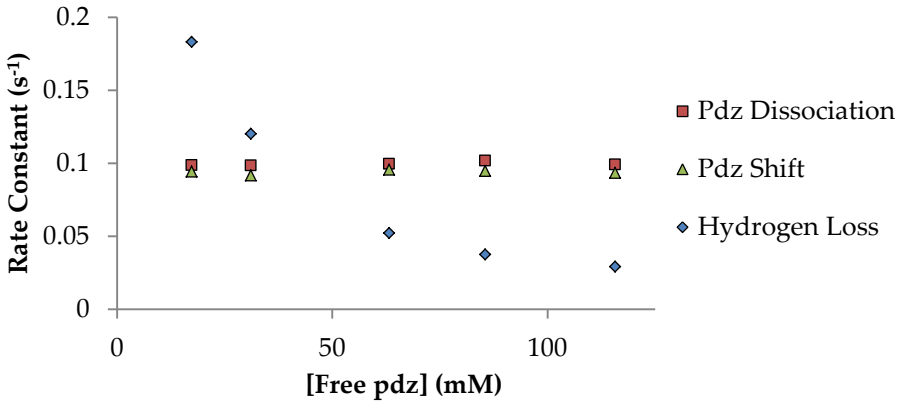

Figure 63: Graph to show the effect of substrate concentration on exchange rate constants in $[Ir(H)_2(IMes)(pdz)_3]Cl$.

Remarkably, the rate of hydrogen loss is inhibited by an increase in the concentration of free *N*-heterocycle in solution. This suggests that hydrogen loss occurs after dissociation or shifting of the *N*-heterocycle. DFT predictions for hydrogen exchange in the related pyridine system, $[Ir(H)_2(IMes)(py)_3]Cl$, propose the involvement of a dihydrogen-dihydride intermediate, $[Ir(H)_2(\eta^2\text{-}H_2)(IMes)(py)_2]Cl$.[149] To form this, a pyridine ligand must first dissociate from $[Ir(H)_2(IMes)(py)_3]Cl$, forming $[Ir(H)_2(IMes)(py)_2(sol)]Cl$, where sol is a stabilisng solvent molecule. A second hydrogen molecule then binds, displacing the solvent molecule, and then exchanges with the first hydrogen molecule. Excess *N*-heterocycle inhibits the formation of $[Ir(H)_2(\eta^2\text{-}H_2)(IMes)(sub)_2]Cl$, as $[Ir(H)_2(IMes)(sub)_2(sol)]Cl$ can reform $[Ir(H)_2(IMes)(sub)_3]Cl$ by reaction with the *N*-heterocycle.

Both the 1,2-metallotropic shifting and dissociation of the *N*-heterocycle are independent of the concentration of *N*-heterocycle in solution. All of the free substrate concentrations used were in excess of the iridium concentration, hence the free substrate concentration is not a limiting factor in *N*-heterocycle exchange.

The likely mechanism of substrate and hydrogen exchange is shown for $[Ir(H)_2(IMes)(pdz)_3]Cl$ (**A**) in Figure 64. Intermediates $[Ir(H)_2(IMes)(pdz)_2(sol)]Cl$ (**B**) and $[Ir(H)_2(\eta^2\text{-}H_2)(IMes)(pdz)_2]Cl$ (**C**) are short-lived, with unobservable NMR signals, thus it can be assumed that their concentrations in solution do not change. Steady-state principles can be applied to derive a rate law for the formation of **C**, which is a key step to hydrogen loss. This is shown below.

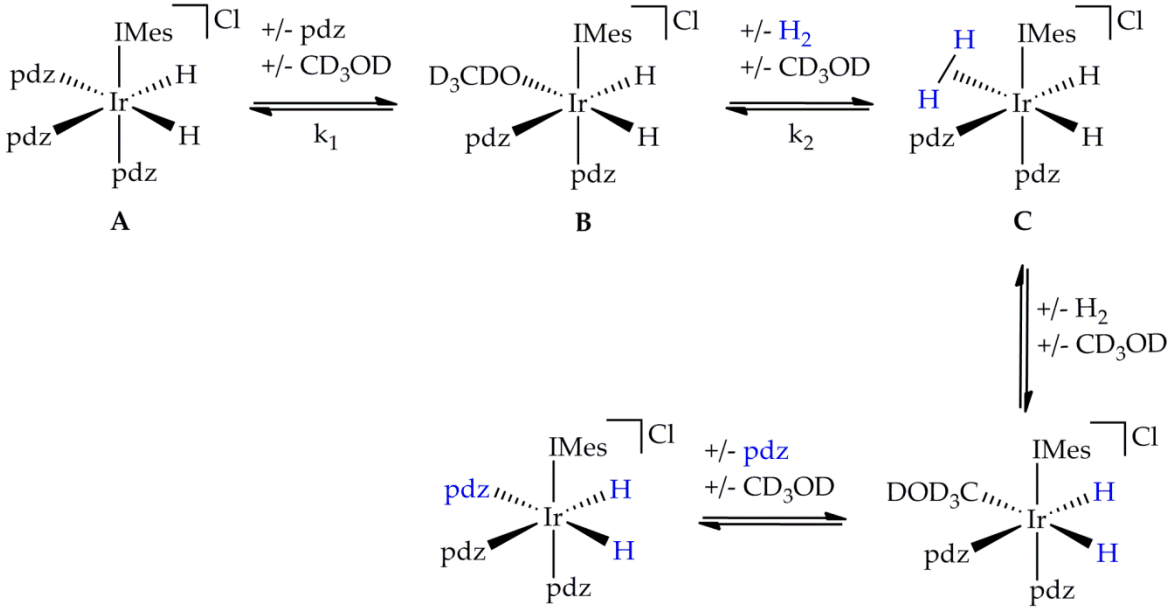

Figure 64: The substrate and hydrogen exchange mechanism in $[Ir(H)_2(IMes)(pdz)_3]Cl$.

$$\frac{\delta[\boldsymbol{C}]}{\delta t} = k_2[\boldsymbol{B}][H_2] - k_{-2}[\boldsymbol{C}] = 0$$

$$\frac{\delta[\boldsymbol{B}]}{\delta t} = k_1[\boldsymbol{A}] + k_{-2}[\boldsymbol{C}] - k_{-1}[\boldsymbol{B}][pdz] - k_1[\boldsymbol{B}][H_2] = 0$$

A rate law for the formation of **C** is shown below. The full derivation of this is given in Appendix A, section A.1.11. The formation of **C**, and therefore the rate of hydrogen loss, is proportional to the concentration of hydrogen, which reflects the increase in the observed rate of hydrogen loss with pressure, shown in Figure 62. The concentration of **C** is inversely proportional to the concentration of free pyridazine in solution, which reflects the inhibition of hydrogen loss with increasing concentration of *N*-heterocycle, shown in Figure 63.

$$[\boldsymbol{C}] = \frac{k_2 k_1[A][H_2]}{k_{-2} k_1[pdz]}$$

A plot of the reciprocal observed rate of hydrogen loss, as a function of free substrate concentration, is shown in Figure 65 and supports this rate law. Interestingly, hydrogen loss is inhibited to a greater extent by an increase in pyridazine concentration, rather than phthalazine, despite phthalazine being the more basic substrate.

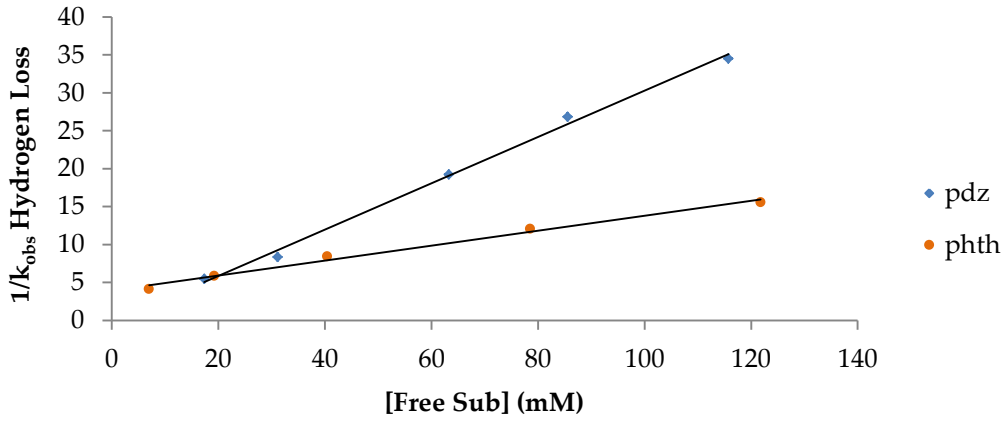

Figure 65: Graph to show the inversely proportional relationship between the observed rate of hydrogen loss, and the concentration of free substrate in solution in $[Ir(H)_2(IMes)(pdz)_3]Cl$ (pdz), and $[Ir(H)_2(IMes)(phth)_3]Cl$ (phth).

2.3.6 Competition Studies between Pyridazine and Phthalazine

To compare the reactivity of the iridium complexes that form with pyridazine and phthalazine, a d_4-methanol solution was prepared that contained approximately equal amounts of pyridazine and phthalazine (6.73 equivalents of phthalazine and 6.16 equivalents of pyridazine, measured by NMR). The [Ir(COD)(IMes)(pdz)]Cl and [Ir(COD)(IMes)(phth)]Cl complexes formed immediately, in a 1:3.71 ratio. When corrected for the slightly unequal proportions, this ratio becomes 1:3.40. As these two complexes are in equilibrium, the $\Delta G^{\ddagger}_{240\,K}$ value of this equilibrium can be calculated using the formula shown below, where K_{eq} is the equilibrium constant (taken as the ratio of the two complexes), R is the gas constant (8.314 $JK^{-1}mol^{-1}$), and T is the temperature (K).

$$\Delta G^{\ddagger} = -RT(lnK_{eq})$$

$\Delta G^{\ddagger}_{240\,K}$ for the conversion of [Ir(COD)(IMes)(pdz)]Cl to [Ir(COD)(IMes)(phth)]Cl is calculated to be −2.44 KJ mol^{-1}. The iridium complex with phthalazine is more stable than the pyridazine analogue, which reflects the more basic nature of phthalazine.[192]

Addition of hydrogen, at 240 K, results in the formation of $[Ir(COD)(H)_2(IMes)(pdz)]Cl$ and $[Ir(COD)(H)_2(IMes)(phth)]Cl$ in a ratio of 1:3.21 respectively, measured using the hydride signals in the ^1H NMR spectrum shown in Figure 66. $\Delta G^{\ddagger}_{240\,K}$ is equal to −2.33 kJ mol^{-1}.

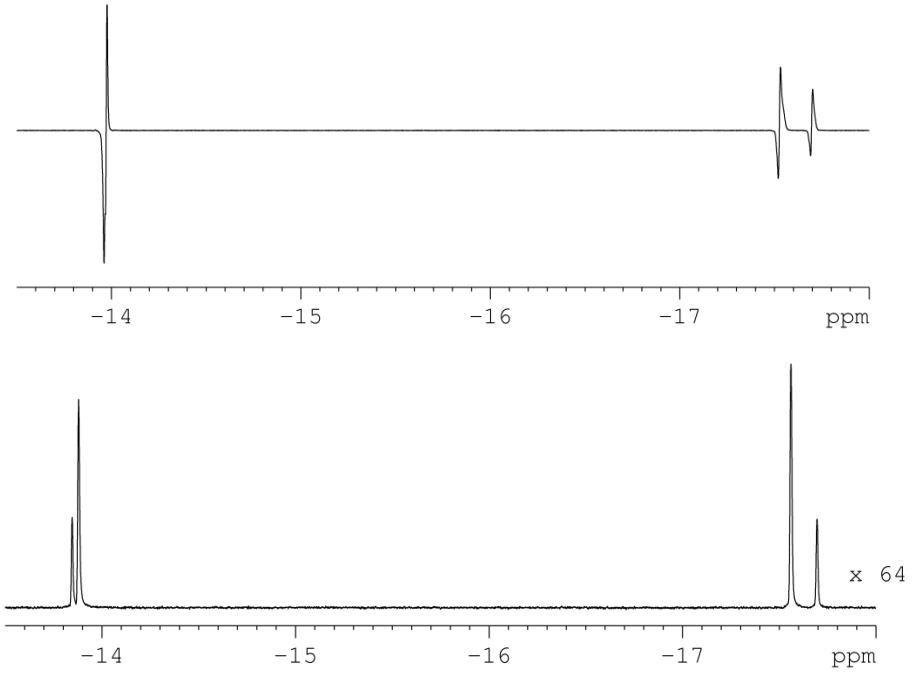

Figure 66: Hydride regions of ^{1}H NMR spectra of [Ir(H)$_2$(COD)(IMes)(sub)]Cl, comparing PHIP-enhanced signals (above) with thermal signals (below, magnified 64-fold. The larger signals at δ −13.88 and −17.56 correspond to [Ir(H)$_2$(COD)(IMes)(phth)]Cl and the smaller signals at δ −13.85 and −17.70 correspond to [Ir(H)$_2$(COD)(IMes)(pdz)]Cl.

On replacing hydrogen with *para*-H_2, the PHIP enhancements produced by this sample (at δ −17.55 for [Ir(COD)(H)$_2$(IMes)(phth)]Cl and −17.69 for [Ir(COD)(H)$_2$(IMes)(pdz)]Cl) are shown in Figure 66, and are 37.3-fold and 49.8-fold, respectively. The *para*-H_2 concentration in solution is constant, and [Ir(COD)(H)$_2$(IMes)(phth)]Cl is in a greater abundance (x 3.71). The rate of *para*-H_2 addition to [Ir(COD)(H)$_2$(IMes)(phth)]Cl must therefore be slower than the rate of addition to [Ir(COD)(H)$_2$(IMes)(pdz)]Cl, leading to proportionally smaller hydride enhancements, assuming their relaxations are equal.

Warming the solution up to 298 K resulted in the formation of the six iridium species shown in Figure 67. Due to overlapping NMR signals, these complexes have not been fully characterised, however, their hydride NMR signals are diagnostic (Figure 68). The two singlets at δ −21.10 and −21.38 are present in a ratio of 1:0.18, and correspond to species **d** and **a** respectively, which have already been fully characterised (see Experimental section E.3.3). The additional two singlets at δ −21.15 and −21.34 are present in a ratio of 0.90:0.20 with respect to **d**, and must correspond to species **c** and **f** respectively, as the hydride ligands in these species are chemically equivalent. As all

previous work has shown that phthalazine binds preferentially over pyridazine, it can be reasonably assumed that the signal at δ −21.15 corresponds to species **c** and the signal at δ −21.34 corresponds to species **f**. In addition to these singlets, four doublets are also present at δ −21.13, −21.17, −21.25, and −21.30. COSY NMR spectra contain cross peaks between the signals at δ −21.12 and −21.25 (J_{HH} = 8.1) and the signals at δ −21.17 and −21.30 (J_{HH} = 8.0). The two species are present in a ratio of 0.44:0.37, with respect to **d**. It is therefore likely that the former correspond to species **e** and the latter correspond to species **b**.

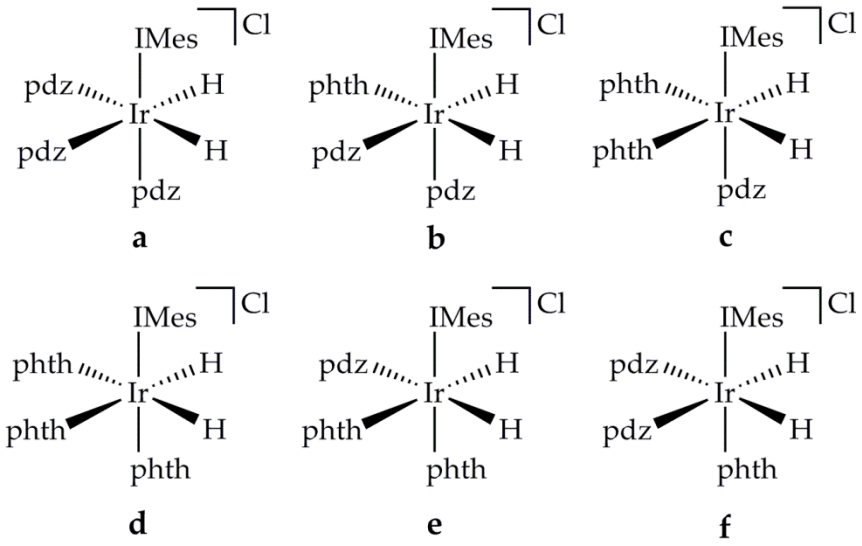

Figure 67: The six [Ir(H)$_2$(IMes)(sub)$_3$]Cl complexes that form with an excess of both free pdz and free phth in solution.

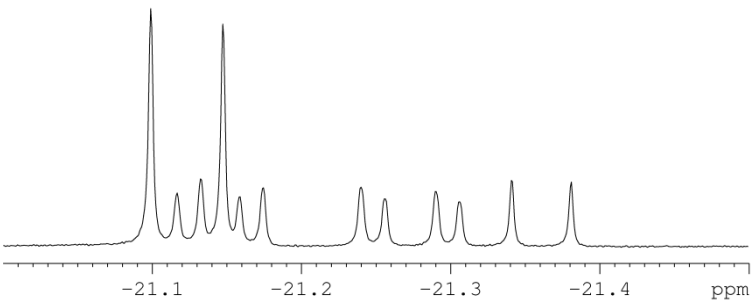

Figure 68: Hydride region of the ^{1}H NMR spectrum of [Ir(H)$_2$(IMes)(sub)$_3$], where sub = a combination of pdz or phth, resulting in the six complexes shown in Figure 67.

On replacing hydrogen with *para*-H_2, shaking the sample at ~ 65 G, and immediately collecting a ^{1}H NMR spectrum, dramatic signal enhancements of free pyridazine and phthalazine were observed as a result of SABRE. The enhancement factor of the signals

corresponding to the *ortho* protons of free phthalazine and pyridazine are 68-fold and 200-fold respectively. Despite the greater abundance of **d** and **c** with respect to **a** and **f**, and thus more bound phthalazine relative to pyridazine, the enhancements of the signals corresponding to free phthalazine are significantly lower than those corresponding to free pyridazine. This observation reflects the slower addition of *para*-H_2 to binding sites that lie *trans* to phthalazine, and the slightly larger $\Delta G^{\ddagger}$ for phthalazine dissociation, relative to pyridazine dissociation (Table 7).

2.4 Conclusion

The SABRE active catalysts $[Ir(H)_2(IMes)(sub)_3]Cl$, where sub is pyridazine or phthalazine, have been synthesised according to the route shown in Figure 69. This involved the immediate displacement of the chloride by the *N*-heterocycle to form [Ir(COD)(IMes)(sub)]Cl, followed by the oxidative addition of hydrogen over the C-Ir-pdz axis to selectively form the isomer of $[Ir(H)_2(COD)(IMes)(sub)]Cl$ shown in Figure 69. These complexes were stable at temperatures below 250 K, and their NMR signals could be fully assigned. This is the first example of the complete NMR characterisation of such SABRE-active intermediates. On replacement of the hydrides with *para*-H_2-derived hydrides, PHIP was observed in the ^1H NMR signals corresponding to the hydrides as well as the bound *N*-heterocycle and COD. No PHIP signals were observed for the second isomer shown in Figure 52, thus there is no evidence that this forms. Finally, hydrogenation of the COD at temperatures above 250 K formed $[Ir(H)_2(IMes)(sub)_3]Cl$, and COA.

Due to the more basic nature of phthalazine relative to pyridazine,[192] it binds preferentially to all of these iridium complexes and forms more stable complexes than with pyridazine. As a result, the rate of hydrogen addition to [Ir(COD)(IMes)(pdz)]Cl is faster than to [Ir(COD)(IMes)(phth)]Cl, and the rate of hydrogen addition to binding sites that lie *trans* to pyridazine is faster than to binding sites that lie *trans* to phthalazine. It is therefore likely that under the same conditions, pyridazine will become more polarised *via* SABRE than phthalazine, and its corresponding NMR signals will be enhanced to a greater degree.

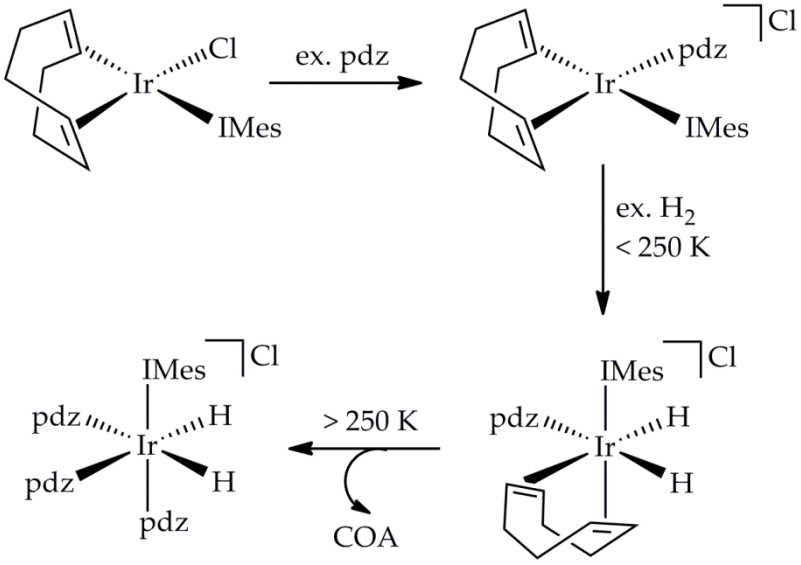

Figure 69: Synthetic pathway for the formation of the SABRE-active catalysts, showing $[Ir(H)_2(IMes)(pdz)_3]Cl$ as the example.

Both pyridazine and phthalazine undergo a haptotropic shift on the NMR timescale, the rates of which were analysed in the two temperature-stable complexes, [Ir(COD)(IMes)(sub)]Cl and $[Ir(H)_2(IMes)(sub)_3]Cl$. To the best of our knowledge, there are no other examples of the haptotropic shifting of pyridazine and phthalazine ligands in iridium complexes, and the effect of such a process on SABRE has not previously been explored. The haptotropic shifting of both substrates proceeded with similar Gibb's free energies of activation.

The bound pyridazine or bound phthalazine, in $[Ir(H)_2(COD)(IMes)(sub)]Cl$ and $[Ir(H)_2(IMes)(sub)_3]Cl$ exchange with the free substrate in solution. The bound hydrides also exchange with free hydrogen in solution. This results in both complexes being SABRE-active, however, it was only possible to analyse the substrate and hydrogen exchange in the temperature-stable $[Ir(H)_2(IMes)(sub)_3]Cl$. Substrate shifting and dissociation in this complex were found to be independent of the concentration of hydrogen and free substrate in solution. As with the haptotropic shift, dissociation of both substrates proceeded with similar Gibb's free energies of activation. Hydrogen dissociation, however, was found to be directly proportional to the concentration of hydrogen, and inversely proportional to the concentration of free substrate. This suggests that hydrogen dissociation proceeds after perturbation of the Ir-N bond (either by substrate dissociation or by a haptotropic shift), and the subsequent addition of a second hydrogen molecule.

Both $[Ir(H)_2(IMes)(sub)_3]Cl$ complexes promise to be useful as SABRE catalysts for the hyperpolarisation of pyridazine and phthalazine. These *N*-heterocycles are found as moieties in a number of drug molecules that could potentially be used as hyperpolarised MRI contrast agents. Optimisation of the enhancements of the proton NMR signals of free pyridazine and phthalazine, and their potential use as hyperpolarised MRI contrast agents is explored in Chapter 3.

3 Optimising SABRE of Pyridazine and Phthalazine

Optimising SABRE catalysis is essential for imaging applications so that large signals can be observed using minimal hyperpolarised agent. This reduces the possibility of negative symptoms in patients which result from contrast agent metabolism.[201] SABRE levels fluctuate according to a number of variables. As the enhancements are the result of reversible *para*-H_2 and substrate exchange at an iridium centre, ligand exchange rates play a significant role in controlling enhancement levels. As discussed in Chapter 2, exchange rates are dependent on the temperature, the concentration of catalyst, the ratio of catalyst to substrate, and the pressure of hydrogen.[145,149,150]

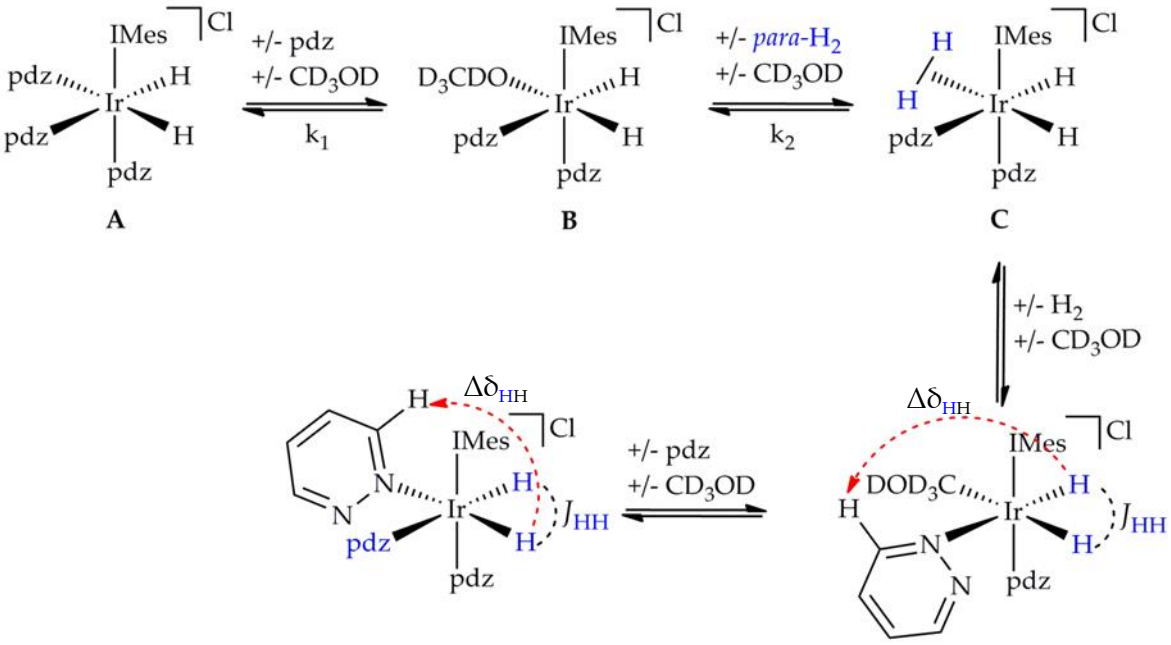

Figure 70: Mechanism of pyridazine and hydrogen exchange in d_4-methanol solutions of $[Ir(H)_2(IMes)(pdz)_3]Cl$ containing excess pyridazine and hydrogen. The same exchange mechanism is true for phthalazine exchange.

The mechanism of exchange of pyridazine or phthalazine and hydrogen at the iridium centre in the $[Ir(H)_2(IMes)(sub)_3]Cl$ catalysts was elucidated in the previous chapter and is shown in Figure 70. Hydrogen dissociation occurs after dissociation of the *N*-heterocycle, and is therefore inhibited by higher ratios of *N*-heterocycle:catalyst. Both higher hydrogen pressures and lower catalyst concentrations result in a larger ratio of hydrogen:catalyst in solution, thereby increasing the rate of hydrogen exchange. If faster hydrogen exchange

leads to larger SABRE enhancements then lower *N*-heterocycle ratios, lower catalyst concentrations, and higher hydrogen pressures will be favoured. Similarly, higher temperatures lead to faster *N*-heterocycle and hydrogen exchange, and may be favoured if faster exchange leads to larger signal enhancements.

Polarisation transfer from the *para*-H_2-derived hydrides to the protons on the *N*-heterocycle occurs *via* long-range $^4J_{HH}$ scalar coupling at low magnetic fields (~ 65 G).[157,160,163] The extent of polarisation transfer is dependent on the strength of the magnetic field. Surprisingly, the field strength that leads to optimum polarisation transfer is dictated by the $^2J_{HH}$ scalar coupling between the *para*-H_2-derived hydrides (J_{HH}), shown in Figure 70, and not the long-range $^4J_{HH}$ scalar coupling between the hydrides and the *N*-heterocycle protons.[146] Lowering the magnetic field strength results in smaller chemical shift differences between NMR signals due to the Zeeman effect, discussed in Chapter 1. Optimum polarisation transfer occurs at the magnetic field strength at which the chemical shift differences between the *para*-H_2-derived hydrides and the protons on the *N*-heterocycle ($\Delta\delta_{HH}$) match the $^2J_{HH}$ scalar coupling between the *para*-H_2-derived hydrides (J_{HH}), shown in Figure 70.[146]

Herein, all of the aforementioned variables will be investigated in order to optimise SABRE of pyridazine and phthalazine.

3.1 SABRE-active Complexes

Formation of SABRE-active complexes for the transfer of polarisation from *para*-H_2 to pyridazine and phthalazine, *via* the route shown in Figure 71, was discussed in the previous chapter. Although the intermediate $[Ir(H)_2(COD)(IMes)(sub)]Cl$ complexes (where sub is pyridazine or phthalazine) are SABRE-active, they are not stable at temperatures above 250 K, and are therefore not suitable as catalysts for this process.

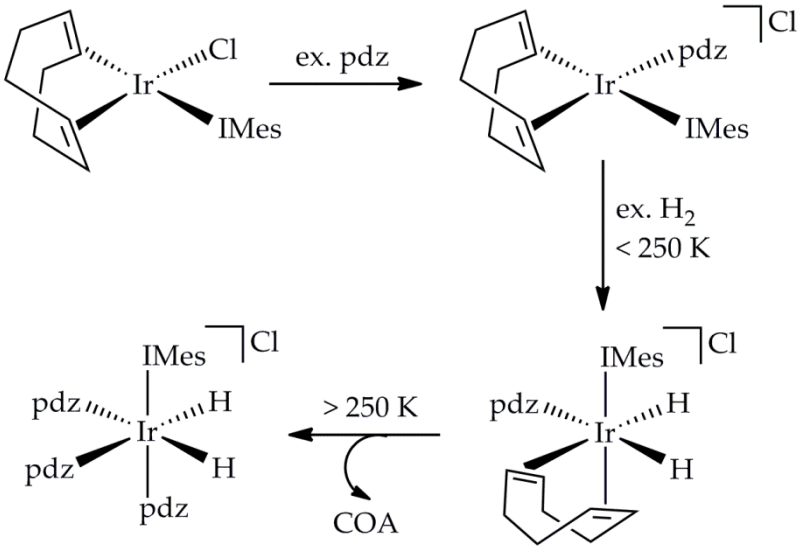

Figure 71: Synthetic pathway for the formation of the SABRE-active catalysts, showing $[Ir(H)_2(IMes)(pdz)_3]Cl$ as the example.

To test SABRE in d_4-methanol solutions of $[Ir(H)_2(IMes)(sub)_3]Cl$, containing excess substrate (7 equivalents), the hydrogen in solution was replaced with *para*-H_2. The solutions were then shaken at low magnetic field for 10 seconds, and a ^{1}H NMR spectrum was immediately acquired. Dramatic signal enhancements of the ^{1}H NMR resonances that correspond to both the bound (*) and free *N*-heterocycles (*) were observed. This is shown for $[Ir(H)_2(IMes)(pdz)_3]Cl$ in Figure 72 and $[Ir(H)_2(IMes)(phth)_3]Cl$ in Figure 73.

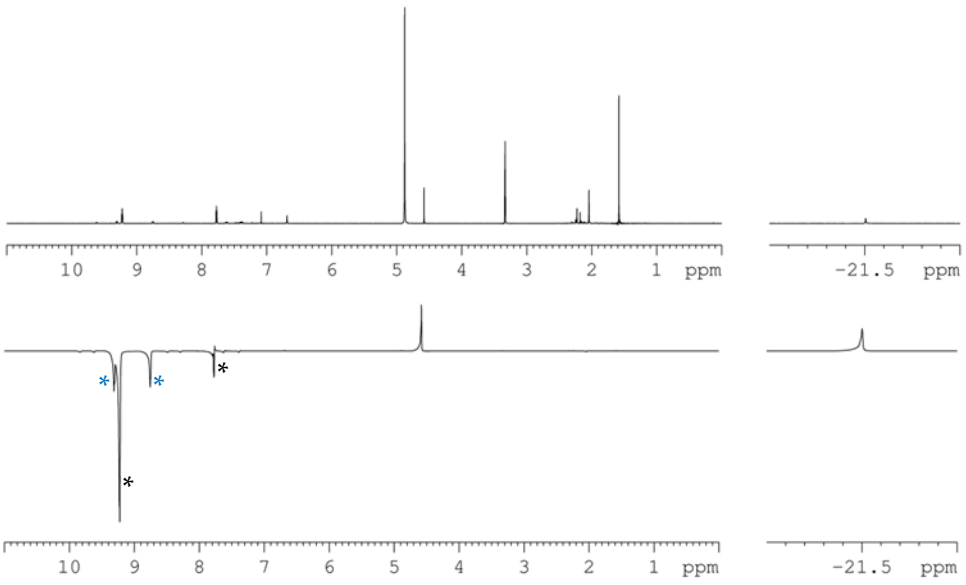

Figure 72: ^{1}H NMR spectra of $[Ir(H)_2(IMes)(pdz)_3]Cl$, comparing thermal signals (above) with SABRE-enhanced signals (below).

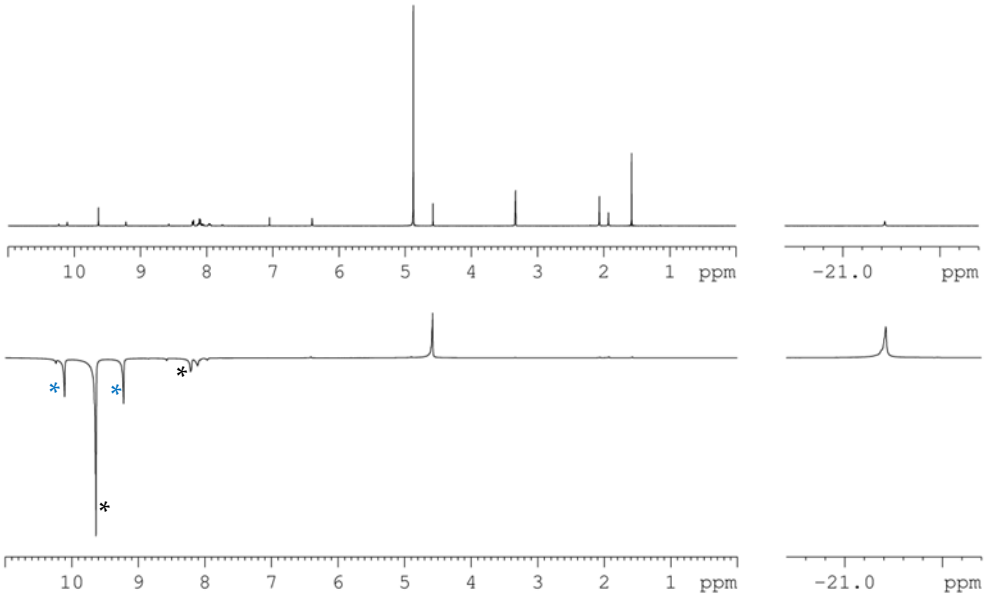

Figure 73: ^{1}H NMR spectra of [Ir(H)$_2$(IMes)(phth)$_3$]Cl, comparing thermal signals (above) with SABRE-enhanced signals (below).

SABRE-enhanced spectra of [Ir(H)$_2$(IMes)(pdz)$_3$]Cl (Figure 72) show enhanced emissive signals corresponding to free pyridazine in solution (NC**H** at δ 9.22, NCHC**H** at δ 7.77), as well as equatorially-bound pyridazine signals (IrNC**H** at δ 9.31, IrNNC**H** at δ 8.75). Enhancement factors of the two proton resonances of free pyridazine differ considerably; enhancement factors of the NC**H** resonance are consistently larger than those of the NCHC**H** resonance.

SABRE-enhanced spectra of [Ir(H)$_2$(IMes)(phth)$_3$]Cl (Figure 73) also show enhanced emissive signals, which correspond to free phthalazine in solution (NC**H** at δ 9.64, NCHCC**H** at δ 8.21, NCHCCHC**H** at δ 8.10), as well as equatorially-bound phthalazine signals (IrNC**H** at δ 10.12, IrNNC**H** at δ 9.23). Enhancement factors of the three proton resonances of free phthalazine also differ considerably; enhancement factors of the NC**H** resonance are consistently larger than those of the NCHCC**H** and NCHCCHC**H** resonances.

Enhanced absorptive signals corresponding to the *para*-H$_2$-derived hydride signals ([Ir(**H**)$_2$(IMes)(pdz)$_3$]Cl at δ −21.50, [Ir(**H**)$_2$(IMes)(phth)$_3$]Cl at δ −21.16), and dissolved hydrogen in solution (δ 4.58) are also observed. In order to optimise SABRE enhancements, efficient polarisation transfer from the *para*-H$_2$-derived hydrides, across the iridium catalyst, to the *N*-heterocycle is desirable. If this is the case, polarisation of the

hydride ligands will be minimal, resulting in hydride signals with small enhancement factors.

3.2 *J*-couplings in Pyridazine and Phthalazine

During SABRE, polarisation transfers from the *para*-H_2-derived hydrides to the substrate protons *via* long-range *J*-coupling. Unpublished work, in the Duckett group, on SABRE of pyridine using $[Ir(H)_2(IMes)(py)_3]Cl$ has revealed that at 65 G (the optimum polarisation transfer field for this substrate) the majority of polarisation transfers *via* $^4J_{HH}$ scalar coupling into the *ortho* protons of the *N*-heterocycle. Polarisation can then transfer from the *ortho* protons to the *meta* and *para* protons *via* $^3J_{HH}$ or $^4J_{HH}$ couplings. When the *ortho* and *para* protons are replaced with deuterium, which is not polarised *via* SABRE under the conditions used, the level of polarisation that transfers into the *meta* protons reduces to 18% of the original level. Furthermore, on replacing the *ortho* and *meta* protons with deuterium the level of polarisation that transfers into the *para* protons reduces to 0.3% of the original level. These data are given in Figure 74.

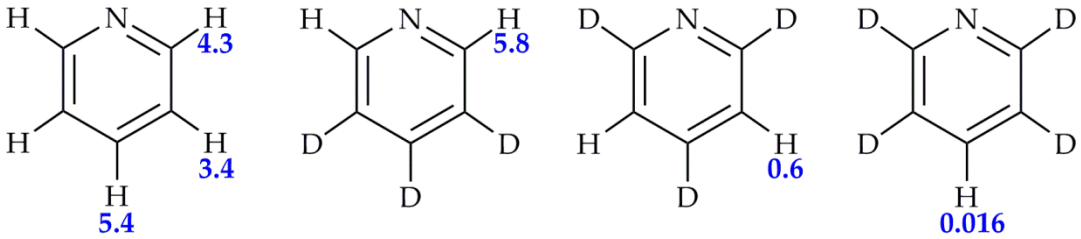

Figure 74: The percentage level of polarisation in the ortho, meta, and para protons of pyridine and its deuterated analogues, after SABRE with $[Ir(H)_2(IMes)(py)_3]Cl$ and 1 equivalent of pyridine. Courtesy of Ryan Mewis.

Polarisation transfer from the *para*-H_2-derived hydrides into the *ortho* protons of a substrate occurs whilst the substrate is bound to the iridium.[101] If the lifetime of the complex allows, polarisation can also transfer from the *ortho* protons to the other protons of the substrate whilst bound. However, the T_1 values of bound substrate protons are shorter than unbound substrate protons (~ 27.5 s for free pyridine and 3.6 s for bound),[163,202] therefore longer complex lifetimes lead to faster relaxation of the polarisation, and this is disadvantageous.

If the complex lifetime is shorter, polarisation transfer from the *ortho* protons to the other protons of the substrate is likely to occur after dissociation of the substrate. To better understand the enhancement levels in the individual proton resonances of dissociated pyridazine and phthalazine, the *J*-couplings between these resonances are required. Both *N*-heterocycles exhibit C_{2v} symmetry and as a result contain sets of two protons that are chemically equivalent, but magnetically inequivalent. This gives rise to second-order coupling constants. To calculate the coupling constants, the magnet inside the NMR spectrometer must be well-shimmed in order to resolve the splitting patterns in the ^{1}H NMR spectra.

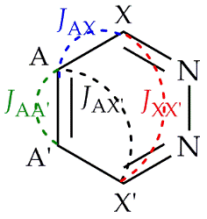

Figure 75: The four different coupling constants between the protons of pyridazine.

In pyridazine there are two chemically distinct proton resonances and both couple to each other. Both first and second order couplings give rise to four different coupling constants between the protons of pyridazine, $J_{AX} \equiv J_{A'X'}$, $J_{AX'} \equiv J_{A'X}$, $J_{AA'}$, and $J_{XX'}$ shown in Figure 75, which give rise to an AA'XX' splitting pattern. The splitting patterns of both proton resonances in pyridazine are identical and are shown for the signal at δ 7.77 (NCHC**H**) in Figure 76.

The Hamiltonian of an AA'XX' four-spin system has been solved by McConnell *et. al.*[203], who use 1,1-difluoroethylene as their example molecule. There are 10 distinct, allowed transitions between the spin states of an AA'XX' spin system, and they have been labelled in Figure 76. Transitions 1 and 2, 9 and 6, 7 and 12, and 3 and 4, are too similar in energy to be distinguished from one another. McConnell *et. al.* found a similar apparent degeneracy in their NMR spectra of 1,1-difluoroethylene.

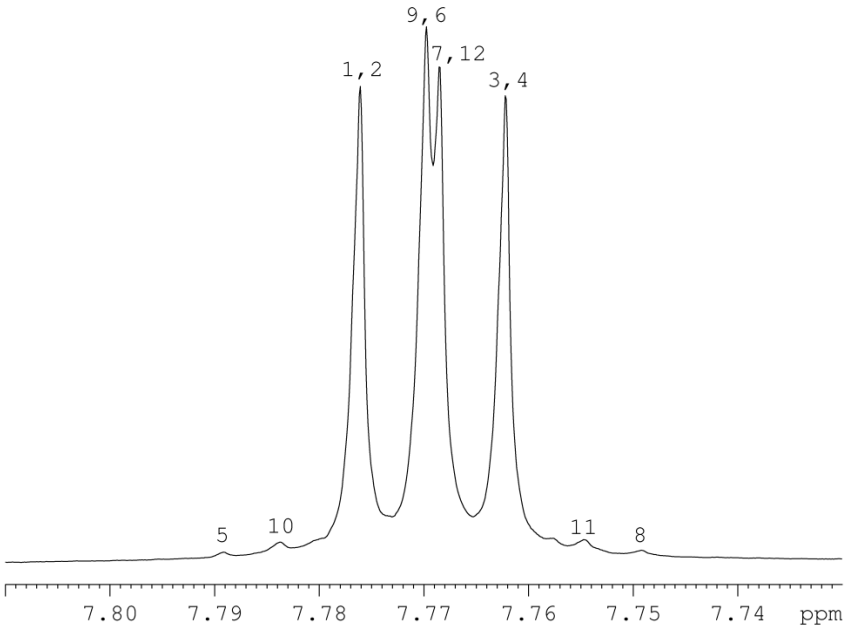

Figure 76: ^{1}H NMR resonance corresponding to NCHC<u>H</u> of free pyridazine.

The energies of the nuclear spin transitions are related to the coupling constants as shown in the formulae below. See Appendix A section A.2.1 for their derivation.

$$1 - 3 = J_{AX} + J_{AX'}$$

$$5 - 6 = J_{XX'} + J_{AA'}$$

$$6 - 8 = \sqrt{(J_{XX'} + J_{AA'})^2 + (J_{AX} - J_{AX'})^2}$$

$$10 - 9 = J_{XX'} - J_{AA'}$$

The transition frequency differences are calculated by simply measuring the difference, in Hz, between their NMR resonances. The above formulae can then be solved simultaneously to give the desired coupling constants. A full description of this is also given in Appendix A section A.2.1.

Table 9: The four coupling constants between the protons of pyridazine.

Coupling Constant	Frequency (Hz)
$J_{XX'}$	1.35
$J_{AA'}$	8.35
J_{AX}	5.22
$J_{AX'}$	1.73

The four coupling constants between the protons of pyridazine are given in Table 9. Predictably, as the number of bonds between the protons increases, the coupling constants decrease. The largest coupling therefore exists between protons A and A', which are connected by three bonds, and the smallest coupling exists between protons X and X', which are connected by five bonds. Polarisation from the *para*-H_2-derived hydrides most likely transfers to protons A and A' from the adjacent X and X' protons, respectively.

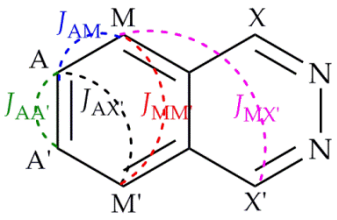

Figure 77: The five different coupling constants between the protons of phthalazine.

In phthalazine there are three chemically distinct proton resonances, which are also magnetically inequivalent due to second-order couplings. The NC**H** proton resonance at δ 9.56 (corresponding to protons X and X' in Figure 77) exhibits a small splitting of 0.43 Hz, shown in Figure 78. This is due to coupling to the NCHCC**H** protons (M' and M respectively) and is shown as $J_{MX'} \equiv J_{M'X}$ in Figure 77. The NCHCC**H** proton resonance at δ 8.12 is an AA'MM'-type multiplet but also exhibits small splittings of 0.43 Hz due to $J_{MX'}$ couplings. The NCHCCHC**H** proton resonance at δ 8.02 exhibits an AA'MM' splitting pattern, shown in Figure 78, due to the four couplings, $J_{AM} \equiv J_{A'M'}$, $J_{AM'} \equiv J_{A'M}$, $J_{AA'}$, and $J_{MM'}$, shown in Figure 77. There are no visible couplings to the NC**H** protons.

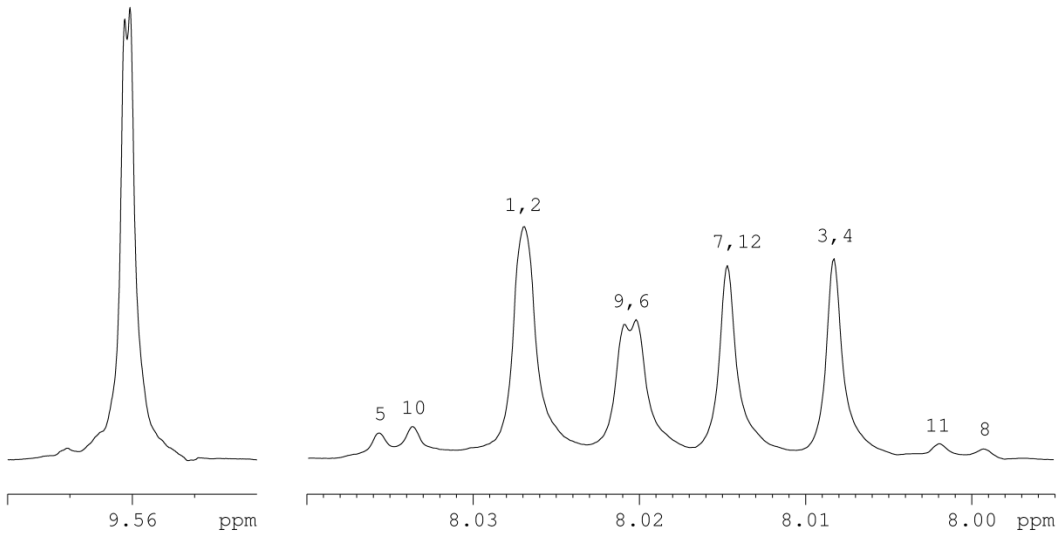

Figure 78: ^{1}H NMR resonances corresponding to NC<u>H</u> (left), and NCHCCHC<u>H</u> (right) of free phthalazine.

Akin to pyridazine, the transitions in the NCHCCHC**H** resonance of phthalazine, at δ 8.02, were used to calculate the four coupling constants of the AA'MM' spin-system. This is fully explained in Appendix A, and the values are given in Table 10.

Table 10: The five coupling constants between the protons of phthalazine.

Coupling Constant	Frequency (Hz)
$J_{MX'}$	0.43
$J_{MM'}$	0.7
$J_{AA'}$	7.05
J_{AM}	10.48
$J_{AM'}$	1.16

Again, as the number of bonds between the protons increases, the coupling constants decrease. The largest coupling constant is between protons A and M, which are connected by three bonds, and the smallest coupling exists between protons M and X', which are connected by five bonds. This small coupling of 0.43 Hz is all that connects the first and second rings of phthalazine to allow polarisation transfer. The polarisation that transfers from the *para*-H_2-derived hydrides to protons X and X' becomes almost 'trapped', resulting in consistently larger enhancements of the NC**H** protons of free phthalazine, and almost negligible enhancements on the NCHCC**H** and NCHCCHC**H** protons of the second ring.

3.3 Effect of Exchange Rates on SABRE

As previously discussed, exchange rates are dependent on the temperature, concentration of catalyst, ratio of catalyst to substrate, and pressure of hydrogen. The effect of these variables on the observed rate constants of hydrogen loss, *N*-heterocycle dissociation, and *N*-heterocycle haptotropic shifting has been thoroughly explored in Chapter 2. Herein, the effect of these variables on SABRE levels is explored.

3.3.1 Temperature

In a typical complex, an increase in temperature results in an increased rate of hydrogen and substrate exchange. Previous studies on SABRE enhancements of pyridine in d_4-methanol solutions of $[Ir(H)_2(IMes)(py)_3]Cl$, have shown an optimum rate of

exchange at 274 K, above which enhancement levels decrease.[149,150] This plateau reflects the optimum lifetime of the SABRE catalyst. At lower temperatures, the slower exchange rates reduce the amount of polarised pyridine that builds-up in solution. At higher temperatures, the faster exchange rates prevent efficient polarisation transfer from the polarised hydrides to the pyridine.

The optimum temperature for SABRE differs depending on the iridium exchange catalyst used, however, the optimum lifetime of the SABRE catalyst has also been shown to vary between 2 and 6 s (calculated as the inverse of twice the rate of pyridine dissociation).[150] Optimum catalyst lifetimes correspond to the inverse of the spin mixing frequency,[202] which is in turn proportional to $\frac{1}{2J_{HH}}$, where J_{HH} is the long-range $^4J_{HH}$ scalar coupling between the *para*-H_2-derived hydrides and the *ortho* protons on the substrate. A method to determine these $^4J_{HH}$ scalar couplings has recently been reported by Eshuis *et. al.*[204] The $^4J_{HH}$ coupling between the hydrides and *ortho* protons of pyridine in $[Ir(H)_2(IMes)(MeCN)(py)_2]Cl$ was reported to be 1.13 Hz, which corresponds to an optimum catalyst lifetime of approximately 2.3 s. Although this is optimised for a different, asymmetric SABRE catalyst, it is similar to the optimum lifetime of $[Ir(H)_2(IMes)(py)_3]Cl$ which is reported to be 2 s at 274 K.[150]

SABRE of the free pyridazine and phthalazine in d_4-methanol solutions of $[Ir(H)_2(IMes)(pdz)_3]Cl$ and $[Ir(H)_2(IMes)(phth)_3]Cl$, containing 3 bar of *para*-H_2, was investigated at temperatures ranging from 273 to 323 K. The results are shown in Figure 79 and Figure 80 and tabulated data with errors are in Appendix A, section A.2.2. They reveal that for both pyridazine and phthalazine, there is a continuous growth in hyperpolarisation level with increase in temperature up to 323 K, which is the safety limit in these measurements.

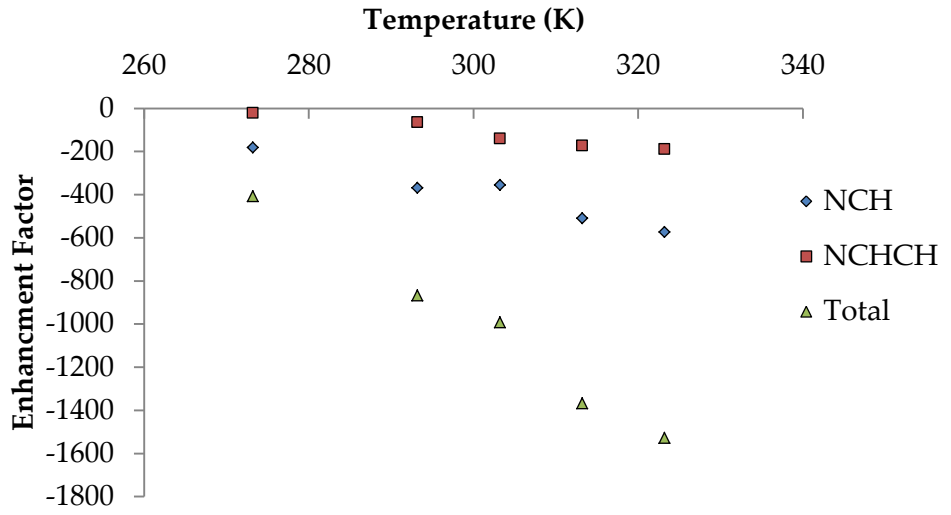

Figure 79: Graph to show the effect of temperature on SABRE of free pdz in d_4-methanol, using the $[Ir(H)_2(IMes)(pdz)_3]Cl$ exchange catalyst, with 12.3 mM free pdz.

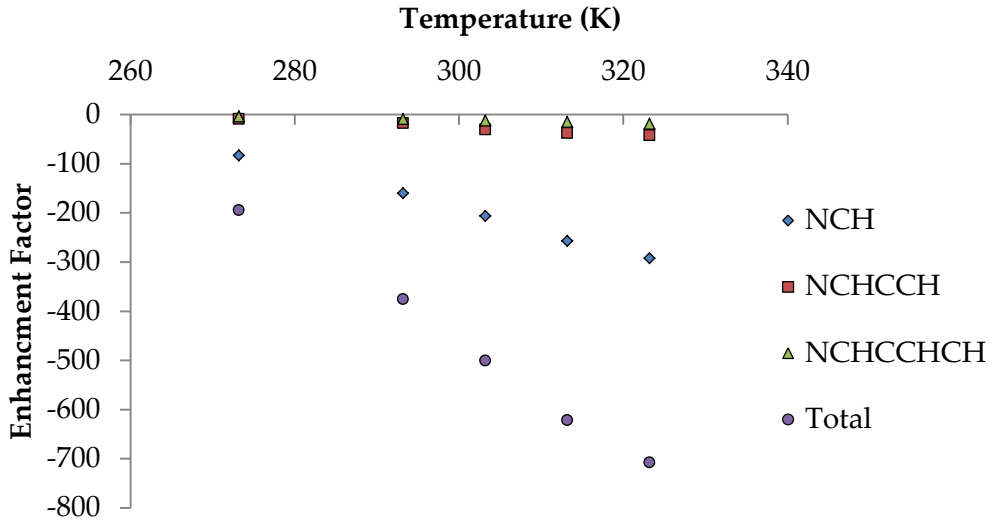

Figure 80: Graph to show the effect of temperature on SABRE of free phth in d_4-methanol, using the $[Ir(H)_2(IMes)(phth)_3]Cl$ exchange catalyst, with 14.1 mM free phth.

The lifetimes of the $[Ir(H)_2(IMes)(pdz)_3]Cl$ and $[Ir(H)_2(IMes)(phth)_3]Cl$ SABRE catalysts are calculated to be 0.05 and 0.08 s, at 323 K. As the enhancements are yet to reach a plateau at this temperature, the optimum complex lifetimes must be shorter than those reported for pyridine. This is likely to be due to the higher probability of the *N*-heterocycles undergoing a haptotropic shift (~ 55%), instead of dissociating to form free *N*-heterocycle (~ 45%), at these temperatures. Although the lifetime of the complex has technically terminated on perturbation of the Ir-N bond, a haptotropic shift allows further polarisation transfer into the second *ortho* proton (Figure 81). Without a haptotropic shift, the second *ortho* proton would receive very little polarisation directly from the polarised

hydrides, and the small J_{XX}, couplings (equal to 1.35 Hz for pyridazine and negligible for phthalazine) would limit further polarisation transfer between the *ortho* protons. The haptotropic shift is therefore beneficial to SABRE of pyridazine and phthalazine as it allows more polarisation to transfer to the protons of both *N*-heterocycles. Haptotropic shifting lowers the optimum lifetime of these SABRE catalysts relative to $[Ir(H)_2(IMes)(py)_3]Cl$.

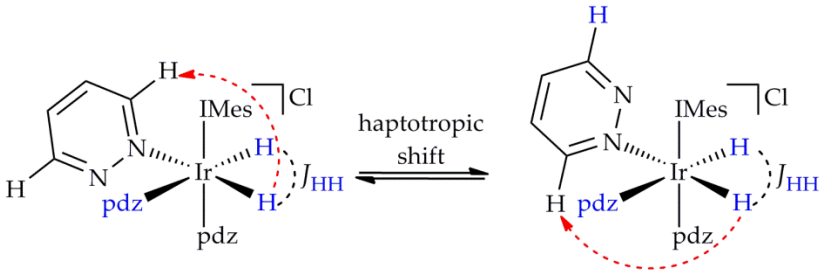

Figure 81: Further polarisation transfer from the para-H_2-derived hydrides to the ortho protons of pyridazine following a haptotropic shift. The same may also occur with phthalazine.

Furthermore, the long-range $^4J_{HH}$ couplings between the hydrides and *ortho* protons of pyridazine and phthalazine in these SABRE-active catalysts are unlikely to be identical to those reported for the pyridine analogue. Eshuis *et. al.* reported $^4J_{HH}$ values that varied from 0.61 Hz to 1.26 Hz for $[Ir(H)_2(IMes)(MeCN)(sub)_2]Cl$ complexes, where sub was equal to various *N*-heterocycles but not pyridazine or phthalazine. The method used by Eshuis *et. al.*, to determine $^4J_{HH}$ values, involved collecting *J*-modulated NMR spectra using SEPP (selective excitation of polarisation using PASADENA)[205] pulse sequences at low temperatures (268 K), where substrate dissociation rates were minimal and hydride T_2 values were suitably long.[204] The modulation of the NMR signal intensity as a function of the long-range $^4J_{HH}$ values could be isolated from the modulations caused by the $^2J_{HH}$ values, therefore this method could potentially be adapted to find the $^4J_{HH}$ values in the $[Ir(H)_2(IMes)(sub)_3]Cl$ complexes. Unfortunately, the equipment needed to acquire such data at low temperatures using an NMR flow system[163] is not currently available to us.

The correlations of the pyridazine and phthalazine ^{1}H NMR signal intensities as a function of temperature, appear to be linear. The gradients of the slopes fall with distance from the nitrogen ligation site. In pyridazine the gradients are −7.7 for NC**H**, and −3.7 for NCHC**H**, and for phthalazine they are −4.3 for NC**H**, −0.7 for NCHCC**H**, and −0.3 for

NCHCCHC**H**. This change mirrors the efficiency of their polarisation; at the polarisation transfer field used (65 G), transfer of polarisation into the remote protons in pyridazine and phthalazine occurs mainly *via* $^{3}J_{HH}$ and $^{4}J_{HH}$ scalar couplings to the NC**H** protons. The gradients shown for the pyridazine signals are larger than those for phthalazine due to the greater exchange rate sensitivity to temperature, discussed in Chapter 2, section 2.3.4.

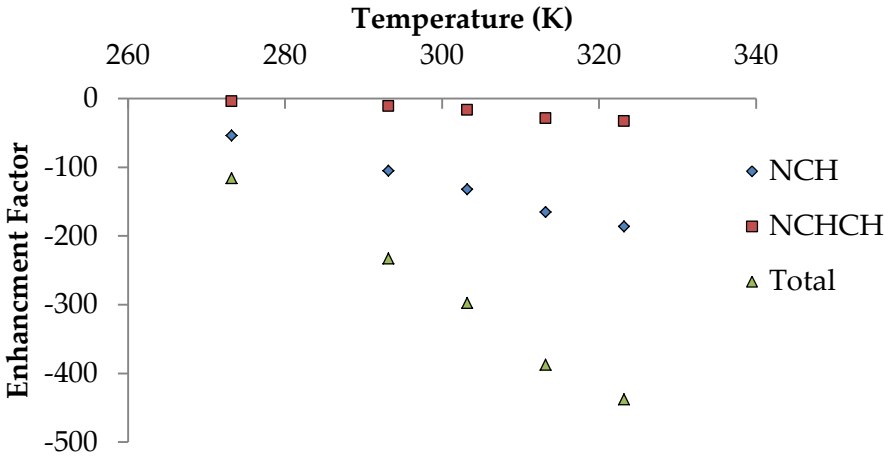

Figure 82: Graph to show the effect of temperature on SABRE of free pdz in d_4-methanol, using the $[Ir(H)_2(IMes)(pdz)_3]Cl$ exchange catalyst, with 75.1 mM free pdz.

A comparison of the plots in Figure 79 and Figure 82 reveals a drop in the sensitivity of pyridazine ^{1}H NMR signal enhancements with temperature as the substrate excess increases. The gradient of the slope corresponding to enhancements of the NC**H** signal falls from −7.7 to −6.6. This observation can be rationalised by the fall in hydrogen exchange rates with an increase in *N*-heterocycle concentration, which is also discussed in Chapter 2, section 2.3.5.

3.3.2 Concentration of *N*-heterocycle

The hydrogen exchange rates decrease with an increase in the concentration of *N*-heterocycle whereas dissociation and haptotropic shifting of the *N*-heterocycle are independent of *N*-heterocycle concentration. Previous studies on SABRE enhancements of pyridine in d_4-methanol solutions of $[Ir(H)_2(IMes)(py)_3]Cl$, have shown a drop in enhancement levels as the concentration of pyridine increases, although the effect differs depending on the iridium exchange catalyst used.[150]

SABRE of the free pyridazine and phthalazine in d_4-methanol solutions of $[Ir(H)_2(IMes)(pdz)_3]Cl$ and $[Ir(H)_2(IMes)(phth)_3]Cl$ (5.2 mM), containing 3 bar of *para*-H_2,

was investigated at 298 K, with *N*-heterocycle concentrations that varied from 17 to 122 mM. As with pyridine, enhancement factors of both the pyridazine and phthalazine proton resonances decrease as the *N*-heterocycle concentration increases, shown for pyridazine in Figure 83 and phthalazine in Figure 84, with tabulated data and errors given in Appendix A, section A.2.3. This decrease in enhancement factors is likely to be the result of slower hydrogen dissociation. At higher *N*-heterocycle concentrations, the amount of catalyst and *para*-H_2 in solution also becomes limiting and this may also contribute to the decrease in enhancement levels.

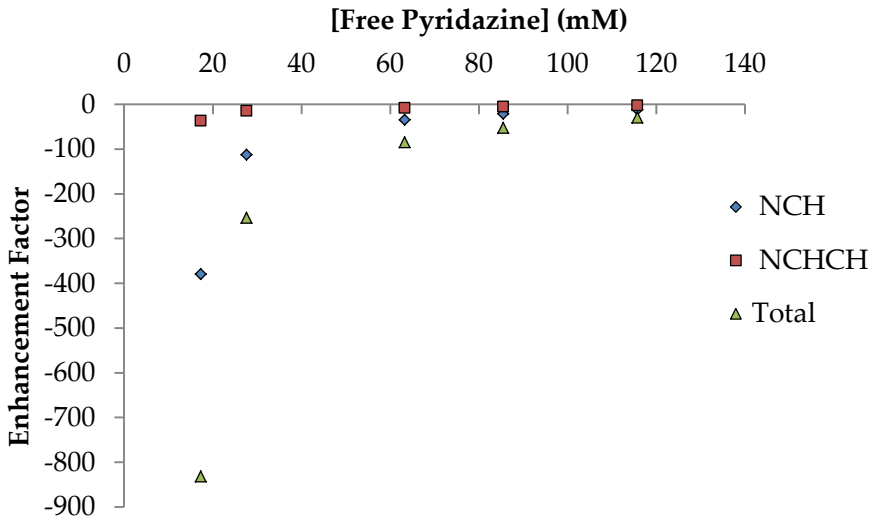

Figure 83: Graph to show the effect of pdz concentration on SABRE of free pdz in d_4-methanol, using the $[Ir(H)_2(IMes)(pdz)_3]Cl$ exchange catalyst.

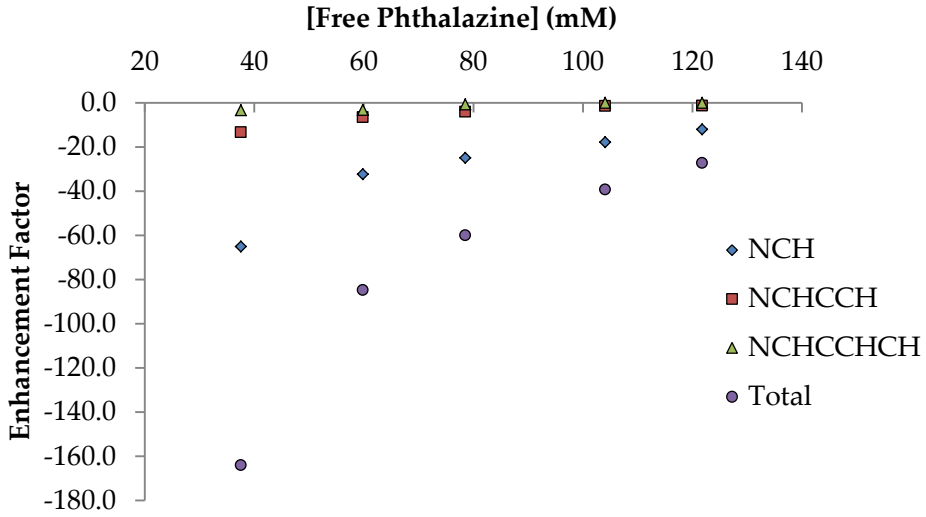

Figure 84: Graph to show the effect of phth concentration on SABRE of free phth in d_4-methanol, using the $[Ir(H)_2(IMes)(phth)_3]Cl$ exchange catalyst.

The rate of hydrogen loss is consistently slower than the sum of the rates of the *N*-heterocycle shift and *N*-heterocycle dissociation; hydrogen loss occurs after perturbation of the Ir-N bond of the *N*-heterocycle, as shown in Figure 70. As the rate of hydrogen loss slows, the frequency of oxidative addition of *para*-H_2 to the iridium centre is reduced therefore less polarisation is available to the bound *N*-heterocycles despite their dissociation rates remaining constant. A small excess of *N*-heterocycle (~ 5 equivalents) is optimum for SABRE. This is also beneficial for imaging applications, as minimal hyperpolarised contrast agent is desirable.

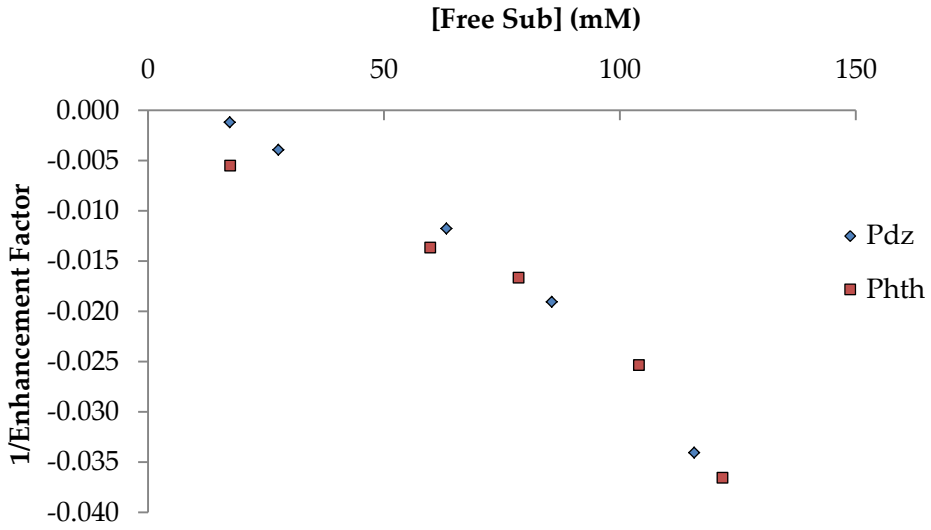

Figure 85: Graph to show the linear correlation between the N-heterocycle concentration and the reciprocal of the SABRE enhancements of free N-heterocycle.

A plot of the reciprocal enhancement factors as a function of the concentration of *N*-heterocycle shows a linear correlation to a point (approximately 80 mM), after which the enhancements tails off due to nuclear spin dilution, i.e. there is too much excess substrate so enhancements become limited by the amount of catalyst and *para*-H_2 present. This linear correlation mirrors the correlation between the reciprocal rate of hydrogen loss and the free substrate concentration, discussed in Chapter 2 section 2.3.5, and highlights the importance of fast rates of hydrogen exchange at the iridium centre for SABRE.

3.3.3 Catalyst Concentration

The effect of *N*-heterocycle concentration on SABRE enhancements has been rigorously studied however, the enhancements observed with different concentrations of SABRE catalyst also differ. Previous studies on SABRE enhancements of pyridine in d_4-

methanol solutions of $[Ir(H)_2(IMes)(py)_3]Cl$ have shown large proton enhancements at low catalyst concentrations, due to a higher proportion of *para*-H_2:catalyst in solution. However, these enhancements sharply drop on lowering the catalyst concentration below 2.5 mM, as the catalyst concentration now limits SABRE.[150]

The concentration of $[Ir(H)_2(IMes)(pdz)_3]Cl$, with 4.07 equivalents of free pyridazine in solution, was lowered by repeatedly taking aliquots and diluting with known quantities of d_4-methanol. In this way, the ratio of complex:free pyridazine remained constant, but their concentrations were reduced. The resulting enhancements and signal-to-noise ratios (SNRs) are given in Figure 86. Again, tabulated data with errors are given in Appendix A, section A.2.4.

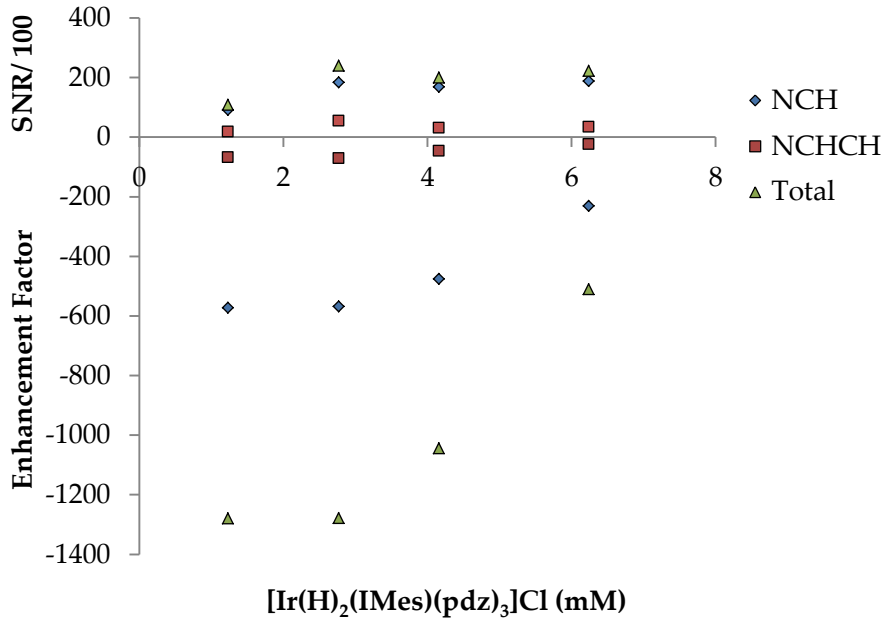

Figure 86: Graph to show the enhancement factors and SNRs (which have been divided by 100) of the proton resonances of free pyridazine, as a function of $[Ir(H)_2(IMes)(pdz)_3]Cl$ concentration.

Hyperpolarisation levels increase considerably, as the sample becomes less concentrated, due to a greater ratio of *para*-H_2:$[Ir(H)_2(IMes)(pdz)_3]Cl$ in solution. The mechanism of pyridazine and hydrogen exchange in $[Ir(H)_2(IMes)(pdz)_3]Cl$ is shown in Figure 70. From this mechanism, a formula was derived in Chapter 2 section 2.3.5, for the concentration of intermediate **C**, $[Ir(H)_2(\eta^2\text{-}H_2)(IMes)(pdz)_2]Cl$, which is a key intermediate required for SABRE:

$$[\boldsymbol{C}] = \frac{k_2 k_1 [A][H_2]}{k_{-2} k_1 [pdz]}$$

The formation of **C** is promoted at higher concentrations of *para*-H_2, thus SABRE enhancements are larger when the ratio of *para*-H_2:$[Ir(H)_2(IMes)(pdz)_3]Cl$ is higher. This effect tails off at lower concentrations, however, where the concentration of $[Ir(H)_2(IMes)(pdz)_3]Cl$ becomes the limiting factor. As the above formula shows, the formation of **C** is also promoted at higher concentrations of **A,** $[Ir(H)_2(IMes)(pdz)_3]Cl$. The results presented here differ from those published using pyridine, where optimum enhancements were achieved using a $[Ir(H)_2(IMes)(py)_3]Cl$ concentration of 5 mM, below which enhancement factors quickly dropped.[150] In this case, a metal concentration of 2.8 mM is optimal, with the maximum total enhancement observed for pyridazine being 1278-fold. This is a huge improvement on the 511-fold enhancement observed with no dilution. The repercussions are that a more dilute catalyst and substrate solution leads to far better enhancements, which is very beneficial for *in vivo* studies.

Usually, the SNR associated with a given resonance is proportional to concentration. Here, however, the SNR is linked to both the concentration and the SABRE level. There was no obvious change in the detected signal strength of the proton resonances in pyridazine for samples lying between 2.8 mM and 6.2 mM. There is therefore no benefit to working at higher concentrations, even if there is an abundance of available substrate, since the fall in SABRE level offsets the gain in signal.

3.4 Effect of Polarisation Transfer Field on SABRE

As discussed earlier, optimum polarisation transfer occurs at the magnetic field strength at which the chemical shift differences between the *para*-H_2-derived hydrides and the protons on the *N*-heterocycle match the $^2J_{HH}$ scalar coupling between the *para*-H_2-derived hydrides.[146] The chemical shift differences are dependent on the strength of the magnetic field experienced by the SABRE-active complex during polarisation transfer.[149,150] Chemical shift differences ($\Delta\delta_{HH}$) are larger in stronger magnetic fields as a result of the Zeeman effect, illustrated both in Figure 87 and in the equation given below, where ω is the operating frequency (MHz), γ is the gyromagnetic ratio ($MHzT^{-1}$), and B_0 is the applied magnetic field strength (T).[206]

$$\omega = \gamma B_0$$

At high-field, for example inside a 500 MHz spectrometer, the field strength is equal to 117,400 G. At this field, $\Delta\delta_{HH}$ (~ 30 ppm) is equal to 15,000 Hz, which is far from the value of $^{2}J_{HH}$, estimated to be approximately 5-10 Hz.[146,155] At lower magnetic fields, $\Delta\delta_{HH}$ is reduced, and is equal to approximately 8 Hz at 65 G, thus 65 G is often found to be the optimum polarisation transfer field for proton polarisation.[150,163] Polarisation transfer to heteronuclei requires even lower magnetic fields, for example the chemical shift differences between ^{1}H and ^{13}C nuclei inside a 500 MHz spectrometer are equal to approximately 374 MHz. To reduce this difference to 5-10 Hz, magnetic fields in the order of mG have to be used,[155,156] and the sample requires shielding from the Earth's magnetic field.

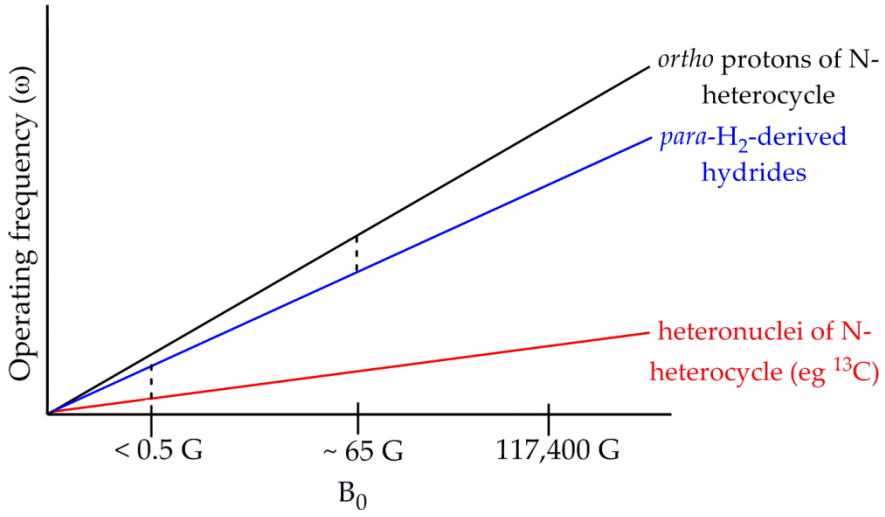

Figure 87: Diagram to show the increase in energy difference, and thus chemical shift difference with increasing magnetic field for two spin ½ nuclei.

Previous research by Dücker *et. al.*[207] has investigated the effect of the *N*-heterocycle structure on the relationship between polarisation transfer field (PTF) and enhancement. It was observed that the shape of plots of proton enhancement as a function of PTF were only weakly dependent on the structure of the *N*-heterocycle, but very strongly dependent on the J_{HH} scalar coupling between the *para*-H_2-derived hydrides and the closest substrate proton. Substrates, like pyridine and pyrazole, with a $^{4}J_{HH}$ coupling between the hydrides and the *ortho* substrate protons exhibit similar relationships between the PTF and the enhancement factors, whereas substrates like 3,5-dimethylpyrazole, with a $^{5}J_{HH}$ coupling, exhibit different relationships and require stronger PTFs for optimum polarisation transfer.[208]

3.4.1 Spin States in Pyridazine and Phthalazine

The different longitudinal spin states generated by SABRE of pyridazine and phthalazine can be selectively probed using the 'only *para*-H_2 spectroscopy' (OPSY) protocol, where only PHIP-derived signals are observed and thermal signals are suppressed.[209] For pyridazine, longitudinal spin states generated by SABRE are exemplified by four one-spin order combinations (I_z^A, $I_z^{A'}$, I_z^X, $I_z^{X'}$), four two-spin order combinations ($I_z^A I_z^{A'}$, $I_z^X I_z^{X'}$, $I_z^A I_z^X$, $I_z^A I_z^{X'}$), two three-spin order combinations ($I_z^{A'} I_z^A I_z^X$, $I_z^A I_z^X I_z^{X'}$) and one four-spin order term ($I_z^A I_z^{A'} I_z^X I_z^{X'}$), see Figure 75. In phthalazine, the coupling between the first and second rings is negligible (0.43 Hz), and the two rings can be considered as separate coupling systems. There are six one-spin order combinations (I_z^A, $I_z^{A'}$, I_z^M, $I_z^{M'}$, I_z^X, $I_z^{X'}$), four two-spin order combinations ($I_z^A I_z^{A'}$, $I_z^M I_z^{M'}$, $I_z^A I_z^M$, $I_z^A I_z^{M'}$), two three-spin order combinations ($I_z^{A'} I_z^A I_z^M$, $I_z^A I_z^M I_z^{M'}$) and one four-spin order term ($I_z^A I_z^{A'} I_z^M I_z^{M'}$), see Figure 77. Further details of the experimental methods used for magnetic state interrogation can be found in Appendix A, section A.2.5.

3.4.2 Effect of Polarisation Transfer Field on SABRE of Select Spin States of Pyridazine and Phthalazine

Thus far, the variables investigated have affected the exchange rates, which have in turn affected signal enhancements of all spin states, unselectively. Each spin state lies at a different energy, which is dependent on the magnetic field strength applied (see Figure 87). A change in the magnetic field experienced by the iridium exchange catalyst during polarisation transfer, from the *para*-H_2-derived hydrides to the *N*-heterocycle, will therefore change the relative energies of the spin states and influence their degree of polarisation.

A flow system was used to investigate the influence of the PTF on the SABRE enhancement levels in specific spin states of pyridazine and phthalazine.[163] For this, d_4-methanol solutions of $[Ir(H)_2(IMes)(sub)_3]Cl$, containing ~ 5 equivalents of free *N*-heterocycle were used. The PTF experienced by the sample was increased from 0 (Earth's field = ~ 0.5 G) to 140 G in 10 G intervals. If an enhancement maximum was apparent, the magnetic fields around the position of the maximum were investigated to find the true maximum. Calculations of enhancements for each probed state are explained in detail in Appendix A, section A.2.6.

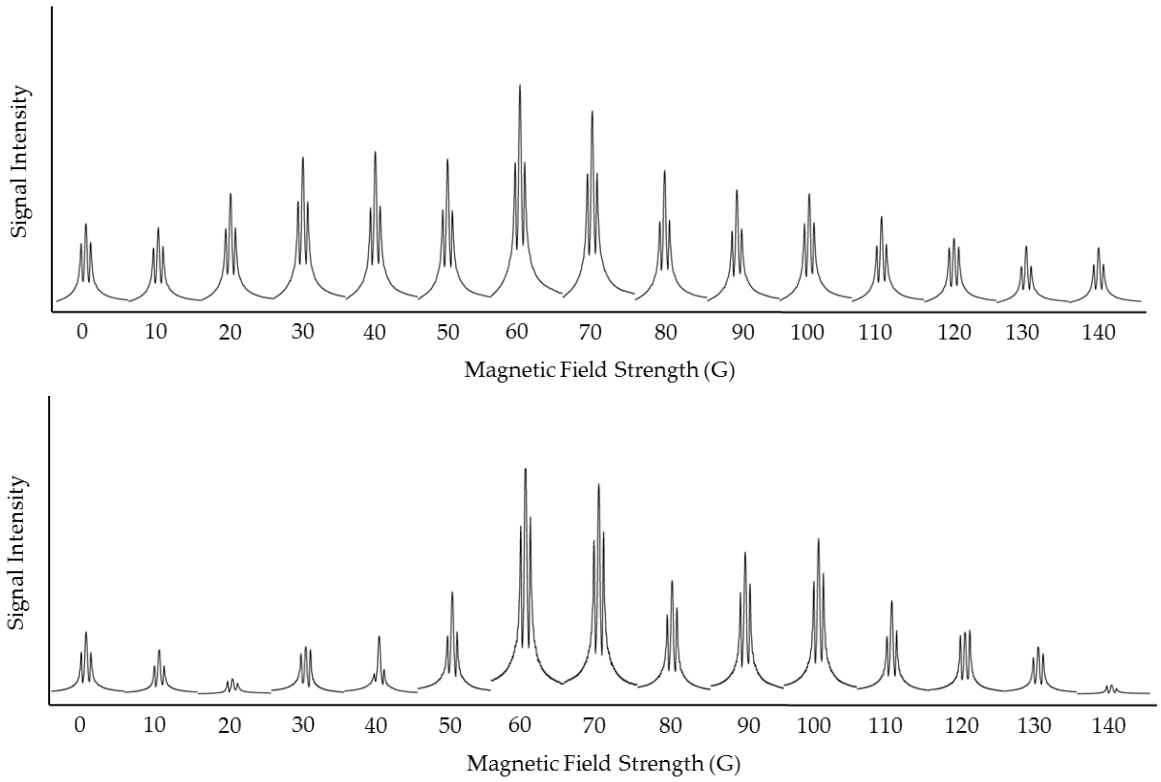

Figure 88: Effect of the polarisation transfer field on the SABRE signal enhancements of the NC<u>H</u> (above) and NCHC<u>H</u> (below) proton resonances of pyridazine.

The influence of the PTF on the single quantum signal enhancements of the NC**H** and NCHC**H** protons of free pyridazine are shown in Figure 88. Both signals exhibit optimised signal enhancements at 65 G, which is typical of such *N*-heterocycles.[157,160,163,207] The total signal enhancements for the single quantum states are also maximised at 65 G, shown in Figure 89. The single quantum states give rise to the most signal and their optimisation takes preference for imaging applications. Signal enhancements in pyridazine are therefore optimised with a PTF of 65 G.

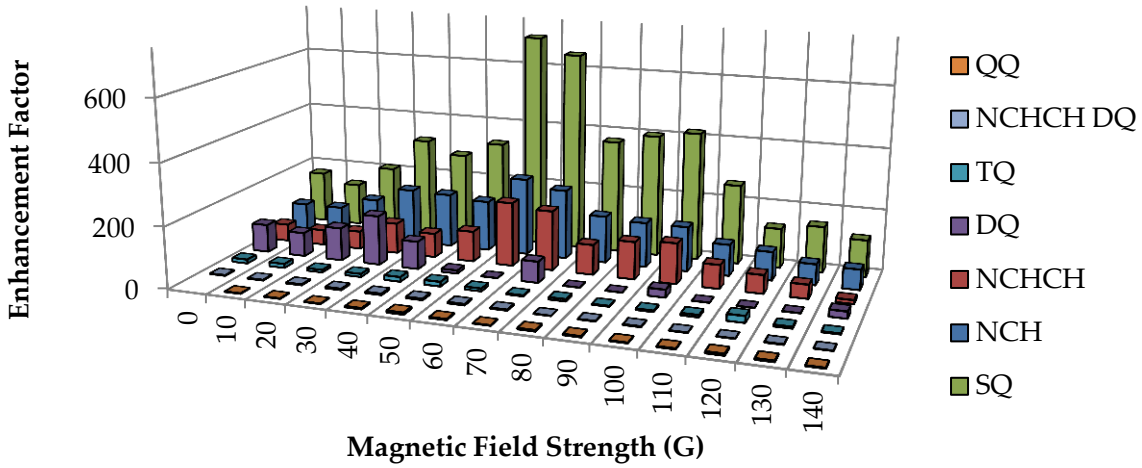

Figure 89: Effect of the polarisation transfer field on the SABRE signal enhancements of select spin states of pyridazine, where SQ = single quantum, DQ = double quantum, TQ = triple quantum, QQ = quadruple quantum.

Interestingly, SABRE enhancements of the double, triple, and quadruple quantum states of pyridazine are optimised with different PTFs as these states are preferentially populated at different fields. Producing a theoretical model of polarisation transfer to the different states of pyridazine at different magnetic fields is complex, and requires the inclusion of the two hydrides of the SABRE-active complex, in addition to the four protons of bound pyridazine. This is beyond the scope of this thesis. Three-spin and four-spin theoretical models that include the *para*-H_2-derived hydrides and one or two *ortho* substrate protons have been reported.[146,210,211] In these models, the effect of the PTF on the resulting single quantum states are considered, however, higher-order terms are not included. When using a flow system, the polarised sample experiences a range of different magnetic fields as it is shuttled from the fixed magnetic field in the reaction chamber, into the NMR spectrometer. This has not yet been accounted for in any of the existing theoretical SABRE models and further complicates comparisons of experimental data with theory.

The signal enhancements of the double, triple, and quadruple quantum states are much smaller due to their smaller populations. The double quantum transitions give optimum enhancements at 40 G, with a second smaller maximum at 70 G. The double quantum NCHC**H** state ($I_z^A I_z^{A'}$), shown in Figure 90, exhibits a similar profile to that of the total double quantum transitions, however optimum enhancements are at 50 G, with a second smaller maximum at 100 G. The triple quantum transitions give optimum signal enhancements at 120 G, with a smaller maximum at 40-50 G, and the quadruple quantum

transitions give optimum signal enhancements of almost equal intensity at 50 and 120 G. Interestingly, the NMR signal resulting from these higher order terms is minimised at 65 G, which is the field used to optimise single quantum NMR signals.

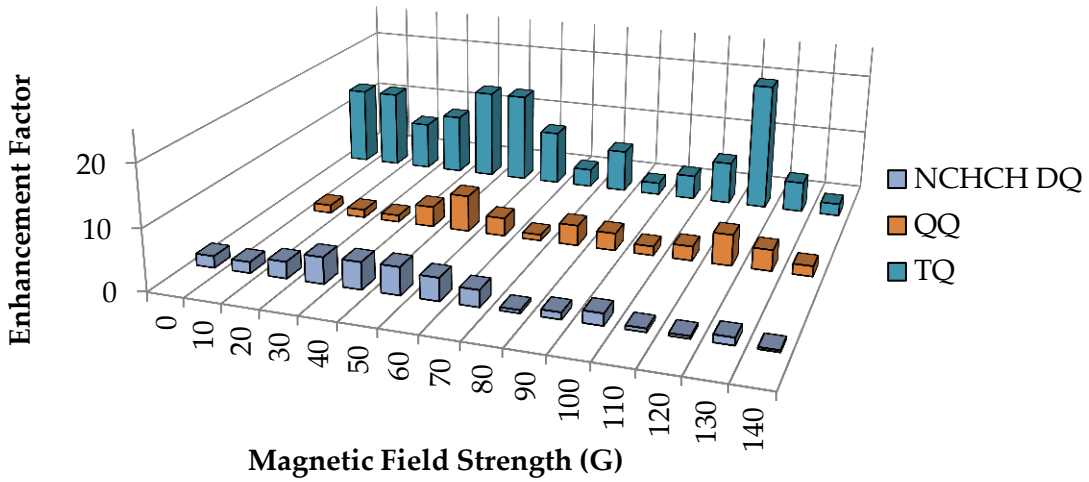

Figure 90: Effect of the polarisation transfer field on the SABRE signal enhancements of select spin states of pyridazine, where DQ = double quantum, TQ = triple quantum, QQ = quadruple quantum.

The effect of the PTF on the single quantum signal enhancements of the NC**H**, NCHCC**H**, and NCHCCHC**H** proton resonances of phthalazine are shown in Figure 91. As with pyridazine, all the proton resonances exhibit similar profiles, with maximum signal enhancements obtained at 65 G. The total signal enhancements for the single quantum states are also maximised at 65 G, shown in Figure 92, and give rise to the most signal.

The enhancement factors of the individual proton resonances of phthalazine decrease dramatically on going from the first ring (NC**H**) to the second ring (NCHCC**H**, NCHCCHC**H**, also shown in Figure 93), due to the weak coupling between the rings (0.43 Hz). This limited polarisation transfer resulted in no observable ^{1}H NMR signals for the triple quantum and quadruple quantum states.

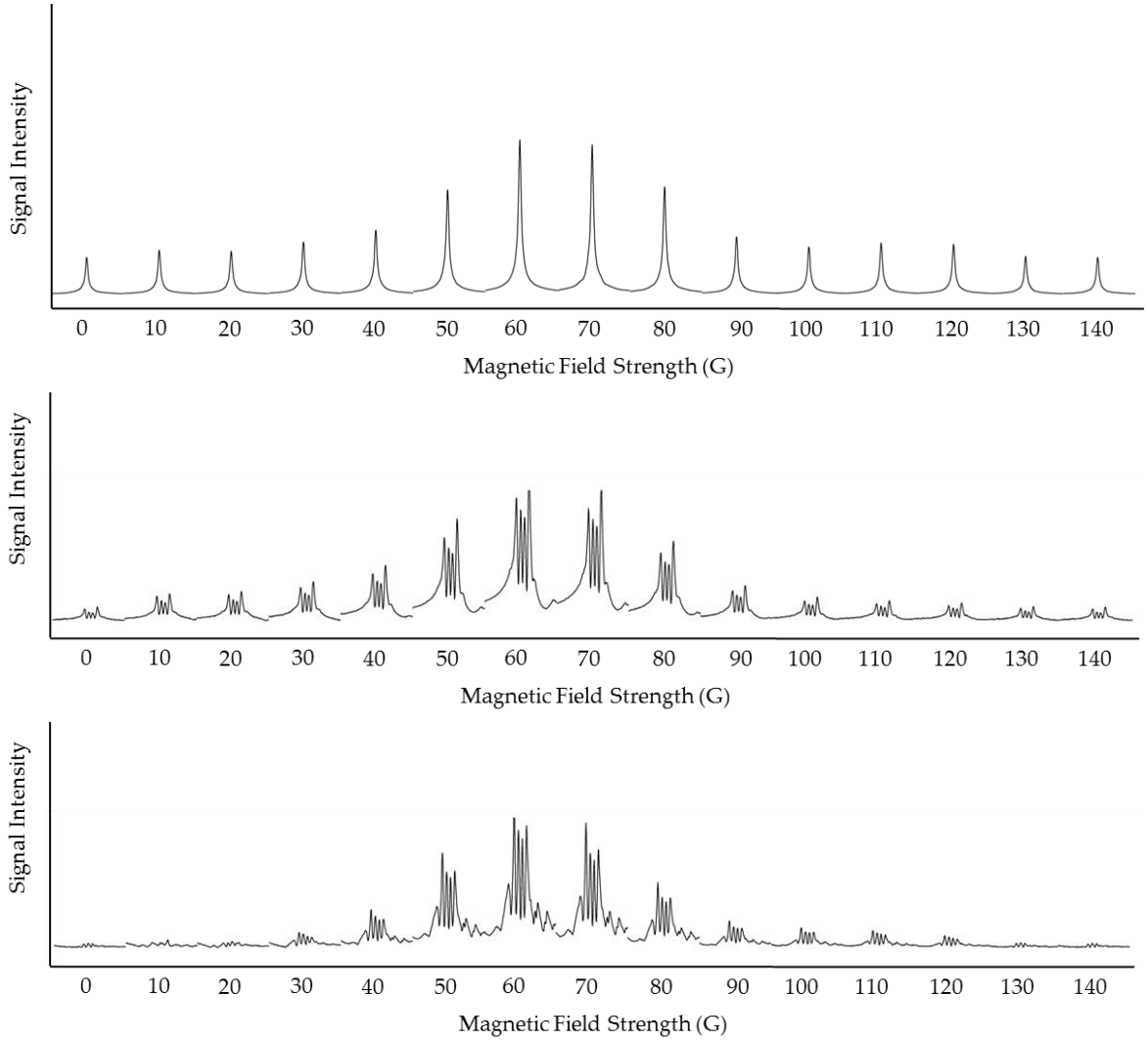

Figure 91: Effect of the polarisation transfer field on the SABRE signal enhancements of the NC<u>H</u> (above), NCHCC<u>H</u> (middle), and NCHCCHC<u>H</u> (below) proton resonances of phthalazine.

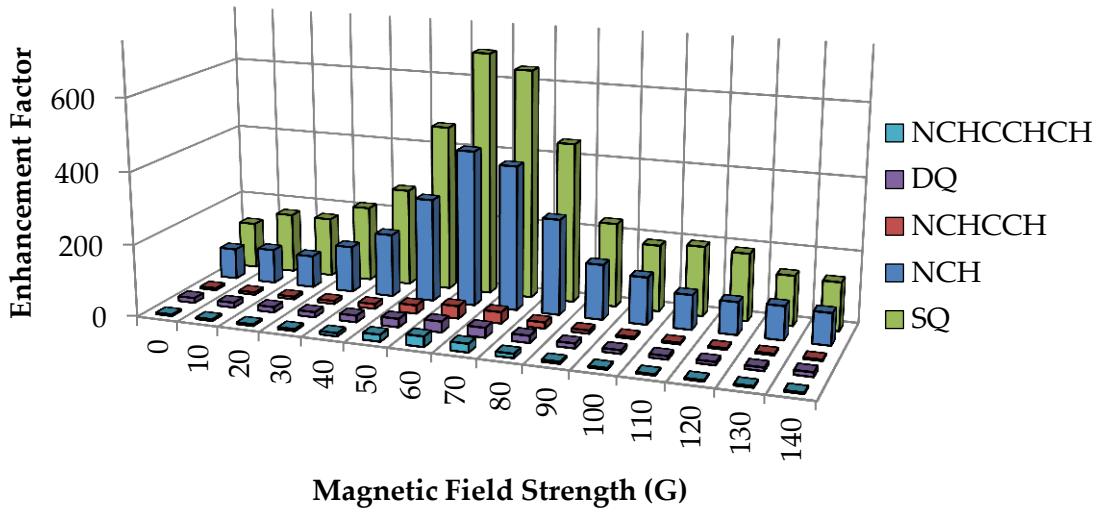

Figure 92: Effect of the polarisation transfer field on the SABRE signal enhancements of select spin states of phthalazine, where SQ = single quantum, DQ = double quantum.

Unlike pyridazine, the signal enhancements of the double quantum transitions in phthalazine were also optimised at 65 G. As expected, the signal resulting from these transitions was mainly observed in the NCHCC**H** and NCHCCHC**H** proton resonances. Akin to pyridazine, signal enhancements in phthalazine are optimised with a PTF of 65 G.

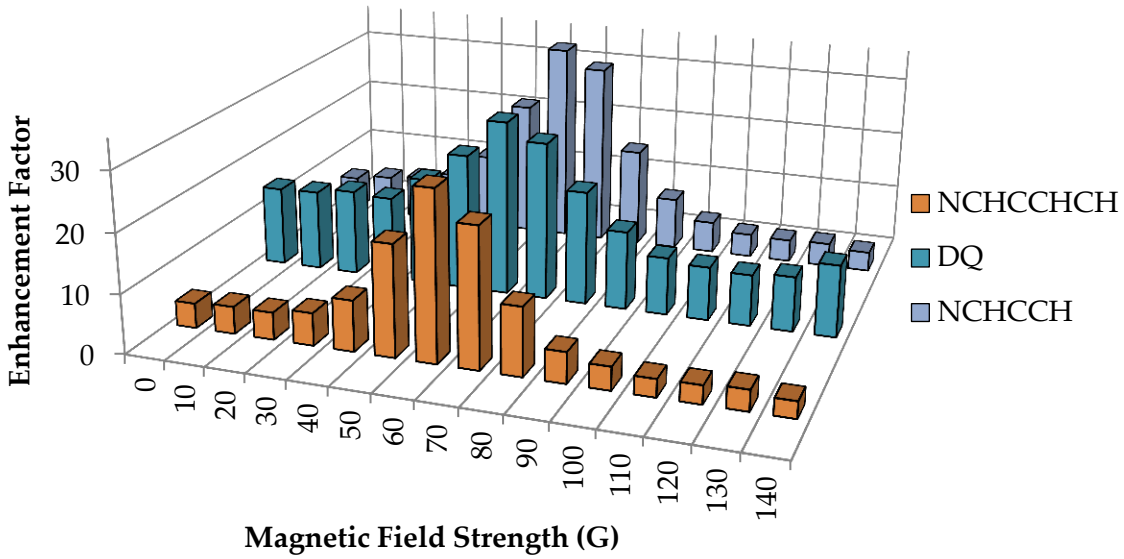

Figure 93: Effect of the polarisation transfer field on the SABRE signal enhancements of select spin states of phthalazine, where DQ = double quantum.

The higher order transitions of pyridazine are affected differently by the PTF. This interesting observation has not yet been reported for any other substrates, and highlights the significance of the PTF when probing specific spin states using SABRE.

3.5 Effect of polarisation Transfer Time on SABRE

Intuitively, the time during which excess *para*-H_2 and *N*-heterocycle exchange with the iridium exchange catalyst influences the level of polarisation transferred to the *N*-heterocycle, and thus the enhancement factors. Increasing the polarisation transfer time (PTT) results in more 'visits' from the *para*-H_2 and *N*-heterocyle and allows more of the *N*-heterocycle to polarise, as shown in Figure 94. As the polarisation transfer time is increased, the enhancement factors increase. Longitudinal relaxation of the *N*-heterocycle protons counteracts the increasing enhancement levels, which consequently plateau at a maximum.

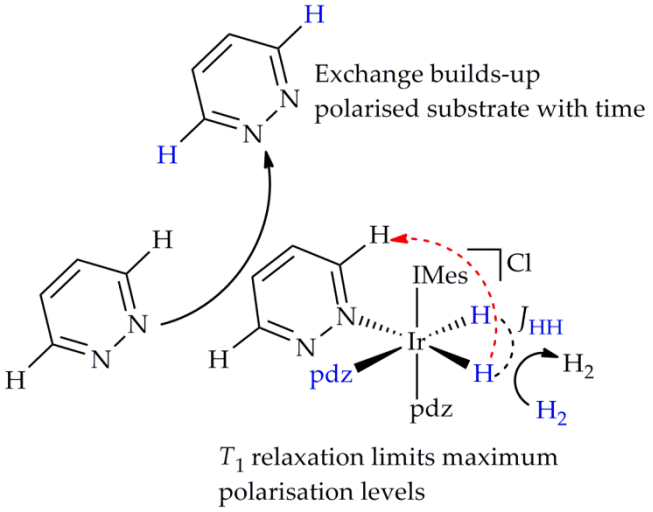

Figure 94: Scheme showing the increase in pyridazine polarisation with longer PTTs.

Previous studies on the effect of the *para*-H_2 bubbling time on enhancements in nicotinamide revealed an increase in the rate of polarisation build-up for higher-order spin states.[163] This was observed qualitatively by comparing plots of enhancement factors as a function of PTT. The smaller levels of polarisation reached for the higher-order spin states was attributed to their shorter T_1 values, although smaller spin state populations will likely have played an additional role.

As before, a flow system was used to investigate the influence of the PTT on the SABRE enhancement levels in specific spin states of pyridazine and phthalazine.[163] For this, d_4-methanol solutions of $[Ir(H)_2(IMes)(sub)_3]Cl$, containing ~ 5 equivalents of free *N*-heterocycle were used. The optimum PTFs were used to probe the different spin states, in order to achieve the best enhancement levels. The *para*-H_2 bubbling time was increased from 1.25 to 7.5 s in 1.25 s intervals, and then increased from 7.5 to 30 s in 2.5 s intervals. By 30 s, there was no discernible increase in the enhancement factors.

The enhancement factors were then plotted as a function of time, and the data was fitted according to the formula given, to calculate the observed rate of polarisation build-up (k_{obs}), where $[B_t]$ is the concentration of hyperpolarised substrate at time t (s), and $[B_e]$ is the concentration of hyperpolarised substrate at equilibrium. The derivation of this formula is described in Appendix A, section A.2.7. The k_{obs} values reflect both the rates of polarisation build-up and the rates of polarisation relaxation (T_1 values).

$$[B_t] = [B_e] - \frac{[B_e]}{exp^{(k_{obs})t}}$$

In order to calculate the rate of polarisation build-up (k), the T_1 values are required. Unfortunately, it has not been possible to measure the spin-lattice relaxation of every probed state in pyridazine and phthalazine. The T_1 values of the I_Z^X, I_Z^A, and single quantum states in pyridazine, however, have been calculated in addition to the I_Z^X, I_Z^M, I_Z^A, and single quantum states in phthalazine, using the inversion-recovery method which was discussed in Chapter 2. The conditions used for the T_1 experiments replicated those used to investigate *para*-H_2 bubbling times (~ 5 equivalents of free *N*-heterocycle with 3 bar of hydrogen). Plots of the change in magnetisation as a function of delay time for the states probed in pyridazine are shown in Figure 95.

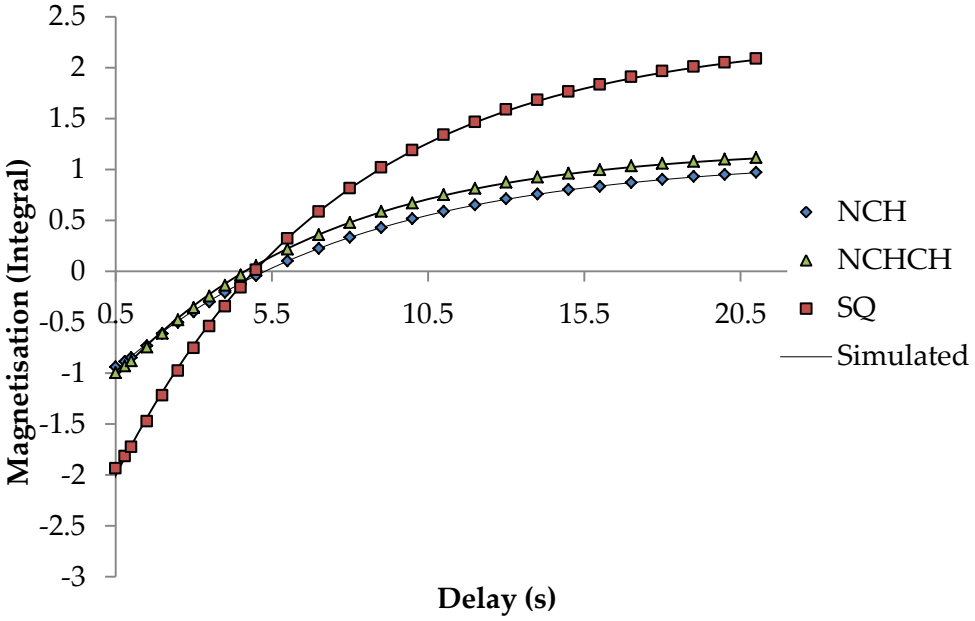

Figure 95: Graph to show the change in magnetisation intensity, with respect to the intensity when τ = 0.001 s, as a function of the delay time (τ) in an inversion recovery experiment used to calculate the T_1 values of specific spin states in pyridazine.

T_1 values for the higher-order spin states could not be calculated due to insufficient signal-to-noise, however reported T_1 values for select double quantum states in nicotinamide are much shorter than the values for the single quantum states as a result of the larger number of nuclear spins involved.[163] It can be assumed that the same principle applies to the spin states in pyridazine and phthalazine.

The effect of the PTT on the enhancement factors of the different proton resonances of pyridazine are shown in Figure 96, with the observed rate constants of polarisation build-up given in Table 11. Tabulated data and graphs are given in Appendix A, section A.2.8. The calculated T_1 values are included, and were used to calculate the true rate constants of polarisation build-up. The errors in these values were calculated using the Jack-knife method.[191]

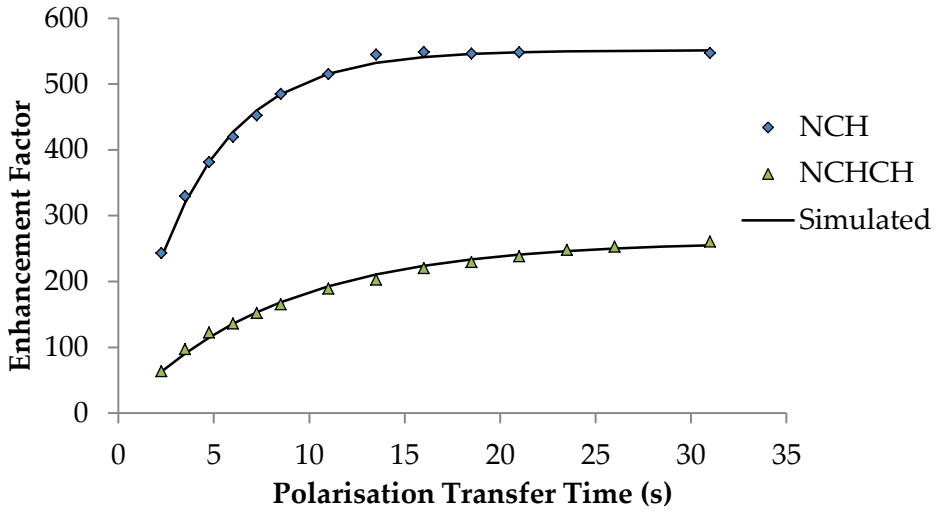

Figure 96: Plot of enhancement factors of the NCH and NCHCH proton resonances of pyridazine (selectively irradiated), as a function of polarisation transfer time.

Table 11: The observed rate constants, and true rate constants, for the build-up of polarisation, with polarisation transfer time, into specific spin states of pyridazine.

Magnetic state	k_{obs} polarisation build-up (s^{-1})	T_1 (s)	k polarisation build-up (s^{-1})
NC**H** (I_z^X, $I_z^{X'}$)	0.249 ± 0.007	7.613 ± 0.001	0.380 ± 0.007
NCHC**H** (I_z^A, $I_z^{A'}$)	0.122 ± 0.005	6.697 ± 0.001	0.271 ± 0.005
NCHC**H** DQ ($I_z^A I_z^{A'}$)	0.177 ± 0.005	-	-
SQ (I_z^A, $I_z^{A'}$, I_z^X, $I_z^{X'}$)	0.207 ± 0.007	7.118 ±0.001	0.347 ± 0.007
DQ ($I_z^A I_z^{A'}$, $I_z^X I_z^{X'}$, $I_z^A I_z^X$, $I_z^A I_z^{X'}$)	0.213 ± 0.006	-	-
TQ ($I_z^{A'} I_z^A I_z^X$, $I_z^A I_z^X I_z^{X'}$)	0.268 ± 0.007	-	-
QQ ($I_z^A I_z^{A'} I_z^M I_z^{M'}$)	0.244 ± 0.005	-	-

Polarisation builds-up more quickly into the I_z^X state (0.249 s^{-1} or 0.380 s^{-1}) than in the I_z^A state (0.122 s^{-1} or 0.271 s^{-1}); the NC**H** proton is closer to the ligating nitrogen, hence polarisation transfer into this proton *via J*-coupling is more facile than into the NCHC**H** proton, which occurs *via* transfer from the NC**H** proton. The single quantum terms are comprised of the I_z^X and I_z^A terms, hence the observed rate of polarisation build-up into

the single quantum terms (0.207 s^{-1} or 0.347 s^{-1}) lies in between the observed rates for the I_z^X and I_z^A terms. Although it appears, from the k_{obs} values, that polarisation into the higher-order states proceeds at a similar rate as the single quantum states, the T_1 values are likely to be much shorter for the higher-order states[163] therefore the true k values are likely to be much faster.

The effect of the PTT on the enhancement factors of the different proton resonances of phthalazine are shown in Figure 97, with the observed rate constants of polarisation build-up given in Table 12. The calculated T_1 values are included, and were used to calculate the true rate constants of polarisation build-up. The errors were calculated using the Jack-knife method.[191]

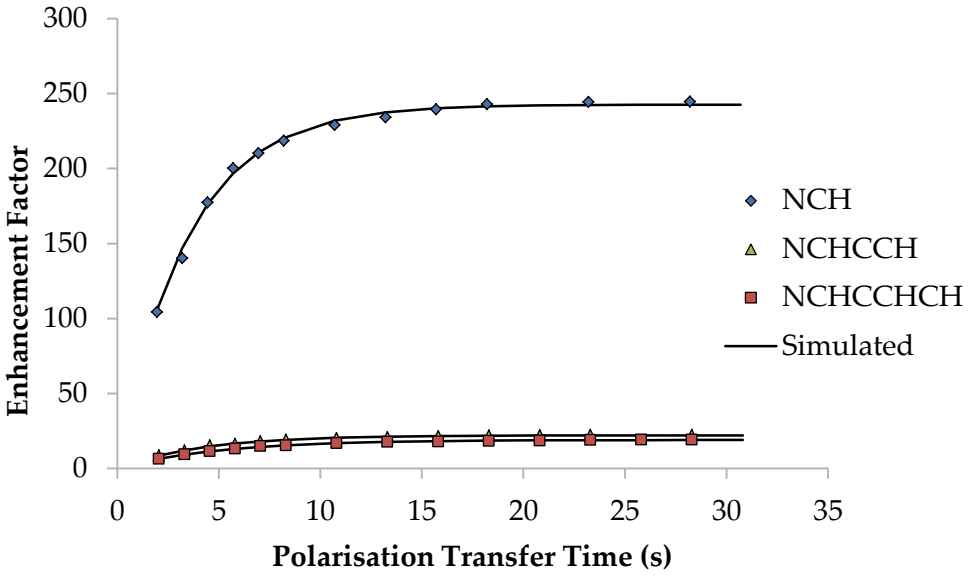

Figure 97: Plot of enhancement factors of the NC<u>H</u>, NCHCC<u>H</u>, and NCHCCHC<u>H</u> proton resonances of phthalazine (selectively irradiated), as a function of polarisation transfer time.

Table 12: The observed rate constants, and true rate constants, for the build-up of polarisation, with polarisation transfer time, into specific spin states of phthalazine.

Magnetic state	k_{obs} polarisation build-up (s^{-1})	T_1 (s)	k polarisation build-up (s^{-1})
NCH (I_z^X, $I_z^{X'}$)	0.292 ± 0.006	5.335 ± 0.001	0.477 ± 0.006
NCHCCH (I_z^M, $I_z^{M'}$)	0.240 ± 0.006	4.0375 ± 0.0009	0.488 ± 0.006
NCHCCHCH (I_z^A, $I_z^{A'}$)	0.201 ± 0.003	3.615 ± 0.001	0.477 ± 0.003
SQ (I_z^A, $I_z^{A'}$, I_z^X, $I_z^{X'}$)	0.28 ± 0.01	4.1523 ± 0.0007	0.52 ± 0.01
DQ ($I_z^M I_z^{M'}$, $I_z^A I_z^{A'}$, $I_z^A I_z^M$, $I_z^A I_z^{M'}$)	0.32 ± 0.01	-	-

As with pyridazine, polarisation builds up more quickly on the protons that lie closer to the ligating nitrogen atom; k_{obs} decreases in the order of $I_z^X > I_z^M > I_z^A$. This suggests that the NCHCC**H** and NCHCCHC**H** protons are polarised *via* transfer from the NC**H** proton, rather than directly from the *para*-H_2-derived dihydrides. Once again, the observed rate of polarisation build-up into the single quantum terms (0.28 s^{-1}) lies in between the observed rates for the I_z^X, I_z^M, and I_z^A terms. Unlike pyridazine, the rate of build-up, when including the T_1 values, does not follow the same trend. In this case, the rate is greatest for the single quantum states (0.52 s^{-1}), and polarisation is transferred into I_z^M (0.488 s^{-1}) more quickly than both I_z^A and I_z^X(0.477 s^{-1}).

Interestingly, the rate of polarisation build-up into pyridazine is slower than into phthalazine, despite enhancements of pyridazine being consistently larger than those of phthalazine. As the exchange rates of both pyridazine and phthalazine are comparable at room temperature, the larger enhancements are likely the result of faster hydrogen addition to binding sites positioned *trans* to pyridazine, and stronger *J*-coupling between the *para*-H_2-derived hydrides and the NC**H** protons of pyridazine. This is consistent with the predicted shorter Ir-N bond length in $[Ir(H)_2(IMes)(pdz)_3]Cl$, rather than $[Ir(H)_2(IMes)(phth)_3]Cl$. The T_1 values of the single quantum states of pyridazine are also longer than those of phthalazine, which allows more time for polarisation to build-up.

The enhancement factors of all spin states in both pyridazine and phthalazine plateau after bubbling *para*-H_2 into solution for approximately 20 s. SABRE is therefore optimised with a PTT / shaking time of 20 s.

3.6 Steps Towards Imaging Applications

In order to demonstrate the applicability of hyperpolarised pyridazine and phthalazine as MRI contrast agents, several one-shot hyperpolarised images were collected and compared with their thermally-equilibrated images, which required 512 averages for an observable signal (Figure 98). The pulse sequences used to collect these images are outlined in the Experimental. The samples used contained d_4-methanol solutions of $[Ir(H)_2(IMes)(sub)_3]Cl$, with ~ 5 equivalents of free *N*-heterocycle, and 3 bar of *para*-H_2. It is clear, when qualitatively comparing the images, that the signal levels in the hyperpolarised samples far exceed those in the thermally-equilibrated samples.

Furthermore, the time required to collect the hyperpolarised images was a mere 260 ms, whereas several hours were required to collect the thermal images. This is over 6 orders of magnitude longer.

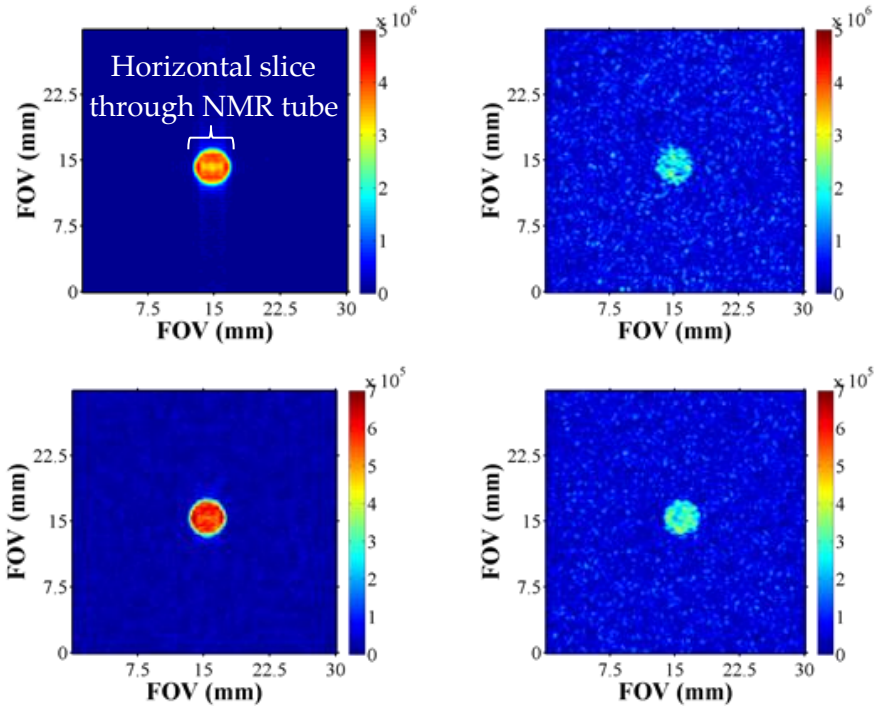

Figure 98: Hyperpolarised one-shot images of pyridazine (upper left) and phthalazine (lower left) in d_4-methanol solutions containing $[Ir(H)_2(IMes)(sub)_3]Cl$ with ~ 5 equivalents of free substrate. Each image is compared with its thermally-equilibrated image (right), which was collected using 512 averages.

Table 13: The SNRs of one-shot images of hyperpolarised pyridazine and phthalazine, and the ratio of these to the SNRs of thermally-equilibrated solutions collected using 512 averages.

Complex	SNR (hyperpolarised)	SNR (hyperpolarised)/ SNR (thermal)
$[Ir(H)_2(IMes)(pdz)_3]Cl$	185	1100
$[Ir(H)_2(IMes)(phth)_3]Cl$	72	229

In order to quantitatively compare signal levels, five one-shot hyperpolarised images were collected, and their SNRs averaged. The resulting values are given in Table 13. The average SNR of the image of hyperpolarised pyridazine is more than double that of hyperpolarised phthalazine. The SNR improvement is considerable for both substrates, although the improvement in SNR using pyridazine is almost an order of magnitude

better than with phthalazine. Both substrates display promising signal levels, suggesting that drug derivatives could potentially be used as hyperpolarised contrast agents.

To test this possibility, the optimum conditions used to hyperpolarise pyridazine and phthalazine were applied to 5-aminophthalazine, shown in Figure 99, which has antifungal properties.[212]

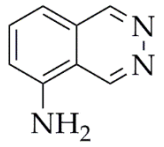

Figure 99: 5-aminophthalazine.

The resulting hyperpolarised proton resonances of 5-aminophthalazine are shown in Figure 100, and were enhanced by a factor of 500-fold, which is a very promising preliminary result. Functionalisation of the remote ring of phthalazine does not prevent polarisation transfer to the NC**H** protons and, as these protons exhibit the strongest *J*-coupling to the *para*-H_2-derived hydrides, they are the most enhanced signals. This is significant, as the NC**H** signals in an assortment of such functionalised phthalazines could potentially be enhanced using this method. These types of molecules exhibit antibacterial properties,[213-217] and could be used as hyperpolarised contrast agents.

3.6.1.1 Biologically-compatible Solvents

A substantial challenge in the use of SABRE to produce hyperpolarised contrast agents is the need to use a biologically-compatible solvent. Methanol is not biologically-compatible, therefore alternatives are required. Water is the most obvious solvent choice however SABRE has not yet been shown to work effectively in this solvent,[161,162] which is most likely due to the limited solubility of hydrogen in water.[218] Alternatively, ethanol-water mixtures are biocompatible, and the use of ethanol, followed by dilution with water has been reported to be feasible.[161,163,218]

Samples containing d_6-ethanol solutions of $[Ir(H)_2(IMes)(sub)_3]Cl$, with *para*-H_2 (3 bar) and excess pyridazine or phthalazine were prepared. Preliminary results reveal superior SABRE in ethanol, with the total pyridazine signal enhancement being approximately 400-fold (9.62-fold excess, 60 mM free pyridazine) which is 33% more enhanced than in methanol. For phthalazine, the total signal enhancement was 480-fold (2.12-fold excess,

13.2 mM free phthalazine) which is 20% more enhanced than in methanol. Unfortunately, when the optimum conditions used to hyperpolarise pyridazine and phthalazine were applied to 5-aminophthalazine in d_6-ethanol, rather than d_4-methanol, negligible polarisation transferred to the proton resonances of 5-aminophthalazine. The SABRE-enhanced ^{1}H NMR spectra of 5-aminophthalazine in d_4-methanol and d_6-ethanol are compared in Figure 100. The spectral signals corresponding to the protons on the iridium exchange catalyst are complicated due to the loss of C_{2v} symmetry when incorporating an amino group into the 5-position of phthalazine. This is particularly noticeable in the hydride regions, which contain multiple overlapping signals. The two nitrogen binding centres in 5-aminophthalazine are chemically inequivalent, which results in a minimum of six iridium complexes present in solution.

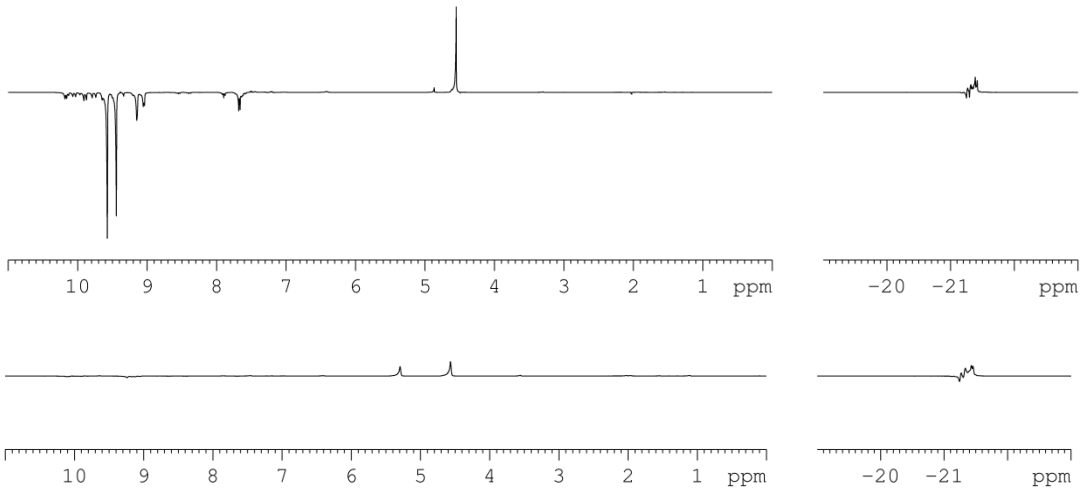

Figure 100: ^{1}H NMR spectra of [Ir(H)$_2$(IMes)(5-aminophth)$_3$]Cl, comparing SABRE-enhanced signals in d_4-methanol (above) with SABRE-enhanced signals in d_6-ethanol (below).

Although the hydride NMR resonances are enhanced to a similar degree in both d_4-methanol and d_6-ethanol, the polarisation does not transfer from the hydrides, to the proton resonances of the bound 5-aminopthalazine in d_6-ethanol. As hydrogen is reported to be more soluble in ethanol,[219] and the J-coupling between the hydrides and the substrate protons should be independent of the solvent, the lack of polarisation transfer in d_6-ethanol is likely to be the result of different rates of 5-aminophthalazine and hydrogen exchange. These can be optimised using different temperatures and concentrations, as already shown for pyridazine and phthalazine. The T_1 values of spin-1/2 nuclei are solvent specific and can differ significantly when dissolved in ethanol rather than

methanol.[153] Polarisation of 5-aminopthalazine may be shorter-lived in d_6-ethanol. In addition, the viscosity of ethanol is higher than methanol,[220] and may prevent hydrogen dissolution during the 'shake and drop' method described in the Experimental due to limited flow as a result of increased capillary action.

3.7 Conclusion

The complexes $[Ir(H)_2(IMes)(sub)_3]Cl$, where sub is pyridazine or phthalazine, are effective SABRE catalysts for the hyperpolarisation of pyridazine and phthalazine. The efficiency of polarisation transfer from the *para*-H_2-derived hydrides to the protons of the *N*-heterocycles is dependent on a number of variables, which have been optimised herein.

The rates of substrate and hydrogen exchange affect the lifetime of the polarisation transfer catalyst, thus a change in temperature, *N*-heterocycle concentration, and/or catalyst concentration affects the enhancement levels. Enhancement factors were optimised at 323 K, with 5 equivalents of *N*-heterocycle with respect to $[Ir(H)_2(IMes)(sub)_3]Cl$, and between 2.8 mM to 6.2 mM of $[Ir(H)_2(IMes)(sub)_3]Cl$. It should be noted that the 'optimum' temperature of 323 K is the safety limit when using pressurised samples in methanol. The enhancements, however, do not reach a plateau at this temperature, and higher temperatures are likely to give better enhancements. The optimum complex lifetimes appear to be shorter than those reported for pyridine, which reflects the greater probability of the *N*-heterocycles undergoing a haptotropic shift instead of dissociation, and the different *J*-coupling networks that are present.

The efficiency of polarisation transfer from *para*-H_2 to the *N*-heterocycle depends on the *J*-coupling between the *para*-H_2-derived hydrides and the protons of the substrate, and the difference in their chemical shifts,[146] which is dependent on the PTF.[149,150] Polarisation transfer into the proton resonances of both pyridazine and phthalazine was optimised using a PTF of 65 G and a PTT of 20 s. In the case of pyridazine, the enhancements of different magnetic spin states were optimised using different magnetic field strengths, however the enhancements from single quantum transitions, which are of interest when forming long-lived singlet states, were optimal at 65 G.

In Chapter 2, the rate of hydrogen addition to binding sites positioned *trans* to pyridazine was found to be faster than to binding sites positioned *trans* to phthalazine. It

was therefore predicted that under the same conditions, pyridazine would be hyperpolarised to a greater extent, *via* SABRE, than phthalazine. This has been confirmed - the total signal enhancements of the proton resonances in pyridazine are consistently larger than those in phthalazine. This may also result from stronger *J*-coupling between the *para*-H_2-derived hydrides and the NC**H** protons of pyridazine which is consistent with the predicted shorter Ir-N bond length in $[Ir(H)_2(IMes)(pdz)_3]Cl$. The T_1 values of the single quantum states of pyridazine are also longer than those of phthalazine, which allows more time for polarisation to build-up.

The suitability of pyridazine and phthalazine drug derivatives as potential hyperpolarised contrast agents has been verified by collecting several images of phantoms containing hyperpolarised pyridazine and phthalazine. Both *N*-heterocycles exhibit dramatic signal enhancements in ethanol which, when diluted, is a biologically-compatible solvent. The antifungal, 5-aminophthalazine, has been successfully polarised, which verifies that drug derivatives of phthalazine, where functionalisation is on the second ring, have the potential to be used as hyperpolarised contrast agents.

4 Synthesis and Reactivity of Palladium Monomers

The nature of the true active catalysts in palladium-catalysed reactions, particularly in carbon coupling reactions, is debated. Early mechanistic hypotheses assume a homogeneous catalytic cycle, in which the active catalyst is free Pd^0 in solution.[2-6,12] More recently, a plethora of studies in support of a heterogeneous catalytic cycle have been reported,[221,222] fuelling the mechanistic debate.

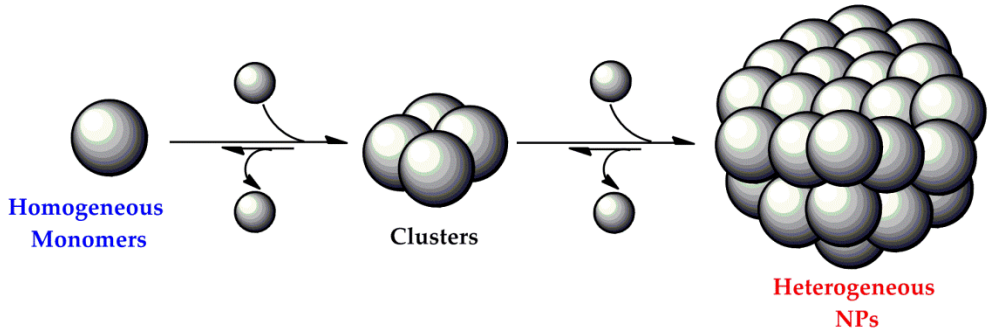

Figure 101: Scheme to illustrate the equilibria between the palladium monomers, clusters, and nanoparticles in solution during carbon-coupling reactions.

Despite most arguments focussing on these two distinct catalytic phases, it is likely that the intermediate palladium cluster phase (Figure 101) contains relevant, active palladium catalysts, however, few studies focus on the clusters that bridge palladium monomers and nanoparticles.[223,224] Herein, the formation of palladium clusters from palladium monomers - with the general structure $[Pd(OTf)_2(XR_3)_2]$, where X can be As or P, and R can be aryl or alkyl - on the pathway to nanoparticle formation, is investigated predominantly by NMR spectroscopy. The palladium monomers are highly reactive, as a result of the lability of the triflate groups,[225] and they find use as hydrogenation pre-catalysts.[115-117,226,227]

4.1 Synthesis of $[Pd(OTf)_2(XR_3)_2]$

$[Pd(OTf)_2(XR_3)_2]$, where XR_3 = $AsPh_3$, PPh_3, PPh_2Me, $P(Ph(p\text{-}OMe))_3$, $P(Ph(p\text{-}CF_3))_3$, $PPh_2(PhCH_2Ph)$, $PPh_2(PhPh)$, and $P(PhPh)_3$ (see XR_3 ligand terminology in Figure 102), were synthesised from $PdCl_2$ following the reaction scheme shown in Figure 102. The synthetic procedure used by Slzyk[228] was adapted to form *trans*-$[PdCl_2(PhCN)_2]$ on heating $PdCl_2$ in neat benzonitrile. Ligand exchange, with two equivalents of XR_3 ligand, produced both *trans*-$[PdCl_2(XR_3)_2]$ and *cis*-$[PdCl_2(XR_3)_2]$, which are air-stable complexes. The three PR_3 ligands, $PPh_2(PhCH_2Ph)$, $PPh_2(PhPh)$, and $P(PhPh)_3$, used in this step were not commercially-available, and were synthesised from available precursors.

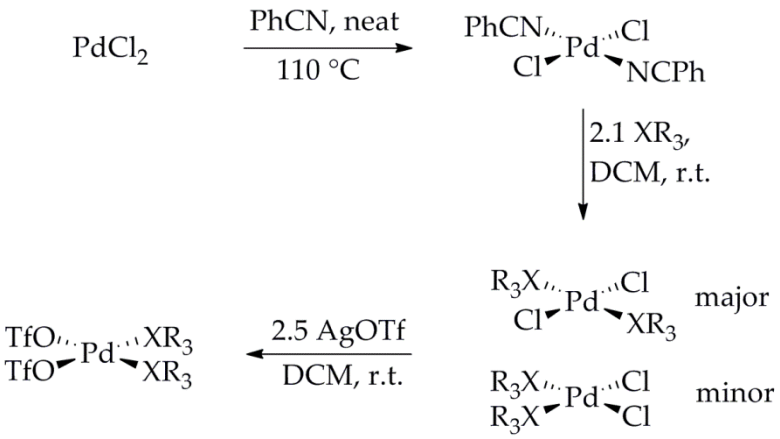

XR_3 ligand terminology for phosphines

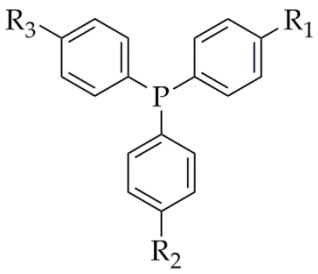

$R_1=R_2=R_3=H$	**PPh_3**
$R_1=R_2=H$ $R_3=Me$	**PPh_2Me**
$R_1=R_2=R_3=OMe$	**$P(Ph(p\text{-}OMe))_3$**
$R_1=R_2=R_3=CF_3$	**$P(Ph(p\text{-}CF_3))_3$**
$R_1=R_2=H$ $R_3=CH_2Ph$	**$PPh_2(PhCH_2Ph)$**
$R_1=R_2=H$ $R_3=Ph$	**$PPh_2(PhPh)$**
$R_1=R_2=R_3=Ph$	**$P(PhPh)_3$**

Figure 102: Scheme to show the synthetic pathway followed for the synthesis of $[Pd(OTf)_2(XR_3)_2]$ and XR_3 ligand terminology.

The methods used are shown in Figure 103, and involved either bromine-lithium exchange of an aryl precursor, followed by S_N2 nucelophilic substitution with chlorodiphenylphosphine (**A**), or reacting the commercially-available Grignard reagent with phosphorus trichloride (**B**).[229]

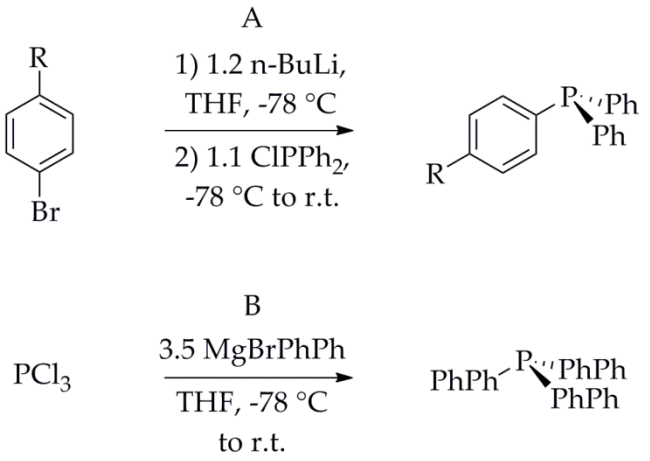

Figure 103: Scheme to show the synthetic pathways used to synthesise PR_3 ligands. Route A was used to synthesise $PPh_2(PhPh)$, and $PPh_2(PhCH_2Ph)$. Route B was used to synthesise $P(PhPh)_3$.

Trans-$[PdCl_2(XR_3)_2]$ was consistently produced as the major geometrical isomer, however, the *cis*:*trans* ratio was dependent on the XR_3 ligand used. The ^{31}P NMR signals of these species were used to calculate the *cis*:*trans* ratio (X = As produced solely the *trans*-isomer). In these $[PdCl_2(XR_3)_2]$ complexes, the chemical shifts of ^{31}P NMR resonances that correspond to phosphines in a *cis*-geometry are consistently located down-field from those that correspond to phosphines in a *trans*-geometry.[230] This is due to the larger *trans*-effect of phosphine with respect to chloride;[231] the stronger σ-donation and π-acceptance of phosphine result in an up-field chemical shift. The ^{31}P NMR spectrum of $[PdCl_2(P(Ph(p\text{-}OMe))_3)_2]$ exemplifies this, and is shown in Figure 104.

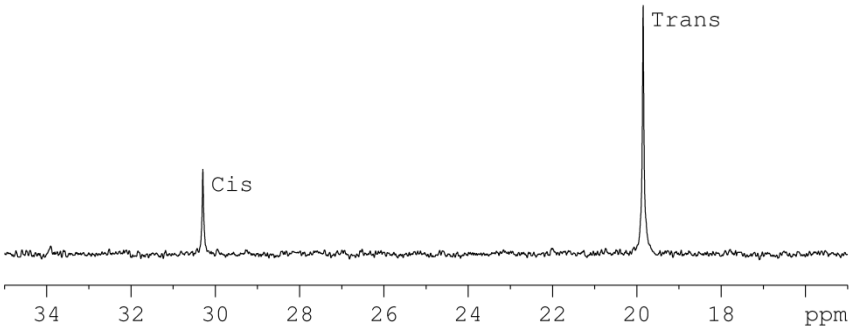

Figure 104: ^{31}P NMR spectrum showing the up-field chemical shift of the phosphorus resonances of trans-$[PdCl_2(P(Ph(\mathbf{p\text{-}OMe}))_3)_2]$ with respect to cis-$[PdCl_2(P(Ph(\mathbf{p\text{-}OMe}))_3)_2]$.

Cis-trans isomerisation of square planar palladium bisphosphine complexes, including similar dichloride complexes, has been previously reported.[232,233] The *trans*-configuration is less polar and is therefore favoured over the *cis*-configuration in non-polar solvents.[232]

Here, dichloromethane was employed as the solvent, which is relatively polar and therefore favours the *cis*-configuration. The equilibrated *cis*:*trans* ratios of the $[PdCl_2(XR_3)_2]$ complexes reflect their σ-donation and π-acceptance properties, and are given in Table 14. The electron-donating methoxy group of $P(Ph(p\text{-}OMe))_3$ is conjugated into the phenyl ring and thus increases the σ-donation from the phosphorus atom. This phosphine exhibits the largest *trans*-effect and, due to its *trans*-influence, the *trans*-configuration of $[PdCl_2(P(Ph(p\text{-}OMe)_3)_2]$ is the least stable with respect to its *cis* counterpart. As XR_3 becomes less σ-donating, the ratio of *cis* isomer decreases.

Table 14: The cis : trans ratios of $[PdCl_2(XR_3)_2]$, calculated from the ratio of the ^{31}P NMR peak integrals.

XR_3	***Cis* : *trans* ratio (%)**	
	Cis	*Trans*
$P(Ph(p\text{-}OMe))_3$	26	74
$P(PhPh)_3$	20	80
$PPh_2(PhPh)$	6	94
$PPh_2(PhCH_2Ph)$	5	95
PPh_2Me	-	100
PPh_3	-	100
$AsPh_3$	-	100
$P(Ph(p\text{-}CF_3))_3$	-	100

Crystal structures of the *trans*-configurations of the complexes where $XR_3 = P(PhPh)_3$, $PPh_2(PhPh)$, PPh_3, and $P(Ph(p\text{-}CF_3))_3$, are given in the Experimental and all exhibit distorted square planar structures. The final synthetic step for the synthesis of $[Pd(OTf)_2(XR_3)_2]$ required chloride abstraction, using two equivalents of silver triflate to form *cis*-$[Pd(OTf)_2(XR_3)_2]$. With the exception of $XR_3 = PPh_3$ or PPh_2Me, these $[Pd(OTf)_2(XR_3)_2]$ compounds are novel. In the case of $[Pd(OTf)_2(PPh_3)_2]$, the ^1H, ^{13}C and ^{31}P NMR spectral assignments agree with those of Murata and Ido,[234] who synthesised *trans*-$[Pd(OTf)_2(PPh_3)_2]$ by the addition of two equivalents of triphenylphosphine to $[Pd(OTf)_2].2H_2O$. Unfortunately, spectroscopic data for $[Pd(OTf)_2(PPh_2Me)_2]$ has not yet been published.

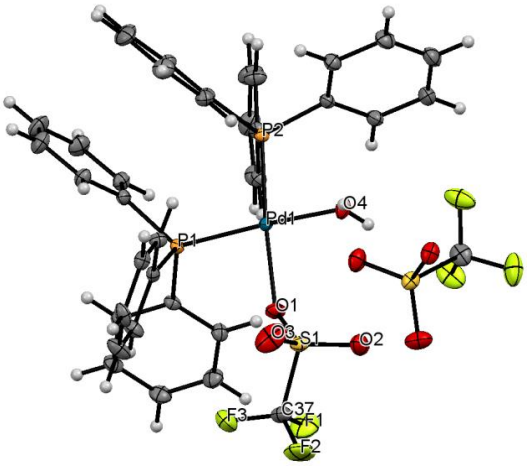

Figure 105: Crystal structure of [Pd(OTf)(H_2O)(PPh_3)$_2$]OTf, formed from [Pd(OTf)$_2$(PPh_3)$_2$] by displacement, by water, of a triflate. Atom colours: C-grey, F-yellow, H-white, O-red, P-orange, Pd-blue, S-gold.

Single crystals of both [Pd(OTf)$_2$(PPh_3)$_2$] and [Pd(OTf)$_2$(P(Ph(*p*-CF_3))$_3$)$_2$] have been grown and their crystal structures solved by single-crystal XRD. Both crystal structures exhibit a distorted square planar geometry, and that of [Pd(OTf)$_2$(PPh_3)$_2$] is shown in Figure 105. Unfortunately, due to the hygroscopic nature of these species, which has been reported for similar palladium complexes,[235] it was not possible to grow crystals of the pure complexes, under an inert atmosphere. Both crystal structures show the displacement of a triflate ligand by a water molecule. The resulting positive charge of the palladium(II) complex is stabilised by the displaced triflate, which now acts as a counter-ion. Interestingly, both crystal structures show *cis*-configurations of the phosphine ligands, despite the dominance of the *trans*-configurations in the dichloride precursors. This contradicts Murata's proposed *trans*-configuration, which was based on NMR characterisation, and therefore not proven.[234] Furthermore, it is well-reported that triflate ligands are rarely stable unless they lie *trans* to amine-type ligands,[236] therefore they are likely to be stable when positioned *trans* to phosphines and arsines. Chloride dissociation is reported to occur stepwise,[225] hence the intermediate [PdCl(OTf)(XR_3)$_2$] complexes can isomerise, as shown in Figure 106. Once the triflate and chloride ligands lie *cis* to one another, chloride dissociation reportedly occurs more quickly, forming [Pd(OTf)$_2$(XR_3)$_2$].[236] Diagnostic ^{19}F NMR spectra confirmed the successful formation of the bis-triflate complexes.

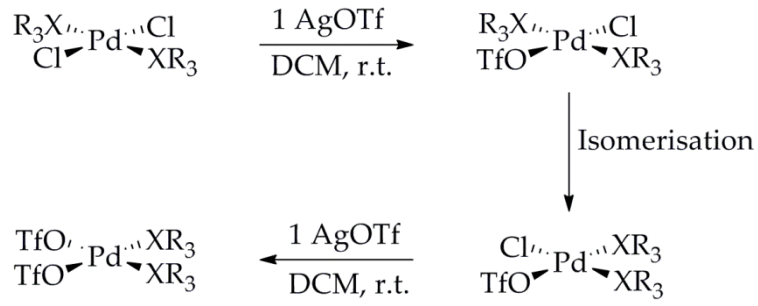

Figure 106: Possible isomerisation pathway to form cis-$[Pd(OTf)_2(XR_3)_2]$ from trans-$[PdCl_2(XR_3)_2]$.

4.2 Suitability of $[Pd(OTf)_2(XR_3)_2]$ Complexes for these Studies

The aim is to identify palladium cluster intermediates that form en-route to palladium nanoparticles. To be suitable for this study, the $[Pd(OTf)_2(XR_3)_2]$ monomers must reduce to palladium(0) nanoparticles in solution. $[Pd(OTf)_2(XR_3)_2]$ monomers find use as hydrogenation catalysts and have been used alongside *para*-H_2 to investigate hydrogenation mechanisms[115-117,226]. To replicate these reaction conditions, the $[Pd(OTf)_2(XR_3)_2]$ complexes were dissolved in dichloromethane, the solutions were degassed, and hydrogen gas was added. In theory, addition of hydrogen reduces $[Pd(OTf)_2(PPh_3)_2]$ to Pd(0), with triflic acid produced as a side product.[117] In all cases, with the exception of $XR_3 = P(Ph(p\text{-}CF_3))_3$, the solutions darkened from bright yellow, to murky dark red (Figure 107). The darkening of the solutions suggested the formation of nanoparticles, which was confirmed by TEM analysis, thus verifying the suitability of the $[Pd(OTf)_2(XR_3)_2]$ monomers for this study.

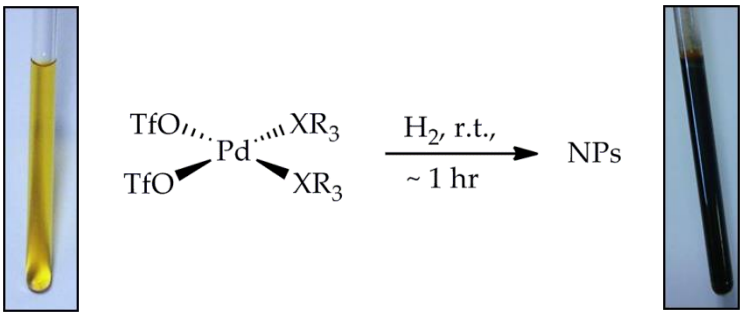

Figure 107: Evidence of nanoparticle (NP) formation on addition of hydrogen to $[Pd(OTf)_2(XR_3)_2]$. The photographs shown are using $[Pd(OTf)_2(PPh_3)_2]$ as the example complex.

The palladium nanoparticles that formed on addition of 3 bar of hydrogen to a 7.6 mM dichloromethane solution of $[Pd(OTf)_2(XR_3)_2]$, where $XR_3 = PPh_3$ or $AsPh_3$, were compared. Their transmission electron microscopy (TEM) images are shown in Figure 109. Polyvinylpyrrolidone (PVP), shown in Figure 108, was used as a control during TEM sample preparation because it is known to coat and stabilise nanoparticles (Figure 108), preventing palladium aggregation occurring during the TEM analysis of palladium nanoparticles, under working reaction conditions as described by the Fairlamb group.[51,52] In this way, any changes in palladium nanoparticle size *ex situ* can be assessed, however, in this case there were no discernible changes, highlighting the stability of the palladium nanoparticles that formed.

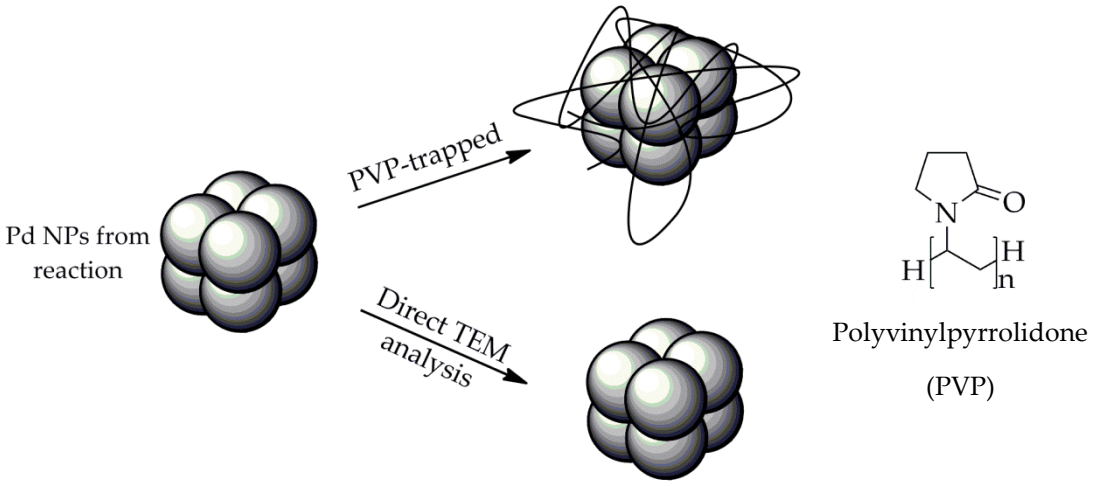

Figure 108: Schematic showing the trapping of nanoparticles by PVP, used as a control in TEM imaging. The structure of PVP is given on the right.

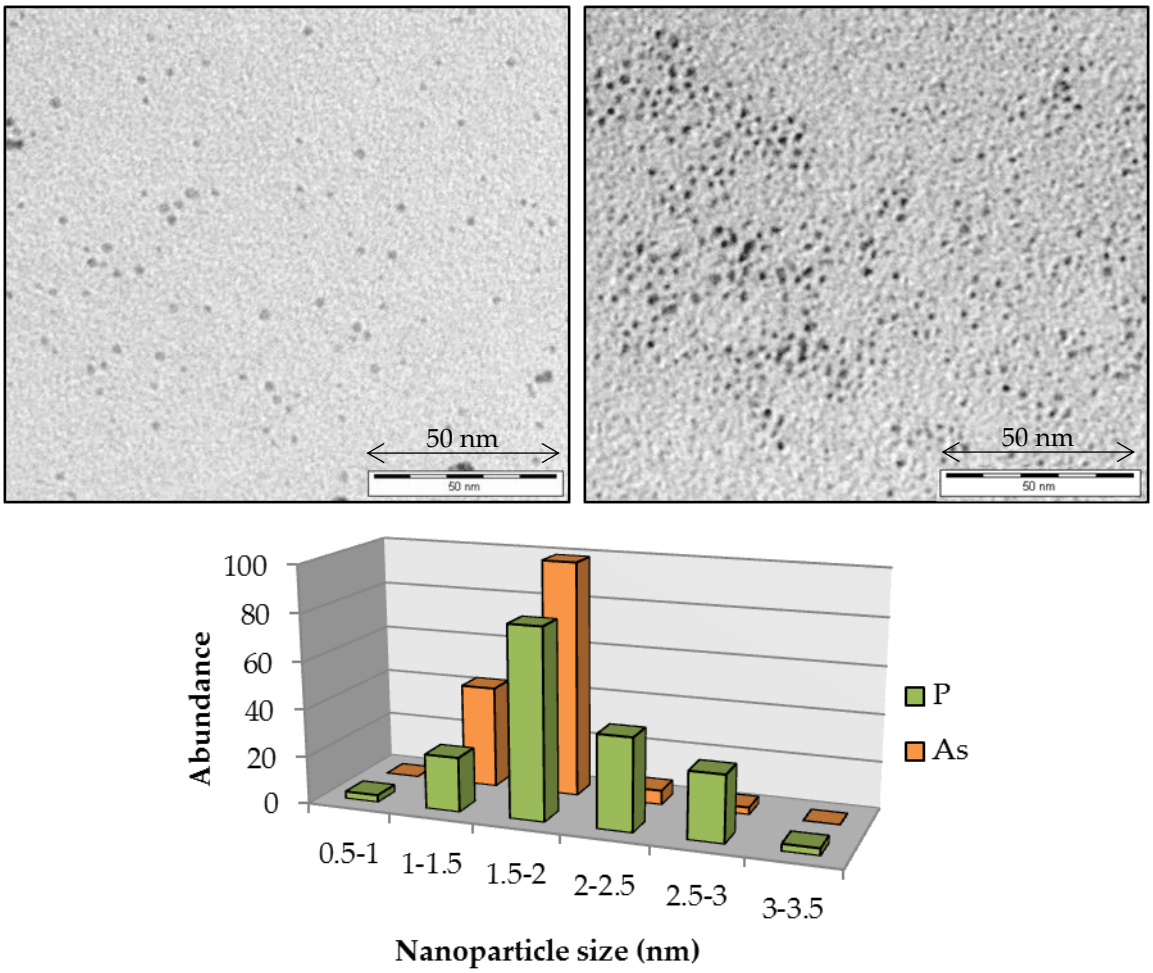

Figure 109: TEM images of the palladium nanoparticles that form on addition of hydrogen to (top left) [Pd(OTf)$_2$(PPh$_3$)$_2$], and (top right) [Pd(OTf)$_2$(AsPh$_3$)$_2$]. The nanoparticle size distributions that form from the AsPh$_3$ and PPh$_3$-stabilised precursors are compared in the histogram (below).

The TEM images were analysed to calculate the size distributions of the nanoparticles (Figure 109). All of the TEM images used for this are given in Appendix B, section B.1.1. The nanoparticles most likely have either an icosahedral or cuboctahedral geometry, depending on the level of hydrogen absorption; a greater number of bound hydrides favours a cuboctahedral geometry.[237] The range of nanoparticle sizes is small, from 1 to 4 nm, with no discernible difference between the mean sizes of those that form from the addition of hydrogen to [Pd(OTf)$_2$(PPh$_3$)$_2$] or [Pd(OTf)$_2$(AsPh$_3$)$_2$], when taking errors into account. The mean nanoparticle sizes are given in Table 15. These small (~ 2 nm) palladium nanoparticles are likely to exhibit activity in a range of cross-couplings reactions,[238] such as those reported by Fairlamb and co-workers.[53]

Table 15: The mean, mode, and median nanoparticle (NP) sizes formed on the addition of hydrogen to $[Pd(OTf)_2(PPh_3)_2]$ and $[Pd(OTf)_2(AsPh_3)_2]$. Y = yes (PVP used), N = no (PVP not used).

Complex	PVP	Mean NP size (nm)	Standard deviation (nm)	Mode NP size (nm)	Median NP size (nm)
$[Pd(OTf)_2(PPh_3)_2]$	Y	1.9	0.5	1.7	1.8
$[Pd(OTf)_2(PPh_3)_2]$	N	2.0	0.5	1.7	1.9
$[Pd(OTf)_2(AsPh_3)_2]$	Y	1.6	0.3	1.7	1.6
$[Pd(OTf)_2(AsPh_3)_2]$	N	1.7	0.3	1.7	1.7

4.3 PHIP of Unsaturated Substrates Using $[Pd(OTf)_2(PPh_3)_2]$

As previously mentioned, palladium bis-triflate complexes have been used as hydrogenation pre-catalysts.[115-117,226] When used in conjunction with *para*-H_2, the ^{1}H NMR signals of the *para*-H_2-derived protons become substantially enhanced. This allows for the detection of palladium intermediates that would otherwise be unobservable in ^{1}H NMR spectra. PHIP could potentially enhance the ^{1}H NMR signals of palladium clusters that form as intermediates, en-route to nanoparticles, with the requirement that *para*-H_2 is incorporated into such clusters.

Herein, $[Pd(OTf)_2(PPh_3)_2]$, has been used to test the application of PHIP for the detection of palladium clusters. It was selected because of the C_3 symmetry of the triphenylphosphine ligands which arises from the equivalent phenyl rings and helps to simplify NMR spectra. Furthermore, the spin-½ ^{31}P is a good 'NMR handle' with which intermediates may be characterised more easily.

4.3.1 *Para*-hydrogenation of Phenylacetylene

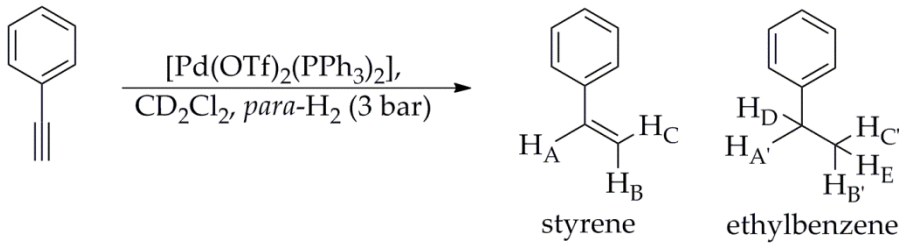

Figure 110: Hydrogenation of phenylacetylene, ^{1}H NMR (500 MHz, $CDCl_3$): 7.53 (d.d, J_{HH} = 7.3, 1.4, 2H, HCCCCHCHCH), 7.36 (m, 3H, HCCCCHCHCH), 3.10 (s, 1H, HCCCCHCHCH), to form styrene and ethylbenzene.

Under nitrogen, $[Pd(OTf)_2(PPh_3)_2]$ (5 mg, 5.38 μmol) was dissolved in d_2-dichloromethane (0.6 mL) containing 10 equivalents of phenylacetylene (6 μL, 53.8 μmol). A black solution immediately formed and was degassed. A comparison of the ^{1}H NMR signals with those of pure phenylacetylene showed a significant loss of the signal corresponding to the acetylene proton at δ 3.10. It is reported that, in the presence of a palladium catalyst, phenylacetylene can dimerise to form diphenylbutadiyne[239] or trimerise to form triphenylbenzene,[240] which would account for the loss of the acetylene proton however there was no NMR evidence for the formation of these species. Furthermore, the ^{31}P {^{1}H} NMR spectrum contains a singlet at δ 38.15, which is diagnostic of unreacted $[Pd(OTf)_2(PPh_3)_2]$. Replacement of the acetylene proton with deuterium is possible through the activation of d_2-dichloromethane at palladium.[241]

A ^{1}H NMR spectrum taken immediately after the addition of 3 bar of *para*-H_2, contains significant signal enhancements at δ 6.77, and 5.28, shown in Figure 111. A COSY NMR spectrum, shown in Figure 112, contains cross peaks between these enhanced signals and another weakly enhanced signal at δ 5.81. There is no evidence of any ^{31}P couplings to these enhanced signals, hence they must be caused by hydrogenation products dissociated from the catalyst. A previous publication by Eichhorn *et. al.*,[123] in which a colloidal $Pd_x[(N(octyl)_4Cl]_y$ catalyst was used to *para*-hydrogenate phenylacetylene contained similar findings. The signals at δ 6.77, 5.81, and 5.28 correspond to the *para*-H_2-derived protons in styrene as shown in Figure 110; the antiphase doublet of doublets at δ 6.77 corresponds to H_A, the very slightly enhanced antiphase doublet at δ 5.81

corresponds to H_C and the enhanced antiphase doublet at δ 5.28 corresponds to H_B. *Para*-H_2 is selectively added across the same face of the alkyne, resulting in stronger enhancements of H_A and H_B, relative to H_C, by a factor of 6.7.

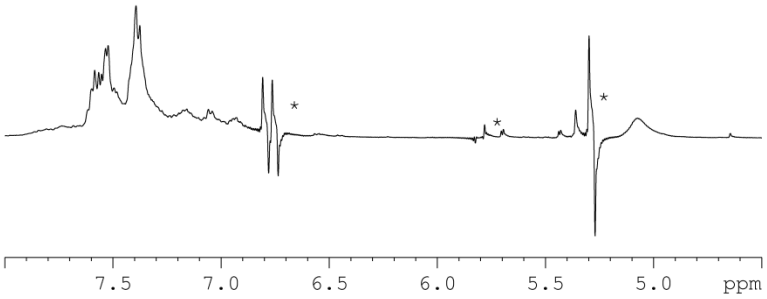

Figure 111: ^{1}H NMR spectrum showing PASADENA signals that correspond to the para-H_2-derived protons in styrene.

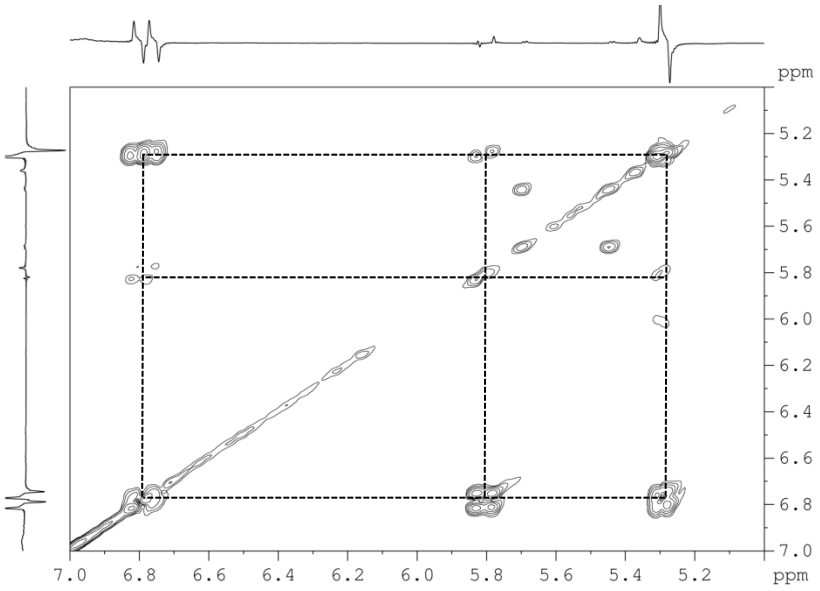

Figure 112: COSY NMR spectrum showing coupling between the PASADENA signals that correspond to the para-H_2-derived protons in styrene.

Two smaller enhanced NMR signals are also visible at δ 2.68 and 1.27, shown in Figure 113. A COSY NMR spectrum, shown in Figure 114, contains cross peaks between these two enhanced signals, which correspond to the *para*-H_2-derived protons in ethylbenzene, predominantly H_D (antiphase quartet at δ 2.68) and H_E (antiphase triplet at δ 1.27) in Figure 110, although any existing polarisation in $H_{A'}$, $H_{B'}$, and $H_{C'}$ will also contribute to these signals.

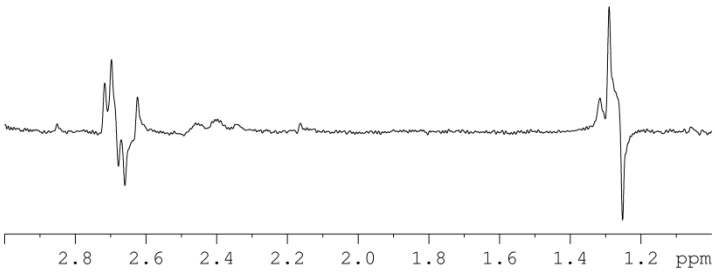

Figure 113: ^{1}H NMR spectrum showing PASADENA signals that correspond to the para-H_2-derived protons in ethylbenzene.

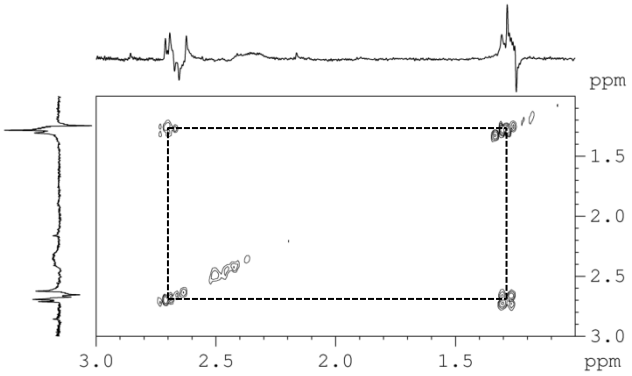

Figure 114: COSY NMR spectrum showing coupling between the PASADENA signals that correspond to the para-H_2-derived protons in ethylbenzene.

The enhanced *para*-H_2-derived NMR signals of styrene and ethylbenzene all exhibit the in-phase/antiphase shaping that is characteristic of PASADENA. This confirms that polarisation transfer from the *para*-H_2-derived hydrides occurs at high field; phenylacetylene is hydrogenated inside the NMR spectrometer. Unfortunately, no additional enhanced NMR signals were observed, and no palladium intermediates were detected. This suggests that such intermediates are too short-lived for observation.

4.3.2 *Para*-hydrogenation of Styrene

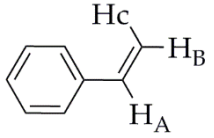

Figure 115: Styrene, ^{1}H NMR (400 MHz, $CDCl_3$): 7.49 (d, J_{HH} = 7.3, 2H, CC<u>H</u>), 7.40 (t, J_{HH} = 7.4, CCHC<u>H</u>), 7.32 (t, J_{HH} = 7.4, CCHCHC<u>H</u>), 6.80 (dd, J_{HH} = 17.5, 10.6, H_A), 5.82 (d, J_{HH} = 17.5, H_C), 5.32 (d, J_{HH} = 10.6, H_B).

As before, under nitrogen, $[Pd(OTf)_2(PPh_3)_2]$ (5 mg, 5.38 μmol) was dissolved in d_2-dichloromethane (0.6 mL) containing 10 equivalents of styrene (6.2 μL, 53.8 μmol). The bright yellow solution was degassed. $^{31}P\{^1H\}$ NMR spectra of this mixture contained a singlet at δ 38.15 which is diagnostic of unreacted $[Pd(OTf)_2(PPh_3)_2]$. A ^1H NMR spectrum, acquired immediately after addition of *para*-H_2 (~ 3 bar) to the sample, contained two enhanced hydride signals at δ −15.43 and −8.17, shown in Figure 116. Cross peaks between the two hydride signals can be observed in the COSY NMR spectrum shown in Figure 117, hence both hydrides must couple to each other as part of the same molecule. The antiphase splitting reveals a J_{HH} coupling constant of 7 Hz. There is no evidence of any coupling to ^{31}P.

The integral ratios of enhanced signals cannot be definitively used to quantify the number of protons they correspond to, as they are very sensitive to the proton environment and spin-lattice relaxation rate. This is exemplified in Chapter 2 where the integrals of the SABRE-enhanced hydrides in $[Ir(H)_2(COD)(IMes)(sub)]Cl$ differ considerably, despite both signals corresponding to a single proton. Although the hydride signal at δ −15.43 appears to be twice the size of that at δ −8.17, both signals may correspond to one proton each. Unfortunately, this NMR data does not provide enough information to quantitatively characterise this palladium hydride species. The same hydride NMR signals have also been observed on *para*-hydrogenation of diphenylacetylene and *trans*-stilbene, using the same palladium catalyst. They are discussed in more detail in sections 4.3.3 and 4.3.4.

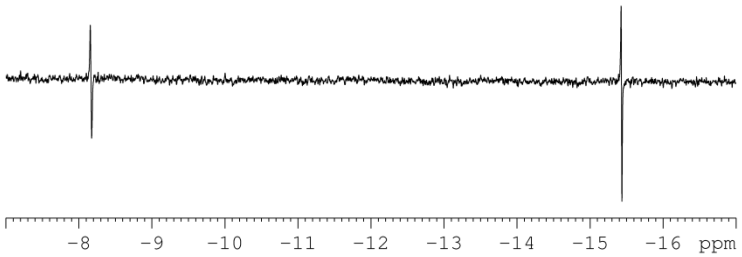

Figure 116: ^1H NMR spectrum showing PASADENA signals that correspond to the para-H_2-derived hydrides that form using $[Pd(OTf)_2(PPh_3)_2]$ with 10 equivalents of styrene, and para-H_2 (~3 bar).

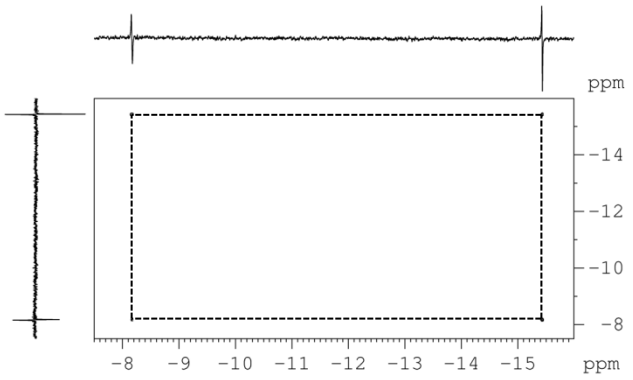

Figure 117: COSY NMR spectrum showing coupling between the PASADENA signals that correspond to the para-H_2-derived hydrides that form using $[Pd(OTf)_2(PPh_3)_2]$ with 10 equivalents of styrene, and para-H_2 (~3 bar).

No other enhanced resonances were observed and the styrene was not hydrogenated by $[Pd(OTf)_2(PPh_3)_2]$. The enhanced ^1H NMR signals corresponding to ethylbenzene that are observed immediately on *para*-hydrogenation of phenylacetylene, are unlikely to be forming by *para*-hydrogenation of free styrene. The styrene is more likely undergoing a sequential *para*-hydrogenation whilst complexed to palladium.

4.3.3 *Para*-hydrogenation of Diphenylacetylene

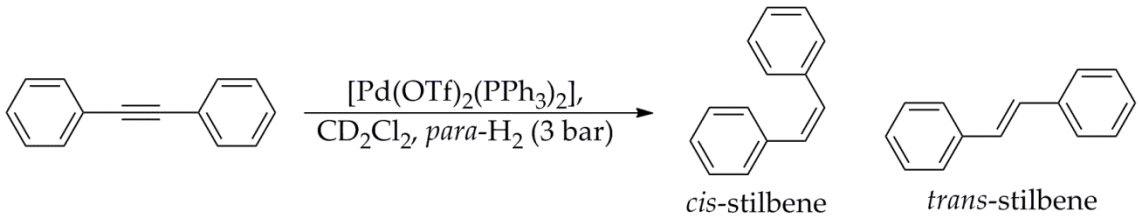

Figure 118: Hydrogenation of diphenylacetylene, ^1H NMR (400 MHz, CD_2Cl_2): 7.60 – 7.58 (m, 4H, CCH), 7.42 – 7.41 (m, 6H, CCHCHCH), to form cis and trans-stilbene.

Under nitrogen, diphenylacetylene (10 mg, 53.8 μmol) and $[Pd(OTf)_2(PPh_3)_2]$ (5 mg, 5.38 μmol) were dissolved in d_2-dichloromethane (0.6 mL), and the sample was degassed. Prior to the addition of *para*-H_2, there was no reaction and only the signals corresponding to diphenylacetylene are visible in ^1H NMR spectra. The triphenylphosphine signals of the catalyst are hidden beneath these, but a $^{31}P\{^1H\}$ NMR spectrum contained a single peak at δ 38.7, which corresponds to the single phosphorus environment in $[Pd(OTf)_2(PPh_3)_2]$.

Addition of *para*-H_2 (~3 bar) resulted in the immediate observation of two enhanced signals in the ^{1}H NMR spectrum, a *pseudo*-antiphase multiplet at δ 7.27 and an emissive singlet at δ 6.66, shown in Figure 119. These signals correspond to the protons in *cis*-stilbene, shown in Figure 118. As expected, *para*-H_2 is selectively added across the same face of the alkyne, resulting in observed enhancements of the protons in *cis*-stilbene, but no enhancements observed for the protons in *trans*-stilbene (also shown in Figure 118). *Trans*-stilbene is observed to form in this reaction, as the thermally-stable isomer, however the lack of proton enhancements suggest that it forms *via* isomerisation of *cis*-stilbene.[242]

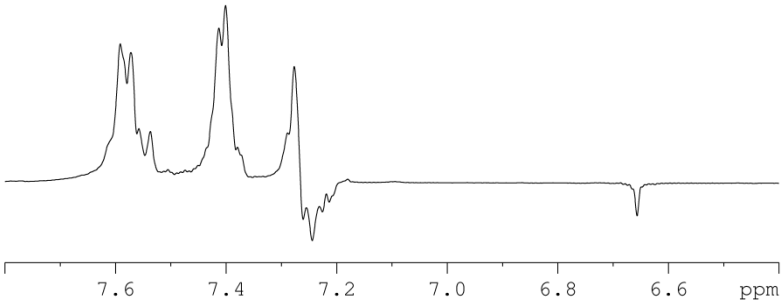

Figure 119: ^{1}H NMR spectrum showing ALTADENA signals that correspond to cis-stilbene.

The emissive nature of the vinylic C**H** signal at δ 6.66 is characteristic of one-hydrogen PHIP, which was first experimentally observed by the Eisenberg group in 2002, but had been postulated by Natterer prior to this.[243] One-hydrogen PHIP results when two *para*-H_2-derived hydrides form a strongly-coupled system at a metal catalyst, so that although just one hydride transfers to the product, spin correlation is retained resulting in emissive enhancements. This has been reported for the *para*-hydrogenation of diphenylacetylene using similar palladium systems.[226] A possible route to the generation of one-hydrogen PHIP in the vinylic-CH of *cis*-stilbene is shown in Figure 120. The aromatic C**H** signals of *cis*-stilbene are also polarised and appear as the *pseudo*-antiphase multiplet at δ 7.27.

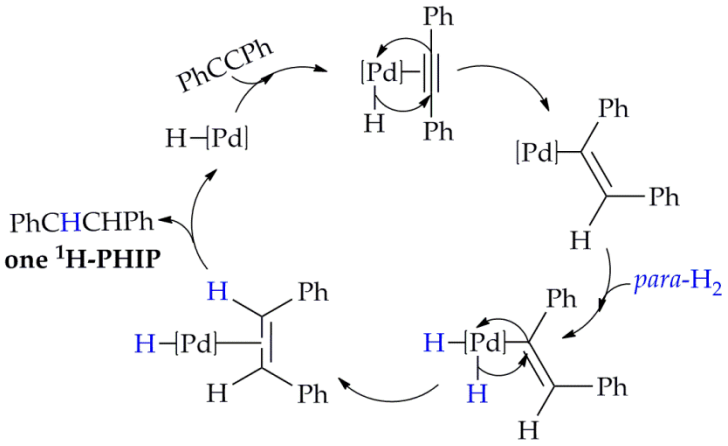

Figure 120: A potential route to the generation of one-hydrogen PHIP in the vinylic CH of cis-stilbene.

Several, less intense, enhanced signals were also observed, including two hydride signals at δ −15.43 and −8.17, which were also seen in the analogous experiment in which styrene was used as the substrate. These signals initially grew in intensity, but were no longer visible after approximately 15 minutes, despite the availability of *para*-H_2 and diphenylacetylene. There are no visible phosphorus splittings of the two hydride signals, and a ^{31}P-optimised HMQC showed no cross peaks, indicating no phosphorus couplings. As with styrene, a COSY NMR spectrum contained cross peaks between the two hydride signals, but to no other protons.

In addition to these two enhanced hydride resonances, several enhanced signals became visible in the alkyl region of the ^{1}H NMR spectrum, at δ 2.93, 2.59 and 2.18, shown in Figure 121. A COSY NMR spectrum, shown in Figure 122, revealed the presence of two further signals at δ 4.08 and 3.58 that cannot be identified in the ^{1}H NMR spectrum. The COSY NMR spectrum clearly shows two coupling systems, both of which couple to the signal at δ 2.93, which is complicated by the overlap of two peaks. The signals at δ 4.08, 2.93 and 2.59 form one system (blue), and those at δ 3.58, 2.93 and 2.18 form the other (black). A COSY NMR spectrum, with a spectral window scanning both the hydride and alkyl region, indicated no coupling between the hydrides and the two alkyl species. It can be assumed that the two palladium alkyl species do not contain hydrides.

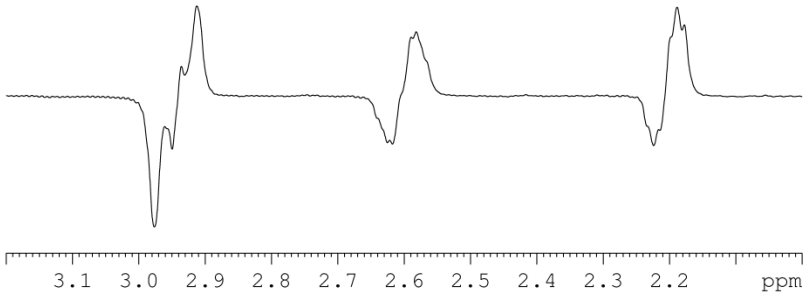

Figure 121: ^{1}H NMR spectrum showing PASADENA signals that correspond to two palladium alkyl species.

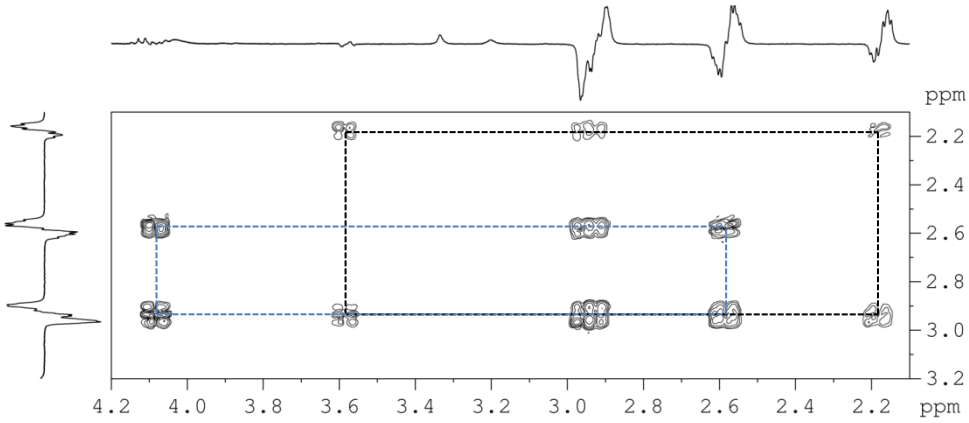

Figure 122: COSY NMR spectrum showing coupling between the PASADENA signals that correspond to the para-H_2-derived hydrides in two palladium alkyl species.

A ^{31}P-optimised HMQC NMR spectrum, shown in Figure 123, reveals three different phosphorus environments, at δ 33.56, 29.93 and 22.22. The phosphorus signals at δ 33.56 and 22.22 couple to one spin system and that at δ 29.93 couples to the other. The results are consistent with the presence of the two palladium alkyl species shown in Figure 124. Species **1** contains two inequivalent phosphines at δ 33.56 and 22.22, which couple to the proton signals at δ 3.58, 2.93 and 2.18, and species **2** contains two equivalent phosphines at δ 29.93, which couple to the proton signals at δ 4.08, 2.93 and 2.59. Similar species have been reported to form on *para*-hydrogenating diphenylacetylene using related palladium systems with bidentate phosphines, whereby the palladium alkyl complexes are stabilised by η^2-coordination of the phenylic π-system, rather than a triflate ligand.[115,226,227] There is no NMR evidence for this interaction in these palladium alkyl complexes hence it is assumed that triflate ligands bind to stabilise the palladium complexes and raise the electron count to 16.

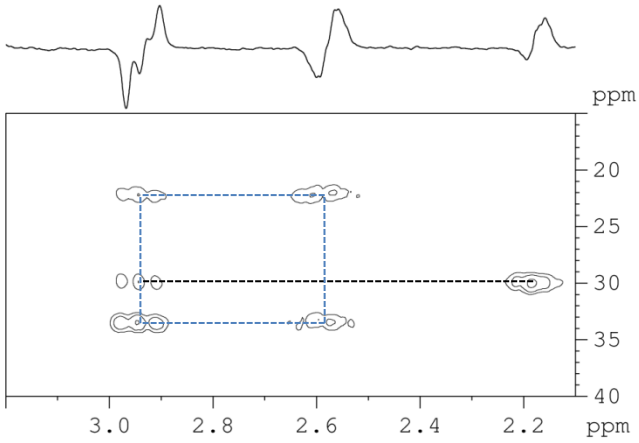

Figure 123: ^{31}P-optimised HMQC NMR spectrum showing coupling between the PASADENA signals that correspond to the para-H_2-derived hydrides in two palladium alkyl species, and ^{31}P signals of triphenylphosphine ligands.

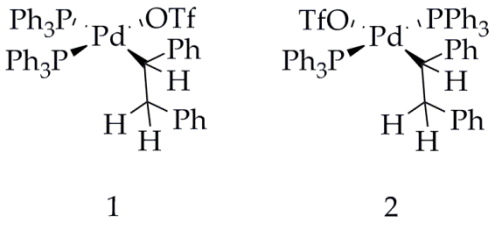

1 2

Figure 124: The two possible geometric isomers of [Pd(OTf)$_2$(CHPhCH$_2$Ph)(PPh$_3$)$_2$].

As expected, on repeating the reaction with $^{13}C_2$-labelled diphenylacetylene, with ^{13}C at the alkynyl positions, the PASADENA ^{1}H NMR signals, shown in Figure 125, become complicated by extra scalar couplings to the ^{13}C, and overlapping signals. ^{13}C-optimised HMQC spectra, probing strong CH coupling interactions, revealed four different carbon environments, at δ 77.0, 60.7, 36.4, and 35.6, further proving structures **1** and **2** shown in Figure 124. The carbon signals at δ 77.0 and 60.7 couple to the proton signals at 4.08 and 3.58, respectively, and are therefore the Pd**C**H signals in **2** and **1**, respectively. The carbon signals at δ 36.4 and 35.6 couple to the proton signals at δ 2.93 and 2.18, and δ 2.93 and 2.59, and are therefore the **C**H$_2$ signals in **1** and **2**, respectively. Interestingly, ^{13}C-optimised HMQC spectra, probing weak CH coupling interactions, revealed cross-peaks between the C**H$_2$** proton signals at δ 2.93 and the carbon signals at δ 77.0 and 60.7, but not between the C**H$_2$** proton signals at δ 2.59 and 2.18. Presumably, these lie at a different angle with respect to the Pd**C**H which is less conducive to *J* coupling.[244]

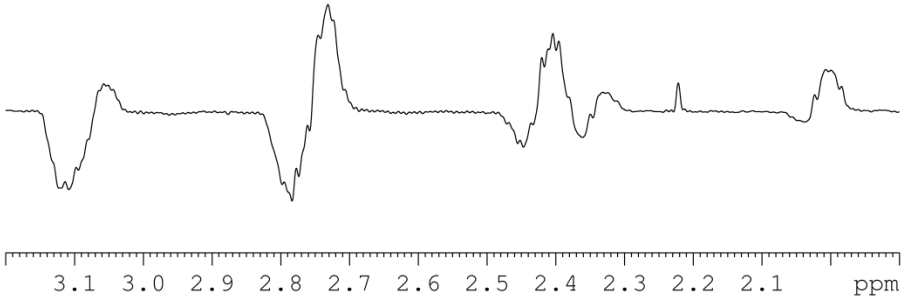

Figure 125: ^{1}H NMR spectrum showing PASADENA signals, split by couplings to ^{13}C, that correspond to two palladium alkyl species.

On heating the reaction mixture to 40 °C, two new hydride signals appeared at δ −7.10 and −8.20, shown in Figure 126. A COSY NMR spectrum, Figure 127, shows cross peaks between the two hydrides, which must be part of the same species. ^{31}P-optimised HMQC NMR spectra, supported by a ^{1}H {^{31}P} NMR spectrum shown in Figure 126, revealed a *trans*-coupling of 56 Hz between the hydride at δ −8.22 and a phosphine signal at δ 22.86. There is also a *trans*-coupling of 81 Hz with a phosphine at δ 34.23. The hydride at δ −7.11 exhibits a *cis*-coupling of 22 Hz with the same phosphine at δ 34.23. Furthermore, there was no observable change in the splitting patterns of the hydride signals on repeating the reaction with $^{13}C_2$-labelled diphenylacetylene, which suggests that this species does not contain any bound alkyne, alkene, or alkyl. It is possible that the resonances correspond to a di-palladium species, like that shown in Figure 128, where X may be chloride produced by activation of the d_2-dichloromethane solvent at palladium, and R may be chloride or triflate. The activation of dichloromethane at transition metal centres has been previously reported for iridium,[245] palladium,[241] platinum,[246] rhodium,[247] and ruthenium.[248] Palladium is generally considered to be the most active metal for this.[241] The proposed di-palladium complex in Figure 128 has one 14 electron and one 16 electron palladium centre. It could be stabilised through the formation of a metal-metal bond between the two palladium centres, leading to two 16 electron palladium centres.

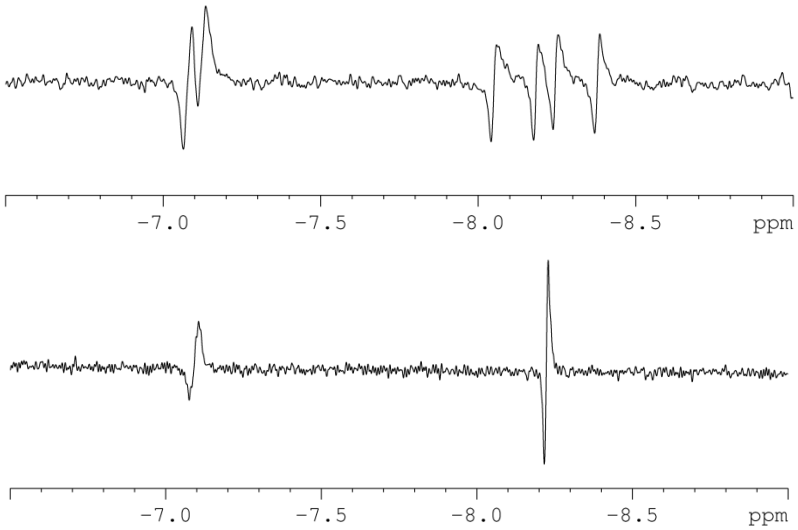

Figure 126: ^{1}H NMR (above) and $^{1}H\{^{31}P\}$ NMR (below) spectra showing signals that correspond to the para-H_2-derived hydrides in a palladium dihydride species.

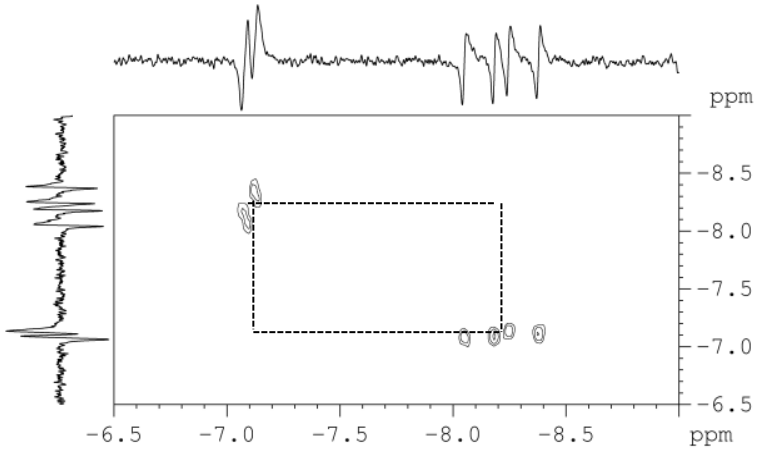

Figure 127: COSY NMR spectrum showing coupling between the PASADENA signals that correspond to the para-H_2-derived hydrides in a palladium dihydride species.

Figure 128: Potential structure of the palladium dihydride species that forms on addition of para-H_2 (~3 bar) to $[Pd(OTf)_2(PPh_3)_2]$ with 10 equivalents of diphenylacetylene, where X = Cl or OTf.

4.3.4 *Para*-hydrogenation of *Trans*-stilbene

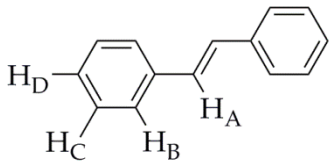

Figure 129: Trans-stilbene, ^{1}H NMR (400 MHz, CD_3Cl): 7.55 (d, J_{HH} = 7.5, 4H, H_B), 7.40 (t, J_{HH} = 7.7, 4H, H_C), 7.30 (t, J_{HH} = 7.2, 1H, H_D), 7.15 (s, 2H, H_A).

Under nitrogen, *trans*-stilbene (9.7 mg, 53.8 μmol) and $[Pd(OTf)_2(PPh_3)_2]$ (5 mg, 5.38 μmol) were dissolved in d_2-dichloromethane (0.6 mL), and the sample was degassed. Prior to the addition of *para*-H_2, there was no reaction and only the signals corresponding to $[Pd(OTf)_2(PPh_3)_2]$ and *trans*-stilbene are visible in ^{1}H NMR spectra. Addition of *para*-H_2 (~3 bar) yielded no enhanced alkene or alkyl ^{1}H NMR signals, although thermal bibenzyl signals were identified after an hour. As the enhanced ^{1}H NMR signals that correspond to the palladium alkyl species form almost immediately on hydrogenating diphenylacetylene, they are unlikely to be forming from *para*-hydrogenation of free stilbene. The stilbene is more likely undergoing a second *para*-hydrogenation whilst complexed to palladium, as has been reported previously.[117]

The two hydride signals at δ −15.43 and −8.17, which were observed in the analogous experiments in which styrene and diphenylacetylene were *para*-hydrogenated, were immediately visible on addition of *para*-H_2. These signals are compared in Figure 130. The chemical shifts of these hydride signals are independent of the substrate used, which suggests that substrate is not present in this palladium species. The lack of phosphine and substrate is surprising, as this suggests that the palladium species is stabilised solely by hydride, and triflate or chloride ligands. It is possible that the hydride signals correspond to the monomeric palladium species shown in Figure 131, which is a palladium(IV) species, where L is a neutral 2 electron donor, and is likely to be bound dichloromethane. Many palladium(IV) species have been speculated to form as intermediates in palladium-catalysed reactions, but there are no reported examples of palladium(IV) hydride species.[249] The enhanced NMR signals are phase-inverted, and thus have an 'up-down' pattern rather than the 'down-up' pattern typically observed in PHIP signals. Phase-inversion reflects a positive scalar coupling constant between the two hydride ligands. Negative scalar ^2J couplings are reported for transition metal complexes in which a

hydride ligand is positioned *cis* to the second NMR-active nucleus, as in the proposed structure in Figure 131.[250] Positive scalar couplings exist between protons that are connected by 3 bonds, thus it is possible that these NMR signals correspond to hydride ligands bound to contiguous palladium atoms in a palladium cluster or colloid and interact *via* positive scalar $^{3}J_{HH}$ couplings.

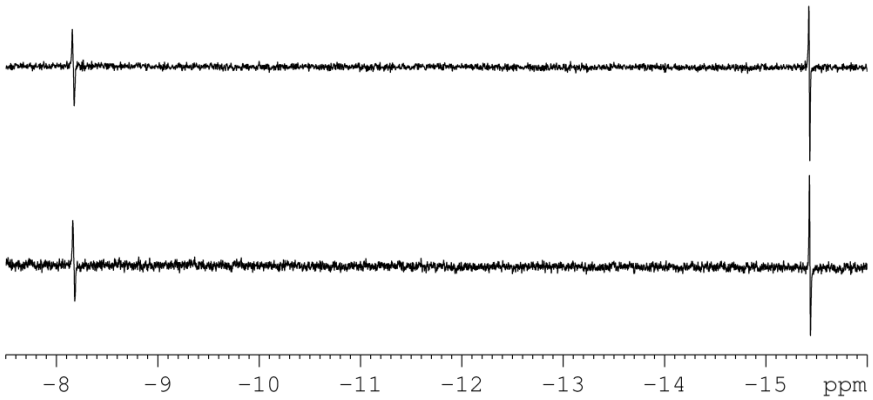

Figure 130: ^{1}H NMR spectra showing signals that correspond to para-H_2-derived hydrides in a palladium dihydride species that forms on addition of para-H_2 (~3 bar) to [Pd(OTf)$_2$(PPh$_3$)$_2$] with 10 equivalents of styrene (above), and trans-stilbene (below).

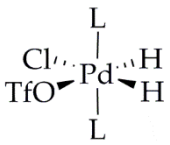

Figure 131: Possible monomeric structure of the unknown palladium hydride species, where L is likely to be dichloromethane.

4.4 Conclusion

A series of novel *cis*-[Pd(OTf)$_2$(XR$_3$)$_2$] complexes, where X = As or P, and R = aryl or alkyl, have been synthesised. These complexes are reactive palladium monomers due to the lability of their triflate ligands,[225] and have been targeted for the study of palladium cluster intermediates that form en-route to palladium nanoparticles. Palladium bis-triflate complexes have been reported to find use as pre-catalysts in hydrogenation reactions.[115-117,226] Their suitability for this study was tested through the addition of hydrogen gas, which acts as a reducing agent. All of the *cis*-[Pd(OTf)$_2$(XR$_3$)$_2$] monomers, with the exception of XR$_3$ = P(Ph(*p*-CF$_3$))$_3$, were reduced and formed palladium aggregates in solution, verifying their suitability for this study.

The palladium nanoparticles that formed on reduction of $[Pd(OTf)_2(AsPh_3)_2]$ and $[Pd(OTf)_2(PPh_3)_2]$ were analysed using TEM. Size distributions of these nanoparticles were calculated from their TEM images, and were found to be similar. The mean nanoparticle sizes were indistinguishable (~ 2 nm) when taking errors into account. Such small nanoparticles are likely to be active in a range of cross-coupling reactions.[53,238]

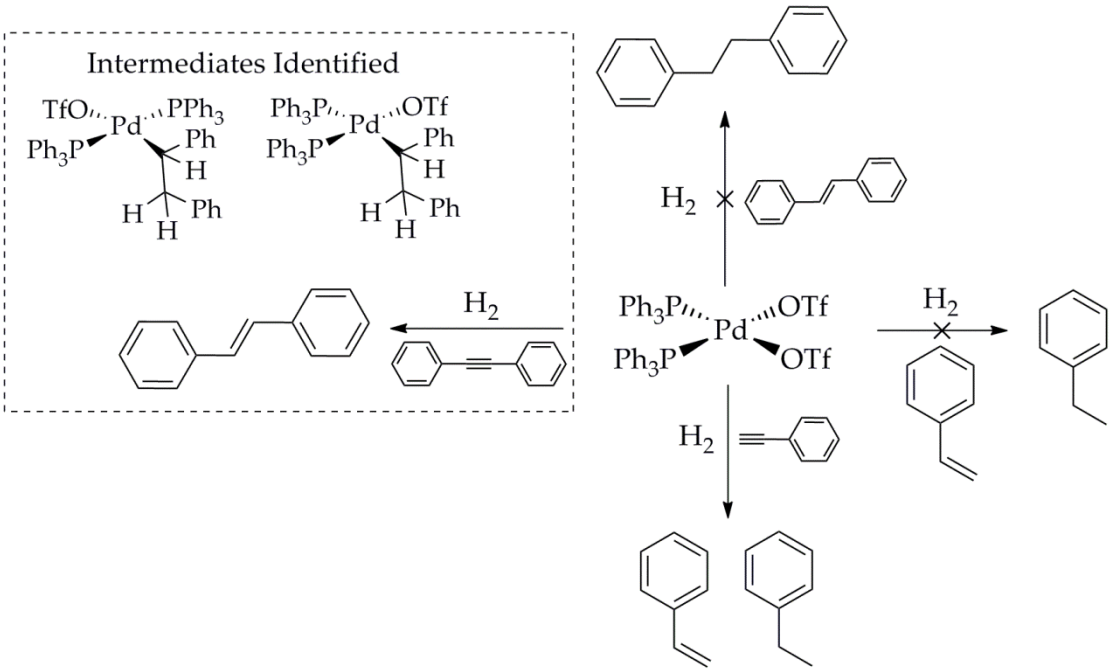

Figure 132: Hydrogenation of some unsaturated substrates using the $[Pd(OTf)_2(PPh_3)_2]$ pre-catalyst.

$[Pd(OTf)_2(PPh_3)_2]$ was used as a hydrogenation pre-catalyst to hydrogenate a number of unsaturated organic substrates, in conjunction with *para*-H_2, as shown in Figure 132. The ^{1}H NMR signals of the *para*-H_2-derived protons were substantially enhanced, which in some cases allowed palladium intermediates to be detected that would otherwise have been unobservable in ^{1}H NMR spectra. *Para*-hydrogenation of phenylacetylene did not produce any PHIP-enhanced NMR signals corresponding to palladium intermediates, whereas *para*-hydrogenation of diphenylacetylene allowed for the detection of multiple palladium species. The analogous palladium intermediates are likely to form when using phenylacetylene, but are predicted to be less stable. This is exemplified in Figure 133, where the activated carbon in $[Pd(OTf)(PPh_3)_2(bibenzyl)]$ is stabilised by electron induction from the phenyl group, whereas that in $[Pd(OTf)(PPh_3)_2(benzyl)]$ cannot be stabilised in this manner. Additionally, η^2-coordination of the phenyl ring to palladium has been reported to occur in similar palladium bibenzyl species, but cannot occur in the

benzyl analogues.[226] The [Pd(OTf)(PPh_3)$_2$(benzyl)] intermediate is therefore likely to be very short-lived and thus not observable.

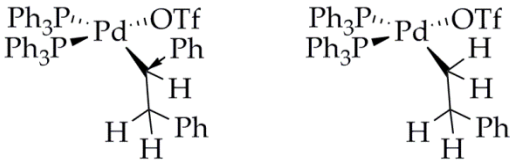

Figure 133: [Pd(OTf)(PPh_3)$_2$(bibenzyl)] (left) and [Pd(OTf)(PPh_3)$_2$(benzyl)] (right).

The observed PHIP signals also provided mechanistic information; the detection of the two geometric isomers of [Pd(OTf)(PPh_3)$_2$(bibenzyl)] supports an ionic rather than a neutral hydrogenation catalytic cycle, as previously reported.[116] *Para*-H_2 was consistently selectively added to the same face of the alkyne, selectively forming the *cis*-alkene prior to *cis-trans* isomerisation.[242] Furthermore, hydrogenation of alkynes to alkanes proceeded through two sequential hydrogenations whilst the substrate remained bound to the palladium. Hydrogenation of free alkene was limited due to the lower binding affinity of alkenes to palladium, relative to alkynes.[251] The type of enhanced signal also provided information about the mechanism of hydrogenation; the enhanced in-phase signals observed on *para*-hydrogenation of diphenylacetylene to *cis*-stilbene confirm that hydrogenation is not pairwise, but occurs *via* one-hydrogen PHIP.

Although the palladium alkyl intermediate, [Pd(OTf)(PPh_3)$_2$(bibenzyl)] was well-characterised by its PHIP-enhanced NMR signals, it was not possible to fully characterise the other palladium intermediates with the limited information gathered from their PHIP-enhanced hydride NMR signals. Furthermore, it is not known if any of the intermediates detected are multi-palladium species that form en-route to nanoparticles, or are palladium monomers. The limited information gathered using this method, led me to use a slightly different approach, whereby *para*-H_2 was added to the [Pd(OTf)$_2$(XR_3)$_2$] complexes without the presence of substrate. The results from this more successful method are described in Chapter 5.

5 Detection of Palladium Intermediates En-route to Palladium Nanoparticles

Several novel palladium(II) bis-triflate complexes with the general formula $[Pd(OTf)_2(XR_3)_2]$, where X = As or P and R = aryl or alkyl, have been synthesised for the study of palladium cluster intermediates that form en-route to palladium nanoparticles. With the exception of $XR_3 = P(Ph(p\text{-}CF_3))_3$, all of these palladium monomers are reduced by hydrogen gas to form palladium colloids. *Para*-hydrogenation of a number of alkynes with the $[Pd(OTf)_2(PPh_3)_2]$ pre-catalyst was monitored by NMR spectroscopy. This gave information about the mechanism of the hydrogenation process, but NMR data on palladium intermediates was limited. Furthermore, PHIP-enhanced signals can only result if *para*-H_2 is incorporated into the species of interest, which limits the palladium intermediates that can be detected in this way.

Herein, the $[Pd(OTf)_2(XR_3)_2]$ pre-catalysts are reduced by *para*-H_2 in the absence of substrate, and palladium intermediates that form are detected by predominantly NMR spectroscopy. The study is supported by liquid injection field desorption/ionisation (LIFDI) mass spectrometry (MS). Field desorption (FD) is a particularly soft ionisation technique which uses strong electric fields to ionise molecules *via* electron tunneling. This results in the formation of predominantly molecular radical cations ($[M]^{+\cdot}$) and allows for the detection of less stable species, including reactive transition metal complexes that contain weakly-bound ligands.[35,252]

5.1 Detection of Monohydride Species

Addition of excess *para*-H_2 (~3 bar) to d_2-dichloromethane solutions of $[Pd(OTf)_2(XR_3)_2]$ (7 mM) resulted in the formation of a number of XR_3-stabilised palladium monohydride species, which are discussed in detail in the sections that follow. Polarisation was not transferred from *para*-H_2 to any of the new proton signals, thus there was no benefit in using *para*-H_2 over normal hydrogen. Species derived from $[Pd(OTf)_2(AsPh_3)_2]$ are more difficult to characterise by NMR than their phosphine analogues because spin-½ ^{31}P has been replaced with quadrupolar ^{75}As which is effectively NMR silent in these studies.[253]

However, LIFDI-MS can be used to support NMR spectroscopic analysis by determining the molecular mass of species that form.

On addition of hydrogen to the d_2-dichloromethane solutions of $[Pd(OTf)_2(XR_3)_2]$, the formation of nanoparticles resulted in the production of free XR_3 in solution, which goes on to form $[HXR_3]^+$. Consequently, the signals in the aromatic regions of ^{1}H NMR spectra were overlapped and complex. The hydride regions of the ^{1}H NMR spectra are therefore significant in characterising the palladium monohydride species, in combination with ^{1}H $\{^{31}P\}$,^{31}P $\{^1H\}$, ^{31}P-optimised HMQC, and ^{13}C-optimised HMQC NMR spectra.

5.1.1 Formation of $[Pd(H)(OTf)(XR_3)_2]$

The first type of monohydride species, which formed immediately on addition of hydrogen, was observed by ^{1}H NMR spectroscopy as a triplet at ~ δ −17.5 where X = P, or as a singlet at δ −20.5 where X = As. These species were observed to form in all complexes, except XR_3 = P(Ph(*p*-OMe)$_3$)$_3$, which is not stable in solution and degrades to form palladium black and free phosphine ligand. Examples of the hydride ^{1}H NMR signals observed for these species are given in Figure 134.

As triplet splittings are only observed in the hydride signals that form on addition of hydrogen to $[Pd(OTf)_2(PR_3)_2]$, they must be caused by J_{HP} couplings. This was confirmed by the observed simplification of the triplet splittings to singlets on decoupling to ^{31}P. These monohydride species must therefore be stabilised by complexation of two XR_3 ligands. The hydride J_{HP} couplings are relatively small, indicating *cis*-couplings between the hydrides and phosphorus nuclei; the triplet splitting patterns suggest that the two XR_3 ligands are chemically equivalent. ^{31}P-optimised HMQC NMR spectra revealed couplings between the triplet hydride signals and single ^{31}P environments. The diagnostic ^{1}H and ^{31}P NMR signals are given in Table 16. The magnitude of the scalar coupling between the hydride and phosphine ligands reflects the structure of the complexes; couplings are larger when H-Pd-P distances are smaller and when H-Pd-P angles are close to 180 °.[254] The similarity of the J_{HP} values suggests that these complexes are all similar in structure.

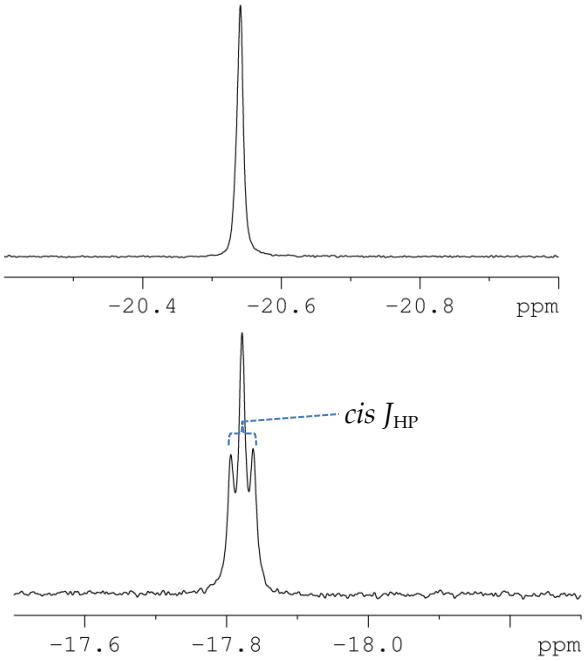

Figure 134: ^{1}H NMR spectra showing initial hydride signals observed to form on addition of H_2 (~3 bar) to d_2-dichloromethane solutions of $[Pd(OTf)_2(XR_3)_2]$, where $XR_3 = AsPh_3$ (above), and PPh_3 (below) at 250 K.

Table 16: Diagnostic ^{1}H and ^{31}P NMR signals for $[Pd(H)(OTf)(XR_3)_2]$ complexes that form on addition of H_2 (~3 bar) to d_2-dichloromethane solutions of $[Pd(OTf)_2(XR_3)_2]$. n.d. = not detected due to low SNR.

$[Pd(H)(OTf)(XR_3)_2]$			
XR_3	**$^{31}P\{^{1}H\}$ NMR (J in Hz)**	**^{1}H NMR hydride (J in Hz)**	**LIFDI-MS (m/z)**
PPh_3	25.27 (s.)	−17.80 (t. J_{HP} = 6.5)	779.0 $[C_{37}H_{30}F_3O_3P_2PdS]^+$
PPh_2Me	11.30 (s.)	−17.70 (t. J_{HP} = 5.7)	656.0 $[C_{27}H_{27}F_3O_3P_2PdS]^+$
$P(Ph(p\text{-}CF_3))_3$	25.83 (s.)	−17.50 (t. J_{HP} = 7.2)	n.d.
$P(PhPh)_3$	23.82 (s.)	−17.34 (t. J_{HP} = 6.1)	1235.3 $[C_{73}H_{55}F_3O_3P_2PdS]^+$
$PPh_2(PhPh)$	24.98 (s.)	−17.46 (br.)	931.1 $[C_{49}H_{38}F_3O_3P_2PdS]^+$
$PPh_2(PhCH_2Ph)$	25.02 (br.)	−17.6 (br.)	960.0 $[C_{51}H_{42}F_3O_3P_2PdS]^+$
$AsPh_3$	-	−20.54 (s.)	867.0 $[C_{37}H_{30}F_3O_3As_2PdS]^+$

The up-field chemical shifts of the hydride signals indicate that they are positioned *trans* to the π and σ-donating triflate ligand, rather than the π-accepting XR_3 ligand. Despite the *cis*-configurations of the original $[Pd(OTf)_2(XR_3)_2]$ complexes, it is clear that in these monohydride species, the hydrides lie *trans* to the triflate ligand, and *cis* to two XR_3 ligands, as shown in Figure 135. Substitution of the original triflate ligand by a hydride ligand must therefore result in a ligand rearrangement.

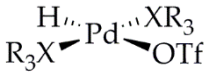

Figure 135: $[Pd(H)(OTf)(XR_3)_2]$.

The formation of $[Pd(H)(OTf)(XR_3)_2]$ from $[Pd(OTf)_2(XR_3)_2]$ potentially proceeds *via* an associative pathway shown in Figure 136. This involves the initial binding of hydrogen to palladium to form the 18 electron five-coordinate trigonal bipyramidal $[Pd(OTf)_2(H_2)(XR_3)_2]$ complex. The dihydrogen molecule is then cleaved, forming the 16 electron $[Pd(H)(OTf)_2(XR_3)_2]$ complex in which the hydride is positioned *cis* to triflate. Triflic acid is also produced during this mechanistic step. The hydride ligand exhibits a strong *trans*-effect, which labilises the XR_3 ligand positioned *trans* to it. Rearrangement of the ligands results in the hydride ligand now lying *trans* to the triflate and the XR_3 ligands lying *trans* to one another. This complex is the more stable isomer and is the only one observed experimentally.

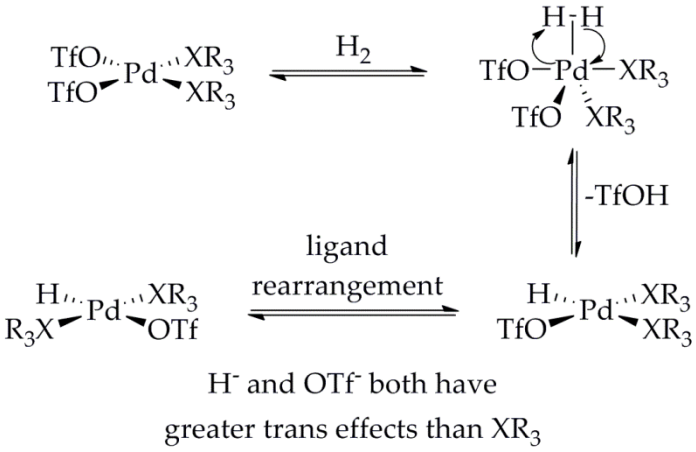

Figure 136: Likely pathway for the formation of $[Pd(H)(OTf)(XR_3)_2]$.

Signals for the $[Pd(OTf)(XR_3)_2]$ cations were observed in the corresponding LIFDI mass spectra, and their experimentally-observed *m*/*z* values are given in Table 16. Their

isotope distribution patterns match with those simulated for these complexes. This is exemplified by the LIFDI-MS signal observed for $[Pd(OTf)(PPh_3)_2]^+$, shown in Figure 137. A complete set of LIFDI-MS data is given in Appendix B, section B.2.1. These data confirm that the proposed $[Pd(H)(OTf)(XR_3)_2]$ species are present in solution.

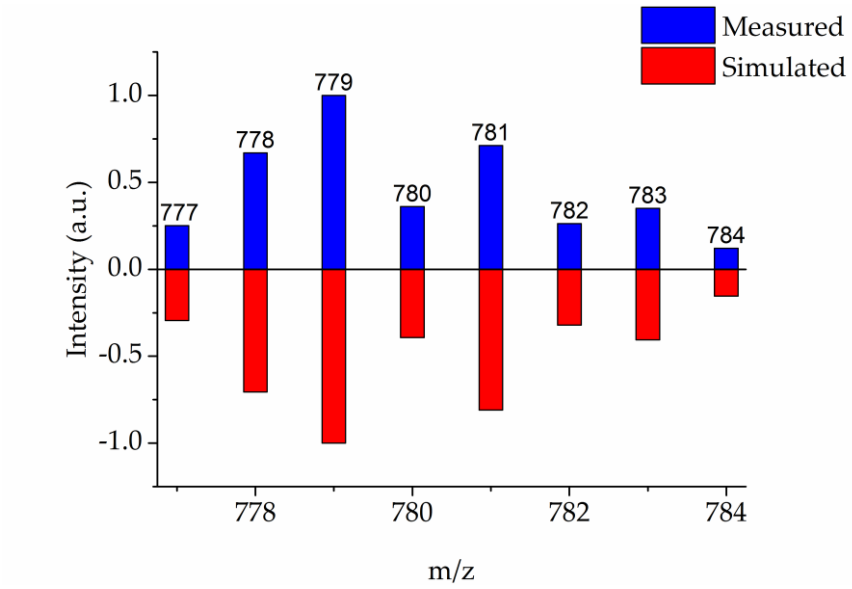

Figure 137: Histogram of the experimental and simulated LIFDI-MS data for the $[Pd(OTf)(PPh_3)_2]^+$ cation.

In the case of XR_3 = $P(Ph(p\text{-}CF_3))_3$, the resulting $[Pd(H)(OTf)(P(Ph(p\text{-}CF_3))_3)_2]$ complex forms quantitatively, is stable to hydrogen reduction, and does not go on to form palladium nanoparticles. Presumably, the electron-withdrawing inductive effect of the trifluoromethyl groups stabilises the complex, which would otherwise react further due to the instability of a hydride positioned *trans* to triflate.

It was anticipated that platinum analogues could be used in this study, as spin-½ ^{195}Pt is a useful NMR handle for metal cluster characterisation. Addition of hydrogen to d_2-dichloromethane solutions of $[Pt(OTf)_2(PPh_3)_2]$, however, resulted in the quantitative formation of $[Pt(H)(OTf)(PPh_3)_2]$ with no further reduction, as observed with XR_3 = $P(Ph(p\text{-}CF_3))_3$. These complexes have been fully characterised by NMR spectroscopy and this data is given in the Experimental.

5.1.2 Formation of $[Pd(H)(XR_3)_3]OTf$

After a time period of a few minutes, a second type of monohydride palladium species formed. These were identified by ^1H NMR spectroscopy as a doublet of triplets at ~ δ −6.8 where X = P, or as a singlet at δ −7.6 where X = As. Examples of the corresponding hydride NMR signals are shown in Figure 138.

Again, splitting of the hydride NMR signals is only observed when X = P, as a result of J_{HP} couplings. The doublet of triplets splitting confirms that these monohydride complexes now contain three phosphine ligands, two of which are chemically equivalent. A large J_{HP} coupling of ~ 180 Hz, which gives rise to the doublet, is due to coupling with a phosphorus nucleus that lies *trans* to the hydride, and a small J_{HP} coupling of ~ 13 Hz, which gives rise to the triplet character, is due to coupling with two phosphorus nuclei that lie *cis* to the hydride. The smaller intensities of the inner triplet peaks relative to the outer peaks are indicative of ligand exchange at palladium. This is discussed in more detail later in this section.

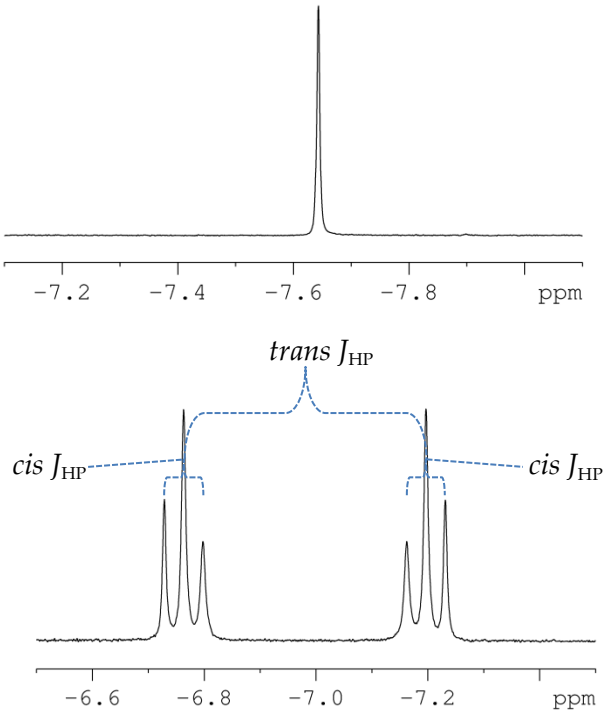

Figure 138: ^1H NMR spectra showing hydride signals observed to form on addition of H_2 (~3 bar) to d_2-dichloromethane solutions of $[Pd(OTf)_2(XR_3)_2]$, where $XR_3 = AsPh_3$ (above), and PPh_3 (below) at 250 K.

Cross-peaks observed in ^{31}P-optimised HMQC spectra confirm that there are two phosphorus signals due to two distinct phosphine environments - a doublet at lower

magnetic field with a relative signal integration of 2, which corresponds to the phosphines that lie *cis* to the hydride, and a triplet at higher magnetic field with a relative signal integration of 1, which corresponds to the phosphines that lie *trans* to the hydride. This is exemplified in the ^{31}P NMR spectrum in Figure 139, where X = PPh_3.

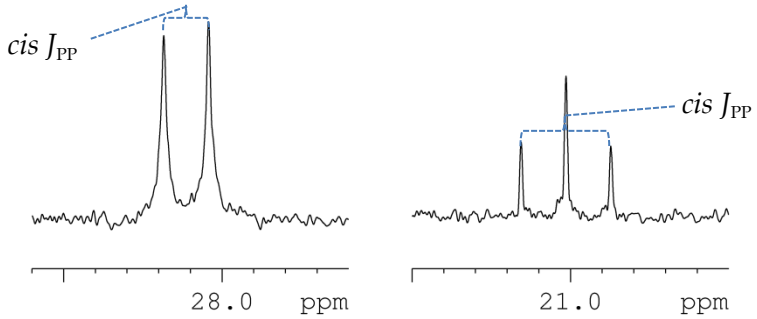

Figure 139: ^{31}P NMR spectra at 298 K, showing the ^{31}P signals observed to couple to the hydride signal at δ −6.98, which forms on addition of H_2 (~3 bar) to d_2-dichloromethane solutions of $[Pd(OTf)_2(PPh_3)_2]$.

These ^{1}H and ^{31}P NMR signals correspond to $[Pd(H)(XR_3)_3]OTf$, shown in Figure 140, where the triflate in the previously formed $[Pd(H)(OTf)(XR_3)_2]$ has been displaced by free XR_3 ligand, and is now acting as a counterion to stabilise the resulting positive charge. The extra XR_3 ligand required to form $[PdH(XR_3)_3]OTf$ becomes available on reduction of $[Pd(OTf)_2(XR_3)_2]$ to the palladium colloids observed by TEM imaging, with free XR_3 ligands visible in NMR spectra, as well as triflic acid.

The diagnostic ^{1}H and ^{31}P NMR signals are given in Table 17, in addition to the J_{HP} values. The J_{HP} couplings are similar in all of the complexes with the exception of XR_3 = PPh_2Me, which is the phosphine with the smallest cone angle,[255] and which has a significantly larger $J_{HP(trans)}$ value. Larger couplings arise when H-Pd-P angles are close to 180 °. A perfectly square-planar complex exhibits H-Pd-P_{trans} angles of 180 °, however, this angle decreases as the structure becomes distorted. In the $[Pd(H)(XR_3)_3]OTf$ complexes, bulkier phosphines with larger cone angles will distort the H-Pd-P_{trans} angle to < 180 °, resulting in smaller $J_{HP(trans)}$ values. Smaller phosphines, like PPh_2Me, will cause less of a distortion, resulting in H-Pd-P_{trans} angles closer to 180 °, and consequently larger $J_{HP(trans)}$ values.

Table 17: Diagnostic ^{1}H and ^{31}P NMR signals for $[Pd(H)(XR_3)_3]OTf$ complexes that form on addition of H_2 (~3 bar) to d_2-dichloromethane solutions of $[Pd(OTf)_2(XR_3)_2]$. * Due to the stability of $[Pd(H)(OTf)(P(Ph(p\text{-}CF_3))_3)_2]$, excess $P(Ph(p\text{-}CF_3))_3$ was required to form $[Pd(H)(P(Ph(p\text{-}CF_3))_3)_3]OTf$. This complex was also stable to further reduction. n.d = not detected due to low SNR.

$[Pd(H)(XR_3)_3]OTf$			
XR_3	**$^{31}P\{^{1}H\}$ NMR (J in Hz)**	**^{1}H NMR hydride (J in Hz)**	**LIFDI-MS (m/z) ($[M\text{-}OTf]^+$)**
PPh_3	27.63 (d. J_{PP} = 28.9), 21.24 (t. J_{PP} = 29.1)	−6.98 (d.t. J_{PH} = 173.5, 13.9)	893.1 $[C_{54}H_{46}P_3Pd]^+$
PPh_2Me	10.08 (d. J_{PP} = 31.1), 0.84 (t. J_{PP} = 32.8)	−6.65 (d.t. J_{HP} = 187.7, 9.7)	707.1 $[C_{39}H_{40}P_3Pd]^+$
$P(Ph(p\text{-}CF_3))_3$*	26.1 (br.) 20.4 (br.)	−6.89 (d.t. J_{HP} = 174.7, 15.4)	n.d.
$P(PhPh)_3$	26.44 (d. J_{PP} = 28.6), 18.94 (t. J_{PP} = 28.6)	−6.45 (d.t. J_{HP} = 175.6, 13.7)	1577.6 $[C_{108}H_{82}P_3Pd]^+$
$PPh_2(PhPh)$	28.19 (d. J_{PP} = 28.8), 20.56 (t. J_{PP} = 28.8)	−6.57 (d.t J_{HP} = 175.0, 13.9)	1121.2 $[C_{72}H_{58}P_3Pd]^+$
$PPh_2(PhCH_2Ph)$	36.6 (br.) 19.7 (br.)	−6.85 (d.t J_{HP} = 175.1, 14.1)	1164.1 $[C_{75}H_{64}P_3Pd]^+$
$AsPh_3$	-	−7.64 (s.)	1025.0 $[C_{54}H_{46}As_3Pd]^+$

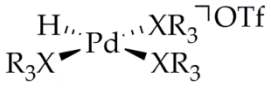

Figure 140: $[Pd(H)(XR_3)_3]OTf$.

The experimentally-observed m/z values of the $[Pd(H)(XR_3)_3]$ cations are also given in Table 17, and the LIFDI-MS signal observed for $[Pd(H)(PPh_3)_3]^+$ is shown, as an example, in Figure 141. A complete set of LIFDI-MS data is given in Appendix B, section B.2.2. These data confirm the presence of $[Pd(H)(OTf)(XR_3)_2]$ species in solution.

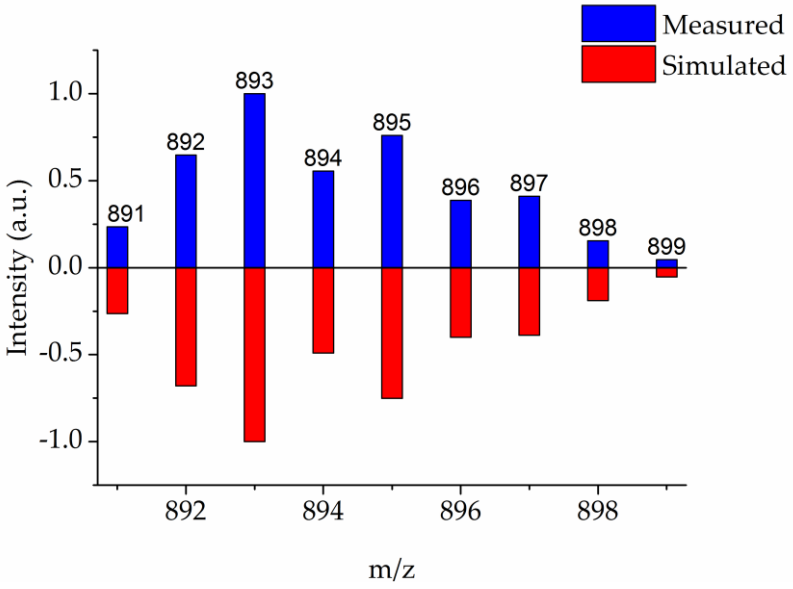

Figure 141: Histogram of the experimental and simulated LIFDI-MS data for the $[Pd(H)(PPh_3)_3]^+$ cation.

The formation of $[Pd(H)(PPh_3)_3]^+$ in solution has been observed previously by Zudin *et. al.*[256] They dissolved $[Pd(CF_3COO)_2(PPh_3)_2]$ in aqueous trifluoroacetic acid, containing an excess of triphenylphosphine, and added hydrogen at 343 K. Their published NMR data is in very good agreement with that reported here. Furthermore, they argue that the reduced stability of $[Pd(H)(PPh_3)_3]^+$ in more acidic solutions results from the equilibrium shown below.

$$H^+ + [Pd(H)(PPh_3)_3]OOCCF_3 \rightleftharpoons [Pd(H)(OOCCF_3)(PPh_3)_2] + [HPPh_3]^+$$

Equilibrium shifts to the right in more acidic solutions, producing $[PdH(CF_3COO)(PPh_3)_2]$, which can subsequently be protolysed by the acid to produce the original $[Pd(CF_3COO)_2(PPh_3)_2]$ and hydrogen gas (not shown here).

Exchange between $[Pd(H)(XR_3)_3]OTf$ and $[Pd(H)(OTf)(XR_3)_2]$ was confirmed in this study using EXSY. Each hydride signal was selectively excited, and left for a specified mixing time after which a ^1H NMR spectrum was acquired. In this way, any exchange between the palladium hydride species was observed as magnetisation transfer between the hydride NMR signals. This is exemplified in Figure 142, where the hydride signal corresponding to $[Pd(\mathbf{H})(PPh_3)_3]OTf$ has been irradiated, and a $^1H\{^{31}P\}$ NMR spectrum acquired after 1 s contains a peak corresponding to $[Pd(\mathbf{H})(OTf)(PPh_3)_2]$.

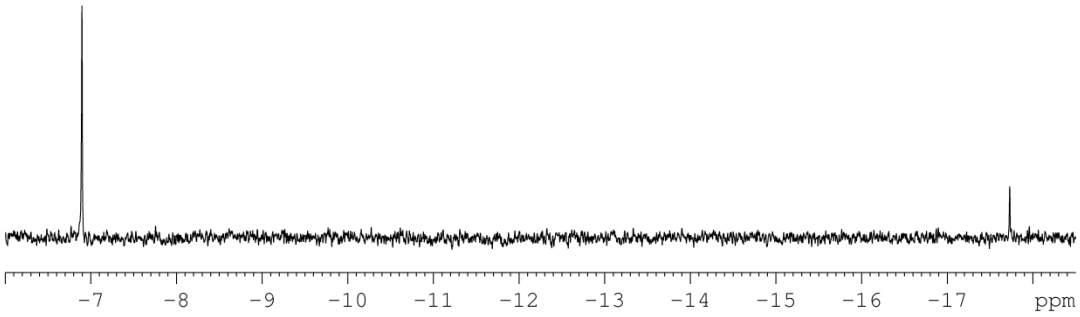

Figure 142: {^{31}P} EXSY NMR spectrum acquired with a mixing time of 1 s, after irradiating the hydride NMR signal at δ -6.98 corresponding to [Pd(H)(PPh$_3$)$_3$]OTf, at 298 K.

This hydride exchange confirms that these palladium species exist in equilibrium, where K_{eq}~1.95 mol^{-1}dm^3 at 298 K, as measured from the ^{1}H hydride NMR signal areas. The formation of [Pd(H)(XR$_3$)$_3$]OTf from [Pd(H)(OTf)(XR$_3$)$_2$] is likely to occur *via* associative substitution,[257] where initial addition of XR$_3$ forms the 18 electron trigonal bipyramidal complex shown in Figure 143, followed by the dissociation of triflate. This is likely to be a lower-energy pathway than dissociative substitution, which would involve the 14 electron [Pd(H)(XR$_3$)$_2$]OTf complex.

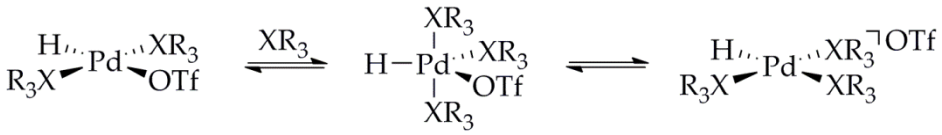

Figure 143: Likely pathway for the formation of [Pd(H)(XR$_3$)$_3$]OTf.

According to Le Chatelier's principle,[258] addition of excess XR$_3$ ligand should shift the position of equilibrium to the right. This was observed experimentally; addition of excess triphenylphosphine (10 equivalents) to a d_2-dichloromethane solution of [Pd(H)(OTf)(PPh$_3$)$_2$] and [Pd(H)(XR$_3$)$_3$]OTf shifted equilibrium to the far right, so that only the hydride signal corresponding to [Pd(H)(PPh$_3$)$_3$]OTf was observed, shown in Figure 144 (a). This hydride signal appears broad, and the triplet splitting is no longer resolved, even at low temperatures, due to the fast exchange of the bound phosphines with the free triphenylphosphine.

Similarly, addition of excess tris(4-trifluoromethylphenyl)phosphine (5 equivalents) to a d_2-dichloromethane solution of [Pd(H)(OTf)(P(Ph(*p*-CF$_3$))$_3$)$_2$], resulted in quantitative conversion to [Pd(H)(P(Ph(*p*-CF$_3$))$_3$)$_3$]OTf. The hydride region of the corresponding ^{1}H

NMR spectrum is shown in Figure 144 (b) and contains only the hydride signal for [Pd(**H**)(P(Ph(*p*-CF_3))$_3$)$_3$]OTf. This tris-phosphine complex was only accessible *via* this route and was not observed to form on addition of hydrogen to d_2-dichloromethane solutions of solely [Pd(OTf)$_2$(P(Ph(*p*-CF_3))$_3$)$_2$].

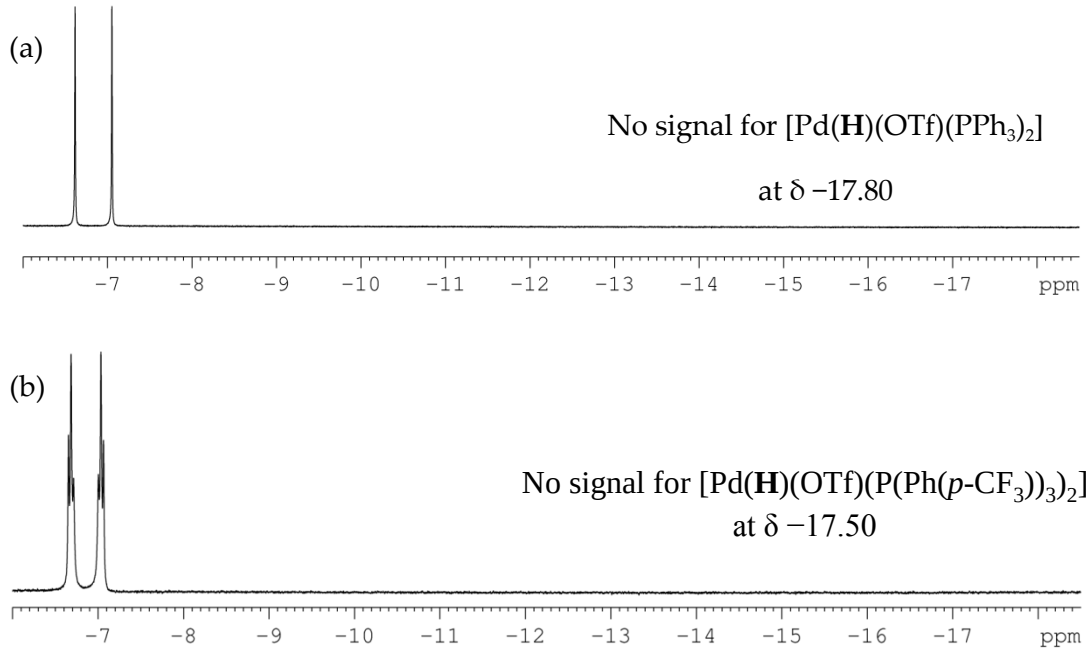

Figure 144: ^{1}H NMR spectrum collected at (a) 298 K, showing only the hydride signal corresponding to [Pd(H)(PPh$_3$)$_3$]OTf due to reaction of [Pd(H)(OTf)(PPh$_3$)$_2$] with excess PPh$_3$, and (b) 235 K, showing only the hydride signal corresponding to [Pd(H)(P(Ph(p-CF$_3$))$_3$)$_3$]OTf due to reaction of [Pd(H)(OTf)(P(Ph(p-CF$_3$))$_3$)$_2$] with excess P(Ph(p-CF$_3$))$_3$.

5.1.3 Non-innocent Dichloromethane

In the case of X = $AsPh_3$, two additional hydride NMR signals were observed to form at δ −9.43 and −9.93. Analogous signals were not observed to form from any of the palladium bis-triflate complexes stabilised by the other XR_3 ligands. Variable temperature NMR studies, shown in Figure 145, reveal that these new monohydride species (*) appear at 265 K, after the formation of [Pd(H)(OTf)(AsPh$_3$)$_2$] (* observed at T = 255 K) and before the formation of [Pd(H)(AsPh$_3$)$_3$]OTf (* observed at T = 270 K).

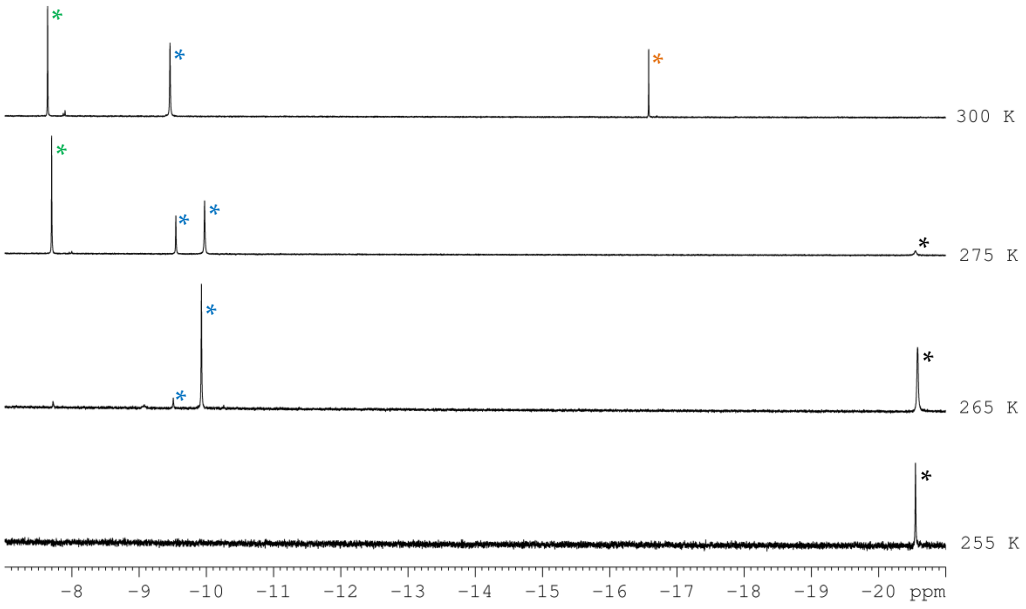

Figure 145: ^{1}H NMR spectra of the hydride signals that correspond to [Pd(H)(OTf)(AsPh$_3$)$_2$] (*), [Pd(H)(Cl$_2$CD$_2$)(AsPh$_3$)$_2$] (*), [Pd(H)(AsPh$_3$)$_3$]OTf (*), and [Pd(Cl)(H)(AsPh$_3$)$_2$] (*), that form on addition of H$_2$ (~3 bar) to d$_2$-dichloromethane solutions of [Pd(OTf)$_2$(AsPh$_3$)$_2$].

EXSY was used to probe exchange between these new palladium monohydride species. Closer examination revealed that the hydride signal at δ −9.43 exchanges with those at δ – 20.54 ([Pd(**H**)(OTf)(AsPh$_3$)$_2$]) and – 7.64 ([Pd(**H**)(AsPh$_3$)$_3$]OTf), however, the signal at δ −9.93 does not exchange on the NMR timescale. Furthermore, magnetisation was found to transfer from these two new hydride signals into protons in residual CHDCl$_2$ molecules, which suggests that dichloromethane is bound to palladium. The hydride signals at δ −9.43 and −9.93 most likely correspond to the hydride ligands in the two geometric isomers of [Pd(**H**)(Cl$_2$CD$_2$)(AsPh$_3$)$_2$]OTf, shown in Figure 146, where the triflate ligand in [Pd(H)(OTf)(AsPh$_3$)$_2$] has been replaced with a molecule of dichloromethane, which is binding through the chlorine. The triflate is now acting as a counterion to stabilise the resulting positive charge.

Table 18: Diagnostic ^{1}H NMR signals for [Pd(H)(CD$_2$Cl$_2$)(AsPh$_3$)$_2$]OTf complexes that form on addition of H$_2$ (~3 bar) to d$_2$-dichloromethane solutions of [Pd(OTf)$_2$(AsPh$_3$)$_2$].

[Pd(H)(Cl$_2$CD$_2$)(AsPh$_3$)$_2$]	
XR$_3$	**^{1}H NMR hydride (*J* in Hz)**
AsPh$_3$ (two geometric isomers)	−9.43 (s.) −9.93 (s.)

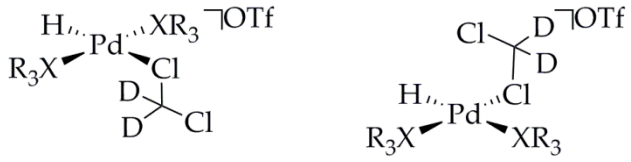

Figure 146: The two geometric isomers of [Pd(H)(Cl$_2$CD$_2$)(XR$_3$)$_2$].

The NMR spectroscopic data for these two species are given in Table 18. Splitting of the hydride NMR signals by $^4J_{HD}$ couplings is not observed due to exchange of the dichloromethane. The mechanism for the formation of [Pd(H)(Cl$_2$CD$_2$)(AsPh$_3$)$_2$]OTf from [Pd(H)(OTf)(AsPh$_3$)$_2$] is shown in Figure 147. Initial coordination of dichloromethane forms an 18 electron trigonal bipyramidal intermediate. This is followed by loss of a triflate ligand to form the isomer of [Pd(H)(Cl$_2$CD$_2$)(AsPh$_3$)$_2$]OTf in which the hydride is positioned *trans* to the bound dichloromethane. A ligand rearrangement forms the isomer in which the hydride lies *cis* to the bound dichloromethane. The geometric isomer in which the hydride lies *trans* to the dichloromethane ligand is therefore most likely to be in equilibrium with [Pd(H)(OTf)(AsPh$_3$)$_2$] on the NMR timescale, thus this likely corresponds to the hydride signal at δ −9.43. The isomer in which the hydride lies *cis* to the dichloromethane ligand requires rearrangement of the palladium complex, in addition to exchange, and this is less likely to occur on the NMR timescale, hence this isomer likely gives rise to the hydride signal at δ −9.93.

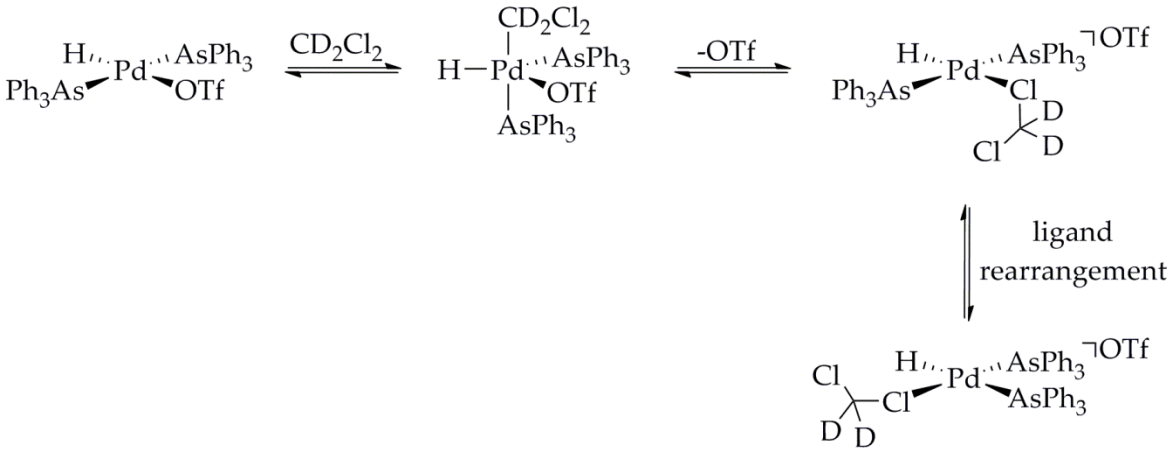

Figure 147: Likely pathway for the formation of the two geometric isomers of [Pd(H)(Cl$_2$CD$_2$)(AsPh$_3$)$_2$]OTf.

In these hydrogenation reactions, dichloromethane is not an innocent solvent. As previously discussed, a range of transition metals are known to activate

dichloromethane,[241,245-248] and palladium is generally considered to be the most active metal for this.[241] Formation of the Pd←Cl bond in $[Pd(H)(Cl_2CD_2)(AsPh_3)_2]$ weakens the Cl-C bond of the bound dichloromethane, which is now more likely to break. Previous studies on the hydrodechlorination of dichloromethane report methane, methyl chloride, ethane, and ethylene as the main products, with little known about the mechanism, which is presumed to be radical in nature.[241] In these studies, ^{1}H NMR signals appear at δ 0.82 and 0.23, which agree with the chemical shifts of ethane and methane respectively.[259] There is no ^{1}H NMR evidence for the formation of ethylene, and it was not possible to analyse the spectroscopic region at which methyl chloride would be observed (δ 7.32) due to signal overlap.

At the higher temperatures used in the variable temperature NMR studies discussed above, a new hydride signal is observed to form at δ −15.56. Similar hydride signals are also observed when XR_3 = $P(PhPh)_3$, $PPh_2(PhPh)$, and $PPh_2(PhCH_2Ph)$, and these are shown in Figure 148. The triplet splitting of ~ 12 Hz is due to J_{HP} coupling to phosphines positioned *cis* to the hydride – all of these signals simplify to singlets in ^{1}H {^{31}P} NMR spectra. The diagnostic phosphorus and hydride NMR shifts are given in Table 19. The chemical shifts are similar to literature values for hydrides positioned *trans* to chloride in palladium bis-phosphine complexes, for example the hydride in $[Pd(Cl)(H)(PPh_3)_2]$ resonates at δ −13.2.[260] Furthermore, *m*/*z* values corresponding to dicationic dimers, $[Pd(Cl)(XR_3)_2]_2^{2+}$, are observed in LIFDI mass spectra (see Appendix B, section B.2.3) and their isotope distributions match with simulations. The LIFDI-MS signal observed for $[Pd(Cl)(P(PhPh)_3)_2]_2^{2+}$ is given in Figure 150. Despite NMR evidence for the $[PdH(Cl_2CD_2)(XR_3)_2]OTf$ complex being limited to XR_3 = $AsPh_3$, such complexes most likely form as precursors to $[Pd(Cl)(H)(XR_3)_2]$ (Figure 149).

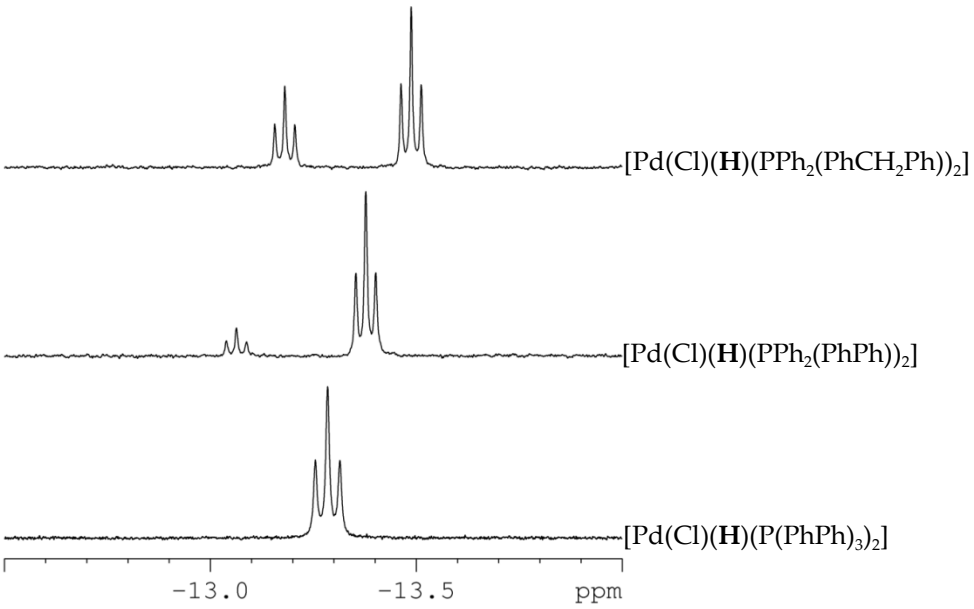

Figure 148: *^{1}H NMR spectra, collected at 250 K, showing the hydride signals that correspond to [Pd(H)(Cl)(P(PhPh)$_3$)$_2$]* **(below)**, *[Pd(Cl)(H)(PPh$_2$(PhPh))$_2$] (middle), and [Pd(Cl)(H)(PPh$_2$(PhCH$_2$Ph))$_2$] (above), that form on addition of H_2 (~3 bar) to d$_2$-dichloromethane solutions of [Pd(OTf)$_2$(PR$_3$)$_2$].*

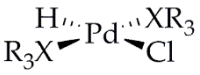

Figure 149: [Pd(Cl)(H)(XR$_3$)$_2$].

Table 19: Diagnostic ^{1}H and ^{31}P NMR signals for [Pd(Cl)(H)(XR$_3$)$_2$] complexes that form on addition of H_2 (~3 bar) to d$_2$-dichloromethane solutions of [Pd(OTf)$_2$(XR$_3$)$_2$].

[Pd(Cl)(H)(XR$_3$)$_2$]			
XR$_3$	**^{31}P {^{1}H} NMR (*J* in Hz)**	**^{1}H NMR hydride (*J* in Hz)**	**LIFDI-MS *m/z***
P(PhPh)$_3$	28.02 (s.)	−13.29 (t. J_{HP} = 11.9)	1124.1 $[C_{144}H_{108}Cl_2P_4Pd_2]_2^{2+}$
PPh$_2$(PhPh) (two isomers)	29.38 (s.), 29.29 (s.)	−13.06 (t. J_{HP} = 12.2) −13.38 (t. J_{HP} = 12.2)	818.6 $[C_{96}H_{76}Cl_2P_4Pd_2]_2^{2+}$
PPh$_2$(PhCH$_2$Ph) (two isomers)	29.4 (s.), 29.1 (s.)	−13.20 (t. J_{HP} = 12.2) −13.50 (t. J_{HP} = 12.2)	-
AsPh$_3$	-	−15.56 (s.)	-

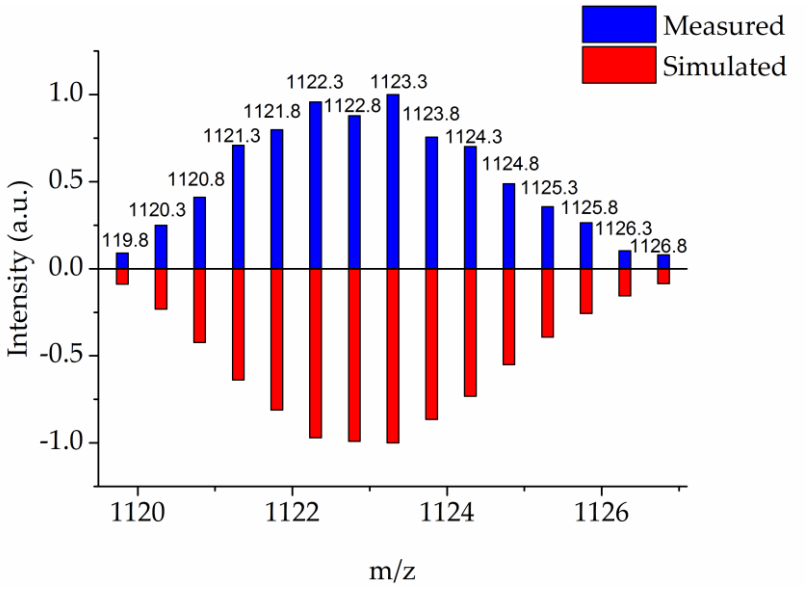

Figure 150: Histogram of the experimental and simulated LIFDI-MS data for the $[Pd(Cl)(P(PhPh)_3)_2]_2^{2+}$ dication.

To further confirm the $[Pd(Cl)(\mathbf{H})(XR_3)_2]$ assignments of the observed ^1H hydride NMR signals, the reactions were repeated in the absence of a chloride source. Therefore, d_2-dichloromethane was replaced with d_6-benzene. The ^1H NMR signals corresponding to $[Pd(Cl)(\mathbf{H})(XR_3)_2]$ were no longer observed. Interestingly, only the $[Pd(\mathbf{H})(OTf)(XR_3)_2]$ signals were observed, as shown in Figure 151 using $XR_3 = P(PhPh)_3$ as the example. This suggests that dichloromethane is required for the formation of $[Pd(H)(XR_3)_3]OTf$, which is presumably because it can bind to the palladium to stabilise the $[Pd(H)(XR_3)_2]^+$ intermediate and its polarity stabilises the ionic charges in $[Pd(H)(XR_3)_3]OTf$. Addition of d_2-dichloromethane to the d_6-benzene solutions containing $[Pd(H)(OTf)(XR_3)_2]$ resulted in the formation of the hydride signals corresponding to $[Pd(Cl)(\mathbf{H})(XR_3)_2]$ and $[Pd(\mathbf{H})(XR_3)_3]OTf$.

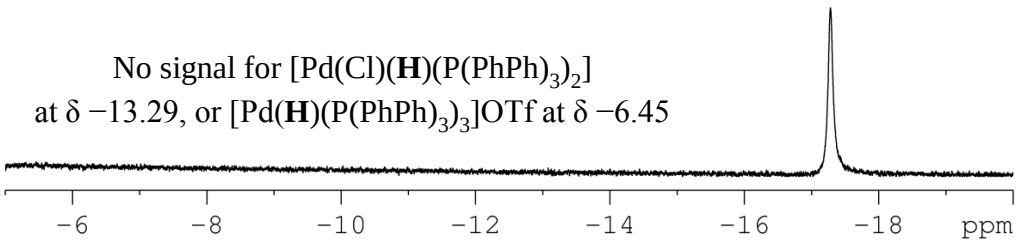

Figure 151: ^1H NMR spectrum of the hydride signal that corresponds to $[Pd(\underline{H})(OTf)(P(PhPh)_3)_2]$, which forms on addition of H_2 (~3 bar) to d_6-benzene solutions of $[Pd(OTf)_2(P(PhPh)_3)_2]$, at 275 K.

The chemical shifts of the hydride signals in the palladium monohydride arsine complexes are consistently located up-field, relative to the phosphine complexes. For example, the hydride signal corresponding to [Pd**H**(OTf)($AsPh_3$)$_2$] (δ −20.53) is shifted 2.8 ppm up-field with respect to [Pd**H**(OTf)(PPh_3)$_2$] (δ −17.73). This reflects the greater electron-donation exhibited by arsine ligands. The hydride signal of the proposed [Pd**H**(Cl)($AsPh_3$)$_2$] lies at δ −15.56, whereas that of [Pd**H**(Cl)(PPh_3)$_2$] lies at δ −13.2. The up-field shift seen for [Pd**H**(Cl)($AsPh_3$)$_2$] is as expected.

Interestingly, when XR_3 = PPh_2(PhPh), or PPh_2($PhCH_2Ph$), two hydride signals, with identical J_{HP} coupling constants of 12.2 Hz, are observed at chemical shifts that correspond to [Pd(Cl)(**H**)(XR_3)$_2$] (Figure 148). These are not observed at room temperature due to line broadening, but resolve at lower temperatures (~ 250 K). Two sets of signals are most likely the result of two different rotamers (*anti* and *syn*) present in solution, which are shown for XR_3 = PPh_2(PhPh) in Figure 152. These are observed due to restricted rotation about the Pd-P bonds, which results from steric clashes with the chloride ligand. The smaller down-field triplet signals likely correspond to the hydrides in complexes with *syn* phosphine orientations, which are sterically disfavoured. The larger up-field triplet signals correspond to the more favoured *anti* orientation. A larger *syn*:*anti* ratio (0.5:1 rather than 0.1:1) is observed when XR_3 = PPh_2($PhCH_2Ph$), and only one isomer is possible when XR_3 = P(PhPh)$_3$. Unequally populated rotamers have been reported for similar palladium phosphine and palladium carbene complexes.[261,262]

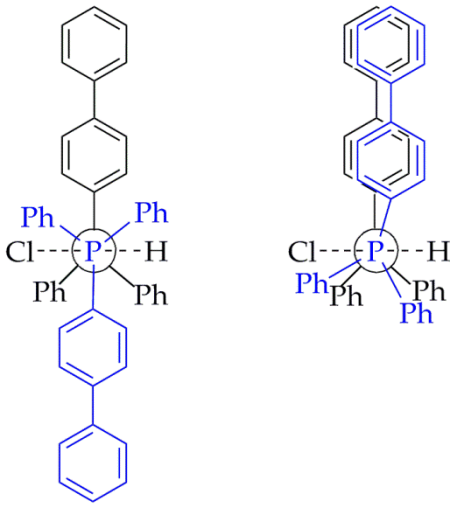

Figure 152: Anti (left) and syn (right) rotamers of [Pd(Cl)(H)(PPh_2(PhPh))$_2$].

Rotamers should also be observed in the [Pd(**H**)(OTf)(PR_3)$_2$] and [Pd(**H**)(PR_3)$_3$]OTf complexes, due to steric clashes with the triflate and phosphine ligands, respectively. Due to exchange, the hydride signals corresponding to [Pd(**H**)(OTf)(PR_3)$_2$] are broad even at the low temperatures used, therefore rotamers could not be distinguished. Additional small hydride signals corresponding to a second rotamer of [Pd(**H**)(PR_3)$_3$]OTf are present, however these signals overlap with those of the major rotamer, and as a result, cannot be characterised.

Activation of dichloromethane is only observed when the stabilising XR_3 ligands are relatively bulky and electron-donating. Presumably, bulkier ligands disfavour the formation of [Pd(H)(XR_3)$_3$]OTf due to the steric implications of three bulky ligands positioned *cis* to one another. Furthermore, electron-donation from the XR_3 ligand positioned *trans* to the hydride also destabilises [Pd(H)(XR_3)$_3$]OTf. The equilibrium, shown in Figure 153 therefore shifts towards the [Pd(H)(Cl_2CD_2)(XR_3)$_2$]OTf complex, increasing the probability of C-Cl bond cleavage.

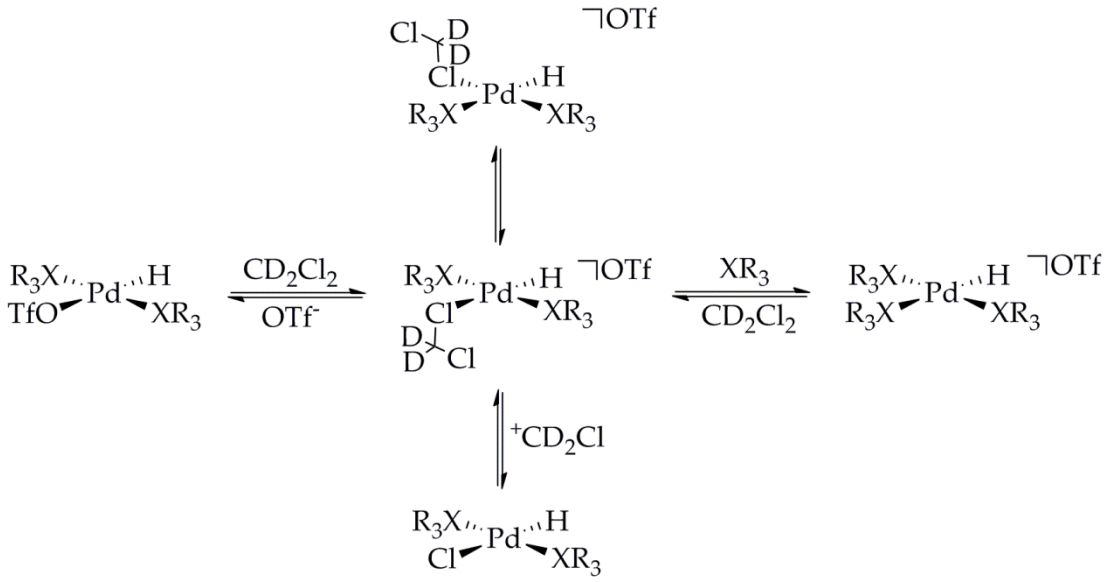

Figure 153: Exchange between the different hydride species that form on addition of hydrogen to [Pd(OTf)$_2$(XR$_3$)$_2$].

This study has revealed the importance of dichloromethane, for the stabilisation of [Pd(H)(XR_3)$_2$]OTf intermediates during exchange between [Pd(H)(OTf)(XR_3)$_2$] and [Pd(H)(XR_3)$_3$]OTf. In the absence of a coordinating solvent, for example when using benzene, the formation of [Pd(H)(XR_3)$_3$]OTf is not observed. Coordination of

dichloromethane to palladium results in its activation and consequently the formation of $[Pd(Cl)(H)(XR_3)_2]$ species.

5.1.4 Depletion of Monohydride Species

Over time, the hydride NMR signals corresponding to $[Pd(\mathbf{H})(OTf)(XR_3)_2]$, $[Pd(\mathbf{H})(XR_3)_3]OTf$, $[Pd(\mathbf{H})(Cl_2CD_2)(XR_3)_2]$, and $[Pd(Cl)(\mathbf{H})(XR_3)_2]$ reduce in intensity and eventually disappear from the ^1H NMR spectra. The hydride signals corresponding to $[Pd(Cl)(\mathbf{H})(XR_3)_2]$ remain visible in ^1H NMR spectra for far longer than the other hydride signals. This confirms that under these conditions, $[Pd(Cl)(H)(XR_3)_2]$ is the most thermally-stable monohydride species in equilibria. Over time, more triflic acid and $[HXR_3]^+$ ligand are produced thus less triflate and XR_3 ligand are available in solution. As a result, equilibrium is shifted towards the $[Pd(Cl)(H)(XR_3)_2]$ species.

5.2 Detection of Palladium Clusters

As the hydride NMR signals corresponding to the palladium monohydride species reduce in intensity, several unusual ^1H and ^{31}P NMR signals are observed to form. Initially, the signals produced on addition of hydrogen (~3 bar) to d_2-dichloromethane solutions of $[Pd(OTf)_2(PPh_3)_2]$, were analysed as the C_3 symmetry of the triphenylphosphine ligands helps to simplify NMR spectra. Furthermore, the spin-½ ^{31}P is a good 'NMR handle' with which these new intermediates were characterised more easily.

5.2.1 Characterisation of $[Pd_3(PPh_3)_4][OTf]_2$

The most identifiable of the new NMR signals are the ^1H NMR signals shown in Figure 154. Although they appear as simple triplets, their chemical shifts are very unusual. Aside from hydride and d_2-dichloromethane signals, all other proton NMR signals must correspond to the protons in triphenylphosphine ligands. As these are aromatic, they are expected to lie between δ 7-8, however these signals are shifted considerably up-field to δ 5.98 and 4.74. Up-field shifts result from the shielding of signals from the applied magnetic field by a small, localised magnetic field,[263] which is caused by

an area of high electron density positioned near the nucleus of interest. Often, this will be a metal interaction, as the substantial electron density surrounding a metal nucleus will induce a localised magnetic field and shield any nearby nuclei from the applied field. These unusual up-field signals are therefore likely to correspond to the protons on a triphenylphosphine ligand which are interacting with a palladium centre.

These NMR signals have integral ratios of 1:1 and coupling between them was confirmed by a COSY NMR spectrum. Cross-peaks were also observed to form between the signal at δ 5.98 and a third aromatic signal at δ 7.07. This is unidentifiable in ^{1}H NMR spectra due to peak overlap in the aromatic region. A ^{1}H {^{31}P} NMR spectrum is also shown in Figure 154. The signal at δ 5.98 is unaffected by de-coupling to phosphorus, however, the signal at δ 4.74 simplifies to a doublet. The original *pseudo*-triplet splitting is therefore the result of both J_{HH} and J_{HP} couplings. This signal is likely to correspond to *ortho* protons of triphenylphosphine, as it is positioned close to a phosphorus nucleus and adjacent to one proton. The signal at δ 5.98 therefore corresponds to *meta* protons, and that at δ 7.07 corresponds to *para* protons.

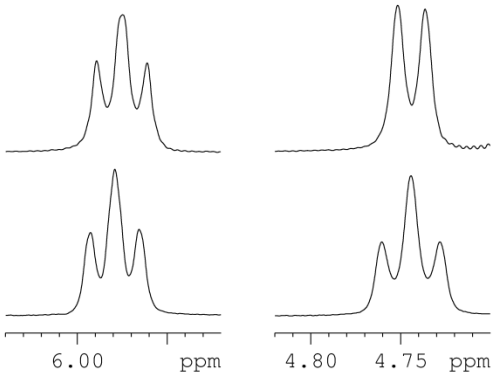

Figure 154: ^{1}H NMR spectrum (below) and ^{1}H {^{31}P} NMR spectrum (above) of the unusual up-field signals corresponding to protons on triphenylphosphine, which form on addition of H_2 (~3 bar) to d_2-dichloromethane solutions of $[Pd(OTf)_2(PPh_3)_2]$, at 298 K.

^{31}P-optimised HMQC spectra reveal a cross-peak between the ^{1}H NMR signal at δ 4.74 and a ^{31}P NMR signal at δ 43.53. This ^{31}P {^{1}H} signal is shown in Figure 155, and displays an unusual splitting pattern. This is an AA'XX' splitting pattern, and is similar to those observed in the aromatic proton signals of pyridazine and phthalazine discussed in Chapter 3. These patterns are only observed if there are four magnetically inequivalent spins, consisting of two pairs of chemically equivalent spins. This palladium species must

therefore contain four magnetically inequivalent phosphorus environments, but only two chemically inequivalent phosphorus environments. This is supported by the $^{31}P\{^{1}H\}$ NMR spectrum, where a second AA'XX' signal was observed at δ 9.06, with a respective integral ratio of 1.

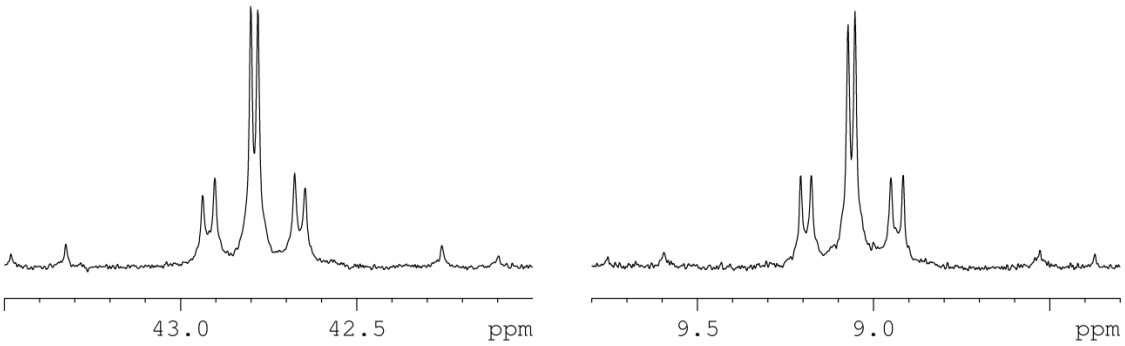

Figure 155: $^{31}P\{^{1}H\}$ NMR spectrum of the unusual ^{31}P NMR signals corresponding to phosphorus nuclei of triphenylphosphine, which form on addition of H_2 (~3 bar) to d_2-dichloromethane solutions of $[Pd(OTf)_2(PPh_3)_2]$.

^{31}P-optimised HMQC spectra also reveal cross-peaks between the ^{31}P NMR signal at δ 45.53, and a second aromatic proton signal at δ 7.49. This presumably corresponds to the *ortho* protons on a second, chemically inequivalent phenyl ring bound to the same phosphorus nucleus as that which is interacting with the palladium centre. Cross-peaks are also observed between the ^{31}P NMR signal at δ 9.06 and an aromatic ^{1}H NMR signal at δ 7.24. This is likely to correspond to the *ortho* protons of a second, chemically different triphenylphosphine ligand. Both proton signals at δ 7.49 and 7.24 appear at standard chemical shifts for such aromatic protons. This suggests that these triphenylphosphine phenyl rings are bound in a conventional manner, with no evidence of a palladium interaction.

Single crystals were grown from this d_2-dichloromethane solution by opening the Young's NMR tubes to air, and layering wet hexane. The solvents were then allowed to slowly diffuse. Surprisingly, crystals could not be grown under an inert atmosphere, but did form in the presence of air and water. The crystal structure was solved using single crystal XRD and is shown in Figure 156. The presence of water appears to have aided crystallisation by forming a hydrogen bonding network with the triflate counterions. The position of the water molecule is disordered, and this is shown in the crystal structure.

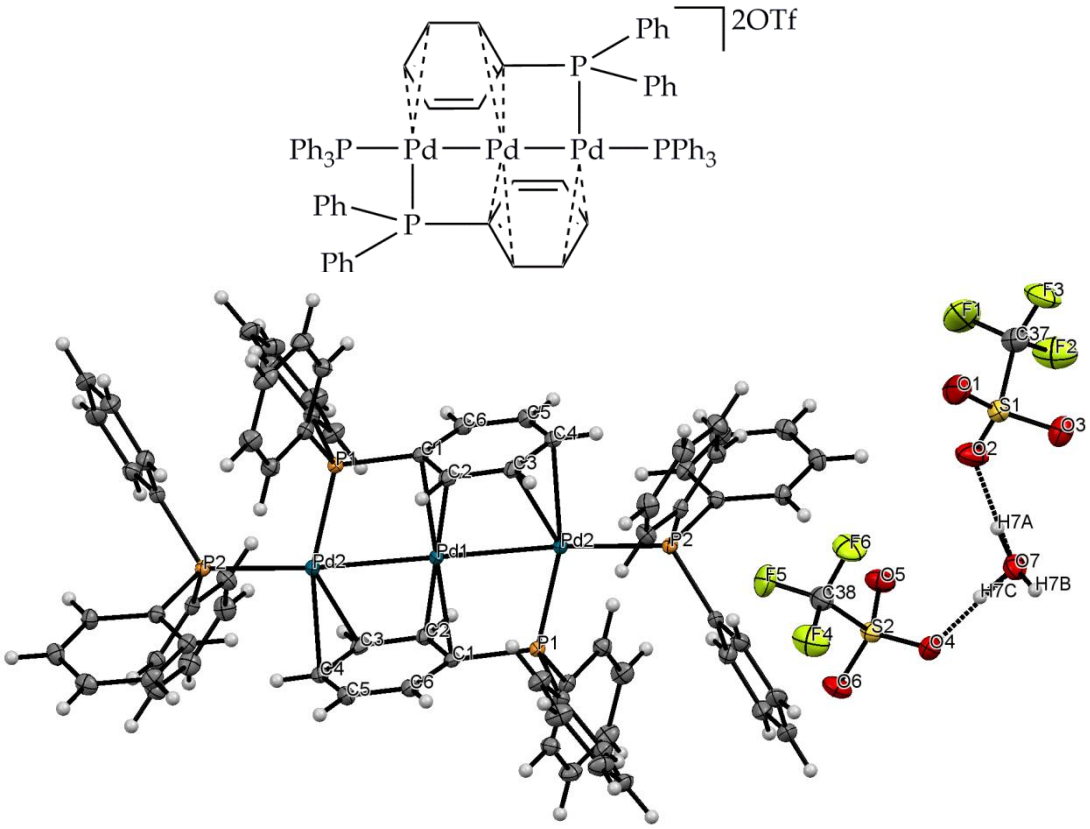

Figure 156: Schematic (above) and crystal structure (below) of $[Pd_3(PPh_3)_4][OTf]_2$, formed by addition of H_2 (~3 bar) to d_2-dichloromethane solutions of $[Pd(OTf)_2(PPh_3)_2]$. Atom colours: C-grey, F-yellow, H-white, O-red, P-orange, Pd-blue, S-gold.

The crystal structure shows three palladium atoms bonded linearly to form a tri-palladium complex which is stabilised by four triphenylphosphine ligands; two of which lie perfectly in the Pd-Pd-Pd plane, and two that are positioned outside this plane. Intriguingly, the triphenylphosphine ligands that lie outside the Pd-Pd-Pd plane are coordinating to the palladium not only by sigma donation from the phosphorus atoms, but also by η^2-bonds from one of the three phenyl rings in each, so that there are a total of four η^2-bonds stabilising the palladium. A free palladium(0) atom appears to have become trapped between two $[Pd(OTf)_2(PPh_3)_2]$ monomers, which have lost their triflate ligands in the process and these are now acting as counterions. In order to stabilise the tri-palladium complex *via* η^2 coordination, the phenyl rings have lost aromaticity, which has resulted in longer C-C bond lengths, given in Table 20. The uncoordinated C5-C6 bonds, however, have shortened and now resemble isolated double bonds.[264] The complex must have a low-energy ground state to compensate for this loss of aromaticity.

Table 20: Bond lengths of interest in $[Pd_3(PPh_3)_4][OTf]_2$ and $[Pd_3(AsPh_3)_4][OTf]_2$, with the arbitrary bond numbering scheme shown.

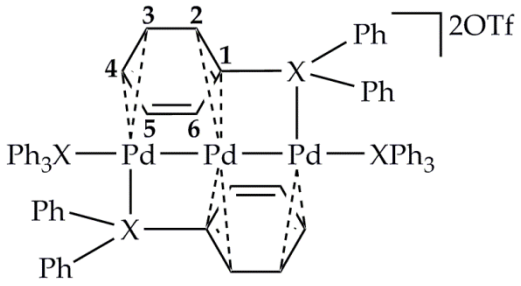

Bond	Bond length / Å	
	PPh	AsPh
C1-C2	1.424(2)	1.39(1)
C2-C3	1.411(2)	1.41(1)
C3-C4	1.399(3)	1.40(1)
C4-C5	1.419(3)	1.42(1)
C5-C6	1.374(2)	1.395(9)
C6-C1	1.429(2)	1.43(1)
Mean C-C in terminal XPh_3	1.388(2)	1.39(1)
Mean η^2 bond length	2.286(2)	2.276(7)

This triphenylphosphine-stabilised tri-palladium complex is solvated by triflate anions and has an overall charge of +2. The Pd-Pd bond length in the crystal structure is 2.631 Å, which is very slightly longer than typical Pd(I)-Pd(I) bond lengths,[265] and supports a Pd(I)-Pd(0)-Pd(I) structure. There is an overall reduction of palladium, which suggests that the tri-palladium complexes are likely to be stable intermediates on the route to formation of palladium nanoparticles. Furthermore, LIFDI-MS was used to analyse a d_2-dichloromethane solution containing $[Pd_3(PPh_3)_4][OTf]_2$. A new signal was observed at *m*/*z* 684.54, which corresponds to the dicationic tri-palladium cluster ($[M-2OTf]^{2+}$), which has a molecular mass of 1368.40 $gmol^{-1}$. This confirms that this tri-palladium complex is present in solution, and does not just form in the solid state.

Despite its unusual appearance, $[Pd_3(PPh_3)_4]^{2+}$ is a known compound, stabilised by tetrafluoroborate rather than triflate ligands.[266] It was previously formed by adding ethanol to a dichloromethane solution of $[Pd(\mu\text{-}OH)(PPh_3)_2]_2$. The ethanol reduces the

palladium(II), forming palladium in both the (I) and (0) oxidation states, and ethanal. Triphenylphosphine is oxidised by the oxygen in solution, forming triphenylphosphine oxide, which helps to drive the reaction forward. The η^2-coordination of triphenylphosphine to palladium has only been seen in this tri-palladium species, although η^1-coordination from the *ipso*-carbon atoms has also been reported in a di-palladium complex, shown in Figure 157 (a).[267] In addition to this tri-palladium species, some palladium sandwich complexes have been synthesised, an example of which is given in Figure 157 (b).[268-270] Furthermore, the handful of palladium(I) dimers that are stabilised *via* η-coordination of bridging arenes[271-274] (an example is given in Figure 157 (c)) do not form as reaction intermediates, but have been synthesised either as catalysts for Suzuki-Miyaura cross-coupling, or as complexes that are interesting in their own right. Longer, linear palladium clusters stabilised by η-coordination from polyenes are also known[275,276] but have not yet proven to be catalytically viable. They are proposed to be promising catalysts for alkyne polymerisation.

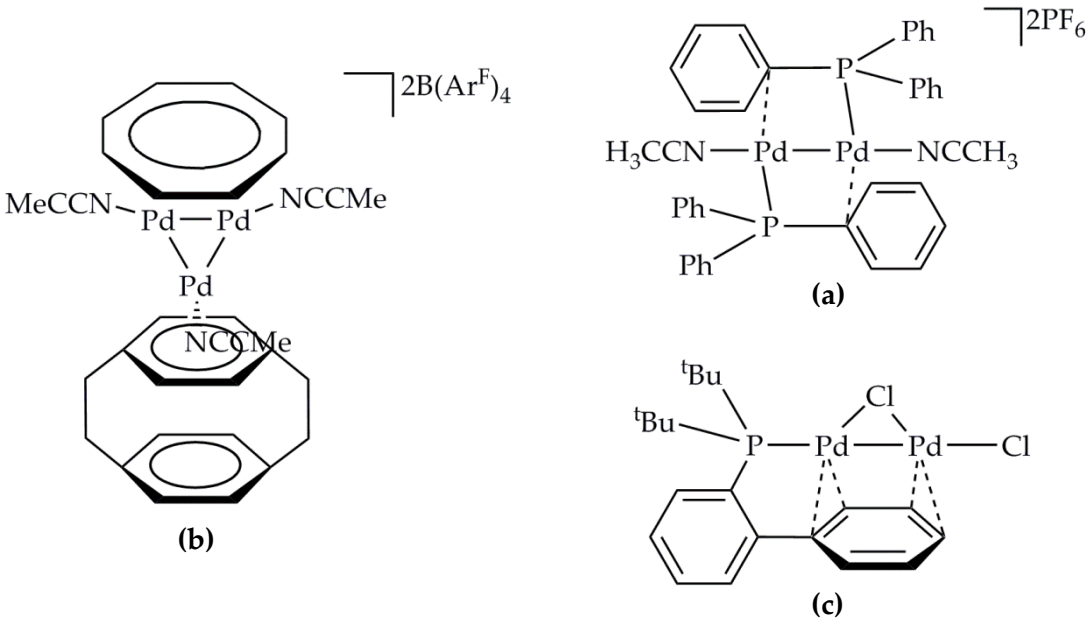

Figure 157: Examples of (a) η^1-coordination from triphenylphosphine to palladium,[277] (b) a tri-palladium sandwich complex stabilized by three η^2-coordinations between the [2.2]paracyclophane ligand and palladium atoms, and a combination of η^3 and η^2-coordinations between the cyclooctatraene ligand and the palladium atoms[268] and (c) a di-palladium complex stabilized by η^2-coordinations.[272]

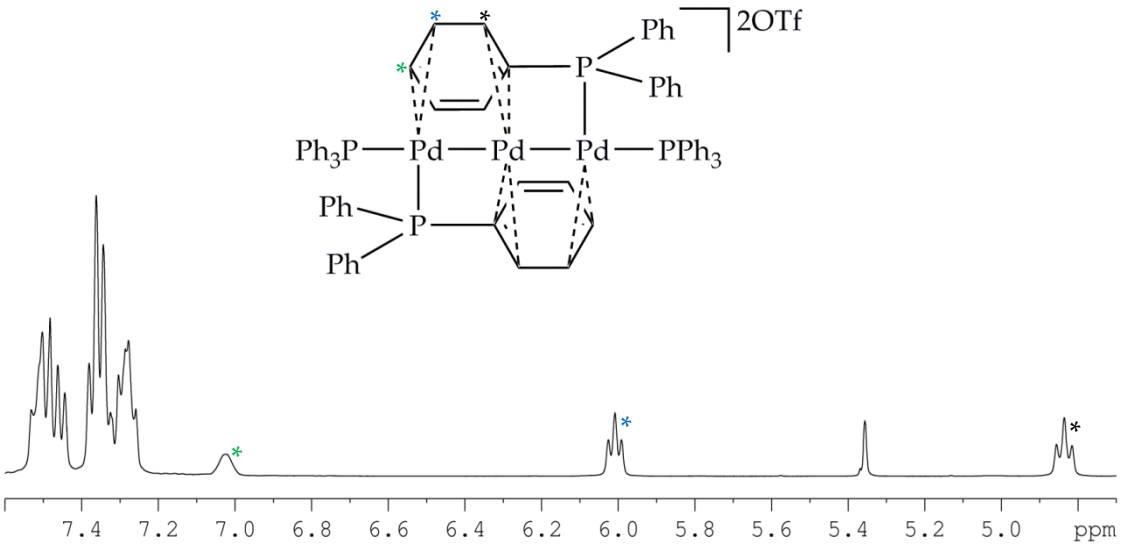

Figure 158: ^{1}H NMR spectrum of the signals corresponding to $[Pd_3(PPh_3)_4][BF_4]_2$.

$[Pd_3(PPh_3)_4]^{2+}$ was synthesised and isolated following the procedure used by Kannan *et. al.*[266] The ^{1}H NMR spectrum is given in Figure 158. Interestingly, the proton resonance corresponding to the *para* protons of the η^2-coordinated phenyl rings appears broad, which typically suggests exchange. The signal simplifies, however, to a sharp *pseudo*-triplet in ^{1}H $\{^{31}P\}$ NMR spectra hence this apparent broadening is due to J_{HP} coupling.

5.2.2 Characterisation of $[Pd_3(XR_3)_4][OTf]_2$

The clean ^{1}H NMR spectrum of $[Pd_3(PPh_3)_4][BF_4]_2$, shown in Figure 158, which has been fully assigned, is compared with all of the δ 6.5-4 ^{1}H NMR spectral regions containing the diagnostic up-field signals that form on addition of hydrogen to d_2-dichloromethane solutions of $[Pd(OTf)_2(XR_3)_2]$ in Figure 159. The ^{1}H NMR signals that form when $XR_3 = AsPh_3$ (spectrum **(a)** in Figure 159) are similar in appearance and chemical shift to those that correspond to $[Pd_3(PPh_3)_4]^{2+}$. This is because they belong to the triphenyarsine analogue of the triphenylphosphine-stabilised cluster.

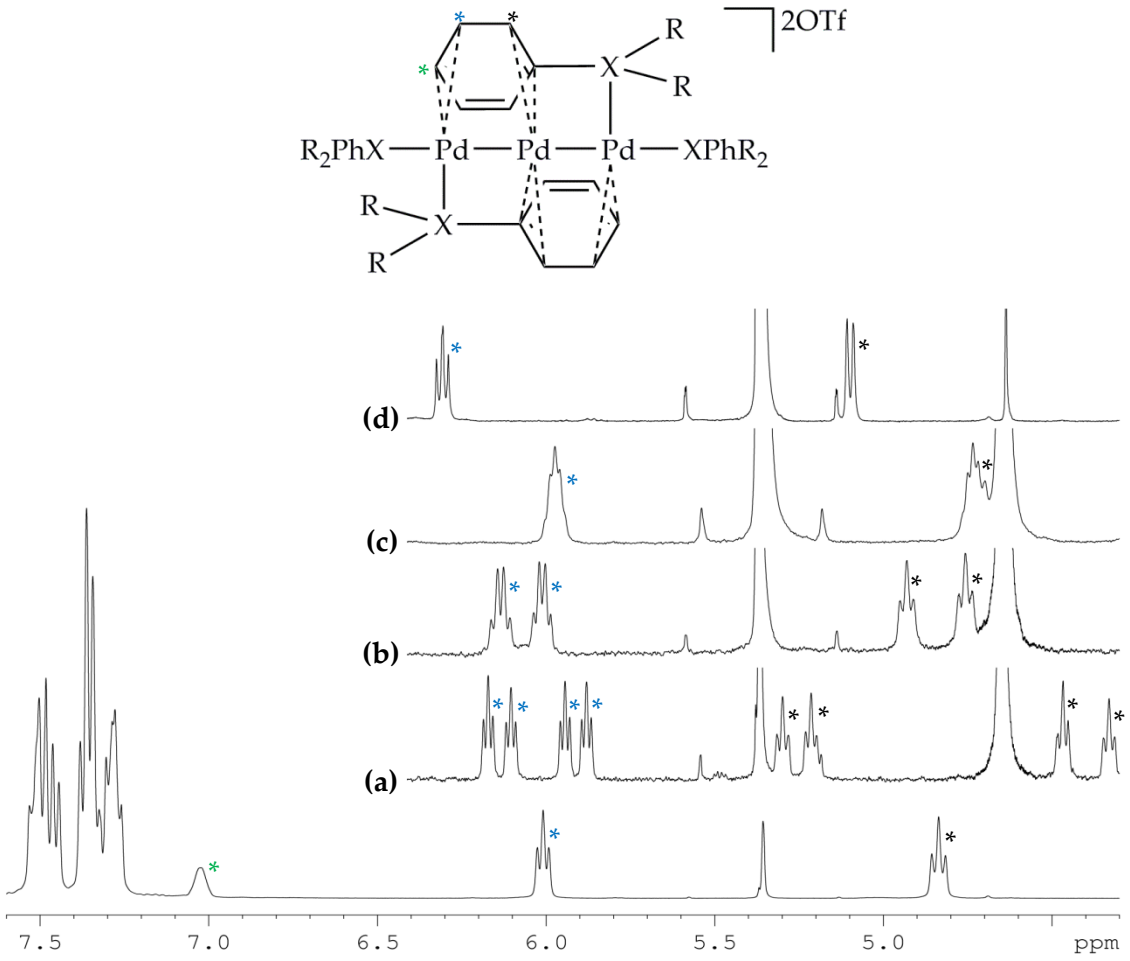

Figure 159: The ^{1}H NMR spectrum of $[Pd_3(PPh_3)_4]^{2+}$ (below), and the δ 6.4-4.3 region of interest, which contains the diagnostic aromatic signals for (a) $[Pd_3(PPh_2Me)_4]^{2+}$, (b) $[Pd_3(PPh_2(PhPh))_4]^{2+}$, (c) $[Pd_3(PPh_2(PhCH_2Ph))_4]^{2+}$, and (d) $[Pd_3(AsPh_3)_4]^{2+}$.

$[Pd_3(AsPh_3)_4]^{2+}$ is much more difficult to characterise by NMR as the spin-½ ^{31}P has been replaced with quadrupolar ^{75}As, however, crystals were grown and the crystal structure was solved by single-crystal XRD. This is shown in Figure 160. The triflate counterions have been omitted, however, they do not appear to form a hydrogen bond network with water to assist crystallisation. The equivalence of the R groups in these XR_3 ligands leads to the η^2-coordinated phenyl rings having two equivalent *ortho* and two equivalent *meta* protons, hence there are just two diagnostic up-field signals in the ^{1}H NMR spectra. As there is no J_{HP} coupling, the *ortho* signals at δ 5.09 appear as doublets, rather than *pseudo*-triplets. As with $[Pd_3(PPh_3)_4][OTf]_2$, η^2-coordination of the phenyl rings results in a loss of aromaticity, which results in longer C-C bond lengths, given in Table 20.

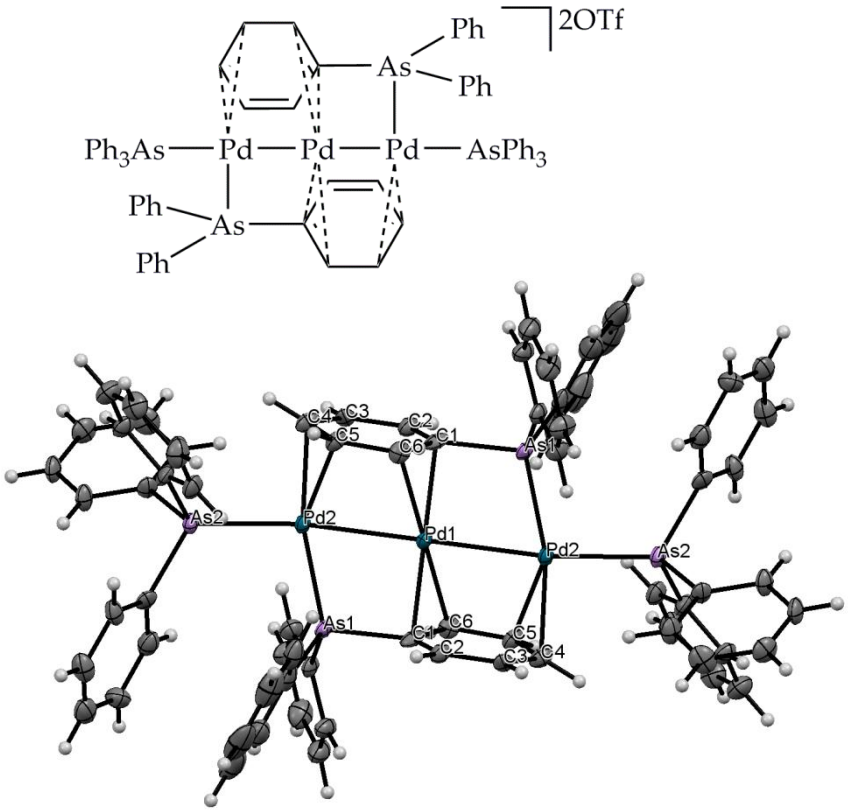

Figure 160: Schematic (above) and crystal structure (below) of $[Pd_3(AsPh_3)_4][OTf]_2$, formed by addition of H_2 (~3 bar) to d_2-dichloromethane solutions of $[Pd(OTf)_2(AsPh_3)_2]$. The triflate counterions have been omitted for clarity. Atom colours: As-purple, C-grey, H-white, Pd-blue.

Introducing an inequivalent R group to the stabilising XR_3 ligands complicates the ^1H NMR spectra. In the case where $XR_3 = PPh_2Me$, there are now eight diagnostic proton NMR signals which, on integration, correspond to two different tri-palladium complexes, each with four signals. These are two diastereoisomers; in this case, the η^2-coordination of a phenyl ring results in chirality at the phosphorus centre. There are two chiral centres per tri-palladium complex, giving rise to two possible diastereoisomers (Figure 161). The *ortho* and *meta* protons on the η^2-coordinated phenyls are inequivalent, hence there are four diagnostic proton signals per diastereoisomer. Initially, the ^1H NMR signal integrals were inequivalent for the two diastereoisomers – one was formed preferentially over the other in a ratio of 1:0.6, as shown in Figure 162, however, it is not known which is the major isomer. This is a kinetic effect, and over time the ^1H NMR signal integrals equalise due to the similar thermal stabilities of the two diastereoisomers.

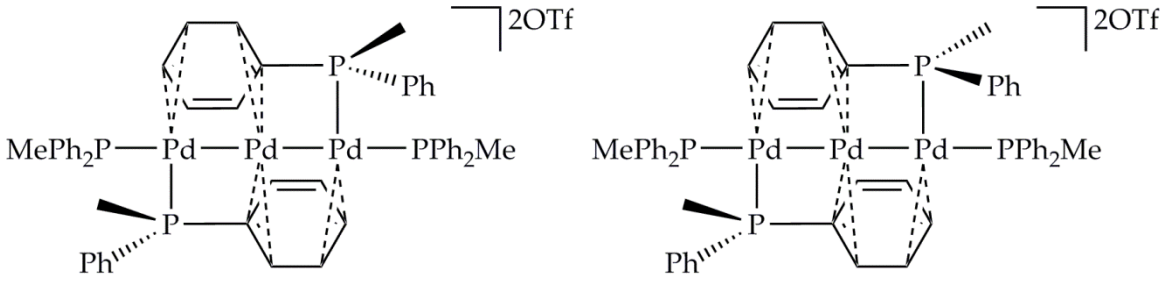

Figure 161: Diastereoisomers of $[Pd_3(PPh_2Me)_4][OTf]_2$.

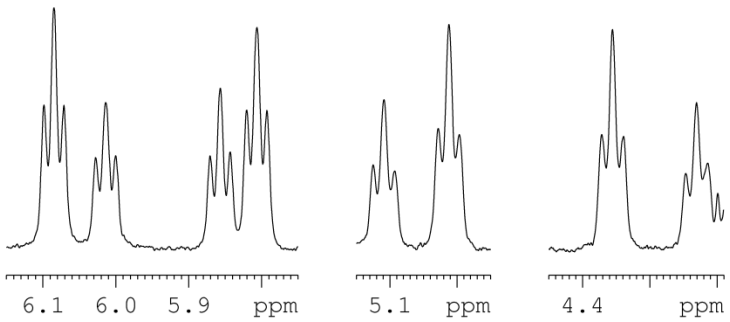

Figure 162: ^1H NMR spectrum of the signals corresponding to $[Pd_3(PPh_2Me)_4][OTf]_2$. There are two sets of four proton signals which correspond to the two diastereoisomers that form. One set is more intense than the other as it is formed preferentially.

The same is also true when XR_3 = $PPh_2(PhPh)$ and $PPh_2(PhCH_2Ph)$, however, in these cases it appears, in Figure 159, that only one diastereoisomer forms, which leads to just four proton signals and in the case of XR_3 = $PPh_2(PhCH_2Ph)$, the two *ortho* proton signals and the two *meta* proton signals are overlapping. On cooling the spectrometer to 270 K, signals that were originally overlapping separate to reveal the presence of two diastereoisomers of both $[Pd_3(PPh_2(PhPh))_4][OTf]_2$ and $[Pd_3(PPh_2(PhCH_2Ph))_4][OTf]_2$. This is demonstrated in Figure 163 for signals corresponding to the *ortho* protons of the η^2-coordinated phenyls in $[Pd_3(PPh_2(PhPh))_4][OTf]_2$ that lie at δ 4.91. A ^1H $\{^{31}P\}$ NMR spectrum clearly shows two doublets, which correspond to *ortho* protons of two diastereoisomers. Again, the ^1H NMR signal integrals are equal due to the equivalent thermal stabilities of the two diastereoisomers.

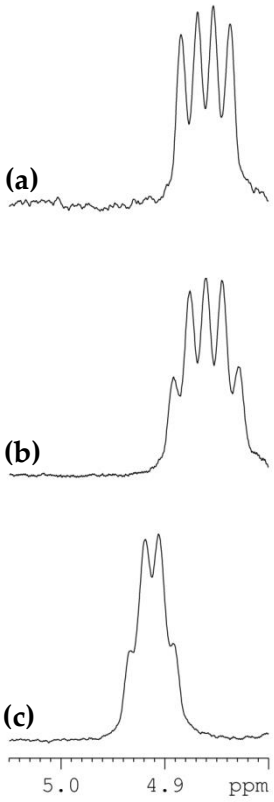

Figure 163: ^{1}H NMR spectrum of the signals corresponding to ortho protons of the η^{2}-coordinated phenyl rings in $[Pd_3(PPh_2(PhPh))_4][OTf]_2$ at (c) 298 K, (b) 270 K, (a) $^{1}H\{^{31}P\}$ NMR spectrum at 270 K.

The longer R groups (PhPh and $PhCH_2Ph$) were incorporated into the XR_3 groups in an attempt to lengthen the tri-palladium complexes to penta-palladium complexes (shown in Figure 164). Similar linear multi-palladium complexes have been reported, predominantly by Murahashi *et. al.*,[275,276,278-280] which are stabilised by η-coordination with long conjugated, polyene ligands. These are also shown in Figure 164. No NMR or MS evidence was found to suggest that the desired penta-palladium complexes had formed. The longer R groups do not form η^{2}-coordinations to the palladium, thus when XR_3 = $P(PhPh)_3$, no tri-palladium or penta-palladium complexes were observed to form. This is presumably due to unfavourable steric interactions caused by the bulkier R groups, which prevent the palladium atoms from coming into close contact.

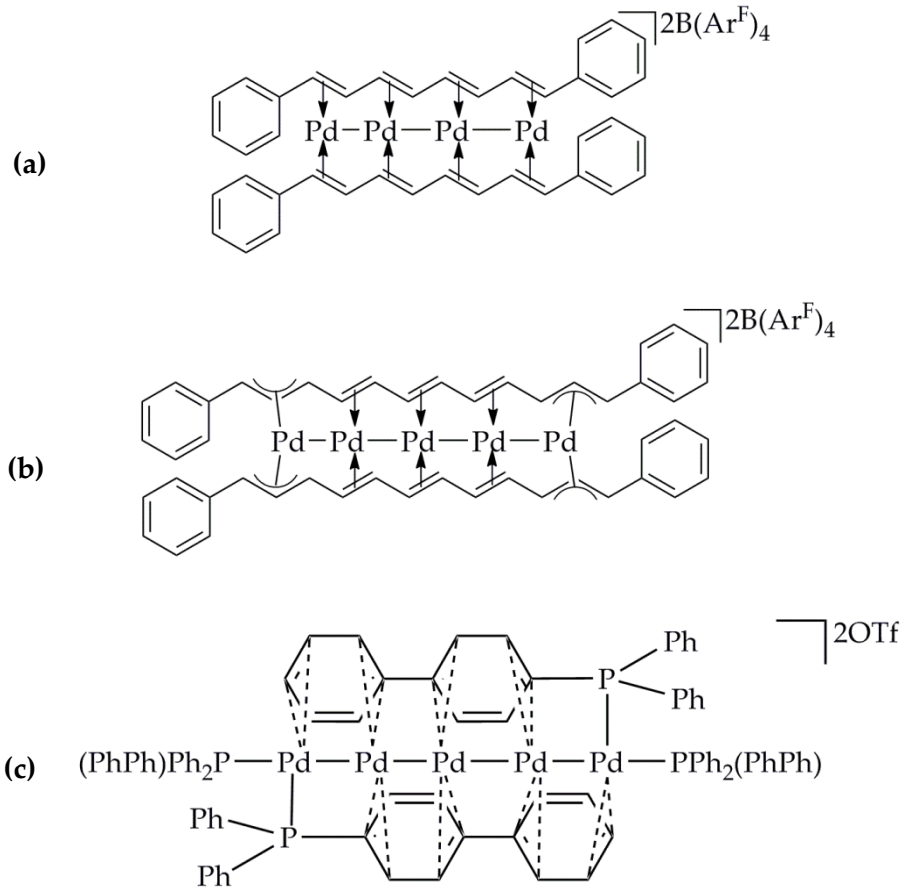

Figure 164: (c) The desired penta-palladium complexes, exemplified by $[Pd_5(PPh_2(PhPh))_4][OTf]$. (a) and (b) are examples of reported linear multi-palladium complexes stabilised by conjugated polyenes.

The diagnostic ^1H and $^{31}P\{^1H\}$ NMR signals of all the tri-palladium complexes are given in Table 21, including all J_{HH}, J_{HP}, and J_{PP} coupling constants. The J_{PP} coupling constants of the AA'XX' $^{31}P\{^1H\}$ NMR signals were calculated using the same method as that used to calculate the J_{HH} coupling between the aromatic protons of pyridazine and phthalazine. This is described in detail in Appendix A, section A.2.1. Coupling between the phosphorus nuclei that are positioned *trans* to one another ($J_{XX'}$) is very strong (~ 98 Hz), despite this being a 4-bond coupling. Presumably, the linear alignment of the palladium atoms is conducive to strong J_{PP} coupling. As expected, coupling between the phosphorus nuclei that are positioned *cis* to one another (J_{AX} ~ 35 Hz) is stronger than the coupling between the more remote AX' phosphines ($J_{AX'}$ ~ 9 Hz). All of the identified tri-palladium complexes exhibit similar coupling constants, which suggests that they all have similar structures. The four η^2-coordinations from the phenyl rings most likely lock the complexes into the same geometries, with similar bond lengths and bond angles (see Table 20).

Table 21: Diagnostic ^{1}H and ^{31}P NMR signals for $[Pd_3(XR_3)_4][OTf]_2$ complexes that form on addition of H_2 (~3 bar) to d_2-dichloromethane solutions of $[Pd(OTf)_2(XR_3)_2]$, with the phosphorus guide shown.

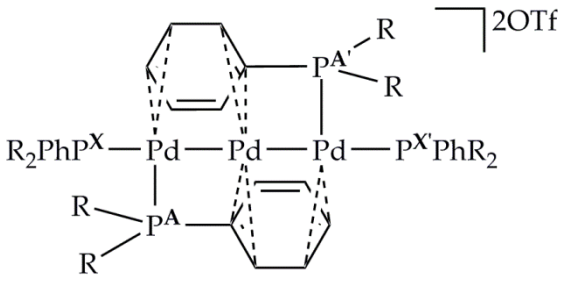

$[Pd_3(XR_3)_4][OTf]_2$				
XR_3		**$^{31}P\{^{1}H\}$ NMR (AA'XX', *J* in Hz)**	**^{1}H NMR (*J* in Hz)**	**LIFDI-MS *m/z***
PPh_3		42.79 (X), 9.07 (A). ($J_{AA'}$ = 12, J_{AX} = 30.9, $J_{AX'}$ = 10.4, $J_{XX'}$ = 97.5)	6.00 (d.d. J_{HH} = 8.3, 7.8), 4.80 (t. J_{HP} = 9.3, J_{HH} = 8.2)	683.6 $[C_{72}H_{60}P_4Pd_3]^{2+}$
PPh_2Me	**Major isomer**	26.18 (X), −7.64 (A). ($J_{AA'}$ = 14.1, J_{AX} = 37.1, $J_{AX'}$ = 8.3, $J_{XX'}$ = 98.9)	6.16 (d.d. J_{HH} = 7.8, 7.6), 5.86 (d.d. J_{HH} = 8.1, 7.7), 5.16 (t. J_{HP} = 9.4, J_{HH} = 8.2), 4.45 (t. J_{HP} = 9.5, J_{HH} = 8.1)	559.4 $[C_{52}H_{52}P_4Pd_3]^{2+}$
	Minor isomer	27.02 (X), −7.60 (A). ($J_{AA'}$ = 14.1, J_{AX} = 37.1, $J_{AX'}$ = 8.3, $J_{XX'}$ = 98.9)	6.08 (d.d. J_{HH} = 8.1, 7.8), 5.93 (d.d. J_{HH} = 8.0, 7.4), 5.23 (t. J_{HP} = 9.2, J_{HH} = 8.2), 4.34 (t. J_{HP} = 9.2, J_{HH} = 7.7)	559.4 $[C_{52}H_{52}P_4Pd_3]^{2+}$
$PPh_2(PhPh)$		43.00 (X), 8.65 (A). ($J_{AA'}$ = 10.1, J_{AX} = 32.2, $J_{AX'}$ = 8.0, $J_{XX'}$ = 97.5)	6.13 (q. J_{HH} = 7.0), 6.00 (q. J_{HH} = 7.0), 4.93 (t. J_{HP} = 10.6, J_{HH} = 7.5), 4.75 (t. J_{HP} = 10.6, J_{HH} = 7.6)	-
$PPh_2(PhCH_2Ph)$		43.13 (X), 8.43 (A).*	5.97 (m.), 4.75 (m.)	865.0 $[C_{100}H_{84}P_4Pd_3]^{2+}$
$AsPh_3$		-	6.27 (d.d. J_{HH} = 8.0, 6.3), 5.04 (d.d. J_{HH} = 8.2, 1.1)	772.0 $[C_{72}H_{60}As_4Pd_3]^{2+}$

Experimental *m*/*z* values, which correspond to the dicationic tri-palladium clusters ([M-2OTf]$^{2+}$), are given in Table 21 and further prove that these species are present in solution. Their isotope distribution patterns match with those simulated for these complexes. This is exemplified by the LIFDI-MS signal for $[Pd_3(PPh_3)_4]^{2+}$ shown in Figure 165, with a complete set of LIFDI-MS data given in Appendix B, section B.2.4.

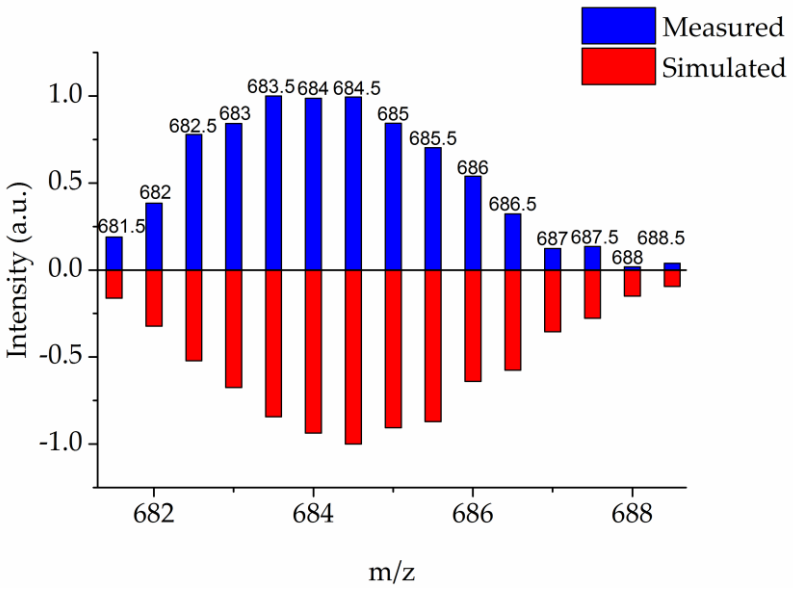

Figure 165: Histogram of the experimental and simulated LIFDI-MS data for the $[Pd_3(PPh_3)_4]^{2+}$ dication.

5.2.3 Competition Studies between $AsPh_3$ and PPh_3

To compare the stabilities of the monohydride and tri-palladium species when stabilised with triphenylarsine or triphenylphosphine ligands, a d_2-dichloromethane solution was prepared that contained equal quantities of $[Pd(OTf)_2(AsPh_3)_2]$ (2.63 mg, 2.58 mmol) and $[Pd(OTf)_2(PPh_3)_2]$ (2.40 mg, 2.58 mmol). The sample was degassed, and cooled to 195 K with an acetone/dry ice bath. Prior to the addition of hydrogen, $^{31}P\{^1H\}$ NMR spectra were collected at 250 K, and contained only a singlet at δ 38.9, which is diagnostic for unreacted $[Pd(OTf)_2(PPh_3)_2]$. This confirms that the phosphine and arsine ligands do not exchange prior to hydrogen addition. Hydrogen (3 bar) was added to the sample, and ^1H NMR spectra were subsequently collected at 250 K. Palladium colloids again formed on the addition of hydrogen, which resulted in the production of free phosphine and arsine ligands.

5.2.3.1 Monohydride Species

Initial ^{1}H NMR spectra contained hydride signals at δ −7.64, −9.43, −9.93, and −20.54, which correspond to the hydride ligands of the triphenylarsine-stabilised monohydride species previously observed - [Pd(**H**)($AsPh_3$)$_3$]OTf, the two geometrical isomers of [Pd(**H**)(Cl_2CD_2)($AsPh_3$)$_2$]OTf, and [Pd(**H**)(OTf)($AsPh_3$)$_2$], respectively. These are labelled * in spectrum **(a)** of Figure 166.

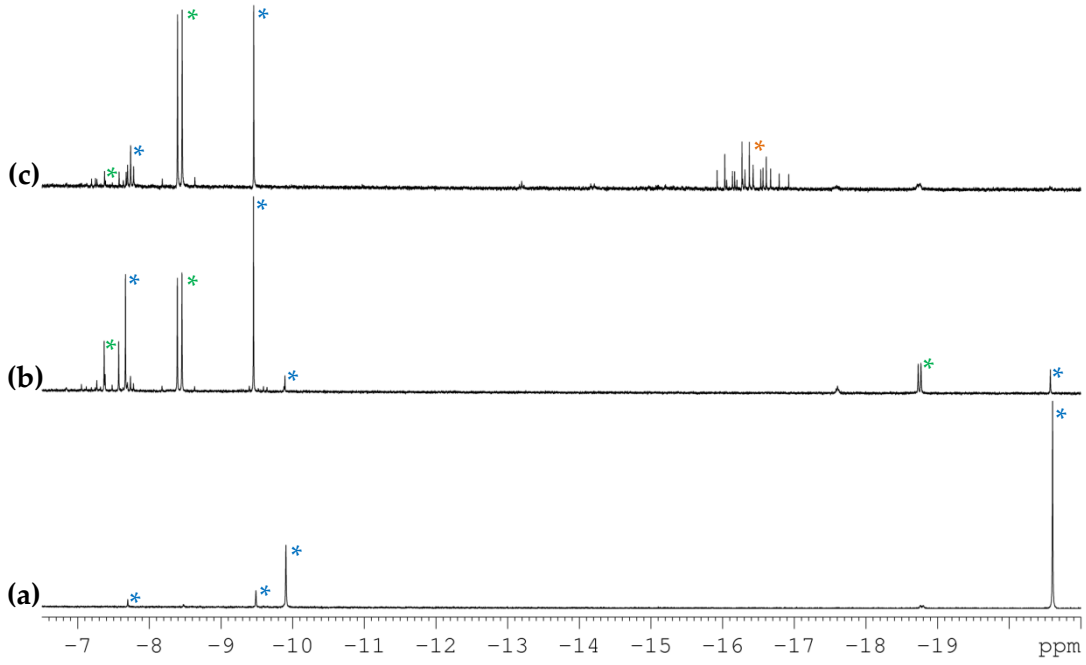

Figure 166: ^{1}H NMR spectra of the hydride signals that form on addition of H_2 (~3 bar) to d_2-dichloromethane solutions containing equal molar quantities of [Pd(OTf)$_2$($AsPh_3$)$_2$] and [Pd(OTf)$_2$(PPh_3)$_2$]. (a) triphenylarsine-stabilised monohydride species (*) observed to form at 250 K, (b) mixed triphenylarsine and triphenylphosphine-stabilised monohydride species (*) observed to form at 290 K, and (c) mixed triphenylarsine and triphenylphosphine-stabilised [Pd(Cl)(H)(XR_3)$_2$] species (*) observed to form at 298 K.

On warming the sample to 290 K, several new hydride signals appeared, and are labelled * in spectrum **(b)** of Figure 166. These correspond to the hydride ligands in palladium monohydride species that contain a mixture of both triphenylarsine and triphenylphosphine ligands. The doublets observed at δ −7.47 and −8.42 are likely to correspond to hydride ligands in complexes of the type [Pd(**H**)(XPh_3)$_3$]OTf, as their chemical shifts lie within the range typically observed for such species. The former hydride signal exhibits a large J_{HP} coupling of 81.1 Hz, caused by coupling to one phosphorus nucleus positioned *trans* to the hydride. The latter hydride signal, however, exhibits a small J_{HP} coupling of 25.7 Hz, caused by coupling to one ^{31}P nucleus positioned

cis to the hydride. As both signals are doublets, their corresponding species must contain just one phosphine ligand, with the two other sites occupied by arsine ligands. These signals therefore correspond to the hydride ligands in the two geometrical isomers of [Pd(**H**)($AsPh_3$)$_2$(PPh_3)]OTf, shown in Figure 167.

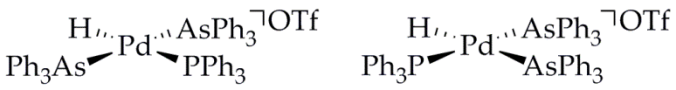

Figure 167: Two geometrical isomers of [Pd(H)($AsPh_3$)$_2$(PPh_3)]OTf.

An additional small doublet is observed at δ −18.75. This chemical shift is consistent with a hydride ligand in a complex of the type [Pd(H)(OTf)(XPh_3)$_2$], where the hydride is positioned *trans* to the triflate ligand. The small J_{HP} coupling of 15.7 Hz, exhibited by this signal, agrees with a *cis*-arrangement of the hydride and phosphine. This therefore corresponds to the hydride of [Pd(**H**)(OTf)($AsPh_3$)(PPh_3)], shown in Figure 168.

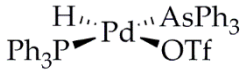

Figure 168:[Pd(H)(OTf)($AsPh_3$)(PPh_3)].

Warming the sample further, to 298 K, results in a significant reduction in the intensity of the ^{1}H NMR hydride signals corresponding to the triphenylarsine-stabilised monohydride species. This suggests that these are kinetic products, and incorporation of phosphine ligands into the monohydride species appears to form more stable complexes. Several additional new signals, labelled * in spectrum **(c)** of Figure 168, are also observed to form at δ ~ −16.44. This chemical shift correlates to hydride ligands in complexes of the type [Pd(Cl)(**H**)(XPh_3)$_2$], however substantial overlap of these signals prevents further NMR characterisation. Such complex hydride signals reflect the formation of several different geometric isomers of this monohydride species.

5.2.3.2 Tri-palladium Species

In contrast to the palladium monohydride species, the initial tri-palladium species that formed on addition of hydrogen at 250 K contained a combination of phosphine and arsine ligands. Their diagnostic up-field ^{1}H NMR signals are shown in Figure 169. The signals that correspond to the *ortho*-protons of the η^2-coordinated phenyl rings specify the

nature of 'X'; *pseudo*-triplet splitting indicates that the proton is coupling to an adjacent proton, as well as a phosphorus nucleus thus X = P, whereas doublet splitting indicates that the proton is coupling to an adjacent proton only, thus X = As.

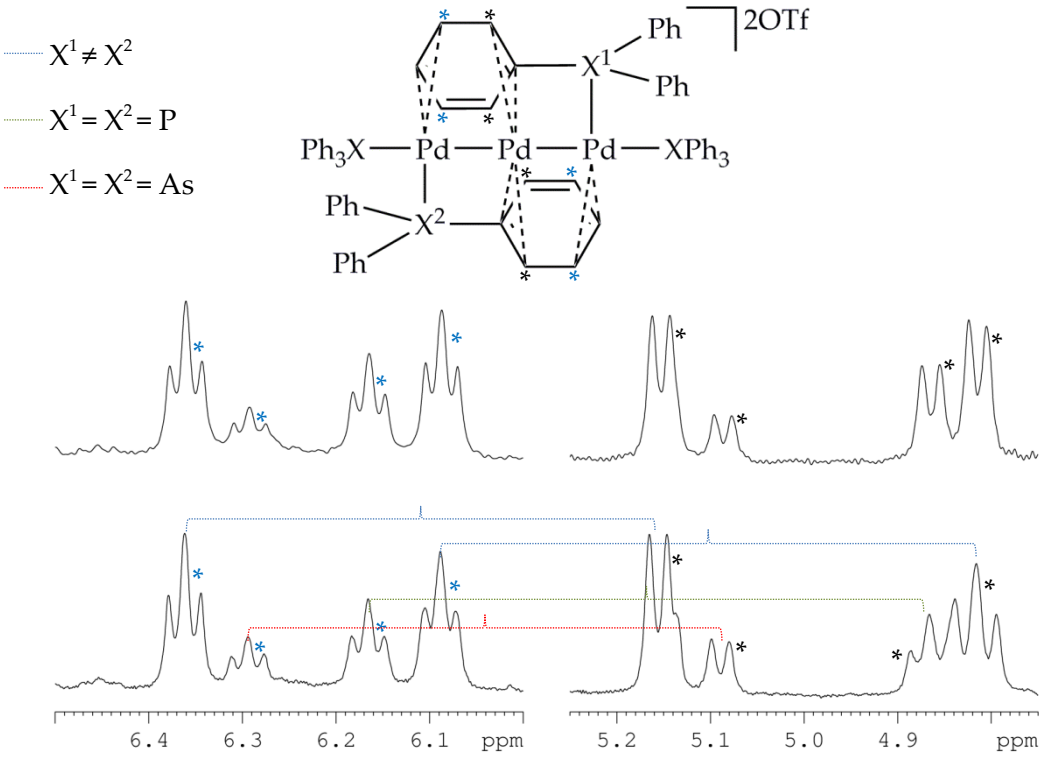

Figure 169: ^{1}H NMR spectrum (below) and $^{1}H\{^{31}P\}$ NMR spectrum (above) showing the diagnostic up-field signals of the tri-palladium species that form on addition of H_2 (~3 bar) to a d_2-dichloromethane solution containing equal molar quantities of $[Pd(OTf)_2(AsPh_3)_2]$ and $[Pd(OTf)_2(PPh_3)_2]$. Signals observed to couple are connected with faint dashed lines (see key).

The doublets at δ 5.16 and 5.09 correspond to the *ortho* proton signals of an η^2-coordinated triphenylarsine, whereas the *pseudo*-triplets at δ 4.87 and 4.82 correspond to the *ortho* proton signals of an η^2-coordinated triphenylphosphine. COSY NMR spectra reveal coupling between the *ortho* and *meta* proton signals of the η^2-coordinated phenyl rings at δ 6.36 and 5.16, and δ 6.09 and 4.82 (connected with blue dashed lines in Figure 169). These signals have equivalent integral values, thus they likely correspond to a tri-palladium complex with one η^2-coordinated arsine and one η^2-coordinated phosphine. Coupling is also revealed between the signals at δ 6.30 and 5.09 (connected with a red dashed line in Figure 169), which correspond to a tri-palladium complex with two η^2-coordinated arsines, and δ 6.17 and 4.87 (connected with a green dashed line in Figure 169), which correspond to a tri-palladium complex with two η^2-coordinated phosphines.

Due to complexity and signal overlap in the aromatic region, and in ^{31}P NMR spectra, it is not possible to decipher the nature of the terminal ligands that stabilise these tri-palladium complexes, however, the percentage of η^2-coordinated triphenylarsine and triphenylphosphine can be calculated from the *ortho*-proton NMR signals. This is calculated to be 45% triphenylarsine and 55% triphenylphosphine.

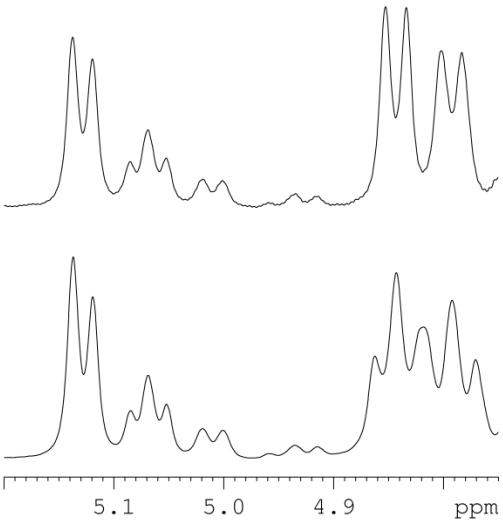

Figure 170: ^{1}H NMR spectrum (below) and $^{31}P\{^{1}H\}$ NMR spectrum (above) showing the diagnostic up-field signals of the tri-palladium species that form on addition of H_2 (~3 bar) to a d_2-dichloromethane solution containing equal molar quantities of $[Pd(OTf)_2(AsPh_3)_2]$ and $[Pd(OTf)_2(PPh_3)_2]$.

On warming the solution to 310 K, the same tri-palladium species remain in solution in addition to some new, minor tri-palladium species. The ^{1}H NMR signals that correspond to the *meta* protons of the η^2-coordinated phenyl rings are now overlapping, which limits further NMR characterisation. The ^{1}H NMR signals that correspond to the *ortho* protons are shown in Figure 170. The signals at δ 5.13, 5.00, 4.84, and 4.79 were observed previously, at 250 K, and have slightly shifted due to the temperature change. The new *pseudo*-triplets observed at δ 5.07 and 4.94 each consist of two overlapping doublets, and therefore correspond to the *ortho* protons of η^2-coordinated triphenylarsine ligands. The percentage of η^2-coordinated triphenylarsine and triphenylphosphine is now calculated to be 43% triphenylarsine and 57% triphenylphosphine.

Single crystals were grown from this d_2-dichloromethane solution, by opening the Young's NMR tube to air, and layering wet hexane. The solvents were then allowed to

slowly diffuse. The crystal structure was solved using single crystal XRD and is shown in Figure 171.

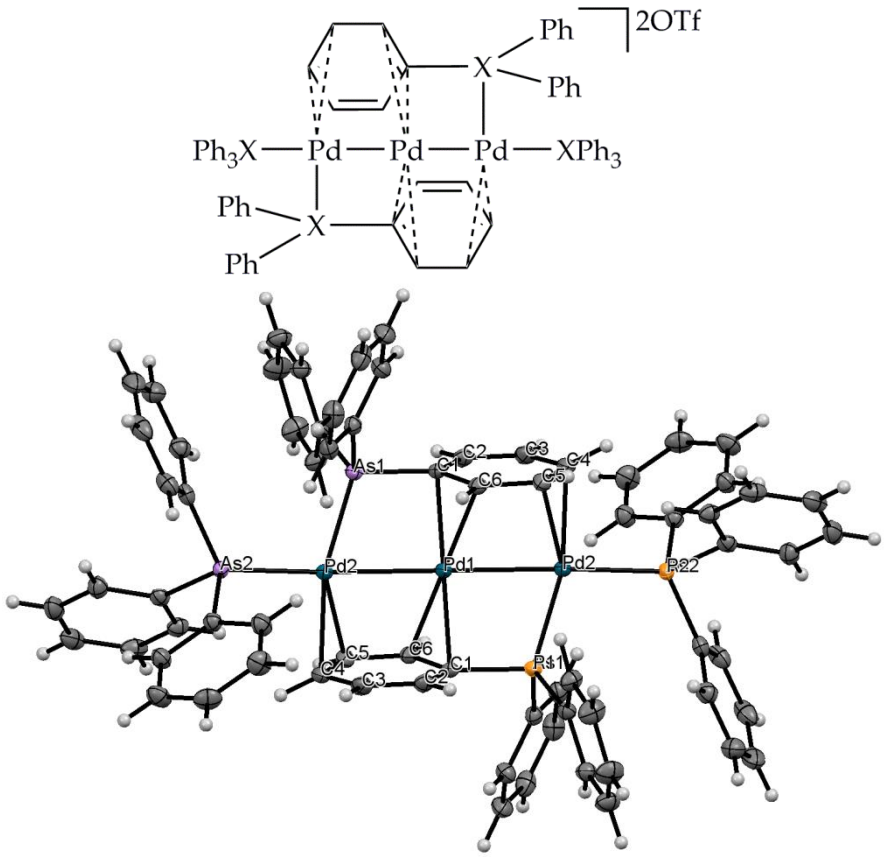

Figure 171: Schematic (above) and crystal structure (below) of $[Pd_3(AsPh_3)_{1.6}(PPh_3)_{2.4}][OTf]_2$, formed by the addition of H_2 (~3 bar) to d_2-dichloromethane solutions containing equal molar quantities of $[Pd(OTf)_2(AsPh_3)_2]$ and $[Pd(OTf)_2(PPh_3)_2]$. The triflate counterions have been omitted for clarity. Atom colours: As-purple, C-grey, H-white, P-orange, Pd-blue.

The structure appears to show a tri-palladium species containing two triphenylphosphine and two triphenylarsine ligands, one of each as a terminal ligand and one of each as an η^2-coordinated ligand. This arrangement, however, simply reflects the probability of finding a phosphorus or an arsenic nucleus at the 'X' positions shown in the schematic. In reality, the crystal contained a mixture of tri-palladium complexes, where both phosphorus and arsenic atoms could be found at each 'X' position, in multiple combinations. The molecular formula calculated from the crystal structure is $C_{72}H_{60}As_{1.6}P_{2.4}Pd_3$ which confirms the incorporation of 40% triphenylarsine and 60% triphenylphosphine into the tri-palladium species. This is consistent with the corresponding ^{1}H NMR data.

Triphenylphosphine ligands are slightly favoured, relative to triphenylarsine ligands, in the formation of these tri-palladium complexes. Despite this, tri-palladium complexes containing multiple combinations of phosphine and arsine ligands form, with no obvious preference at each binding site.

5.3 Conclusion

Addition of hydrogen to d_2-dichloromethane solutions of $[Pd(OTf)_2(XR_3)_2]$ results in the formation of several novel palladium monohydride species. The dichloromethane is not innocent in these reactions as it was observed to coordinate to palladium. NMR and LIFDI-MS evidence confirms that the C-Cl bond of dichloromethane is activated at the palladium centre to form palladium chloride species, $[Pd(Cl)(H)(XR_3)_2]$, *via* an intermediate palladium species, $[Pd(H)(Cl_2CD_2)(XR_3)_2]OTf$, in which dichloromethane is bound. This species also mediates exchange between $[Pd(H)(OTf)(XR_3)_2]$ and $[Pd(H)(XR_3)_3]OTf$, the latter of which does not form on replacement of dichloromethane with benzene.

These palladium monomers are the kinetic products of this reaction. Their NMR signals disappear from NMR spectra over several hours, during which time NMR signals corresponding to the tri-palladium species, $[Pd_3(XR_3)_4][OTf]_2$, form. All except $[Pd_3(PPh_3)_4]^{2+}$ are novel cluster species[266] and appear to be intermediate between $[Pd(OTf)_2(XR_3)_2]$ monomers and palladium nanoparticles. Furthermore, the synthetic method reported for the synthesis of $[Pd_3(PPh_3)_4][BF_4]_2$ cannot be successfully applied to synthesise the other tri-palladium complexes,[266] hence reduction with hydrogen is a more general method for the synthesis of a range of such tri-palladium species.

The reported synthesis of $[Pd_3(PPh_3)_4][BF_4]_2$ was not en-route to nanoparticle formation,[266] and as such, these tri-palladium species have not previously been identified as nanoparticle precursors. As these species form with commonly-used phosphines, and arsines that are becoming more prevalent in palladium catalysis,[281,282] it is possible that they form in a range of palladium reactions. They may be active catalysts in their own right, or conduits for the active catalysts. Minimal research into the reactivity of these tri-palladium complexes has been reported, therefore it has been investigated herein and the results are discussed in Chapter 6.

6 Reactivity of $[Pd_3(PPh_3)_4][BF_4]_2$

The formation of $[Pd_3(PPh_3)_4][BF_4]_2$ was reported in 1998 by Kannan, James, and Sharp,[266] however, minimal research into its reactivity was included and little has been reported since. The original paper reported a slow reaction of $[Pd_3(PPh_3)_4][BF_4]_2$ with triphenylphosphine and dichloromethane, to form $[Pd(Cl)(PPh_3)_3]BF_4$ and $[Pd(PPh_3)_4]$ (shown in Figure 172) which took place over several hours. These results further prove the active role of dichloromethane in palladium chemistry. It was reported that no reaction takes place between $[Pd_3(PPh_3)_4][BF_4]_2$ and carbon monoxide or methyl iodide, but it is suggested that $[Pd_3(PPh_3)_4][BF_4]_2$ may be a useful catalyst precursor, and an intermediate in P-C bond cleavage reactions.[266]

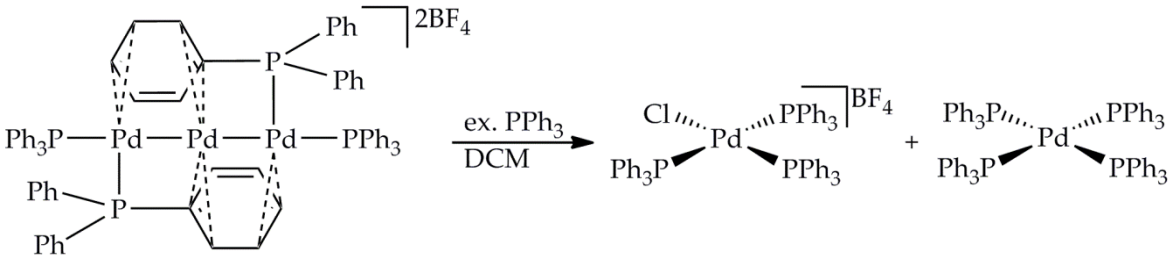

Figure 172: Reported reaction of $[Pd_3(PPh_3)_4][BF_4]_2$ with excess triphenylphosphine, forming $[Pd(Cl)(PPh_3)_3]BF_4$ and $[Pd(PPh_3)_4]$.

More recently, $[Pd_3(PPh_3)_4][BF_4]_2$ was reported to be an active pre-catalyst for the hydromethoxycarbonylation of alkenes.[283] It is reacted with triphenylphosphine and triflic acid, which forms the catalytically-active monomeric species $[Pd(H)(OTf)(PPh_3)_2]$, as well as $[Pd(OTf)_2(PPh_3)_2]$. This is shown in Figure 173.

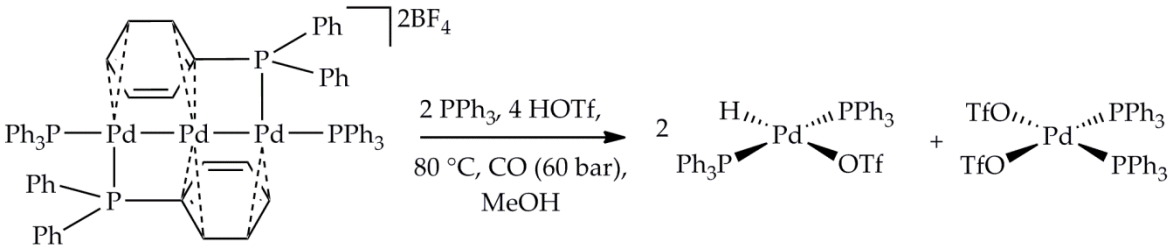

Figure 173: Reported reaction of $[Pd_3(PPh_3)_4][BF_4]_2$ with 2 equivalents of triphenylphosphine, and 4 equivalents of triflic acid, forming 2 equivalents of $[Pd(H)(OTf)(PPh_3)_2]$ and 1 equivalent of $[Pd(OTf)_2(PPh_3)_2]$.

The reported reactions have focussed on fragmentation to form catalytically-active palladium monomers from $[Pd_3(PPh_3)_4][BF_4]_2$ for use in homogeneous catalysis. There are no existing publications that use solely $[Pd_3(PPh_3)_4][BF_4]_2$ as a catalyst, or that take advantage of the facile conversion of $[Pd_3(PPh_3)_4][BF_4]_2$ to nanoparticles for use in heterogeneous catalysis.

Herein, the reactivity of $[Pd_3(PPh_3)_4][BF_4]_2$ is explored, with a focus on photoactivity, and on catalytic properties in hydrogenation and cross-coupling reactions.

6.1 Photoactivity

All of the tri-palladium complexes detected form brightly coloured dichloromethane solutions, ranging from yellow/orange to red/purple. The UV-*vis* absorption spectra of pure dichloromethane solutions of $[Pd_3(PPh_3)_4][OTf]_2$ and $[Pd_3(AsPh_3)_4][OTf]_2$ are compared in Figure 174. These were collected using optically-dilute samples, with maximum absorptions lying between 0.5-1.0, which were prepared by the successive dilution of standard solutions of known concentrations. The molar absorption coefficients (ε, $mol^{-1}dm^3cm^{-1}$) at the wavelengths of maximum absorption (λ_{max}, nm) are given in Table 22 and were calculated from the Beer-Lambert law, shown below, where A is absorbance, c is concentration ($moldm^{-3}$), and l is sample length (cm).

$$A = \epsilon cl$$

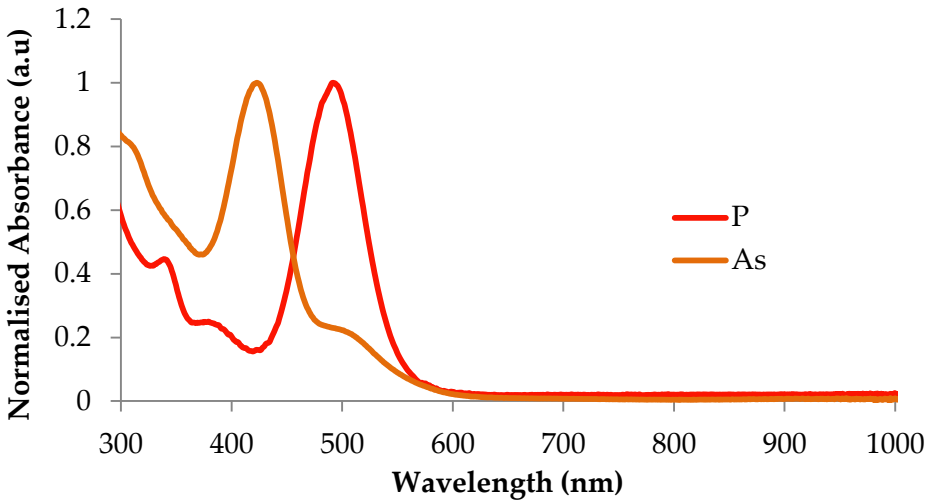

Figure 174: Normalised UV-vis absorption spectra of dichloromethane solutions of $[Pd_3(PPh_3)_4][OTf]_2$ (P), and $[Pd_3(AsPh_3)_4][OTf]_2$ (As).

Table 22: Wavelengths of maximum absorption (λ_{max}) and the corresponding molar absorption coefficients (ε, $mol^{-1}dm^3cm^{-1}$) of dichloromethane solutions of $[Pd_3(PPh_3)_4][OTf]_2$ and $[Pd_3(AsPh_3)_4][OTf]_2$ determined from a single analysis. Pd-Pd bond lengths were measured from crystal structures. *Molar absorption coefficients given in SI units ($mol^{-1}m^2$).

Complex	λ_{max} (nm)	ε ($mol^{-1}dm^3cm^{-1}$)	Pd-Pd bond length (Å)
$[Pd_3(PPh_3)_4][OTf]_2$	492	37, 000 (3, 700)*	2.6314(2)
$[Pd_3(AsPh_3)_4][OTf]_2$	423	47, 000 (4, 700)*	2.6809(5)

Both complexes exhibit strong absorption bands in the visible region of the EM spectrum. The λ_{max} of 492 nm observed for dichloromethane solutions of $[Pd_3(PPh_3)_4][OTf]_2$ corresponds to the absorption of blue/green light, of which red is the complimentary colour. This agrees with the bright red colour of this solution. The λ_{max} of 423 nm observed for dichloromethane solutions of $[Pd_3(AsPh_3)_4][OTf]_2$ corresponds to the absorption of violet light, of which orange/yellow is the complimentary colour. This also agrees with the observed colour of this solution.

In both cases, the molar absorption coefficients are too large to correspond to d-d transitions, which are Laporte forbidden and typically less than 20 $mol^{-1}dm^3cm^{-1}$.[284] The absorption bands are more likely to be the result of charge transfer and, due to the close proximity of the palladium atoms, may be the result of metal-metal-to-ligand charge transfer (MMLCT) from a filled Pd-Pd antibonding orbital to an empty π^* orbital on the η^2-coordinated phenyl rings.[285] This type of transition has been reported for several platinum aggregates and dimers.[286-290] The energy required for MMLCT is strongly dependent on the M-M distance. The MMLCT band is reported to become red-shifted as the Pt-Pt distance decreases.[285,291] This trend is mirrored with $[Pd_3(PPh_3)_4][OTf]_2$ and $[Pd_3(AsPh_3)_4][OTf]_2$; smaller Pd-Pd distances are measured in the crystal structure of $[Pd_3(PPh_3)_4][OTf]_2$ which exhibits a longer wavelength of maximum absorption.

Little is known about the photoactivity induced by MMLCT, however, MLCT is known to induce a wealth of photochemistry.[292] For this reason, the photoactivity of $[Pd_3(PPh_3)_4][BF_4]_2$ was investigated.

6.1.1 Reaction with Triphenylphosphine

As previously stated, a very slow reaction of $[Pd_3(PPh_3)_4][BF_4]_2$ with triphenylphosphine, was reported to form $[Pd(Cl)(PPh_3)_3]BF_4$ and $[Pd(PPh_3)_4]$ (shown in Figure 172) which took place over several hours.[266] To investigate the potential photoactivity of $[Pd_3(PPh_3)_4][BF_4]_2$, this reaction was repeated under broadband UV irradiation, and probed by NMR in d_2-dichloromethane.

After just 5 minutes of irradiation at room temperature, all of the NMR signals corresponding to $[Pd_3(PPh_3)_4][BF_4]_2$ had disappeared from the acquired NMR spectra. Several very minor new NMR signals were observed, but the major NMR signals corresponded to $[Pd(Cl)(PPh_3)_3][BF_4]$, which is easily identified from its diagnostic ^{31}P NMR signals shown in Figure 175. These consist of a triplet with *cis* J_{PP} coupling of 15.4 Hz and an integral ratio of 1, observed at δ 32.18, and a doublet with *cis* J_{PP} coupling of 15.4 Hz and an integral ratio of 2, observed at δ 29.48. The former signal corresponds to the phosphine that lies *trans* to the chloride, and the latter corresponds to the two chemically equivalent phosphines that lie *cis* to the chloride. These NMR signals agree with the reported values for this complex.[293]

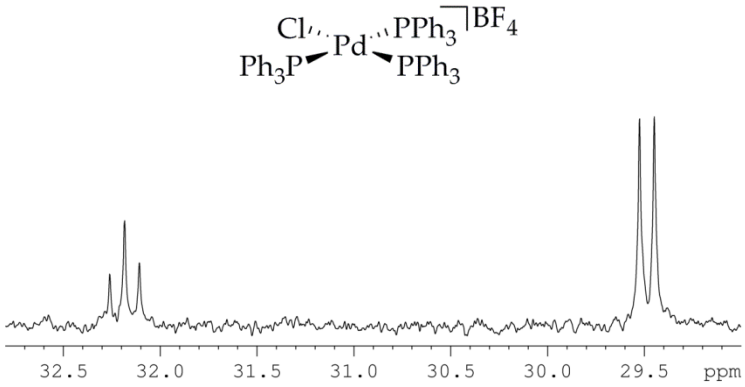

Figure 175: [Pd(Cl)(PPh$_3$)$_3$][BF$_4$] (above) and its diagnostic $^{31}P\{^1H\}$ NMR signals (below), recorded with inverse gated decoupling to allow integration.

As the reaction proceeds much more quickly when irradiated with broadband UV light, the $[Pd_3(PPh_3)_4][BF_4]_2$ complex is likely to be photoactive.

6.1.2 Photoisomerisation

The effect of UV irradiation was further investigated by analysing NMR spectral changes on irradiation, at low temperatures (~ 250 K), of d_2-dichloromethane solutions of $[Pd_3(PPh_3)_4][BF_4]_2$ (2.16 mM), which were prepared under nitrogen. After three hours of UV irradiation, a colour change from red/orange to pink/purple could be observed. This change is shown in Figure 176, alongside the UV-*vis* absorption spectra of the solutions before and after irradiation.

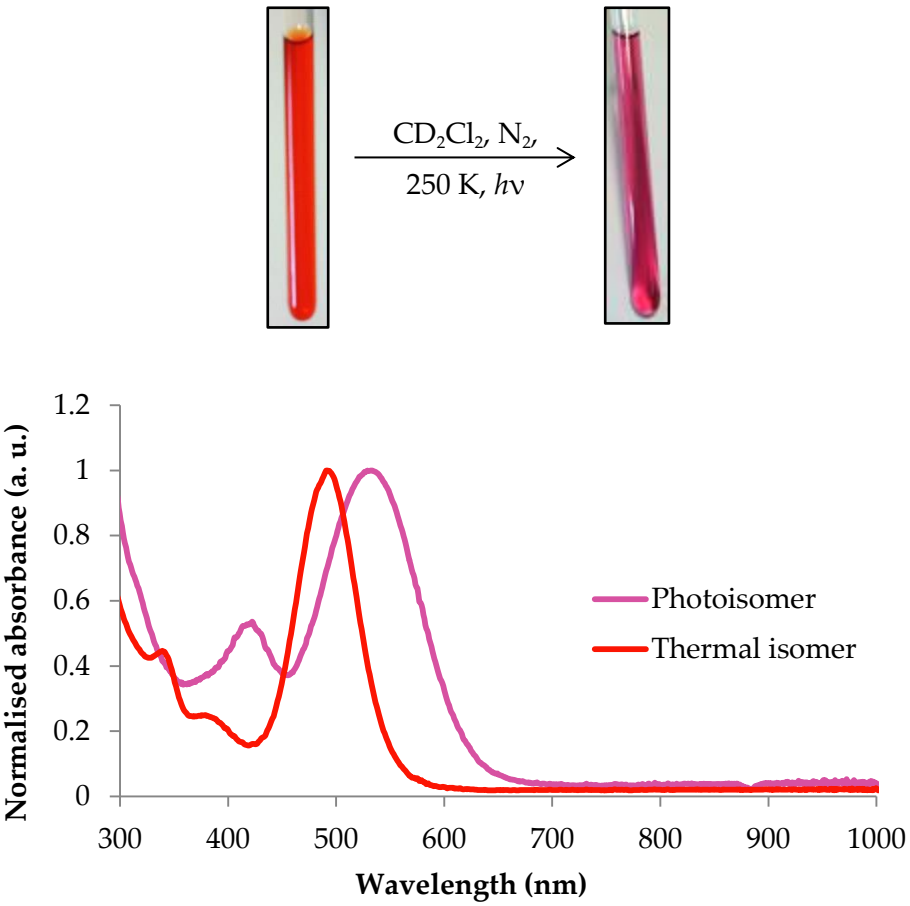

Figure 176: Normalised UV-vis absorption spectra of d_2-dichloromethane solutions of $[Pd_3(PPh_3)_4][OTf]_2$ before (thermal isomer) and after (photoisomer) irradiation with broadband UV light.

The absorption spectrum of the solution after irradiation contains a strong band with a λ_{max} at 532 nm. This corresponds to the absorption of green light, of which violet is the complimentary colour. This agrees with the pink/purple colour of this solution, shown in Figure 176. The molar absorption coefficient of this band could not be calculated by standard means, as the concentration of the diluted solution was not known. Instead, the ERETIC2 quantification tool,[294] provided by Topspin 3.1, was used whereby the signal intensities of solutions of known concentration are compared with the signal intensities of

solutions of unknown concentration in order to calculate their concentration. This method is explained in more detail in Appendix B, section B.3.1. A standard solution of dibenzylideneacetone (Figure 177) was prepared in d_2-dichloromethane, in an NMR tube. The signal intensity of the two protons in the labelled positions (*) shown in Figure 177, at δ 7.18, were used to calibrate the spectrometer. The concentration of the irradiated d_2-dichloromethane solution of $[Pd_3(PPh_3)_4][BF_4]_2$ was calculated using ERETIC2, and the molar absorption coefficient given in Table 23, was calculated using the Beer-Lambert law.

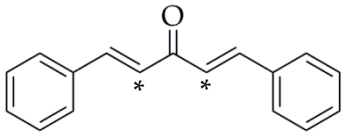

Figure 177: Dibenzylideneacetone.

Table 23: Wavelengths of maximum absorption (λ_{max}) and the corresponding molar absorption coefficients (ε) of d_2-dichloromethane solutions of $[Pd_3(PPh_3)_4][OTf]_2$ before (thermal isomer) and after (photoisomer) irradiation. *Molar absorption coefficients given in SI units ($mol^{-1}m^2$).

Complex	λ_{max} (nm)	ε ($mol^{-1}dm^3cm^{-1}$)
Thermal isomer	492	37, 000 (3, 700)*
Photoisomer	532	30, 500 (3, 500)*

The molar absorption coefficient of the λ_{max}, at 532 nm, is too large to correspond to d-d transitions, and is likely to be due to MMLCT, as with the pre-irradiated solution. The colour change observed on irradiation of the sample confirms a chemical change in $[Pd_3(PPh_3)_4][BF_4]_2$. NMR spectroscopy was used to further analyse the photo-induced chemical change.

The ^{1}H NMR spectra before and after broadband UV irradiation are given in Figure 178. Irradiation leads to the quantitative conversion of the thermal isomer to a new species with fairly similar ^{1}H NMR spectra. The two up-field signals, corresponding to the *ortho* and *meta* protons on the η^2-coordinated phenyl rings remain, although the *ortho* signal now lies at δ 5.18 and the *meta* lies at δ 5.88. The *ortho* signal appears broad, which is typically attributed to exchange, however the signal simplifies to a sharp doublet in ^{1}H

{^{31}P} NMR spectra (Figure 178), hence this apparent broadening is due to coupling of the *ortho* protons to phosphorus nuclei.

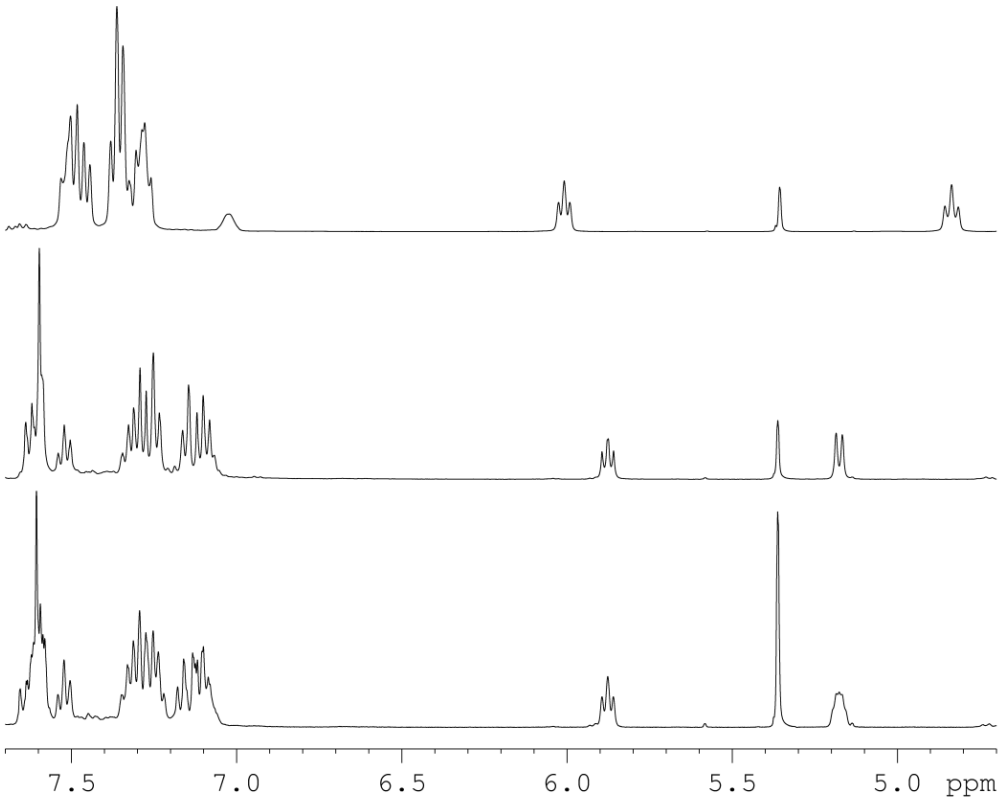

Figure 178: ^{1}H NMR spectrum of d_2-dichloromethane solutions of $[Pd_3(PPh_3)_4][BF_4]_2$ before UV irradiation (above), and after UV irradiation (below). This is compared with the ^{1}H {^{31}P} NMR spectrum of $[Pd_3(PPh_3)_4][BF_4]_2$ after UV irradiation (middle).

The ^{31}P {^{1}H} NMR spectrum of a d_2-dichloromethane solution of $[Pd_3(PPh_3)_4][BF_4]_2$ following broadband UV irradiation is shown in Figure 179. There are now three phosphorus environments, rather than the two AA'XX' environments observed prior to irradiation, thus the symmetry of two of the original phosphine ligands has been lost in this product. The integral ratio of the phosphorus signal at δ 35.69 is double that of the two signals at δ 12.41 and 10.59, therefore it can be concluded that the new species contains four phosphines – two of which are chemically equivalent. The two signals at δ 12.41 and 10.59 are 'roofing'. This effect occurs when the difference in the chemical shift of two signals is similar in magnitude, or less, than the *J* coupling. The formula typically used to predict this type of second order pattern is given below, where $\Delta\nu$ is the chemical shift difference.[263]

$$\frac{\Delta\nu}{J} \leq 10$$

In this case, the chemical shift difference is equal to ~ 300 Hz, and the *J* coupling between these signals is ~ 100 Hz, therefore $\frac{\Delta\nu}{J}$ is equal to 3.

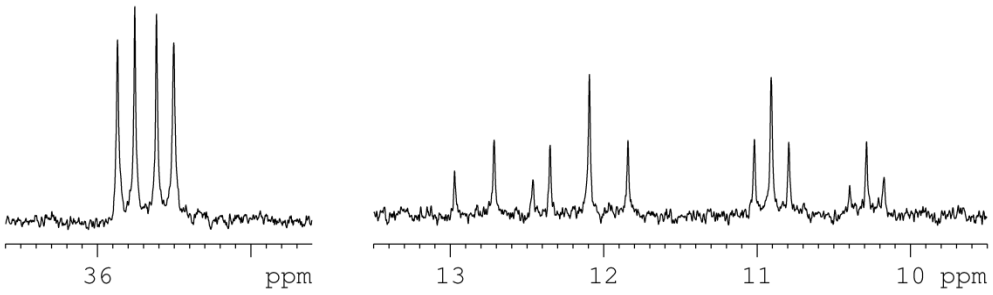

Figure 179: $^{31}P\{^{1}H\}$ NMR spectrum of a d_2-dichloromethane solution of $Pd_3(PPh_3)_4][BF_4]_2$ after UV irradiation.

^{31}P-optimised HMQC NMR spectra contain cross-peaks between the ^{1}H NMR signal corresponding to the *ortho* protons of the η^2-coordinated phenyls at δ 5.18 and the ^{31}P NMR signal at δ 35.69. This must correspond to the phosphorus nuclei of the phosphines that are η^2-coordinated to the palladium. This signal is a doublet of doublets, with *cis* J_{PP} couplings of 41.2 and 18.2 Hz. The coupling values suggest that these phosphorus nuclei are positioned closer to one of the two other phosphines, as shown in Figure 180. The ^{31}P NMR signals at δ 12.41 and 10.59 are both doublet of triplets, which share a large *trans* coupling of 100.7 Hz. The former also exhibits a *cis* coupling of 41.2 Hz, whilst the latter exhibits a *cis* coupling of 18.2 Hz. As no cross peaks were observed between these up-field phosphorus signals and the up-field proton signals of the η^2-coordinated phenyls, they are likely to correspond to terminal phosphines on a linear palladium complex, which matches with their mutual *trans* coupling. This is also shown in Figure 180.

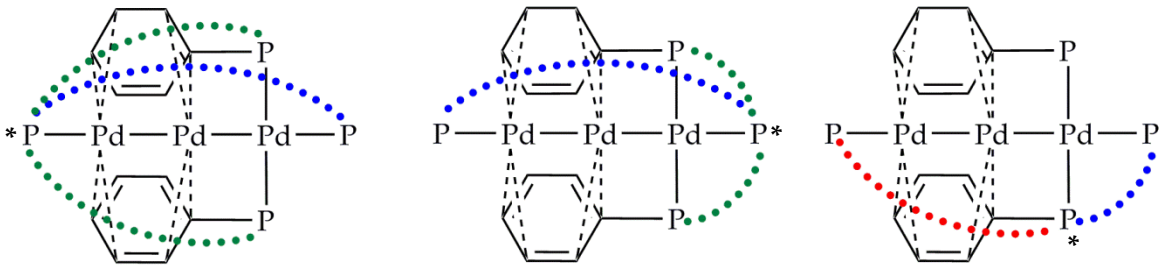

Figure 180: Schematic showing the J_{PP} coupling that gives rise to the phosphorus splitting observed in the ^{31}P NMR spectra.

Table 24: Diagnostic ^{1}H and ^{31}P NMR signals for the photoisomer of $[Pd_3(PPh_3)_4][BF_4]_2$ that forms on UV irradiation of d_2-dichloromethane solutions of $[Pd_3(PPh_3)_4][BF_4]_2$.

$[Pd_3(PPh_3)_4][BF_4]_2$		
$^{31}P\{^{1}H\}$ NMR (J in Hz)	**^{1}H NMR (J in Hz)**	**LIFDI-MS (m/z)**
35.69 (d.d. $J_{PP'}$ = 41.2, $J_{PP''}$ = 18.2, P), 12.41 (d.t. $J_{P'P''}$ = 100.7, $J_{P'P}$ = 41.4, P'), 10.59 (d.t, $J_{P''P'}$ = 100.7, $J_{P''P}$ = 18.4, P'')	5.88 (d.d. J_{HH} = 8.1, 6.4), 5.17 (m. J_{HP} = 14.0)	683.6 $[C_{72}H_{60}P_4Pd_3]^{2+\cdot}$

LIFDI-MS was used to probe the species in solution. The only signal observed appeared at m/z 683.6, which is identical to the m/z of the dicationic tri-palladium cluster $[Pd_3(PPh_3)_4]^{2+\cdot}$. This confirms that the new palladium species that forms on irradiation of d_2-dichloromethane solution of $[Pd_3(PPh_3)_4][BF_4]_2$ is a photoisomer. The diagnostic NMR and LIFDI-MS data is given in Table 24. All of this evidence points towards the structure shown in Figure 181. Now, one terminal palladium binds to three phosphorus nuclei, whilst the other binds to just one and is stabilised by two η^2-coordinations from the phenyls of triphenylphosphine. The η^2-coordinated phosphines are now chemically and magnetically equivalent, giving rise to a doublet of doublets in ^{31}P NMR spectra due to *cis* coupling to the two inequivalent terminal phosphines. Both terminal phosphines give rise to doublet of triplets due to their mutual *trans* coupling, and further *cis* couplings to the two equivalent η^2-coordinated phosphines.

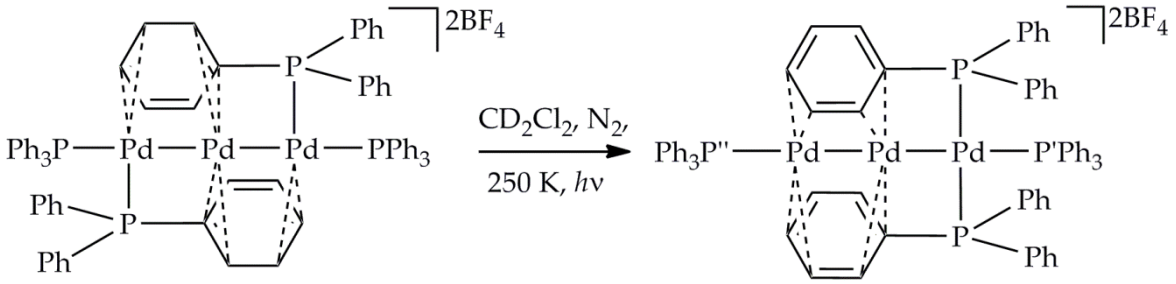

Figure 181: Photoisomerisation of $[Pd_3(PPh_3)_4][BF_4]_2$ using broadband 200-2500 nm UV light.

A single crystal was grown from the d_2-dichloromethane solution of the photoisomer $[Pd_3(PPh_3)_4][BF_4]_2$ by layering dry hexane and allowing the solvents to slowly diffuse at −20 °C. The crystal was suitable for single crystal XRD, and the crystal structure of the photoisomer was solved. This is shown in Figure 182 and confirms the proposed structure.

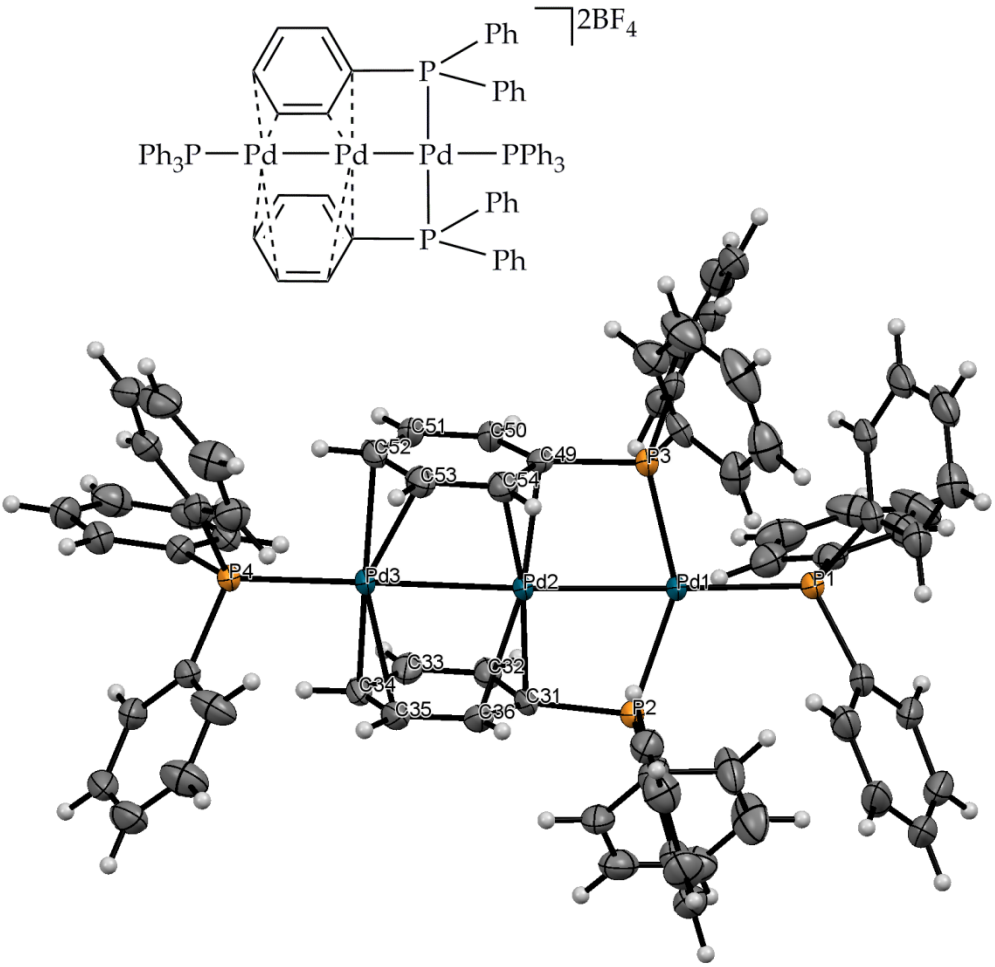

Figure 182: Schematic (above) and crystal structure (below) of the $[Pd_3(PPh_3)_4][BF_4]_2$ photoisomer, formed on UV irradiation of d_2-dichloromethane solutions of $[Pd_3(PPh_3)_4][BF_4]_2$. The tetrafluoroborate counterions have been omitted for clarity. Atom colours: C-grey, H-white, P-orange, Pd-blue.

Again, the three palladium atoms are bonded linearly with the terminal phosphines lying in this plane. Unlike the thermal isomer, the palladium atoms are not perfectly linear; there is a slight bend out of plane so that the Pd-Pd-Pd angle is 171.26 °. As with the thermal isomer, the η^2-coordinated phenyl rings have lost aromaticity in order to stabilise the palladium atoms, however the effect appears to be more severe for the photoisomer – the C-C bonds involved in η^2-coordination are lengthened to a greater degree relative to the C-C bonds in the terminal phosphines, whilst those remote from the η^2-coordination (C5-C6) are shortened to a greater degree and resemble double bonds. The bond lengths of interest are compared in Table 25.

Table 25: Bond lengths of interest in both the thermal and photoisomers of $[Pd_3(PPh_3)_4][BF_4]_2$, with the arbitrary bond numbering scheme shown.

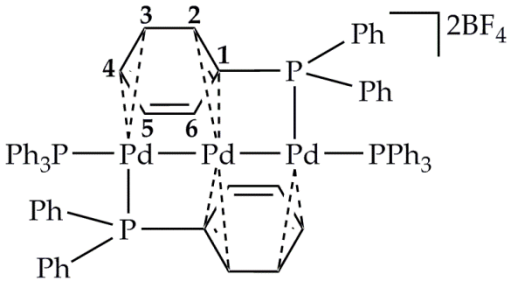

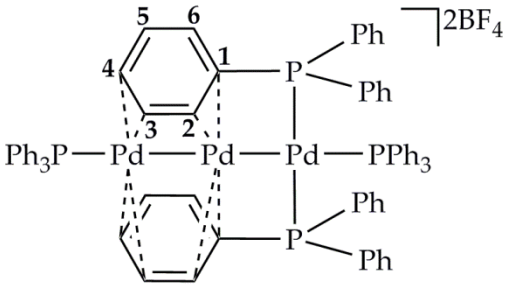

Bond	Bond length / Å	
	Thermal isomer	Photo-isomer
C1-C2	1.424(2)	1.428(6)
C2-C3	1.411(2)	1.414(7)
C3-C4	1.399(3)	1.392(7)
C4-C5	1.419(3)	1.437(7)
C5-C6	1.374(2)	1.361(7)
C6-C1	1.430(2)	1.442(7)
Mean C-C in terminal XPh_3	1.388(2)	1.381(7)
Mean η^2 bond length	2.286(2)	2.264(5)

6.1.2.1 Observed Rate of Photoisomerisation

The rate of formation of this photoisomer is dependent on the concentration of the solution and on the power of the broadband UV lamp used. The observed rate of

formation using a d_2-dichloromethane solution of $[Pd_3(PPh_3)_4][BF_4]_2$ (1.08 mM) with a 200 W broadband UV source, was calculated at 240 K, using ^{1}H NMR spectroscopy. An optic fibre cable was used to refract the light from the lamp to the NMR probe. ^{1}H NMR spectra were collected with 10 minute intervals. The integral ratios of the signals corresponding to the *ortho* protons of the η^2-coordinated phenyl rings of the thermal isomer and photoisomer were converted into the ratio of each species, which was plotted against the time, shown in Figure 183. Rate constants were determined by fitting first order relationships to these data according to the formulae below, where $[A]$ is the concentration of the thermal isomer, $[B]$ is the concentration of the photoisomer, and k_{AB} is the observed rate constant of photoisomerisation. The formulae used are similar to those used to determine the rates of haptotropic shifting of pyridazine and phthalazine discussed in Chapter 2, section 2.3.1.

$$[A]_{t+\delta t} = [A]_t - k_{AB}[A]_t \delta t$$

$$[B]_{t+\delta t} = [B]_t + k_{AB}[A]_t \delta t$$

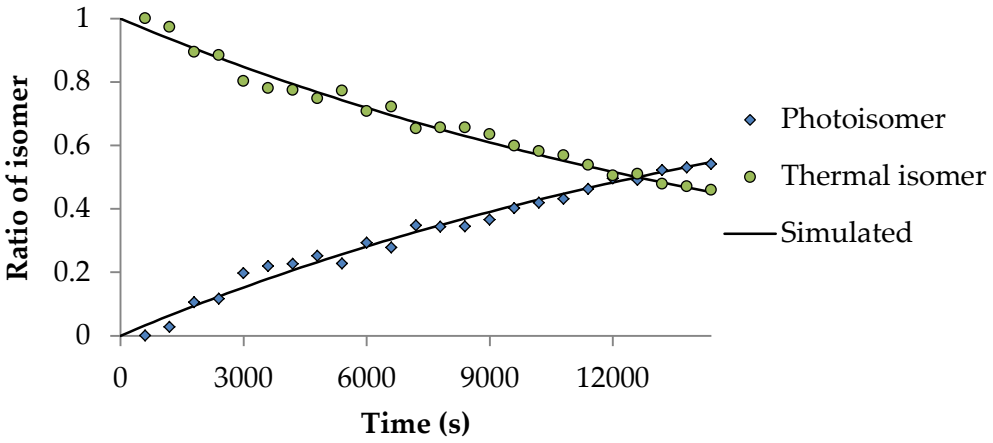

Figure 183: Graph to show the formation of the photoisomer from the thermal isomer of $[Pd_3(PPh_3)_4][BF_4]_2$ on broadband UV irradiation at 240 K.

Under these experimental conditions, the observed rate constant is calculated to be 5.474×10^{-5} s^{-1} ± 5×10^{-8} s^{-1}, which confirms a slow reaction. It should be noted that this is simply an experimental rate and serves to indicate the relatively inefficient nature of this process. The reaction is faster on irradiation of the sample outside the NMR spectrometer, where the sample is rotated to ensure irradiation of the whole sample. Under these conditions, the reaction is complete within 5 hours of irradiation. No evidence for the reformation of the thermal isomer is observed at 240 K.

6.1.2.2 Reverse Isomerisation

On warming d_2-dichloromethane solutions of the $[Pd_3(PPh_3)_4][BF_4]_2$ photoisomer to room temperature, the reverse reaction is observed, as shown in Figure 184. This reaction is not clean, and several minor, uncharacterised species also form (although never more than approximately 7% of the total species). As before, the rate of this isomerisation was calculated using a 1.08 mM solution at the different temperatures given in Table 26, using ^{1}H NMR spectroscopy. Due to the slow nature of this reaction, ^{1}H NMR spectra were recorded with 100 minute intervals. Again, the integral ratios of the signals corresponding to the *ortho* protons of the η^2-coordinated phenyl rings of the thermal isomer and photoisomer were used to determine the ratio of each species, which was plotted against the time. An example plot is shown in Figure 185. Due to signal overlap, the aforementioned minor species cannot be accurately quantified and are therefore not included in the plots. Rate constants were determined by fitting first order relationships to these data according to the formulae discussed above. The exclusion of the minor species leads to slight inaccuracies in the calculated rates.

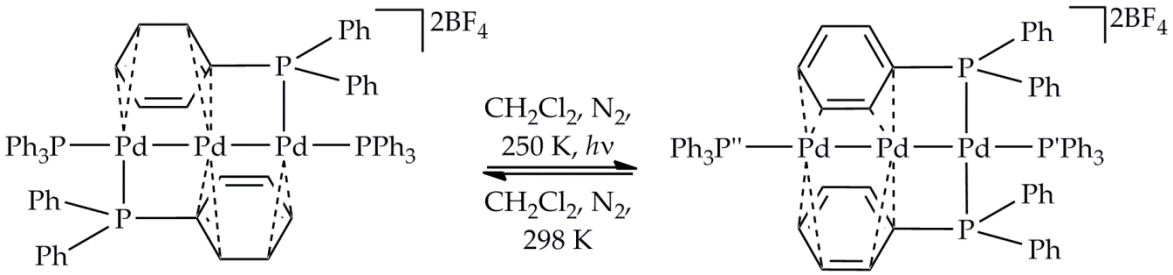

Figure 184: Photoisomerisation and reverse isomerisation of $[Pd_3(PPh_3)_4][BF_4]_2$.

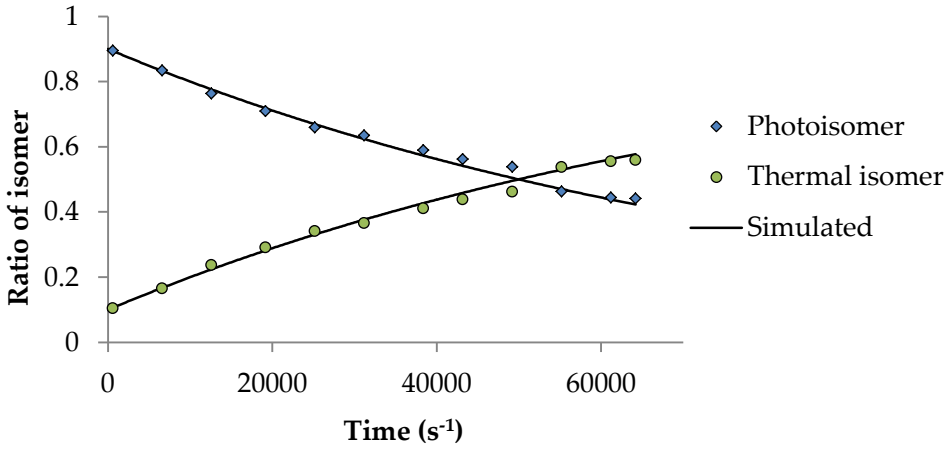

Figure 185: Graph to show the formation of the thermal isomer from the photoisomer of $[Pd_3(PPh_3)_4][BF_4]_2$ at 300 K.

The rates obtained at different temperatures are given in Table 26. Unfortunately, temperatures above 300 K could not be used due to shifting of the NMR signals which resulted in overlap of the signal corresponding to the *ortho* protons of the η^2-coordinated phenyl rings in the photoisomer and the signal corresponding to residual d_1-dichloromethane. Temperatures above 313 K could not be used due to the safety implications of using temperatures above the boiling point of dichloromethane. Temperatures lower than 285 K resulted in isomerisation that was too slow to be accurately measured with this method. The rates of thermal isomerisation are slow, which indicates a large enthalpy of activation ($\Delta H^{\ddagger}$). The enthalpy of activation for this process was calculated from an Eyring plot, given in Appendix B section B.3.2, the method for which is described in detail in Chapter 2, section 2.3.1.

Table 26: Observed rate constants of isomerisation from the photoisomer to the thermal isomer, at the different temperatures shown.

Temperature / K	Rate (x10^{-7} s^{-1})
300	117.7 ± 0.4
295	35.94 ± 0.07
290	48.34 ± 0.03
285	7.92 ± 0.01

The $\Delta H^{\ddagger}$ value was calculated to be 110 ± 10 kJ mol^{-1} and is relatively large, which reflects the slow rates observed for this process. Such a large $\Delta H^{\ddagger}$ suggests that the multiple steps up to and including the rate determining step require substantial energy. The mechanism of isomerisation cannot, however, be elucidated from this experimental data. A complimentary DFT study would be beneficial in determining which reaction pathway is more likely – initial cleavage of the Pd-P bond, or initial dissociation of the η^2-coordinated phenyl ring.

6.1.2.3 Reaction in the Presence of Water and Oxygen

On irradiating d_2-dichloromethane solutions of $[Pd_3(PPh_3)_4][BF_4]_2$ with broadband UV light, in the presence of water and oxygen, the same photoisomerisation is observed to occur. However, under these conditions, the photoisomer is not stable and reacts further. Due to the presence of multiple species in solution, the aromatic regions of the resulting

^{1}H NMR spectra are complicated by the overlap of peaks. The ^{31}P NMR spectra, however, contain diagnostic signals at δ 33.59 (*)and 23.32 (*), shown in Figure 186, which were observed, in ^{31}P-optimised HMQC NMR spectra, to couple only to aromatic proton signals. These ^{31}P NMR signals are singlets and correspond to $[Pd(OH_2)_2(PPh_3)_2][BF_4]_2$, and triphenylphosphine oxide, respectively; their chemical shifts match those reported in the literature.[295,296]

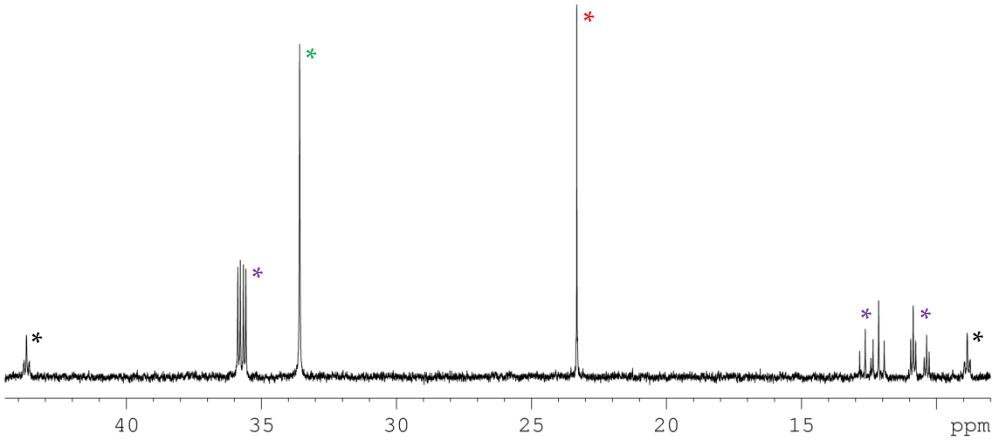

Figure 186: ^{31}P {^{1}H} NMR spectrum showing the diagnostic signals that form on irradiation of $[Pd_3(PPh_3)_4][BF_4]_2$ in the presence of water and oxygen. The signals corresponding to the thermal (*) and photoisomer (*) of $[Pd_3(\underline{P}Ph_3)_4][BF_4]_2$ can be observed, in addition to the signals corresponding to triphenylphosphine oxide (*) and $[Pd(OH_2)_2(\underline{P}Ph_3)_2][BF_4]_2$ (*).

The palladium and triphenylphosphine in the $[Pd_3(PPh_3)_4][BF_4]_2$ photoisomer are therefore oxidised under these conditions. Palladium colloids also form, which is verified by the observation of palladium black coating the glass vessel. As no reaction is observed with the $[Pd_3(PPh_3)_4][BF_4]_2$ thermal isomer in the presence of water and oxygen, the photoisomer is likely to be less stable than the thermal, and potentially a more reactive catalyst. Furthermore, light degradation of the $[Pd_3(PPh_3)_4][BF_4]_2$ thermal isomer is one potential route to nanoparticle formation.

6.2 Hydrogenation Catalysis

In order to investigate the catalytic ability of these tri-palladium complexes, their activity as hydrogenation catalysts was determined. The reaction studied is shown in Figure 187 and is the hydrogenation of phenylacetylene to styrene, which is further hydrogenated to ethylbenzene.

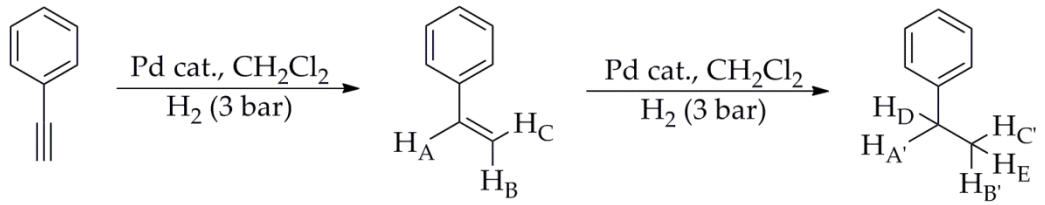

Figure 187: Hydrogenation of phenylacetylene to styrene, and ethylbenzene.

The activity of the tri-palladium catalysts was compared with that of Crabtree's catalyst, $[Ir(COD)(PCy_3)(py)][PF_6]$, where PCy_3 is tricyclohexylphosphine, as this is well known to be a good hydrogenation catalyst for unsaturated hydrocarbons.[297] Dichloromethane was used as the solvent. Crabtree's catalyst is a homogeneous catalyst, and readily deactivates in the absence of a sufficiently ligating substrate, to form $[Ir_3(\mu^3\text{-}H)(PCy_3)_3(Py)_3][PF_6]_2$, shown in Figure 188.[298]

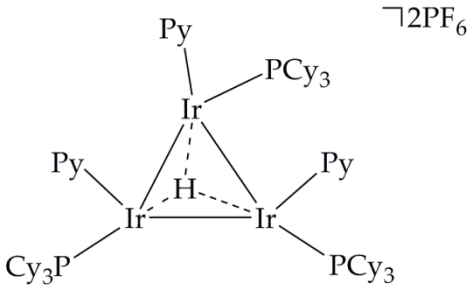

Figure 188: $[Ir_3(\mu^3\text{-}H)(PCy_3)_3(Py)_3][PF_6]_2$.

Phenylacetylene is successfully hydrogenated with both the thermal isomer and photoisomer of $[Pd_3(PPh_3)_4][BF_4]_2$, as well as Crabtree's catalyst. This is therefore a suitable hydrogenation reaction to use for catalyst comparisons. When hydrogen is replaced with *para*-H_2, dramatic PASADENA enhancements of the signals corresponding to the *para*-H_2-derived protons in styrene are observed at δ 6.77 (antiphase d.d, H_A), 5.81 (antiphase d.d, H_C), and 5.28 (antiphase d, H_B). A typical spectrum is shown in Figure 189, using the thermal isomer of $[Pd_3(PPh_3)_4][BF_4]_2$ as the example catalyst. Additional small

PASADENA enhancements of the signals corresponding to the *para*-H_2-derived protons in ethylbenzene are also observed at δ 2.68 (antiphase q, H_D), and 1.27 (antiphase t, H_E). Integrals of these signals are negligible and they disappear from ^{1}H NMR spectra after several seconds, becoming masked by the thermal signals of ethylbenzene.

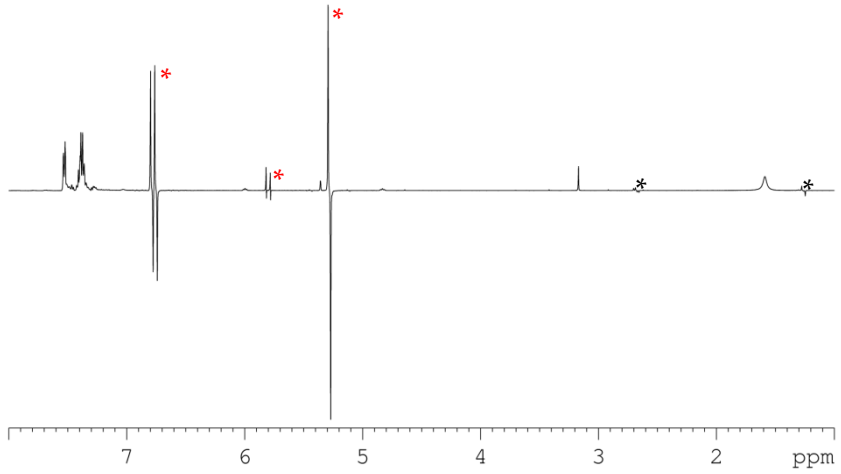

Figure 189: ^{1}H NMR spectrum showing PASADENA signals corresponding to the para-H_2-derived protons in styrene (*) and ethylbenzene (*) that form on addition of para-H_2 (3 bar) to d_2-dichloromethane solutions of $[Pd_3(PPh_3)_4][BF_4]_2$ containing excess phenylacetylene (66 equivalents).

Probing the depletion of these enhanced styrene signals with time is a useful method to calculate effective hydrogenation rates. Using a substantial excess of phenylacetylene (66 equivalents, 85.67 mM) renders the concentration of *para*-H_2 in solution rate-limiting. The rate of depletion of the PASADENA proton signals corresponds to the rate of consumption of *para*-H_2.[299] In order to differentiate thermal signals from PASADENA signals, the OPSY protocol was used, which suppresses thermal signals.[209] Although no longer masked by thermal signals, the enhanced signals corresponding to ethylbenzene could not be observed due to the lower SNR in these single-scan OPSY NMR spectra. Enhanced styrene signals are depleted by probing with OPSY and by T_1 relaxation. The observed signal is therefore caused by the generation of fresh hyperpolarised styrene that has not previously been probed by OPSY. Uniquely, this method probes the reaction rate, rather than the reactant concentration, as a function of reaction time. NMR spectra were collected every eight seconds. This allowed enough time for the probed states to relax but also allowed enough data points to be collected so that even the fastest rates could be calculated within reasonable error.

Pseudo-hydrogenation rate constants were calculated using 1.3 mM d_2-dichloromethane solutions of palladium catalyst with 66 equivalents of phenylacetylene (85.67 mM). The samples were degassed prior to the addition of *para*-H_2 (~ 3 bar). The solutions were then shaken at low magnetic field for 10 seconds, and a series of OPSY NMR spectra were immediately acquired. Once all of the *para*-H_2 in solution had been consumed, the solutions were re-shaken at low magnetic field for 10 seconds, and a second series of OPSY NMR spectra were immediately acquired.

The concentration of hydrogen dissolved in dichloromethane is reported to be 1.51 ± 0.06 mM, at 25 °C, using 1.01 bar.[199] At the pressures studied herein, the mole fraction of hydrogen in solution increases linearly with pressure,[300] thus it can be assumed that the concentration of hydrogen dissolved in dichloromethane at 3 bar is 3 times the concentration at 1 bar, and is equal to 4.49 ± 0.18 mM. This is far lower than the concentration of phenylacetylene in solution, which is equal to 85.67 mM, thus hydrogen concentration is rate-limiting. The amount of hydrogen supplied by the head space can be calculated from the ideal gas law shown below, where P is pressure (Pa), V is volume (m^3), n is the number of moles, R is the ideal gas constant (8.314 J $K^{-1}mol^{-1}$), and T is temperature (K).

$$PV = nRT$$

A typical Young's NMR tube has a volume of approximately 2.4 mL.[301] The sample takes up approximately 0.6 mL of this, leaving 1.8 mL of headspace, which corresponds to 217.8 μmol of hydrogen available. After the first series of OPSY NMR spectra have been acquired, all of the hydrogen in solution has reacted which leads to a loss of 2.7 ± 0.11 μmol of hydrogen. Shaking the sample a second time replaces the hydrogen lost in solution, leaving 215.1 ± 8.76 μmol of hydrogen available in the headspace, which corresponds to a pressure of approximately 2.97 bar. The drop in hydrogen pressure prior to the acquisition of the second series of OPSY NMR spectra is therefore negligible and cannot account for any changes in the effective rates of hydrogen consumption. Similarly, the initial phenylacetylene concentration drops from 51.4 μmol to a minimum of approximately 48.7 μmol (assuming conversion from phenylacetylene to ethylbenzene is negligible), which also cannot account for any changes in hydrogen consumption rates.

The integral ratios of the PASADENA signals corresponding to the *para*-H_2-derived protons of styrene were observed to fall in intensity with time, as the *para*-H_2 in solution was consumed. This is shown in Figure 190, where the thermal isomer of $[Pd_3(PPh_3)_4][BF_4]_2$ is used as the catalyst. The integrals of these signals were calibrated with respect to the integrals in the first OPSY spectrum acquired. These values were plotted against time – an example plot in which $[Pd_3(PPh_3)_4][BF_4]_2$ is used as the catalyst is shown in Figure 191. A complete set of plots is given in Appendix B, section B.3.3. The signal intensity observed for proton H_C is much less than that observed for protons H_A and H_B. This reflects the selectivity of the catalyst to add *para*-H_2 to the same face of the alkyne. The signals corresponding to H_C were not used in rate calculations as their low intensities lead to higher errors.

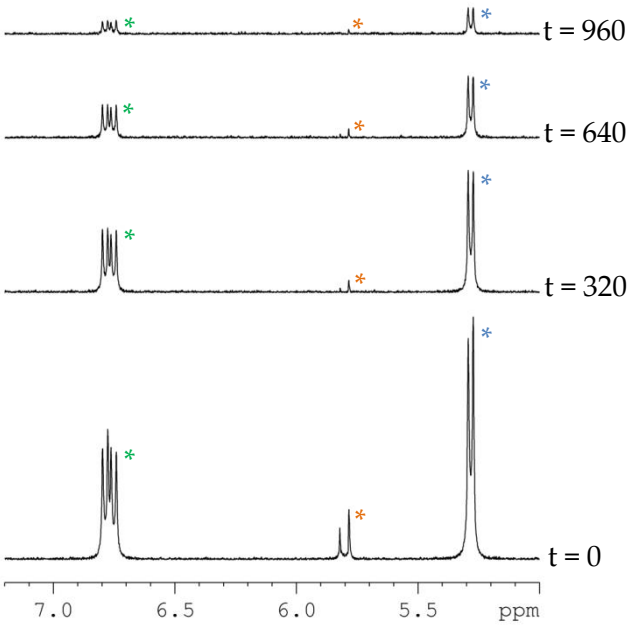

Figure 190: OPSY NMR spectra of d_2-dichloromethane solutions containing 1.3 mM $[Pd_3(PPh_3)_4][BF_4]_2$ with 66 equivalents of phenylacetylene and para-H_2 (3 bar). Spectra were collected t seconds after shaking the sample at low magnetic field and inserting it into the NMR spectrometer. PHIP signals corresponding to protons on styrene (* = H_A, * = H_B, * = H_C) are observed to reduce in intensity as para-H_2 is consumed.

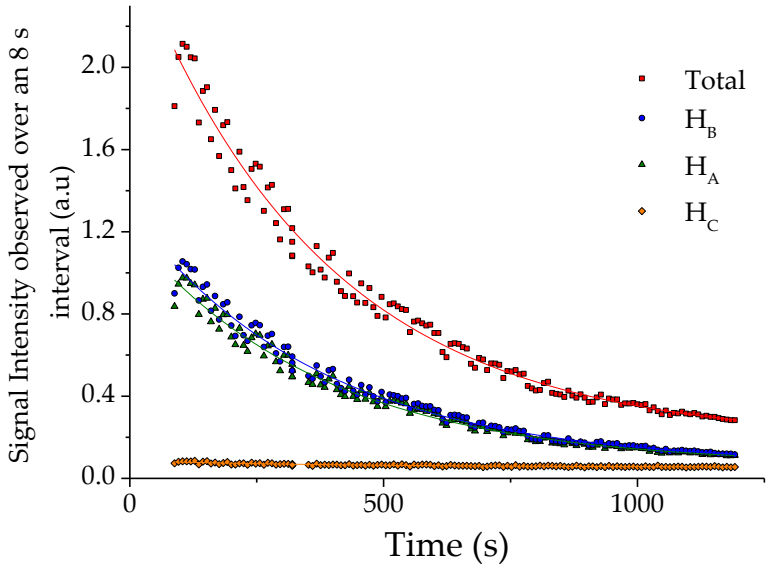

Figure 191: Plot to show the reduction in the change in intensity, over an 8 s interval, of the PASADENA signals corresponding to the para-H_2-derived protons in styrene with time.

The data were plotted using Origin software and were fitted to find the observed rate constant of decay according to the formula given below, where A is the initial amplitude of the signal intensity after 8 s hydrogenation time, t_1 is the decay constant which is equal to $\frac{1}{k_{obs}}$, and y_0 is the offset, from 0, of the signal intensity at $t = \infty$. Simulated fits with lowest errors are found when $y_0 \neq 0$. This is due to the inherent noise in the OPSY spectra, which leads to the detection of residual signal despite the complete relaxation of magnetisation. The effect of this residual signal cancels across all the data points and therefore does not influence the calculated k_{obs}values.

$$y = Aexp^{\frac{-x}{t_1}} + y_0$$

Data fitting is carried out using the Levenberg-Marquardt algorithm,[302] in which the sum of the residuals calculated from a least mean squares analysis are minimised by iterating the variables A, t_1, and y_0. This is identical to the data fitting method used in Excel, to calculate rates, which is explained in full in Appendix A, section A.1.1. Furthermore, the calculation of the standard error is equivalent to the Jack-knife method[191] also detailed in Appendix A, section A.1.2.

The *pseudo*-rate constants of signal depletion, which correspond to the effective rate of *para*-H_2 consumption, are given in Table 27. These values do not truly represent the rate of hydrogenation, as they have been calculated from plots of reaction rate as a function of

time. They effectively represent the rate of decay of the reaction rate as *para*-H_2 is consumed, however the same principles apply – a larger value represents a faster reaction and better catalyst. Probing the reaction rate, rather than the reactant concentration, as a function of reaction time allows the reaction order with respect to hydrogen concentration (n_t) to be found. The reaction order was calculated using Letort's 'order with respect to time, n_t' method[303] which is explained in detail in Appendix B, section B.3.4. The reaction orders with respect to hydrogen concentration are also given in Table 27. Changes in reaction orders suggest changes in catalyst speciation.

Table 27: Pseudo-rate constants and reaction orders, with respect to hydrogen concentration, of hydrogen consumption in the hydrogenation of phenylacetylene, with 1.3 mM d_2-dichloromethane solutions of palladium catalyst with 66 equivalents of phenylacetylene and para-H_2 (3 bar). *'After activation' refers to samples that were left for several days after initial para-H_2 addition. Fresh phenylacetylene was then added, the sample was degassed, and fresh para-H_2 was added.

Catalyst	K_{obs} H_2 depletion ($x10^{-2}$ s^{-2})		Reaction order n_t (a.u.)	
	1	2	1	2
$[Ir(COD)(PCy_3)(py)][PF_6]$	8.5 ± 0.4	2.4 ± 0.1	1.56 ± 0.05	1.13 ± 0.01
$[Pd_3(PPh_3)_4][BF_4]_2$	0.27 ± 0.01	0.50 ± 0.02	0.86 ± 0.02	0.87 ± 0.02
$[Pd_3(PPh_3)_4][BF_4]_2$ (photoisomer)	0.25 ± 0.01	0.50 ± 0.01	0.86 ± 0.02	1.23 ± 0.02
$[Pd_3(PPh_3)_4][BF_4]_2$ (after activation*)	2.80 ± 0.07	2.61 ± 0.06	1.50 ± 0.02	1.47 ± 0.02
$[Pd_3(PPh_3)_4][BF_4]_2$ (+ 10 equiv. PPh_3)	1.25 ± 0.03	0.72 ± 0.03	1.54 ± 0.05	0.92 ± 0.04
$[Pd_3(PPh_3)_4][BF_4]_2$ (+ 10 equiv. PPh_3, after activation*)	-	-	-	-

The fastest *pseudo*-rate constant of hydrogen consumption was calculated to be 8.5 $x10^{-2}$ s^{-2}, observed in the first *para*-H_2 shake with Crabtree's catalyst, which is known to be a very active catalyst for such hydrogenation reactions.[297] This rate drops significantly, to 2.4 $x10^{-2}$ s^{-2}, in the second shake. The aforementioned negligible drop in hydrogen and phenylacetylene concentration cannot account for this change. Rather, the catalyst is likely to be decomposing, which is supported by the change in n_t, which drops from 1.56 to 1.13. Furthermore, the yellow solution was observed to darken. Crabtree's catalyst is

reported to be homogeneous, thus in this case, degradation to iridium clusters and colloids does not produce active catalytic species.[297,304]

There is a significant change in the ^{1}H NMR signals that correspond to the catalyst before and after hydrogenation. This is demonstrated in Figure 192. The doublet observed at δ 8.71, which corresponds to the *ortho* protons of bound pyridine, disappears on addition of *para*-H_2, suggesting that this ligand has dissociated from the iridium. Signals for free pyridine are not observed but may be masked by the aromatic signals corresponding to phenylacetylene and styrene. Furthermore, the multiplets at δ 4.75 and 3.24, which correspond to the vinylic protons of bound COD, also disappear on addition of *para*-H_2, however NMR signals for free COD or COE are not observed to form. Instead, ^{1}H NMR signals corresponding to COA are observed at δ 1.58. The COD has therefore hydrogenated to COA and is no longer ligating to the iridium.

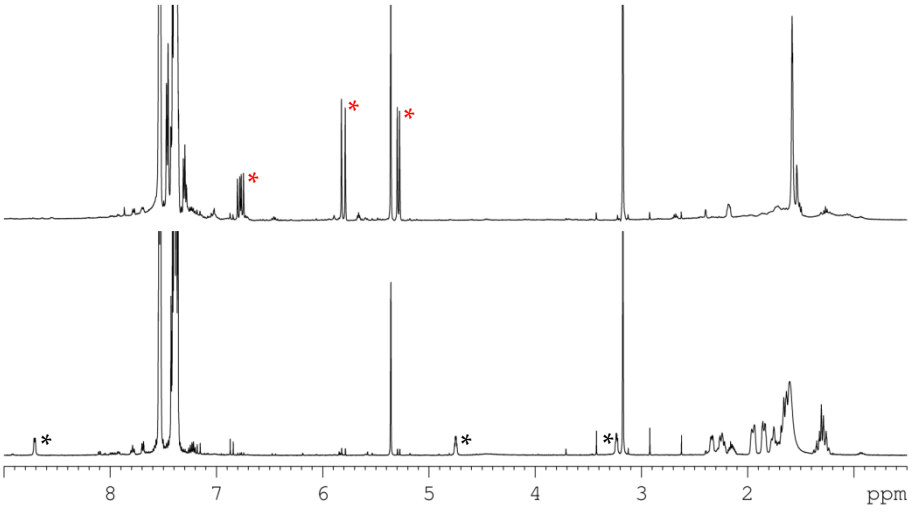

Figure 192: ^{1}H NMR spectra of a 1.3 mM d_2-dichloromethane solution of [Ir(COD)(PCy_3)(py)][PF_6] with 66 equivalents of phenylacetylene (below) prior to para-H_2 addition (above) after addition of para-H_2 (3 bar) followed by shaking at low magnetic field. The thermal signals corresponding to the para-H_2-derived protons in styrene are observed (*).The signals corresponding to protons on [Ir(COD)(PCy_3)(py)][PF_6] are affected (*).

It is reported that the active catalytic species involved in this hydrogenation should be $[Ir(H)_{2n}(sub)_{3-n}(PCy)_2][BF_4]$, where n = 1-3.[297]. The dissociation of pyridine and COD from $[Ir(COD)(PCy_3)(py)][PF_6]$ suggests that these active species have formed. This is also supported by the initial n_t being equal to 1.56 – hydrogen can occupy multiple iridium binding sites. The ^{1}H NMR signal corresponding to hydrogen is never observed in the

OPSY or ^{1}H NMR spectra. This confirms that all of the *para*-H_2 in solution is consumed in the hydrogenation reaction, and none is observed to relax to normal hydrogen neither prior to hydrogenation nor after, *via* a reversible catalytic process.[103] This verifies the suitability of this method for the calculation of the rate of hydrogen consumption.

Interestingly, the observed *pseudo*-rate constants of *para*-H_2 consumption of both the thermal and photoisomers of $[Pd_3(PPh_3)_4][BF_4]_2$ are indistinguishable when taking errors into account. Despite the photoisomer being more reactive than the thermal isomer to oxygen and water, it exhibits identical activity in the hydrogenation of phenylacetylene. The values of n_t, in the first *para*-H_2 shake, for both isomers, are also indistinguishable. The *pseudo*-rate constant of *para*-H_2 consumption in the first *para*-H_2 shake, for both isomers, was 0.26 x10^{-2} s^{-2}, which is over an order of magnitude less than that using Crabtree's catalyst. However, the *pseudo*-rate constant increases significantly with both isomers, to 0.5 x10^{-2} s^{-2} in the second shake. Such an increase implies that the catalyst is activating, and as both the thermal and photoisomers exhibit identical activity, they are likely to be forming identical active species. There were, however, no observable changes in the ^{1}H NMR signals corresponding to the thermal isomer of $[Pd_3(PPh_3)_4][BF_4]_2$ after the second shake with *para*-H_2. The photoisomer was observed to isomerise back to the thermal isomer. Furthermore, the reaction orders with respect to hydrogen did not change significantly on shaking with *para*-H_2 a second time.

To further investigate the activation of the $[Pd_3(PPh_3)_4][BF_4]_2$ catalyst, the same sample was left for several days at room temperature. After this time, all of the phenylacetylene had hydrogenated to ethylbenzene. Fresh phenylacetylene was added to the sample, which was subsequently degassed and fresh *para*-H_2 (3 bar) added. The *pseudo*-rate constant of *para*-H_2 consumption in the first *para*-H_2 shake of this 'activated' sample was 2.80 x10^{-2} s^{-2}. This is 5.6-fold faster than the second shake of the 'unactivated' sample. This is also faster than the second shake with Crabtree's catalyst (2.4 x10^{-2} s^{-2}).

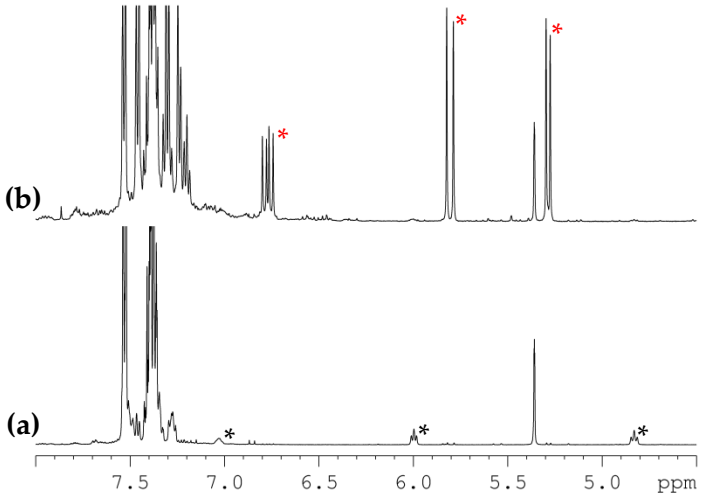

Figure 193: ^{1}H NMR spectra of a 1.3 mM d_2-dichloromethane solution of $[Pd_3(PPh_3)_4][BF_4]_2$ with 66 equivalents of phenylacetylene (a) prior to para-H_2 addition (b) after 'activation' of the catalyst and addition of further para-H_2 (3 bar). The thermal signals corresponding to the para-H_2-derived protons in styrene are observed (*). The signals corresponding to protons on $[Pd_3(PPh_3)_4][BF_4]_2$ are affected (*).

Interestingly, the ^{1}H NMR signals corresponding to $[Pd_3(PPh_3)_4][BF_4]_2$, shown in Figure 193, changed significantly on activation. The signals at δ 7.03, 6.00 and 4.83, which correspond to the protons on the η^2-coordinated phenyl rings of triphenylphosphine have disappeared, which suggests that the catalyst has decomposed to form palladium colloids. The value of n_t also changed significantly, from 0.86 to 1.50. This also supports a change in speciation, with more hydrogen now able to bind to the catalytic species. These changes coincide with the observation of palladium black coating the glass vessel. The increase in the observed rate of hydrogen consumption on catalyst decomposition suggests that this hydrogenation reaction is predominantly heterogeneous.[24]

The OPSY NMR spectra collected during the *para*-hydrogenation of phenylacetylene using both the thermal and photoisomers of $[Pd_3(PPh_3)_4][BF_4]_2$ contained two hydride signals shown in Figure 194. These are singlets and are observed at δ -14.76 and -19.65. Unfortunately, their weak intensity prevented further NMR characterization, however, their sharp, singlet splitting pattern provides no evidence of J_{HP} couplings, which suggests an absence of phosphine ligands. These signals may therefore correspond to hydride ligands bound to small palladium colloidal species[305]. Their observation with both isomers of $[Pd_3(PPh_3)_4][BF_4]_2$ is further proof that these catalysts break down to form identical species.

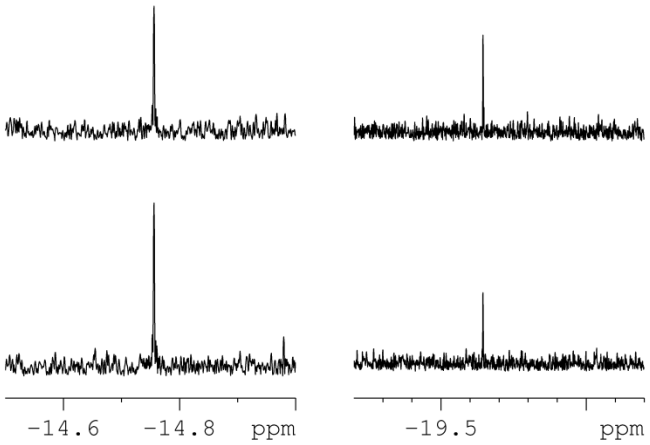

Figure 194: OPSY NMR spectra showing para-H_2-derived hydride signals that form on para-hydrogenation of phenylacetylene using a 1.3 mM d_2-dichloromethane solution of the thermal (below) and photoisomer (above) of $[Pd_3(PPh_3)_4][BF_4]_2$.

The nature of the active catalytic species that form from $[Pd_3(PPh_3)_4][BF_4]_2$ was further investigated. Degradation of this catalyst may form colloids, as is suggested by the evidence hitherto discussed, but can also form palladium monomers that are stabilised by phosphine ligands. To distinguish which are most likely to be contributing to the activity of this catalyst, a second 1.3 mM d_2-dichloromethane sample of $[Pd_3(PPh_3)_4][BF_4]_2$ (thermal isomer) with 66 equivalents of phenylacetylene and 10 equivalents of triphenylphosphine was prepared and degassed. As discussed previously, excess triphenylphosphine is known to react with $[Pd_3(PPh_3)_4][BF_4]_2$ to form the monomeric species $[Pd(PPh_3)_4]$ and $[Pd(Cl)(PPh_3)_3][BF_4]$. The hydrogenation activity of this sample was compared with that of $[Pd_3(PPh_3)_4][BF_4]_2$ without additional triphenylphosphine.

The *pseudo*-rate constant of *para*-H_2 consumption, on addition of *para*-H_2 to this sample and shaking for the first time, was calculated to be 1.25 $x10^{-2}$ s^{-2}, given in Table 27, which is 4.6-fold faster than the same catalyst without additional phosphine. This rate reduces after the second shake to 0.72 $x10^{-2}$ s^{-2}, which suggests that the catalyst is deactivating. This coincides with a reduction in n_t, from 1.54 to 0.92 which is similar to that observed using Crabtree's catalyst. This sample was left for several days at room temperature. After this time, much of the phenylacetylene had not reacted. Fresh phenylacetylene was added to the sample, which was subsequently degassed and fresh *para*-H_2 (3 bar) added, however no further hydrogenation was observed to occur – the catalyst had completely

deactivated. Furthermore, no hydride signals were observed to form in any of the acquired OPSY spectra.

The activity of $[Pd_3(PPh_3)_4][BF_4]_2$ is dramatically altered on the addition of excess triphenylphosphine. It is therefore unlikely that these triphenylphosphine-stabilised monomeric palladium species are the relevant catalytic species on degradation of $[Pd_3(PPh_3)_4][BF_4]_2$. Although a homogeneous catalytic pathway cannot be ruled out, the evidence collected suggests that a heterogeneous pathway is more likely.

6.3 Carbon-coupling Catalysis

As the $[Pd_3(PPh_3)_4][BF_4]_2$ complex exhibited promising activity as a hydrogenation catalyst, its potential as a carbon-coupling catalyst was briefly examined.

6.3.1 Suzuki-Miyaura Coupling

The first carbon-coupling reaction studied is shown in Figure 195 and is a Suzuki-Miyaura coupling of 4-bromo-6-methyl-pyran-2-one with 4-methylphenylboronic acid to form 6-methyl-4-(4-methylphenyl)-pyran-2-one. This is a known reaction,[306,307] and the conditions used here are typical for such Suzuki-Miyaura cross-couplings.[308]

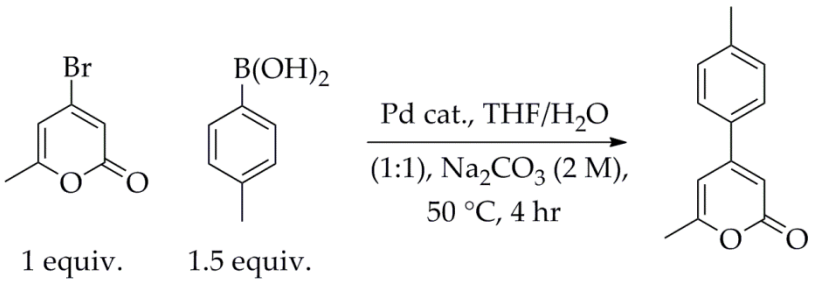

Figure 195: Suzuki-Miyaura cross-coupling of 4-bromo-6-methyl-pyran-2-one with 4-methylphenylboronic acid to form 6-methyl-4-(4-methylphenyl)-pyran-2-one, using the reaction conditions shown.

In cross-coupling reactions, oxidative addition of an aryl, heteroaryl, or vinyl halide to the palladium catalyst is typically the rate-determining step.[309] The barrier to oxidative addition is reduced when the halide used is a better leaving group (I > OTf > Br >> Cl), and when the aryl-halide bond is made more electropositive by the close proximity of electron-withdrawing groups. In the case of 4-bromo-6-methyl-pyran-2-one, the electron-withdrawing nature of the pyrone moiety, combined with bromine as a leaving group

leads to relatively fast oxidative addition to palladium. Although high temperatures (~80 °C) are typically used for the Suzuki-Miyaura reaction, lower temperatures (50 °C) can be employed when using this 2-pyrone starting material. Full details of the procedure used for this reaction are given in the Experimental.

The activity of $[Pd_3(PPh_3)_4][BF_4]_2$ as a catalyst for this Suzuki-Miyaura coupling reaction was compared to that of $[Pd(PPh_3)_4]$, as this is the most commonly-used palladium catalyst for Suzuki-Miyaura reactions.[309] The bis-triflate precursor, $[Pd(OTf)_2(PPh_3)_2]$, which forms $[Pd_3(PPh_3)_4][OTf]_2$ on reduction with hydrogen, was also compared. The conversion of 4-bromo-6-methyl-pyran-2-one to 6-methyl-4-(4-methylphenyl)-pyran-2-one, after four hours of reaction time, was calculated by comparing the relevant proton peak integrals in ^{1}H NMR spectra of crude product mixtures. Long delay times of 15 s were used between NMR scans to ensure that most of the magnetisation had relaxed back to equilibrium. This enabled the extraction of accurate peak integrals. Methyl groups were desirable in the starting materials, as they act as useful NMR 'handles' that are easily identifiable in ^{1}H NMR spectra. All of the resulting ^{1}H NMR signals of the crude product mixtures, however, were well-resolved and easily characterised.

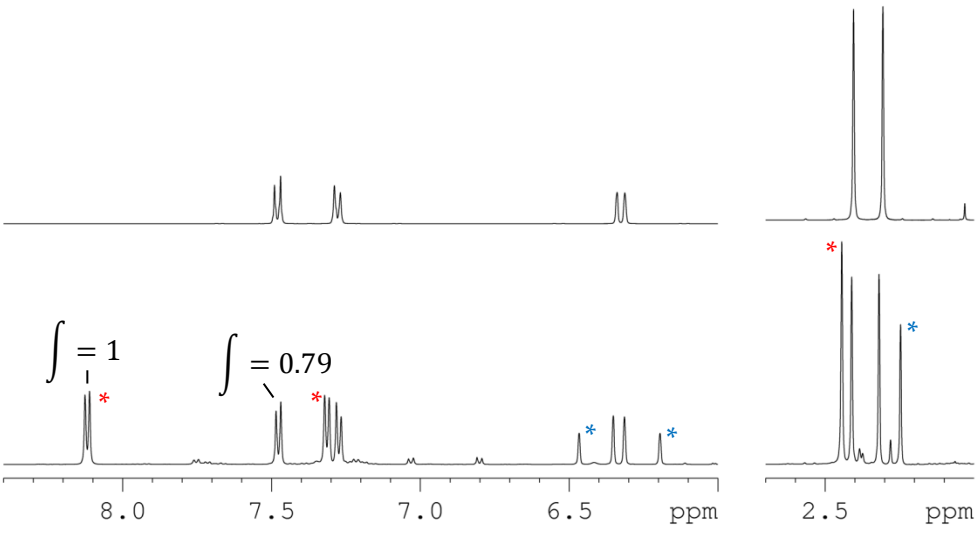

Figure 196: ^{1}H NMR spectra of (below) the crude product mixture on coupling 4-bromo-6-methyl-pyran-2-one (*) with 4-methylphenylboronic acid (*) to form 6-methyl-4-(4-methylphenyl)-pyran-2-one using $[Pd(PPh_3)_4]$ (1 mol%), and (above) isolated 6-methyl-4-(4-methylphenyl)-pyran-2-one.

An exemplar ^{1}H NMR spectrum of the crude product mixture obtained using [Pd(PPh$_3$)$_4$] (1 mol%) is shown in Figure 196, where it is compared with the ^{1}H NMR spectrum of pure 6-methyl-4-(4-methylphenyl)-pyran-2-one. The signals observed in the crude product mixture at δ 8.12 (d, J_{HH} = 7.5), 7.31 (d, J_{HH} = 7.5), and 2.45 (s), labelled * in Figure 196, correspond to the aromatic protons in the 2 and 3 positions, and the methyl protons of 4-methylphenylboronic acid, respectively. The singlets at δ 6.47, 6.19, and 2.25, labelled * in Figure 196, correspond to the aromatic protons in the, 3 and 5 positions, and the methyl protons of 4-bromo-6-methyl-pyran-2-one, respectively. In addition to the percentage conversion by ^{1}H NMR, the yield of the isolated product of 6-methyl-4-(4-methylphenyl)-pyran-2-one was calculated. 6-methyl-4-(4-methylphenyl)-pyran-2-one was isolated using the method described in the Experimental.

Table 28: Percentage conversion by NMR and percentage yield of isolated 6-methyl-4-(4-methylphenyl)-pyran-2-one, formed by coupling 4-bromo-6-methyl-pyran-2-one with 4-methylphenylboronic acid, using the palladium catalysts given.

Catalyst	Mol% of catalyst	Conversion by NMR (%)	Yield of isolated product (%)
[Pd(PPh$_3$)$_4$]	1	44	42
[Pd(OTf)$_2$(PPh$_3$)$_2$]	1	77	76
[Pd$_3$(PPh$_3$)$_4$][BF$_4$]$_2$	1	80	76
[Pd$_3$(PPh$_3$)$_4$][BF$_4$]$_2$	0.33	85	80

The percentage conversions and yields of isolated 6-methyl-4-(4-methylphenyl)-pyran-2-one, synthesised using different palladium catalysts, are given in Table 28. Surprisingly, the lowest conversion of just 44%, and yield of just 42% was obtained for the reaction in which the most commonly used catalyst, [Pd(PPh$_3$)$_4$], was employed. The palladium in [Pd(PPh$_3$)$_4$] is in the catalytically-active Pd(0) oxidation state, therefore it is often considered to be an ideal catalyst for carbon-couplings, as it does not require reducing and ought to exhibit a short inductive period. [Pd(PPh$_3$)$_4$] is reported to be present in solution as predominantly [Pd(PPh$_3$)$_3$], which exchanges rapidly with free phosphine at ambient temperatures.[310] Assuming homogeneous catalysis, the active catalyst formed from [Pd(PPh$_3$)$_3$] is reported to be [Pd(PPh$_3$)$_2$], which is in fast equilibrium with [Pd(PPh$_3$)$_3$],[311] and can oxidatively add an aryl halide. More recent reports have

indicated that just one equivalent of phosphine ligand per palladium atom ([Pd(PPh_3)]) gives rise to even higher activities.[312] The low conversion obtained when using [Pd(PPh_3)$_4$] suggests that, under the conditions used, few active palladium species are present in solution. During this Suzuki reaction, the colour of the solution remained yellow/orange, and there was no observable evidence of palladium deposition. Presumably, the surplus of triphenylphosphine (four for every palladium atom), stabilised the monomeric palladium species and prevented their decomposition to colloidal species.

Figure 197: Dark brown, translucent THF layer, which forms after the Suzuki-Miyaura coupling of 4-bromo-6-methyl-pyran-2-one with 4-methylphenylboronic acid to form 6-methyl-4-(4-methylphenyl)-pyran-2-one, using the [$Pd_3(PPh_3)_4$][BF_4]$_2$ catalyst.

Interestingly, the highest conversion of 85% and yield of 80% were obtained using [$Pd_3(PPh_3)_4$][BF_4]$_2$ (0.33 mol%, which is equal to 1 mol% palladium). The THF reaction solution was observed to change colour from a bright red, transparent solution, to the dark brown translucent solution shown in Figure 197, and palladium black was observed to coat the glass vessel. The ^{1}H NMR spectra that were subsequently acquired did not contain any of the proton signals corresponding to [$Pd_3(PPh_3)_4$][BF_4]$_2$. Furthermore, reducing the amount of catalyst used from 1 mol% to 0.33 mol% was not detrimental to the percentage conversion. On the contrary, the conversion increased from 80% to 85%. This confirms that the active catalytic species is not [$Pd_3(PPh_3)_4$][BF_4]$_2$, as reducing the amount of catalyst by a third would have resulted in a significant drop in catalytic activity. Such inverse correlations between catalyst concentration and conversion to product often suggest a heterogeneous reaction, whereby more dilute solutions prevent palladium aggregation to inactive palladium black, and therefore exhibit a higher activity.[8,9] A higher activity can, however, also be attributed to the leaching of palladium monomers from smaller nanoparticles that act as a monomer reservoir (see Figure 198). The high conversions achieved using [$Pd_3(PPh_3)_4$][BF_4]$_2$ confirm that, even under the mild

conditions used here, the tri-palladium complex decomposes to form active catalytic species.

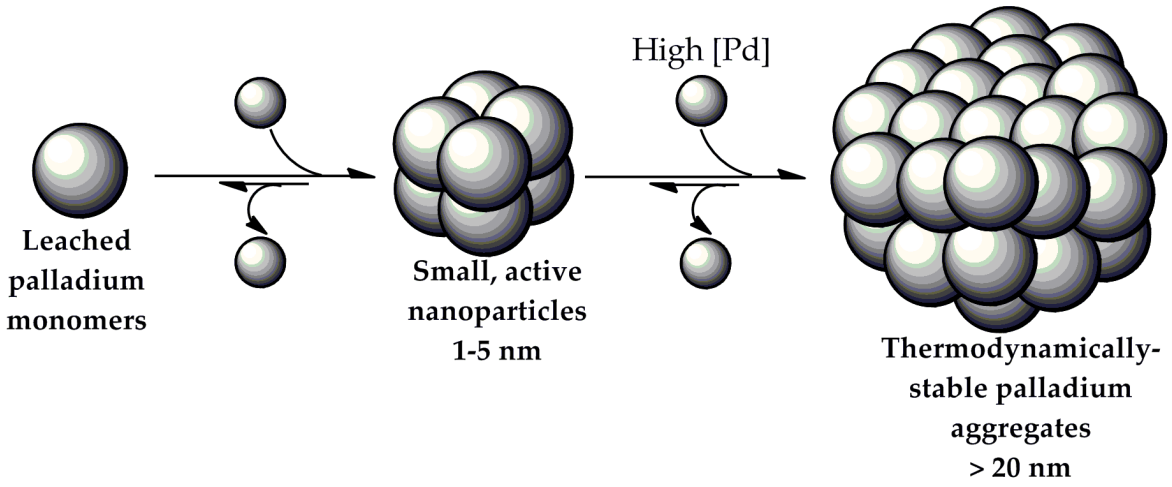

Figure 198: The formation of large, catalytically-inactive palladium aggregates, which is promoted at higher palladium concentrations.

A similarly high percentage conversion of 77%, with a yield of 76%, was obtained using $[Pd(OTf)_2(PPh_3)_2]$. This is a surprising result as this complex exhibited very low activity in the hydrogenation of phenylacetylene, and consequently a rate of hydrogen consumption could not be calculated. As with the $[Pd_3(PPh_3)_4][BF_4]_2$ catalyst, the THF layer was observed to change colour during the Suzuki reaction, from an orange/yellow transparent solution, to a dark brown translucent solution, and palladium black was observed to form. This bis-triflate palladium species is the precursor to $[Pd_3(PPh_3)_4][OTf]_2$, which forms on its reduction with hydrogen. It is possible that during the Suzuki reaction, the reduction of $[Pd(OTf)_2(PPh_3)_2]$ to palladium black also occurs *via* the formation of $[Pd_3(PPh_3)_4][OTf]_2$, which accounts for the similarly high conversions. The slightly lower conversion obtained for the bis-triflate palladium catalyst may be due to a longer induction period needed to form active colloidal species *via* the $[Pd_3(PPh_3)_4][OTf]_2$ tri-palladium species.

6.3.2 Heck Coupling

The second carbon-coupling reaction studied is shown in Figure 199 and is a Heck coupling of *n*-butyl acrylate with 4-bromoanisole to form butyl (2*E*)-3-(4-methoxyphenyl)acrylate. The *trans*-isomer forms selectively due to an internal rotation of the intermediate alkylpalladium species prior to elimination; the β hydrogen of the

alkylpalladium species must be positioned *syn* to the palladium for hydride elimination to occur, and this produces the *trans*-isomer.[313] This Heck reaction is known and the conditions used, detailed in the Experimental, are typical for such couplings.[314] The high temperatures (130 °C) are required to solubilise the potassium carbonate in the DMF solvent.

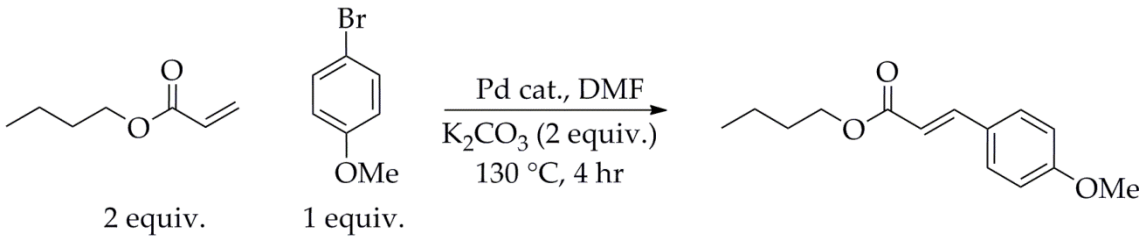

Figure 199: Heck cross-coupling of butyl acrylate with 4-bromoanisole to form butyl (2E)-3-(4-methoxyphenyl)acrylate, using the reaction conditions shown.

As before, the activity of $[Pd_3(PPh_3)_4][BF_4]_2$ as a catalyst for this Heck coupling was compared to that of $[Pd(PPh_3)_4]$, which is commonly-used for such couplings,[313] as well as the bis-triflate complex $[Pd(OTf)_2(PPh_3)_2]$. Again, the percentage conversion of 4-bromoanisole to butyl (2*E*)-3-(4-methoxyphenyl)acrylate, after four hours of reaction time, was calculated by comparing the relevant proton peak integrals in ^{1}H NMR spectra of crude product mixtures. The methoxy aryl bromide derivative was used because, again, methyl groups were desirable in the starting materials, as they are useful NMR 'handles', however all of the resulting ^{1}H NMR signals of the crude product mixtures were well-resolved and easily characterised.

The ^{1}H NMR spectrum of the crude product mixture obtained after four hours, using $[Pd(PPh_3)_4]$ (1 mol%), is compared with that of pure butyl (2*E*)-3-(4-methoxyphenyl)acrylate in Figure 200. The signals observed in the crude product mixture at δ 7.40 (*p*-d, J_{HH} = 8.9), 6.81 (*p*-d, J_{HH} = 8.9), and 3.81 (s), labelled * in Figure 200, correspond to the aromatic protons at the 3 and 2 positions, and the methyl protons of 4-bromoanisole, respectively. Although the reaction clearly did not go to completion, ^{1}H NMR signals corresponding to butyl acrylate cannot be observed in the crude product mixture. This is because most of this species is lost due to evaporation in the reaction work-up. When appropriate, the isolated yield of butyl (2*E*)-3-(4-methoxyphenyl)acrylate

was also calculated, in addition to the percentage conversion. Butyl (2*E*)-3-(4-methoxyphenyl)acrylate was isolated using the method described in the Experimental.

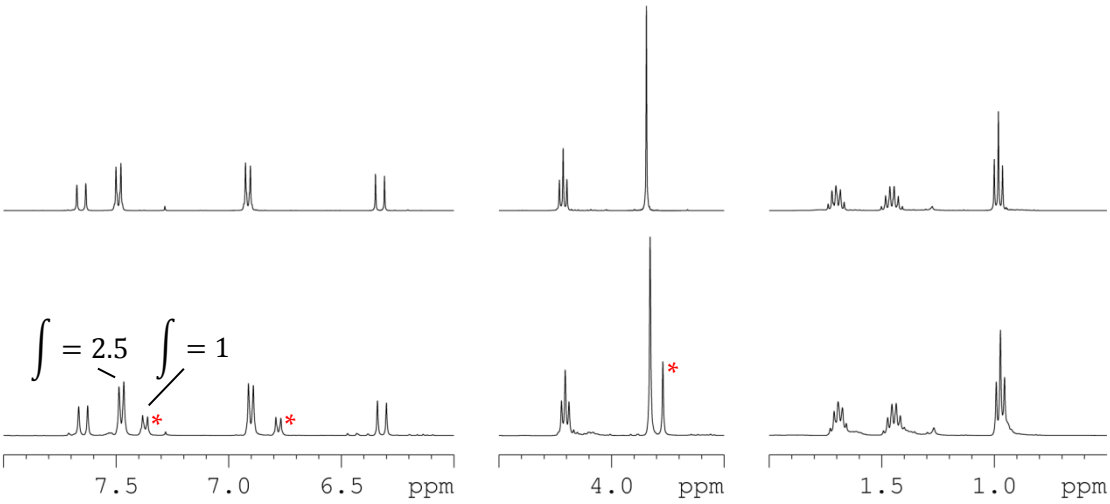

Figure 200: ^{1}H NMR spectra of (below) the crude product mixture on coupling butyl acrylate with 4-bromoanisole (*) to form butyl (2E)-3-(4-methoxyphenyl)acrylate, using [Pd(PPh$_3$)$_4$] (1 mol%), and (above) isolated butyl (2E)-3-(4-methoxyphenyl)acrylate.

Table 29: Percentage conversion by NMR and percentage yield of isolated butyl (2E)-3-(4-methoxyphenyl)acrylate, formed by coupling butyl acrylate with 4-bromoanisole, using the palladium catalysts given.

Catalyst	Mol% of catalyst	Conversion by NMR (%)	Yield of isolated product (%)
[Pd(PPh$_3$)$_4$]	1	71	55
[Pd(OTf)$_2$(PPh$_3$)$_2$]	1	17	-
[Pd$_3$(PPh$_3$)$_4$][BF$_4$]$_2$	0.33	8	-

The percentage conversions and yields of butyl (2*E*)-3-(4-methoxyphenyl)acrylate, synthesised using the different palladium catalysts, are compared in Table 29. Interestingly, the highest percentage conversion of 71% was obtained when using [Pd(PPh$_3$)$_4$], and the lowest of just 8% was obtained when using [Pd$_3$(PPh$_3$)$_4$][BF$_4$]$_2$. This is the opposite trend to that observed when comparing the same catalysts in the Suzuki-Miyaura coupling reaction. In every Heck reaction, the solution was observed to change colour to a translucent dark brown and palladium black was observed to deposit on the glassware. This colour change was most rapid for the solutions that contained [Pd$_3$(PPh$_3$)$_4$][BF$_4$]$_2$ and [Pd(OTf)$_2$(PPh$_3$)$_2$], where the solution turned dark brown/black

immediately on addition of the palladium catalyst. This is in contrast with the Suzuki-Miyaura, where all colour changes were more gradual.

It is possible that the facile conversion of $[Pd_3(PPh_3)_4][BF_4]_2$ molecules to nanoparticles is actually detrimental under these harsh reaction conditions, and the nanoparticles quickly aggregate to form inactive palladium black. The DMF solvent used is reported to promote palladium nanoparticle formation by coating nanoparticles, however, this typically leads to the formation of small, catalytically-active nanoparticles.[53] Nevertheless, the high temperatures used (130 °C), may have led to fast nanoparticle formation and aggregation when using $[Pd_3(PPh_3)_4][BF_4]_2$ and $[Pd(OTf)_2(PPh_3)_2]$.

At the high temperature used for the Heck reaction, deposition of palladium black was observed from the $[Pd(PPh_3)_4]$ catalyst, and a high percentage conversion to product was obtained. Formation of palladium black leads to an excess of free phosphine in solution which ought to disfavour the formation of the reported homogeneous active catalysts.[311,312] At the low temperature used for the Suzuki-Miyaura reaction, no palladium black was deposited, yet the percentage conversion to product was low. Although this is suggestive of a heterogeneous pathway, a homogeneous pathway cannot be ruled out, as the lower temperatures used for the Suzuki coupling may inhibit dissociation of the phosphine from the palladium and thus inhibit formation of $[Pd(PPh_3)_2]$ or $[Pd(PPh_3)]$.

6.4 Conclusions

The research presented herein has confirmed that the tri-palladium complex, $[Pd_3(PPh_3)_4][BF_4]_2$, is a reactive palladium species and a useful pre-catalyst for low-temperature hydrogenations and cross-couplings. Due to the strong MMLCT bands observed in corresponding UV-*vis* absorption spectra, $[Pd_3(PPh_3)_4][BF_4]_2$ was tested for photoactivity. Its reaction with triphenylphosphine in dichloromethane to form $[Pd(PPh_3)_4]$ and $[Pd(Cl)(PPh_3)_3]BF_4$ is dramatically faster on exposure to broadband UV light. Furthermore, prolonged UV irradiation of dichloromethane solutions of $[Pd_3(PPh_3)_4][BF_4]_2$, at low temperatures and in the absence of water and oxygen, results in the quantitative formation of a photoisomer. This photoisomer slowly converts back to the thermal isomer at room temperature.

Investigations into the catalytic activity of both the thermal and photoisomers of $[Pd_3(PPh_3)_4][BF_4]_2$, in the hydrogenation of phenylacetylene, confirmed their suitability as pre-catalysts. Both isomers exhibited identical *pseudo*-rate constants of hydrogen consumption, as well as reaction orders with respect to hydrogen concentration, suggesting that they both degrade to form the same active catalytic species. Furthermore, their *pseudo*-rate constants of hydrogen consumption increased over time, which confirmed a long inductive period during which more catalytically-active species were produced. Once activated, the rates of hydrogen consumption using $[Pd_3(PPh_3)_4][BF_4]_2$ rivalled those obtained using Crabtree's catalyst, which was observed to quickly deactivate. Interestingly, the samples that exhibited better catalytic activity also exhibited n_t values equal to approximately 1.5, thus the more active catalytic species are able to bind multiple molecules of hydrogen. The least active samples, however, exhibit n_t values equal to < 1. Addition of excess triphenylphosphine dramatically altered the activity of $[Pd_3(PPh_3)_4][BF_4]_2$, which quickly deactivated before reaction completion. Hydrogenation using $[Pd_3(PPh_3)_4][BF_4]_2$ is therefore likely to be heterogeneous in nature.

$[Pd_3(PPh_3)_4][BF_4]_2$ was found to be an active pre-catalyst in low-temperature (50 °C) Suzuki carbon-coupling. Here, the facile conversion of $[Pd_3(PPh_3)_4][BF_4]_2$ to nanoparticles was advantageous, and high conversions to product (85%) were obtained with low catalyst loadings (0.33%) after just four hours of reaction time. Furthermore, $[Pd_3(PPh_3)_4][BF_4]_2$ was found to be more active than commonly-used $[Pd(PPh_3)_4]$, at this low temperature. Conversely, $[Pd_3(PPh_3)_4][BF_4]_2$ was found to be an inactive pre-catalyst for high-temperature (130 °C) Heck carbon-coupling, where inactive palladium black was quickly produced, leading to low conversion to product after four hours (8%). In this case, $[Pd(PPh_3)_4]$ was found to be the most active pre-catalyst.

The $[Pd_3(PPh_3)_4][BF_4]_2$ complex therefore promises to be a useful pre-catalyst for low-temperature Suzuki reactions, which are widely-used in the total synthesis of natural products.[315] Here, the ability to carbon-couple at low temperatures is important as sensitive reagents are often used. $[Pd_3(PPh_3)_4][BF_4]_2$ also has the potential to be a useful pre-catalyst for other low-temperature cross-coupling reactions, however this requires further study.

7 Significance of Work and Future Study

The two main aims, set out in the Introduction chapter of this thesis, were:

- To explore the palladium cluster phase that lies between homogeneous palladium monomers and heterogeneous palladium nanoparticles, using advanced NMR techniques including PHIP.
- To develop the relatively new SABRE technique for use with functionalised diazines such as pyridazine and phthalazine, with a view to generating a new class of contrast agents for use in MRI.

As such, this discussion of conclusions and future work is divided into two sections.

7.1 Palladium Cluster Formation

7.1.1 Suitable Palladium Complexes

In order to investigate palladium clusters that form, en-route to nanoparticles, suitable reactive palladium monomers were required. Monomers with the general formula $[Pd(OTf)_2(XR_3)_2]$, where X is arsenic or phosphorus and R is an alkyl or aryl group, were successfully synthesised following the procedures discussed in Chapter 4 and given in the Experimental. Similar bis-triflate species are reported to be useful hydrogenation pre-catalysts and have been used alongside *para*-H_2 to investigate low-concentration palladium intermediates that form during the hydrogenation of alkynes.[115-117,226]

The suitability of the $[Pd(OTf)_2(XR_3)_2]$ monomers was verified by replicating hydrogenation conditions through the dissolution of the complex into dichloromethane and the addition of hydrogen gas. In all cases, with the exception of $XR_3 = P(Ph(p\text{-}CF_3))_3$, the solutions darkened and palladium colloid formation was observed in the form of a palladium black precipitate. The formation of palladium nanoparticles from the bis-triflate complexes stabilised by triphenylphosphine and triphenylarsine was also confirmed by TEM images.

7.1.2 Use of PHIP to Detect Reaction Intermediates

The potential of PHIP to identify palladium clusters that form upon the *para*-hydrogenation of alkynes was tested using the $[Pd(OTf)_2(PPh_3)_2]$ hydrogenation pre-catalyst. Phenylacetylene and diphenylacetylene were *para*-hydrogenated and short-lived palladium intermediates were detected through the observation of their PHIP-enhanced ^1H NMR signals.

No intermediates were detected during the *para*-hydrogenation of phenylacetylene although the *para*-hydrogenation of diphenylacetylene did produce PHIP-enhanced NMR signals that corresponded to the palladium intermediate complexes given in Figure 201. Their characterisation is described in detail in Chapter 4. Palladium alkyl species, like **1** and **2**, are commonly detected during the *para*-hydrogenation of alkynes using palladium bis-triflate pre-catalysts.[115,116] Intermediate **3** is a di-palladium complex, and its identification suggests that it may be possible to detect higher-order palladium species using PHIP. It was not possible, however, to fully characterise intermediate **3** with the limited information gathered from its PHIP-enhanced hydride NMR signals. The limited information gathered using this method led to the use of a different approach, whereby hydrogen was added to the $[Pd(OTf)_2(XR_3)_2]$ complexes without the presence of substrate.

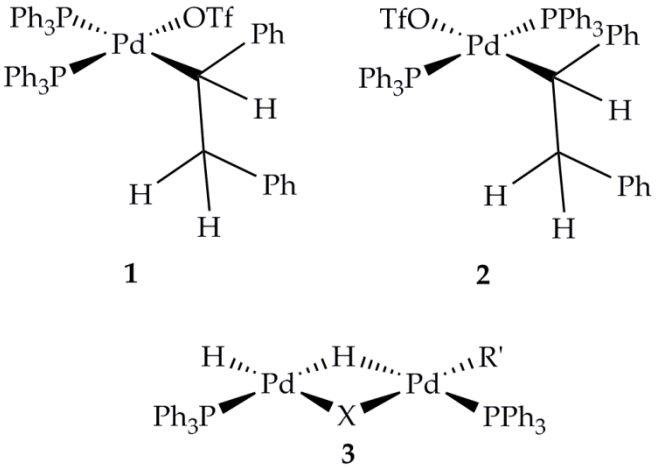

Figure 201: Two isomers of $[Pd(OTf)(bibenzyl)(PPh_3)_2]$ (1 and 2) and a di-palladium species (3, where X = chloride and R′ = chloride or triflate) detected from PHIP-enhanced ^1H NMR signals observed on para-hydrogenation of diphenylacetylene using a $[Pd(OTf)(PPh_3)_2]$ pre-catalyst.

7.1.3 Detection of Palladium Clusters

Addition of hydrogen to d_2-dichloromethane solutions of the palladium bis-triflate complexes led to the formation of several novel palladium monohydride species. These are shown in Figure 202, and include species with bound dichloromethane, which activates to form palladium chloride intermediates. Their NMR and LIFDI-MS characterisation is described in detail in Chapter 5. EXSY measurements confirmed that these monohydride species exist in equilibrium with one another, however their abundance decreases with time, thus they appear to be kinetic rather than thermodynamic products.

Over time, NMR signals that corresponded to the linear tri-palladium clusters shown in Figure 202 were observed to grow in intensity and they reflect the thermodynamic product. These species have been characterised by NMR, LIFDI-MS, and single-crystal XRD and detailed characterisation is discussed in Chapter 5. They are unusual species as the palladium atoms are stabilised by η^2-coordination from the phenyl rings of the phosphine or arsine ligands, which results in a loss of ring aromaticity. Such η^2-coordination of phenyl rings directly bound to phosphorus and arsenic is rare and has only been observed in these tri-palladium species, although η^1-coordination from the *ipso*-carbon atoms of triphenylphosphine has been reported in a di-palladium complex.[267] The triphenylphosphine-stabilised tri-palladium complex is a known species, and was first reported by Kannan *et. al.* in 1998 and synthesised by adding ethanol to a dichloromethane solution of $[Pd(\mu\text{-}OH)(PPh_3)_2]_2$.[266] It was not previously identified as a precursor to nanoparticle formation. All of the other tri-palladium complexes reported here are novel. The overall charge of the tri-palladium species is +2, therefore the palladium(II) monomers have been reduced so that each palladium atom now has an average oxidation state of +2/3. This reduction of palladium suggests that the tri-palladium complexes are likely to be stable intermediates that form en-route to palladium nanoparticles, as shown in Figure 202.

Palladium clusters that form en-route to palladium nanoparticles have therefore been successfully identified and characterised. Interestingly, reducing $[Pd(OTf)_2(XR_3)_2]$ complexes with hydrogen is a general method to successfully produce tri-palladium complexes, with the constraint that at least one R group is a phenyl ring. Functionalising

the phenyl ring at the *para* position with the electron-withdrawing trifluoromethyl group and the electron-donating methoxy group prevented tri-palladium cluster formation. An extension of this study to other functional groups of varying electronic and steric properties, in addition to functionalisation at the *ortho* and *meta* positions of phenyl rings, would enable a better understanding of the parameters required for efficient cluster formation. Efforts were made to extend the palladium clusters to penta-palladium complexes through the use of phosphines with longer R groups (PhPh and $PhCH_2Ph$) that have the potential to stabilise five palladium atoms *via* η^2-coordinations. Unfortunately, no penta-palladium complexes were detected, presumably due to unfavourable steric interactions caused by the bulkier R groups, which prevent the palladium atoms from coming into close contact. Nevertheless, this study could be extended to include R groups with longer vinylic chains, in a similar manner to those reported by the Murahashi group discussed in Chapter 5.[275,276,278-280] Although such unsaturated ligands have the potential to hydrogenate under the reducing conditions used, styrene and stilbene did not hydrogenate under the same conditions in Chapter 4, therefore hydrogenation is unlikely to be an issue.

The tri-palladium clusters that have been identified cannot form when the R groups used are alkylic. This means that the formation of nanoparticles from palladium monomers that are stabilised with alkylated phosphines or arsines must occur *via* a different mechanism, with different intermediate cluster species. Furthermore, the formation of tri-palladium clusters from palladium monomers stabilised by bidentate phosphines or arsines is unlikely due to the increased stability of the monomer. Bidentate phosphines, such as 1,1'-bis(diphenylphosphino)ferrocene (dppf) are commonly used industrially to stabilise palladium monomers during homogeneous catalysis.[316] The formation of nanoparticles from both alkylated and bidentate phosphines and arsines could be investigated using the methods described in Chapters 4 and 5 as a future study.

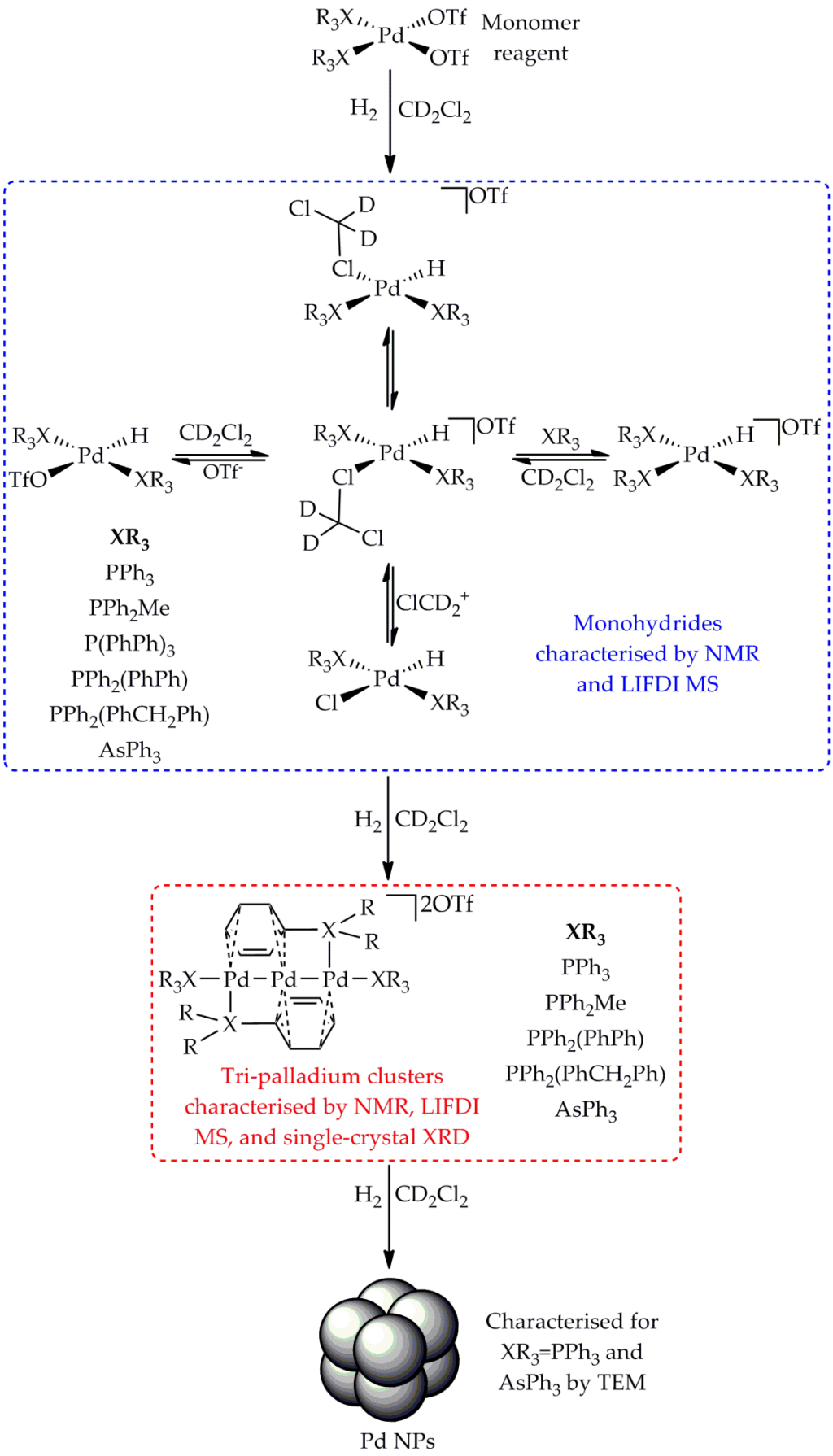

Figure 202: Schematic to show the formation of palladium monohydride species, tri-palladium species, and palladium nanoparticles on addition of hydrogen to [Pd(OTf)$_2$(XR$_3$)$_2$].

7.1.4 Reactivity of Palladium Clusters

As the tri-palladium species form with commonly-used phosphines and arsines, it is possible that they form in a range of palladium-catalysed reactions and are active catalysts in their own right, or conduits for the active catalysts. The reactivity of the $[Pd_3(PPh_3)_4][BF_4]_2$ complex is discussed in detail in Chapter 6.

The tri-palladium complexes form brightly-coloured solutions due to CT electronic transitions which give rise to large molar absorption coefficients in the visible spectral region. Irradiation of the $[Pd_3(PPh_3)_4][BF_4]_2$ complex with broadband UV light resulted in photoisomerisation to the photoisomer shown in Figure 203, which was characterised by NMR, LIFDI-MS, and single-crystal XRD, all of which is discussed in Chapter 6.

Both the thermal and photoisomers were tested for their reactivity in the *para*-hydrogenation of phenylacetylene to styrene, and were compared to Crabtree's catalyst which is known to be an active homogeneous hydrogenation catalyst.[297] The *pseudo*-hydrogenation rate constants of hydrogen depletion were calculated using OPSY, and the reaction orders, with respect to hydrogen, were calculated from this data, as described in Chapter 6 and Appendix B. Although Crabtree's catalyst initially gave the fastest *pseudo*-hydrogenation rate constant, it deactivated over time whereas both the thermal and photoisomers of $[Pd_3(PPh_3)_4][BF_4]_2$ became more active with time, with *pseudo*-rate constants that rivalled Crabtree's catalyst. Both isomers exhibited identical *pseudo*-rate constants and similar reaction orders with respect to hydrogen, which increased over time thus supporting catalyst activation. Furthermore, $[Pd_3(PPh_3)_4][BF_4]_2$ deactivated on addition of excess triphenylphosphine, therefore the reaction is unlikely to be homogeneous. The evidence suggests that the tri-palladium species are conduits for the active catalytic species, which are likely to be heterogeneous in nature and may be colloidal palladium, or 'naked' palladium atoms, shown in Figure 203.

The thermal isomer of $[Pd_3(PPh_3)_4][BF_4]_2$ was also tested for its reactivity in the Suzuki-Miyaura and Heck cross-coupling reactions, discussed in Chapter 6, and was compared to $[Pd(PPh_3)_4]$, which is typically used for such reactions, and the bis-triflate precursor, $[Pd(OTf)_2(PPh_3)_2]$. Interestingly, opposite trends were observed for the two reactions, which is likely due to the different reaction conditions used.

The Suzuki-Miyaura reaction was carried out at 50 °C for four hours using a biphasic solvent mixture of THF and basic water. Under these mild conditions, the $[Pd(PPh_3)_4]$ catalyst performed poorly, with a conversion of just 44%, whereas the $[Pd(OTf)_2(PPh_3)_2]$ and $[Pd_3(PPh_3)_4][BF_4]_2$ pre-catalysts performed well, with conversions of 77% and 80% respectively. The reaction solutions gradually darkened when using $[Pd(OTf)_2(PPh_3)_2]$ and $[Pd_3(PPh_3)_4][BF_4]_2$ and palladium black was observed to form as a precipitate. Furthermore, on reducing the amount of $[Pd_3(PPh_3)_4][BF_4]_2$ pre-catalyst used by a third, the conversion increased to 85%, suggesting a role for the heterogeneous catalysis shown in Figure 203.

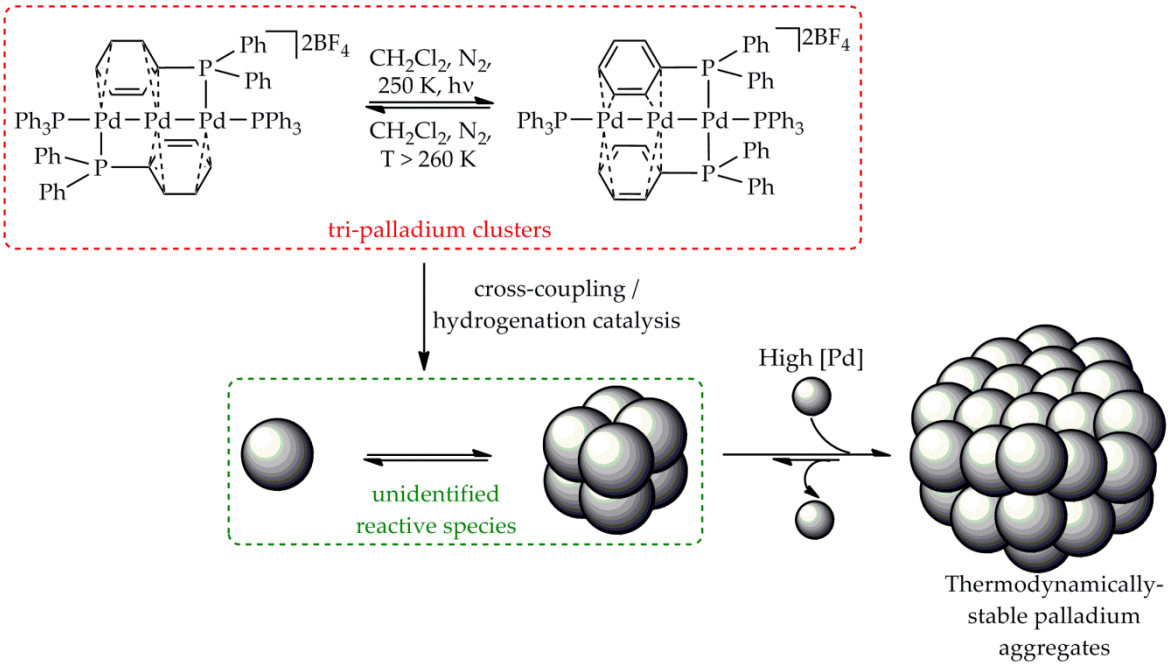

Figure 203: Schematic to show the formation of unidentified reactive species during cross-coupling and hydrogenation reactions using the $[Pd_3(PPh_3)_4][BF_4]_2$ pre-catalyst.

The Heck reaction was carried out at 130 °C for four hours, using a basic DMF solvent. Under these harsh conditions, the $[Pd(PPh_3)_4]$ catalyst improved significantly and gave a conversion of 71%. The $[Pd(OTf)_2(PPh_3)_2]$ and $[Pd_3(PPh_3)_4][BF_4]_2$ pre-catalysts, on the other hand, deteriorated significantly and gave conversions of just 17% and 8%, respectively. The rapid darkening of the reaction solutions containing $[Pd(OTf)_2(PPh_3)_2]$ and $[Pd_3(PPh_3)_4][BF_4]_2$ suggested that, under these harsh reaction conditions, the facile conversion to nanoparticles is detrimental, and the nanoparticles quickly aggregate to form inactive palladium black.

The improved performance of $[Pd_3(PPh_3)_4][BF_4]_2$ under the mild conditions used in the Suzuki-Miyaura cross-coupling reaction suggests that this pre-catalyst could be useful for other low-temperature cross-coupling reactions, which are widely-used in the total synthesis of natural products.[315] The ability to carbon-couple at low temperatures enables the use of sensitive reagents. Suzuki-Miyaura cross-couplings of similar 2-pyrones with arylboronic acids have been reported to function at room temperature[317] using the conditions outlined by the Buchwald group, which require either of the phosphine ligands shown in Figure 204, used alongside $Pd(OAc)_2$ and KF in THF.[318] This reactivity study could therefore be extended by testing the activity of the $[Pd_3(PPh_3)_4][BF_4]_2$ pre-catalyst at lower temperatures for the same Suzuki-Miyaura cross-coupling with a range of bases, including KF. In addition to catalysing the reductive elimination step, anionic bases, like F^- and OH^-, have been reported to increase the rate of transmetallation during Suzuki-Miyaura cross-couplings as they act as ligands and form reactive palladium intermediates.[319] The identity of the cation is also important; cations that form insoluble halide salts, like Ag^+, accelerate the reaction due to the quenching of the halide, whereas more soluble cations, like K^+, decelerate the reaction by hindering transmetallation.[320] If room temperature Suzuki-Miyaura carbon-coupling is achieved, then sensitive reagents could also be tested.

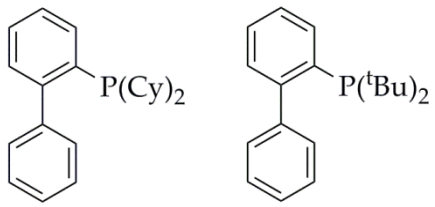

Figure 204: ortho-(di-cyclohexylphosphino)biphenyl (left) and ortho-(di-tert-butylphosphino)biphenyl (right).

Another interesting expansion to the research on Suzuki-Miyaura coupling is to research the regioselectivity of the $[Pd_3(PPh_3)_4][BF_4]_2$ catalyst, when coupling an aryl dihalide to an arylboronic acid, and compare it to that of $[Pd(PPh_3)_4]$ and $[Pd(OTf)_2(PPh_3)_2]$. A recent report by Sicre *et. al.* has shown that 2,4-dibromopyridine (shown in Figure 205) undergoes regioselective Suzuki-Miyaura carbon-coupling, to several different arylboronic acids, at the 2-position when using $[Pd(PPh_3)_4]$ with aqueous

TlOH in THF or $Pd_2(dba)_3/PCy_3$ with K_3PO_4 in dioxane.[321] The proposed mechanism is homogeneous, and the regioselectivity may differ when using heterogeneous catalysts.

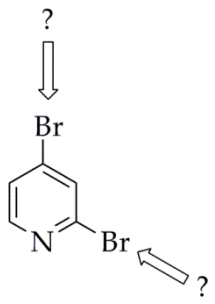

Figure 205: Dibromopyridine used to investigate regioselectivity.

A comparison of the reactivity of $[Pd_3(PPh_3)_4][BF_4]_2$ with the other tri-palladium complexes identified and characterised in Chapter 5 in order to assess the influence of the stabilising ligand on reactivity would also be interesting. Unfortunately, synthesis and isolation of useable quantities of these complexes has not yet been achieved; the synthetic procedure reported by Kannan *et. al.*[266] to form the triphenylphosphine-stabilised tri-palladium complex is not successful when using the other stabilising ligands.

7.1.5 Summary

Novel tri-palladium clusters that form from palladium monomers, en-route to palladium nanoparticles have been successfully identified and characterised. Their formation requires the presence of stabilising ligands that can η^2-coordinate to palladium. Commonly-used ligands, like triphenylphosphine are suitable, suggesting that these species may form in a range of different palladium-catalysed reactions. The tri-palladium clusters have proven to be photoactive and useful pre-catalysts for hydrogenation and Suzuki-Miyaura cross-coupling reactions. The clusters appear to be a conduit for the active catalytic species, which are likely to be heterogeneous in nature and may be colloidal palladium, or 'naked' palladium atoms.

7.2 SABRE with Pyridazine and Phthalazine

7.2.1 Formation of a SABRE-active Catalyst

The SABRE-active catalysts $[Ir(H)_2(IMes)(sub)_3]Cl$, where sub is pyridazine or phthalazine, were synthesised *via* the route shown in Figure 206, and their properties are discussed in detail in Chapter 2. Addition of an excess of pyridazine or phthalazine to [IrCl(COD)(IMes)] resulted in the displacement of the chloride by the *N*-heterocycle to form [Ir(COD)(IMes)(sub)]Cl. Oxidative addition of hydrogen to these species proceeds selectively over the C-Ir-sub axis, forming solely the isomer of $[Ir(H)_2(COD)(IMes)(sub)]Cl$ shown in Figure 206. This complex is only stable at temperatures below 250 K; the bound COD is hydrogenated to COA above this temperature, and is no longer able to ligate. The two free binding sites that result are then occupied by two molecules of substrate, forming $[Ir(H)_2(IMes)(sub)_3]Cl$.

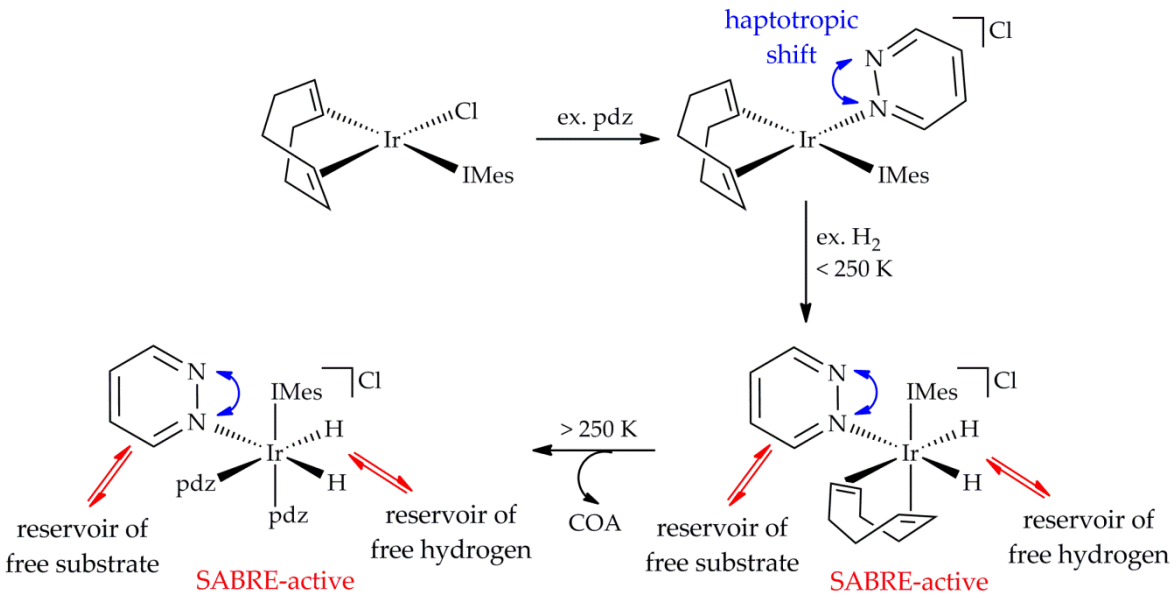

Figure 206: Schematic showing the synthetic pathway used to form the SABRE-active $[Ir(H)_2(IMes)(sub)_3]Cl$ catalysts. Pyridazine is shown as the example substrate, but the same also occurs when using phthalazine. Both N-heterocycles can undergo haptotropic shifts shown in blue, as well as exchange with free N-heterocycles.

The bound *N*-heterocycles undergo a haptotropic shift on the NMR timescale and this type of behaviour had not previously been reported in iridium complexes. This interconversion was monitored for the temperature-stable [Ir(COD)(IMes)(sub)]Cl and

$[Ir(H)_2(IMes)(sub)_3]Cl$ complexes using EXSY. Both *N*-heterocycles exhibited similar Gibb's free energies of activation for this interchange, implying a common process.

Competition studies confirmed that phthalazine binds preferentially to all of the iridium complexes and forms more stable complexes due to its greater basicity.[192] The rate of *para*-H_2 addition to the [Ir(COD)(IMes)(sub)]Cl complexes was analysed by comparing the magnitude of the resulting PHIP-enhanced hydride NMR signals. Addition to [Ir(COD)(IMes)(pdz)]Cl is faster than to [Ir(COD)(IMes)(phth)]Cl, and the rate of hydrogen addition to binding sites that lie *trans* to pyridazine is faster than to binding sites that lie *trans* to phthalazine. This emulates the greater basicity of phthalazine.

Both the $[Ir(H)_2(COD)(IMes)(sub)]Cl$ and $[Ir(H)_2(IMes)(sub)_3]Cl$ complexes undergo exchange with hydrogen and substrate on the NMR timescale. These complexes are therefore SABRE-active, and replacing normal H_2 with *para*-H_2 leads to SABRE-enhanced ^1H NMR signals corresponding to both the bound and free *N*-heterocycles. As the $[Ir(H)_2(COD)(IMes)(sub)]Cl$ complexes are not stable above temperatures of 250 K, they are unlikely to be suitable for MRI applications. Exchange in these complexes was therefore not investigated however this study could be extended to probe low temperature exchange within these complexes.

The mechanism of hydrogen and substrate exchange in the temperature-stable $[Ir(H)_2(IMes)(sub)_3]Cl$ complexes was investigated by fitting kinetic data obtained using EXSY to the model discussed in Chapter 2 and Appendix A. Substrate shifting and dissociation, in these complexes, were found to be independent of the concentration of hydrogen and free substrate in solution. As with the haptotropic shift, dissociation of both substrates proceeded with similar Gibb's free energies of activation. Hydrogen dissociation however, was found to be directly proportional to the concentration of hydrogen, and inversely proportional to the concentration of free substrate. This suggests that hydrogen dissociation proceeds after perturbation of the Ir-N bond (either by substrate dissociation or by a haptotropic shift), and the subsequent addition of a second hydrogen molecule to form the short-lived $[Ir(H)_2(\eta^2\text{-}H_2)(IMes)(sub)_2]Cl$ complexes, shown as **C** in Figure 207, where sub is pyridazine. This hydrogen exchange mechanism has been reported for the analogous pyridine complex, $[Ir(H)_2(IMes)(py)_3]Cl$, and was supported by DFT calculations.[149]

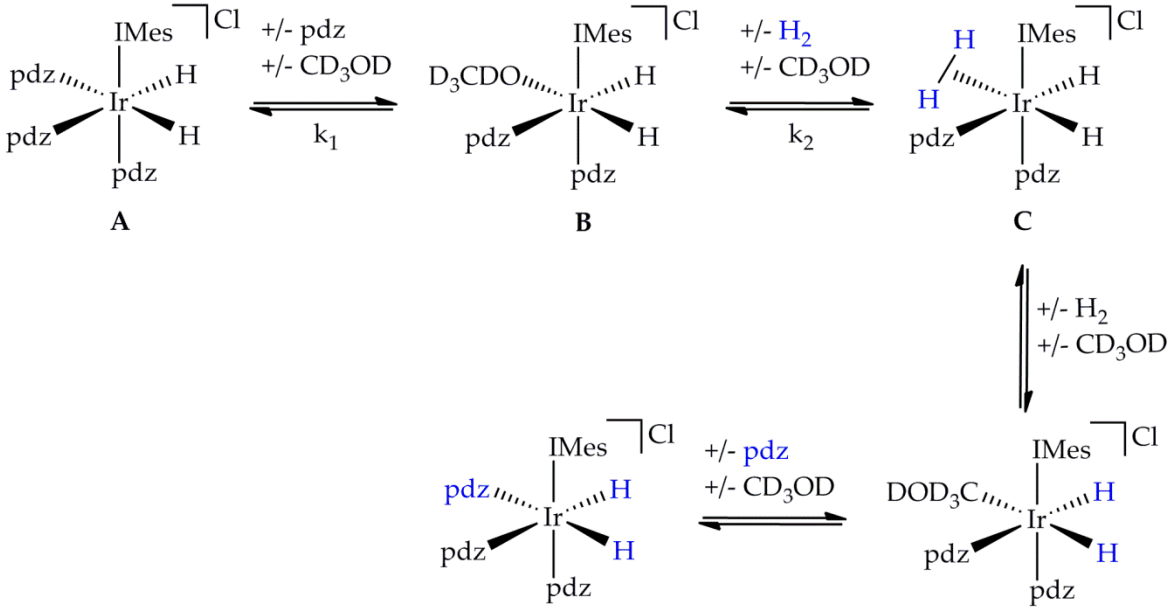

Figure 207: The substrate and hydrogen exchange mechanism in $[Ir(H)_2(IMes)(pdz)_3]Cl$. The same mechanism also occurs when using phthalazine in place of pyridazine.

Complexes **B** and **C** have not been observed by NMR spectroscopy and are likely to be short-lived. The observation of SABRE-enhancements confirms that intermediate **C** is short-lived; the T_1 values of η^2-coordinated H_2 molecules are typically just tens of milliseconds.[151,152] Such fast relaxation of η^2-coordinated H_2 molecules could lead to the relaxation of *para*-H_2 to normal H_2, resulting in very little signal enhancement if the species were long-lived.

The hydrogen and substrate exchange mechanism indicates that faster hydrogen exchange occurs with larger hydrogen pressures, and smaller substrate concentrations. The lifetimes of the $[Ir(H)_2(IMes)(sub)_3]Cl$ SABRE complexes can therefore be lengthened/shortened by lowering/increasing hydrogen pressures or increasing/lowering substrate concentrations. Optimisation of the lifetimes of the SABRE-active catalysts is necessary for the optimisation of SABRE enhancements.

7.2.2 Optimising SABRE of Pyridazine and Phthalazine

The $[Ir(H)_2(IMes)(sub)_3]Cl$ complexes, where sub is pyridazine or phthalazine, are effective SABRE catalysts. Optimisation of polarisation transfer from the *para*-H_2-derived hydrides to pyridazine and phthalazine is discussed in Chapter 3. The polarisation transfer catalyst lifetimes are longer than optimum at room temperature, therefore polarisation transfer was made more efficient by altering the temperature, *N*-heterocycle

concentration, and the catalyst concentration to shorten the catalyst lifetimes. The optimum complex lifetimes are shorter than those reported for pyridine, which may be due to the equal probability of the *N*-heterocycles undergoing a haptotropic shift instead of dissociation, and the different *J*-coupling networks that are present.

Enhancement factors were optimised at 323 K (the safety limit when using pressurised samples in methanol), with 5 equivalents of *N*-heterocycle with respect to $[Ir(H)_2(IMes)(sub)_3]Cl$, and between 2.8 mM to 6.2 mM of $[Ir(H)_2(IMes)(sub)_3]Cl$, as shown in Figure 208. It should be noted that SABRE enhancements do not reach a plateau at 323 K, and higher temperatures are likely to give better enhancements. Furthermore, SABRE enhancements are likely to increase when higher hydrogen pressures are used however 3 bar was the safety limit of the NMR tubes that were used.

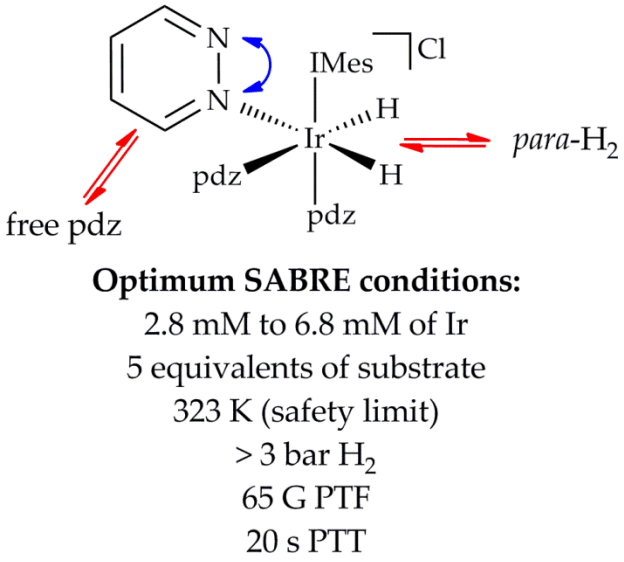

Figure 208: Optimum SABRE conditions for polarisation transfer to pyridazine or phthalazine.

In addition to the lifetimes of the polarisation transfer catalysts, the efficiency of polarisation transfer from *para*-H_2 to the *N*-heterocycle depends on the *J*-coupling between the *para*-H_2-derived hydrides and the protons of the substrate, as well as the difference in their chemical shifts. The latter is dependent on the PTF. Polarisation transfer into the proton resonances of both pyridazine and phthalazine was optimised using a PTF of 65 G and a PTT of 20 s. Interestingly in the case of pyridazine, the enhancements of different magnetic spin states were optimised using different magnetic field strengths. These are given in Table 30, using the arbitrary proton labels shown in Figure 209. The

enhancements from single quantum transitions, which lead to the largest signals and are of interest when forming long-lived singlet states, were optimal at 65 G.

Table 30: The optium PTFs for the enhancement of the different magnetic states of pdz.

Magnetic state	Optimum PTF (G)	Enhancement Factor
NCH (I_z^X, $I_z^{X'}$)	65	284 ± 2
NCHCH (I_z^A, $I_z^{A'}$)	65	238 ± 2
NCHCH DQ ($I_z^A I_z^{A'}$)	50	4.5 ± 0.1
SQ (I_z^A, $I_z^{A'}$, I_z^X, $I_z^{X'}$)	60	680 ± 10
DQ ($I_z^A I_z^{A'}$, $I_z^X I_z^{X'}$, $I_z^A I_z^X$, $I_z^A I_z^{X'}$)	30	162 ± 5
TQ ($I_z^{A'} I_z^A I_z^X$, $I_z^A I_z^X I_z^{X'}$)	40, 120	15 ± 2, 21 ± 2
QQ ($I_z^A I_z^{A'} I_z^M I_z^{M'}$)	50, 120	5.97 ± 0.05, 5.06 ± 0.05

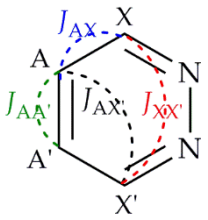

Figure 209: The four different coupling constants between the protons of pyridazine.

The C_{2v} symmetry exhibited by both pyridazine and phthalazine gives rise to potential polarisation storage properties. A current drawback to the use of the SABRE technique for *in vivo* studies is the short lifetime of the signal enhancements that result. The lifetime is limited by the T_1 values of the polarised nuclei. The T_1 values measured for the protons of pyridazine and phthalazine (26 mM in d_4-methanol) are given in blue in Figure 210. These values are not practical for *in vivo* applications, as most of the polarisation would relax in under a minute. Furthermore, the T_1 values measured for the same protons in d_4-methanol (10.4 mM) with $[Ir(H)_2(IMes)(sub)_3]Cl$ (5.2 mM) are equal to approximately 6 s, and were discussed in detail in section 3.5.

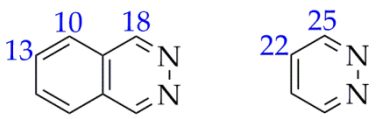

Figure 210: The T_1 values, in seconds, of the protons of phthalazine (left) and pyridazine (right).

The presence of the iridium SABRE catalyst significantly reduces the T_1 values of the protons on pyridazine and phthalazine, as once bound to iridium their longitudinal relaxation rates increase. The T_1 values can be restored to those measured in the absence of catalyst if exchange with the SABRE catalyst is halted. This can be achieved by deactivating the iridium catalyst with a chelating ligand, like 1,10-phenanthroline, as discussed in Chapter 1.[164]

The more commercially-developed DNP technique, discussed in Chapter 1, is often used to polarise the ^{13}C nucleus of [1-^{13}C] pyruvate, shown in Figure 211.[322] The rate of cellular pyruvate up-take is fast relative to the T_1 values of the ^{13}C nuclei, which are approximately 30 s *in vivo*, at magnetic fields greater than 1 T,[323] thus the metabolism of hyperpolarised pyruvate can be monitored by MRI. The rate of pyruvate metabolism can be used to identify cancerous tissues, and this has recently been applied to clinical trials of hyperpolarised [1-^{13}C] pyruvate for the detection of prostate cancer.[323] The short *in vivo* T_1 of the ^{13}C nucleus of pyruvate, however, also limits its use as a hyperpolarised contrast agent.

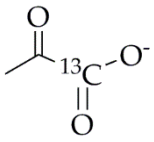

Figure 211: [1-^{13}C] pyruvate.

At low magnetic fields, the protons of pyridazine and phthalazine potentially form singlet states. As discussed in Chapter 1, in order to form a singlet state, a molecule must contain a pair of spin-½ nuclei which are positioned away from other nuclear spins to prevent relaxation, and the two nuclei must be magnetically inequivalent so that, at high field, the spin state can be probed.[142] Phthalazine matches these criteria, as the NC**H** protons of the first ring are isolated from the protons on the second ring, with a very weak coupling of 0.43 Hz. The NC**H** protons of pyridazine, however, couple very strongly (5.22 Hz) to their neighbouring NCHC**H** protons, thus a singlet state would relax very quickly. This could be prevented by replacing the NCHC**H** protons with deuterium atoms. This study could therefore be extended to investigate polarisation transfer into long-lived singlet states. Polarisation can potentially be stored in singlet states *via* polarisation transfer at high field, after which storage and 'release' is achieved by simply shuttling the

sample between low and high magnetic field, respectively,[133] or by using a 'spin locking' pulse sequence, in which a radiofrequency is applied to prevent singlet-triplet mixing.[138] The ability to store polarisation and 'release' it when desired would be a major breakthrough towards MRI applications.

A recent report by Theis *et. al.* highlights the potential of long-lived singlet states for use in biomedical imaging.[324] The diazirine molecule shown in Figure 212 was synthesised by the authors and the ^{15}N nuclei were polarised *via* SABRE with an $[Ir(H)_2(IMes)(py)(Diaz)][PF_6]$ SABRE catalyst, where Diaz is the diazirine given in Figure 212. Typically, polarisation transfer to the ^{15}N nuclei is optimised at a PTF of approximately 6 mG,[155,156,324] however polarisation transfer to the singlet state was optimised at PTFs between 0.5 to 200 G. ^{15}N NMR signal enhancements of 5000-fold were observed for the singlet state, and a ^{15}N T_1 of 5.8 minutes (340 s) was reported. Polarisation of this duration would be incredibly useful for *in vivo* MRI, as it allows more time for the polarised contrast agent to travel to different areas of the body prior to detection.

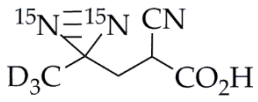

Figure 212: 2-cyano-3-(D_3-methyl-$^{15}N_2$-diazirine)-propanoic acid.

Singlet states in [1,2-$^{13}C_2$] pyruvate have also been accessed,[323] however they are not preserved on metabolism of pyruvate to lactate. Polarising singlet states may generalise the use of DNP to produce hyperpolarised contrast agents, however its high financial and time costs will limit its progression if the same results can be achieved using SABRE.

The total signal enhancements of the proton resonances of pyridazine were consistently larger than those of phthalazine. This is likely to be due to a faster rate of hydrogen addition to binding sites positioned *trans* to pyridazine than to binding sites positioned *trans* to phthalazine. In addition, *J*-coupling between the *para*-H_2-derived hydrides and the NC**H** protons of pyridazine may be stronger than that to the NC**H** protons of phthalazine, which is consistent with the predicted shorter Ir-N bond length in $[Ir(H)_2(IMes)(pdz)_3]Cl$. The T_1 values of the single quantum states of pyridazine are also longer than those of phthalazine, which allows polarisation to build-up over a longer period of time.

The suitability of pyridazine and phthalazine drug derivatives as potential hyperpolarised contrast agents was verified in Chapter 3 by collecting several images of phantoms containing hyperpolarised pyridazine and phthalazine. Both *N*-heterocycles exhibited dramatic signal enhancements in ethanol, which can be diluted to produce a biologically-compatible solvent. The antifungal, 5-aminophthalazine, was successfully polarised in Chapter 3, which verifies that drug derivatives of phthalazine, where functionalisation is on the second ring, have the potential to be used as hyperpolarised contrast agents. These studies could be extended by optimising polarisation transfer into the resonances of 5-aminophthalazine and collecting hyperpolarised images of phantoms containing this antifungal. Furthermore, the effect of dilution of ethanol solutions, containing polarisation transfer catalysts and substrates of interest, could be investigated. Dilution is likely to have an effect on the exchange of hydrogen, as hydrogen is far less soluble in water (mole fraction at 298 K, with ~1 atmosphere of H_2 in water = 1.4×10^{-5}, in methanol = 1.6×10^{-4})[325] therefore exchange rates are likely to be slower. Furthermore, the solubility of polarisation transfer catalysts with the general formula $[Ir(H)_2(IMes)(sub)_3]Cl$ in aqueous media is limited, and other water-soluble exchange catalysts, for example those synthesised by Fekete *et. al.* containing water-solubilising phosphine ligands,[218] might be preferable.

7.2.3 Summary

Iridium polarisation transfer catalysts have been used to successfully enhance the ^1H NMR signals corresponding to pyridazine and phthalazine *via* the SABRE technique. Exchange of substrate and hydrogen at iridium was monitored under different conditions to assess the mechanism of exchange, which was used to predict the optimum conditions for efficient polarisation transfer from *para*-H_2. SABRE was optimised by adjusting the concentration of polarisation transfer catalyst, the equivalents of substrate with respect to the catalyst, the temperature, the pressure of *para*-H_2, the PTF, and the PTT. Enhancement factors of > 1000-fold have been achieved for pyridazine, which consistently performed better than phthalazine. Images of phantoms containing hyperpolarised pyridazine and phthalazine were also substantially enhanced with respect to their thermal counterparts (1100-fold increase in signal when using hyperpolarised pyridazine). The potential to use drug derivatives of pyridazine and phthalazine as MRI contrast agents has been verified. This research was successfully published in *Chemical Science*.[326]

Appendix A

The following is the supplementary information for Chapters 2 and 3, which has been cross-referenced throughout.

A.1SABRE of Pyridazine and Phthalazine

A.1.1 Fitting Kinetic Data in order to Abstract Rate Constants

The 1,2-metallotropic shifting of pyridazine in [Ir(COD)(IMes)(pdz)]Cl, shown in Figure 213, at 245 K, is used as the example kinetic process. In this case, 2-D NOESY was used to probe exchange of the protons labelled as * in Figure 213, however 1-D EXSY has also been used whenever NMR signals could be selectively irradiated. The percentage abundance of the irradiated signal (IrNCHC**H**, species **A**), and the signal that polarisation transfers into due to exchange (IrNNCHC**H**, species **B**), were plotted against the mixing time. This is shown in Figure 214.

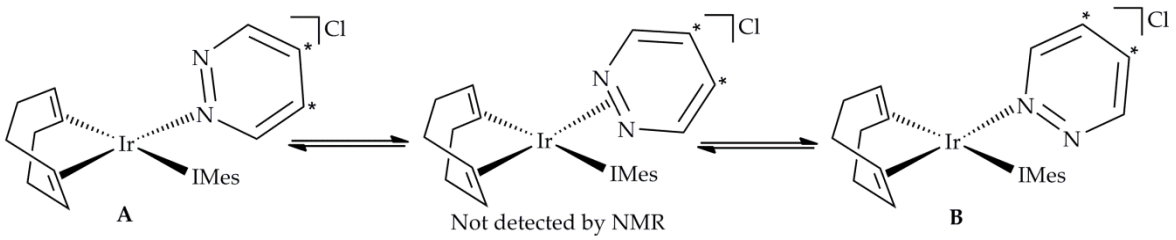

Figure 213: Haptotropic shift of pyridazine in [Ir(COD)(IMes)(pdz)]Cl.

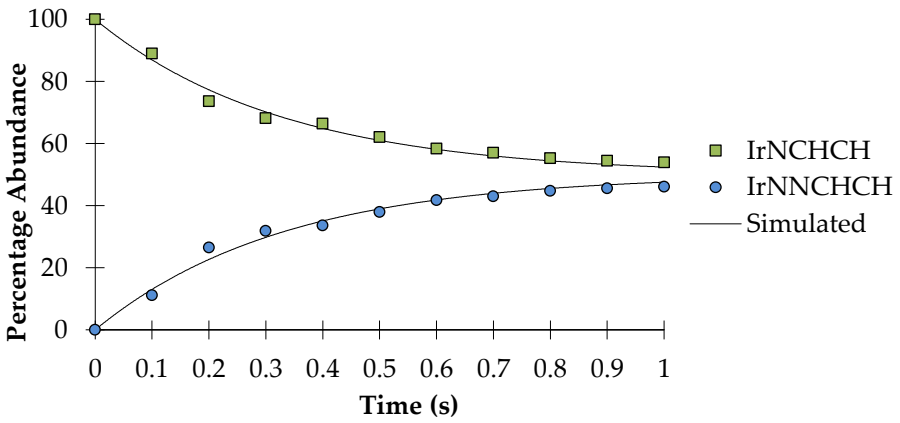

Figure 214: Graph to show the transfer of polarisation from IrNCHC<u>H</u> to IrNNCHC<u>H</u> in the bound pyridazine of [Ir(COD)(IMes)(pdz)]Cl, as a result of a haptotropic shift, at 245 K.

These data were simulated using the Solver package in Microsoft Excel, according to the formulae given below, where [A] is the percentage abundance of species A, [B] is the percentage abundance of species **B**, and k_{AB} is the observed rate constant of the haptotropic shift.

$$[A]_{t+\delta t} = [A]_t - k_{AB}[A]_t\delta t + k_{BA}[B]_t\delta t$$

$$[B]_{t+\delta t} = [B]_t + k_{AB}[A]_t\delta t - k_{BA}[B]_t\delta t$$

This was achieved by creating a set of simulated data in Microsoft Excel, in which the percentage abundances of **A** and **B** were calculated according to the formulae given, from t = 0 s, to t = 1 s (the longest time tested). Time increments were used that are a minimum of four times smaller than those used to collect the experimental data. In this example, time increments of 0.01 s were used, which is ten times smaller than those used to collect experimental data (0.1), however different increments were used depending on the experimental conditions. The value of $[A]_0$was assumed to be equal to 100%, and the value of $[B]_0$ was assumed to be equal to 0%. The calculations require a value of k_{AB}, thus an estimated value was used. The resulting Excel cell inputs used to calculate the simulated data are shown in Figure 215. The inputs used to calculate [A] and [B] at t = 0.01 s can be applied to all the other time values by simply substituting the suitable cells in place of B2, C2, A3 and A2.

	A	B	C	N	O
1	Time (s)	[A]	[B]		
2	0	100	0	k_{AB}	k_{BA}
3	0.01	=B2−(N3*B2*(A3−A2))+(O3*C2*(A3−A2))	=C2+(N3*B2*(A3−A2))−(O3*C2*(A3−A2))	1.5	1.5

Figure 215: The Excel cell inputs used to calculate the simulated data for the haptotropic shifting of pdz in [Ir(COD)(IMes)(pdz)]Cl. The same inputs can be used for any first-order reaction.

Once the simulated data were created, according to estimated values of k_{AB} and k_{BA}, they were fitted to the experimental data using Excel's Solver package. It is assumed that each value of y has the same uncertainty therefore the unweighted least squares method has been used. First, a least squares analysis was required in which the residuals were calculated by subtracting the appropriate simulated values of [A] and [B] from the experimental values, *i.e.* those corresponding to the same time increments. Each residual was then squared and all were summed to find the sum of the squared residuals,

according to the formula given below where S is the sum of the squared residuals, n is the number of data points, i is a given data point, and r_i is the residual of a given data point.[327] The Excel cell inputs are given in Figure 216.

$$S = \sum_{n}^{i} r_i^2$$

	E	F	G	H	I	J
1	Time (s)	[A]	[B]	(Residual [A])^2	(Residual [B])^2	Sum of residuals
2	0	100	0	=(F2−B2)^2	=(G2−C2)^2	=H2+I2
3	0.1	88.9	11.1	=(F3−B12)^2	=(G3−C12)^2	=H3+I3
					S	=J2+J3

Figure 216: The Excel cell inputs used to calculate the sum of the squared residuals showing the experimental data in columns E-G, and using the cell references given in Figure 215 for the simulated data.

Solver was then used to minimise the value of the sum of the squared residuals (S), thereby fitting the simulated data to the experimental data. To do this, specified variables are iterated until S is minimised, according to the constraints specified. The values of k_{AB} and k_{BA} were therefore iterated, with the constraints $[A]_0 = 100$, $[B]_0 = 0$, $k_{AB} \geq 0$, and $k_{BA} \geq 0$. Solver uses a generalised reduced gradient algorithm to iterate the data,[328] in which the outputs are analysed to speed-up data fitting. The first derivative of the overall input function is analysed to methodically vary the value of the variables (k_{AB} and k_{BA}). The data has been fitted when the first derivative has been minimised; if an increase in k_{AB} increases the value of the first derivative, then k_{AB} will be decreased in the next iteration.

If, after several Solver cycles, the output values of k_{AB} and k_{BA} had not changed, then the optimum fit had been obtained. Of course, a plot of the simulated data was always compared with the experimental data to ensure a suitable fit.

A.1.2 Calculating the Errors in Data Fitting

On fitting data using the Microsoft Excel's Solver package, no error values are given. Errors must therefore be calculated using the Jack-knife method.[191] Although time-consuming, this is a very simple way to calculate the errors in the fit. Here, the error associated with the value of k_{AB} is used as the example. The Excel cell inputs for this are

given in Figure 217. The first data point was omitted, (row 2 in Figure 217) and the Solver package was used to obtain the k_{AB} value using all the data except the first point. The k_{AB} value was recorded (in cell P2 in Figure 217). The first data point was then re-inserted and the second data point was omitted (row 3 in Figure 217) and again, Solver was used to obtain the k_{AB} value using all the data except the second point. The k_{AB} value was recorded (in cell P3 in Figure 217). This was repeated so that a k_{AB} value was obtained after the omission, and then re-insertion, of every data point (n times for n data points).

	H	I	J	O	P
1	(Residual [A])^2	(Residual [B])^2	Sum of residuals	Row emitted	k_{AB}
2	=(F2−B2)^2	=(G2−C2)^2	=H2+I2	2	
3	=(F3−B12)^2	=(G3−C12)^2	=H3+I3	3	
11				Standard deviation	=(stdev(P2:P3))
12				Standard error	=P11/(sqrt(10))

Figure 217: The Excel cell inputs used to calculate the errors in the data fit using the Jack-knife method. The cell references from Figure 215 and Figure 216 are used.

The standard deviation of the 10 different k_{AB} values was calculated, and was used to calculate the standard error according to the formula given below, where s is the standard deviation, and n is the number of data points.

$$SE = \frac{s}{\sqrt{n}}$$

The standard error is quoted for every rate constant given.

A.1.3 Eyring Plot for the Haptotropic Shift of Phthalazine in [Ir(COD)(IMes)(phth)]Cl

Eyring analysis is discussed in detail in Chapter 2 and the Eyring plot used to calculate the activation parameters for the haptotropic shifting of pyridazine in [Ir(COD)(IMes)(pdz)]Cl is also given.

The Eyring plot from which the activation parameters for the haptotropic shifting of phthalazine in [Ir(COD)(IMes)(phth)]Cl were calculated, is shown in Figure 218. The $\Delta H^{\ddagger}$ and $\Delta S^{\ddagger}$ values were calculated from linear regression of this plot, thus the errors

associated with these values can be calculated using the Jack-knife approach discussed above.

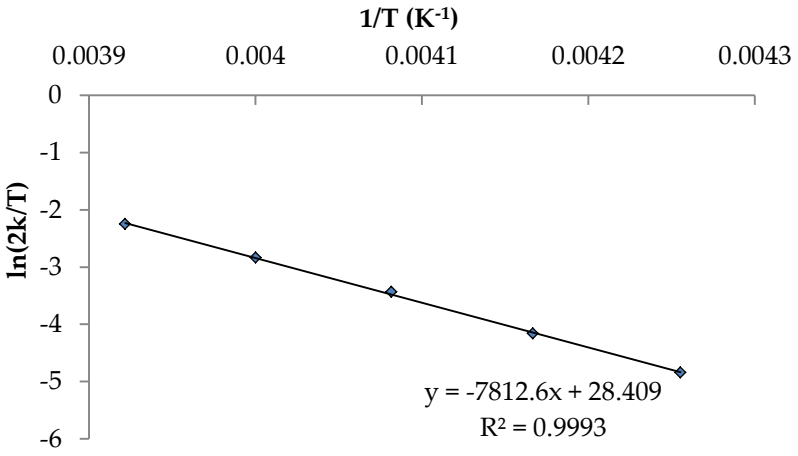

Figure 218: Eyring plot to calculate the activation parameters of the 1,2-metallotropic shift of the bound phthalazine in [Ir(COD)(IMes)(phth)]Cl.

A.1.4 Calculation of Errors from Propagation of Error

On calculating a value from others with known errors, the error associated with the new value can be calculated according to the propagation of errors. In this work, only the two formulae given below were required. Where q is the sum of the measured quantities including x and y:

$$\delta q = \sqrt{\delta x^2 + \cdots + \delta y^2}$$

Where q is the product of the measured quantities including x and y:

$$\frac{\delta q}{q} = \sqrt{\left(\frac{\delta x}{x}\right)^2 + \cdots + \left(\frac{\delta y}{y}\right)^2}$$

For example, $\Delta G^{\ddagger}$ is calculated from $\Delta H^{\ddagger}$ and $\Delta S^{\ddagger}$, according to the formula given below, where T is the temperature (K).

$$\Delta G^{\ddagger} = \Delta H^{\ddagger} - T\Delta S^{\ddagger}$$

As the errors in $\Delta H^{\ddagger}$ ($\delta\Delta H^{\ddagger}$) and $\Delta S^{\ddagger}$ ($\delta\Delta S^{\ddagger}$) were calculated using the Jack-knife method discussed previously, the error in $\Delta G^{\ddagger}$ ($\delta\Delta G^{\ddagger}$) can therefore be calculated by combining the formulae above to give:

$$\delta\Delta G^{\ddagger} = \sqrt{\delta\Delta H^{\ddagger 2} + T\delta\Delta S^{\ddagger 2}}$$

A.1.5 Plot used to Calculate the T_1 Values of the Hydride NMR Signals in [Ir(H)$_2$(COD)(IMes)(pdz)]Cl

Calculation of T_1 values using inversion recovery experiments is discussed in detail in Chapter 2. Fitting of the data was achieved using Excel's Solver package, in an identical manner to that discussed previously, using the formula given in Chapter 2 to simulate data and obtain the T_1 values. The plot used to calculate the T_1 values of the hydride NMR signals in [Ir(H)$_2$(COD)(IMes)(phth)]Cl is also given in Chapter 2.

The plot used to calculate the T_1 values of the hydride NMR signals in [Ir(H)$_2$(COD)(IMes)(pdz)]Cl is shown in Figure 219. The T_1 values calculated from this are given in Chapter 2.

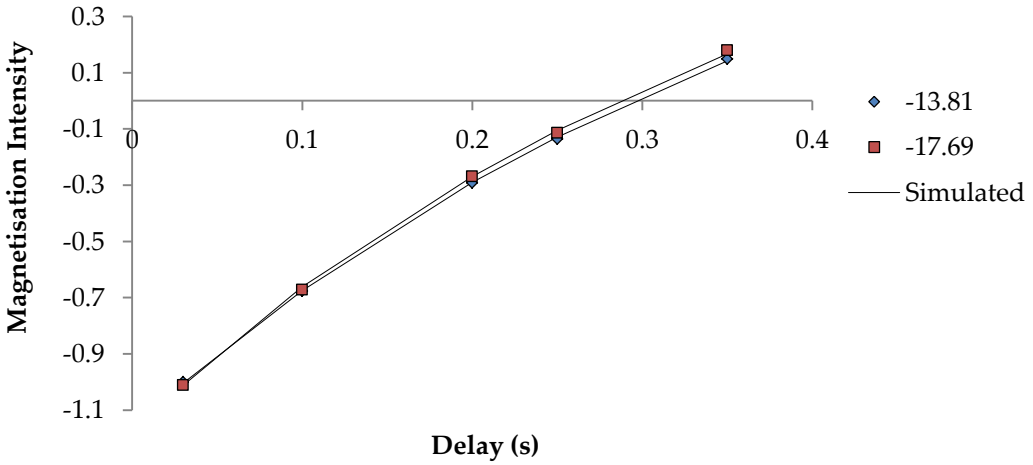

Figure 219: Graph to show the change in magnetisation intensity, with respect to the intensity when τ = 0.03 s, as a function of the delay time (τ) in an inversion recovery experiment used to calculate the T_1 of the hydride NMR signals in [Ir(H)$_2$(COD)(IMes)(pdz)]Cl.

A.1.6 Modelling Substrate Exchange in [Ir(H)$_2$(IMes)(sub)$_3$]Cl

Fitting the data for *N*-heterocycle exchange in [Ir(H)$_2$(IMes)(sub)]Cl was challenging. In these complexes, the substrate can dissociate or undergo a haptotropic shift and, in order to obtain rate constants for these two processes, an equation that accurately describes the transfer of magnetic polarisation from the irradiated bound species to the free and shifted species *via* exchange was required. Despite some papers reporting a

dissociative 1,2-metallotropic shift mechanism of pyridazine-like *N*-heterocycles, our exchange data would only fit to a model in which the 1,2-metallotropic shift is assumed to be haptotropic in nature. Eleven different polarised species, including unobservable intermediates, can form and these are labelled **A-K** in Figure 220. In this model, it is assumed that only one substrate dissociates at a time to form 16 electron complexes. Dissociation of two substrates would lead to the formation of 14 electron complexes, which would lack stability.

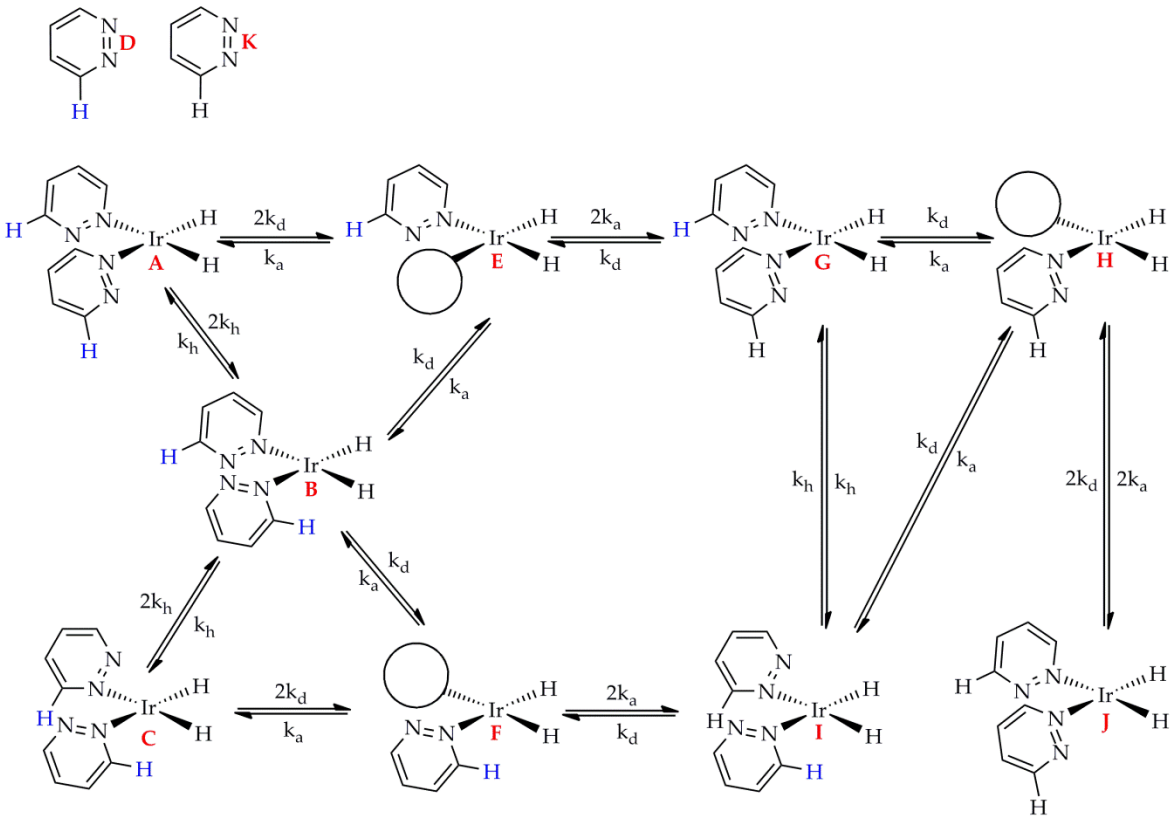

Figure 220: The potential pathways to exchange polarisation from the irradiated species (A) to the shifted species and free N-heterocycle detected in EXSY spectra for $[Ir(H)_2(IMes)(pdz)_3]Cl$. The carbene (IMes), axial N-heterocycles, and chloride counterions have been omitted from each iridium species for simplification. These ligands are not involved in exchange. Identical pathways are possible with $[Ir(H)_2(IMes)(phth)_3]Cl$.

In the case of $[Ir(H)_2(IMes)(pdz)_3]Cl$, the irradiated signal at δ 8.75 is that which corresponds to the IrNNC**H** protons. Species **A** is therefore created on selectively irradiating this signal. The polarised protons of species **A** are highlighted in blue in Figure 220. During the delay time used in EXSY, prior to spectral acquisition, one of the polarised pyridazine ligands can dissociate to form species **E** and **D** at a rate equal to k_d or one can undergo a haptotropic shift to form species **B** at a rate equal to k_h. As either one of the

two pyridazine ligands can dissociate or shift to form species **E** and **D** or **B**, the probability of these processes occurring is twice that of a scenario where only one of the ligands can exchange, therefore the rates are doubled ($2k_d$ or $2k_h$).

Once **E** has formed, a molecule of **D** can re-associate to re-form **A** at a rate equal to k_a. Alternatively, a molecule of **K** (unpolarised free pyridazine) can associate to form **G**. As the unpolarised pyridazine can bind at either nitrogen atom to form **G**, the probability of this process occurring is double that of binding a molecule of **D**, which must bind at the nitrogen situated farthest from the polarised proton to re-form **A**. The rate of forming **G** from **E** and **K** is therefore double ($2k_h$).

In total, three 16 electron intermediates, **E**, **F**, and **H**, can form from the pathways shown in Figure 220, in which a pyridazine ligand has dissociated to leave an empty binding site. These species are not observed by NMR and therefore do not contribute to the signals observed in the acquired EXSY spectra. The irradiated IrNNC**H** ^{1}H NMR signal observed at δ 8.75 is produced by species **A** (in which there are two of these polarised proton environments), **B**, and **G**, and its intensity is equal to $2[\boldsymbol{A}] + [\boldsymbol{B}] + [\boldsymbol{G}]$. The signal observed at δ 9.31 corresponds to IrNC**H** protons and is produced by species **B**, **C** (in which there are two of these polarised proton environments), and **I**. Its intensity is therefore equal to $[\boldsymbol{B}] + 2[\boldsymbol{C}] + [\boldsymbol{I}]$. Finally, the signal observed at δ 9.23 corresponds to the NC**H** protons of free pyridazine and is produced by species **D**, with an intensity simply equal to $[\boldsymbol{D}]$.

In order to model the experimental data, formulae for the concentration of each species, **A**-**K**, at time t were derived from the kinetic pathways given in Figure 220. These formulae are given below, and were used to produce the simulated data needed, in Microsoft Excel. The value of $[A]_0$ was assumed to be 5.2 mM, and the value of $[K]_0$ was assumed to be 2.8-fold larger than this, as free pyridazine was measured to be in a 2.8-fold excess with respect to the iridium catalyst. The initial concentrations of all other species were assumed to be equal to 0. Values of k_a, k_d, and k_h were estimated.

$$[\boldsymbol{A}]_t = [\boldsymbol{A}]_0 - (2k_d[\boldsymbol{A}])t + (k_a[\boldsymbol{E}][\boldsymbol{D}])t + (k_h[\boldsymbol{B}])t$$

$$[\boldsymbol{B}]_t = [\boldsymbol{B}]_0 - (2k_h[\boldsymbol{B}])t - (2k_d[\boldsymbol{B}])t + (2k_h[\boldsymbol{A}])t + (2k_h[\boldsymbol{C}])t + (k_a[\boldsymbol{E}][\boldsymbol{D}])t + (k_a[\boldsymbol{F}][\boldsymbol{D}])t$$

$$[\boldsymbol{C}]_t = [\boldsymbol{C}]_0 - (2k_h[\boldsymbol{C}])t - (2k_d[\boldsymbol{C}])t + (k_h[\boldsymbol{B}])t + (k_a[\boldsymbol{F}][\boldsymbol{D}])t$$

$$[\boldsymbol{D}]_t = [\boldsymbol{D}]_0 - (2k_a[\boldsymbol{E}][\boldsymbol{D}])t - 2k_a[\boldsymbol{F}][\boldsymbol{D}])t - (2k_a[\boldsymbol{H}][\boldsymbol{D}])t + (2k_d[\boldsymbol{A}])t + (2k_d[\boldsymbol{B}])t + (2k_d[\boldsymbol{C}])t + (k_d[\boldsymbol{G}])t + (k_d[\boldsymbol{I}])t$$

$$[\boldsymbol{E}]_t = [\boldsymbol{E}]_0 - (2k_a[\boldsymbol{E}][\boldsymbol{K}])t - (2k_a[\boldsymbol{E}][\boldsymbol{D}]) + (2k_d[\boldsymbol{A}])t + (k_d[\boldsymbol{G}])t + (k_d[\boldsymbol{B}])t$$

$$[\boldsymbol{F}]_t = [\boldsymbol{F}]_0 - (2k_a[\boldsymbol{F}][\boldsymbol{K}])t - (2k_a[\boldsymbol{F}][\boldsymbol{D}])t + (2k_d[\boldsymbol{C}])t + (k_d[\boldsymbol{B}])t + (k_d[\boldsymbol{I}])t$$

$$[\boldsymbol{G}]_t = [\boldsymbol{G}]_0 - (2k_d[\boldsymbol{G}])t - (k_h[\boldsymbol{G}])t + (2k_a[\boldsymbol{E}][\boldsymbol{K}])t + (k_a[\boldsymbol{H}][\boldsymbol{D}])t + (k_h[\boldsymbol{I}])t$$

$$[\boldsymbol{H}]_t = [\boldsymbol{H}]_0 - (2k_a[\boldsymbol{H}][\boldsymbol{D}])t - (2k_a[\boldsymbol{H}][\boldsymbol{K}])t + (k_d[\boldsymbol{G}])t + (k_d[\boldsymbol{I}])t + (2k_d[\boldsymbol{J}])t$$

$$[\boldsymbol{I}]_t = [\boldsymbol{I}]_0 - (2k_d[\boldsymbol{I}])t - (k_h[\boldsymbol{I}])t + (k_a[\boldsymbol{H}][\boldsymbol{D}])t + (2k_a[\boldsymbol{F}][\boldsymbol{K}])t + (k_h[\boldsymbol{G}])t$$

$$[\boldsymbol{J}]_t = [\boldsymbol{J}]_0 - (2k_d[\boldsymbol{J}])t + (2k_a[\boldsymbol{H}][\boldsymbol{K}])t$$

$$[\boldsymbol{K}]_t = [\boldsymbol{K}]_0 - (2k_a[\boldsymbol{E}][\boldsymbol{K}])t - (2k_a[\boldsymbol{F}][\boldsymbol{K}])t - (2k_a[\boldsymbol{H}][\boldsymbol{K}])t + (2k_d[\boldsymbol{J}])t + (2k_d[\boldsymbol{G}])t + (k_d[\boldsymbol{I}])t$$

As mentioned previously, the relative intensities of the observed NMR signals resulting from the polarised protons in these species were calculated using the formulae given below, where δ 8.75 corresponds to IrNNC**H**, δ 9.31 corresponds to IrNC**H**, and δ 9.23 corresponds to NC**H** on free pyridazine.

$$\delta\ 8.75 = 2[\boldsymbol{A}] + [\boldsymbol{B}] + [\boldsymbol{G}]$$

$$\delta\ 9.31 = [\boldsymbol{B}] + [\boldsymbol{2C}] + [\boldsymbol{I}]$$

$$\delta\ 9.23 = [\boldsymbol{D}]$$

These values were then converted into the percentage abundance of each species, which was used as the simulated data. The experimental peak integrals had also been converted into percentage abundances. The simulated data was fitted to the experimental data according to the Solver protocol discussed previously, where values of k_a, k_d, and k_h were iterated under the constraints $k_a \geq 0$, $k_d \geq 0$, and $k_h \geq 0$, until the optimum fit was obtained. The values of $k_a$were ignored as their accuracy could not be confirmed due to a lack of experimental data for the associative process. The errors in the values of k_d and k_h were calculated using the Jack-knife method discussed previously.

The exchange of phthalazine in $[Ir(H)_2(IMes)(phth)_3]Cl$ was modelled in an identical fashion.

A.1.7 Modelling Hydrogen Exchange in $[Ir(H)_2(IMes)(sub)_3]Cl$

In the case of hydrogen exchange, signals corresponding to the selectively irradiated hydrides in the $[Ir(\mathbf{H})_2(IMes)(sub)_3]Cl$ species are observed, as well as signals corresponding to polarised hydrogen. In the case of $[Ir(H)_2(IMes)(pdz)_3]Cl$, selective irradiation of the hydride signal at δ −21.47, followed by a specified delay and spectral acquisition leads to the observation of the same hydride signal and free hydrogen at δ 4.58. No other signals are detected. Although hydrogen exchange requires the dissociation of a substrate molecule followed by the association of a hydrogen molecule, as discussed in Chapter 1, the full procedure cannot be modelled with the experimental data as signals corresponding to the short-lived intermediates are not observed. As a result, a simplified model is used, shown for $[Ir(H)_2(IMes)(pdz)_3]Cl$ in Figure 221.

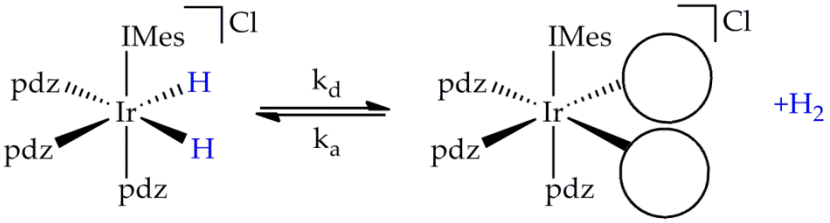

Figure 221: Simplified model for hydrogen exchange in $[Ir(H)_2(IMes)(pdz)_3]Cl$.

Simulated data can be calculated from formulae derived from this simplified model, given below, where A is $[Ir(\mathbf{H})_2(IMes)(sub)_3]Cl$, B is $\mathbf{H_2}$, and C is $[Ir(IMes)(pdz)_3]$.

$$[A]_{t+\delta t} = [A]_t - k_{AB}[A]_t\delta t + k_{BA}[B]_t[C]_t\delta t$$

$$[B]_{t+\delta t} = [B]_t + k_{AB}[A]_t\delta t - k_{BA}[B]_t[C]_t\delta t$$

Although the $k_{BA}[B]_t[C]_t\delta t$ term includes the concentration of the 16 electron intermediate $[Ir(IMes)(pdz)_3]$, this intermediate is not observed by NMR and is likely to be very short-lived, therefore its concentration is unlikely to change with time. As a result, the C term can be combined with the k_{BA} term to give $k_{com} = k_{BA}[C]_t$, and the formulae below.

$$[A]_{t+\delta t} = [A]_t - k_{AB}[A]_t\delta t + k_{com}[B]_t\delta t$$

$$[B]_{t+\delta t} = [B]_t + k_{AB}[A]_t\delta t - k_{com}[B]_t\delta t$$

Simulated data were calculated using these formulae and fitted to the experimental data using the Solver protocol described previously, where k_{com} and k_{AB} are iterated with the constraints $k_{com} \geq 0$, and $k_{AB} \geq 0$. The values obtained for k_{com} were ignored as their accuracy could not be confirmed due to a lack of experimental data for the associative process. The errors in the k_{AB} values were calculated using the Jack-knife method discussed previously. The k_{AB} values have been determined using a simplified model and reflect the observed rate constant of hydrogen dissociation from $[Ir(H)_2(IMes)(sub)_3]Cl$, which is comprised of several processes that were discussed in detail in the introduction. Although their values do not reflect the true rates of hydrogen dissociation, their use in the mechanistic studies of hydrogen exchange is invaluable.

A.1.8 Eyring Plots used to Calculate the Activation Parameters of Substrate and Hydrogen Exchange in $[Ir(H)_2(IMes)(sub)_3]Cl$

The activation parameters for substrate dissociation and haptotropic shifting, and hydrogen dissociation from the $[Ir(H)_2(IMes)(sub)_3]Cl$ complexes were calculated from the Eyring plots given below, using the method detailed in Chapter 2. The plots used to calculate the activation parameters of substrate and hydrogen exchange in $[Ir(H)_2(IMes)(pdz)_3]Cl$ and $[Ir(H)_2(IMes)(phth)_3]Cl$ are shown in Figure 222 and Figure 223 respectively, along with their corresponding formulae which were obtained using linear regression.

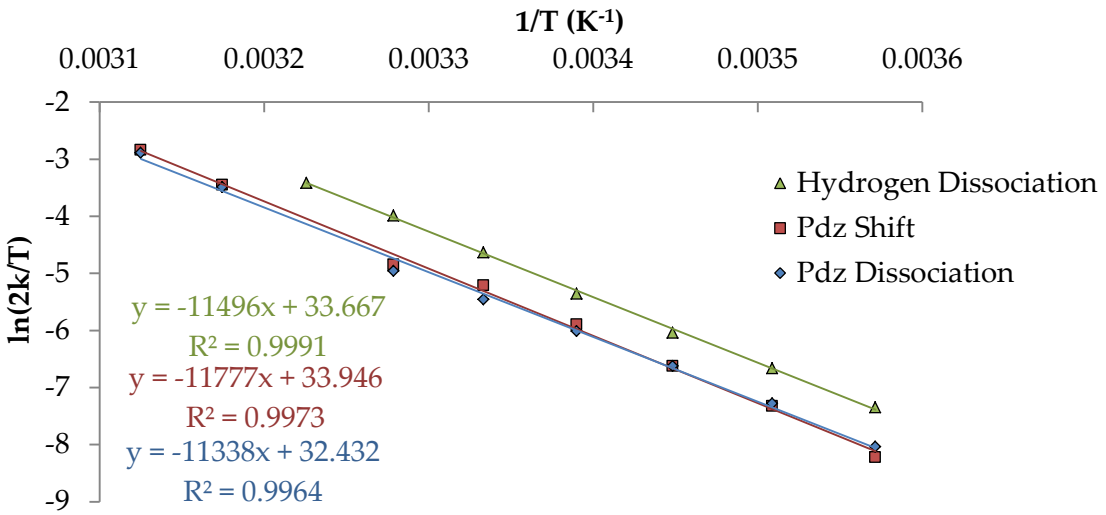

Figure 222: Eyring plot used to calculate the activation parameters of hydrogen dissociation, pyridazine shifting and pyridazine dissociation in $[Ir(H)_2(IMes)(pdz)_3]Cl$ and their corresponding formulae (shown in the same colour as the plot) obtained from linear regression analysis.

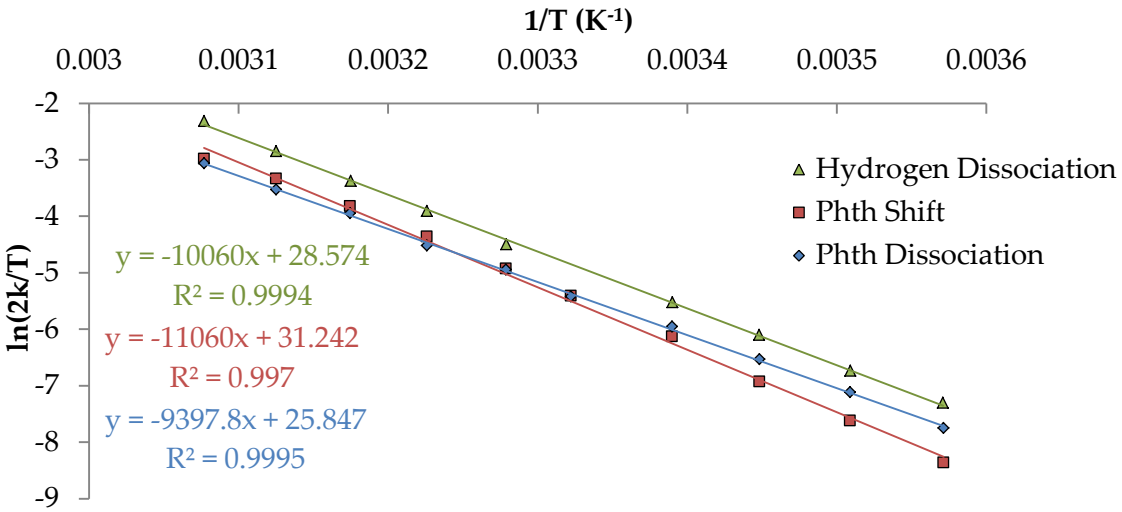

Figure 223: Eyring plot used to calculate the activation parameters of hydrogen dissociation, phthalazine shifting and phthalazine dissociation in $[Ir(H)_2(IMes)(phth)_3]Cl$ and their corresponding formulae (shown in the same colour as the plot) obtained from linear regression analysis.

A.1.9 Rate Data Obtained to Investigate the Effect of Hydrogen Pressure on Exchange

Hydrogen and pyridazine exchange were examined at a constant temperature (298 K), iridium concentration (5.2 mM), and free substrate concentration (8.4 mM), with varying pressures of hydrogen. The observed rate constants are given in Table 31. The errors given are for the fitting of the data and were calculated using the Jack-knife procedure.

Table 31: Observed rate constants of hydrogen and pdz exchange in d_4-methanol solutions of $[Ir(H)_2(IMes)(pdz)_3]Cl$ at 298 K, at the various pressures of hydrogen given.

H_2 pressure (bar)	Rate of exchange in $[Ir(H)_2(IMes)(pdz)_3]Cl$ (s^{-1})		
	H_2 dissociation	Pdz dissociation	Pdz haptotropic shift
0.445	0.428 ± 0.001	0.466 ± 0.003	0.800 ± 0.001
1.032	0.790 ± 0.003	0.456 ± 0.003	0.797 ± 0.001
1.515	0.94 ± 0.02	0.456 ± 0.003	0.780 ± 0.001
2.000	1.03 ± 0.01	0.451 ± 0.003	0.778 ± 0.002
2.495	1.10 ± 0.02	0.456 ± 0.003	0.785 ± 0.002
2.99	1.16 ± 0.03	0.458 ± 0.003	0.780 ± 0.001

A.1.10 Rate Data Obtained to Investigate the Effect of Substrate Concentration on Exchange

Hydrogen and substrate exchange were examined at a constant temperature (285 K), iridium concentration (5.2 mM), and hydrogen pressure (3 bar), with varying concentrations of substrate. The observed rate constants for exchange in $[Ir(H)_2(IMes)(pdz)_3]Cl$ and $[Ir(H)_2(IMes)(phth)_3]Cl$ are given in Table 32 and Table 33, respectively. The errors given are of the fitting of the data and were calculated using the Jack-knife procedure.

Table 32: Observed rate constants of hydrogen and pdz exchange in d_4-methanol solutions of $[Ir(H)_2(IMes)(pdz)_3]Cl$ at 285 K, at the various free pdz concentrations given.

[free pdz] (mM)	Rate of exchange in $[Ir(H)_2(IMes)(pdz)_3]Cl$ (s^{-1})		
	H_2 dissociation	Pdz dissociation	Pdz haptotropic shift
17.35	0.183 ± 0.003	0.0986 ± 0.0001	0.0942 ± 0.0001
27.64	0.120 ± 0.003	0.0982 ± 0.0002	0.0914 ± 0.0002
63.27	0.052 ± 0.001	0.0994 ± 0.0002	0.0955 ± 0.0002
85.55	0.037 ± 0.001	0.1017 ± 0.0003	0.0945 ± 0.0002
115.75	0.029 ± 0.001	0.0989 ± 0.0002	0.0932 ± 0.0003

Table 33: Observed rate constants of hydrogen and phth exchange in d_4-methanol solutions of $[Ir(H)_2(IMes)(phth)_3]Cl$ at 285 K, at the various free phth concentrations given.

[free phth] (mM)	Rate of exchange in $[Ir(H)_2(IMes)(phth)_3]Cl$ (s^{-1})		
	H_2 dissociation	Phth dissociation	Phth haptotropic shift
6.99	0.243 ± 0.007	0.1001 ± 0.0001	0.0618 ± 0.0001
19.22	0.172 ± 0.004	0.1192 ± 0.0002	0.0711 ± 0.0002
40.44	0.119 ± 0.005	0.1168 ± 0.0003	0.0694 ± 0.0003
78.56	0.083 ± 0.005	0.1037 ± 0.0002	0.0630 ± 0.0001
121.80	0.0643 ± 0.003	0.1000 ± 0.0002	0.0615 ± 0.0001

A.1.11 Derivation of Rate Law for the Formation of $[Ir(H)_2(\eta^2\text{-}H_2)(IMes)(pdz)_2]Cl$

The likely mechanism of substrate and hydrogen exchange is shown for $[Ir(H)_2(IMes)(pdz)_3]Cl$ in Figure 224. As intermediates $[Ir(H)_2(IMes)(pdz)(sol)]Cl$ (**B**) and $Ir(H)_2(\eta^2\text{-}H_2)(IMes)(pdz)_2]Cl$ (**C**) are short-lived, it can be assumed that their concentrations in solution do not change, and steady-state principles can be applied to derive a rate law for the formation of **C**, which is a key step to hydrogen loss.

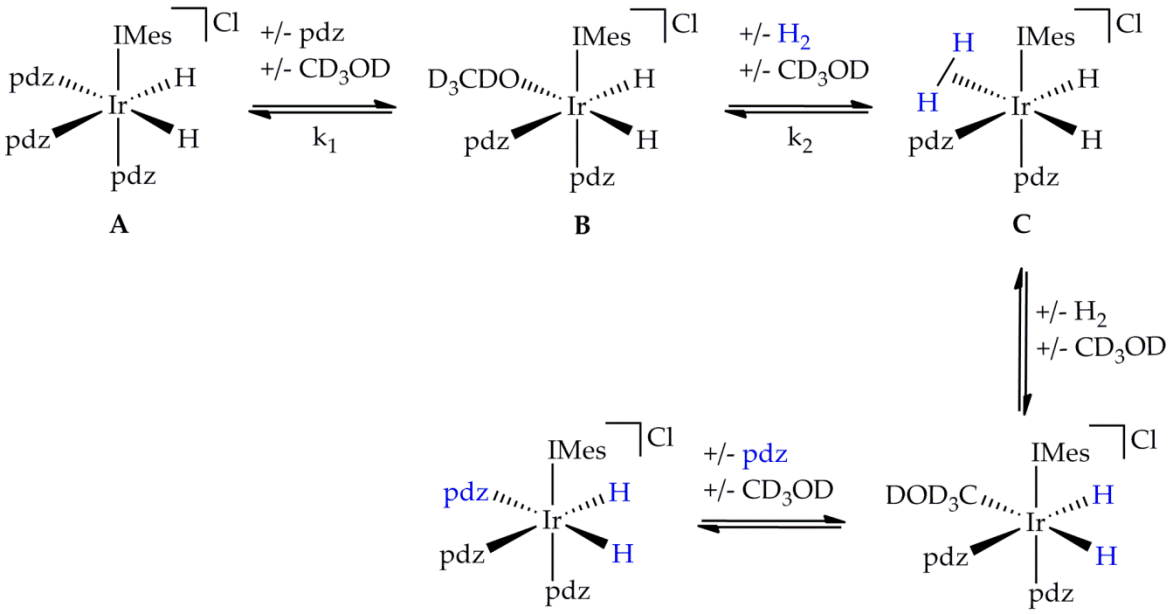

Figure 224: The substrate and hydrogen exchange mechanism in $[Ir(H)_2(IMes)(pdz)_3]Cl$.

From the above kinetic pathway, a formula for the concentration of C can be derived:

$$\frac{\delta[C]}{\delta t} = k_2[B][H_2] - k_{-2}[C] = 0$$

$$[C] = \frac{k_2[B][H_2]}{k_{-2}}$$

Also from the above kinetic pathway, a formula for the concentration of B can be derived:

$$\frac{\delta[B]}{\delta t} = k_1[A] + k_{-2}[C] - k_{-1}[B][pdz] - k_2[B][H_2] = 0$$

$$k_1[A] + k_{-2}[C] = k_{-1}[B][pdz] + k_2[B][H_2]$$

$$k_1[A] + k_2[B][H_2] = k_{-1}[B][pdz] + k_2[B][H_2]$$

$$k_1[A] = k_{-1}[B][pdz]$$

$$[B] = \frac{k_1[A]}{k_{-1}[pdz]}$$

Substituting this formula for the [B] term in the above formula gives:

$$[C] = \frac{k_2 k_1[A][H_2]}{k_{-2}k_{-1}[pdz]}$$

A.1.12 Rate Data used to Support the Derived Rate Law for the Formation of $[Ir(H)_2(\eta^2\text{-}H_2)(IMes)(pdz)_2]Cl$

Plots of the reciprocal observed rate of hydrogen loss, as a function of free substrate concentration are linear, supporting the rate law derived above. The data used to plot these graphs are given in Table 34, for $[Ir(H)_2(IMes)(pdz)_3]Cl$, and Table 35, for $[Ir(H)_2(IMes)(phth)_3]Cl$. The errors of the reciprocal rates were calculated using the propagation of errors formulae discussed previously.

Table 34: Observed rate constants of hydrogen exchange in d_4-methanol solutions of $[Ir(H)_2(IMes)(pdz)_3]Cl$ at 285 K, at the various free pdz concentrations given.

[free pdz] (mM)	Rate of H_2 dissociation (s^{-1})	1/Rate of H_2 dissociation (s)
17.35	0.183 ± 0.003	5.46 ± 0.09
27.64	0.120 ± 0.003	8.3 ± 0.2
63.27	0.052 ± 0.001	19.2 ± 0.4
85.55	0.037 ± 0.001	26.8 ± 0.7
115.75	0.029 ± 0.001	34 ± 1

Table 35: Observed rate constants of hydrogen exchange in d_4-methanol solutions of $[Ir(H)_2(IMes)(phth)_3]Cl$ at 285 K, at the various free phth concentrations given.

[free phth] (mM)	Rate of H_2 dissociation (s^{-1})	1/Rate of H_2 dissociation (s)
6.99	0.243 ± 0.007	4.1 ± 0.1
19.22	0.172 ± 0.004	5.8 ± 0.1
40.44	0.119 ± 0.005	8.4 ± 0.4
78.56	0.083 ± 0.005	12.1 ± 0.7
121.80	0.0643 ± 0.003	15.6 ± 0.7

A.2 Optimising SABRE of Pyridazine and Phthalazine

A.2.1 Calculating *J*-Couplings in an AA'XX' system

The Hamiltonian of an AA'XX' four-spin system has been solved by McConnell *et. al.*[203] Herein, pyridazine is used as the example AA'XX' system, and contains the four coupling constants $J_{AA'}$, J_{AX}, $J_{AX'}$, and $J_{XX'}$, shown in Figure 225.

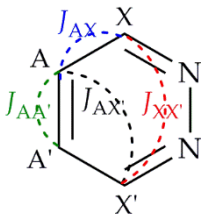

Figure 225: The four different coupling constants between the protons of pyridazine.

There are 10 distinct, allowed transitions between the spin states of an AA'XX' spin system, and they are labelled, in Figure 226, for the NCHC**H** ^{1}H NMR signal of pyridazine, which lies at δ 7.77. Their related energies are given in Table 36, where $K = J_{AA'} + J_{XX'}$, $L = J_{AX} - J_{AX'}$, $M = J_{AA'} - J_{XX'}$, and $N = J_{AX} + J_{AX'}$.

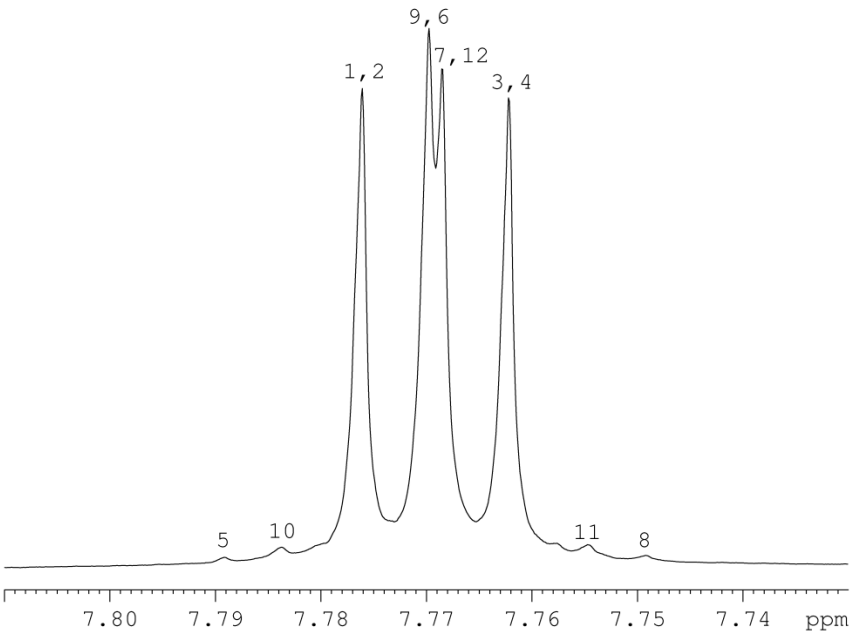

Figure 226: ^{1}H NMR resonance corresponding to NCHCH of free pyridazine.

Table 36: Energies for the given transitions in an AA'XX' coupling system.

Transition number	Transition energy
1	$\frac{1}{2}N$
3	$-\frac{1}{2}N$
5	$\frac{1}{2}K+\frac{1}{2}\sqrt{K^2+L^2}$
6	$-\frac{1}{2}K+\frac{1}{2}\sqrt{K^2+L^2}$
8	$-\frac{1}{2}K-\frac{1}{2}\sqrt{K^2+L^2}$
9	$\frac{1}{2}M+\frac{1}{2}\sqrt{M^2+L^2}$
10	$-\frac{1}{2}M+\frac{1}{2}\sqrt{M^2+L^2}$

Coupling values can be found by measuring the energy differences between specific transitions, in Hz. The transitions and formulae used are given below.

$$Transition\ 1-3=\frac{1}{2}N+\frac{1}{2}N=N$$

$$Transition\ 5-6=\frac{1}{2}K+\frac{1}{2}\sqrt{K^2+L^2}+\frac{1}{2}K-\frac{1}{2}\sqrt{K^2+L^2}=K$$

$$Transition\ 9-10=\frac{1}{2}M+\frac{1}{2}\sqrt{M^2+L^2}+\frac{1}{2}M-\frac{1}{2}\sqrt{M^2+L^2}=M$$

$$Transition\ 6-8=-\frac{1}{2}K+\frac{1}{2}\sqrt{K^2+L^2}+\frac{1}{2}K+\frac{1}{2}\sqrt{K^2+L^2}=\sqrt{K^2+L^2}$$

The energy differences between the transitions given above were calculated from the NCHC**H** ^{1}H NMR signal of pyridazine, simply by measuring the difference, in Hz, between the appropriate spectral lines.

$$(1)N=6.95=J_{AX}+J_{AX'}$$

$$(2)K=9.70=J_{AA'}+J_{XX'}$$

$$(3)M=7.00=J_{AA'}-J_{XX'}$$

$$\sqrt{K^2+L^2}=10.31;\ \sqrt{94.09+L^2}=10.31;\ 94.09+L^2=106.30;\ L^2=12.21;$$

$$(4)L=3.49=J_{AX}-J_{AX'}$$

The coupling constants were then calculated using these derived simultaneous equations.

$$(1) + (4): 6.95 + 3.49 = 2J_{AX} = 10.44;\ \boldsymbol{J_{AX} = 5.22}$$

$$(1): 5.22 + J_{AX'} = 6.95;\ \boldsymbol{J_{AX'} = 1.73}$$

$$(2) + (3): 9.70 + 7.00 = 2J_{AA'} = 16.70;\ \boldsymbol{J_{AA'} = 8.35}$$

$$(2): 8.35 + J_{XX'} = 9.70;\ \boldsymbol{J_{XX'} = 1.35}$$

The same method was used to calculate the four coupling constants in all AA'XX' coupling systems, including the phosphorus couplings in the tri-palladium species discussed in Chapter 5.

A.2.2 Data Obtained to Investigate the Effect of Temperature on Enhancements of Free Substrate using $[Ir(H)_2(IMes)(sub)_3]Cl$

SABRE of the free pyridazine and phthalazine in d_4-methanol solutions of $[Ir(H)_2(IMes)(pdz)_3]Cl$ and $[Ir(H)_2(IMes)(phth)_3]Cl$, containing 3 bar of *para*-H_2, was investigated at temperatures ranging from 273 to 323 K. To ensure that the sample was at the desired temperature when acquiring enhanced spectra, *para*-H_2 (3 bar) was added to the sample, which was submerged in a water bath set to the desired temperature. The sample was left in the water bath for 3 minutes prior to spectral acquisition. The enhancement factors of the ^1H NMR resonances of pyridazine with $[Ir(H)_2(IMes)(pdz)_3]Cl$, at different temperatures, are given in Table 37 and Table 38. The enhancement factors of the ^1H NMR resonances of phthalazine with $[Ir(H)_2(IMes)(phth)_3]Cl$, at different temperatures, are given in Table 39. Each enhancement factor is the average of 3 values that lay within 5 units. The errors were therefore calculated using the propagation of errors formulae discussed above.

Table 37: Calculated enhancement factors of the proton NMR resonances of free pdz in d_4-methanol, using the $[Ir(H)_2(IMes)(pdz)_3]Cl$ exchange catalyst, with 75.1 mM free pdz, at the various temperatures given.

Temperature (K)	Enhancement Factor		
	NC**H**	NCHC**H**	Total
273.2	−54 ± 1	−4 ± 1	−116 ± 3
293.2	−105 ± 1	−11 ± 1	−233 ± 3
303.2	−132 ± 1	−16 ± 1	−297 ± 3
313.2	−165 ± 1	−29 ± 1	−387 ± 3
323.2	−186 ± 1	−33 ± 1	−438 ± 3

Table 38: Calculated enhancement factors of the proton NMR resonances of free pdz in d_4-methanol, using the $[Ir(H)_2(IMes)(pdz)_3]Cl$ exchange catalyst, with 12.3 mM free pdz, at the various temperatures given.

Temperature (K)	Enhancement Factor		
	NC**H**	NCHC**H**	Total
273.2	−182 ± 1	−22 ± 1	−409 ± 3
293.2	−369 ± 1	−65 ± 1	−868 ± 3
303.2	−356 ± 1	−141 ± 1	−993 ± 3
313.2	−510 ± 1	−174 ± 1	−1368 ± 3
323.2	−574 ± 1	−190 ± 1	−1528 ± 3

Table 39: Calculated enhancement factors of the proton NMR resonances of free phth in d_4-methanol, using the $[Ir(H)_2(IMes)(phth)_3]Cl$ exchange catalyst, with 14.1 mM free phth, at the various temperatures given.

Temperature (K)	Enhancement Factor			
	NC**H**	NCHCC**H**	NCHCCHC**H**	Total
273.2	−84 ± 1	−10 ± 1	−4 ±1	−195 ± 3
293.2	−161 ± 1	−18 ± 1	−9 ± 1	−376 ± 3
303.2	−207 ± 1	−31 ± 1	−13 ± 1	−501 ± 3
313.2	−257 ± 1	−38 ± 1	−16 ± 1	−622 ± 3
323.2	−292 ± 1	−42 ± 1	−19 ± 1	−708 ± 3

A.2.3 Data Obtained to Investigate the Effect of Substrate Concentration on Enhancements of Free Substrate using $[Ir(H)_2(IMes)(sub)_3]Cl$

SABRE of the free pyridazine and phthalazine in d_4-methanol solutions of $[Ir(H)_2(IMes)(pdz)_3]Cl$ and $[Ir(H)_2(IMes)(phth)_3]Cl$, containing 3 bar of *para*-H_2, was investigated at different concentrations of free substrate. The concentration of free substrate was calculated from the ratio of free substrate:one bound substrate ligand, as the concentration of one bound substrate is equal to the concentration of iridium catalyst (5.2 mM). The ratio of free:bound substrate was calculated using the integral ratios of their corresponding ^{1}H NMR signals.

The enhancement factors of the ^{1}H NMR resonances of pyridazine with $[Ir(H)_2(IMes)(pdz)_3]Cl$, at different substrate concentrations, are given in Table 40. The enhancement factors of the ^{1}H NMR resonances of phthalazine with $[Ir(H)_2(IMes)(phth)_3]Cl$, at different substrate concentrations, are given in Table 41. Both tabulated data sets include values for the reciprocal total enhancements, the errors of which were calculated using the propagation of errors formulae discussed previously.

Table 40: Calculated enhancement factors of the proton NMR resonances of free pdz in d_4-methanol, using the $[Ir(H)_2(IMes)(pdz)_3]Cl$ exchange catalyst, at 298 K, with the various concentrations of free pdz given.

[free pdz] (mM)	Enhancement Factor			
	NC**H**	NCHC**H**	Total	1/Total
17.35	−379 ± 1	−37 ± 1	−832 ± 3	−0.001202 ± 0.000004
27.64	−112 ± 1	−15 ± 1	−254 ± 3	−0.00394 ± 0.00005
63.27	−35 ± 1	−8 ± 1	−85 ± 3	−0.0118 ± 0.0004
85.55	−21 ± 1	−5 ± 1	−53 ± 3	−0.019 ± 0.001
115.75	−12 ± 1	−3 ± 1	−29 ± 3	−0.034 ± 0.004

Table 41: Calculated enhancement factors of the proton NMR resonances of free phth in d_4-methanol, using the $[Ir(H)_2(IMes)(phth)_3]Cl$ exchange catalyst, at 298 K, with the various concentrations of free phth given.

[free phth] (mM)	Enhancement Factor				
	NC**H**	NCHCC**H**	NCHCCHC**H**	Total	1/Total
37.56	−65 ± 1	−13 ± 1	−3 ± 1	−164 ± 3	−0.0061 ± 0.0001
59.84	−32 ± 1	−7 ± 1	−3 ± 1	−85 ± 3	−0.0118 ± 0.0004
78.56	−25 ± 1	−4 ± 1	−1 ± 1	−60 ± 3	−0.0167 ± 0.0008
104.08	−18 ± 1	−2 ± 1	0 ± 1	−39 ± 3	−0.025 ± 0.002
121.80	−12 ± 1	−1 ± 1	0 ± 1	−27 ± 3	−0.037 ± 0.004

A.2.4 Data Obtained to Investigate the Effect of Catalyst Concentration on Enhancements and SNRs of Free Pyridazine using $[Ir(H)_2(IMes)(pdz)_3]Cl$

SABRE of the free pyridazine in d_4-methanol solutions of $[Ir(H)_2(IMes)(pdz)_3]Cl$, containing 3 bar of *para*-H_2, and 4.07 equivalents of free pyridazine, was investigated at different concentrations of catalyst. The initial sample was prepared by reacting a degassed d_4-methanol solution (0.5 mL) of [Ir(Cl)(COD)(IMes)] (2 mg, 3.12 μmol) with ~ 7 equivalents of pyridazine, and hydrogen (3 bar). Samples were then successively diluted 1.5-fold by removing 0.4 mL from the previous sample solution and adding 0.2 mL of d_4-methanol.

The enhancement factors of the ^1H NMR resonances of pyridazine, using different concentrations of $[Ir(H)_2(IMes)(pdz)_3]Cl$, are given in Table 42, alongside the SNRs, which were calculated using Bruker Topspin 3.1 software.

Table 42: Calculated enhancement factors and SNRs of the proton NMR resonances of free pdz in d_4-methanol, at 298 K, using the $[Ir(H)_2(IMes)(pdz)_3]Cl$ exchange catalyst at the concentrations given, with 4.07 equivalents of free pdz.

$[Ir(H)_2(IMes)(pdz)_3]Cl$ (mM)	Enhancement Factor			Signal to noise ratio		
	NC**H**	NCHC**H**	Total	NC**H**	NCHC**H**	Total
6.24	−232 ± 1	−24 ± 1	−511 ± 3	18840	3400	22240
4.16	−476 ± 1	−46 ± 1	−1044 ± 3	16800	3130	19930
2.77	−568 ± 1	−71 ± 1	−1278 ± 3	18400	5500	23910
1.23	−573 ± 1	−67 ± 1	−1280 ± 3	9120	1760	10880

A.2.5 Spin States in Pyridazine and Phthalazine

The different longitudinal spin states generated by SABRE of pyridazine and phthalazine can be selectively probed using the 'only *para*-H_2 spectroscopy' (OPSY) protocol.[209] The general pulse sequence uses a $\frac{\pi}{2}$ pulse, in the x-plane, to unselectively create all the different spin states, which are then detected following the application of a second $\frac{\pi}{2}$ pulse, in the y-plane. Different quantum coherences are selected by applying a pair of gradient pulses in between the $\frac{\pi}{2}$ pulses. A gradient pair with a ratio of 1:n selects n quantum coherence pathways, for example a gradient pair with a ratio of 1:0 selects zero quantum coherence pathways. Specific resonances can also be selectively probed, simply by selectively irradiating with radiowaves of the corresponding frequencies.

In pyridazine, there are four one-spin order combinations (I_z^A, $I_z^{A\prime}$, I_z^X, $I_z^{X\prime}$), four two-spin order combinations ($I_z^A I_z^{A\prime}$, $I_z^X I_z^{X\prime}$, $I_z^A I_z^X$, $I_z^A I_z^{X\prime}$), two three-spin order combinations ($I_z^{A\prime} I_z^A I_z^X$, $I_z^A I_z^X I_z^{X\prime}$) and one four-spin order term ($I_z^A I_z^{A\prime} I_z^X I_z^{X\prime}$). The four-spin order term is probed by selecting quadruple quantum coherence pathways, however this results in the loss of signals derived from the other coherence orders generated by the four-spin order term. The coherence orders generated from the four-spin order term are given below. Each is shown in one phase, but the nuclear spins can also exist in the opposite phase, thus each represents two coherences.

$$+\frac{1}{2}+\frac{1}{2}+\frac{1}{2}+\frac{1}{2}=QQ$$

$$+\frac{1}{2}+\frac{1}{2}+\frac{1}{2}-\frac{1}{2}=DQ$$

$$+\frac{1}{2}+\frac{1}{2}-\frac{1}{2}+\frac{1}{2}=DQ$$

$$+\frac{1}{2}-\frac{1}{2}+\frac{1}{2}+\frac{1}{2}=DQ$$

$$-\frac{1}{2}+\frac{1}{2}+\frac{1}{2}+\frac{1}{2}=DQ$$

$$+\frac{1}{2}+\frac{1}{2}-\frac{1}{2}-\frac{1}{2}=ZQ$$

$$+\frac{1}{2}-\frac{1}{2}-\frac{1}{2}+\frac{1}{2}=ZQ$$

$$+\frac{1}{2}-\frac{1}{2}+\frac{1}{2}-\frac{1}{2}=ZQ$$

There are six zero quantum coherences, eight double quantum coherences, and two quadruple quantum coherences, but when the gradient ratio is 1:4, only one pathway is probed using the OPSY protocol. The sensitivity is therefore one in sixteen, thus the signal intensity that results when probing the four-spin term is multiplied by sixteen to account for the loss of signal.

The coherence orders generated from each three-spin order term are given below. Again, the nuclear spins can also exist in the opposite phase, thus each represents two coherences.

$$+\frac{1}{2}+\frac{1}{2}+\frac{1}{2}=TQ$$

$$+\frac{1}{2}+\frac{1}{2}-\frac{1}{2}=SQ$$

$$+\frac{1}{2}-\frac{1}{2}+\frac{1}{2}=SQ$$

$$-\frac{1}{2}+\frac{1}{2}+\frac{1}{2}=SQ$$

There are two triple quantum coherences and six single quantum coherences, thus the sensitivity when probing three-spin order terms, with a 1:3 gradient ratio, is one in eight, and the signal intensities are multiplied by eight to account for this.

The coherence orders generated from each two-spin order term are given below. Again, the nuclear spins can also exist in the opposite phase, thus each represents two coherences.

$$+\frac{1}{2}+\frac{1}{2}=DQ$$

$$+\frac{1}{2}-\frac{1}{2}=ZQ$$

There are two double quantum coherences and two zero quantum coherences, thus the sensitivity when probing two-spin order terms with a gradient ratio of 1:2 is one in four, and the signal intensities are multiplied by four to account for this. The 8 double quantum terms in the four-spin order also contribute to the NMR signal, therefore 8x the amplitude of the four-spin order is subtracted.

The coherence orders generated from each one-spin order term are given below.

$$+\frac{1}{2}=SQ$$

There are two single quantum coherences, thus the sensitivity is one in two, and the signal intensities are multiplied by two to account for this. The 6 single quantum terms in the three-spin order also contribute to the NMR signal, therefore 6x the amplitude of the three-spin orders is subtracted.

In phthalazine, the coupling between the first and second rings is negligible, and the two rings can be considered as separate coupling systems. There are six one-spin order combinations (I_z^A, $I_z^{A\prime}$, I_z^M, $I_z^{M\prime}$, I_z^X, $I_z^{X\prime}$), four two-spin order combinations ($I_z^A I_z^{A\prime}$, $I_z^M I_z^{M\prime}$, $I_z^A I_z^M$, $I_z^A I_z^{M\prime}$), two three-spin order combinations ($I_z^{A\prime} I_z^A I_z^M$, $I_z^A I_z^M I_z^{M\prime}$) and one four-spin order term ($I_z^A I_z^{A\prime} I_z^M I_z^{M\prime}$). The quantum coherences generated from each term are identical to the terms in pyridazine, and the signals were multiplied to the same extent; 2, 4, 8, 16 times for the one-spin, two-spin, three-spin, and four-spin terms.

A.2.6 Data Obtained to Investigate the Effect of PTF on Enhancements of Free Substrate using $[Ir(H)_2(IMes)(sub)_3]Cl$

To investigate the effect of PTF on the enhancement levels of specific terms, d_4-methanol solutions of $[Ir(H)_2(IMes)(sub)_3]Cl$, containing ~ 5 equivalents of free *N*-

heterocycle were used. The PTF experienced by the sample was increased from 0 (Earth's field = ~ 0.5 G) to 140 G in 10 G intervals.

A.2.6.1 Pyridazine

The data obtained for the selectively excited NC**H** and NCHC**H** proton resonances of free pyridazine are given in Table 43 and Table 44.

Table 43: Enhancements in the NC<u>H</u> resonance of free pdz in d_4-methanol, at 298 K, using the $[Ir(H)_2(IMes)(pdz)_3]Cl$ exchange catalyst (5.2 mM), with 5 equivalents of free pdz, as a function of PTF.

Field (G)	Enhancement Factor		Correction for Receiver Gain (/1)
	NC**H**	Total	
0	46 ± 1	92 ± 2	92 ± 2
10	47 ± 1	93 ± 2	93 ± 2
20	66 ± 1	132 ± 2	132 ± 2
30	90 ± 1	179 ± 2	179 ± 2
40	88 ± 1	176 ± 2	176 ± 2
50	83 ± 1	165 ± 2	165 ± 2
60	126 ± 1	253 ± 2	253 ± 2
65	142 ± 1	284 ± 2	284 ± 2
70	114 ± 1	228 ± 2	228 ± 2
80	77 ± 1	154 ± 2	154 ± 2
90	73 ± 1	146 ± 2	146 ± 2
100	73 ± 1	146 ± 2	146 ± 2
110	51 ± 1	102 ± 2	102 ± 2
120	46 ± 1	93 ± 2	93 ± 2
130	34 ± 1	68 ± 2	68 ± 2
140	33 ± 1	66 ± 2	66 ± 2

Table 44: Enhancements in the NCHC<u>H</u> resonance of free pdz in d_4-methanol, at 298 K, using the $[Ir(H)_2(IMes)(pdz)_3]Cl$ exchange catalyst (5.2 mM), with 5 equivalents of free pdz, as a function of PTF.

Field (G)	Enhancement Factor		Correction for Receiver Gain (/1)
	NCHC**H**	Total	
0	28 ± 1	56 ± 2	56 ± 2

10	25 ± 1	50 ± 2	50 ± 2
20	30 ± 1	59 ± 2	59 ± 2
30	50 ± 1	100 ± 2	100 ± 2
40	40 ± 1	79 ± 2	79 ± 2
50	50 ± 1	100 ± 2	100 ± 2
60	105 ± 1	209 ± 2	209 ± 2
65	119 ± 1	238 ± 2	238 ± 2
70	98 ± 1	195 ± 2	195 ± 2
80	49 ± 1	98 ± 2	98 ± 2
90	61 ± 1	122 ± 2	122 ± 2
100	66 ± 1	132 ± 2	132 ± 2
110	39 ± 1	77 ± 2	77 ± 2
120	30 ± 1	60 ± 2	60 ± 2
130	23 ± 1	45 ± 2	45 ± 2
140	6 ± 1	12 ± 2	12 ± 2

The data obtained for the single spin, two spin, NCHC**H** double quantum, three spin, and four spin terms of free pyridazine are given in Table 45, Table 46, Table 47, Table 48, and Table 49, respectively.

Table 45: Enhancements in the single spin terms of free pdz in d_4-methanol, at 298 K, using the $[Ir(H)_2(IMes)(pdz)_3]Cl$ exchange catalyst (5.2 mM), with 5 equivalents of free pdz, as a function of PTF.

Field (G)	**Enhancement Factor**			**Correction for observation of 1 of 2 terms**	**Subtraction of 6x TQ**	**Correction for Receiver Gain (/1)**
	NC**H**	NCHC**H**	Total			
0	45 ± 2	18 ± 2	127 ± 6	250 ± 10	170 ± 10	170 ± 10
10	42 ± 2	12 ± 2	110 ± 6	220 ± 10	140 ± 10	140 ± 10
20	59 ± 2	4 ± 2	127 ± 6	250 ± 10	210 ± 10	210 ± 10
30	79 ± 2	17 ± 2	192 ± 6	380 ± 10	320 ± 10	320 ± 10
40	78 ± 2	15 ± 2	185 ± 6	370 ± 10	280 ± 10	280 ± 10
50	75 ± 2	29 ± 2	208 ± 6	420 ± 10	330 ± 10	330 ± 10
60	114 ± 2	75 ± 2	377 ± 6	750 ± 10	700 ± 10	700 ± 10
70	102 ± 2	66 ± 2	336 ± 6	670 ± 10	650 ± 10	650 ± 10
80	68 ± 2	36 ± 2	208 ± 6	420 ± 10	370 ± 10	370 ± 10

90	59 ± 2	45 ± 2	208 ± 6	420 ± 10	400 ± 10	400 ± 10
100	62 ± 2	49 ± 2	222 ± 6	440 ± 10	420 ± 10	420 ± 10
110	47 ± 2	28 ± 2	148 ± 6	300 ± 10	260 ± 10	260 ± 10
120	40 ± 2	23 ± 2	126 ± 6	250 ± 10	130 ± 10	130 ± 10
130	30 ± 2	16 ± 2	92 ± 6	180 ± 10	150 ± 10	150 ± 10
140	31 ± 2	3 ± 2	66 ± 6	130 ± 10	120 ± 10	120 ± 10

Table 46: Enhancements in the two spin terms of free pdz in d_4-methanol, at 298 K, using the $[Ir(H)_2(IMes)(pdz)_3]Cl$ exchange catalyst (5.2 mM), with 5 equivalents of free pdz, as a function of PTF.

Field (G)	**Enhancement Factor**			**Correction for observation of 1 of 4 terms**	**Correction for Receiver Gain (/16)**	**Subtraction of 8x QQ**
	NC**H**	NCHC**H**	Total			
0	87 ± 7	97 ± 8	370 ± 20	1480 ± 80	92 ± 5	92 ± 5
10	83 ± 7	93 ± 8	350 ± 20	1410 ± 80	88 ± 5	78 ± 5
20	111 ± 7	126 ± 8	470 ± 20	1900 ± 80	119 ± 5	108 ± 5
30	159 ± 7	182 ± 8	680 ± 20	2730 ± 80	170 ± 5	162 ± 5
40	109 ± 7	126 ± 8	470 ± 20	1880 ± 80	118 ± 5	91 ± 5
50	52 ± 7	63 ± 8	230 ± 20	920 ± 80	57 ± 5	10 ± 5
60	19 ± 7	24 ± 8	90 ± 20	350 ± 80	22 ± 5	0 ± 5
70	71 ± 7	82 ± 8	310 ± 20	1220 ± 80	76 ± 5	69 ± 5
80	26 ± 7	27 ± 8	100 ± 20	420 ± 80	26 ± 5	0 ± 5
90	19 ± 7	20 ± 8	80 ± 20	310 ± 80	20 ± 5	0 ± 5
100	33 ± 7	40 ± 8	150 ± 20	590 ± 80	37 ± 5	25 ± 5
110	13 ± 7	14 ± 8	50 ± 20	220 ± 80	14 ± 5	0 ± 5
120	32 ± 7	38 ± 8	150 ± 20	560 ± 80	35 ± 5	0 ± 5
130	9 ± 7	7 ± 8	30 ± 20	130 ± 80	8 ± 5	0 ± 5
140	33 ± 7	37 ± 8	140 ± 20	560 ± 80	35 ± 5	22 ± 5

Table 47: Enhancements in the NCHC<u>H</u> double quantum resonances of free pdz in d_4-methanol, at 298 K, using the $[Ir(H)_2(IMes)(pdz)_3]Cl$ exchange catalyst (5.2 mM), with 5 equivalents of free pdz, as a function of PTF.

Field (G)	**Enhancement Factor**		**Correction for observation of 1 of 4 terms**	**Correction for Receiver Gain (/16)**
	NCHC**H**	Total		

0	3.7 ± 0.2	7.4 ± 0.4	30 ± 2	1.9 ± 0.1
10	3.5 ± 0.2	7.0 ± 0.4	28 ± 2	1.8 ± 0.1
20	5.3 ± 0.2	10.7 ± 0.4	43 ± 2	2.7 ± 0.1
30	8.6 ± 0.2	17.1 ± 0.4	68 ± 2	4.3 ± 0.1
40	8.8 ± 0.2	17.6 ± 0.4	70 ± 2	4.4 ± 0.1
50	8.9 ± 0.2	17.8 ± 0.4	71 ± 2	4.5 ± 0.1
60	7.4 ± 0.2	14.8 ± 0.4	59 ± 2	3.7 ± 0.1
70	5.3 ± 0.2	10.6 ± 0.4	42 ± 2	2.7 ± 0.1
80	0.9 ± 0.2	1.8 ± 0.4	7 ± 2	0.5 ± 0.1
90	2.2 ± 0.2	4.4 ± 0.4	18 ± 2	1.1 ± 0.1
100	3.8 ± 0.2	7.6 ± 0.4	30 ± 2	1.9 ± 0.1
110	1.2 ± 0.2	2.3 ± 0.4	9 ± 2	0.58 ± 0.1
120	0.8 ± 0.2	1.6 ± 0.4	6 ± 2	0.4 ± 0.1
130	2.4 ± 0.2	4.7 ± 0.4	19 ± 2	1.18 ± 0.1
140	0.6 ± 0.2	1.2 ± 0.4	5 ± 2	0.3 ± 0.1

Table 48: Enhancements in the three spin terms of free pdz in d_4-methanol, at 298 K, using the $[Ir(H)_2(IMes)(pdz)_3]Cl$ exchange catalyst (5.2 mM), with 5 equivalents of free pdz, as a function of PTF.

Field (G)	**Enhancement Factor**			**Correction for observation of 1 of 8 terms**	**Correction for Receiver Gain (/912)**
	NC**H**	NCHC**H**	Total		
0	500 ± 70	270 ± 70	1500 ± 200	6100 ± 800	13 ± 2
10	420 ± 70	290 ± 70	1400 ± 200	5700 ± 800	13 ± 2
20	330 ± 70	100 ± 70	900 ± 200	3400 ± 800	8 ± 2
30	340 ± 70	250 ± 70	1200 ± 200	4700 ± 800	10 ± 2
40	120 ± 70	730 ± 70	1700 ± 200	6800 ± 800	15 ± 2
50	200 ± 70	640 ± 70	1700 ± 200	6700 ± 800	15 ± 2
60	90 ± 70	410 ± 70	1000 ± 200	4000 ± 800	9 ± 2
70	50 ± 70	130 ± 70	300 ± 200	1400 ± 800	3 ± 2
80	240 ± 70	160 ± 70	800 ± 200	3200 ± 800	7 ± 2
90	20 ± 70	90 ± 70	200 ± 200	900 ± 800	2 ± 2
100	170 ± 70	40 ± 70	400 ± 200	1700 ± 800	4 ± 2
110	110 ± 70	280 ± 70	800 ± 200	3100 ± 800	7 ± 2
120	710 ± 70	490 ± 70	2400 ± 200	9600 ± 800	21 ± 2
130	170 ± 70	120 ± 70	600 ± 200	2300 ± 800	5 ± 2

140	40 ± 70	60 ± 70	200 ± 200	800 ± 800	2 ± 2

Table 49: Enhancements in the four spin terms of free pdz in d_4-methanol, at 298 K, using the $[Ir(H)_2(IMes)(pdz)_3]Cl$ exchange catalyst (5.2 mM), with 5 equivalents of free pdz, as a function of PTF.

Field (G)	**Enhancement Factor**			**Correction for observation of 1 of 16 terms**	**Correction for Receiver Gain (/2050)**
	NC**H**	NCHC**H**	Total		
0	-	-	-	-	-
10	35 ± 2	50 ± 4	169 ± 9	2700 ± 100	1.32 ± 0.05
20	35 ± 2	48 ± 4	165 ± 9	2600 ± 100	1.29 ± 0.05
30	29 ± 2	42 ± 4	141 ± 9	2300 ± 100	1.10 ± 0.05
40	85 ± 2	129 ± 4	428 ± 9	6800 ± 100	3.34 ± 0.05
50	155 ± 2	230 ± 4	764 ± 9	12200 ± 100	5.97 ± 0.05
60	76 ± 2	114 ± 4	381 ± 9	6100 ± 100	2.97 ± 0.05
70	27 ± 2	35 ± 4	123 ± 9	2000 ± 100	0.96 ± 0.05
80	88 ± 2	126 ± 4	428 ± 9	6800 ± 100	3.34 ± 0.05
90	71 ± 2	110 ± 4	363 ± 9	5800 ± 100	2.83 ± 0.05
100	39 ± 2	56 ± 4	190 ± 9	3000 ± 100	1.48 ± 0.05
110	60 ± 2	89 ± 4	297 ± 9	4800 ± 100	2.32 ± 0.05
120	133 ± 2	192 ± 4	648 ± 9	10400 ± 100	5.06 ± 0.05
130	88 ± 2	132 ± 4	439 ± 9	7000 ± 100	3.43 ± 0.05
140	44 ± 2	63 ± 4	214 ± 9	3400 ± 100	1.67 ± 0.05

A.2.6.2 Phthalazine

The data obtained for the selectively excited NC**H,** NCHCC**H**, and NCHCCHC**H** proton resonances of free phthalazine are given in Table 50, Table 51, and Table 52 respectively.

Table 50: Enhancements in the NC<u>H</u> resonance of free phth in d_4-methanol, at 298 K, using the $[Ir(H)_2(IMes)(phth)_3]Cl$ exchange catalyst (5.2 mM), with 5 equivalents of free phth, as a function of PTF.

Field (G)	**Enhancement Factor**		**Correction for Receiver Gain (/1)**
	NC**H**	Total	
0	43 ± 2	86 ± 4	86 ± 4

10	48 ± 2	96 ± 4	96 ± 4
20	45 ± 2	90 ± 4	90 ± 4
30	64 ± 2	129 ± 4	129 ± 4
40	88 ± 2	176 ± 4	176 ± 4
50	143 ± 2	287 ± 4	287 ± 4
60	217 ± 2	433 ± 4	433 ± 4
65	222 ± 2	443 ± 4	443 ± 4
70	201 ± 2	402 ± 4	402 ± 4
80	133 ± 2	266 ± 4	266 ± 4
90	76 ± 2	153 ± 4	153 ± 4
100	65 ± 2	131 ± 4	131 ± 4
110	48 ± 2	96 ± 4	96 ± 4
120	45 ± 2	90 ± 4	90 ± 4
130	46 ± 2	93 ± 4	93 ± 4
140	44 ± 2	88 ± 4	88 ± 4

Table 51: Enhancements in the NCHCC<u>H</u> resonance of free phth in d_4-methanol, at 298 K, using the $[Ir(H)_2(IMes)(phth)_3]Cl$ exchange catalyst (5.2 mM), with 5 equivalents of free phth, as a function of PTF.

Field (G)	**Enhancement Factor**		**Correction for Receiver Gain (/1)**
	NCHCC**H**	Total	
0	3.0 ± 0.1	5.9 ± 0.2	5.9 ± 0.2
10	3.4 ± 0.1	6.8 ± 0.2	6.8 ± 0.2
20	3.8 ± 0.1	7.5 ± 0.2	7.5 ± 0.2
30	4.4 ± 0.1	8.8 ± 0.2	8.8 ± 0.2
40	6.5 ± 0.1	13.0 ± 0.2	13.0 ± 0.2
50	11.7 ± 0.1	23.3 ± 0.2	23.3 ± 0.2
60	17.2 ± 0.1	34.5 ± 0.2	34.5 ± 0.2
65	18.7 ± 0.1	37.4 ± 0.2	37.4 ± 0.2
70	15.7 ± 0.1	31.5 ± 0.2	31.5 ± 0.2
80	8.5 ± 0.1	17.0 ± 0.2	17.0 ± 0.2
90	4.4 ± 0.1	8.9 ± 0.2	8.9 ± 0.2
100	2.7 ± 0.1	5.4 ± 0.2	5.4 ± 0.2
110	2.0 ± 0.1	4.0 ± 0.2	4.0 ± 0.2
120	1.9 ± 0.1	3.8 ± 0.2	3.8 ± 0.2

130	2.0 ± 0.1	4.0 ± 0.2	4.0 ± 0.2
140	1.6 ± 0.1	3.3 ± 0.2	3.3 ± 0.2

Table 52: Enhancements in the NCHCCHCH resonance of free phth in d_4-methanol, at 298 K, using the $[Ir(H)_2(IMes)(phth)_3]Cl$ exchange catalyst (5.2 mM), with 5 equivalents of free phth, as a function of PTF.

Field (G)	**Enhancement Factor**		**Correction for Receiver Gain (/1)**
	NCHCCHC***H***	Total	
0	2.1 ± 0.1	4.2 ± 0.2	4.2 ± 0.2
10	2.3 ± 0.1	4.6 ± 0.2	4.6 ± 0.2
20	2.3 ± 0.1	4.6 ± 0.2	4.6 ± 0.2
30	2.7 ± 0.1	5.5 ± 0.2	5.5 ± 0.2
40	4.3 ± 0.1	8.6 ± 0.2	8.6 ± 0.2
50	9.4 ± 0.1	18.8 ± 0.2	18.8 ± 0.2
60	14.3 ± 0.1	28.5 ± 0.2	28.5 ± 0.2
65	15.3 ± 0.1	30.5 ± 0.2	30.5 ± 0.2
70	11.8 ± 0.1	23.5 ± 0.2	23.5 ± 0.2
80	5.7 ± 0.1	11.5 ± 0.2	11.5 ± 0.2
90	2.6 ± 0.1	5.2 ± 0.2	5.2 ± 0.2
100	1.9 ± 0.1	3.9 ± 0.2	3.9 ± 0.2
110	1.5 ± 0.1	3.0 ± 0.2	3.0 ± 0.2
120	1.6 ± 0.1	3.1 ± 0.2	3.1 ± 0.2
130	1.8 ± 0.1	3.5 ± 0.2	3.5 ± 0.2
140	1.4 ± 0.1	2.8 ± 0.2	2.8 ± 0.2

The data obtained for the single quantum, and double quantum, coherence-derived resonances of free phthalazine are given in Table 53, and Table 54.

Table 53: Enhancements in the single quantum resonances of free phth in d_4-methanol, at 298 K, using the $[Ir(H)_2(IMes)(phth)_3]Cl$ exchange catalyst (5.2 mM), with 5 equivalents of free phth, as a function of PTF.

Field (G)	**Enhancement Factor**				**Correction for observation of 1 of 2 terms**	**Correction for Receiver Gain (/1)**
	NC**H**	NCHCC**H**	NCHCCHC**H**	Total		
0	29.0 ± 0.6	2.9 ± 0.2	0.8 ± 0.1	65 ± 1	130 ± 2	130 ± 2

10	37.2 ± 0.6	4.0 ± 0.2	0.9 ± 0.1	84 ± 1	168 ± 2	168 ± 2
20	36.7 ± 0.6	4.3 ± 0.2	0.8 ± 0.1	84 ± 1	167 ± 2	167 ± 2
30	45.1 ± 0.6	5.7 ± 0.2	1.8 ± 0.1	105 ± 1	211 ± 2	211 ± 2
40	55.6 ± 0.6	8.2 ± 0.2	4.4 ± 0.1	136 ± 1	273 ± 2	273 ± 2
50	90.0 ± 0.6	14.9 ± 0.2	11.2 ± 0.1	232 ± 1	464 ± 2	464 ± 2
60	130.8 ± 0.6	22.0 ± 0.2	17.1 ± 0.1	340 ± 1	679 ± 2	679 ± 2
65	161.4 ± 0.6	27.0 ± 0.2	20.0 ± 0.1	417 ± 1	833 ± 2	833 ± 2
70	126.1 ± 0.6	20.0 ± 0.2	14.0 ± 0.1	320 ± 1	640 ± 2	640 ± 2
80	92.0 ± 0.6	12.0 ± 0.2	7.4 ± 0.1	223 ± 1	446 ± 2	446 ± 2
90	50.1 ± 0.6	5.3 ± 0.2	3.0 ± 0.1	117 ± 1	234 ± 2	234 ± 2
100	40.5 ± 0.6	3.5 ± 0.2	2.2 ± 0.1	93 ± 1	185 ± 2	185 ± 2
110	43.7 ± 0.6	3.0 ± 0.2	1.9 ± 0.1	97 ± 1	194 ± 2	194 ± 2
120	42.7 ± 0.6	2.6 ± 0.2	1.4 ± 0.1	93 ± 1	187 ± 2	187 ± 2
130	32.1 ± 0.6	2.0 ± 0.2	0.5 ± 0.1	69 ± 1	139 ± 2	139 ± 2
140	31.3 ± 0.6	1.9 ± 0.2	0.4 ± 0.1	67 ± 1	134 ± 2	134 ± 2

Table 54: Enhancements in the double quantum resonances of free phth in d_4-methanol, at 298 K, using the $[Ir(H)_2(IMes)(phth)_3]Cl$ exchange catalyst (5.2 mM), with 5 equivalents of free phth, as a function of PTF.

Field (G)	**Enhancement Factor**				**Correction for observation of 1 of 4 terms**	**Correction for Receiver Gain (/128)**
	NC**H**	NCHCC**H**	NCHCCHC**H**	Total		
0	13 ± 1	105 ± 8	99 ± 8	440 ± 30	1700 ± 100	13.6 ± 0.8
10	16 ± 1	105 ± 8	99 ± 8	440 ± 30	1800 ± 100	13.8 ± 0.8
20	17 ± 1	112 ± 8	106 ± 8	470 ± 30	1900 ± 100	14.7 ± 0.8
30	15 ± 1	107 ± 8	107 ± 8	460 ± 30	1800 ± 100	14.3 ± 0.8
40	17 ± 1	127 ± 8	151 ± 8	590 ± 30	2400 ± 100	18.4 ± 0.8
50	29 ± 1	137 ± 8	209 ± 8	750 ± 30	3000 ± 100	23.4 ± 0.8
60	72 ± 1	152 ± 8	254 ± 8	960 ± 30	3800 ± 100	29.9 ± 0.8
65	119 ± 1	173 ± 8	291 ± 8	1170 ± 30	4700 ± 100	36.4 ± 0.8
70	97 ± 1	133 ± 8	203 ± 8	870 ± 30	3500 ± 100	27.0 ± 0.8
80	73 ± 1	103 ± 8	134 ± 8	620 ± 30	2500 ± 100	19.4 ± 0.8
90	34 ± 1	84 ± 8	96 ± 8	430 ± 30	1700 ± 100	13.4 ± 0.8
100	24 ± 1	61 ± 8	72 ± 8	310 ± 30	1300 ± 100	9.8 ± 0.8
110	18 ± 1	59 ± 8	69 ± 8	290 ± 30	1200 ± 100	9.1 ± 0.8

120	16 ± 1	59 ± 8	66 ± 8	280 ± 30	1100 ± 100	8.7 ± 0.8
130	15 ± 1	67 ± 8	67 ± 8	300 ± 30	1200 ± 100	9.3 ± 0.8
140	20 ± 1	87 ± 8	87 ± 8	390 ± 30	1600 ± 100	12.2 ± 0.8

A.2.7 Derivation of the Formula used to Calculate the Observed Rate of Polarisation Build-up (k_{obs})

The equilibrium between the unpolarised and hyperpolarised substrate is represented by that shown in Figure 227, where k_f is the observed rate constant of the forward reaction, and k_b is the observed rate constant of the backward reaction, which is equal to the T_1 value of the resonance.

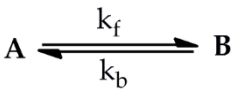

Figure 227: Equilibrium between unpolarised substrate (A) and polarised substrate (B).

At equilibrium, the concentration of species A_t and A_e are given by the formulae below, where $[A_t]$ is the concentration of A at time t, $[A_0]$ is the concentration of A at time $t = 0$, $[A_e]$ is the concentration of A at equilibrium, $[B]_t$ is the concentration of B at time t, and $[B_e]$ is the concentration of B at equilibrium.

$$[A_t] = [A_0] - [B_t]$$

$$[A_e] = [A_0] - [B_e]$$

Solving the equilibria for the concentration of B gives the following formulae.

$$\frac{\delta[B_t]}{\delta t} = k_f[A_t] - k_b[B_t]$$

$$\frac{\delta[B_t]}{\delta t} = k_f([A_0] - [B_t]) - k_b[B_t]$$

$$(\mathbf{1})\ \boldsymbol{\frac{\delta[B_t]}{\delta t} = k_f[A_0] - k_f[B_t] - k_b[B_t]}$$

Furthermore, the equilibrium constant, K is given by the formulae below.

$$K = \frac{k_f}{k_b} = \frac{[B_e]}{[A_e]}$$

$$[B_e] = \frac{k_f[A_e]}{k_b} = \frac{k_f([A_0] - [B_e])}{k_b} = \frac{k_f[A_0] - k_f[B_e]}{k_b}$$

$$[B_e]k_b + [B_e]k_f = k_f[A_0];\ [B_e](k_b + k_f) = k_f[A_0]$$

$$(\mathbf{2})[\boldsymbol{B_e}] = \frac{\boldsymbol{k_f[A_0]}}{\boldsymbol{k_b + k_f}}$$

Substituting (**2**) into (**1**) gives the following:

$$\frac{\delta[B_t]}{\delta t} = [B_e](k_f + k_b) - [B_t](k_f + k_b) = ([B_e] - [B_t])(k_f + k_b)$$

This can then be solved to find $[B_t]$ by taking integrals:

$$\int \frac{1}{[B_e] - [B_t]} \delta[B_t] = \int (k_f + k_b)\, \delta t$$

$$-\ln([B_e] - [B_t]) = (k_f + k_b)t + c$$

When $t = 0$, $[B_0] = 0$, therefore $c = -ln[B_e]$

$$-\ln([B_e] - [B_t]) = (k_f + k_b)t - ln[B_e]$$

$$ln\frac{[B_e]}{[B_e] - [B_t]} = (k_f + k_b)t;\ [B_e] - [B_t] = \frac{[B_e]}{exp^{(k_f + k_b)t}}$$

$$[\boldsymbol{B_t}] = [\boldsymbol{B_e}] - \frac{[\boldsymbol{B_e}]}{\boldsymbol{exp^{(k_f + k_b)t}}}$$

A.2.8 Data Obtained to Investigate the Effect of the PTT on Enhancements of Free Substrate using $[Ir(H)_2(IMes)(sub)_3]Cl$

To investigate the effect of the PTT on the enhancement levels of specific terms, d_4-methanol solutions of $[Ir(H)_2(IMes)(sub)_3]Cl$, containing ~ 5 equivalents of free *N*-heterocycle were prepared. The optimum PTFs were used to probe the different spin states, in order to achieve the best enhancement levels. The *para*-H_2 bubbling time was increased from 1.25 to 7.5 s in 1.25 s intervals, and then increased from 7.5 to 30 s in 2.5 s intervals.

A.2.8.1 Pyridazine

The data obtained for the selectively excited NC**H** and NCHC**H** proton resonances of free pyridazine are given in Table 55 and Table 56.

Table 55: Enhancements in the NC<u>H</u> resonance of free pdz in d_4-methanol, at 298 K and 65 G, using the $[Ir(H)_2(IMes)(pdz)_3]Cl$ exchange catalyst (5.2 mM), with 5 equivalents of free pdz, as a function of PTT.

PTT (s)	Enhancement Factor		Correction for Receiver Gain (/1)
	NC**H**	Total	
1.25	122 ± 2	243 ± 4	243 ± 4
2.5	165 ± 2	330 ± 4	330 ± 4
3.75	191 ± 2	381 ± 4	381 ± 4
5	210 ± 2	420 ± 4	420 ± 4
6.25	226 ± 2	452 ± 4	452 ± 4
7.5	243 ± 2	485 ± 4	485 ± 4
10	258 ± 2	515 ± 4	515 ± 4
12.5	272 ± 2	544 ± 4	544 ± 4
15	274 ± 2	549 ± 4	549 ± 4
17.5	273 ± 2	546 ± 4	546 ± 4
20	274 ± 2	548 ± 4	548 ± 4
30	274 ± 2	547 ± 4	547 ± 4

Table 56: Enhancements in the NCHC<u>H</u> resonance of free pdz in d_4-methanol, at 298 K and 65 G, using the $[Ir(H)_2(IMes)(pdz)_3]Cl$ exchange catalyst (5.2 mM), with 5 equivalents of free pdz, as a function of PTT.

PTT (s)	Enhancement Factor		Correction for Receiver Gain (/1)
	NCHC**H**	Total	
1.25	32 ± 1	63 ± 2	63 ± 2
2.5	49 ± 1	97 ± 2	97 ± 2
3.75	61 ± 1	123 ± 2	123 ± 2
5	68 ± 1	136 ± 2	136 ± 2
6.25	76 ± 1	152 ± 2	152 ± 2
7.5	83 ± 1	165 ± 2	165 ± 2
10	95 ± 1	189 ± 2	189 ± 2
12.5	101 ± 1	203 ± 2	203 ± 2

15	110 ± 1	220 ± 2	220 ± 2
17.5	115 ± 1	229 ± 2	229 ± 2
20	119 ± 1	238 ± 2	238 ± 2
22.5	124 ± 1	248 ± 2	248 ± 2
25	126 ± 1	253 ± 2	253 ± 2
30	130 ± 1	261 ± 2	261 ± 2

The plots and data obtained for the single and two spin terms are given in Figure 228, Table 57, and Table 58.

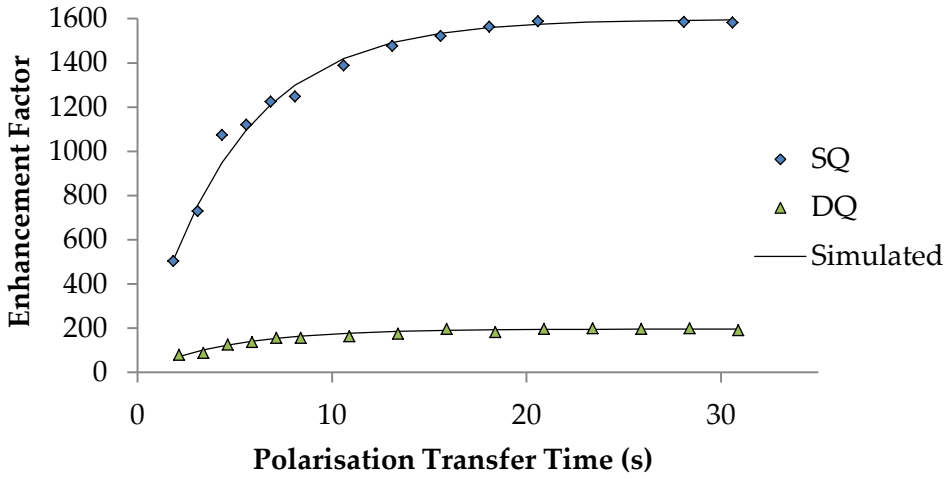

Figure 228: Plot of enhancement factors of the single quantum (SQ) and double quantum (DQ) coherence-derived resonances of free pdz in d_4-methanol, at 298 K, using the $[Ir(H)_2(IMes)(pdz)_3]Cl$ exchange catalyst (5.2 mM), with 5 equivalents of free pdz, as a function of PTT.

Table 57: Enhancements in the single spin terms of free pdz in d_4-methanol, at 298 K and 65 G, using the $[Ir(H)_2(IMes)(pdz)_3]Cl$ exchange catalyst (5.2 mM), with 5 equivalents of free pdz, as a function of PTT.

PTT (s)	**Enhancement Factor**			**Correction for observation of 1 of 2 terms**	**Correction for Receiver Gain (/1)**	**Subtraction of and 6x TQ**
	NC**H**	NCHC**H**	Total			
1.25	93 ± 2	59 ± 1	305 ± 4	611 ± 8	611 ± 8	503 ± 8
2.5	134 ± 2	85 ± 1	439 ± 4	879 ± 8	879 ± 8	729 ± 8
3.75	185 ± 2	131 ± 1	632 ± 4	1266 ± 8	1266 ± 8	1074 ± 8
5	194 ± 2	140 ± 1	669 ± 4	1337 ± 8	1337 ± 8	1121 ± 8
6.25	212 ± 2	153 ± 1	730 ± 4	1459 ± 8	1459 ± 8	1225 ± 8
7.5	214 ± 2	158 ± 1	744 ± 4	1488 ± 8	1488 ± 8	1248 ± 8

10	232 ± 2	179 ± 1	820 ± 4	1641 ± 8	1641 ± 8	1389 ± 8
12.5	247 ± 2	188 ± 1	870 ± 4	1741 ± 8	1741 ± 8	1477 ± 8
15	251 ± 2	195 ± 1	893 ± 4	1785 ± 8	1785 ± 8	1521 ± 8
17.5	256 ± 2	204 ± 1	919 ± 4	1839 ± 8	1839 ± 8	1563 ± 8
20	262 ± 2	202 ± 1	929 ± 4	1858 ± 8	1858 ± 8	1588 ± 8
22.5	262 ± 2	207 ± 1	939 ± 4	1877 ± 8	1877 ± 8	1601 ± 8
25	268 ± 2	214 ± 1	964 ± 4	1927 ± 8	1927 ± 8	1651 ± 8
27.5	258 ± 2	207 ± 1	931 ± 4	1861 ± 8	1861 ± 8	1585 ± 8
30	261 ± 2	205 ± 1	933 ± 4	1865 ± 8	1865 ± 8	1583 ± 8

Table 58: Enhancements in the two spin terms of free pdz in d_4-methanol, at 298 K and 30 G, using the $[Ir(H)_2(IMes)(pdz)_3]Cl$ exchange catalyst (5.2 mM), with 5 equivalents of free pdz, as a function of PTT.

PTT (s)	**Enhancement Factor**			**Correction for observation of 1 of 4 terms**	**Correction for Receiver Gain (/16)**	**Subtraction of 8x QQ**
	NC**H**	NCHC**H**	Total			
1.25	122 ± 6	136 ± 7	520 ± 20	2060 ± 80	129 ± 5	79 ± 5
2.5	158 ± 6	176 ± 7	670 ± 20	2670 ± 80	167 ± 5	89 ± 5
3.75	214 ± 6	238 ± 7	900 ± 20	3620 ± 80	226 ± 5	126 ± 5
5	239 ± 6	268 ± 7	1010 ± 20	4060 ± 80	254 ± 5	138 ± 5
6.25	261 ± 6	292 ± 7	1110 ± 20	4420 ± 80	276 ± 5	156 ± 5
7.5	273 ± 6	305 ± 7	1160 ± 20	4620 ± 80	289 ± 5	156 ± 5
10	290 ± 6	325 ± 7	1230 ± 20	4920 ± 80	307 ± 5	163 ± 5
12.5	302 ± 6	338 ± 7	1280 ± 20	5120 ± 80	320 ± 5	175 ± 5
15	325 ± 6	363 ± 7	1380 ± 20	5500 ± 80	344 ± 5	196 ± 5
17.5	319 ± 6	357 ± 7	1350 ± 20	5400 ± 80	338 ± 5	183 ± 5
20	333 ± 6	372 ± 7	1410 ± 20	5640 ± 80	353 ± 5	196 ± 5
22.5	335 ± 6	375 ± 7	1420 ± 20	5690 ± 80	355 ± 5	199 ± 5
25	334 ± 6	373 ± 7	1410 ± 20	5650 ± 80	353 ± 5	196 ± 5
27.5	336 ± 6	376 ± 7	1420 ± 20	5700 ± 80	356 ± 5	200 ± 5
30	325 ± 6	362 ± 7	1370 ± 20	5500 ± 80	344 ± 5	191 ± 5

The plots and data obtained for the NCHC**H** double quantum, three spin, and four spin terms of free pyridazine are given in Figure 229, Table 59, Table 60, and Table 61 respectively.

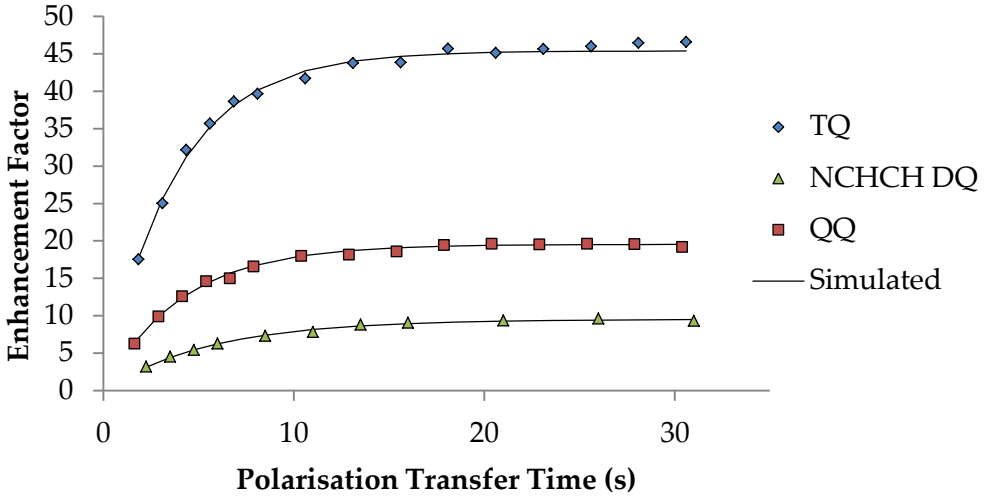

Figure 229: Plot of enhancement factors of the Triple Quantum (TQ), NCHCH double quantum (DQ), and Quadruple Quantum (QQ) coherence-derived resonances of free pdz in d_4-methanol, at 298 K, using the $[Ir(H)_2(IMes)(pdz)_3]Cl$ exchange catalyst (5.2 mM), with 5 equivalents of free pdz, as a function of PTT.

Table 59: Enhancements in the triple quantum resonances of free pdz in d_4-methanol, at 298 K and 120 G, using the $[Ir(H)_2(IMes)(pdz)_3]Cl$ exchange catalyst (5.2 mM), with 5 equivalents of free pdz, as a function of PTT.

PTT (s)	Enhancement Factor			Correction for observation of 1 of 8 terms	Correction for Receiver Gain (/114)
	NCH	NCHCH	Total		
1.25	80 ± 10	40 ± 10	250 ± 30	2000 ± 200	18 ± 2
2.5	120 ± 10	60 ± 10	360 ± 30	2900 ± 200	25 ± 2
3.75	150 ± 10	80 ± 10	460 ± 30	3700 ± 200	32 ± 2
5	160 ± 10	90 ± 10	510 ± 30	4100 ± 200	36 ± 2
6.25	180 ± 10	100 ± 10	550 ± 30	4400 ± 200	39 ± 2
7.5	180 ± 10	100 ± 10	570 ± 30	4500 ± 200	40 ± 2
10	180 ± 10	110 ± 10	590 ± 30	4800 ± 200	42 ± 2
12.5	200 ± 10	120 ± 10	620 ± 30	5000 ± 200	44 ± 2
15	200 ± 10	120 ± 10	620 ± 30	5000 ± 200	44 ± 2
17.5	200 ± 10	120 ± 10	650 ± 30	5200 ± 200	46 ± 2
20	200 ± 10	120 ± 10	640 ± 30	5100 ± 200	45 ± 2
22.5	200 ± 10	120 ± 10	650 ± 30	5200 ± 200	46 ± 2
25	200 ± 10	130 ± 10	660 ± 30	5200 ± 200	46 ± 2
27.5	210 ± 10	130 ± 10	660 ± 30	5300 ± 200	46 ± 2
30	200 ± 10	130 ± 10	660 ± 30	5300 ± 200	47 ± 2

Table 60: Enhancements in the NCHCH double quantum resonances of free pdz in d_4-methanol, at 298 K and 50 G, using the $[Ir(H)_2(IMes)(pdz)_3]Cl$ exchange catalyst (5.2 mM), with 5 equivalents of free pdz, as a function of PTT.

PTT (s)	Enhancement Factor		Correction for observation of 1 of 4 terms	Correction for Receiver Gain (/64)
	NCHCH	Total		
1.25	26 ± 1	51 ± 2	205 ± 8	3.2 ± 0.1
2.5	36 ± 1	72 ± 2	288 ± 8	4.5 ± 0.1
3.75	43 ± 1	87 ± 2	347 ± 8	5.4 ± 0.1
5	50 ± 1	100 ± 2	402 ± 8	6.3 ± 0.1
7.5	58 ± 1	117 ± 2	467 ± 8	7.3 ± 0.1
10	63 ± 1	125 ± 2	501 ± 8	7.8 ± 0.1
12.5	70 ± 1	140 ± 2	561 ± 8	8.8 ± 0.1
15	72 ± 1	144 ± 2	578 ± 8	9.0 ± 0.1
20	75 ± 1	149 ± 2	598 ± 8	9.3 ± 0.1
25	77 ± 1	154 ± 2	615 ± 8	9.6 ± 0.1
30	74 ± 1	149 ± 2	596 ± 8	9.3 ± 0.1

Table 61: Enhancements in the quadruple quantum resonances of free pdz in d_4-methanol, at 298 K and 50 G, using the $[Ir(H)_2(IMes)(pdz)_3]Cl$ exchange catalyst (5.2 mM), with 5 equivalents of free pdz, as a function of PTT.

PTT (s)	Enhancement Factor			Correction for observation of 1 of 16 terms	Correction for Receiver Gain (/2050)
	NCH	NCHCH	Total		
1.25	170 ± 10	230 ± 10	800 ± 30	12800 ± 500	6.2 ± 0.2
2.5	270 ± 10	370 ± 10	1260 ± 30	20200 ± 500	9.8 ± 0.2
3.75	340 ± 10	470 ± 10	1610 ± 30	25700 ± 500	12.5 ± 0.2
5	380 ± 10	550 ± 10	1860 ± 30	29800 ± 500	14.5 ± 0.2
6.25	400 ± 10	560 ± 10	1920 ± 30	30700 ± 500	15.0 ± 0.2
7.5	450 ± 10	620 ± 10	2120 ± 30	33900 ± 500	16.6 ± 0.2
10	480 ± 10	670 ± 10	2300 ± 30	36800 ± 500	18.0 ± 0.2
12.5	490 ± 10	670 ± 10	2320 ± 30	37100 ± 500	18.1 ± 0.2
15	490 ± 10	700 ± 10	2380 ± 30	38000 ± 500	18.5 ± 0.2
17.5	510 ± 10	730 ± 10	2490 ± 30	39800 ± 500	19.4 ± 0.2
20	520 ± 10	730 ± 10	2510 ± 30	40200 ± 500	19.6 ± 0.2

22.5	520 ± 10	730 ± 10	2500 ± 30	40000 ± 500	19.5 ± 0.2
25	520 ± 10	730 ± 10	2510 ± 30	40200 ± 500	19.6 ± 0.2
27.5	520 ± 10	730 ± 10	2510 ± 30	40100 ± 500	19.5 ± 0.2
30	520 ± 10	710 ± 10	2500 ± 30	39300 ± 500	19.1 ± 0.2

A.2.8.2 Phthalazine

The plots used to calculate the the T_1 values of the resonances of phthalazine are given in Figure 230 and the data obtained for the selectively excited NC**H**, NCHCC**H**, and NCHCCHC**H** resonances of free pyridazine are given in Figure 230, Table 62, Table 63, and Table 64 respectively.

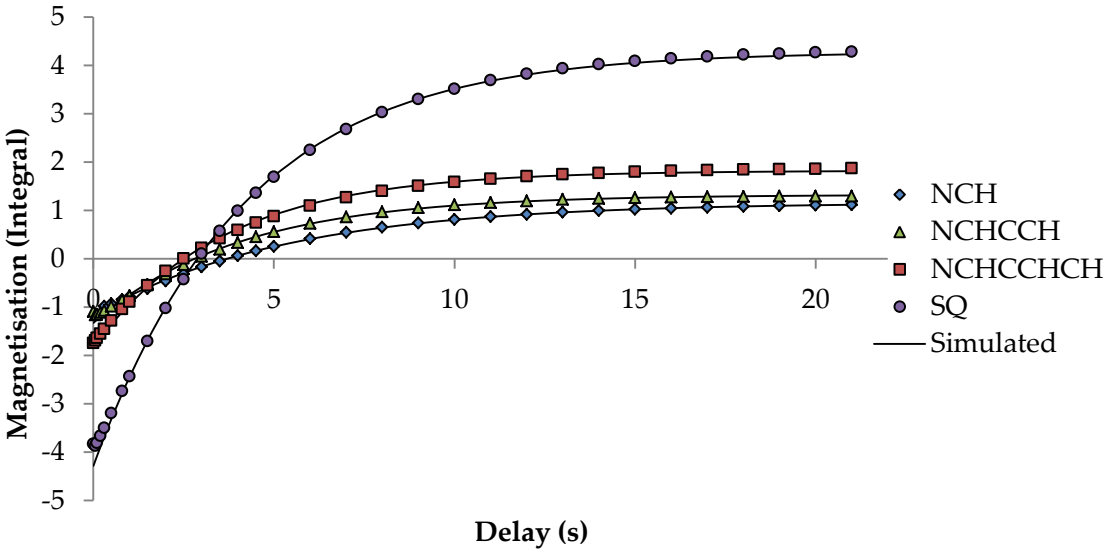

Figure 230: Graph to show the change in magnetisation intensity, with respect to the intensity when τ = 0.001 s, as a function of the delay time (τ) in an inversion recovery experiment used to calculate the T_1 values of specific spin states in phthalazine.

Table 62: Enhancements in the NC<u>H</u> resonance of free phth in d_4-methanol, at 298 K and 65 G, using the $[Ir(H)_2(IMes)(phth)_3]Cl$ exchange catalyst (5.2 mM), with 5 equivalents of free phth, as a function of PTT.

PTT (s)	**Enhancement Factor**		**Correction for Receiver Gain (/1)**
	NC**H**	Total	
1.25	52 ± 1	104 ± 2	104 ± 2
2.5	70 ± 1	140 ± 2	140 ± 2
3.75	89 ± 1	177 ± 2	177 ± 2
5	100 ± 1	200 ± 2	200 ± 2
6.25	105 ± 1	210 ± 2	210 ± 2

7.5	109 ± 1	219 ± 2	219 ± 2
10	115 ± 1	229 ± 2	229 ± 2
12.5	117 ± 1	234 ± 2	234 ± 2
15	120 ± 1	240 ± 2	240 ± 2
17.5	121 ± 1	243 ± 2	243 ± 2
22.5	122 ± 1	244 ± 2	244 ± 2
27.5	122 ± 1	245 ± 2	245 ± 2

Table 63: Enhancements in the NCHCCH resonance of free phth in d_4-methanol, at 298 K and 65 G, using the $[Ir(H)_2(IMes)(phth)_3]Cl$ exchange catalyst (5.2 mM), with 5 equivalents of free phth, as a function of PTT.

PTT (s)	Enhancement Factor		Correction for Receiver Gain (/16)
	NCHCC**H**	Total	
1.25	69 ± 2	138 ± 4	8.6 ± 0.2
2.5	96 ± 2	192 ± 4	12.0 ± 0.2
3.75	123 ± 2	245 ± 4	15.3 ± 0.2
5	130 ± 2	261 ± 4	16.3 ± 0.2
6.25	146 ± 2	291 ± 4	18.2 ± 0.2
7.5	154 ± 2	307 ± 4	19.2 ± 0.2
10	162 ± 2	324 ± 4	20.3 ± 0.2
12.5	167 ± 2	333 ± 4	20.8 ± 0.2
15	172 ± 2	344 ± 4	21.5 ± 0.2
17.5	175 ± 2	350 ± 4	21.8 ± 0.2
20	177 ± 2	354 ± 4	22.1 ± 0.2
22.5	178 ± 2	357 ± 4	22.3 ± 0.2
27.5	180 ± 2	359 ± 4	22.4 ± 0.2

Table 64: Enhancements in the NCHCCHCH resonance of free phth in d_4-methanol, at 298 K and 65 G, using the $[Ir(H)_2(IMes)(phth)_3]Cl$ exchange catalyst (5.2 mM), with 5 equivalents of free phth, as a function of PTT.

PTT (s)	Enhancement Factor		Correction for Receiver Gain (/16)
	NCHCCHC**H**	Total	
1.25	51.7 ± 0.7	103 ± 1	6.47 ± 0.06
2.5	74.6 ± 0.7	149 ± 1	9.33 ± 0.06

3.75	92.4 ± 0.7	185 ± 1	11.55 ± 0.06
5	105.4 ± 0.7	211 ± 1	13.18 ± 0.06
6.25	118.7 ± 0.7	237 ± 1	14.83 ± 0.06
7.5	122.3 ± 0.7	245 ± 1	15.29 ± 0.06
10	135.3 ± 0.7	271 ± 1	16.91 ± 0.06
12.5	141.5 ± 0.7	283 ± 1	17.68 ± 0.06
15	144.0 ± 0.7	288 ± 1	18.00 ± 0.06
17.5	147.2 ± 0.7	294 ± 1	18.40 ± 0.06
20	149.0 ± 0.7	298 ± 1	18.63 ± 0.06
22.5	151.8 ± 0.7	304 ± 1	18.97 ± 0.06
25	153.5 ± 0.7	307 ± 1	19.18 ± 0.06
27.5	154.0 ± 0.7	308 ± 1	19.26 ± 0.06

The plots and data obtained for the single and double quantum coherence-derived resonances of free phthalazine are given in Figure 231, Table 65, and Table 66 respectively.

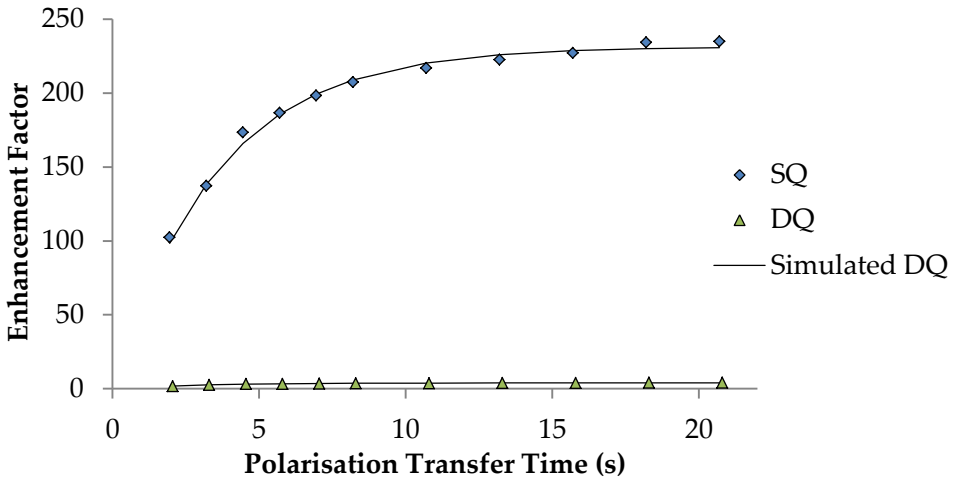

Figure 231: Plot of enhancement factors of the Single Quantum (SQ), and Double quantum (DQ) coherence-derived resonances of free phth in d_4-methanol, at 298 K, using the $[Ir(H)_2(IMes)(phth)_3]Cl$ exchange catalyst (5.2 mM), with 5 equivalents of free phth, as a function of PTT.

Table 65: Enhancements in the single quantum resonances of free phth in d_4-methanol, at 298 K and 65 G, using the $[Ir(H)_2(IMes)(phth)_3]Cl$ exchange catalyst (5.2 mM), with 5 equivalents of free phth, as a function of PTT.

PTT (s)	**Enhancement Factor**				**Correction for detection of 1 of 2**	**Correction for Receiver**
	NC**H**	NCHCC**H**	NCHCCHC**H**	Total		

					terms	Gain (/4)
1.25	155 ± 3	29.7 ± 0.7	20.2 ± 0.5	409 ± 6	820 ± 10	205 ± 2
2.5	205 ± 3	40.9 ± 0.7	28.3 ± 0.5	549 ± 6	1100 ± 10	275 ± 2
3.75	256 ± 3	53.3 ± 0.7	37.5 ± 0.5	694 ± 6	1390 ± 10	347 ± 2
5	274 ± 3	58.0 ± 0.7	41.7 ± 0.5	747 ± 6	1490 ± 10	373 ± 2
6.25	289 ± 3	62.1 ± 0.7	45.4 ± 0.5	793 ± 6	1590 ± 10	397 ± 2
7.5	301 ± 3	65.7 ± 0.7	48.4 ± 0.5	830 ± 6	1660 ± 10	415 ± 2
10	312 ± 3	69.6 ± 0.7	52.1 ± 0.5	867 ± 6	1730 ± 10	434 ± 2
12.5	319 ± 3	71.7 ± 0.7	54.6 ± 0.5	890 ± 6	1780 ± 10	445 ± 2
15	324 ± 3	73.8 ± 0.7	56.6 ± 0.5	909 ± 6	1820 ± 10	455 ± 2
17.5	333 ± 3	76.3 ± 0.7	59.1 ± 0.5	937 ± 6	1870 ± 10	468 ± 2
20	334 ± 3	76.7 ± 0.7	59.6 ± 0.5	940 ± 6	1880 ± 10	470 ± 2

Table 66: Enhancements in the double quantum resonances of free phth in d_4-methanol, at 298 K and 65 G, using the $[Ir(H)_2(IMes)(phth)_3]Cl$ exchange catalyst (5.2 mM), with 5 equivalents of free phth, as a function of PTT.

PTT (s)	**Enhancement Factor**				**Correction for detection of 1 of 4 terms**	**Correction for Receiver Gain (/128)**
	NC**H**	NCHCC**H**	NCHCCHC**H**	Total		
1.25	20 ± 2	38 ± 2	55 ± 4	220 ± 10	900 ± 40	7.0 ± 0.3
2.5	33 ± 2	53 ± 2	81 ± 4	330 ± 10	1340 ± 40	10.5 ± 0.3
3.75	41 ± 2	63 ± 2	96 ± 4	400 ± 10	1600 ± 40	12.5 ± 0.3
5	44 ± 2	65 ± 2	102 ± 4	420 ± 10	1690 ± 40	13.2 ± 0.3
6.25	49 ± 2	68 ± 2	108 ± 4	450 ± 10	1800 ± 40	14.0 ± 0.3
7.5	51 ± 2	70 ± 2	111 ± 4	460 ± 10	1860 ± 40	14.5 ± 0.3
10	54 ± 2	72 ± 2	114 ± 4	480 ± 10	1920 ± 40	15.0 ± 0.3
12.5	56 ± 2	74 ± 2	119 ± 4	500 ± 10	2000 ± 40	15.6 ± 0.3
15	56 ± 2	75 ± 2	120 ± 4	500 ± 10	2010 ± 40	15.7 ± 0.3
17.5	58 ± 2	76 ± 2	122 ± 4	510 ± 10	2050 ± 40	16.0 ± 0.3
20	59 ± 2	76 ± 2	123 ± 4	520 ± 10	2060 ± 40	16.1 ± 0.3

Appendix B

The following is supplementary information for Chapters 3, 4, and 5, which has been cross-referenced throughout.

B.1 Synthesis and Reactivity of Palladium Monomers

B.1.1 TEM images used to Calculate the Size Distributions of Palladium Nanoparticles

The palladium nanoparticles that formed on addition of 3 bar of hydrogen to a 7.6 mM dichloromethane solution of $[Pd(OTf)_2(XR_3)_2]$, where $XR_3 = PPh_3$ or $AsPh_3$, were compared using their TEM images. PVP was used as a control during TEM sample preparation because it prevents palladium aggregation occurring during TEM analysis [51,52] and any changes in palladium nanoparticle size *ex situ* can be assessed.

For each complex, two TEM images collected in the absence of PVP and two TEM images collected in the presence of PVP were used to calculate the size distributions of the nanoparticles. The images were printed on A1 paper, and the scale given on the TEM images was used to convert from cm to nm. The nanoparticles were measured with a ruler and tallied into size groupings, producing the histograms given in Chapter 4. In the experience of the Fairlamb group, this method is more reliable than using computer software packages, for example ImageJ, to automatically calculate the size of the different particles.

B.1.1.1 $[Pd(OTf)_2(AsPh_3)_2]$

The four TEM images used to calculate the size distribution of the palladium nanoparticles that formed on addition of hydrogen to $[Pd(OTf)_2(AsPh_3)_2]$ are shown in Figure 232. The size distributions calculated from the TEM images are compared in Figure 233. There is no discernible difference in the size distributions of the nanoparticles exposed to PVP relative to those prepared without PVP.

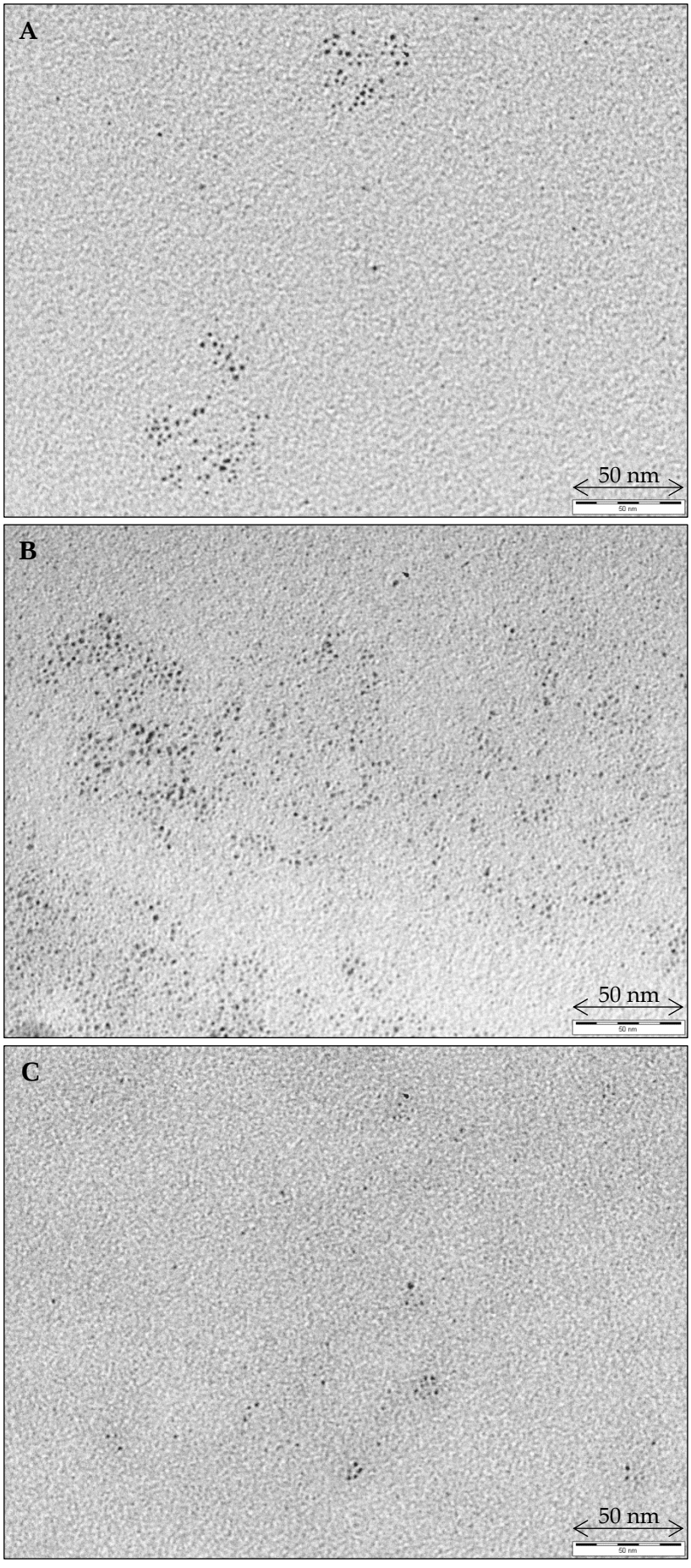
A
50 nm
B
50 nm
C
50 nm

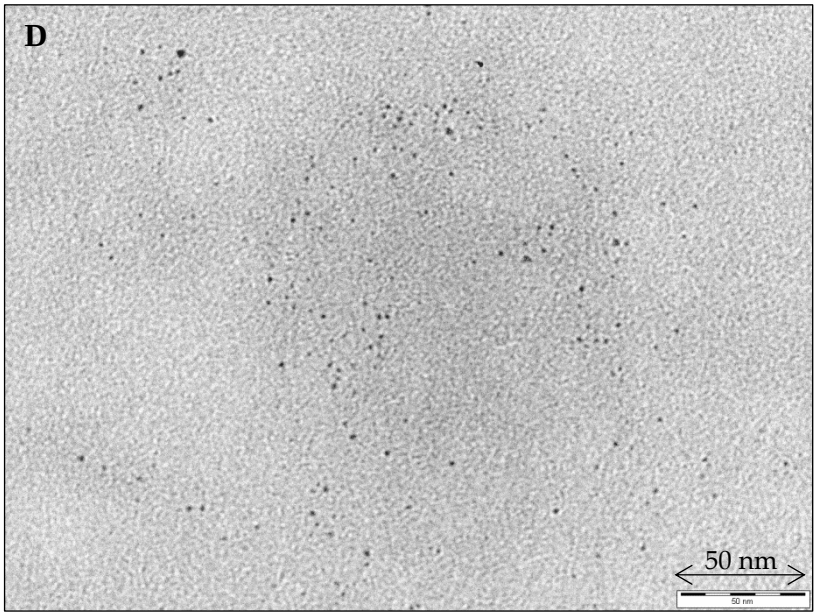

Figure 232: TEM images of the palladium nanoparticles that form on addition of hydrogen to $[Pd(OTf)_2(AsPh_3)_2]$ collected (A and B) in the absence of PVP and (C and D) in the presence of PVP.

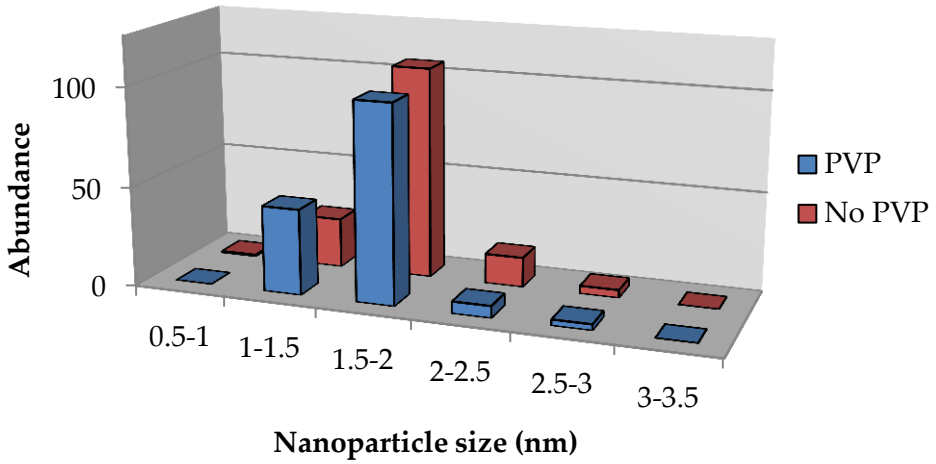

Figure 233: Histogram comparing the nanoparticle sizes that form on addition of hydrogen to $[Pd(OTf)_2(AsPh_3)_2]$, calculated from TEM images in which samples were prepared with or without PVP.

B.1.1.2 $[Pd(OTf)_2(PPh_3)_2]$

The four TEM images used to calculate the size distribution of the palladium nanoparticles that formed on addition of hydrogen to $[Pd(OTf)_2(PPh_3)_2]$ are shown in Figure 234. The size distributions calculated from the TEM images are compared in Figure 235. Again, there is no discernible difference in the size distributions of the nanoparticles exposed to PVP relative to those prepared without PVP.

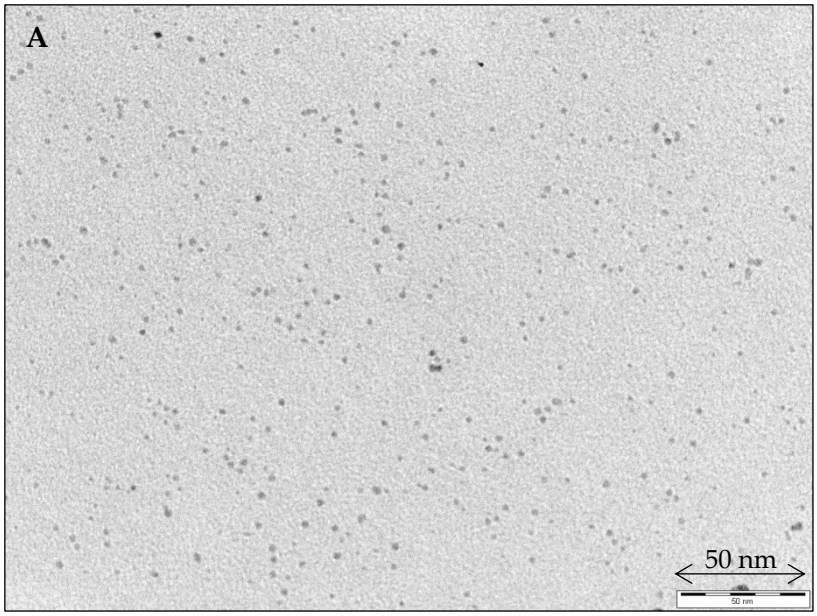
A
50 nm

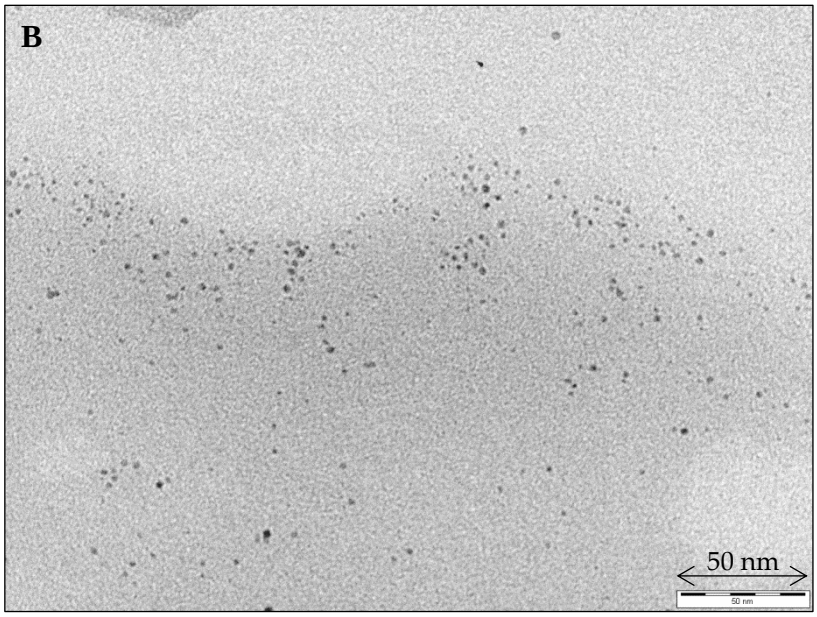
B
50 nm

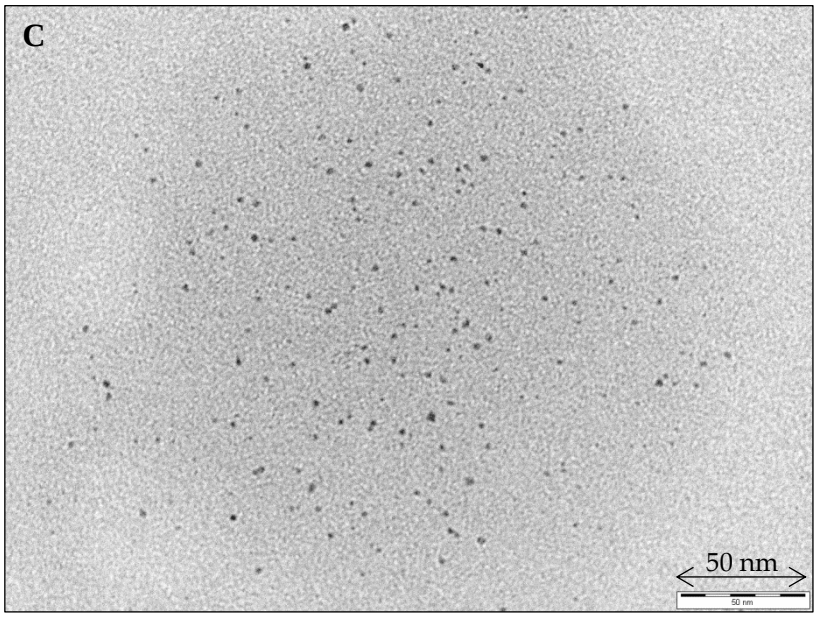
C
50 nm

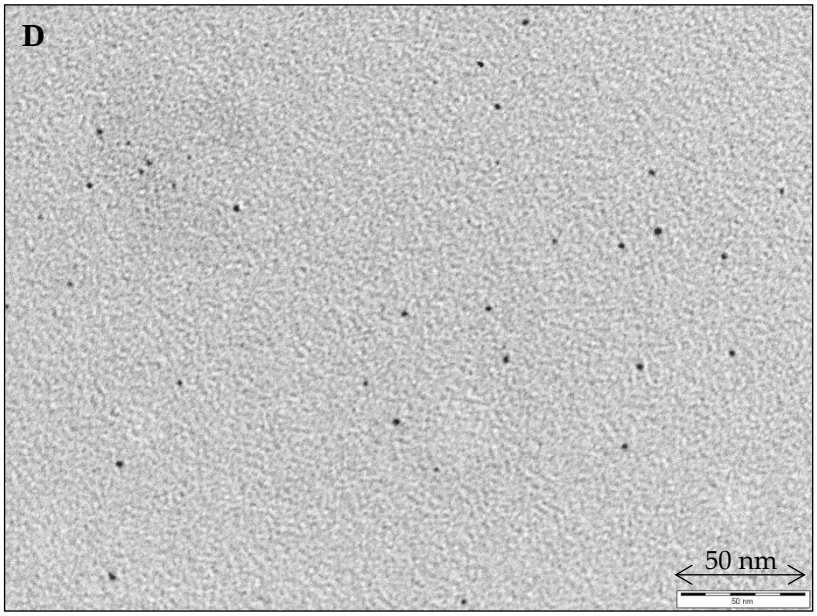

Figure 234: TEM images of the palladium nanoparticles that form on addition of hydrogen to [Pd(OTf)$_2$(PPh$_3$)$_2$] collected (A and B) in the absence of PVP and (C and D) in the presence of PVP.

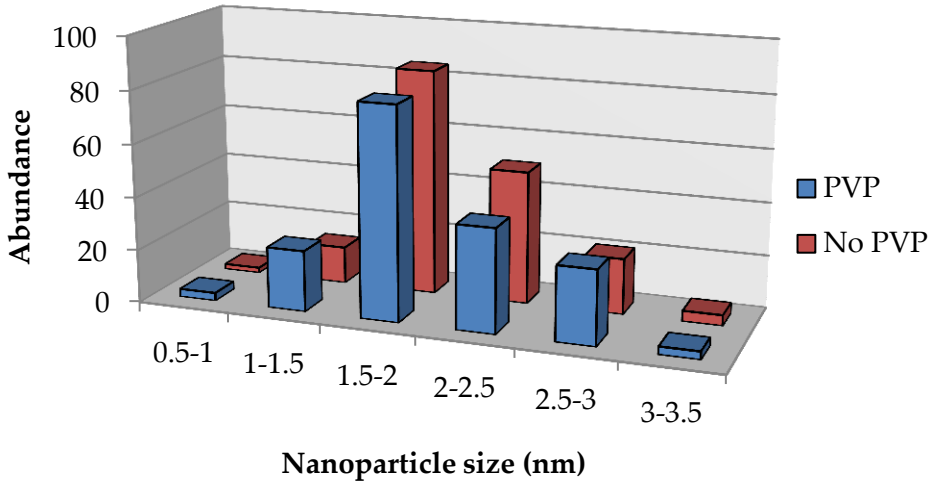

Figure 235: Histogram comparing the nanoparticle sizes that form on addition of hydrogen to [Pd(OTf)$_2$(PPh$_3$)$_2$], calculated from TEM images in which samples were prepared with or without PVP.

B.2 Detection of Palladium Intermediates En-route to Palladium Nanoparticles

B.2.1 LIFDI-MS Data for [Pd(H)(OTf)(XR$_3$)$_2$] Complexes

All experimental LIFDI-MS data was compared to simulated isotope patterns of the complex of interest in histogram plots. In every case, the experimental data is displayed in

the positive phase (blue) and the simulated data is displayed in the negative phase (red). The $[Pd(H)(OTf)(XR_3)_2]$ complexes were either detected as the radical cation of the complete complex, or as the cation of the complex without the hydride ligand, $[Pd(OTf)(XR_3)_2]^+$.

B.2.1.1 $[Pd(H)(OTf)(PPh_3)_2]$

Signals for the $[Pd(OTf)(PPh_3)_2]^+$ cation were observed in LIFDI mass spectra, and these match with the simulated isotope distributions, shown in Figure 236.

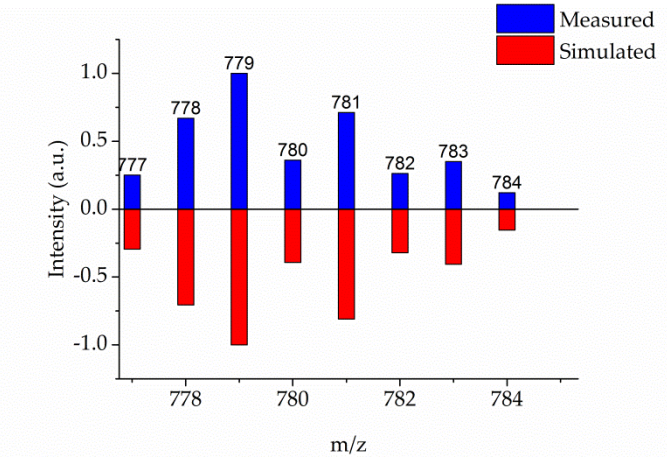

Figure 236: Histogram of the experimental and simulated LIFDI-MS data for the $[Pd(OTf)(PPh_3)_2]^+$ cation.

B.2.1.2 $[Pd(H)(OTf)(PPh_2Me)_2]$

Signals for the $[Pd(H)(OTf)(PPh_2Me)_2]^{+\cdot}$ radical cation were observed in LIFDI mass spectra, and these match with the simulated isotope distributions, shown in Figure 237.

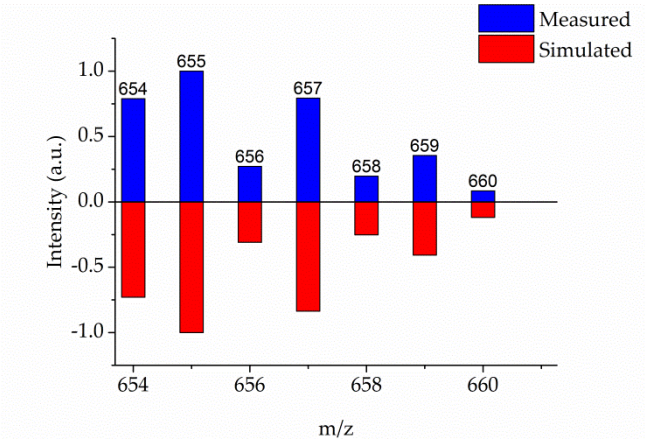

Figure 237: Histogram of the experimental and simulated LIFDI-MS data for the $[Pd(H)(OTf)(PPh_2Me)_2]^{+\cdot}$ radical cation.

B.2.1.3 [Pd(H)(OTf)(P(PhPh$_3$)$_2$)$_2$]

Signals for the [Pd(H)(OTf)(P(PhPh$_3$)$_2$)$_2$]$^{+\cdot}$ radical cation were observed in LIFDI mass spectra, and these match with the simulated isotope distributions, shown in Figure 238.

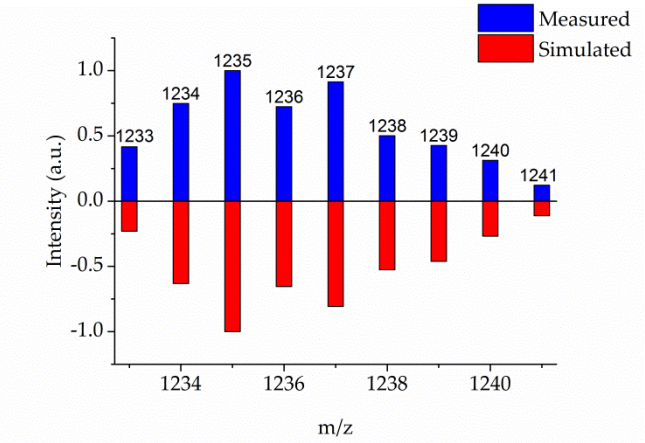

Figure 238: Histogram of the experimental and simulated LIFDI-MS data for the [Pd(H)(OTf)(P(PhPh$_3$)$_2$)$_2$]$^{+\cdot}$ radical cation.

B.2.1.4 [Pd(H)(OTf)(PPh$_2$(PhPh))$_2$]

Signals for the [Pd(OTf)(PPh$_2$(PhPh))$_2$]$^+$ cation were observed in LIFDI mass spectra, and these match with the simulated isotope distributions, shown in Figure 239.

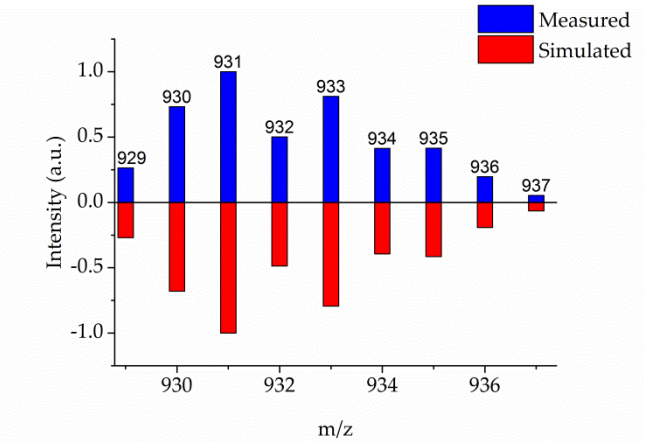

Figure 239: Histogram of the experimental and simulated LIFDI-MS data for the [Pd(OTf)(PPh$_2$(PhPh))$_2$]$^+$ cation.

B.2.1.5 [Pd(H)(OTf)(PPh$_2$(PhCH$_2$Ph))$_2$]

Signals for the [Pd(OTf)(PPh$_2$(PhCH$_2$Ph))$_2$]$^+$ cation were observed in LIFDI mass spectra, and these match with the simulated isotope distributions, shown in Figure 240.

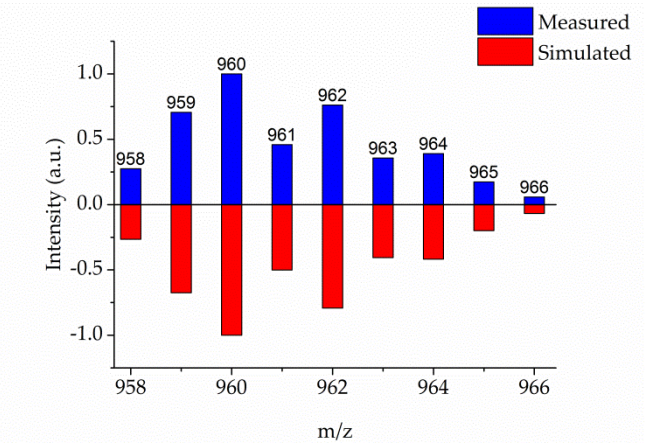

Figure 240: Histogram of the experimental and simulated LIFDI-MS data for the $[Pd(OTf)(PPh_2(PhCH_2Ph))_2]^+$ cation.

B.2.1.6 $[Pd(H)(OTf)(AsPh_3)_2]$

Signals for the $[Pd(OTf)(AsPh_3)_2]^+$ cation were observed in LIFDI mass spectra, and these match with the simulated isotope distributions, shown in Figure 241.

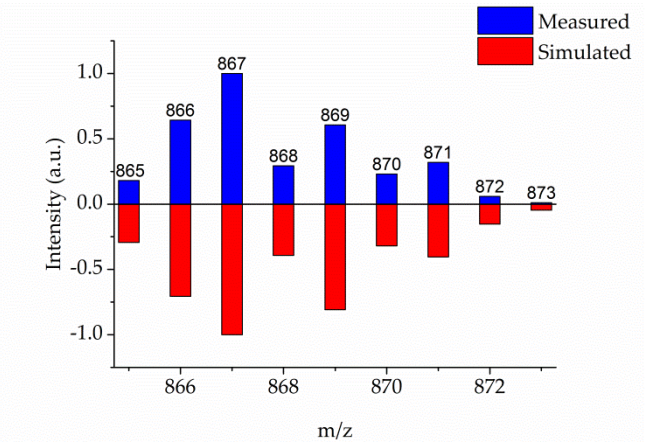

Figure 241: Histogram of the experimental and simulated LIFDI-MS data for the $[Pd(OTf)(AsPh_3)_2]^+$ cation.

B.2.2 LIFDI-MS Data for $[Pd(H)(XR_3)_3]OTf$ Complexes

The $[Pd(H)(XR_3)_3]OTf$ complexes were detected as the cation of the complex without the triflate counterion.

B.2.2.1 $[Pd(H)(PPh_3)_3]OTf$

Signals for the $[Pd(H)(PPh_3)_3]^+$ cation were observed in LIFDI mass spectra, and these match with the simulated isotope distributions, shown in Figure 242.

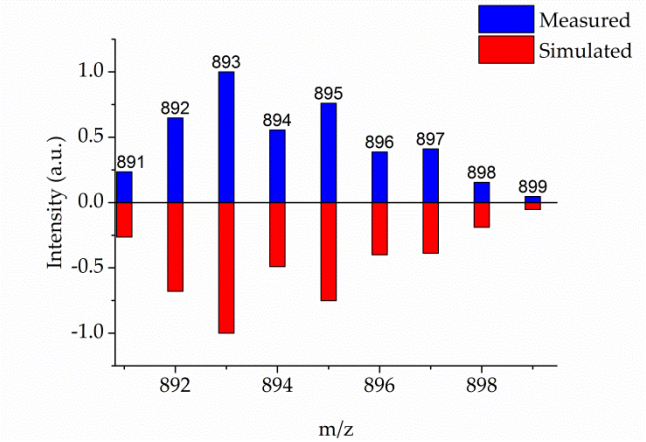

Figure 242: Histogram of the experimental and simulated LIFDI-MS data for the $[Pd(H)(PPh_3)_3]^+$ cation.

B.2.2.2 $[Pd(H)(PPh_2Me)_3]OTf$

Signals for the $[Pd(H)(PPh_2Me)_3]^+$ cation were observed in LIFDI mass spectra, and these match with the simulated isotope distributions, shown in Figure 243.

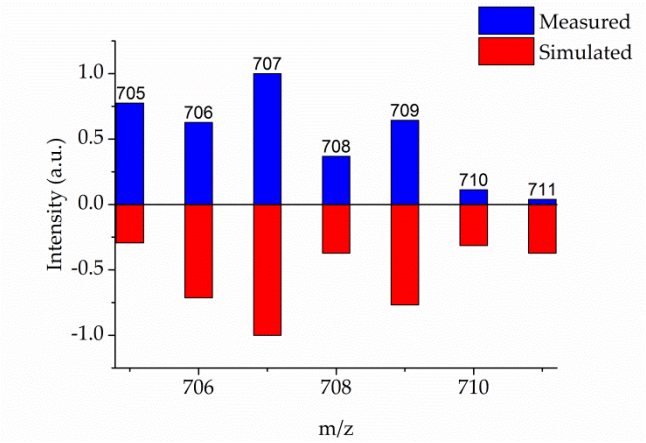

Figure 243: Histogram of the experimental and simulated LIFDI-MS data for the $[Pd(H)(PPh_2Me)_3]^+$ cation.

B.2.2.3 $[Pd(H)(P(PhPh)_3)_3]OTf$

Signals for the $[Pd(H)(P(PhPh)_3)_3]^+$ cation were observed in LIFDI mass spectra, and these match with the simulated isotope distributions, shown in Figure 244.

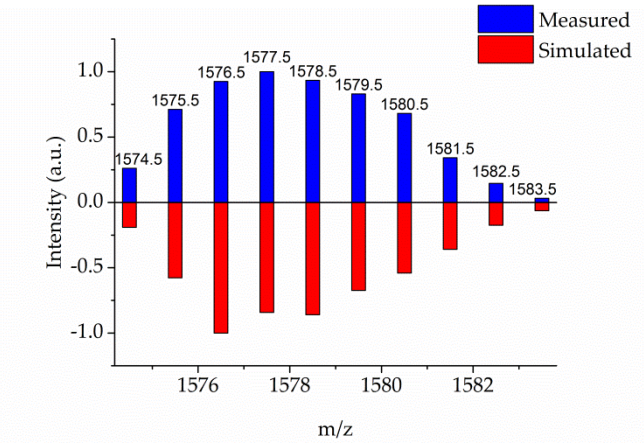

Figure 244: Histogram of the experimental and simulated LIFDI-MS data for the $[Pd(H)(P(PhPh)_3)_3]^+$ cation.

B.2.2.4 $[Pd(H)(PPh_2(PhPh))_3]OTf$

Signals for the $[Pd(H)(PPh_2(PhPh))_3]^+$ cation were observed in LIFDI mass spectra, and these match with the simulated isotope distributions, shown in Figure 245.

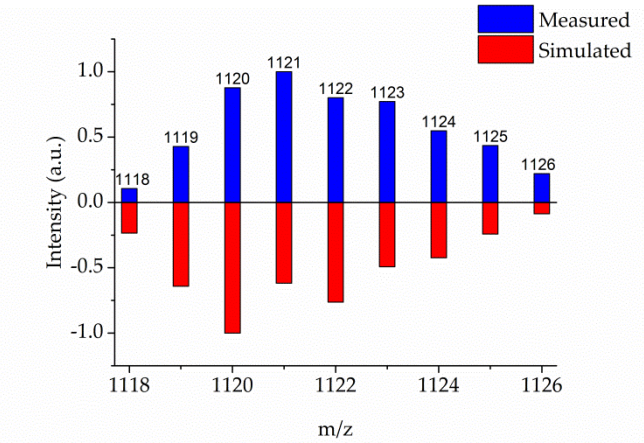

Figure 245: Histogram of the experimental and simulated LIFDI-MS data for the $[Pd(H)(PPh_2(PhPh))_3]^+$ cation.

B.2.2.5 $[Pd(H)(PPh_2(PhCH_2Ph))_3]OTf$

Signals for the $[Pd(H)(PPh_2(PhCH_2Ph))_3]^+$ cation were observed in LIFDI mass spectra, and these match with the simulated isotope distributions, shown in Figure 246.

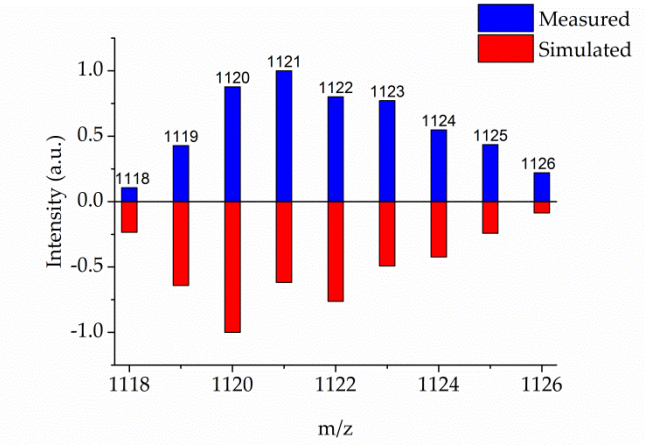

Figure 246: Histogram of the experimental and simulated LIFDI-MS data for the $[Pd(H)(P(PhPh)_3)_3]^+$ cation.

B.2.2.6 $[Pd(H)(AsPh_3)_3]OTf$

Signals for the $[Pd(H)(AsPh_3)_3]^+$ cation were observed in LIFDI mass spectra, and these match with the simulated isotope distributions, shown in Figure 247.

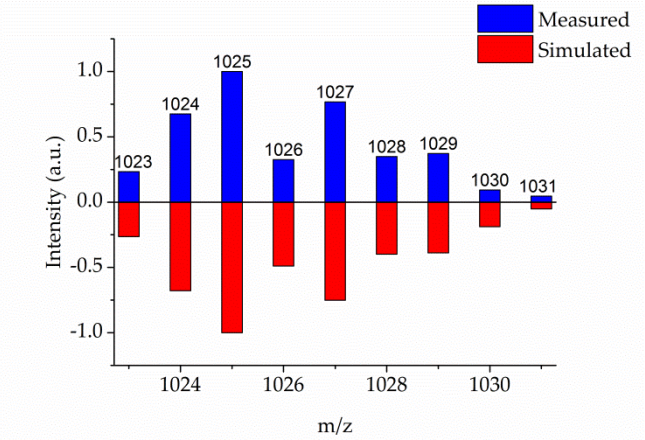

Figure 247: Histogram of the experimental and simulated LIFDI-MS data for the $[Pd(H)(AsPh_3)_3]^+$ cation.

B.2.3 LIFDI-MS Data for $[Pd(Cl)(H)(XR_3)_2]$ Complexes

The $[Pd(Cl)(H)(XR_3)_2]$ complexes were detected as the dicationic dimers, $[Pd(Cl)(XR_3)_2]_2^{2+}$.

B.2.3.1 $[Pd(Cl)(H)(P(PhPh)_3)_2]$

Signals for the $[Pd(Cl)(P(PhPh)_3)_2]_2^{2+}$ dication were observed in LIFDI mass spectra, and these match with the simulated isotope distributions, shown in Figure 248.

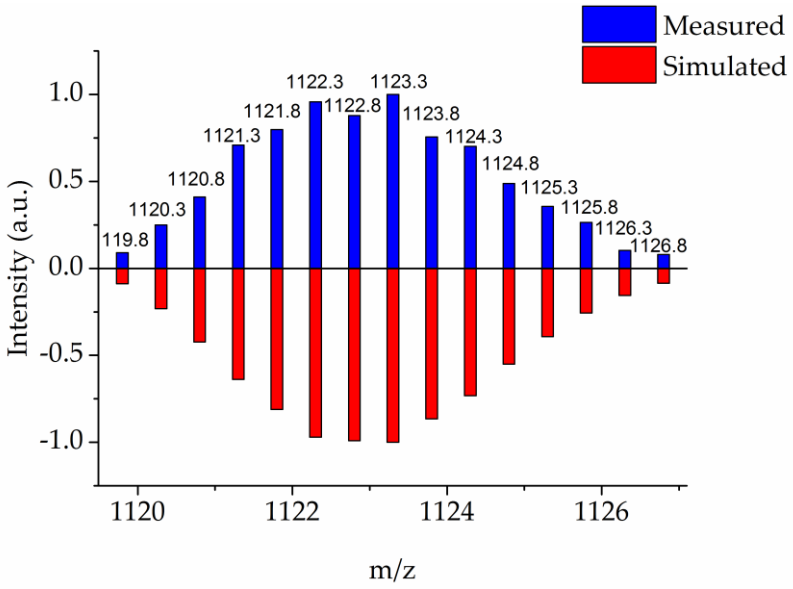

Figure 248: Histogram of the experimental and simulated LIFDI-MS data for the $[Pd(Cl)(P(PhPh)_3)_2]_2^{2+}$ dication.

B.2.3.2 $[Pd(Cl)(H)(PPh_2(PhPh))_2]$

Signals for the $[Pd(Cl)(PPh_2(PhPh))_2]_2^{2+}$ dication were observed in LIFDI mass spectra, and these match with the simulated isotope distributions, shown in Figure 249.

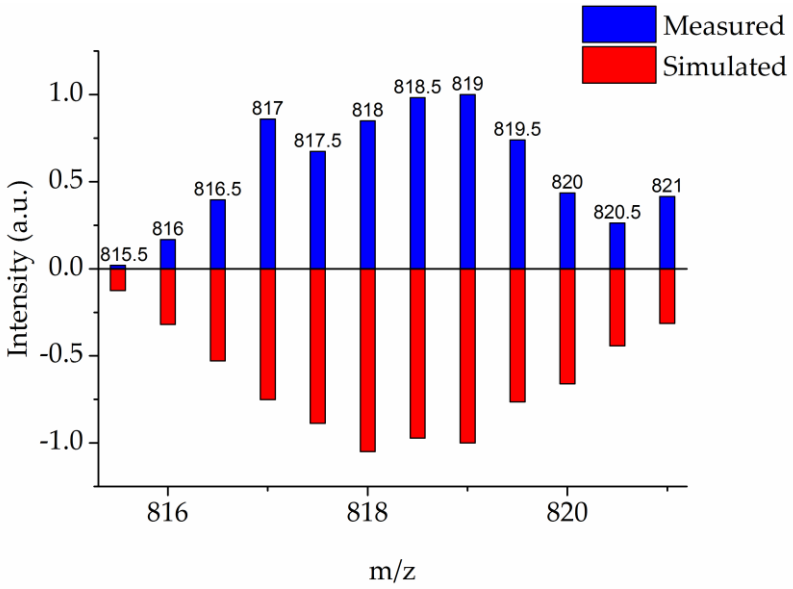

Figure 249: Histogram of the experimental and simulated LIFDI-MS data for the $[Pd(Cl)(H)(PPh_2(PhPh))_2]_2^{2+}$ dication.

B.2.4 LIFDI-MS Data for $[Pd_3(XR_3)_4][OTf]_2$ Complexes

The $[Pd_3(XR_3)_4][OTf]_2$ complexes were detected as the dication of the complex, without the two triflate counterions.

B.2.4.1 $[Pd_3(PPh_3)_4][OTf]_2$

Signals for the $[Pd_3(PPh_3)_4]^{2+}$ dication were observed in LIFDI mass spectra, and these match with the simulated isotope distributions, shown in Figure 250.

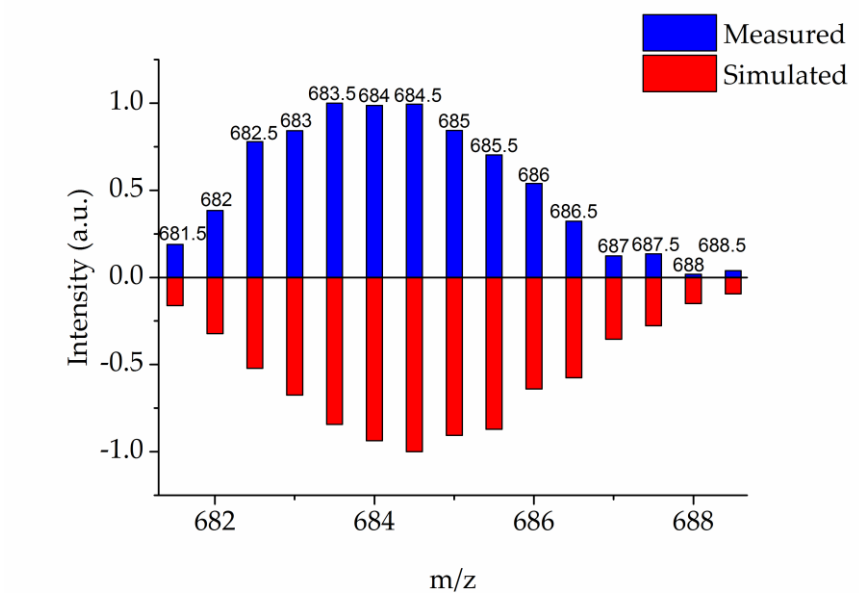

Figure 250: Histogram of the experimental and simulated LIFDI-MS data for the $[Pd_3(PPh_3)_4]^{2+}$ dication.

B.2.4.2 $[Pd_3(PPh_2Me)_4][OTf]_2$

Signals for the $[Pd_3(PPh_2Me)_4]^{2+}$ dication were observed in LIFDI mass spectra, and these match with the simulated isotope distributions, shown in Figure 251.

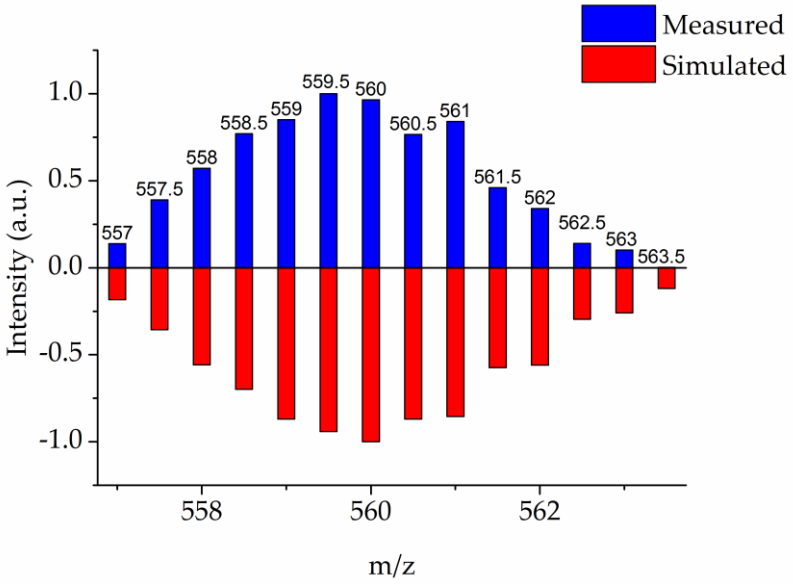

Figure 251: Histogram of the experimental and simulated LIFDI-MS data for the $[Pd_3(PPh_2Me)_4]^{2+}$ dication.

B.2.4.3 $[Pd_3(PPh_2(PhCH_2Ph))_4][OTf]_2$

Signals for the $[Pd_3(PPh_2(PhCH_2Ph))_4]^{2+}$ dication were observed in LIFDI mass spectra, and these match with the simulated isotope distributions, shown in Figure 252.

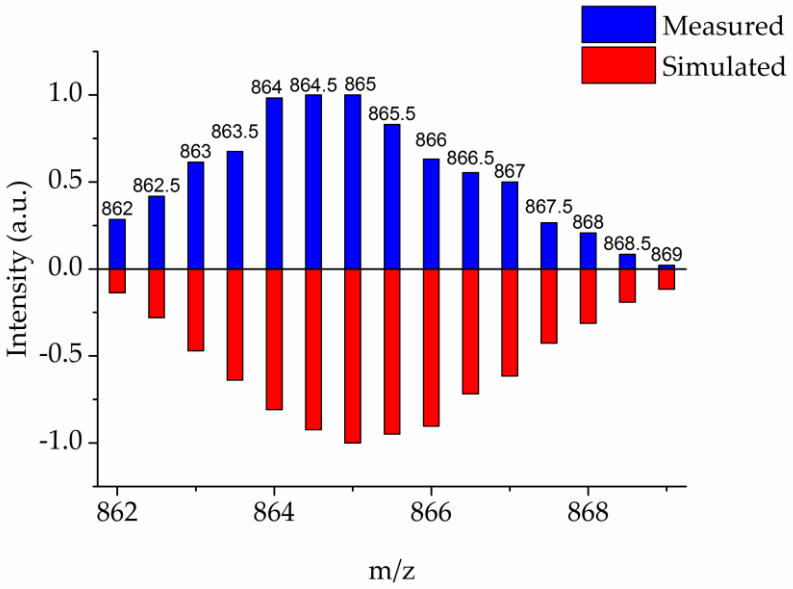

Figure 252: Histogram of the experimental and simulated LIFDI-MS data for the $[Pd_3(PPh_2(PhCH_2Ph))_4]^{2+}$ dication.

B.2.4.4 $[Pd_3(AsPh_3)_4][OTf]_2$

Signals for the $[Pd_3(AsPh_3)_4]^{2+}$ dication were observed in LIFDI mass spectra, and these match with the simulated isotope distributions, shown in Figure 253.

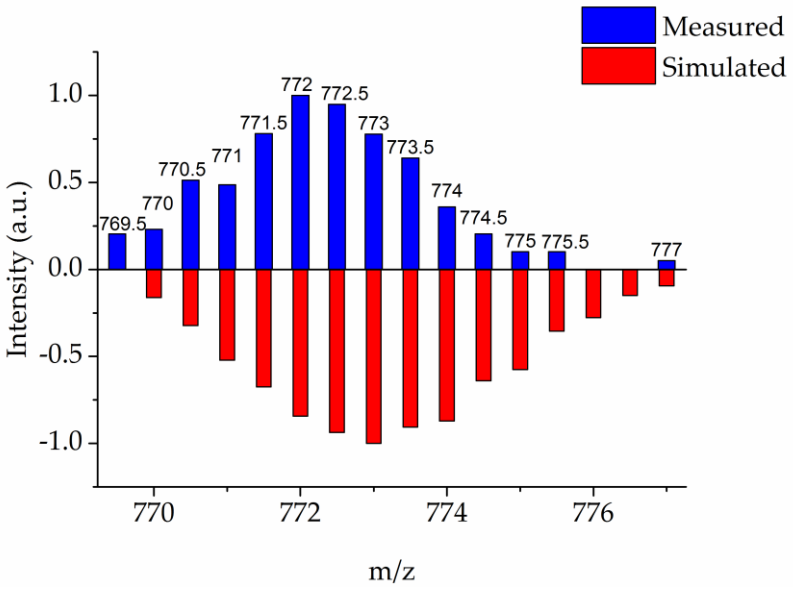

Figure 253: Histogram of the experimental and simulated LIFDI-MS data for the $[Pd_3(AsPh_3)_4]^{2+}$ dication.

B.3 Reactivity of $[Pd_3(PPh_3)_4][BF_4]_2$

B.3.1 The use of Topspin's ERETIC2 Quantification Tool to Calculate Unknown Sample Concentrations

The molar absorption coefficient of the $[Pd_3(PPh_3)_4][OTf]_2$ photoisomer was calculated from the absorbance value of a sample of unknown concentration. The concentration of the sample was calculated using the ERETIC2 quantification tool provided by Topspin 3.1.[294] This is based on PULCON,[329] which is a method that correlates the intensities of signals in two different NMR spectra, using the equation given below where C_x is the concentration (A is the unknown species and B is the reference sample), k is a correction factor that takes number of protons, receiver gain, and relaxation into account, Int_x is the integral area, T_x is the temperature, θ_{90}^x is the length of the 90 ° pulse, and n_x is the number of scans used.

$$C_A = kC_B \frac{Int_A T_A \theta_{90}^A n_A}{Int_B T_B \theta_{90}^B n_B}$$

The same spectrometer and tuned and matched probe were used to collect the spectra and, as the temperature, pulse length and number of scans were equivalent, the aforementioned equation simplifies to:

$$C_A = kC_B \frac{Int_A}{Int_B}$$

The 90 ° pulse was calibrated and a long delay time (30 s) was used between scans to allow the magnetisation to fully relax, providing accurate integrals. The value of k therefore simply corresponds to the number of protons in the molecule that the NMR signal corresponds to.

The integrals of well-resolved NMR signals corresponding to known proton environments were compared for the reference compound and the sample of unknown concentration. The unknown concentration was calculated using the formula above. In this case, the two protons of dibenzylideneacetone, labelled * in Figure 254, were compared with the four protons of the $[Pd_3(PPh_3)_4][BF_4]_2$ photoisomer, labelled * in Figure 255.

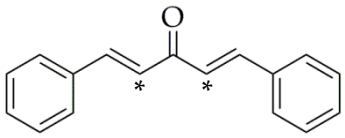

Figure 254: Dibenzylideneacetone. The proton NMR signal used to calibrate the spectrometer using the ERETIC2 quantification tool corresponds to the protons labelled *.

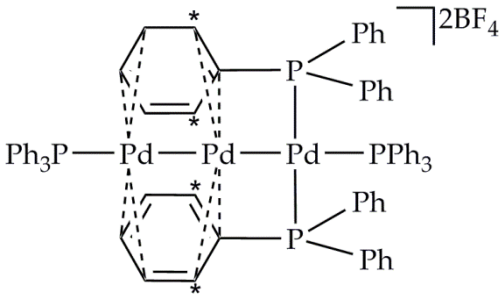

Figure 255: $[Pd_3(PPh_3)_4][BF_4]_2$ photoisomer. The proton NMR signal used to calibrate the spectrometer using the ERETIC2 quantification tool corresponds to the protons labelled *.

B.3.2 Eyring Plot used to Calculate the Enthalpy of Activation of Reverse Isomerisation

The observed rates of reverse isomerisation from the $[Pd_3(PPh_3)_4][BF_4]_2$ photoisomer to the thermal isomer were calculated at different temperatures, using 1.08 mM d_2-dichloromethane solutions of $[Pd_3(PPh_3)_4][BF_4]_2$. The enthalpy of activation was calculated from the Eyring plot given in Figure 256, using the method detailed in Chapter 2.

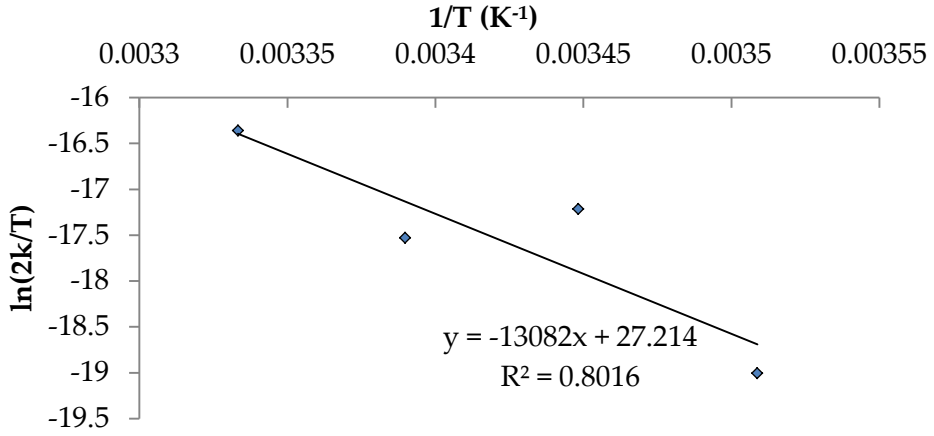

Figure 256: Eyring plot used to calculate the enthalpy of activation of reverse isomerisation from the $[Pd_3(PPh_3)_4][BF_4]_2$ photoisomer to the $[Pd_3(PPh_3)_4][BF_4]_2$ thermal isomer, obtained from linear regression analysis.

B.3.3 Plots used to Calculate the Observed Rate of Hydrogen Depletion during the Hydrogenation of Phenylacetylene using Different Hydrogenation Catalysts

The *pseudo* rate constants of hydrogen depletion were calculated using 1.3 mM d_2-dichloromethane solutions of palladium catalyst with 66 equivalents of phenylacetylene (85.67 mM). The samples were degassed prior to the addition of *para*-H_2 (~ 3 bar), after which the solutions were shaken at low magnetic field for 10 seconds, and a series of OPSY NMR spectra were immediately acquired, with 8 s intervals. Once all of the *para*-H_2 in solution had been consumed, the solutions were re-shaken at low magnetic field for 10 seconds, and a second series of OPSY NMR spectra were immediately acquired.

Plots showing the reduction in intensity of the enhanced signals corresponding to the protons in styrene, observed over an 8 s interval, over time using different hydrogenation catalysts are presented below. These plots are showing the rate of decay of the rate of

hydrogenation. The results using [Ir(COD)(PCy_3)(py)][PF_6], [$Pd_3(PPh_3)_4$][BF_4]$_2$, the [$Pd_3(PPh_3)_4$][BF_4]$_2$ photoisomer, 'activated' [$Pd_3(PPh_3)_4$][BF_4]$_2$, and [$Pd_3(PPh_3)_4$][BF_4]$_2$ with 10 equivalents of triphenylphosphine, are given in Figure 257, Figure 258, Figure 259, Figure 260, and Figure 261 respectively. The rates of hydrogen depletion were calculated by fitting these plots according to the method discussed in Chapter 6.

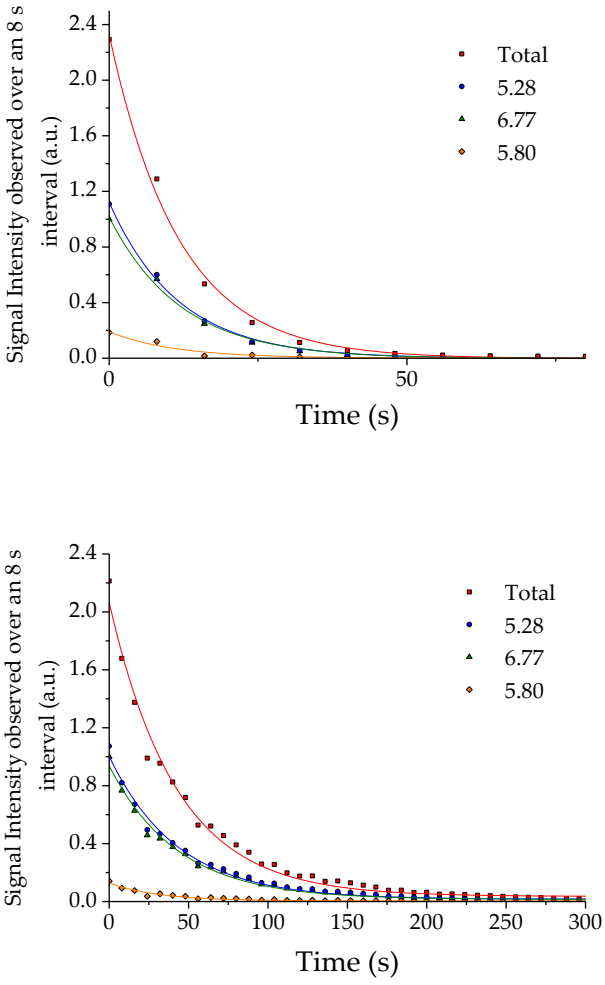

Figure 257: Plot to show the reduction in the change in intensity, over an 8 s interval, of the PASADENA signals corresponding to the para-H_2-derived protons in styrene, observed at the chemical shifts indicated in the key, with time using [Ir(COD)(PCy_3)(py)][PF_6]. First shake (above), second shake (below).

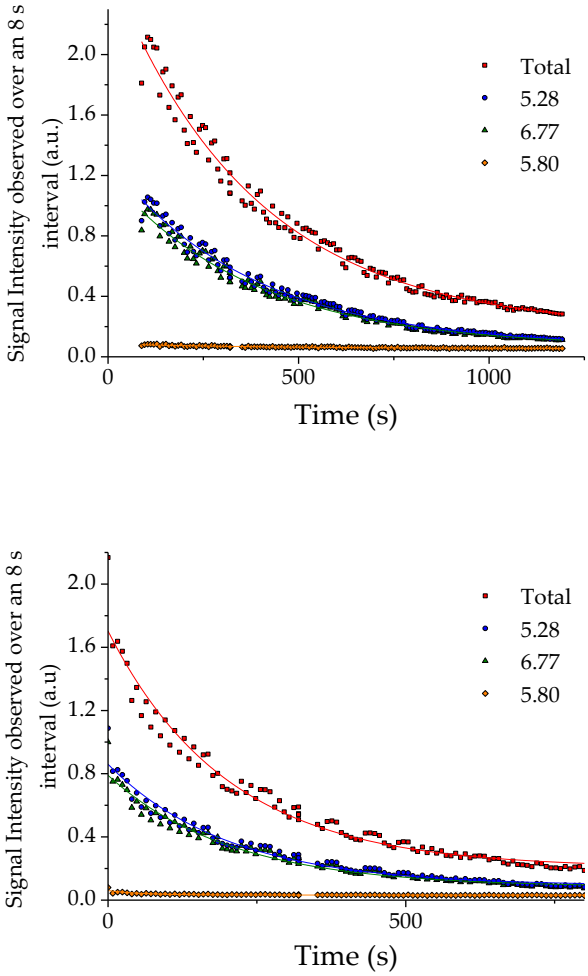

Figure 258: Plot to show the reduction in the change in intensity, over an 8 s interval, of the PASADENA signals corresponding to the para-H_2-derived protons in styrene, observed at the chemical shifts indicated in the key, with time, using $[Pd_3(PPh_3)_4][BF_4]_2$. First shake (above), second shake (below).

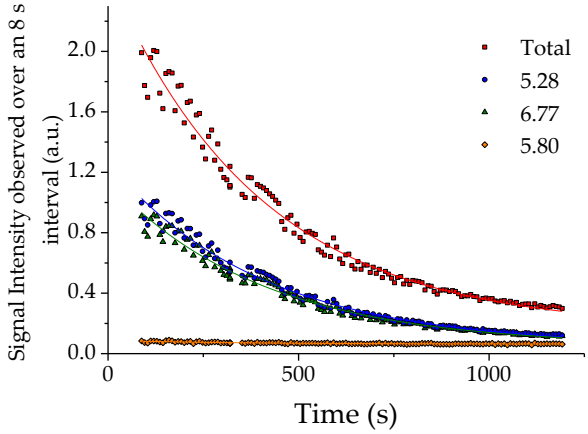

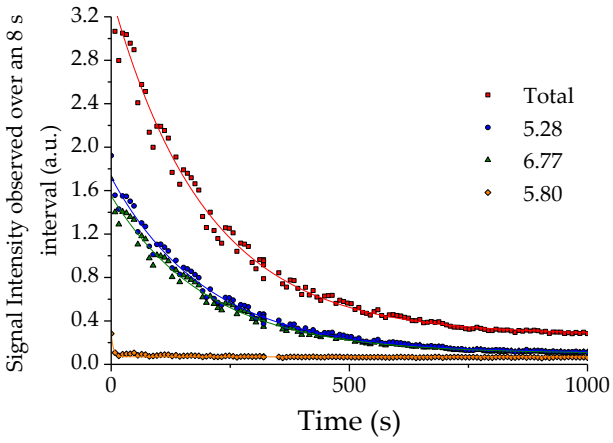

Figure 259: Plot to show the reduction in the change in intensity, over an 8 s interval, of the PASADENA signals corresponding to the para-H_2-derived protons in styrene, observed at the chemical shifts indicated in the key, with time, using the $[Pd_3(PPh_3)_4][BF_4]_2$ photoisomer. First shake (above), second shake (below).

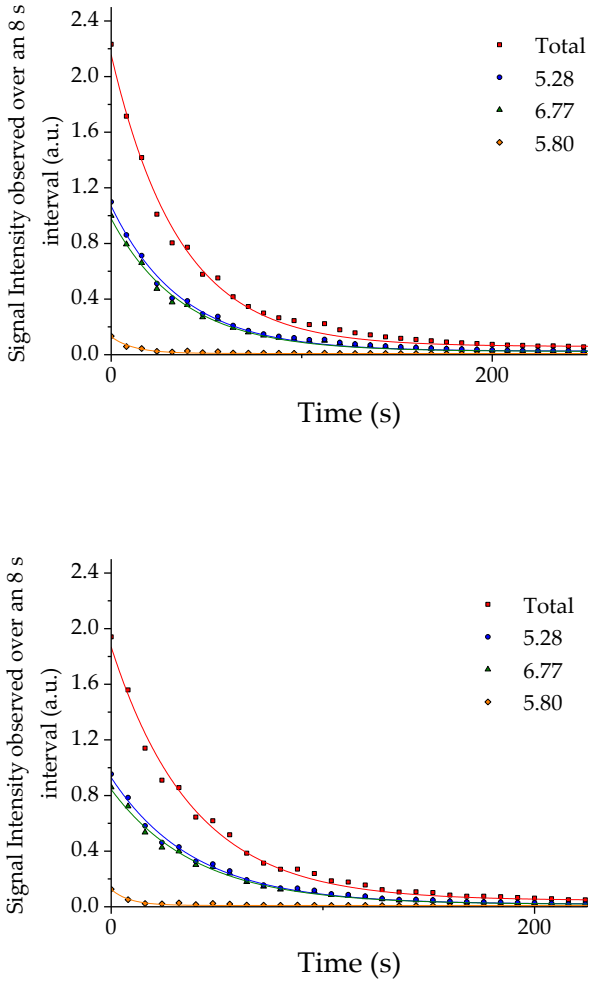

Figure 260: Plot to show the reduction in the change in intensity, over an 8 s interval, of the PASADENA signals corresponding to the para-H_2-derived protons in styrene, observed at the chemical shifts indicated in the key, with time, using 'activated' $[Pd_3(PPh_3)_4][BF_4]_2$. First shake (above), second shake (below).

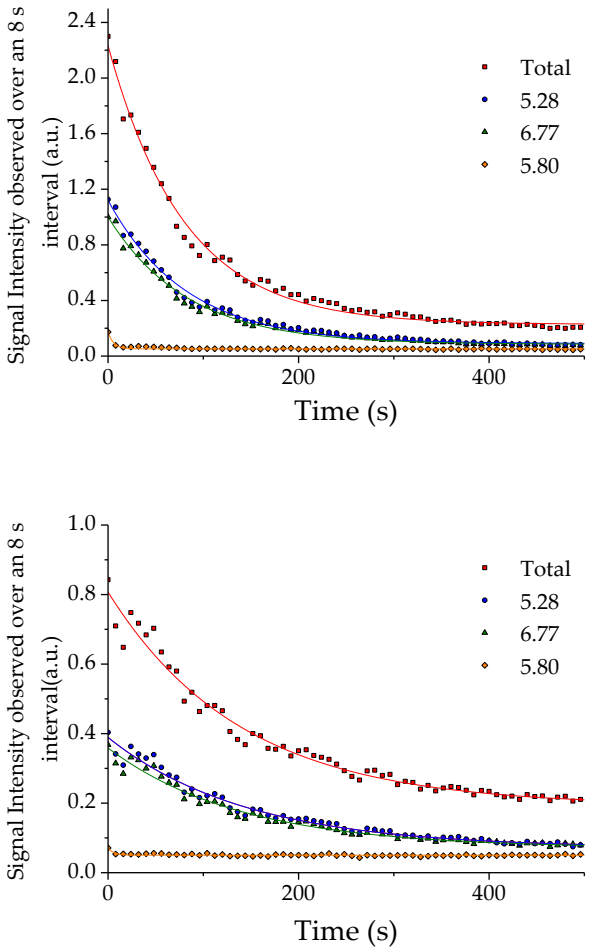

Figure 261: Plot to show the reduction in the change in intensity, over an 8 s interval, of the PASADENA signals corresponding to the para-H_2-derived protons in styrene, observed at the chemical shifts indicated in the key, with time, using $[Pd_3(PPh_3)_4][BF_4]_2$ with 10 equivalents of triphenylphosphine. First shake (above), second shake (below).

B.3.4 Letort's 'Order with Respect to Time, n_t' Method for Calculating Reaction Orders

Uniquely, the OPSY method used to compare the catalytic activity of the tri-palladium complexes with Crabtree's catalyst, in hydrogenation reactions, probes the reaction rate, rather than the reactant concentration, as a function of reaction time (see Figure 262). The resulting data can be used to calculate the reaction order with respect to hydrogen concentration, according to the formulae given below, where v is equal to the reaction rate, k is the rate constant, n is the reaction order, and c is the concentration of hydrogen.[303]

$$v = kc^n$$

$$log_{10}v = log_{10}k + nlog_{10}c$$

The gradient of a linear plot of $log_{10}v$ as a function of $log_{10}c$ is equal to the reaction order with respect to hydrogen concentration. Two different procedures can be used to obtain the data required for such a plot. The first is the 'order with respect to concentration, n_c' in which initial reaction rates are measured at various initial hydrogen concentrations. The second is the 'order with respect to time, n_t' in which the reaction rate is measured at different points in a reaction, as the hydrogen concentration changes. In implementing the OPSY method, the latter procedure has been followed, thus the reaction orders with respect to time, n_t have been calculated.

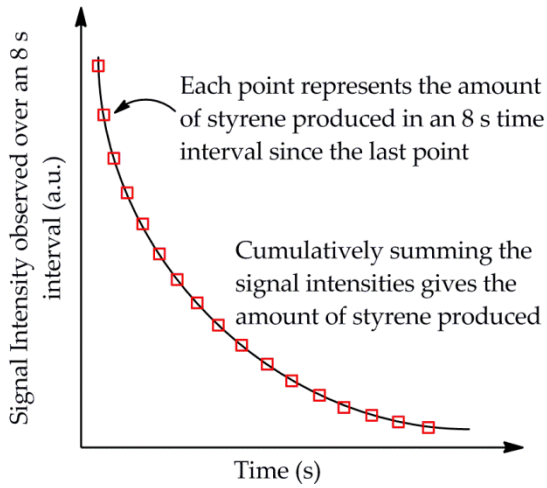

Figure 262: Plot to show the reduction in the change in signal intensity, over an 8 s interval, of the PASADENA signals corresponding to the para-H_2-derived protons in styrene, over time.

The concentration of hydrogen at different times can also be calculated from the OPSY data collected. The amount of styrene produced over time can be found by cumulatively summing the signal intensities, as described in Figure 262. An example plot is shown in Figure 263, which corresponds to the styrene produced on the second shake, using Crabtree's catalyst. Observed rate constants can also be calculated from these plots, and are given in Table 67. The trends observed with these values mirror the *pseudo*-rate constants discussed in Chapter 6.

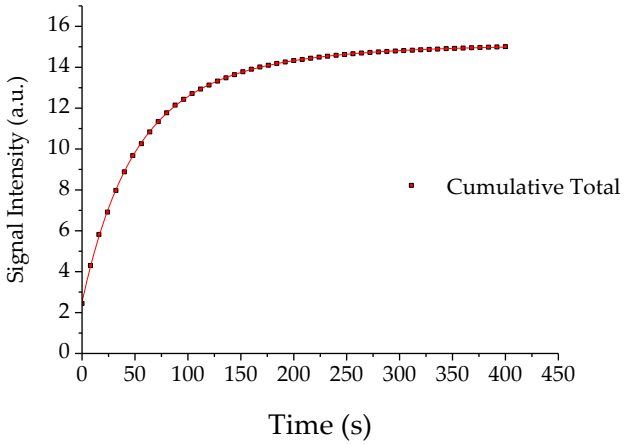

Figure 263: Plot of the cumulative sum of the signal intensity, observed over an 8 s interval, of the PASADENA signals corresponding to the para-H_2-derived protons in styrene, with time. This now corresponds to the amount of styrene produced, with time.

*Table 67: Pseudo rate constants and observed rate constants, of hydrogen consumption and styrene production respectively, in the hydrogenation of phenylacetylene, with 1.3 mM d_2-dichloromethane solutions of palladium catalyst with 66 equivalents of phenylacetylene and para-H_2 (3 bar). *'After activation' refers to samples that were left for several days after initial para-H_2 addition. Fresh phenylacetylene was then added, the sample was degassed, and fresh para-H_2 was added.*

Catalyst	*Ps* K_{obs} H_2 depletion ($x10^{-2}$ s^{-2})		K_{obs} H_2 depletion ($x10^{-2}$ s^{-1})	
	1	**2**	**1**	**2**
[Ir(COD)(PCy_3)(py)][PF_6]	8.5 ± 0.4	2.4 ± 0.1	9.5 ± 0.3	1.68 ± 0.02
[$Pd_3(PPh_3)_4$][BF_4]$_2$	0.27 ± 0.01	0.50 ± 0.02	0.198 ± 0.001	0.278 ± 0.003
[$Pd_3(PPh_3)_4$][BF_4]$_2$ (photoisomer)	0.25 ± 0.01	0.50 ± 0.01	0.204 ± 0.003	0.376 ± 0.003
[$Pd_3(PPh_3)_4$][BF_4]$_2$ (after activation*)	2.80 ± 0.07	2.61 ± 0.06	1.50 ± 0.05	1.60 ± 0.05
[$Pd_3(PPh_3)_4$][BF_4]$_2$ (+ 10 equiv. PPh_3)	1.25 ± 0.03	0.72 ± 0.03	0.49 ± 0.02	0.261 ± 0.007
[$Pd_3(PPh_3)_4$][BF_4]$_2$ (+ 10 equiv. PPh_3, after activation*)	-	-	-	-

The concentration of hydrogen in solution was calculated from the amount of styrene using the formula given below. Each shake dissolves 2.7 μmol of hydrogen (calculated in Chapter 6) which corresponds to an initial hydrogen concentration of 4.49 mM.

$$[H_2]_t = \frac{[styrene]_t[H_2]_{t=0}}{[styrene]_{t=\infty}}$$

Plots of $log_{10}v$ as a function of $log_{10}c$ are shown for all the catalysts used in Figure 264-Figure 268. These graphs were plotted using the Origin software, and were fitted to find n_t using linear regression. The errors in the data were calculated by the Origin software using an identical method to the Jack-knife method described in Appendix A.

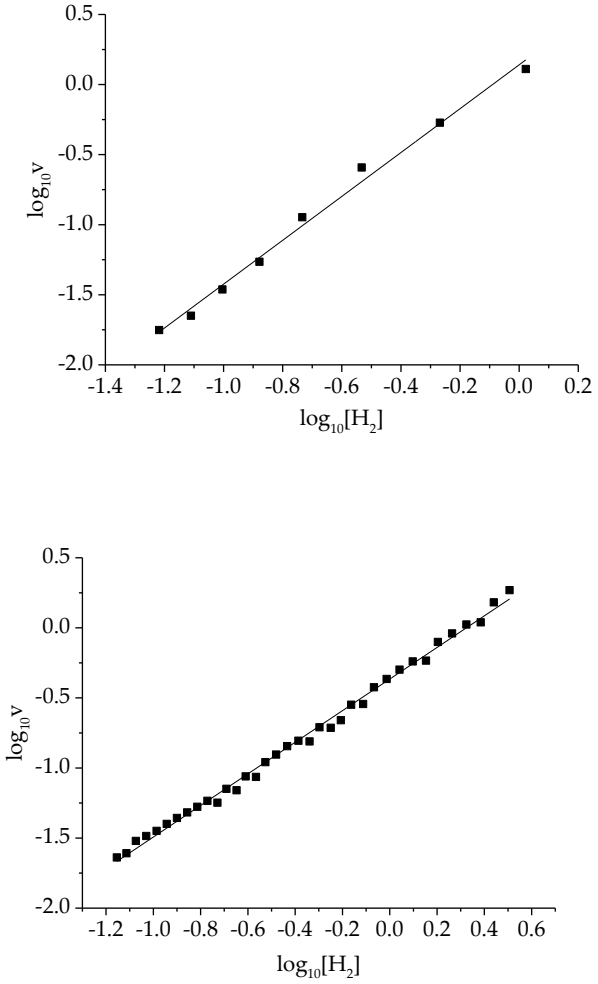

Figure 264: Double logarithmic plot of rate against hydrogen concentration of the para-hydrogenation of phenylacetylene using [Ir(COD)(PCy_3)(py)][PF_6]. First shake (above), second shake (below).

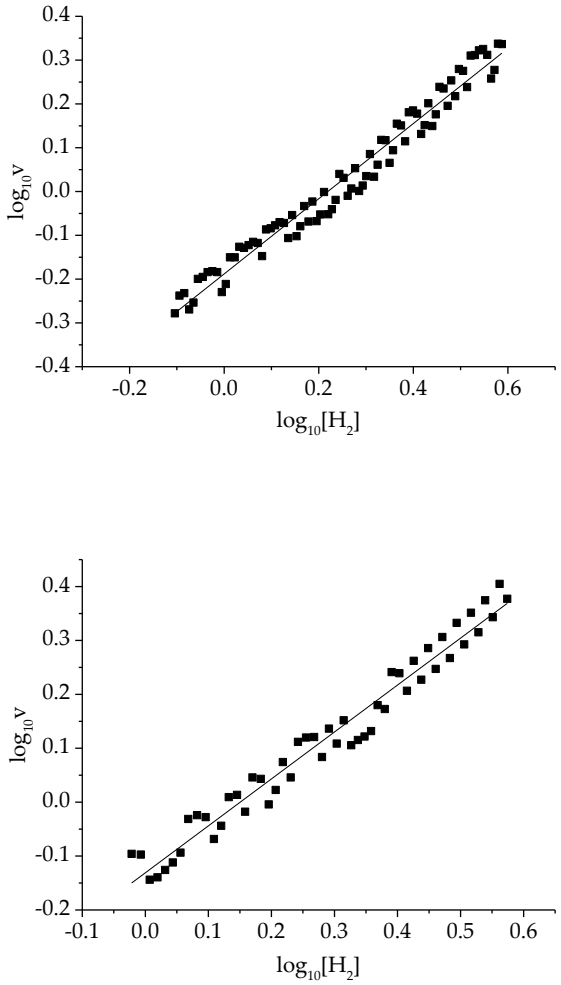

Figure 265: Double logarithmic plot of rate against hydrogen concentration of the para-hydrogenation of phenylacetylene using the thermal isomer of $[Pd_3(PPh_3)_4][BF_4]_2$. First shake (above), second shake (below).

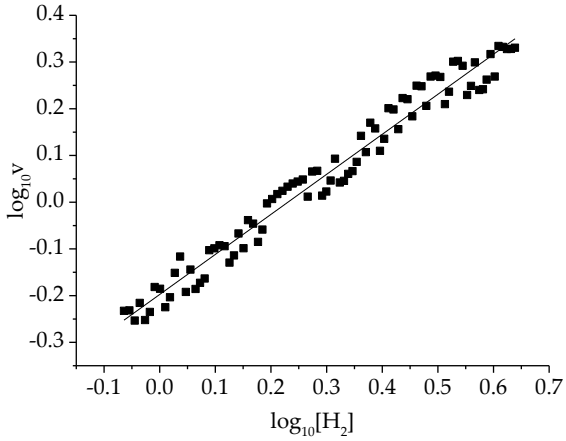

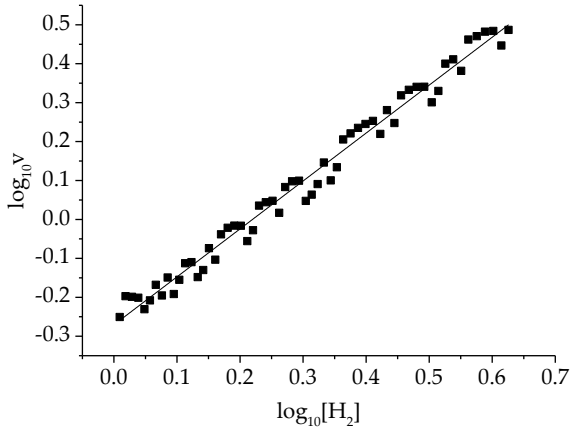

Figure 266: Double logarithmic plot of rate against hydrogen concentration of the para-hydrogenation of phenylacetylene using the photoisomer of $[Pd_3(PPh_3)_4][BF_4]_2$. First shake (above), second shake (below).

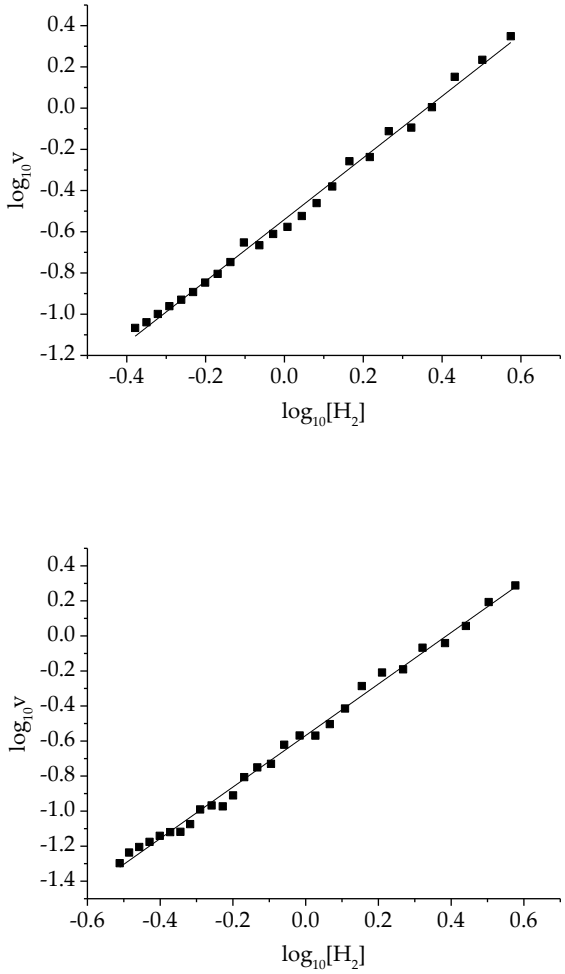

Figure 267: Double logarithmic plot of rate against hydrogen concentration of the para-hydrogenation of phenylacetylene using 'activated' $[Pd_3(PPh_3)_4][BF_4]_2$. First shake (above), second shake (below).

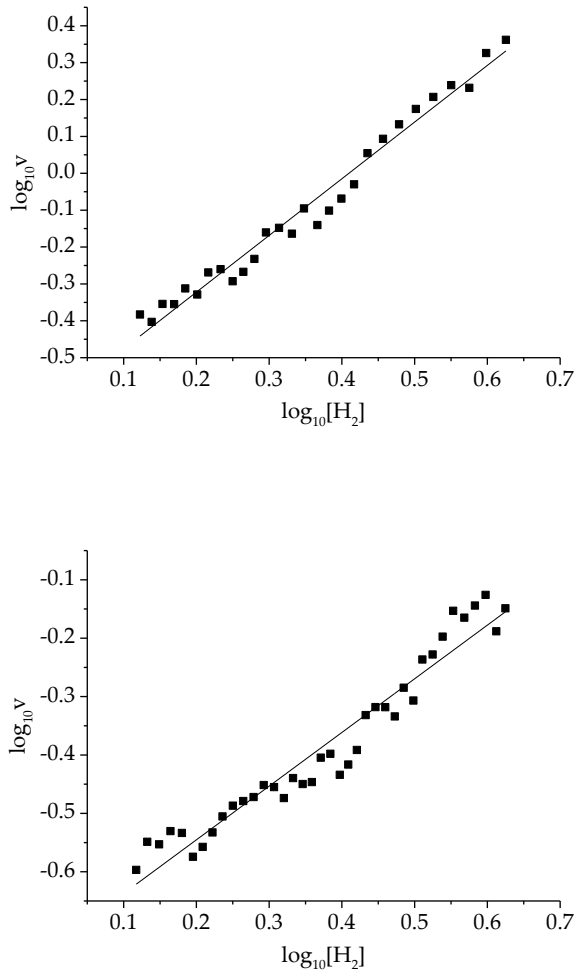

Figure 268: Double logarithmic plot of rate against hydrogen concentration of the para-hydrogenation of phenylacetylene using $[Pd_3(PPh_3)_4][BF_4]_2$ with 10 equivalents of triphenylphosphine. First shake (above), second shake (below).

Experimental

E.1 Instrumentation

E.1.1 NMR Spectrometers and Solvents

All NMR characterisation was conducted on Bruker NMR spectrometers, using Avance III 400, and 500 MHz spectrometers, where the ^{1}H NMR frequency is measured at 400.1, and 500.1, MHz, respectively. The ^{13}C NMR frequency is measured at 100.6 (400), and 125.8 (500) MHz, ^{15}N NMR frequency at 50.7 (500) MHz, ^{31}P NMR frequency at 162.0 (400) and 202.5 (500) MHz, and ^{19}F frequency at 470.5 (500) MHz. Bruker Topspin software, versions 3.17 and 3.26, was used for data acquisition and processing.

Chemical shifts are given in parts per million (ppm) with respect to the residual solvent signal. The deuterated solvents used for NMR samples were d_2-dichloromethane, where the proton in residual d_1-dichloromethane is the reference signal; d_1-chloroform, where the proton in residual chloroform is the reference; d_6-benzene, where the proton in residual d_5-benzene is the reference; d_6-acetone, where the proton in residual d_5-acetone is the reference; d_6-dimethylsulfoxide, where the proton in residual d_5-dimethylsulfoxide is the reference; d_4-methanol, where the proton in residual d_3-methanol is the reference; and d_6-ethanol, where the proton in residual d_5-ethanol is the reference. Herein, multiplicities are quoted as s (singlet), d (doublet), t (triplet), q (quartet), m (multiplet), br. (broad), *ps* (pseudo), and AA'XX'. *J* couplings are given in Hz. The method used to calculate *J* couplings from AA'XX' splitting patterns is given in Appendix A.

E.1.2 UV-vis Spectrometer

All UV-vis absorption spectra were recorded using an Evolution Array UV-vis spectrophotometer, with a window of 190-1100 nm. Data was processed using VISION*collect* software. 'Background' absorption spectra of the solvents used were subtracted from sample spectra. Herein, the wavelengths of maximum absorption (λ_{max}) are given in nm, and molar absorption coefficients (ε) are given in $mol^{-1}dm^{3}cm^{-1}$.

E.1.3 Mass Spectrometers

All molecular ion signals were observed using either electrospray ionisation (ESI) or liquid introduction field desorption ionisation (LIFDI) techniques. The latter technique is a soft ionisation technique used for non-polar, or unstable metal complexes to prevent fragmentation. Accurate mass is not possible with LIFDI. A Bruker micrOTOF time of flight mass spectrometer, with an ESI source was used to collect all ESI-MS data. A Waters GCT Premier time of flight mass spectrometer with LIFDI was used to collect all LIFDI MS data. Herein, all mass spectrometry data is given in *m*/*z* ratio.

E.1.4 Elemental Analysis

Samples were prepared using a Sartorius SE2 analytical balance, capable of weighing accurately to four decimal places on a milligram. An Exeter Analytical CE-440 elemental analyser was used to collect all elemental analysis data, which is calibrated against acetanilide standards. Samples are run as duplicates. Herein, the amounts of carbon (C), hydrogen (H), and nitrogen (N) are given as mean percentages.

E.1.5 X-ray Crystallography

Suitable single crystals were selected and crystallography data was collected on a SuperNova, single source at offset, Eos diffractometer which has dual Mo & Cu sources. The crystal was kept at 110.05(10) K during data collection. Using Olex2[330], the structure was solved with the ShelXS[331] structure solution program using Direct Methods and refined with the ShelXL refinement package using Least Squares minimisation. Mercury software was used to visualise structures. Herein, crystal structures are presented (solvent molecules and counterions have been omitted for clarity), alongside crystallographic data.

E.1.6 *Para*-H_2 Rig

Para-H_2 of 99% purity was generated using a *para*-H_2 rig. In this, hydrogen gas is cooled to 30 K, using a closed cycle helium refrigeration unit, and passed over paramagnetic Fe_2O_3, which converts *ortho*-H_2 to *para*-H_2. Unless stated otherwise, H_2 pressures of 3 bar were used.

E.1.7 Flow System

A Bruker hydrogen generator was used to supply *para*-H_2 in this setup. This generates hydrogen through the electrolysis of water. This is then converted to *para*-H_2 in a similar way to the *para*-H_2 rig. The *para*-H_2 generated is connected to a reaction cell which allows a sample to be hyperpolarized in a predefined magnetic field. The sample can then be transferred to the flow probe integrated into the NMR spectrometer.[149] This allows the study of the hyperpolarisation levels in the created nuclear spin states.

E.2 General Experimental Procedures

All commercially sourced solvents were purchased from VWR, Cambridge Isotope Laboratories, and Goss Scientific. Commercially sourced reagents were purchased from Alfa Aesar, Acros, and Sigma Aldrich. Herein, any procedures that required nitrogen atmospheres were carried out using standard Schlenk techniques, or in an MBraun Unilab glovebox. When necessary, solvents were dried using an Innovative Technology anhydrous solvent system, or distilled from an appropriate drying agent under nitrogen. A LOT Hg/Xe Arc lamp, model LSE 139, with an output of 200-2500 nm, was used with a LOT LSN 271 power supply to irradiate samples, when necessary. Samples were irradiated in an NMR probe, with a liquid nitrogen cooling system, and a EUROTHERM B-VT 2000 variable temperature unit.

E.2.1 NMR Pulse Lengths used to Probe PHIP

The product operator formalism is a useful quantum mechanical approach to describe NMR experiments. Product operators represent measurable quantities, including angular momentum, and operate on functions to give new functions. Nuclear spins have spin angular momentum, with x, y and z components. These are represented by the operators I_x, I_y, and I_z, and the density operator at time t, σ_t can be expressed as a sum of these. At equilibrium σ_{eq} is given by the formula below.

$$\sigma_{eq} = I_z$$

To simplify the theory, the evolution of spin angular momentum under coupling is not considered. Application of a pulse, of duration t_p, in the x-plane, to magnetization at

equilibrium gives the product operators shown below, where ω_1 is the frequency of rotation, which is equal to the larmor frequency of the probed nucleus, $\omega = -\gamma B$.

$$I_z \xrightarrow{\omega_1 I_x t_p} cos\omega_1 t_p I_z - sin\omega_1 t_p I_y$$

The application of a pulse in the x-plane rotates the magnetisation, so that the nucleus now possesses angular momentum in both the −y and z planes. The diagram in Figure 269 shows the rotation of magnetisation on application of a pulse in the z, x or y plane.

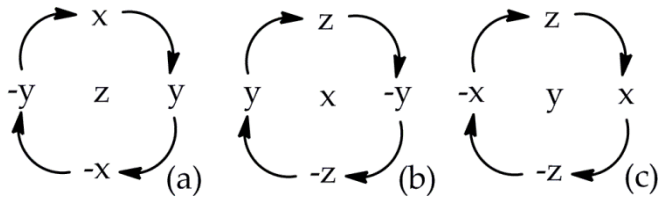

Figure 269: Diagram to show the rotation of magnetisation on application of a pulse in the (a) z-plane, (b) x-plane and (c) y-plane.

Magnetisation in the xy plane is detected and gives rise to free induction decay (FID), hence the spin angular momentum in the z plane ($cos\omega_1 t_p I_z$) does not contribute to the signal. Only the second term ($sin\omega_1 t_p I_y$) need be considered as this is the only term that contributes to the FID. This term is maximised when $sin\omega_1 t_p = 1$, i.e. when a π/2 pulse is used to give $\sigma = -I_y$.

Similarly, ALTADENA leads to antiphase peaks with density operators at equilibrium equal to $\sigma_{eq} = -I_z$. Application of a pulse in the x-plane to such magnetization gives the following product operators:

$$-I_z \xrightarrow{\omega_1 I_x t_p} -cos\omega_1 t_p I_z + sin\omega_1 t_p I_y$$

The magnetisation is rotated, so that the nucleus now possesses angular momentum in both the y and −z planes. As before, magnetisation detected in the xy plane is optimised with a π/2 pulse.

In the case of PASADENA, where polarisation is transferred and detected at high field, peaks are absorptive and emissive. Density operators at equilibrium are equal to $\sigma_{eq} = -I_z^A I_z^B$. Application of a pulse in the x-plane to such magnetization gives the following product operators:

$$-I_z^A I_z^B \xrightarrow{\omega_1 I_x^A t_p} -cos\omega_1 t_p I_z^A I_z^B + sin\omega_1 t_p I_y^A I_z^B$$

$$-cos\omega_1 t_p I_z^A I_z^B + sin\omega_1 t_p I_y^A I_z^B \xrightarrow{\omega_1 I_x^B t_p} -cos^2\omega_1 t_p I_z^A I_z^B + cos\omega_1 t_p sin\omega_1 t_p I_z^A I_y^B + cos\omega_1 t_p sin\omega_1 t_p I_y^A I_z^B + sin^2\omega_1 t_p I_y^A I_y^B$$

Again, the $I_z I_z$ term is not detected, nor is the $I_y I_y$ term, which leaves only $cos\omega_1 t_p sin\omega_1 t_p I_z^A I_y^B + cos\omega_1 t_p sin\omega_1 t_p I_y^A I_z^B$ for consideration. As this term contains both cosine and sine functions, it is maximised when using a π/4 pulse, giving:

$$\sigma = I_z^A I_y^B + I_y^A I_z^B$$

1-D SABRE and ALTADENA NMR spectra were collected using π/2 pulses and 1-D and 2-D PASADENA NMR spectra were collected using π/4 pulses.

E.2.2 Hyperpolarisation Method – Shake and Drop

NMR samples were prepared using, unless otherwise stated, 2 mg of polarisation transfer catalyst, 5 equivalents of substrate, and solvent (0.6 mL) which was added to a 5 mm NMR tube, fitted with a Young's tap. Samples were degassed, and then activated by the addition of hydrogen gas (3 bar).

Every shake and drop experiment required the evacuation of the headspace of the NMR tube, followed by the addition of *para*-H_2 (3 bar). The sample was then shaken outside the NMR spectrometer at approximately the required magnetic field (measured using a Gaussmeter) for 10 s before insertion into the NMR spectrometer, which was immediately followed by NMR FID acquisition. Unless otherwise stated, a single NMR scan was collected, with a receiver gain of 1, and a pulse angle of π/4.

E.2.3 Hyperpolarisation Method – Flow System

NMR samples were prepared using, unless otherwise stated, 10 mg of polarisation transfer catalyst, 5 equivalents of substrate, and solvent (3 mL) which was added to a Schlenk tube. The solution was degassed, and activated by the addition of hydrogen gas (3 bar). This was allowed to activate overnight.

The solution was transferred into a reaction cell, with a *para*-H_2 supply line. The magnetic field inside the reaction cell can be accurately controlled by a surrounding coil, which produces static fields from −150 to +150 G. The time duration that *para*-H_2 is

bubbled into the sample, prior to sample transfer into the flow probe inside the NMR spectrometer, can also be controlled. Nitrogen gas was used to transfer the sample into, and out of the flow probe. Unless otherwise stated, a *para*-H_2 pressure of 3 bar was used, and a single NMR scan was collected, with a receiver gain of 1, and a pulse angle of $\pi/4$.

E.2.4 Imaging Acquisition

For imaging experiments, all data was acquired on a 400 MHz Bruker spectrometer equipped with a micro imaging gradient system (1 T/m) and a standard 30 mm ^{1}H-^{13}C double resonance birdcage. For SABRE experiments, sample tubes were filled with 3 bars of *para*-H_2 and shaken in the stray field of the MRI magnet (*ca.* 70 G). As a reference, images of the samples with Boltzmann-equilibrated magnetisations were recorded with a recycle delay of 100 s and 512 averages.

A standard rapid acquisition with refocused echoes (RARE) sequence,[332] composed of a train of 64 π pulses separated by an echo time (TE) of 8.15 ms (effective echo time, TE_{eff} = 260 ms), was used to collect images. Using a relatively small number of echoes, combined with a short echo time, minimises the effect of transverse relaxation and image contrast is dictated by spin density. All images used a field of view (FOV) of 30 x 30 mm, a slice thickness of 5 mm and a 64 x 64 matrix size. This led to a raw resolution of 0.47 x 0.47 x 5 mm^3. Data were processed by FT and zero filled to 128 x 128 (resulting digital resolution: 0.23 x 0.23 x 5 mm^3) using a sine-bell noise filter. Signal-to-noise ratio (SNR) values were calculated using an algorithm that assumed a Rice-type noise distribution.

E.2.5 Calculation of NMR Enhancements

NMR enhancements were calculated according to the following formula:

$$Enhancement\ Factor = \frac{Integral\ of\ hyperpolarised\ signal}{Integral\ of\ thermal\ signal}$$

Acquisition of the thermal signals, which possess a Boltzmann distribution of spin states, was conducted after the sample had been allowed ample time to align with the applied magnetic field inside the NMR spectrometer. This was typically around 10 minutes. The same acquisition parameters were used to collect both the hyperpolarised and thermal signals. Emissive hyperpolarised signals are quoted as having negative enhancement factors.

E.3 Synthesis

E.3.1 Palladium Complexes

E.3.1.1 Preparation and Characterisation of Tris(4-biphenyl)phosphine

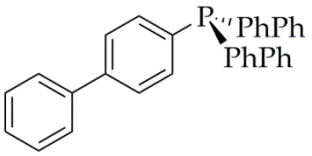

4-biphenylmagnesium bromide solution (0.5 M in THF, 16 mL, 8.0 mmol) was added dropwise to phosphorus trichloride (0.2 mL, 2.3 mmol) in dry, deoxygenated THF (~ 10 mL) at −78 °C, under a N_2 atmosphere. The olive/brown solution was stirred at −78 °C for 30 min., and then at r.t. overnight to form a pale yellow solution with a white MgBrCl precipitate. The reaction mixture was quenched with sat. ammonium chloride solution, extracted with DCM, and purified by column chromatography (silica; hexane:ethyl acetate 99:1 – 95:5). $P(PhPh)_3$ (0.803 g, 1.64 mmol) was isolated as a white solid, in 72% yield. ^{1}H NMR (500 MHz, $CDCl_3$): δ 7.61 (d, J_{HH} = 8.0, 12H, PCCHC**H**CCC**H**), 7.46 (d.d, J_{HP} = 9.0, J_{HH} = 8.0, 6H, PCC**H**), 7.44 (*ps*-t, J_{HH} = 7.4, 6H, PCCHCHCCCHC**H**), 7.35 (t, J_{HH} = 7.4, 3H, PCCHCHCCCHCHC**H**). ^{31}P NMR (203 MHz, $CDCl_3$): δ −7.48 (s.). ^{13}C NMR (126 MHz, $CDCl_3$): δ 141.6 (PCCHCH**C**), 140.5 (PCCHCHC**C**), 136.02 (P**C**), 134.2 (PC**C**H), 128.8 (PCCHCHCCCH**C**H), 127.6 (PCCHCHCCCHCH**C**H), 127.2 (PCCH**C**H), 127.0 (PCCHCHCC**C**H). ESI-MS: Calcd. for $C_{36}H_{28}P$ = 491.1923. Found 491.1898 $[M+H]^+$. Anal. Calcd. for $C_{36}H_{27}P$ (M_r = 490.57): C. 88.14, H. 5.55, N. 0.00. Found C. 87.30, H. 5.50, N. 0.00.

Compound reference kma-3-48

E.3.1.2 General Preparation of Phosphines ((4-Biphenyl)diphenylphosphine, (4-Benzylbenzene)diphenylphosphine)

The synthetic procedure by Tassone *et. al.* was adapted.[229] *n*-Butyllithium (1.2 eq.) was added dropwise to a stirred solution of the appropriate brominated precursor (4-bromobiphenyl or 1-benzyl 4-bromobenzene) in dry, deoxygenated THF (~ 10 mL) at −78 °C, under a N_2 atmosphere. The solution was stirred at −78 °C for 30 min., after which

time chlorodiphenylphosphine (1.1 eq.) was added dropwise to give a dark orange/red solution. This was stirred at −78 °C for 10 min., and then at r.t. for 30 min. The reaction mixture was quenched with sat. ammonium chloride solution, extracted with DCM, and purified by column chromatography (silica; hexane:ethyl acetate 95:5).

E.3.1.3 Characterisation of (4-Biphenyl)diphenylphosphine

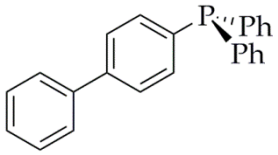

4-biphenyldiphenylphosphine (0.462 g, 1.34 mmol) was produced as a white crystalline solid, in 32% yield. ^{1}H NMR (500 MHz, $CDCl_3$), where C′ is biphenyl: δ 7.60 (dd, J_{HH} = 11.3, 8.2, 4H, PCCHC**H**), 7.46 (t, J_{HH} = 7.4, 2H, PCCHCHC**H**), 7.40 (dd, J_{HP} = 8.9, J_{HH} = 7.9, 4H, PCC**H**), 7.39-7.35 (m, 9H, PC′C**H**C**H**CCC**H**C**H**C**H**). ^{31}P NMR (203 MHz, $CDCl_3$): δ −6.09 (s.). ^{13}C NMR (126 MHz, $CDCl_3$): δ 141.5 (P**C′**), 140.5 (P**C**), 137.3 (PC′CHCH**C**), 137.1 (PC′CHCHC**C**), 133.8 (PC**C**H), 128.8 (PCCHCH**C**H), 127.1 (PCCH**C**H), 134.2, 133.8, 128.8, 128.5, 134.0 (PC′**C**H**C**HCC**C**H**C**H**C**H). ESI-MS: Calcd. for $C_{24}H_{20}P$ = 339.1297. Found 339.1302 $[M+H]^+$. Anal. Calcd. for $C_{24}H_{19}P$ (M_r = 338.38): C. 85.19, H. 5.66, N. 0.00. Found C. 84.37, H. 5.72, N. 0.00.

Compound reference kma-3-10

E.3.1.4 Characterisation of (4-Benzylbenzene)diphenylphosphine

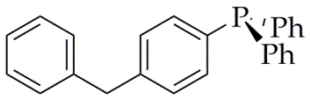

4-benzylbenzenediphenylphosphine (0.640 g, 1.80 mmol) was produced as a colourless oil, in 45% yield. ^{1}H NMR (500 MHz, $CDCl_3$), where C′ is benzylbenzene: δ 7.37-7.32 (m, 10 H, PCC**H**C**H**C**H**), 7.31 (d, J_{HH} = 7.6, 2H, PC′CHCHCCH_2CC**H**), 7.26 (d.d, J_{HP} = 8.0, J_{HH} = 8.0, 2H, PC′C**H**), 7.25-7.21 (m, 3H, PC′CHCHCCH_2CCHC**H**C**H**), 7.19 (d, J_{HH} = 8.0, 2H, PC′CHC**H**), 4.01 (s, 2H, PC′CHCHCC**H_2**). ^{31}P NMR (203 MHz, $CDCl_3$): δ −6.14

(s.). ^{13}C NMR (126 MHz, $CDCl_3$): δ 142.0 (PC'CHCH**C**), 140.6 (PC'CHCHCCH$_2$**C**), 137.2 (P**C**), 134.3 (P**C'**), 133.7 (PC'**C**H), 133.7 (1 of PC**C**H**C**H**C**H), 129.0 (PC'CH**C**H), 129.1 (PC'CHCHCCH$_2$CCH**C**H), 128.7 (1 of PC**C**H**C**H**C**H), 128.4 (PC'CHCHCCH$_2$C**C**H), 128.4 (1 of PC**C**H**C**H**C**H), 126.1 (PC'CHCHCCH$_2$CCH**C**H), 41.7 (PC'CHCH**C**H$_2$). ESI-MS: Calcd. for $C_{25}H_{22}P$ = 353.1454. Found 353.1442 $[M+H]^+$. Anal. Calcd. for $C_{25}H_{21}P$ (M_r = 352.41): C. 85.20, H. 6.01, N. 0.00. Found C. 84.98, H. 6.22, N. 0.00.

Compound reference kma-3-20

E.3.1.5 Preparation and Characterisation of $[Pd(Cl)_2(C_6H_5CN)_2]$

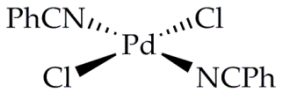

The synthetic procedure by Szlyk *et. al.* was adapted.[228] Benzonitrile (40 mL, 0.4 mol) was added to $PdCl_2$ (1.00 g, 5.64 mmol) and the mixture was stirred at 110 °C for 2 h. The resulting dark orange solution was filtered, whilst hot, and hexane (160 mL) was added to the filtrate at room temperature. Yellow $[Pd(Cl_2)(C_6H_5CN)_2]$ immediately precipitated out of solution. This was filtered, washed with hexane (~ 50 mL), and dried. $[Pd(Cl_2)(C_6H_5CN)_2]$ (1.921 g, 5.01 mmol) was produced as a yellow powder, in 89% yield. ^{1}H NMR (400 MHz, C_6D_6): δ 6.95 (d, J_{HH} = 6, 4H, NCCCHC**H**), 6.79 (t, J_{HH} = 8, 2H, NCCCHCHC**H**), 6.63 (t, J_{HH} = 8, 4H, NCCC**H**). ^{13}C NMR (101 MHz, C_6D_6): δ 131.66 (NCCCH**C**H), 131.61 (NCCCHCH**C**H), 128.47 (NCC**C**H), 112.70 (NC**C**), 118.38 (N**C**). Anal. Calcd. for $C_{14}H_{10}Cl_2N_2Pd$ (M_r = 383.57): C. 43.84, H. 2.63, N. 7.30. Found C. 44.44, H. 2.53, N. 7.31. Spectroscopic data matched that reported in the literature.

Compound reference kma-2-26

E.3.1.6 General Preparation of $[Pd(Cl)_2(XR_3)_2]$, where X = As or P, and R = aryl or alkyl

The synthetic procedure by Brumbaugh *et. al.* was adapted.[333] 2.1 equivalents of phosphine or arsine were dissolved in the minimum amount of dry, deoxygenated dichloromethane, and slowly added to a solution of $[Pd(Cl)_2(C_6H_5CN)_2]$ in dry,

deoxygenated dichloromethane. The mixture was stirred, under N_2, at room temperature for 5 min. The initial dark yellow/orange solution immediately turned bright yellow, and after approximately 2 minutes, the product crashed out of solution as a bright yellow precipitate. Diethy ether was added to encourage precipitation. The precipitate was filtered and washed with diethyl ether.

E.3.1.7 Characterisation of $[Pd(Cl_2)(PPh_3)_2]$

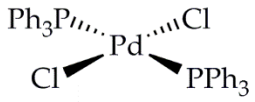

$[Pd(Cl_2)(PPh_3)_2]$ (0.359 g, 0.511 mmol) was produced in the *trans*-configuration as a bright yellow powder, in 98% yield. ^{1}H NMR (400 MHz, C_6D_6): δ 7.94-7.89 (m, 12 H, PCC**H**), 7.01-6.99 (m, 18 H, PCCHC**H**C**H**). ^{31}P NMR (162 MHz, C_6D_6): δ 23.76 (s.). ^{13}C NMR (101 MHz, C_6D_6): δ 135.25 (t., J_{CP} = 6 Hz, PC**C**H), 130.40 (d., J_{CP} = 25, P**C**), 130.15 (s, PCCHCH**C**H), 127.89 (s, PCCH**C**H). LIFDI-MS: 702.02 $[M+H]^+$. Anal. Calcd. for $C_{36}H_{30}Cl_2P_2Pd$ (M_r = 700.02): C. 61.60, H. 4.31, N. 0.00. Found C. 61.72, H. 4.29, N. 0.00. Spectroscopic data matched that reported in the literature.

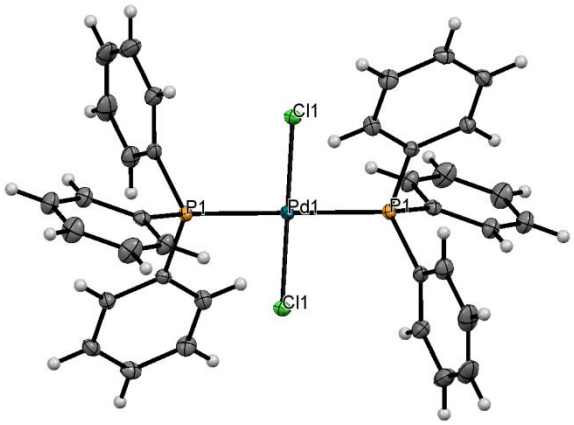

Figure 270: Crystal structure of $[Pd(Cl)_2(PPh_3)_2].(C_6H_6)_3$, with the benzene solvent omitted for clarity. Atom colours: C-grey, Cl-green, H-white, P-orange, Pd-blue.

Empirical formula	**$C_{60}H_{54}Cl_2P_2Pd$**
Formula weight	1014.27
Temperature/K	110.00(10)

Crystal system	triclinic
Space group	P-1
a/Å	10.5290(4)
b/Å	10.8248(5)
c/Å	12.1519(5)
α/°	70.611(4)
β/°	88.029(3)
γ/°	73.052(4)
Volume/Å^3	1246.73(9)
Z	1
ϱ_{calc}mg/mm^3	1.351
m/mm^{-1}	0.582
F(000)	524.0
Crystal size/mm^3	0.2114 × 0.1734 × 0.0927
2Θ range for data collection	6.34 to 60.06°
Index ranges	−14 ≤ h ≤ 14, −15 ≤ k ≤ 15, −17 ≤ l ≤ 17
Reflections collected	12367
Independent reflections	7285[R(int) = 0.0228]
Data/restraints/parameters	7285/0/295
Goodness-of-fit on F^2	1.052
Final R indexes [I>=2σ (I)]	R_1 = 0.0316, wR_2 = 0.0663
Final R indexes [all data]	R_1 = 0.0380, wR_2 = 0.0705
Largest diff. peak/hole / e Å^{-3}	0.52/−0.45

Compound reference kma-1-23

E.3.1.8 Characterisation of [Pd(Cl$_2$)(PPh$_2$Me)$_2$]

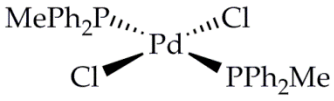

$[Pd(Cl)_2(PPh_2Me)_2]$ (0.140 g, 0.308 mmol) was produced in the *trans*-configuration as a bright orange powder, in 89% yield. ^{1}H NMR (400 MHz, CD_2Cl_2): δ 7.53 (br. d. J_{HH} = 6.2, 8H, PCC**H**), 7.45 (*ps*-t, J_{HH} = 6.9, 4H, PCCHCHC**H**), 7.38 (*ps*-t, J_{HH} = 7.5, 8H, PCCHC**H**), 1.90 (br. s. 6H, PC**H**$_3$). ^{31}P NMR (162 MHz, CD_2Cl_2): δ 17.15 (br. s.). ^{13}C NMR (101 MHz, CD_2Cl_2): δ 132.4 (PC**C**H), 130.0 (PCCHCH**C**H), 128.9 (P**C**), 128.4 (PCCH**C**H), 13.7 (P**C**H$_3$). LIFDI-MS: 577.98 (M^+). APCI-MS: Calcd. for $C_{26}H_{26}ClP_2Pd$ = 541.0234. Found 541.0251 [M-Cl]$^+$. Anal. Calcd. for $C_{26}H_{26}Cl_2P_2Pd$ (M_r = 577.76): C. 54.05, H. 4.54, N. 0.00. Found C. 58.63, H. 4.93, N. 0.00.

Compound reference kma-3-110

E.3.1.9 Characterisation of $[Pd(Cl)_2(P(Ph(p\text{-}OMe))_3)_2]$

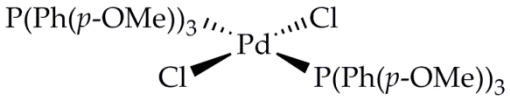

$[Pd(Cl)_2(P(Ph(p\text{-}OMe))_3)_2]$ (0.188 g, 0.213 mmol) was produced in both *cis*- and *trans*-configurations (26:74) as a bright yellow powder, in 82% yield. *Trans*-isomer: ^{1}H NMR (500 MHz, CD_2Cl_2): δ 7.63 (d.d.d, J_{HH} = 8.5, J_{HP} = 12.6, 2.1, 12H, PCC**H**), 6.96 (d, J_{HH} = 8.5, 12H, PCCHC**H**), 3.87 (s, 18H, OC**H**$_3$). ^{31}P NMR (203 MHz, CD_2Cl_2): δ 19.85 (s.). ^{13}C NMR (126 MHz, CD_2Cl_2): δ 161.4 (s, PCCHCH**C**), 136.4 (d, J_{HP} = 13.0, PC**C**H), 121.4 (d, J_{HP} = 66.8, P**C**), 113.5 (s, PCCH**C**H), 55.2 (s, O**C**H$_3$). *Cis*-isomer: ^{1}H NMR (500 MHz, CD_2Cl_2): δ 7.41 (d.d, J_{HH} =8.7, J_{HP} = 11.5, 12H, PCC**H**), 6.76 (d, J_{HH} = 8.7, 12H, PCCHC**H**), 3.84 (s, 18H, OC**H**$_3$). ^{31}P NMR (203 MHz, CD_2Cl_2): δ 30.30 (s.). ^{13}C NMR (126 MHz, CD_2Cl_2): δ 161.5 (s, PCCHCH**C**), 136.2 (d, J_{HP} = 13.0, PC**C**H), 121.8 (d, J_{HP} = 68.0, P**C**), 113.4 (s, PCCH**C**H), 55.3 (s, O**C**H$_3$). LIFDI-MS: 882.02 [M+H]$^+$. Anal. Calcd. for $C_{42}H_{42}Cl_2O_6P_2Pd$ (M_r = 880.09): C. 57.19, H. 4.80, N. 0.00. Found C. 56.63, H. 4.69, N. 0.00.

Compound reference kma-3-38

E.3.1.10 Characterisation of $[Pd(Cl)_2(P(Ph(p\text{-}CF_3))_3)_2]$

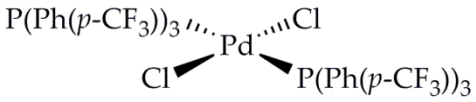

$[Pd(Cl)_2(P(Ph(p\text{-}CF_3))_3)_2]$ (0.214 g, 0.193 mmol) was produced in the *trans*-configuration as a bright yellow powder, in 74% yield. ^{1}H NMR (500 MHz, CD_2Cl_2): δ 7.86 (d.d, J_{HH} = 8.0, J_{HP} = 5.4, 12H, PCC**H**), 7.76 (d, J_{HH} = 8.0, 12H, PCCHC**H**). ^{31}P NMR (203 MHz, CD_2Cl_2): δ 23.35 (s.). ^{13}C NMR (126 MHz, CD_2Cl_2): δ 135.3 (PC**C**H), 133.2 (P**C**), 132.3 (PCCHCH**C**), 125.5 (PCCH**C**H), 122.2 (**C**F_3). ^{19}F NMR (471 MHz, CD_2Cl_2): −63.54. Anal. Calcd. for $C_{42}H_{24}Cl_2F_{18}P_2Pd$ (M_r = 1109.88): C. 45.45, H. 2.18, N. 0.00. Found C. 44.68, H. 2.10, N. 0.00.

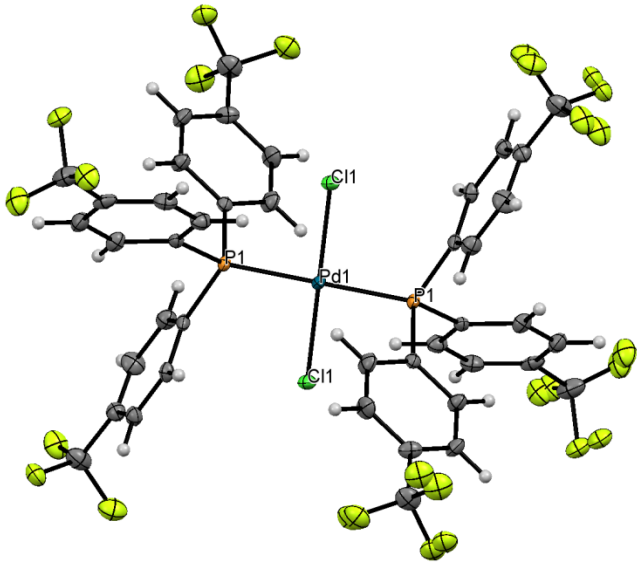

Figure 271: Crystal structure of $[Pd(Cl)_2(P(Ph(p\text{-}CF_3))_3)_2]$. Atom colours: C-grey, Cl-green, F-yellow, H-white, P-orange, Pd-blue.

Empirical formula	**$C_{43}H_{26}Cl_4F_{18}P_2Pd$**
Formula weight	1194.87
Temperature/K	110.00(14)
Crystal system	triclinic
Space group	P-1
a/Å	12.1511(8)
b/Å	14.0134(13)

c/Å	14.4505(10)
α/°	72.814(8)
β/°	78.373(6)
γ/°	75.432(7)
Volume/Å^3	2253.5(3)
Z	2
ϱ_{calc}g/cm^3	1.761
μ/mm^{-1}	0.828
F(000)	1180.0
Crystal size/mm^3	0.2114 × 0.0727 × 0.0502
Radiation	MoKα (λ = 0.71073)
2Θ range for data collection/°	6.932 to 60.518
Index ranges	−17 ≤ h ≤ 17, −19 ≤ k ≤ 19, −20 ≤ l ≤ 20
Reflections collected	14830
Independent reflections	14830 [R_{int} = ?, R_{sigma} = 0.0609]
Data/restraints/parameters	14830/405/743
Goodness-of-fit on F^2	0.919
Final R indexes [I>=2σ (I)]	R_1 = 0.0384, wR_2 = 0.0863
Final R indexes [all data]	R_1 = 0.0653, wR_2 = 0.0926
Largest diff. peak/hole / e Å^{-3}	1.02/−0.63

Compound reference kma-3-39

E.3.1.11 Characterisation of [Pd(Cl)$_2$(P(PhPh)$_3$)$_2$]

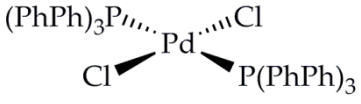

[Pd(Cl)$_2$(P(PhPh)$_3$)$_2$] (0.250 g, 0.216 mmol) was produced in both *cis*- and *trans*-configurations (20:80) as a bright yellow powder, in 83% yield. *Trans*-isomer: ^{1}H NMR (500 MHz, CD_2Cl_2): δ 7.94 (d.d, J_{HP} = 10.80, J_{HH} = 8.3, 12H, PCC**H**), 7.75 (d, J_{HH} = 8.3, 12H,

PCCHC**H**), 7.70 (d, J_{HH} = 8.2, 12H, PCCHCHCCC**H**), 7.50 (*ps*-t, J_{HH} = 7.6, 12H, PCCHCHCCCHC**H**), 7.43 (*ps*-t, J_{HH} = 7.4, 6H, PCCHCHCCCHCHC**H**). ^{31}P NMR (203 MHz, CD_2Cl_2): δ 22.23 (s.). ^{13}C NMR (126 MHz, CD_2Cl_2): δ 143.3 (PCCHCH**C**), 139.8 (PCCHCHC**C**), 135.4 (PC**C**H), 128.9 (PCCHCHCCCH**C**H), 128.4 (P**C**), 128.0 (PCCHCHCCCHCH**C**H), 127.1 (PCCHCHCC**C**H), 126.7 (PCCH**C**H). *Cis*-isomer: ^{31}P NMR (203 MHz, CD_2Cl_2): δ 31.31. LIFDI-MS: 1158.22 $[M]^+$, 1121.26 $[M\text{-}Cl]^+$, 490.17 (free phosphine). Anal. Calcd. for $C_{72}H_{54}Cl_2P_2Pd$ (M_r = 1158.47): C. 74.65, H. 4.70, N. 0.00. Found C. 74.08, H. 4.67, N. 0.00.

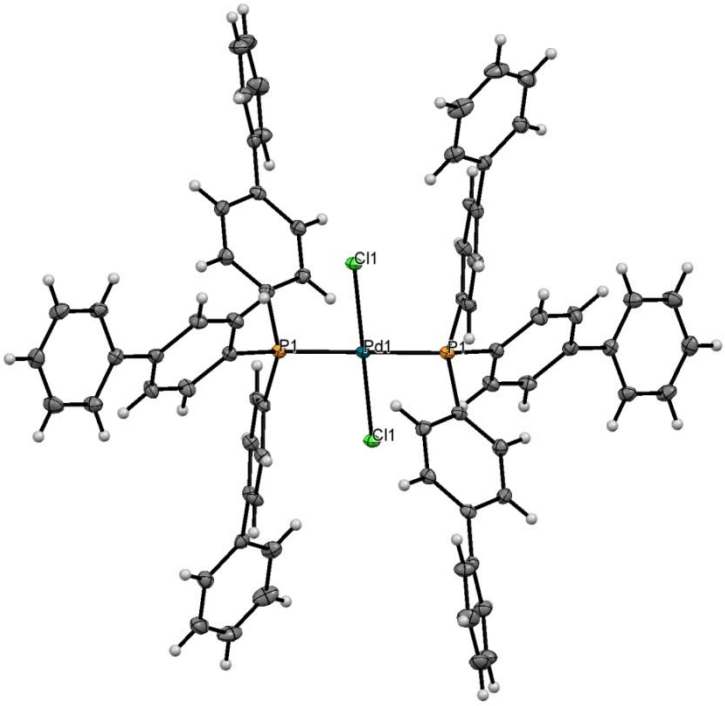

Figure 272: Crystal structure of $[Pd(Cl)_2(P(PhPh)_3)]$. Atom colours: C-grey, Cl-green, H-white, P-orange, Pd-blue.

Empirical formula	**$C_{72}H_{54}Cl_2P_2Pd$**
Formula weight	1158.39
Temperature/K	110.05(10)
Crystal system	triclinic
Space group	P-1
a/Å	10.4772(5)
b/Å	11.3875(4)
c/Å	11.5712(5)

α/°	96.254(3)
β/°	92.184(4)
γ/°	93.175(3)
Volume/Å^3	1368.88(10)
Z	1
ϱ_{calc}g/cm^3	1.405
μ/mm^{-1}	4.525
F(000)	596.0
Crystal size/mm^3	0.181 × 0.1461 × 0.1068
Radiation	CuKα (λ = 1.54184)
2Θ range for data collection/°	7.694 to 142.16
Index ranges	−12 ≤ h ≤ 12, −13 ≤ k ≤ 12, −14 ≤ l ≤ 11
Reflections collected	9196
Independent reflections	5170 [R_{int} = 0.0243, R_{sigma} = 0.0359]
Data/restraints/parameters	5170/0/349
Goodness-of-fit on F^2	1.057
Final R indexes [I>=2σ (I)]	R_1 = 0.0265, wR_2 = 0.0637
Final R indexes [all data]	R_1 = 0.0287, wR_2 = 0.0655
Largest diff. peak/hole / e Å^{-3}	0.43/−0.58

Compound reference kma-3-49

E.3.1.12 Characterisation of [Pd(Cl)$_2$(PPh$_2$(PhPh))$_2$]

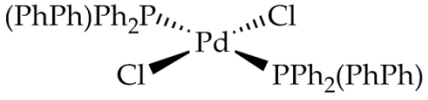

[Pd(Cl)$_2$(PPh$_2$(PhPh))$_2$] (0.156 g, 0.183 mmol) was produced in both *cis*- and *trans*-configurations (6:94) as a bright yellow powder, in 70% yield. *Trans*-isomer: ^{1}H NMR (500 MHz, CD_2Cl_2), where C' is biphenyl: δ 7.83 (d.d, J_{HP} = 5.3, J_{HH} = 8.3, 4H, PC'C**H**), 7.80 (d.d, J_{HP} = 6.0, J_{HH} = 7.2, 8H, PCC**H**), 7.70 (d, J_{HH} = 8.4, 4H, PC'CHC**H**), 7.68 (d, J_{HH} = 7.6, 4H,

PC'CHCHCCC**H**), 7.56 – 7.40 (m, 18H, PCCHC**H**C**H**, PC'CHCHCCCHC**H**C**H**). ^{31}P NMR (203 MHz, CD_2Cl_2): δ 23.09 (s.). ^{13}C NMR: (126 MHz, CD_2Cl_2): δ 143.2 (PC'CHCH**C**), 139.9 (PC'CHCHC**C**), 135.5 (PCCHCH**C**H), 135.4 (PC'**C**H), 134.9 (PC**C**H), 130.6 (PCCH**C**H), 129.7 (P**C**), 128.8 (PC'CHCHCCCH**C**H), 128.4 (P**C**'), 127.9 (PC'CHCHCCCHCH**C**H), 127.1 (PC'CHCHCC**C**H), 126.6 (PC'CH**C**H). *Cis*-isomer: ^{31}P NMR (203 MHz, CD_2Cl_2): δ 32.19 (s.). LIFDI-MS: 854.12 $[M]^+$. Anal. Calcd. for $C_{48}H_{38}P_2Cl_2Pd$ (M_r = 854.09): C. 67.50, H. 4.48, N. 0.00. Found C. 67.17, H. 4.42, N. 0.00.

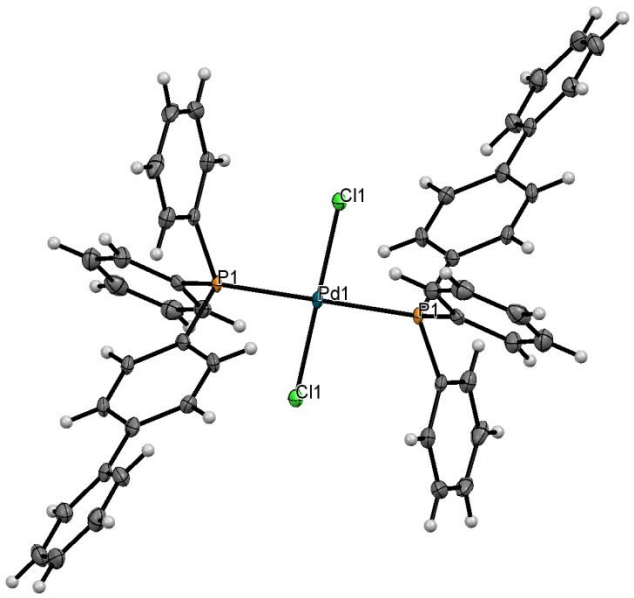

Figure 273: Crystal structure of $[Pd(Cl)_2(P(PhPh)Ph_2)_2]$. Atom colours: C-grey, H-white, P-orange, Pd-blue.

Empirical formula	**$C_{48}H_{38}P_2Cl_2Pd$**
Formula weight	854.02
Temperature/K	109.9(2)
Crystal system	triclinic
Space group	P-1
a/Å	9.9353(11)
b/Å	10.2582(7)
c/Å	11.4139(9)
α/°	79.750(6)
β/°	65.483(9)
γ/°	66.364(9)

Volume/Å^3	969.52(18)
Z	1
ϱ_{calc}g/cm^3	1.463
μ/mm^{-1}	6.166
F(000)	436.0
Crystal size/mm^3	0.2968 × 0.053 × 0.022
Radiation	CuKα (λ = 1.54184)
2Θ range for data collection/°	8.516 to 134.14
Index ranges	−10 ≤ h ≤ 11, −8 ≤ k ≤ 12, −11 ≤ l ≤ 13
Reflections collected	5919
Independent reflections	3407 [R_{int} = 0.0451, R_{sigma} = 0.0662]
Data/restraints/parameters	3407/0/241
Goodness-of-fit on F^2	1.041
Final R indexes [I>=2σ (I)]	R_1 = 0.0422, wR_2 = 0.1030
Final R indexes [all data]	R_1 = 0.0499, wR_2 = 0.1091
Largest diff. peak/hole / e Å^{-3}	0.85/−0.86

Compound reference kma-3-11

E.3.1.13 Characterisation of [Pd(Cl)$_2$(PPh$_2$(PhCH$_2$Ph))$_2$]

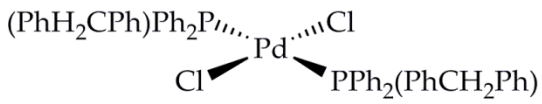

[Pd(Cl)$_2$(PPh$_2$(PhCH$_2$Ph))$_2$] (0.201 g, 0.228 mmol) was produced in both *cis*- and *trans*-configurations (5:95) as a bright yellow powder, in 87% yield. *Trans*-isomer: ^{1}H NMR (500 MHz, $CDCl_3$), where C' is benzylbenzene: δ 7.71 (d.d, J_{HP} = 6.1, J_{HH} = 7.3, 8H, PCC**H**), 7.66 (d.d, J_{HP} = 5.5, J_{HH} = 8.0, 4H, PC'C**H**), 7.43 (*ps*-t, J_{HH} = 7.2, 4H, PCCHCHC**H**), 7.39 (*ps*-t, J_{HH} = 7.3, 8H, PCCHC**H**), 7.32 (*ps*-t, J_{HH} = 7.6, 4H, PC'CHCHCCH2CCHC**H**), 7.24 (*ps*-t., J_{HH} = 7.3, 2H, PC'CHCHCCH$_2$CCHCHC**H**), 7.22 (d, J_{HH} = 7.6, 8H, PC'CHC**H**CCH$_2$CC**H**), 4.01 (s, 4H, PC'CHCHCC**H$_2$**). ^{31}P NMR (203 MHz, $CDCl_3$): δ 22.8 (s.). ^{13}C NMR (126 MHz, $CDCl_3$): δ

143.8 (PC'CHCH**C**), 140.1 (PC'CHCHCCH$_2$**C**), 135.3 (PC'**C**H), 135.0 (PC**C**H), 130.4 (PCCHCH**C**H), 129.1 (PC'CHCHCCH$_2$C**C**H), 128.6 (PC'CH**C**H), 128.5 (PC'CHCHCCH$_2$CCH**C**H), 128.0 (PCCH**C**H), 127.1 (P**C'**), 126.9 (P**C**), 126.3 (PC'CHCHCCH$_2$CCHCH**C**H), 41.8 (PC'CHCHC**C**H$_2$). *Cis*-isomer: ^{31}P NMR (203 MHz, $CDCl_3$): δ 32.02 (s.). LIFDI-MS: 882.13 $[M]^+$. Anal. Calcd. for $C_{50}H_{42}P_2Cl_2Pd$ (M_r = 882.14): C. 68.08, H. 4.80, N. 0.00. Found C. 67.17, H. 5.02, N. 0.00.

Compound reference kma-3-24

E.3.1.14 Characterisation of $[Pd(Cl)_2(AsPh_3)_2]$

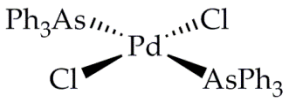

$[Pd(Cl)_2(AsPh_3)_2]$ (0.192 g, 0.243 mmol) was produced in the *trans*-configuration as a bright yellow powder, in 92% yield. ^{1}H NMR (400 MHz, CD_2Cl_2): δ 7.72 (d. J_{HH} = 8.4, 12 H, AsCC**H**), 7.53 (*ps*-t. J_{HH} = 7.4, 6H, AsCCHCHC**H**), 7.46 (*ps*-t, J_{HH} = 7.7, 12H, AsCCHC**H**). ^{13}C NMR (101 MHz, CD_2Cl_2): δ 134.3 (AsC**C**H), 131.6 (As**C**), 130.4 (AsCCHCH**C**H), 128.2 (AsCCH**C**H). LIFDI-MS: 789.9 $[M+H]^+$. Anal. Calcd. for $C_{36}H_{30}As_2Cl_2Pd$ (M_r = 787.92): C. 54.75, H. 3.83, N. 0.00. Found C. 54.21, H. 3.77, N. 0.00.

Compound reference kma-3-79

E.3.1.15 General Preparation of $[Pd(OTf)_2(XR_3)_2]$, where X = As or P, and R = aryl or alkyl

The synthetic procedure by Stang *et. al.* was adapted.[334] $[Pd(Cl)_2(XR_3)_2]$ was suspended in dry, deoxygenated dichloromethane, under N_2. 2.5 equivalents of AgOTf were added and stirred at room temperature, under N_2 for approximately 20 hours. The solution was protected from light during stirring. The resulting orange solution was cannula filtered from the white AgCl precipitate to produce a bright orange solution, which was reduced in volume. Dry hexane was added to encourage precipitation of the product. The solvent was removed by cannula filtration, leaving a precipitate, which was dried in *vacuo*.

E.3.1.16 Characterisation of $[Pd(PPh_3)_2(OTf)_2]$

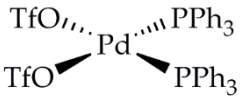

$[Pd(PPh_3)_2(OTf)_2]$ (0.314 g, 0.338 mmol) was isolated in 79% yield, as a yellow crystalline solid. ^{1}H NMR (500 MHz, CD_2Cl_2): δ 7.60 (t, J_{HH} = 7.3, 6H, CCHCHC**H**), 7.56 (d.d, J_{HP} = 6.4, J_{HH} = 7.9, 12H, PCCHC**H**), 7.39 (t.d, J_{HP} = 2.9, J_{HH} = 8.0, 12H, PCC**H**). ^{31}P NMR (203 MHz, CD_2Cl_2): δ 38.67 (s.). ^{13}C NMR (101 MHz, CD_2Cl_2): δ 134.5 (d, J_{PC} = 11.6, PC**C**H), 132.9 (s, PCCHCH**C**H), 129.3 (d, J_{PC} = 12.6, PCCHC**H**), 124.6 (d, J_{PC} = 60.9, P**C**). ^{19}F NMR (471 MHz, CD_2Cl_2): δ −78.42. LIFDI-MS: 779.05 $[M\text{-}OTf]^+$.

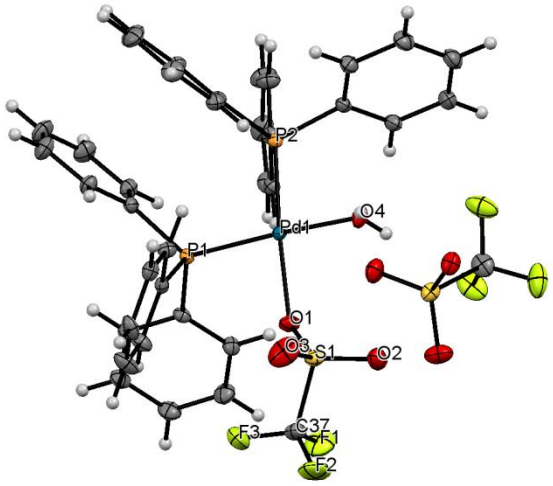

Figure 274: Crystal structure of $[Pd(OTf)(H_2O)(PPh_3)_2][OTf].CH_2Cl_2$, in which one triflate has been displaced by a water molecule and is now acting as a counterion. The CH_2Cl_2 solvent has been omitted for clarity. Atom colours: C-grey, F-yellow, H-white, O-red, P-orange, Pd-blue, S-gold.

Empirical formula	**$C_{39}H_{34}Cl_2F_6O_7P_2PdS_2$**
Formula weight	1032.02
Temperature/K	110.05(10)
Crystal system	triclinic
Space group	P-1
a/Å	13.0478(5)
b/Å	13.3777(7)

c/Å	14.5281(5)
α/°	96.467(4)
β/°	112.826(4)
γ/°	111.608(4)
Volume/Å^3	2074.19(16)
Z	2
ϱ_{calc}mg/mm^3	1.652
m/mm^{-1}	0.830
F(000)	1040.0
Crystal size/mm^3	0.2244 × 0.1744 × 0.1238
2Θ range for data collection	5.7 to 64.36°
Index ranges	−10 ≤ h ≤ 18, −19 ≤ k ≤ 13, −21 ≤ l≤ 19
Reflections collected	19959
Independent reflections	13114[R(int) = 0.0251]
Data/restraints/parameters	13114/0/540
Goodness-of-fit on F^2	1.030
Final R indexes [I>=2σ (I)]	R_1 = 0.0345, wR_2 = 0.0739
Final R indexes [all data]	R_1 = 0.0428, wR_2 = 0.0791
Largest diff. peak/hole / e Å^{-3}	0.98/−0.86

Compound reference kma-1-51

E.3.1.17 Characterisation of [Pd(OTf)$_2$(P(Ph(*p*-OMe))$_3$)$_2$]

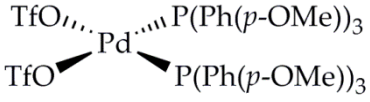

[Pd(OTf)$_2$(P(Ph(*p*-OMe))$_3$)$_2$] (0.087 g, 0.079 mmol) was isolated in 69% yield, as a yellow/orange solid. ^{1}H NMR (500 MHz, CD_2Cl_2): δ 7.46 (d.d, J_{HH} = 8.5, J_{HP} = 11.9, 12H, PCC**H**), 6.90 (d, J_{HH} = 8.5, 12H, PCCHC**H**), 3.89 (s, 18H, OC**H$_3$**). ^{31}P NMR (203 MHz,

CD_2Cl_2): δ 37.57 (s.). ^{13}C NMR (126 MHz, CD_2Cl_2): δ 163.3 (PCCHCH**C**), 136.2 (PC**C**H), 116.5 (P**C**), 114.9 (PCCH**C**H), 55.7 (O**C**H_3). ^{19}F NMR (471 MHz, CD_2Cl_2): δ −78.20.

Compound reference kma-3-41

E.3.1.18 Characterisation of $[Pd(OTf)_2(P(Ph(p\text{-}CF_3))_3)_2]$

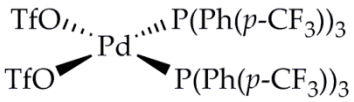

$[Pd(OTf)_2(P(Ph(p\text{-}CF_3))_3)_2]$ (0.093 g, 0.070 mmol) was isolated in 77% yield, as a bright yellow solid. ^{1}H NMR (500 MHz, CD_2Cl_2): δ 7.77 (d.d, J_{HP} = 12.5, J_{HH} = 8.2, 12 H, PCC**H**), 7.72 (d.d, J_{HP} = 1.8, J_{HH} = 8.2, 12 H, PCCHC**H**). ^{31}P NMR (203 MHz, CD_2Cl_2): δ 35.84 (s.). ^{13}C NMR (126 MHz, CD_2Cl_2): δ 135.1 (s, PC**C**H), 127.7 (d, J_{CP} = 95, P**C**), 126.6 (s, PCCH**C**H), 124.1 (s, PCCHCH**C**), 121.9 (PCCHCHC**C**F_3). ^{19}F NMR (471 MHz, CD_2Cl_2): δ −63.96 (PCCHCHCC**F**$_3$), −78.21.

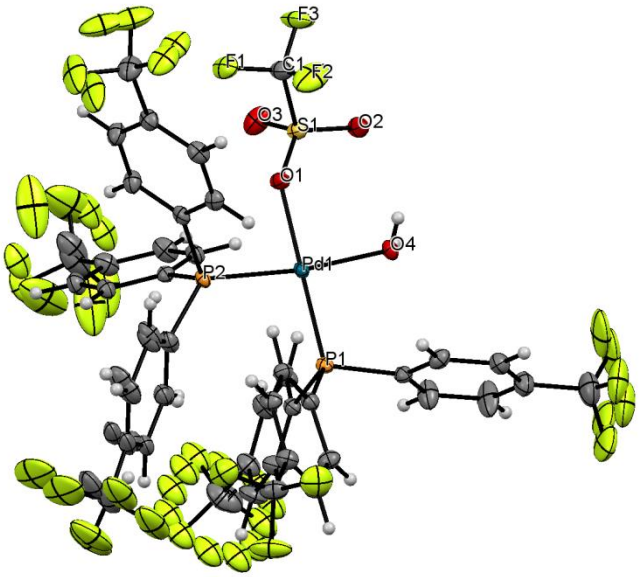

Figure 275: Crystal structure of [Pd(OTf)(H$_2$O)(P(Ph(p-CF$_3$))$_3$)$_2$][OTf], with the triflate counterion omitted for clarity. Atom colours: C-grey, F-yellow, H-white, O-red, P-orange, Pd-blue, S-gold.

Empirical formula	**$C_{44}H_{26}F_{24}O_7P_2PdS_2$**
Formula weight	1356.02
Temperature/K	110.05(10)

Crystal system	Monoclinic
Space group	$P2_1/n$
a/Å	14.4417(2)
b/Å	26.4202(4)
c/Å	14.5018(3)
α/°	90
β/°	102.4602(17)
γ/°	90
Volume/Å^3	5402.87(16)
Z	4
ϱ_{calc}g/cm^3	1.667
μ/mm^{-1}	5.255
F(000)	2682.0
Crystal size/mm^3	0.2898 × 0.0656 × 0.021
Radiation	CuKα (λ = 1.54184)
2Θ range for data collection/°	7.082 to 142.488
Index ranges	−17 ≤ h ≤ 16, −32 ≤ k ≤ 27, −17 ≤ l ≤ 17
Reflections collected	30262
Independent reflections	10285 [R_{int} = 0.0317, R_{sigma} = 0.0317]
Data/restraints/parameters	10285/108/812
Goodness-of-fit on F^2	1.022
Final R indexes [I>=2σ (I)]	R_1 = 0.0327, wR_2 = 0.0822
Final R indexes [all data]	R_1 = 0.0374, wR_2 = 0.0860
Largest diff. peak/hole / e Å^{-3}	0.76/−0.76

Compound reference kma-3-44

E.3.1.19 Characterisation of $[Pd(OTf)_2(P(PhPh)_3)_2]$

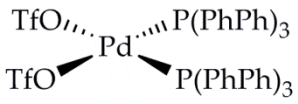

$[Pd(OTf)_2(P(PhPh)_3)_2]$ (0.101 g, 0.073 mmol) was isolated in 84% yield, as a bright orange solid. ^{1}H NMR (500 MHz, CD_2Cl_2): δ 7.77 (d.d, J_{HP} = 12.7, J_{HH} = 8.2, 12H, PCC**H**), 7.66 (d.d, J_{HP} = 2.2, J_{HH} = 8.5, 12H, PCCHC**H**), 7.60 (d, J_{HH} = 8.3, 12H, PCCHCHCCC**H**), 7.51-7.42 (m, 18H, PCCHCHCCCHC**H**C**H**). ^{31}P NMR (203 MHz, CD_2Cl_2): δ 37.38 (s.). ^{13}C NMR (126 MHz, CD_2Cl_2): δ 145.6 (PCCHCH**C**), 138.7 (PCCHCHC**C**), 135.1 (PC**C**H), 129.1 (PCCHCHCCCH**C**H), 128.7 (PCCHCHCCCHCH**C**H), 127.6 (PCCH**C**H), 127.2 (PCCHCHCC**C**H), 123.3 (d, J_{CP} = 69.4, P**C**). ^{19}F NMR (471 MHz, CD_2Cl_2): δ −78.14.

Compound reference kma-3-51

E.3.1.20 Characterisation of $[Pd(OTf)_2(PPh_2(PhPh))_2]$

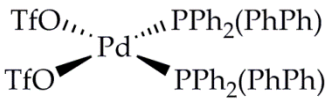

$[Pd(OTf)_2(PPh_2(PhPh))_2]$ (0.048 g, 0.044 mmol) was isolated in 63% yield, as a bright orange/yellow solid. ^{1}H NMR (500 MHz, CD_2Cl_2) where C′ is biphenyl: δ 7.70 (d.d, J_{HP} = 13, J_{HH} = 8.2, 8H, PCC**H**), 7.64 (t, J_{HH} = 7.8, 4H, PCCHCHC**H**), 7.61 (d, J_{HH} = 8.2, 4H, PC′CHCHCCC**H**), 7.56 (d, J_{HP} = 9.0, 8H, PC′C**H**C**H**), 7.51 (t, J_{HH} = 6.9, PC′CHCHCCCHC**H**), 7.45 (t.d, 8H, J_{HP} = 3.0, J_{HH} = 7.8, PCCHC**H**). ^{31}P NMR (203 MHz, CD_2Cl_2): δ 38.3 (s.). ^{13}C NMR: (126 MHz, CD_2Cl_2): δ 145.5 (PC′CHCH**C**), 138.7 (PC′CHCHC**C**), 134.9 (PC′**C**H), 134.7 (PC**C**H), 133.0 (PCCHCH**C**H), 129.3 (PCCH**C**H), 129.1 (PC′CHCHCCCH**C**H), 128.7 (PC′CHCHCCCHCH**C**H), 127.5 (PC′CH**C**H), 127.1 (PC′CHCHCC**C**H), 124.9 (P**C**), 122.7 (P**C′**). ^{19}F NMR (471 MHz, CD_2Cl_2): δ −78.2.

Compound reference kma-3-13

E.3.1.21 Characterisation of $[Pd(OTf)_2(PPh_2(PhCH_2Ph))_2]$

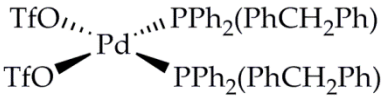

$[Pd(OTf)_2(PPh_2(PhCH_2Ph))_2]$ (0.079 g, 0.071 mmol) was isolated in 62% yield, as a bright orange/yellow solid. ^{1}H NMR (500 MHz, CD_2Cl_2) where C′ is benzylbenzene: δ 7.56 (t, J_{HH} = 7.1, 4H, PCCHCHC**H**), 7.52 (d.d, J_{HP} = 13.0, J_{HH} = 7.6, 8H, PCC**H**), 7.38-7.30 (m, 16H, PCCHC**H**, PC′C**H**CHCCH$_2$CC**H**), 7.28 (t, J_{HH} = 7.3, 2H, PC′CHCHCCH$_2$CCHCHC**H**), 7.21 (d, J_{HH} = 7.8, PC′CHCHCCH$_2$CCHC**H**), 7.13 (d.d, 4H, J_{HP} = 2.0, J_{HH} = 8.2, PC′CHC**H**), 4.00 (s, 4H, PC′CHCHCC**H$_2$**). ^{31}P NMR (203 MHz, CD_2Cl_2): δ 38.12 (s.). ^{13}C NMR (126 MHz, CD_2Cl_2): δ 147.2 (PC′CHCH**C**), 140.0 (PC′CHCHCCH$_2$**C**), 134.7 (PCCH**C**H), 134.5 (PC**C**H), 132.9 (PCCHCH**C**H), 129.5 (s, PC′CH**C**H), 129.2 (PC′**C**H), 128.8 (PC′CHCHCC**H$_2$**CCH**C**H), 128.5 (PC′CHCHCCH$_2$C**C**H), 126.5 (PC′CHCHCCH$_2$CCHCH**C**H), 124.8 (s, P**C**), 121.8 (s, P**C′**), 41.7 (s, PC′CHCHC**C**H$_2$). ^{19}F NMR (471 MHz, CD_2Cl_2): δ −78.1.

Compound reference kma-3-28

E.3.1.22 Characterisation of $[Pd(OTf)_2(AsPh_3)_2]$

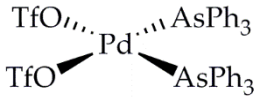

$[Pd(OTf)_2(AsPh_3)_2]$ (0.229 g, 0.241 mmol) was isolated in 86% yield, as a bright yellow powder. ^{1}H NMR (400 MHz, CD_2Cl_2): δ 7.55 (*ps*-t, J_{HH} = 7.4, 6 H, AsCCHCHC**H**), 7.51 (d, J_{HH} = 7.9, 12H, AsCC**H**), 7.36 (*ps*-t, J_{HH} = 7.8, 12H, AsCCHC**H**). ^{13}C NMR (101 MHz, CD_2Cl_2): δ 133.5 (AsC**C**H), 132.0 (AsCCHCH**C**H), 129.5 (AsCCH**C**H), 128.0 (As**C**).

Compound reference kma-3-82

E.3.1.23 Synthesis and Characterisation of [Pd(H)(OTf)(P(Ph(*p*-CF_3))$_3$)$_2$]

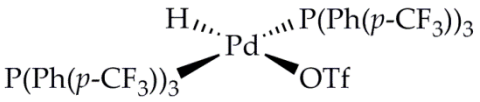

A d_2-dichloromethane (0.6 mL) solution of [Pd(OTf)$_2$(P(Ph(*p*-CF_3))$_3$)$_2$] (5 mg, 3.74 μmol) was inserted into a 5 mm NMR tube and degassed. *Para*-H_2 (3 bar) was added at r.t. to form [Pd(H)(OTf)(P(Ph(*p*-CF_3))$_3$)$_2$] quantitatively. This has not been isolated. ^{1}H NMR (500 MHz, CD_2Cl_2): δ 7.80 (d, J_{HH} = 8.1, 12 H, PCCHC**H**), 7.68 (d.d, J_{PH} = 14.5, J_{HH} = 8.1, 12 H, PCC**H**), −17.50 (t, J_{PH} = 7.3, 1 H, Pd**H**). ^{31}P NMR (203 MHz, CD_2Cl_2): δ 25.83 (s, **P**). ^{13}C NMR (126 MHz, CD_2Cl_2): δ 134.7 (s, PC**C**H), 133.4 (d, J_{PC} = 62.4, P**C**), 126.1 (s, PCCH**C**H), 124.8 (PCCHCHC**C**F_3), 122.2 (PCCHCH**C**).

Compound reference kma-3-45

E.3.1.24 Synthesis and Characterisation of [Pd(μ-OH)(PPh_3)$_2$]$_2$[BF_4]$_2$

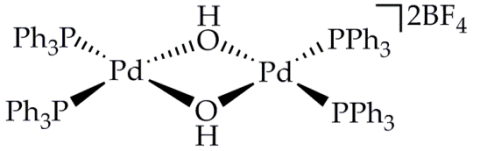

[Pd(μ-OH)(PPh_3)$_2$]$_2$[BF_4]$_2$ was synthesized according to published procedures.[335] [Pd(Cl)$_2$(PPh_3)$_2$] (0.5 g, 0.71 mmol) was dissolved in a mixture of DCM (~20 mL) and acetone (~10 mL). Silver tetrafluoroborate (0.286 g, 1.47 mmol) was dissolved in acetone (~15 mL) and added dropwise to the solution, which was stirred at room temperature for 15 minutes. During this time, white silver chloride precipitated from the solution. This was removed by filtering the solution through celite. Diethyl ether (~ 150 mL) was added to the solution, which was refrigerated overnight. A white powder precipitated and this was isolated by sinter filtration. [Pd(μ-OH)(PPh_3)$_2$]$_2$[BF_4]$_2$ (0.463 g, 0.314 mmol) was isolated in 88% yield as a white powder. ^{1}H NMR (400 MHz, CD_2Cl_2): δ 7.40 (*ps*-t. J_{HH} = 7.7, 12H, PCCHCHC**H**), 7.35 (d.d, J_{HH} = 11.5, 7.6, 24H, PCC**H**), 7.25 (*ps*-t, J_{HH} = 7.6, 24H, PCCHC**H**). ^{31}P NMR (162 MHz, CD_2Cl_2): δ 33.5 (s.). ^{13}C NMR (101 MHz, CD_2Cl_2): δ 134.0

(PC**C**H), 132.4 (PCCHCH**C**H), 129.3 (PCCH**C**H), 125.1 (P**C**). Spectroscopic data matched that reported in the literature.

Compound reference kma-4-04

E.3.1.25 Synthesis and Characterisation of $[Pd_3(PPh_3)_4][BF_4]_2$

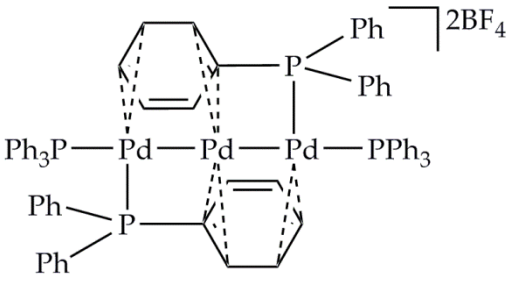

The synthetic procedure by Kannan *et. al.* was adapted.[266] $[Pd(\mu\text{-}OH)(PPh_3)_2]_2[BF_4]_2$ (50.0 mg, 34.0 μmol) was suspended in DCM (~2 mL). Ethanol was added dropwise to this, until the milky-white suspension became a bright red solution. The solution was then reduced in volume to precipitate bright red crystals. The solvent was decanted, and the crystals were washed with cold ethanol (~ 5 mL). $[Pd_3(PPh_3)_4][BF_4]_2$ (21.4 mg, 13.9 μmol) was isolated in 61% yield. ^{1}H NMR (400 MHz, CD_2Cl_2): δ 7.50 (d.d. J_{HP} = 10.8, J_{HH} = 8.1, 8H, PCC**H** of PPh_2), 7.50 (*p*-t, J_{HH} = 7.0, 4H, PCCHCHC**H** of PPh_2), 7.46 (*p*-t, J_{HH} = 7.5, 6H, PCCHCHC**H** of PPh_3), 7.36 (*p*-t, J_{HH} = 7.9, 12H, PCCHC**H** of PPh_3), 7.34 (*p*-t, J_{HH} = 8.0, 8H, PCCHC**H** of PPh_2), 7.28 (d.d. J_{HP} = 12.6, J_{HH} = 7.8, 12H, PCC**H** of PPh_3), 7.03 (s. br., J_{HH} = 6.1, 2H, PCCHCHC**H** of PPh-Pd), 6.0 (*p*-t, J_{HH} = 7.0, 4H, PCCHC**H** of PPh-Pd), 4.83 (*p*-t, J_{HP} = 9.4, J_{HH} = 7.9, 4H, PCC**H** of PPh-Pd). ^{31}P NMR (162 MHz, CD_2Cl_2): δ 42.80(AA'XX', $J_{AA'}$ = 12, J_{AX} = 30.9, $J_{AX'}$ = 10.4, $J_{XX'}$ = 97.5, 2P, **P**Ph-Pd (A)), 9.08 (AA'XX', $J_{AA'}$ = 12, J_{AX} = 30.9, $J_{AX'}$ = 10.4, $J_{XX'}$ = 97.5, 2P, **P**Ph_3 (X)). ^{13}C NMR (101 MHz, CD_2Cl_2): δ 135.3 (t, J_{CP} = 6.9, PC**C**H of PPh_2), 133.4 (t, J_{CP} = 6.4, PC**C**H of PPh_3), 132.6 (s, PCCHCH**C**H of PPh_2), 131.1 (s, PCCHCH**C**H of PPh_3), 129.3 (m, PCCH**C**H of both PPh_2 and PPh_3), 124.7 (d, J_{CP} = 60.9, P**C** of both PPh_2 and PPh_3), 116.7 (t, J_{CP} = 4, PCCH**C**H of PPh-Pd), 107.0 (t, J_{CP} = 4, PC**C**H of PPh-Pd), 87.8 (t, J_{CP} = 7, PCCHCH**C**H of PPh-Pd), 40.9 (d, J_{CP} = 54, P**C** of PPh-Pd). LIFDI-MS: 684.5 $[M\text{-}2BF_4]^{2+}$. UV-vis (CH_2Cl_2, λ_{max}, nm (ε, $mol^{-1}dm^3cm^{-1}$)): 339.14 (16 700), 379.36 (9 300), 491.76 (37 300). Spectroscopic data matched that reported in the literature.

Compound reference kma-4-35

E.3.1.26 Synthesis and Characterisation of $[Pd_3(PPh_3)_4][BF_4]_2$ (Photoisomer)

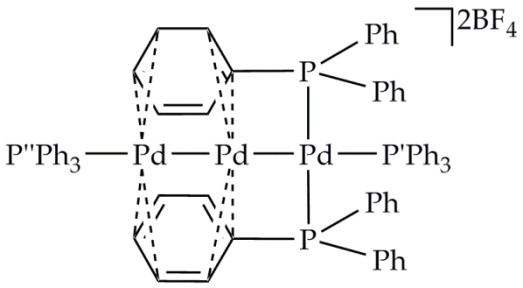

A d_2-dichloromethane (0.5 mL) solution of $[Pd_3(PPh_3)_4][BF_4]_2$ (2 mg, 1.3 μmol) was prepared in the glovebox and inserted into an NMR tube with a Young's cap. The solution was irradiated with UV light for 6 hr, at 240 K. The product has not been isolated. ^{1}H NMR (500 MHz, CD_2Cl_2): δ 7.62 (m, 3H, P''CCHCHC**H**), 7.60 (m, 6H, P''CC**H**), 7.58 (m, 6H, P''CCHC**H**), 7.52 (*ps*-t, J_{HH} = 7.43, 4H, PCCHCHC**H**), 7.33 (*ps*-t, J_{HH} = 7.2, 3H, P'CCHCHC**H**), 7.29 (*ps*-t, J_{HH} = 7.3, 8H, PCCHC**H**), 7.24 (d.d, J_{HP} = 14.0, J_{HH} = 7.9, 8H, PCC**H**), 7.16 (d.d, J_{HP} = 11.1, J_{HH} = 7.6, 6H, P'CC**H**), 7.10 (t.d, J_{HH} = 7.5, J_{HP} = 2.4, 6H, P'CCHC**H**), 7.08 (t, J_{HH} = 6.3, 2H, PCCHCHC**H** of PPh-Pd), 5.88 (d.d, J_{HH} = 8.1, 6.4, 4H, PCCHC**H** of PPh-Pd), 5.17 (m, J_{HP} = 14.0, 4H, PCC**H** of PPh-Pd). ^{31}P NMR (203 MHz, CD_2Cl_2): δ 35.68 (d.d, J_{PP} = 41.2, 18.2, 2P, P), 12.41 (d. t, J_{PP} = 100.7, 41.4, 1P, P'), 10.60 (d.t, J_{PP} = 100.7, 18.4, 1P, P''). ^{13}C NMR (126 MHz, CD_2Cl_2): δ 134.7 (PC**C**H), 134.4 (P''**C**), 133.6 (P'C**C**H), 133.1 (P''CCH**C**H), 132.3 (P'**C** + PCCHCH**C**H), 131.8 (P''CCHCH**C**H), 131.1 (P'CCHCH**C**H), 129.8 (P''C**C**H), 129.4 (PCCH**C**H), 128.9 (P'CCH**C**H), 125.4 (P**C**), 117.1 (PCCH**C**H of PPh-Pd), 107.7 (PC**C**H of PPh-Pd), 86.9 (PCCHCH**C**H of PPh-Pd), 50.0 (P**C** of PPh-Pd). LIFDI-MS: 684.0 $[M\text{-}2BF_4]^{2+}$. UV-vis (CH_2Cl_2, λ_{max}, nm (ε, $mol^{-1}dm^3cm^{-1}$)): 422.13 (7 600), 531.80 (14 100).

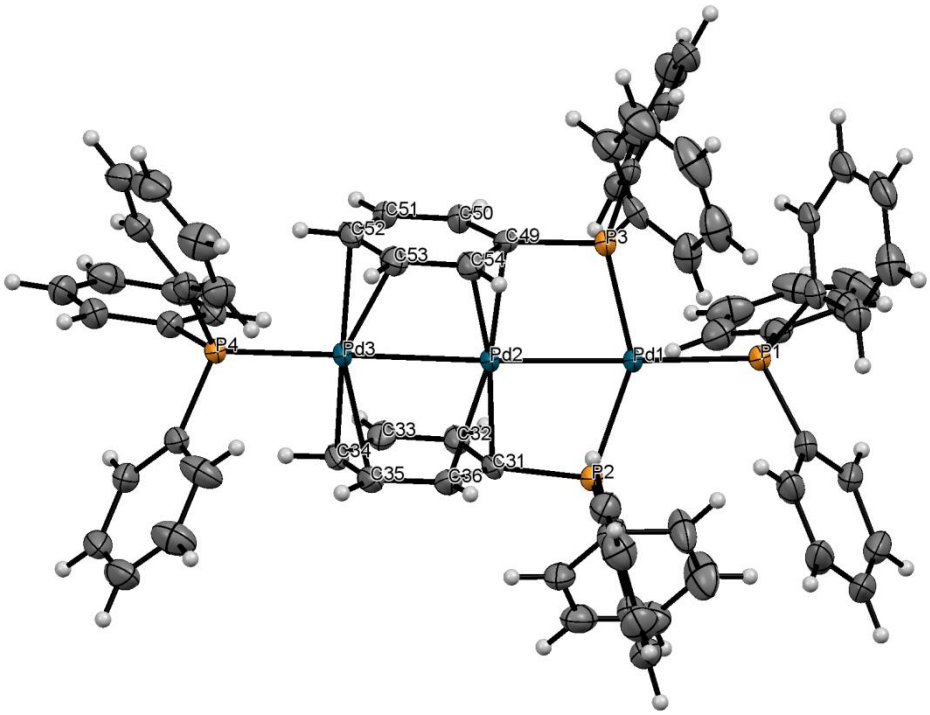

Figure 276: Crystal structure of the photoisomer of $[Pd_3(PPh_3)_4][BF_4]_2.(CH_2Cl_2)_3$, with CH_2Cl_2 solvent and tetrafluoroborate counterions omitted for clarity. Atom colours: C-grey, H-white, P-orange, Pd-blue.

Empirical formula	$C_{75}H_{66}B_2Cl_6F_8P_4Pd_3$
Formula weight	1796.67
Temperature/K	110.05(10)
Crystal system	Triclinic
Space group	P-1
a/Å	16.7741(3)
b/Å	20.8891(5)
c/Å	24.5805(3)
α/°	99.0241(15)
β/°	95.6872(13)
γ/°	112.6718(18)
Volume/Å^3	7727.8(3)
Z	4
ϱ_{calc}g/cm^3	1.544
μ/mm^{-1}	1.041
F(000)	3592.0
Crystal size/mm^3	0.1582 × 0.1083 × 0.0426

Radiation	MoKα (λ = 0.710)
2Θ range for data collection/°	3.156 to 51.622
Index ranges	−19 ≤ h ≤ 20, −25 ≤ k ≤ 24, −22 ≤ l ≤ 29
Reflections collected	56239
Independent reflections	29282 [R_{int} = 0.0516, R_{sigma} = 0.0748]
Data/restraints/parameters	29282/80/1807
Goodness-of-fit on F^2	0.986
Final R indexes [I>=2σ (I)]	R_1 = 0.0464, wR_2 = 0.1118
Final R indexes [all data]	R_1 = 0.0720, wR_2 = 0.1233
Largest diff. peak/hole / e Å^{-3}	1.03/−1.11

Compound reference kma-4-22

E.3.1.27 Synthesis and Characterisation of [Pd(PPh$_3$)$_4$]

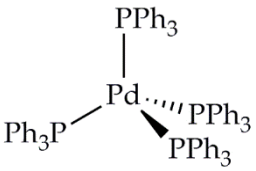

[Pd(PPh$_3$)$_4$] was synthesized according to published procedures.[336] $PdCl_2$ (0.50 g, 2.82 mmol) and triphenylphosphine (3.70 g, 14.12 mmol) were added to dry DMSO (~ 35 mL), under N_2, and refluxed at 140 °C until complete dissolution (~2.5 h). The oil bath was removed and the dark solution was rapidly stirred for ~ 5 min, after which hydrazine hydrate (0.6 mL, 19.1 mmol) was slowly added. A vigorous reaction occurred, and N_2 gas was released. The solution was cooled in a water bath for 5 min, during which bright yellow crystals crashed out of solution. The solution was allowed to slowly cool to room temperature. DMSO was removed by cannula filtration. The product was washed twice with dry ethanol (2 x 7.5 mL), and twice with dry diethyl ether (2 x 7.5 mL). The solvent was removed by cannula filtration after each washing. The product was vacuum dried. Pd(PPh$_3$)$_4$ was produced as a bright yellow precipitate, in 92% yield. ^{1}H NMR (500 MHz, C_6D_6): δ 7.46 (t, J_{HH} = 10, 24 H, PCC**H**), 6.99-6.93 (m, 36 H, PCCHC**H**, PCCHCHC**H**). ^{31}P NMR (203 MHz, C_6D_6): δ 15.6 (s, **P**Ph$_3$). ^{13}C NMR (101 MHz, C_6D_6): δ 139.0 (d, J_{CP} = 11, P**C**),

133.9 (d, J_{CP} = 18, PC**C**H), 128.1 (s, PCCHCH**C**H), 128.0 (s, PCCH**C**H). Spectroscopic data matched that reported in the literature.

Compound reference kma-1-24

E.3.1.28 Synthesis and Characterisation of 6-Methyl-4-(4-methylphenyl)-pyran-2-one; a Comparison of Palladium Catalysts

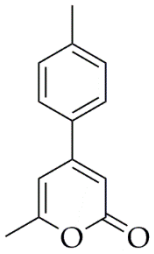

The synthetic procedure by Shah *et. al.* was adapted.[337] 4-Bromo-6-methyl-2-pyrone (47.3 mg, 0.25 mmol) and *para*-tolylboronic acid (51.0 mg, 0.38 mmol) were dissolved in a mixture of THF (2 mL) and aqueous Na_2CO_3 (2 mL, 2M, 2.12 g in 10 mL). The solution was deoxygenated by bubbling N_2 for 10 min. The solution was warmed to 50 °C, and the palladium catalyst (1 mol%, 2.5 μmol) was added. The solution was stirred at 50 °C for 4 hr, after which time the reaction was quenched with saturated aqueous NH_4Cl solution (~ 15 mL). The products were extracted into ethyl actetate, dried over $MgSO_4$, and concentrated in *vacuo*. ^{1}H NMR spectra were used to calculate the conversion of 4-bromo-6-methyl-2-pyrone to 6-methyl-4-(4-methylphenyl)-2*H*-pyran-2-one by comparing their NMR signal integrals. The pyrone product was purified by column chromatography (silica; hexane:ethyl acetate 90:10) and an isolated yield was calculated. These are discussed in Chapter 6. ^{1}H NMR ($CDCl_3$, 400 MHz): δ 7.49 (*p*-d, J_{HH} = 8.1, 2H, OCOCHCCC**H**), 7.23 (*p*-d, J_{HH} = 8.0, 2H, OCOCHCCCHC**H**), 6.35 (s, 1H, OCOC**H**), 6.32 (s, 1H, OC(CH_3)C**H**), 2.42 (s, 3H, OCOCHCCCHCHC(C**H**$_3$)), 2.33 (s, 3H, OC(C**H**$_3$)). ^{13}C NMR ($CDCl_3$, 101 MHz): δ 162.0 (O**C**O), 155.2 (O**C**(CH_3)), 141.1 (OCOCH**C**), 132.8 (OCOCHC**C**), 130.0 (OCOCHCCCHCH**C**(CH_3)), 126.7 (OCOCHCC**C**H), 123.0 (OCOCHCCCH**C**H), 107.5 (OCO**C**H), 103.5 (OC(CH_3)**C**H), 21.4 (OCOCHCCCHCHC(**C**H_3)), 20.3 (OC(**C**H_3)). ESI-MS: Calcd. for $C_{13}H_{12}NaO_2$ = 223.0730. Found 223.0732 $[M+Na]^+$. Calcd. for $C_{13}H_{13}O_2$ = 201.0910. Found 201.0912 $[M+H]^+$. Spectroscopic data matched that reported in the literature.

Compound reference kma-3-93

E.3.1.29 Synthesis and Characterisation of Butyl (2*E*)-3-(4-methoxyphenyl)acrylate; a Comparison of Palladium Catalysts

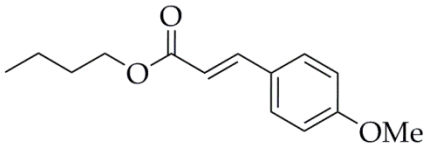

The synthetic procedure by Hierso *et. al.* was adapted.[314] *n*-Butylacrylate (143.4 μL, 1.00 mmol), 4-bromoanisole (62.6 μL, 0.50 mmol), and K_2CO_3 (276 mg, 2.00 mmol) were dissolved in DMF (4 mL). The solution was de-oxygenated by bubbling N_2 for 10 min. The solution was heated to 130 °C and the palladium catalyst (1 mol%, 10 μmol) was added. The solution was stirred at 130 °C for 4 hr, after which time the reaction was quenched with saturated aqueous NH_4Cl solution (~ 15 mL). The products were extracted into ethyl actetate, washed with water, dried over $MgSO_4$, and concentrated in *vacuo*. ^{1}H NMR spectra were used to calculate the conversion of 4-bromoanisole to butyl (2*E*)-3-(4-methoxyphenyl)acrylate by comparing their NMR signal integrals. The product was purified by column chromatography (silica; hexane:ethyl acetate 98:2) and an isolated yield was calculated. These are discussed in Chapter 6. ^{1}H NMR ($CDCl_3$, 400 MHz): δ 7.66 (d, J_{HH} = 16.0, 1H, C(O)CHC**H**), 7.49 (*p*-d, J_{HH} = 8.7, 2H, C(O)CHCHCC**H**), 6.92 (*p*-d, J_{HH} = 8.8, 2H, C(O)CHCHCCHC**H**), 6.33 (d, J_{HH} = 16.0, 1H, C(O)C**H**), 4.22 (t, J_{HH} = 6.7, 2H, C(O)OC$\mathbf{H_2}$), 3.85 (s, 3H, OC$\mathbf{H_3}$), 1.70 (m, 2H, C(O)OCH$_2$C$\mathbf{H_2}$), 1.45 (m, 2H, C(O)OCH$_2$CH$_2$C$\mathbf{H_2}$), 0.98 (t, J_{HH} = 7.4, 3H, C(O)OCH$_2$CH$_2$CH$_2$C$\mathbf{H_3}$). ^{13}C NMR ($CDCl_3$, 101 MHz): δ 167.3 (**C**(O)), 161.1 (C(O)CHCHCCHCH**C**), 144.0 (C(O)CH**C**H), 129.5 (C(O)CHCHC**C**H), 127.1 (C(O)CHCH**C**), 115.6 (C(O)**C**H), 114.2 (C(O)CHCHCCH**C**H), 64.1 (C(O)O**C**H$_2$), 55.3 (O**C**H$_3$), 30.7 (C(O)OCH$_2$**C**H$_2$), 19.1 (C(O)OCH$_2$CH$_2$**C**H$_2$), 13.6 (C(O)OCH$_2$CH$_2$CH$_2$**C**H$_3$). ESI-MS: Calcd. for $C_{14}H_{18}NaO_3$ = 257.1148. Found 257.1144 $[M+Na]^+$. Calcd. for $C_{14}H_{19}O_3$ = 235.1329. Found 235.1326 $[M+H]^+$. Spectroscopic data matched that reported in the literature.

Compound reference kma-4-61

E.3.2 Platinum Complexes

E.3.2.1 Synthesis and Characterisation of $[Pt(Cl)_2(C_6H_5CN)_2]$

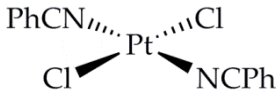

The synthetic procedure by Fraccorollo *et. al.* was adapted.[338] Platinum dichloride (0.50 g, 1.88 mmol) was added to benzonitrile (20 mL, 0.19 mol) and heated to 110 °C. At this temperature the platinum dissolved and formed a yellow solution. The solution was filtered, whilst hot, and allowed to cool to room temperature. Petroleum ether (~100 mL) was added and a pale yellow solid precipitated. This was isolated by cannula filtration and washed with petroleum ether (3 x 5 mL). $[Pt(Cl)_2(C_6H_5CN)_2]$ (0.814 g, 1.72 mmol) was isolated as a pale yellow solid in 92% yield. ^{1}H NMR (400 MHz, $CDCl_3$): δ 7.83 (d. J_{HH} = 7.8, 4H, NCCC**H**), 7.77 (t, J_{HH} = 7.3, 2H, NCCCHCHC**H**), 7.59 (*ps*-t, J_{HH} = 7.8, 4H, NCCCHC**H**). ^{13}C NMR (101 MHz, $CDCl_3$): δ 135.3 (NCCCHCH**C**H), 133.8 (NCC**C**H), 129.5 (NCCCH**C**H), 116.8 (N**C**), 109.1 (NC**C**). LIFDI-MS: 472.00 $[M]^+$. Anal. Calcd. for $C_{14}H_{10}Cl_2N_2Pt$ (M_r = 472.23): C. 35.61, H. 2.13, N. 5.93. Found C. 36.14, H. 2.09, N. 5.97. Spectroscopic data matched that reported in the literature.

Compound reference kma-3-56

E.3.2.2 Synthesis and Characterisation of $[Pt(Cl)_2(PPh_3)_2]$

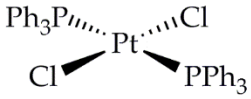

The synthetic procedure by Brumbaugh *et. al.* was adapted.[333] $[Pt(Cl)_2(PhCN)_2]$ (100 mg, 0.212 mmol) was dissolved in the minimum amount of DCM (~ 5 mL). Triphenylphosphine (122 mg, 0.466 mmol) was also dissolved in the minimum amount of DCM (~ 2mL) and added to the platinum solution. A pale yellow solid precipitated from the bright yellow solution. Hexane (~ 50 mL) was added to encourage precipitation and the product was sinter filtered and washed with hexane (3 x 5 mL). $[Pt(Cl)_2(PPh_3)_2]$ (164

mg, 0.207 mmol) was produced in both *cis*- and *trans*-configurations (50:50) as a pale yellow solid in 98% yield. *Trans*-isomer: ^{1}H NMR (500 MHz, $CDCl_3$): δ 7.76 (d.d, J_{HH} = 7.5, J_{HP} = 14.0, 4H, PCC**H**), 7.48-7.38 (m, PCCHC**H**), 7.19 (t, J_{HH} = 7.7, 2H, PCCHCHC**H**). ^{31}P NMR (203 MHz, $CDCl_3$): δ 20.15 (s, J_{PPt} = 2634). ^{13}C NMR (126 MHz, $CDCl_3$): δ 135.2 (PC**C**H), 134.6 (P**C**), 130.5 (PCCH**C**H), 127.9 (PCCHCH**C**H). *Cis*-isomer: ^{1}H NMR (500 MHz, $CDCl_3$): δ 7.51 (d.d, J_{HH} = 7.8, J_{HP} = 11.6, 4H, PCC**H**), 7.48-7.38 (m, PCCHC**H**), 7.35 (t, J_{HH} = 7.2, 2H, PCCHCHC**H**). ^{31}P NMR (203 MHz, $CDCl_3$): δ 14.30 (s, J_{PPt} = 3671). ^{13}C NMR (126 MHz, $CDCl_3$): δ 134.8 (PC**C**H), 130.7 (PCCHCH**C**H), 130.0 (P**C**), 127.9 (PCCH**C**H). LIFDI-MS: 790.08 $[M]^+$. Anal. Calcd. for $C_{36}H_{30}Cl_2P_2Pt$ (M_r = 790.54): C. 54.70, H. 3.83, N. 0.00. Found C. 54.68, H. 3.81, N. 0.00. Spectroscopic data matched that reported in the literature.

Compound reference kma-3-58

E.3.2.3 Synthesis and Characterisation of $[Pt(OTf)_2(PPh_3)_2]$

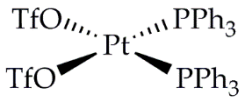

The synthetic procedure by Stang *et. al.* was adapted.[334] $[Pt(Cl)_2(PPh_3)_2]$ (100 mg, 0.13 mmol) and silver triflate (72 mg, 0.28 mmol) were suspended in dry, degassed dichloromethane (20 mL) and stirred for 20 hours, under N_2, at 35 °C. The resulting yellow solution was cannula filtered from the white AgCl precipitate to produce a pale yellow solution. This was reduced in volume to approximately 5 mL. Dry, degassed hexane was added, with vigorous stirring, to encourage precipitation, which resulted in a white product. The pale yellow solution was cannula filtered and the remaining white solid was dried in *vacuo*. $[Pt(OTf)_2(PPh_3)_2]$ (86.8 mg, 85.3 μmol) was isolated as a white solid in 67% yield. ^{1}H NMR (400 MHz, CD_2Cl_2): δ 7.56 (t, J_{HH} = 7.5, 2H, PCCHCHC**H**), 7.49 (d.d, J_{HH} = 7.8, J_{HP} = 12.9, 4H, PCC**H**), 7.36 (*p*-t, J_{HH} = 7.8, 4H, PCCHC**H**). ^{31}P NMR (162 MHz, CD_2Cl_2): δ 5.94 (s, J_{PPt} = 4033). ^{13}C NMR (101 MHz, CD_2Cl_2): δ 134.3 (s, PC**C**H), 132.8 (s, PCCHCH**C**H), 129.2 (s, PCCH**C**H), 124.0 (d, J_{CP} = 74, P**C**). ^{19}F NMR (471 MHz, CD_2Cl_2): −78.61.

Compound reference kma-3-63

E.3.2.4 Synthesis and Characterisation of [Pt(H)(OTf)(PPh_3)$_2$]

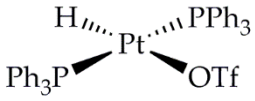

A d_2-dichloromethane (0.6 mL) solution of [Pt(OTf)$_2$(PPh_3)$_2$] (5 mg, 4.9 μmol) was inserted into a 5 mm NMR tube and degassed. *Para*-H_2 (3 bar) was added at r.t. to form [Pt(H)(OTf)(PPh_3)$_2$] quantitatively. This has not been isolated. ^{1}H NMR (400 MHz, CD_2Cl_2): δ 7.58 (d.d, J_{HH} = 7.2, J_{HP} = 14.0, 4H, PCC***H***), 7.55-7.45 (m, 6H, PCCHC***H***C***H***). ^{31}P NMR (162 MHz, CD_2Cl_2): δ 30.99 (s, J_{PPt} = 3043). ^{13}C NMR (101 MHz, CD_2Cl_2): δ 134.4 (s, PC***C***H), 133.8 (s, P***C***), 131.2 (s, PCCHCH***C***H), 128.7 (s, PCCH***C***H).

Compound reference kma-3-66

E.3.3 Iridium Complexes

E.3.3.1 Synthesis and Characterisation of 1,4-Bis-(2,4,6-trimethylphenyl)-1,4-diaza-butadiene

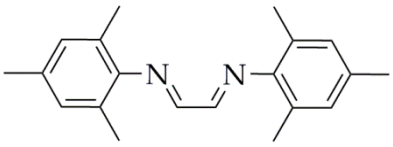

The synthetic procedure by Arduengo *et. al.* was adapted.[184] 2,4,6-Trimethylaniline (7.0 mL, 50 mmol) was added to methanol (100 mL) and acetic acid (1 mL). The mixture was stirred at 50 °C, and a solution of glyoxal (3.1 mL, 40% in H_2O, 27 mmol) in methanol (100 mL) was slowly added. The mixture was stirred, at r.t., for ~ 17 hr, after which the resulting yellow precipitate was filtered and washed with methanol (~ 20 mL). The filtrate was collected and reduced in volume to ~ 25 mL in *vacuo*. The resulting yellow precipitate was filtered to give a 72% yield of 1,4-bis-(2,4,6-trimethylphenyl)-1,4-diaza-butadiene (3.340 g, 15.732 mmol). ^{1}H NMR (500 MHz, $CDCl_3$): δ 8.12 (s, 2H, NC**H**), 6.93 (s, 4H, NCC(CH_3)C**H**), 2.31 (s, 6H, NCC(CH_3)CHC(C**H$_3$**)), 2.18 (s, 12H, NCC(C**H$_3$**)).^{13}C NMR (126 MHz, $CDCl_3$): δ 163.9 (N**C**H), 146.8 (N**C**), 133.8 (NCC(CH3)CH**C**), 129.0 (NCC(CH_3)**C**H),

126.8 (NC**C**), 20.5 (NCC(CH_3)CHC(**C**H_3)), 18.4 (NCC(**C**H_3)). ESI-MS: 293.2 $[M]^+$, 278.1 $[M\text{-}CH_3]^+$. Anal. Calcd. for $C_{20}H_{24}N_2$ (M_r = 292.42): C. 82.15, H. 8.27, N. 9.58. Found C. 82.18, H. 8.26, N. 9.57. Spectroscopic data matched that reported in the literature.

Compound reference kma-2-25

E.3.3.2 Synthesis and Characterisation of 1,3-Bis-(2,4,6-trimethylphenyl)-imidazolium chloride

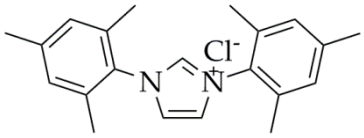

The synthetic procedure by Hintermann *et. al.* was adapted.[185] Ethyl acetate (120 mL) was heated to 70 °C. 1,4-Bis-(2,4,6-trimethylphenyl)-1,4-diaza-butadiene (3.92 g, 13.40 mmol) and paraformaldehyde (0.406 g, 13.50 mmol) were added and the walls of the flask washed with ethyl acetate (5 mL). HCl (4 M in dioxane, 3.7 mL, 14.9 mmol) was added dropwise and the resulting suspension was stirred for 2 hr, at 70 °C. The solution was cooled to r.t. and the white precipitate was isolated by sinter filtration and washed with cold ethyl acetate and diethyl ether. 1,3-Bis(2,4,6-trimethylphenyl)-imidazolium chloride was isolated in 83% yield (3.778 g, 11.1 mmol,) as a white powder. ^{1}H NMR (500 MHz, $CDCl_3$): δ 10.99 (s, 1H, NC**H**), 7.60 (d, J_{HH} = 1.45, 2H, NC**H**, 7.06 (s, 4H, NCC(CH_3)C**H**), 2.37 (s, 6H, NCC(CH_3)CHC(C**H**$_3$)), 2.22 (s, 12H, NCC(C**H**$_3$)).^{13}C NMR (126 MHz, $CDCl_3$): δ 141.4 (NCC(CH_3)CH**C**), 139.9 (N**C**H), 134.1 (N**C**), 130.6 (NC**C**(CH_3)), 129.9 (NCC(CH_3)**C**H), 124.2 (N**C**H), 21.2 (NCC(CH_3)CHC(**C**H_3)), 17.7 (NCC(**C**H_3)). ESI-MS: 340.9 $[M]^+$, 305.4 $[M\text{-}CH_3]^+$. Anal. Calcd. for $C_{21}H_{25}ClN_2$ (M_r = 340.89): C. 73.99, H. 7.39, N. 8.22. Found C. 70.21, H. 7.55, N. 7.73. Spectroscopic data matched that reported in the literature.

Compound reference kma-2-33

E.3.3.3 Synthesis and Characterisation of $[IrCl(COD)]_2$, where COD = 1,5-cyclooctadiene

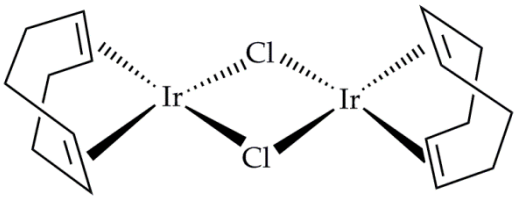

$[IrCl(COD)]_2$ was synthesised according to published procedures.[186] $IrCl_3.3H_2O$ (1.00 g, 2.84 mmol) was added to a solution of propan-2-ol (17 mL) and water (8.5 mL). The solution was deoxygenated with N_2 for ~ 40 min. COD (3.50 mL, 28.5 mmol) was added and the solution deoxygenated for a further 15 min. The solution was refluxed, under N_2, at 115 °C for 18 hr, after which time a red precipitate was seen to form. The solution was cooled and the propan-2-ol removed in *vacuo*. The solution was refrigerated overnight and the red precipitate was isolated by sinter filtration, washed with cold methanol and dried in *vacuo*. $[IrCl(COD)]_2$ (0.507 g, 0.755 mmol) was isolated as a dark red powder, in 53% yield. ^{1}H NMR (400 MHz, $CDCl_3$): δ 4.26 (s, 8H, C**H**), 2.28 (m, 8H, C**H$_2$**), 1.55 (d, J_{HH} = 8, 8H, C**H$_2$**). ^{13}C NMR (101 MHz, $CDCl_3$): δ 62.1 (**C**H), 31.8 (**C**H$_2$). Spectroscopic data matched that reported in the literature.

Compound reference kma-2-38

E.3.3.4 Synthesis and Characterisation of $[Ir(OMe)(COD)]_2$

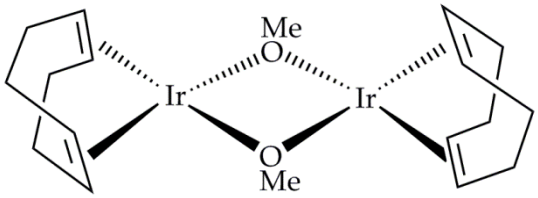

$[Ir(OMe)(COD)]_2$ was synthesised according to published procedures.[186] Potassium hydroxide (0.050 g, 0.89 mmol) was dissolved in dry, degassed methanol (~ 5 mL), which was stirred under N_2 until dissolution. $[IrCl(COD)]_2$ (0.20 mg, 0.30 mmol) was added and the reaction mixture was stirred under N_2 for 1 hr. The resulting yellow precipitate was isolated by sinter filtration and washed with cold water, followed by cold methanol, and dried in *vacuo*. $[Ir(OMe)(COD)]_2$ (0.135 g, 0.204 mmol) was isolated in 69% yield, as a yellow powder. ^{1}H NMR (400 MHz, $CDCl_3$): δ 3.57 (s, 8H, C**H**), 3.27 (s, 6H, C**H$_3$**), 2.25 (s,

8H, C**H**$_2$), 1.39 (d, J_{HH} = 7, 8H, C**H**$_2$). Spectroscopic data matched that reported in the literature.

Compound reference kma-2-39

E.3.3.5 Synthesis and Characterisation of [IrCl(COD)(IMes)], where IMes = 1,3-bis-(2,4,6-trimethylphenyl)-imidazol-2-ylidene

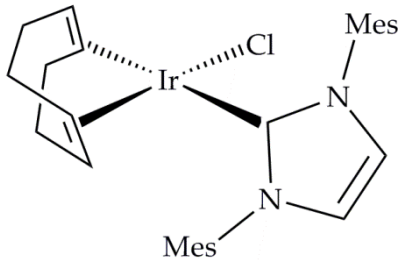

[IrCl(COD)(IMes)] was synthesised according to literature procedures.[187] [Ir(OMe)(COD)]$_2$ (100 mg, 0.15 mmol) was suspended in dry, degassed acetone (~ 5 mL). 1,3-Bis-(2,4,6-trimethylphenyl)-imidazolium chloride (103 mg, 0.302 mmol) was added, and the mixture stirred under N_2, at room temperature, for 1 hr. The acetone was removed in *vacuo.* The resulting dark yellow product was dissolved in the minimum amount of DCM, and flushed through a silica plug using an acetone:DCM (1:8) eluent. The solvent was removed in *vacuo* and the resulting product dried in *vacuo*. [IrCl(COD)(IMes)] (129 mg, 0.201 mmol) was isolated as bright yellow crystals, in a 67% yield. ^{1}H NMR (400 MHz, CD_3OD): δ 7.25 (s, 2H, IrCNC**H**), 7.04 (br. s, 4H, IrCNCC(CH_3)C**H**, 4.02 (br. s, 2H, IrC**H**), 3.09 (br. s, 2H, IrC**H**), 2.38 (s, 6H, IrCNCC(CH_3)CHC(C**H**$_3$)), 2.31 (s, 3H, IrCNCC(C**H**$_3$)), 2.20 (s, 3H, IrCNCC(C**H**$_3$)), 1.69 (m, 4H, C**H**$_2$), 1.33 (m, 4H, C**H**$_2$). ^{13}C NMR (101 MHz, $CDCl_3$): δ 180.5 (Ir**C**), 138.4 (IrCNCC(CH_3)CH**C**(CH_3), 134.4 (IrCNC**C**(CH_3)), 128.7 (IrCNCC(CH_3)**C**H), 123.0 (IrCN**C**H), 120.1 (IrCN**C**), 82.2 (Ir**C**H), 51.5 (Ir**C**H), 34.1 (**C**H$_2$), 32.3 (**C**H$_2$), 29.6 (**C**H$_2$), 28.2 (**C**H$_2$), 20.9 (IrCNCC(CH_3)CHC(**C**H$_3$), 18.1 (IrCNCC(**C**H$_3$)). Spectroscopic data matched that reported in the literature.

Compound reference kma-2-40

E.3.3.6 General Synthesis of [Ir(COD)(IMes)(X)]Cl, where X = pdz or phth

[IrCl(COD)(IMes)] (2.0 mg, 3.1 μmol) and five equivalents of x were dissolved in d_4-methanol (0.5 mL) and degassed in a Young's NMR tube.

E.3.3.7 Characterisation of [Ir(COD)(IMes)(pdz)]Cl

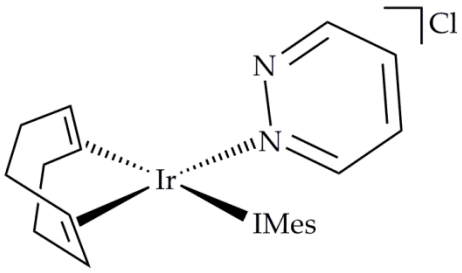

[Ir(COD)(IMes)(pdz)]Cl has not been isolated. ^{1}H NMR (500 MHz, CD_3OD): δ 9.08 (d, 1H, J_{HH} = 4Hz, IrNC**H**), 7.88 (d, 1H, J_{HH} = 5 Hz, IrNNC**H**), 7.70 (m, 1H, IrNCHC**H**), 7.51 (m, 1H, IrNNCHC**H**), 7.43 (s, 2H, IrCNC**H**), 7.23 (s, 2H, NCC(CH_3)C**H**), 6.94 (s, 2H, NCC(CH_3)C**H**), 3.70 (s, 2H, IrC**H**), 3.29 (m, 2H, IrC**H**), 2.45 (s, 6H, NCC(CH_3)CHC(C**H**$_3$)), 2.37 (s, 6H, NCC(C**H**$_3$)), 2.00 (m, 4H, IrCHC**H**$_2$), 1.90 (s, 6H, NCC(C**H**$_3$)), 1.67 (m, 4H, IrCHC**H**$_2$). ^{13}C NMR (101 MHz, CD_3OD): δ 173 (s, Ir**C**N), 155 (s, IrNN**C**H), 153 (s, IrN**C**H), 148 (s, NC**C**(CH_3)), 140 (s, NCC(CH_3)CH**C**(CH_3)), 136 (s, N**C**C(CH_3)), 135 (s, NC**C**(CH_3)), 131 (s, IrNNCH**C**H), 129 (s, NCC(CH_3)**C**H), 127 s, (IrNCH**C**H), 125 (s, IrCN**C**H), 81 (s, Ir**C**H), 65 (s, Ir**C**H), 32 (s, IrCH**C**H$_2$), 29 (s, IrCH**C**H$_2$), 20 (s, NCC(CH_3)CHC(**C**H$_3$)), 17 (s, NCC(**C**H$_3$)). ESI-MS: 685.4 $[M\text{-}Cl]^+$, 605.4 $[M\text{-}Cl\text{-}pdz]^+$.

Compound reference kma-2-48

E.3.3.8 Characterisation of [Ir(COD)(IMes)(phth)]Cl

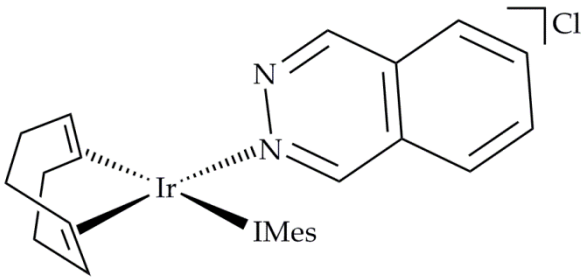

[Ir(COD)(IMes)(phth)]Cl has not been isolated. ^{1}H NMR (400 MHz, CD_3OD): δ 9.55 (s, 1H, IrNC**H**), 8.37 (s, 1H, IrNNC**H**), 8.22-8.18 (m, 3H, IrNNCHCC**H**C**H**C**H**), 7.86 (d, 1H, J_{HH} = 6.6, IrNCHCC**H**), 7.40 (s, 2H, IrCNC**H**), 7.27 (s, 2H, NCC(CH_3)C**H**), 6.61 (s, 2H,

NC(CH_3)C**H**), 3.71 (s (br), 2H, IrC**H**), 3.40 (m, 2H, IrC**H**), 2.43 (s, 6H, NCC(CH_3)CHC(C**H**$_3$)), 2.40 (s, 6H, NCC(C**H**$_3$)), 2.05 (m, 4H, IrCHC**H**$_2$), 1.91 (m, 4H, IrCHC**H**$_2$)), 1.70 (s, 6H, NCC(C**H**$_3$)). ^{13}C NMR (101 MHz, CD_3OD): δ 172 (s, Ir**C**N), 155 (s, IrNN**C**H), 152 (s, IrN**C**H), 139 (s, NCC(CH_3)CH**C**(CH_3)), 136 (s, N**C**C(CH_3)), 135 (s, IrNNCHC**C**H**C**H**C**H), 129 (s, NCC(CH_3)**C**H), 128 (s, NCC(CH_3)**C**H), 128 (s, IrNNCH**C**), 127 (s, IrNNCHC**C**H**C**H**C**H), 127 (s, IrNCHC**C**H), 125 (s, IrNCH**C**), 125 (s, IrCN**C**H), 81 (s, Ir**C**H), 29 (s, IrCH**C**H$_2$), 20 (s, NCC(CH_3)CHC(**C**H$_3$)), 17 (NC**C**(CH_3)). ESI-MS: 735.4 [M-Cl]$^+$, 605.4 [M-Cl-phth]$^+$.

Compound reference kma-2-54

E.3.3.9 General Synthesis of [Ir(H)$_2$(COD)(IMes)(X)]Cl , where X = pdz or phth

[IrCl(COD)(IMes)] (2.0 mg, 3.1 μmol) and five equivalents of X were dissolved in d_4-methanol (0.5 mL) and degassed in a Young's NMR tube. H_2 (3 bar) was added at 240 K.

E.3.3.10 Characterisation of [Ir(H)$_2$(COD)(IMes)(pdz)]Cl

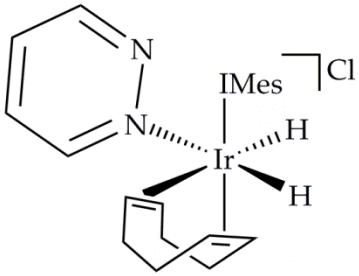

[Ir(H)$_2$(COD)(IMes)(pdz)]Cl has not been isolated. ^{1}H NMR (500 MHz, CD_3OD): δ 9.05 (d, J_{HH} = 4.8, 1H, IrNNC**H**), 9.02 (d, J_{HH} = 5.5, 1H, IrNC**H**), 7.90 (d.d, J_{HH} = 8.3, 5.1, 1H, IrNNCHC**H**), 7.62 (d.d, J_{HH} = 8.3, 5.1, 1H, IrNCHC**H**), 7.36 (s, 2H, IrCNC**H**), 7.03 (s, 2H, NCC(CH_3)C**H**), 7.00 (s, 2H, NCC(CH_3)C**H**), 5.09 (m (br), 1H, IrC**H**) 5.02 (m (br), 1H, IrC**H**), 4.45 (m (br), 1H, IrC**H**), 3.74 (m (br), 1H, IrC**H**), 2.54 (m (br), 1H, IrCHC**H**$_2$), 2.39 (s, 6H, NCC(CH_3)CHC(C**H**$_3$)), 2.23 (m (br), 1H, IrCHC**H**$_2$), 2.19 (s, 6H, NCC(C**H**$_3$)), 2.00 (m (br), 1H, IrCHC**H**$_2$), 1.90 (m (br), 2H, IrCHC**H**$_2$), 1.81 (s, 6H, NCC(C**H**$_3$)), 1.75 (m (br), 1H, IrCHC**H**$_2$), 1.65 (m (br), 1H, IrCHC**H**$_2$), 1.25 (m (br), 1H, IrCHC**H**$_2$), −13.84 (d, J_{HH} = 3.8, 1H, **H**IrCH), −17.69 (d, J_{HH} = 3.8, 1H, **H**IrN). ^{13}C NMR (101 MHz, CD_3OD): δ 163.1 (s, IrNN**C**H), 154.2 (s, Ir**C**N), 153.12 (IrN**C**H), 139.6 (s, NCC(CH_3)CH**C**(CH_3)), 136.6 (s, NC**C**(CH_3)), 135.4 (s, N**C**C(CH_3)), 131.2 (s, IrNCH**C**H), 129.2 (s, NCC(CH_3)**C**H), 128.8 (s, NCC(CH_3)**C**H),

128.1 (s, IrNNCH**C**H), 124.1 (IrCN**C**H), 97.7 (s, Ir**C**H), 95.1 (s, Ir**C**H), 82.6 (s, Ir**C**H), 79.0 (s, Ir**C**H), 34.4 (s, IrCH**C**H_2), 30.8 (s, IrCH**C**H_2), 28.3 (s, IrCH**C**H_2), 27.8 (s, IrCH**C**H_2), 19.7 (s, NCC(CH_3)CHC(**C**H_3)), 17.6 (s, NCC(**C**H_3)), 16.6 (s, NCC(**C**H_3)). ^{15}N NMR (50.7 MHz, CD_3OD): δ 400.1 (IrN**N**), 294.3 (Ir**N**N), 197.8 (IrC**N**).

Compound reference kma-2-63

E.3.3.11 Characterisation of [Ir(H)$_2$(COD)(IMes)(phth)]Cl

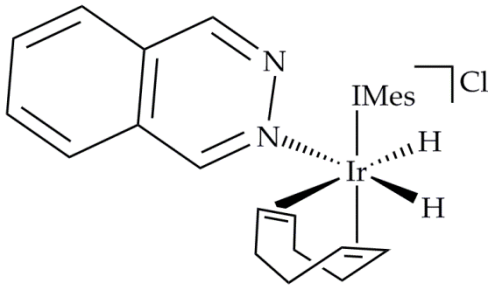

[Ir(H)$_2$(COD)(IMes)(phth)]Cl has not been isolated. ^{1}H NMR (500 MHz, CD_3OD): δ 9.52 (s, 1H, IrNNC**H**), 9.45 (s, 1H, IrNC**H**), 8.31 (d, J_{HH} = 7.9, 1H, IrNNCHCC**H**), 8.27 (t.d, J_{HH} = 7.5, 1.0, 1H, IrNCHCCHC**H**), 8.21 (t.d, J_{HH} = 7.5, 1.0, 1H, IrNNCHCCHC**H**), 8.03 (d, J_{HH} = 8.0, 1H, IrNCHCC**H**), 7.32 (s, 2H, IrCNC**H**), 6.99 (s, 2H, NCC(CH_3)C**H**), 6.76 (s, 2H, NCC(CH_3)C**H**), 5.23 (m, 1H, IrC**H**) 5.18 (m, 1H, IrC**H**), 4.33 (m, 1H, IrC**H**), 3.85 (t.d, J_{HH} = 8.4, 3.9, 1H, IrC**H**), 2.76 (m (br), 1H, IrCHC**H$_2$**), 2.34 (s, 6H, NCC(CH_3)CHC(C**H$_3$**)), 2.26 (s, 6H, NCC(C**H$_3$**)), 2.01 (m (br), 1H, IrCHC**H$_2$**), 1.90 (m (br), 1H, IrCHC**H$_2$**), 1.74 (m (br), 3H, IrCHC**H$_2$**), 1.62 (s, 6H, NCC(C**H$_3$**)), 1.38 (m (br), 2H, IrCHC**H$_2$**), −13.87 (d, J_{HH} = 4.0, 1H, **H**IrCH), −17.55 (d, J_{HH} = 5.1, 1H, **H**IrN). ^{13}C NMR (101 MHz, CD_3OD): δ 162.8 (s, IrN**C**H), 154.2 (s, Ir**C**N), 153.0 (IrNN**C**H), 139.5 (s, NC**C**(CH_3)) 136.8 (s, N**C**C(CH_3)), 135.4 (s, NCC(CH_3)CH**C**(CH_3)), 135.1 (s, IrNCHCCH**C**H**C**H), 129.2 (s, NCC(CH_3)**C**H), 128.7 (s, IrNNCH**C**), 128.4 (s, NCC(CH_3)**C**H), 127.0 (s, IrNCHC**C**H), 126.4 (s, IrNNCHC**C**H), 125.7 (s, IrNCH**C**), 124.0 (IrCN**C**H), 97.3 (s, Ir**C**H), 95.3 (s, Ir**C**H), 83.1 (s, Ir**C**H), 78.6 (s, Ir**C**H), 19.8 (s, NCC(CH_3)CHC(**C**H_3)), 17.6 (s, NCC(**C**H_3)), 16.5 (s, NCC(CH_3)). ^{15}N NMR (50.7 MHz, CD_3OD): δ 368.9 (IrN**N**), 266.6 (Ir**N**N), 198.0 (IrC**N**).

Compound reference kma-2-65

E.3.3.12 General Synthesis of $[Ir(H)_2(IMes)(X)_3]Cl$, where X = pdz or phth

[IrCl(COD)(IMes)] (2 mg, 3.12 μmol) and five equivalents of X were dissolved in d_4-methanol (0.5 mL) in a 5 mm NMR tube and degassed. H_2 (3 bar) was added and the sample was heated to 348 K for 15 minutes to fully activate the complex and form $[Ir(H)_2(IMes)(X)_3]Cl$ in solution.

E.3.3.13 Characterisation of $[Ir(H)_2(IMes)(pdz)_3]Cl$

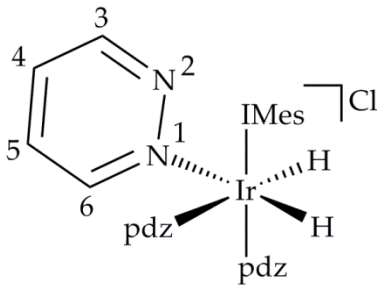

$[Ir(H)_2(IMes)(pdz)_3]Cl$ has not been isolated. ^{1}H NMR (500 MHz, CD_3OD), where ax is axial, and eq is equatorial: δ 9.62 (d.d, J_{HH} = 5.6, 2.4, 1H, **ax. pdz. 6**), 9.32 (d.d, J_{HH} = 5.6, 2.4, 2H, **eq. pdz. 6**), 8.76 (d.d, J_{HH} = 4.8, 3.0, 2H, **eq. pdz. 3**), 8.29 (d.d, J_{HH} = 4.8, 3.0, 1H, **ax. pdz. 3**), 7.62 (m, 2H, **eq. pdz. 5**), 7.48 (m, 1H, **ax. pdz. 5**), 7.42 (m, 1H, **ax. pdz. 4**), 7.39 (m, 2H, **eq. pdz. 4**), 7.09 (s, 2H, IrCNC**H**), 6.69 (s, 4H, IrCNCC(CH_3)C**H**), 2.22 (s, 6H, IrCNCC(CH_3)CHC(C**H**$_3$)), 2.04 (s, 12H, IrCNCC(C**H**$_3$)), −21.47 (s, 2H, Ir**H**). ^{13}C NMR (126 MHz, CD_3OD): δ 162.0 (s, **ax. pdz. 6**), 157.8 (s, **eq. pdz. 6**), 152.4 (s, **ax. pdz. 3**), 151.5 (s, **eq. pdz. 3**), 129.6 (s, **ax. pdz. 4**), 129.2 (s, **eq. pdz. 4**), 126.3 (s, **ax. pdz. 5**), 126.1 (s, **eq. pdz. 5**), 151.7, (s, Ir**C**), 138.1 (s, IrCNCC(CH_3)CH**C**(CH_3)), 137.5 (s, IrCNC**C**(CH_3)), 135.4 (s, IrCN**C**), 128.4 (s, IrCNCC(CH_3)**C**H), 122.4 (s, IrCN**C**H), 19.5 (s, IrCNCC(CH_3)CHC(**C**H_3)), 17.3 (s, IrCNCC(**C**H_3)). ^{15}N NMR (50.7 MHz, CD_3OD): δ 392.2 (s, **ax. pdz. 2**), 390.0 (s, **eq. pdz. 2**), 326.2 (s, **eq. pdz. 1**), 305.8 (s, **ax. pdz. 1**), 194.5 (s, IrC**N**), free pyridazine = 402.7.

Compound reference kma-1-56

E.3.3.14 Characterisation of $[Ir(H)_2(IMes)(phth)_3]Cl$

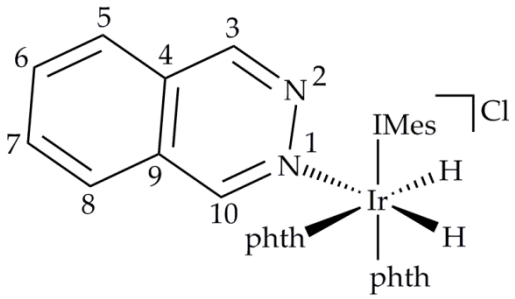

$[Ir(H)_2(IMes)(phth)_3]Cl$ has not been isolated. ^1H NMR (500 MHz, CD_3OD), where ax is axial, and eq is equatorial: δ 10.28 (s, 1H, **ax. phth. 10**), 10.16 (s, 2H, **eq. phth. 10**), 9.27 (s, 2H, **eq. phth. 3**), 8.60 (s, 1H, **ax. phth. 3**), 8.18 (m, 2H, **eq. phth. 5**), 8.17 (m, 1H, **ax. phth. 8**), 8.12 (m, 2H, **eq. phth. 7**), 8.09 (m, 2H, **eq. phth. 6**), 8.07 (m, 1H, **ax. phth. 7**), 8.00 (m, 2H, **eq. phth. 8**), 7.99 (m, 1H, **ax. phth. 6**), 7.78 (m, 1H, **ax. phth. 5**), 7.15 (s, 2H, IrCNC**H**), 6.37 (s, 4H, IrCNCC(CH_3)C**H**), 2.07 (s, 12H, IrCNCC(C**H**$_3$)), 1.92 (s, 6H, IrCNCC(CH_3)CHC(C**H**$_3$)), −21.00 (s, 2H, Ir**H**). ^{13}C NMR (126 MHz, CD_3OD): δ 160.9 (s, **ax. phth. 10**), 157.0 (s, **eq. phth. 10**), 151.9 (s, **ax. phth. 3**), 151.0 (s, **eq. phth. 3**), 133.6 (**s, ax. phth. 6**), 133.6 (s, **eq. phth. 7**), 133.3 (s, **ax. phth. 7**), 133.3 (s, **eq. phth. 6**), 128.3 (s, **ax. phth. 9**), 128.1 (s, **eq. phth. 9**), 126.6 (s, **eq. phth. 8**), 126.3 (s, **ax. phth. 8**), 126.3 (s, **eq. phth. 5**), 126.2 (s, **ax. phth. 5**), 125.5 (s, **eq. phth. 4**), 125.0 (s, **ax. phth. 4**), 151.8 (s, Ir**C**), 137.9 (s, IrCNCC(CH_3)CH**C**(CH_3)**)**, 137.3 (s, IrCNC**C**(CH_3)), 135.2 (s, IrCN**C**), 128.2 (s, IrCNCC(CH_3)**C**H), 122.4 (s, IrCN**C**H), 19.6 (s, IrCNCC(**C**H_3)), 17.5 (s, IrCNCC(CH_3)CHC(**C**H_3)). ^{15}N NMR (50.7 MHz, CD_3OD): δ 362.8 (s, **ax. phth. 2**), 360.9 (s, **eq. phth. 2**), 299.7 (s, **eq. phth. 1**), 278.8 (s, **ax. phth.1**), 194.3 (s, IrC**N**), free phthalazine = 372.4.

Compound reference kma-1-26

List of Abbreviations

ALTADENA	Adiabatic Longitudinal Transport After Dissociation Engenders Net Alignment
APCI	Atmospheric Pressure Chemical Ionisation
CN	Cyano
COA	Cyclooctane
COD	1,5-Cyclooctadiene
COE	Cyclooctene
COSY	Correlation Spectroscopy
Cy	Cyclohexyl
Diaz	2-Cyano-3-(D_3-methyl-$^{15}N_2$-diazirine)-propanoic acid
DFT	Density Functional Theory
DNP	Dynamic Nuclear Polarisation
dppb	1,4-Bis(diphenylphosphino)butane
dppe	1,2-Bis(diphenylphosphino)ethane
dppf	1,1'-Bis(diphenylphosphino)ferrocene
Et	Ethyl
ESI	Electrospray Ionisation
EXAFS	Extended X-ray Absorption Fine Structure
EXSY	Exchange Spectroscopy
FD	Field Desorption
FID	Free Induction Decay

FOV	Field Of View
HMQC	Heteronuclear Multiple Quantum Coherence
INEPT	Insensitive Nuclei Enhanced by Polarisation Transfer
IMes	1,3-Bis(2,4,6-trimethylphenyl)-imidazol-2-ylidene
IR	Infrared
LIFDI	Liquid Injection Field Desorption Ionisation
Me	Methyl
Mes	Mesityl
MRI	Magnetic Resonance Imaging
MS	Mass Spectrometry
m/*z*	Mass/Charge ratio
NHC	*N*-heterocyclic Carbene
NMR	Nuclear Magnetic Resonance
NOESY	Nuclear Overhauser Effect Spectroscopy
OHIP	*Ortho*-H_2 Induced Polarisation
OPSY	Only *para*-H_2 Spectroscopy
OTf	Triflate
PASADENA	*Para*-H_2 And Synthesis Allow Dramatically Enhanced Nuclear Alignment
pdz	Pyridazine
PHIP	*Para*-H_2 Induced Polarisation
phth	Phthalazine

PTF	Polarisation Transfer Field
PTT	Polarisation Transfer Time
PVP	Polyvinylpyrrolidone
py	Pyridine
RARE	Rapid Acquisition with Refocused Echoes
SABRE	Signal Amplification By Reversible Exchange
SEPP	Selective Excitation of Polarisation using PASADENA
SNR	Signal to Noise Ratio
^{t}Bu	*tert*-Butyl
TE	Echo Time
TE_{Eff}	Effective Echo Time
TEM	Transmission Electron Microscopy
TEMPO	(2,2,6,6-Tetramethylpiperidin-1-yl)oxidanyl
TOTAPOL	1-(TEMPO-4-oxy)-3-(TEMPO-4-amino)propan-2-ol
UV-vis	Ultraviolet – Visible light
XAS	X-ray Absorption Spectroscopy
XPS	X-ray Photoelectron Spectroscopy
XRD	X-ray Diffraction

List of References

(1) Phan, N. T. S.; Van Der Sluys, M.; Jones, C. W. *Adv. Synth. Catal.* **2006**, *348*, 609.
(2) Sonogashira, K. *J. Organomet. Chem.* **2002**, *653*, 46.
(3) Negishi, E. I. *Accounts Chem. Res.* **1982**, *15*, 340.
(4) Milstein, D.; Stille, J. K. *J. Am. Chem. Soc.* **1978**, *100*, 3636.
(5) Miyaura, N.; Yano, T.; Suzuki, A. *Tetrahedron Lett.* **1980**, *21*, 2865.
(6) Garrou, P. E.; Heck, R. F. *J. Am. Chem. Soc.* **1976**, *98*, 4115.
(7) Schwartz, J. *Accounts Chem. Res.* **1985**, *18*, 302.
(8) de Vries, A. H. M.; Mulders, J.; Mommers, J. H. M.; Henderickx, H. J. W.; de Vries, J. G. *Org. Lett.* **2003**, *5*, 3285.
(9) Fairlamb, I. J. S.; Kapdi, A. R.; Lee, A. F.; Sanchez, G.; Lopez, G.; Serrano, J. L.; Garcia, L.; Perez, J.; Perez, E. *Dalton Trans.* **2004**, 3970.
(10) Leadbeater, N. E.; Marco, M. *Org. Lett.* **2002**, *4*, 2973.
(11) Deraedt, C.; Astruc, D. *Accounts Chem. Res.* **2014**, *47*, 494.
(12) Lee, A. F.; Ellis, P. J.; Fairlamb, I. J. S.; Wilson, K. *Dalton Trans.* **2010**, *39*, 10473.
(13) Ellis, P. J.; Fairlamb, I. J. S.; Hackett, S. F. J.; Wilson, K.; Lee, A. F. *Angew. Chem. Int. Edit.* **2010**, *49*, 1820.
(14) Collins, G.; Schmidt, M.; Dwyer, C. O.; Holmes, J. D.; McGlacken, G. P. *Angew. Chem. Int. Edit.* **2014**, *53*, 4142.
(15) Huang, Y.; Zheng, Z.; Liu, T.; Lu, J.; Lin, Z.; Li, H.; Cao, R. *Catal. Commun.* **2011**, *14*, 27.
(16) Zhao, N.; Deng, H.-P.; Shu, M.-H. *Chin. J. Inorg. Chem.* **2010**, *26*, 1213.
(17) Zhao, F. Y.; Bhanage, B. M.; Shirai, M.; Arai, M. *Chem-Eur. J.* **2000**, *6*, 843.
(18) Collman, J. P.; Kosydar, K. M.; Bressan, M.; Lamanna, W.; Garrett, T. *J. Am. Chem. Soc.* **1984**, *106*, 2569.
(19) Aiken, J. D.; Lin, Y.; Finke, R. G. *J. Mol. Catal. A: Chem.* **1996**, *114*, 29.
(20) Wang, Z. F.; Shen, B.; He, N. Y. *Mater. Lett.* **2004**, *58*, 3652.
(21) Li, P. H.; Wang, L.; Li, H. J. *Tetrahedron* **2005**, *61*, 8633.
(22) Xu, J.; Zhai, X.; Wu, X.; Zhang, Y. J. *Tetrahedron* **2015**, *71*, 1712.
(23) Hyotanishi, M.; Isomura, Y.; Yamamoto, H.; Kawasaki, H.; Obora, Y. *Chem. Commun.* **2011**, *47*, 5750.
(24) Widegren, J. A.; Finke, R. G. *J. Mol. Catal. A: Chem.* **2003**, *198*, 317.
(25) Vanasselt, R.; Elsevier, C. J. *J. Mol. Catal.* **1991**, *65*, L13.
(26) Lin, Y.; Finke, R. G. *Inorg. Chem.* **1994**, *33*, 4891.
(27) Chen, P. *Angew. Chem. Int. Edit.* **2003**, *42*, 2832.
(28) Aliprantis, A. O.; Canary, J. W. *J. Am. Chem. Soc.* **1994**, *116*, 6985.
(29) Sabino, A. A.; Machado, A. H. L.; Correia, C. R. D.; Eberlin, M. N. *Angew. Chem. Int. Edit.* **2004**, *43*, 2514.
(30) Santos, L. S.; Rosso, G. B.; Pilli, R. A.; Eberlin, M. N. *J. Org. Chem.* **2007**, *72*, 5809.
(31) Ahmadi, Z.; Yunker, L. P. E.; Oliver, A. G.; McIndoe, J. S. *Dalton Trans.* **2015**, *44*, 20367.
(32) Vikse, K.; Naka, T.; McIndoe, J. S.; Besora, M.; Maseras, F. *Chemcatchem* **2013**, *5*, 3604.
(33) Vikse, K. L.; Henderson, M. A.; Oliver, A. G.; McIndoe, J. S. *Chem. Commun.* **2010**, *46*, 7412.
(34) Adlhart, C.; Chen, P. *Helv. Chim. Acta* **2000**, *83*, 2192.
(35) Gross, J. H.; Nieth, N.; Linden, H. B.; Blumbach, U.; Richter, F. J.; Tauchert, M. E.; Tompers, R.; Hofmann, P. *Anal. Bioanal. Chem.* **2006**, *386*, 52.

(36) He, Y.; Fan, J.; Feng, J.; Luo, C.; Yang, P.; Li, D. *J. Catal.* **2015**, *331*, 118.
(37) Chen, C. S.; Lin, J. H.; Chen, H. W. *Appl. Catal., A* **2006**, *298*, 161.
(38) Lavalley, J. C. *Catal. Today* **1996**, *27*, 377.
(39) Palazov, A.; Chang, C. C.; Kokes, R. J. *J. Catal.* **1975**, *36*, 338.
(40) Butler, J. M.; George, M. W.; Schoonover, J. R.; Dattelbaum, D. M.; Meyer, T. J. *Coordin. Chem. Rev.* **2007**, *251*, 492.
(41) Ren, B.; Liu, G.-K.; Lian, X.-B.; Yang, Z.-L.; Tian, Z.-Q. *Anal. Bioanal. Chem.* **2007**, *388*, 29.
(42) Bradley, P. M.; Drummond, M. L.; Turro, C.; Bursten, B. E. *Inorg. Chim. Acta* **2002**, *334*, 371.
(43) McFarlane, K.; Lee, B.; Bridgewater, J.; Ford, P. C. *J. Organomet. Chem.* **1998**, *554*, 49.
(44) George, M. W.; Turner, J. J. *Coordin. Chem. Rev.* **1998**, *177*, 201.
(45) Mulvaney, P. *Langmuir* **1996**, *12*, 788.
(46) Liu, X.; Atwater, M.; Wang, J.; Huo, Q. *Colloid Surface B* **2007**, *58*, 3.
(47) Gaikwad, A. V.; Rothenberg, G. *Phys. Chem. Chem. Phys.* **2006**, *8*, 3669.
(48) Aiken, J. D.; Finke, R. G. *J. Mol. Catal. A: Chem.* **1999**, *145*, 1.
(49) Reetz, M. T.; Maase, M. *Adv. Mater.* **1999**, *11*, 773.
(50) Lewis, L. N.; Lewis, N. *J. Am. Chem. Soc.* **1986**, *108*, 7228.
(51) Papp, S.; Dekany, I. *Colloid Polym. Sci.* **2003**, *281*, 727.
(52) Gniewek, A.; Trzeciak, A. M.; Ziolkowski, J. J.; Kepinski, L.; Wrzyszcz, J.; Tylus, W. *J. Catal.* **2005**, *229*, 332.
(53) Baumann, C. G.; De Ornellas, S.; Reeds, J. P.; Storr, T. E.; Williams, T. J.; Fairlamb, I. J. S. *Tetrahedron* **2014**, *70*, 6174.
(54) Riello, P.; Canton, P.; Benedetti, A. *Langmuir* **1998**, *14*, 6617.
(55) Frenkel, A. I.; Hills, C. W.; Nuzzo, R. G. *J. Phys. Chem. B* **2001**, *105*, 12689.
(56) Mower, M. P.; Blackmond, D. G. *J. Am. Chem. Soc.* **2015**, *137*, 2386.
(57) Soai, K.; Shibata, T.; Morioka, H.; Choji, K. *Nature* **1995**, *378*, 767.
(58) Plasson, R.; Brandenburg, A.; Jullien, L.; Bersini, H. *J. Phys. Chem. A* **2011**, *115*, 8073.
(59) Mathew, S. P.; Klussmann, M.; Iwamura, H.; Wells, D. H., Jr.; Armstrong, A.; Blackmond, D. G. *Chem. Commun.* **2006**, 4291.
(60) Eberhard, M. R. *Org. Lett.* **2004**, *6*, 2125.
(61) Reetz, M. T.; Westermann, E. *Angew. Chem. Int. Edit.* **2000**, *39*, 165.
(62) Watzky, M. A.; Finke, R. G. *J. Am. Chem. Soc.* **1997**, *119*, 10382.
(63) Widegren, J. A.; Aiken, J. D.; Ozkar, S.; Finke, R. G. *Chem. Mater.* **2001**, *13*, 312.
(64) Widegren, J. A.; Bennett, M. A.; Finke, R. G. *J. Am. Chem. Soc.* **2003**, *125*, 10301.
(65) Whitesides, G. M.; Hackett, M.; Brainard, R. L.; Lavalleye, J.; Sowinski, A. F.; Izumi, A. N.; Moore, S. S.; Brown, D. W.; Staudt, E. M. *Organometallics* **1985**, *4*, 1819.
(66) Anton, D. R.; Crabtree, R. H. *Organometallics* **1983**, *2*, 855.
(67) Yu, K. Q.; Sommer, W.; Richardson, J. M.; Weck, M.; Jones, C. W. *Adv. Synth. Catal.* **2005**, *347*, 161.
(68) Yu, K. Q.; Sommer, W.; Weck, M.; Jones, C. W. *J. Catal.* **2004**, *226*, 101.
(69) Sommer, W. J.; Yu, K. Q.; Sears, J. S.; Ji, Y. Y.; Zheng, X. L.; Davis, R. J.; Sherrill, C. D.; Jones, C. W.; Weck, M. *Organometallics* **2005**, *24*, 4351.
(70) Hamlin, J. E.; Hirai, K.; Millan, A.; Maitlis, P. M. *J. Mol. Catal.* **1980**, *7*, 543.
(71) Laine, R. M. *J. Mol. Catal.* **1982**, *14*, 137.
(72) Andrews, S. P.; Stepan, A. F.; Tanaka, H.; Ley, S. V.; Smith, M. D. *Adv. Synth. Catal.* **2005**, *347*, 647.
(73) Djakovitch, L.; Rollet, P. *Adv. Synth. Catal.* **2004**, *346*, 1782.
(74) Handa, P.; Wikander, K.; Holmberg, K. *Micropor. Mesopor. Mat.* **2009**, *117*, 126.

(75) Adams, R. W.; Aguilar, J. A.; Atkinson, K. D.; Cowley, M. J.; Elliott, P. I. P.; Duckett, S. B.; Green, G. G. R.; Khazal, I. G.; Lopez-Serrano, J.; Williamson, D. C. *Science* **2009**, *323*, 1708.
(76) Hore, P. J. *Nuclear Magnetic Resonance*; Oxford University Press: Oxford, 2011.
(77) Frydman, L. *Nature Chem.* **2009**, *1*, 176.
(78) Pietrass, T. *Colloid Surface A* **1999**, *158*, 51.
(79) Kastler, A. *J. Phys. Radium* **1950**, *11*, 255.
(80) Walker, T. G.; Happer, W. *Rev. Mod. Phys.* **1997**, *69*, 629.
(81) Raftery, D.; Reven, L.; Long, H.; Pines, A.; Tang, P.; Reimer, J. A. *J. Phys. Chem.* **1993**, *97*, 1649.
(82) Pietrass, T.; Gaede, H. C.; Bifone, A.; Pines, A.; Ripmeester, J. A. *J. Am. Chem. Soc.* **1995**, *117*, 7520.
(83) Stewart, N. J.; Norquay, G.; Griffiths, P. D.; Wild, J. M. *Magnet. Reson. Med.* **2015**, *74*, 346.
(84) Farrar, C. T.; Hall, D. A.; Gerfen, G. J.; Inati, S. J.; Griffin, R. G. *J. Chem. Phys.* **2001**, *114*, 4922.
(85) Barnes, A. B.; De Paepe, G.; van der Wel, P. C. A.; Hu, K. N.; Joo, C. G.; Bajaj, V. S.; Mak-Jurkauskas, M. L.; Sirigiri, J. R.; Herzfeld, J.; Temkin, R. J.; Griffin, R. G. *Appl. Magn. Reson.* **2008**, *34*, 237.
(86) Hu, K.-N. *Solid State Nucl. Mag.* **2011**, *40*, 31.
(87) Bajaj, V. S.; Hornstein, M. K.; Kreischer, K. E.; Sirigiri, J. R.; Woskov, P. P.; Mak-Jurkauskas, M. L.; Herzfeld, J.; Temkin, R. J.; Griffin, R. G. *J. Magn. Reson.* **2007**, *189*, 251.
(88) Rosay, M.; Lansing, J. C.; Haddad, K. C.; Bachovchin, W. W.; Herzfeld, J.; Temkin, R. J.; Griffin, R. G. *J. Am. Chem. Soc.* **2003**, *125*, 13626.
(89) Wollan, D. S. *Phys. Rev. B* **1976**, *13*, 3671.
(90) Wollan, D. S. *Phys. Rev. B* **1976**, *13*, 3686.
(91) Wind, R. A.; Duijvestijn, M. J.; Vanderlugt, C.; Manenschijn, A.; Vriend, J. *Prog. Nucl. Mag. Res. Sp.* **1985**, *17*, 33.
(92) Hu, K.-N.; Debelouchina, G. T.; Smith, A. A.; Griffin, R. G. *J. Chem. Phys.* **2011**, *134*.
(93) Lee, Y. *Appl. Spectrosc. Rev.* **2016**, *51*, 190.
(94) Lee, D.; Takahashi, H.; Thankamony, A. S. L.; Dacquin, J.-P.; Bardet, M.; Lafon, O.; De Paepe, G. *J. Am. Chem. Soc.* **2012**, *134*, 18491.
(95) Duckett, S. B.; Wood, N. J. *Coordin. Chem. Rev.* **2008**, *252*, 2278.
(96) Natterer, J.; Bargon, J. *Prog. Nucl. Mag. Res. Sp.* **1997**, *31*, 293.
(97) Misra, A.; Panda, A. *J. Low Temp. Phys.* **2011**, *163*, 311.
(98) Berlinsky, A. J.; Hardy, W. N. *Phys. Rev. B* **1973**, *8*, 5013.
(99) Duckett, S. B.; Sleigh, C. J. *Prog. Nucl. Mag. Res. Sp.* **1999**, *34*, 71.
(100) Motizuki, K.; Nagamiya, T. *J. Phys. Soc. Jpn.* **1956**, *11*, 93.
(101) Green, R. A.; Adams, R. W.; Duckett, S. B.; Mewis, R. E.; Williamson, D. C.; Green, G. G. R. *Prog. Nucl. Mag. Res. Sp.* **2012**, *67*, 1.
(102) Tadros, M. E.; Vaska, L. *J. Colloid Interface Sci.* **1982**, *85*, 389.
(103) Brown, J. M.; Canning, L. R.; Downs, A. J.; Forster, A. M. *J. Organomet. Chem.* **1983**, *255*, 103.
(104) Bowers, C. R.; Weitekamp, D. P. *Phys. Rev. Lett.* **1986**, *57*, 2645.
(105) Hommeltoft, S. I.; Berry, D. H.; Eisenberg, R. *J. Am. Chem. Soc.* **1986**, *108*, 5345.
(106) Bowers, C. R.; Weitekamp, D. P. *J. Am. Chem. Soc.* **1987**, *109*, 5541.
(107) Eisenschmid, T. C.; Kirss, R. U.; Deutsch, P. P.; Hommeltoft, S. I.; Eisenberg, R.; Bargon, J.; Lawler, R. G.; Balch, A. L. *J. Am. Chem. Soc.* **1987**, *109*, 8089.
(108) Haake, M.; Barkemeyer, J.; Bargon, J. *J. Phys. Chem.* **1995**, *99*, 17539.

(109) Kirss, R. U.; Eisenschmid, T. C.; Eisenberg, R. *J. Am. Chem. Soc.* **1988**, *110*, 8564.
(110) Bargon, J.; Kandels, J.; Woelk, K. *Angew. Chem. Int. Edit.* **1990**, *29*, 58.
(111) Eisenschmid, T. C.; McDonald, J.; Eisenberg, R.; Lawler, R. G. *J. Am. Chem. Soc.* **1989**, *111*, 7267.
(112) Duckett, S. B.; Newell, C. L.; Eisenberg, R. *J. Am. Chem. Soc.* **1993**, *115*, 1156.
(113) Barkemeyer, J.; Haake, M.; Bargon, J. *J. Am. Chem. Soc.* **1995**, *117*, 2927.
(114) Kirss, R. U.; Eisenberg, R. *J. Organomet. Chem.* **1989**, *359*, C22.
(115) Lopez-Serrano, J.; Duckett, S. B.; Dunne, J. P.; Godard, C.; Whitwood, A. C. *Dalton Trans.* **2008**, 4270.
(116) Lopez-Serrano, J.; Lledos, A.; Duckett, S. B. *Organometallics* **2008**, *27*, 43.
(117) Lopez-Serrano, J.; Duckett, S. B.; Lledos, A. *J. Am. Chem. Soc.* **2006**, *128*, 9596.
(118) Horiuti, I.; Polanyi, M. *Trans. Faraday Soc.* **1934**, *30*, 1164.
(119) Kovtunov, K. V.; Barskiy, D. A.; Salnikov, O. G.; Khudorozhkov, A. K.; Bukhtiyarov, V. I.; Prosvirin, I. P.; Koptyug, I. V. *Chem. Commun.* **2014**, *50*, 875.
(120) Skovpin, I. V.; Zhivonitko, V. V.; Koptyug, I. V. *Appl. Magn. Reson.* **2011**, *41*, 393.
(121) Koptyug, I. V.; Kovtunov, K. V.; Burt, S. R.; Anwar, M. S.; Hilty, C.; Han, S. I.; Pines, A.; Sagdeev, R. Z. *J. Am. Chem. Soc.* **2007**, *129*, 5580.
(122) Kovtunov, K. V.; Zhivonitko, V. V.; Kiwi-Minsker, L.; Koptyug, I. V. *Chem. Commun.* **2010**, *46*, 5764.
(123) Eichhorn, A.; Koch, A.; Bargon, J. *J. Mol. Catal. A: Chem.* **2001**, *174*, 293.
(124) Balu, A. M.; Duckett, S. B.; Luque, R. *Dalton Trans.* **2009**, 5074.
(125) Kovtunov, K. V.; Beck, I. E.; Zhivonitko, V. V.; Barskiy, D. A.; Bukhtiyarov, V. I.; Koptyug, I. V. *Phys. Chem. Chem. Phys.* **2012**, *14*, 11008.
(126) Kovtunov, K. V.; Beck, I. E.; Bukhtiyarov, V. I.; Koptyug, I. V. *Angew. Chem. Int. Edit.* **2008**, *47*, 1492.
(127) Gloggler, S.; Grunfeld, A. M.; Ertas, Y. N.; McCormick, J.; Wagner, S.; Bouchard, L. S. *Chem. Commun.* **2016**, *52*, 605.
(128) Gloggler, S.; Grunfeld, A. M.; Ertas, Y. N.; McCormick, J.; Wagner, S.; Schleker, P. P. M.; Bouchard, L. S. *Angew. Chem. Int. Edit.* **2015**, *54*, 2452.
(129) Sharma, R.; Bouchard, L. S. *Sci. Rep.* **2012**, *2*.
(130) Kovtunov, K. V.; Zhivonitko, V. V.; Skovpin, I. V.; Barskiy, D. A.; Salnikov, O. G.; Koptyug, I. V. *J. Phys. Chem. C* **2013**, *117*, 22887.
(131) Salnikov, O. G.; Kovtunov, K. V.; Koptyug, I. V. *Sci. Rep.* **2015**, *5*.
(132) Kovtunov, K. V.; Barskiy, D. A.; Coffey, A. M.; Truong, M. L.; Salnikov, O. G.; Khudorozhkov, A. K.; Inozemtseva, E. A.; Prosvirin, I. P.; Bukhtiyarov, V. I.; Waddell, K. W.; Chekmenev, E. Y.; Koptyug, I. V. *Chem-Eur. J.* **2014**, *20*, 11636.
(133) Carravetta, M.; Johannessen, O. G.; Levitt, M. H. *Phys. Rev. Lett.* **2004**, *92*.
(134) Shchepin, R. V.; Coffey, A. M.; Waddell, K. W.; Chekmenev, E. Y. *Anal. Chem.* **2014**, *86*, 5601.
(135) Shchepin, R. V.; Coffey, A. M.; Waddell, K. W.; Chekmenev, E. Y. *J. Am. Chem. Soc.* **2012**, *134*, 3957.
(136) Kovtunov, K. V.; Truong, M. L.; Barskiy, D. A.; Salnikov, O. G.; Bukhtiyarov, V. I.; Coffey, A. M.; Waddell, K. W.; Koptyug, I. V.; Chekmenev, E. Y. *J. Phys. Chem. C* **2014**, *118*, 28234.
(137) Levitt, M. H. In *Annual Review of Physical Chemistry, Vol 63*; Johnson, M. A., Martinez, T. J., Eds. 2012; Vol. 63, p 89.
(138) Pileio, G.; Bowen, S.; Laustsen, C.; Tayler, M. C. D.; Hill-Cousins, J. T.; Brown, L. J.; Brown, R. C. D.; Ardenkjaer-Larsen, J. H.; Levitt, M. H. *J. Am. Chem. Soc.* **2013**, *135*, 5084.
(139) Carravetta, M.; Levitt, M. H. *J. Chem. Phys.* **2005**, *122*.

(140) Pileio, G.; Levitt, M. H. *J. Chem. Phys.* **2009**, *130*.
(141) Franzoni, M. B.; Buljubasich, L.; Spiess, H. W.; Munnemann, K. *J. Am. Chem. Soc.* **2012**, *134*, 10393.
(142) Stevanato, G.; Hill-Cousins, J. T.; Hakansson, P.; Roy, S. S.; Brown, L. J.; Brown, R. C. D.; Pileio, G.; Levitt, M. H. *Angew. Chem. Int. Edit.* **2015**, *54*, 3740.
(143) Graafen, D.; Franzoni, M. B.; Schreiber, L. M.; Spiess, H. W.; Munnemann, K. *J. Magn. Reson.* **2016**, *262*, 68.
(144) Claytor, K.; Theis, T.; Feng, Y. S.; Warren, W. *J. Magn. Reson.* **2014**, *239*, 81.
(145) Atkinson, K. D.; Cowley, M. J.; Elliott, P. I. P.; Duckett, S. B.; Green, G. G. R.; Lopez-Serrano, J.; Whitwood, A. C. *J. Am. Chem. Soc.* **2009**, *131*, 13362.
(146) Adams, R. W.; Duckett, S. B.; Green, R. A.; Williamson, D. C.; Green, G. G. R. *J. Chem. Phys.* **2009**, *131*.
(147) Fekete, M.; Bayfield, O.; Duckett, S. B.; Hart, S.; Mewis, R. E.; Pridmore, N.; Rayner, P. J.; Whitwood, A. *Inorg. Chem.* **2013**, *52*, 13453.
(148) Atkinson, K. D.; Cowley, M. J.; Duckett, S. B.; Elliott, P. I. P.; Green, G. G. R.; Lopez-Serrano, J.; Khazal, I. G.; Whitwood, A. C. *Inorg. Chem.* **2009**, *48*, 663.
(149) Cowley, M. J.; Adams, R. W.; Atkinson, K. D.; Cockett, M. C. R.; Duckett, S. B.; Green, G. G. R.; Lohman, J. A. B.; Kerssebaum, R.; Kilgour, D.; Mewis, R. E. *J. Am. Chem. Soc.* **2011**, *133*, 6134.
(150) Lloyd, L. S.; Asghar, A.; Burns, M. J.; Charlton, A.; Coombes, S.; Cowley, M. J.; Dear, G. J.; Duckett, S. B.; Genov, G. R.; Green, G. G. R.; Highton, L. A. R.; Hooper, A. J. J.; Khan, M.; Khazal, I. G.; Lewis, R. J.; Mewis, R. E.; Roberts, A. D.; Ruddlesden, A. J. *Catal. Sci. Tech.* **2014**, *4*, 3544.
(151) Crabtree, R. H.; Lavin, M.; Bonneviot, L. *J. Am. Chem. Soc.* **1986**, *108*, 4032.
(152) Holmes, A. J.; Rayner, P. J.; Cowley, M. J.; Green, G. G. R.; Whitwood, A. C.; Duckett, S. B. *Dalton Trans.* **2015**, *44*, 1077.
(153) Burns, M. J.; Rayner, P. J.; Green, G. G. R.; Highton, L. A. R.; Mewis, R. E.; Duckett, S. B. *J. Phys. Chem. B* **2015**, *119*, 5020.
(154) Pravdivtsev, A. N.; Yurkovskaya, A. V.; Zimmermann, H.; Vieth, H.-M.; Ivanov, K. L. *RSC Adv.* **2015**, *5*, 63615.
(155) Theis, T.; Truong, M. L.; Coffey, A. M.; Shchepin, R. V.; Waddell, K. W.; Shi, F.; Goodson, B. M.; Warren, W. S.; Chekmenev, E. Y. *J. Am. Chem. Soc.* **2015**, *137*, 1404.
(156) Truong, M. L.; Theis, T.; Coffey, A. M.; Shchepin, R. V.; Waddell, K. W.; Shi, F.; Goodson, B. M.; Warren, W. S.; Chekmenev, E. Y. *J. Phys. Chem. C* **2015**, *119*, 8786.
(157) Zeng, H.; Xu, J.; Gillen, J.; McMahon, M. T.; Artemov, D.; Tyburn, J.-M.; Lohman, J. A. B.; Mewis, R. E.; Atkinson, K. D.; Green, G. G. R.; Duckett, S. B.; van Zijl, P. C. M. *J. Magn. Reson.* **2013**, *237*, 73.
(158) Ratajczyk, T.; Gutmann, T.; Bernatowicz, P.; Buntkowsky, G.; Frydel, J.; Fedorczyk, B. *Chem-Eur. J.* **2015**, *21*, 12616.
(159) Gloeggler, S.; Mueller, R.; Colell, J.; Emondts, M.; Dabrowski, M.; Bluemich, B.; Appelt, S. *Phys. Chem. Chem. Phys.* **2011**, *13*, 13759.
(160) Ruddlesden, A. J.; Mewis, R. E.; Green, G. G. R.; Whitwood, A. C.; Duckett, S. B. *Organometallics* **2015**, *34*, 2997.
(161) Truong, M. L.; Shi, F.; He, P.; Yuan, B.; Plunkett, K. N.; Coffey, A. M.; Shchepin, R. V.; Barskiy, D. A.; Kovtunov, K. V.; Koptyug, I. V.; Waddell, K. W.; Goodson, B. M.; Chekmenev, E. Y. *J. Phys. Chem. B* **2014**, *118*, 13882.
(162) Zeng, H.; Xu, J.; McMahon, M. T.; Lohman, J. A. B.; van Zijl, P. C. M. *J. Magn. Reson.* **2014**, *246*, 119.

(163) Mewis, R. E.; Atkinson, K. D.; Cowley, M. J.; Duckett, S. B.; Green, G. G. R.; Green, R. A.; Highton, L. A. R.; Kilgour, D.; Lloyd, L. S.; Lohman, J. A. B.; Williamson, D. C. *Magn. Reson. Chem.* **2014**, *52*, 358.
(164) Mewis, R. E.; Fekete, M.; Green, G. G. R.; Whitwood, A. C.; Duckett, S. B. *Chem. Commun.* **2015**, *51*, 9857.
(165) Blum, J.; Amer, I.; Vollhardt, K. P. C.; Schwarz, H.; Hohne, G. *J. Org. Chem.* **1987**, *52*, 2804.
(166) Weddle, K. S.; Aiken, J. D.; Finke, R. G. *J. Am. Chem. Soc.* **1998**, *120*, 5653.
(167) Khawaja, A. Z.; Cassidy, D. B.; Al Shakarchi, J.; McGrogan, D. G.; Inston, N. G.; Jones, R. G. *Insights Imaging* **2015**, *6*, 553.
(168) Hopkinson, M. N.; Richter, C.; Schedler, M.; Glorius, F. *Nature* **2014**, *510*, 485.
(169) Bourreli, B.; Pinaud, M.; Passuti, N.; Gunst, J. P.; Drouet, J. C.; Remi, J. P. *Can. J. Anaesth.* **1988**, *35*, 242.
(170) Lamberth, C.; Trah, S.; Wendeborn, S.; Dumeunier, R.; Courbot, M.; Godwin, J.; Schneiter, P. *Bioorg. Med. Chem.* **2012**, *20*, 2803.
(171) Livermore, D. G. H.; Bethell, R. C.; Cammack, N.; Hancock, A. P.; Hann, M. M.; Green, D. V. S.; Lamont, R. B.; Noble, S. A.; Orr, D. C.; Payne, J. J.; Ramsay, M. V. J.; Shingler, A. H.; Smith, C.; Storer, R.; Williamson, C.; Willson, T. *J. Med. Chem.* **1993**, *36*, 3784.
(172) Pogacic, V.; Bullock, A. N.; Fedorov, O.; Filippakopoulos, P.; Gasser, C.; Biondi, A.; Meyer-Monard, S.; Knapp, S.; Schwaller, J. *Cancer Res.* **2007**, *67*, 6916.
(173) Chen, L. S.; Redkar, S.; Bearss, D.; Wierda, W. G.; Gandhi, V. *Blood* **2009**, *114*, 4150.
(174) Abel, E. W.; Heard, P. J.; Orrell, K. G.; Hursthouse, M. B.; Malik, K. M. A. *J. Chem. Soc. Dalton Trans.* **1995**, 3165.
(175) Eaton, S. S.; Eaton, G. R.; Holm, R. H. *J. Organomet. Chem.* **1972**, *39*, 179.
(176) Chen, Y.; Shepherd, R. E. *Inorg. Chim. Acta* **1998**, *279*, 85.
(177) Dixon, K. R.; Eadie, D. T.; Stobart, S. R. *Inorg. Chem.* **1982**, *21*, 4318.
(178) Abel, E. W.; Blackwall, E. S.; Heard, P. J.; Orrell, K. G.; Sik, V.; Hursthouse, M. B.; Mazid, M. A.; Malik, K. M. A. *J. Chem. Soc. Dalton Trans.* **1994**, 445.
(179) Abel, E. W.; Heard, P. J.; Orrell, K. G. *Inorg. Chim. Acta* **1997**, *255*, 65.
(180) Abel, E. W.; Heard, P. J.; Orrell, K. G.; Sik, V. *Polyhedron* **1994**, *13*, 2907.
(181) Alvarez, S.; Bermejo, M. J.; Vinaixa, J. *J. Am. Chem. Soc.* **1987**, *109*, 5316.
(182) Tiripicchio, A.; Camellini, M. T.; Neve, F.; Ghedini, M. *J. Chem. Soc. Dalton Trans.* **1990**, 1651.
(183) Oro, L. A.; Carmona, D.; Lahoz, F. J.; Puebla, M. P.; Esteban, M.; Focesfoces, C.; Cano, F. H. *J. Chem. Soc. Dalton Trans.* **1986**, 2113.
(184) Arduengo, A. J.; Krafczyk, R.; Schmutzler, R.; Craig, H. A.; Goerlich, J. R.; Marshall, W. J.; Unverzagt, M. *Tetrahedron* **1999**, *55*, 14523.
(185) Hintermann, L. *Bielstein J. Org. Chem.* **2007**, *3*.
(186) Uson, R.; Oro, L. A.; Cabeza, J. A.; Bryndza, H. E.; Stepro, M. P. *Inorg. Syn.* **1985**, *23*, 126.
(187) Torres, O.; Martin, M.; Sola, E. *Organometallics* **2009**, *28*, 863.
(188) Bain, A. D.; Rex, D. M.; Smith, R. N. *Magn. Reson. Chem.* **2001**, *39*, 122.
(189) Orrell, K. G.; Sik, V.; Stephenson, D. *Prog. Nucl. Mag. Res. Sp.* **1990**, *22*, 141.
(190) Ammann, C.; Meier, P.; Merbach, A. E. *J. Magn. Reson.* **1982**, *46*, 319.
(191) Harris, D. C. *J. Chem. Educ.* **1998**, *75*, 119.
(192) Machado, H. J. S.; Hinchliffe, A. *Theochem-J. Mol. Struc.* **1995**, *339*, 255.
(193) Casarini, D.; Lunazzi, L.; Mazzanti, A. *Eur. J. Org. Chem* **2010**, 2035.
(194) Johnson, C. E.; Eisenberg, R. *J. Am. Chem. Soc.* **1985**, *107*, 3148.
(195) Deutsch, P. P.; Eisenberg, R. *Chem. Rev.* **1988**, *88*, 1147.

(196) Searles, K.; Pink, M.; Caulton, K. G.; Mindiola, D. J. *Dalton Trans.* **2012**, *41*, 9619.
(197) Ammann, C.; Isaia, F.; Pregosin, P. S. *Magn. Reson. Chem.* **1988**, *26*, 236.
(198) Martin, M.; Sola, E.; Torres, O.; Plou, P.; Oro, L. A. *Organometallics* **2003**, *22*, 5406.
(199) Krueger, M. B.; Selle, C.; Heller, D.; Baumann, W. *J. Chem. Eng. Data* **2012**, *57*, 1737.
(200) Michels, A.; Degraaff, W.; Vandersomme, J. *Appl. Sci. Res.* **1953**, *4*, 105.
(201) Hasebroock, K. M.; Serkova, N. J. *Expert Opin. Drug Metab. Toxicol.* **2009**, *5*, 403.
(202) Barskiy, D. A.; Pravdivtsev, A. N.; Ivanov, K. L.; Kovtunov, K. V.; Koptyug, I. V. *Phys. Chem. Chem. Phys.* **2016**, *18*, 89.
(203) McConnell, H. M.; McLean, A. D.; Reilly, C. A. *J. Chem. Phys.* **1955**, *23*, 1152.
(204) Eshuis, N.; Aspers, R. L. E. G.; van Weerdenburg, B. J. A.; Feiters, M. C.; Rutjes, F. P. J. T.; Wijmenga, S. S.; Tessari, M. *J. Magn. Reson.* **2016**, *265*, 59.
(205) Sengstschmid, H.; Freeman, R.; Barkemeyer, J.; Bargon, J. *J. Magn. Reson., Ser A* **1996**, *120*, 249.
(206) Reese, H. M. *Science (New York, N.Y.)* **1900**, *12*, 293.
(207) Duecker, E. B.; Kuhn, L. T.; Muennemann, K.; Griesinger, C. *J. Magn. Reson.* **2012**, *214*, 159.
(208) Mewis, R. E. *Magn. Reson. Chem.* **2015**, *53*, 789.
(209) Aguilar, J. A.; Elliott, P. I. P.; Lopez-Serrano, J.; Adams, R. W.; Duckett, S. B. *Chem. Commun.* **2007**, 1183.
(210) Knecht, S.; Pravdivtsev, A. N.; Hoevener, J.-B.; Yurkovskaya, A. V.; Ivanov, K. L. *RSC Adv.* **2016**, *6*, 24470.
(211) Pravdivtsev, A. N.; Ivanov, K. L.; Yurkovskaya, A. V.; Petrov, P. A.; Limbach, H.-H.; Kaptein, R.; Vieth, H.-M. *J. Magn. Reson.* **2015**, *261*, 73.
(212) Ryu, C.-K.; Park, R.-E.; Ma, M.-Y.; Nho, J.-H. *Bioorg. Med. Chem. Lett.* **2007**, *17*, 2577.
(213) Ibrahim, H. S.; Eldehna, W. M.; Abdel-Aziz, H. A.; Elaasser, M. M.; Abdel-Aziz, M. M. *Eur. J. Med. Chem.* **2014**, *85*, 480.
(214) Barrow, E. W.; Dreier, J.; Reinelt, S.; Bourne, P. C.; Barrow, W. W. *Antimicrob. Agents Ch.* **2007**, *51*, 4447.
(215) Bourne, C. R.; Barrow, E. W.; Bunce, R. A.; Bourne, P. C.; Berlin, K. D.; Barrow, W. W. *Antimicrob. Agents Ch.* **2010**, *54*, 3825.
(216) Bourne, C. R.; Bunce, R. A.; Bourne, P. C.; Berlin, K. D.; Barrow, E. W.; Barrow, W. W. *Antimicrob. Agents Ch.* **2009**, *53*, 3065.
(217) Hollo, B.; Magyari, J.; Ivkovic-Radovanovic, V.; Vuckovic, G.; Tomic, Z. D.; Szilagyi, I. M.; Pokol, G.; Szecsenyi, K. M. *Polyhedron* **2014**, *80*, 142.
(218) Fekete, M.; Gibard, C.; Dear, G. J.; Green, G. G. R.; Hooper, A. J. J.; Roberts, A. D.; Cisnetti, F.; Duckett, S. B. *Dalton Trans.* **2015**, *44*, 7870.
(219) d'Angelo, J. V. H.; Francesconi, A. Z. *J. Chem. Eng. Data* **2001**, *46*, 671.
(220) Motin, M. A.; Kabir, M. H.; Huque, M. E. *Phys. Chem. Liq.* **2005**, *43*, 123.
(221) Borah, B. J.; Saikia, K.; Saikia, P. P.; Barua, N. C.; Dutta, D. K. *Catal. Today* **2012**, *198*, 174.
(222) Beaumont, S. K. *J. Chem. Technol. Biot.* **2012**, *87*, 595.
(223) Ananikov, V. P.; Beletskaya, I. P. *Organometallics* **2012**, *31*, 1595.
(224) Astruc, D. *Inorg. Chem.* **2007**, *46*, 1884.
(225) Diver, C.; Lawrance, G. A. *J. Chem. Soc. Dalton Trans.* **1988**, 931.
(226) Lopez-Serrano, J.; Duckett, S. B.; Aiken, S.; Lenero, K. Q. A.; Drent, E.; Dunne, J. P.; Konya, D.; Whitwood, A. C. *J. Am. Chem. Soc.* **2007**, *129*, 6513.
(227) Dunne, J. P.; Aiken, S.; Duckett, S. B.; Konya, D.; Lenero, K. Q. A.; Drent, E. *J. Am. Chem. Soc.* **2004**, *126*, 16708.
(228) Szlyk, E.; Barwiolek, M. *Thermochim. Acta* **2009**, *495*, 85.
(229) Tassone, J. P.; Mawhinney, R. C.; Spivak, G. J. *J. Organomet. Chem.* **2015**, *776*, 153.

(230) Lu, X. X.; Tang, H. S.; Ko, C. C.; Wong, J. K. Y.; Zhu, N. Y.; Yam, V. W. W. *Chem. Commun.* **2005**, 1572.
(231) Quagliano, J. V.; Schubert, L. *Chem. Rev.* **1952**, *50*, 201.
(232) Redfield, D. A.; Nelson, J. H. *Inorg. Chem.* **1973**, *12*, 15.
(233) Redfield, D. A.; Nelson, J. H. *Inorg. Nucl. Chem. Lett* **1974**, *10*, 931.
(234) Murata, S.; Ido, Y. *Bull. Chem. Soc. Jpn.* **1994**, *67*, 1746.
(235) Stang, P. J.; Cao, D. H.; Poulter, G. T.; Arif, A. M. *Organometallics* **1995**, *14*, 1110.
(236) Bernhardt, P. V.; Lawrance, G. A. *Polyhedron* **1987**, *6*, 1875.
(237) Calvo, F.; Carre, A. *Nanotechnology* **2006**, *17*, 1292.
(238) Stakheev, A. Y.; Mashkovskii, I. S.; Baeva, G. N.; Telegina, N. S. *Russ. J. Gen. Chem.* **2010**, *80*, 618.
(239) Li, J.-H.; Liang, Y.; Xie, Y.-X. *J. Org. Chem.* **2005**, *70*, 4393.
(240) Hilt, G.; Vogler, T.; Hess, W.; Galbiati, F. *Chem. Commun.* **2005**, 1474.
(241) de Pedro, Z. M.; Casas, J. A.; Gomez-Sainero, L. M.; Rodriguez, J. J. *Appl. Catal., B* **2010**, *98*, 79.
(242) Velde, C.; Blockhuys, F.; Van Alsenoy, C.; Lenstra, A. T. H.; Geise, H. J. *Journal of the Chemical Society-Perkin Transactions 2* **2002**, 1345.
(243) Permin, A. B.; Eisenberg, R. *J. Am. Chem. Soc.* **2002**, *124*, 12406.
(244) Karplus, M. *J. Chem. Phys.* **1959**, *30*, 11.
(245) Makkee, M.; Wiersma, A.; van de Sandt, E.; van Bekkum, H.; Moulijn, J. A. *Catal. Today* **2000**, *55*, 125.
(246) Noelke, C. J.; Rase, H. F. *Ind. Eng. Chem. Prod. RD.* **1979**, *18*, 325.
(247) Brunet, J. J.; Couillens, X.; Daran, J. C.; Diallo, O.; Lepetit, C.; Neibecker, D. *Eur. J. Inorg. Chem.* **1998**, 349.
(248) Mori, T.; Yasuoka, T.; Morikawa, Y. *Catal. Today* **2004**, *88*, 111.
(249) Sehnal, P.; Taylor, R. J. K.; Fairlamb, I. J. S. *Chem. Rev.* **2010**, *110*, 824.
(250) Otting, G.; Soler, L. P.; Messerle, B. A. *J. Magn. Reson.* **1999**, *137*, 413.
(251) Dobrovolna, Z.; Kacer, P.; Cerveny, L. *J. Mol. Catal. A: Chem.* **1998**, *130*, 279.
(252) Johnson, B. F. G.; McIndoe, J. S. *Coordin. Chem. Rev.* **2000**, *200*, 901.
(253) Balimann, G.; Pregosin, P. S. *J. Magn. Reson.* **1977**, *26*, 283.
(254) Buergi, H. B.; Fischer, E.; Kunz, R. W.; Parvez, M.; Pregosin, P. S. *Inorg. Chem.* **1982**, *21*, 1246.
(255) Tolman, C. A. *Chem. Rev.* **1977**, *77*, 313.
(256) Zudin, V. N.; Chinakov, V. D.; Nekipelov, V. M.; Likholobov, V. A.; Yermakov, Y. I. *J. Organomet. Chem.* **1985**, *289*, 425.
(257) Basolo, F.; Pearson, R. G.; Chatt, J.; Gray, H. B.; Shaw, B. L. *J. Chem. Soc.* **1961**, 2207.
(258) Paty, M. *Recherche* **1985**, *16*, 520.
(259) Fulmer, G. R.; Miller, A. J. M.; Sherden, N. H.; Gottlieb, H. E.; Nudelman, A.; Stoltz, B. M.; Bercaw, J. E.; Goldberg, K. I. *Organometallics* **2010**, *29*, 2176.
(260) Tanase, T.; Ohizumi, T.; Kobayashi, K.; Yamamoto, Y. *Organometallics* **1996**, *15*, 3404.
(261) Widenhoefer, R. A.; Zhong, H. A.; Buchwald, S. L. *Organometallics* **1996**, *15*, 2745.
(262) Huynh, H. V.; Wu, J. *J. Organomet. Chem.* **2009**, *694*, 323.
(263) Harwood, L. M. C., Timothy, D. W. *Introduction to Organic Spectroscopy*; Oxford University Press: Oxford, 1996.
(264) Zavitsas, A. A. *J. Phys. Chem. A* **2003**, *107*, 897.
(265) Kullberg, M. L.; Lemke, F. R.; Powell, D. R.; Kubiak, C. P. *Inorg. Chem.* **1985**, *24*, 3589.
(266) Kannan, S.; James, A. J.; Sharp, P. R. *J. Am. Chem. Soc.* **1998**, *120*, 215.

(267) Murahashi, T.; Otani, T.; Okuno, T.; Kurosawa, H. *Angew. Chem. Int. Edit.* **2000**, *39*, 537.
(268) Murahashi, T.; Fujimoto, M.; Kawabata, Y.; Inoue, R.; Ogoshi, S.; Kurosawa, H. *Angew. Chem. Int. Edit.* **2007**, *46*, 5440.
(269) Babbini, D. C.; Mulligan, F. L.; Schulhauser, H. R.; Sweigart, T. C.; Nichol, G. S.; Hurst, S. K. *Inorg. Chem.* **2010**, *49*, 4307.
(270) Murahashi, T.; Takase, K.; Usui, K.; Kimura, S.; Fujimoto, M.; Uemura, T.; Ogoshi, S.; Yamamoto, K. *Dalton Trans.* **2013**, *42*, 10626.
(271) Lin, S.; Herbert, D. E.; Velian, A.; Day, M. W.; Agapie, T. *J. Am. Chem. Soc.* **2013**, *135*, 15830.
(272) Christmann, U.; Pantazis, D. A.; Benet-Buchholz, J.; McGrady, J. E.; Maseras, F.; Vilar, R. *Organometallics* **2006**, *25*, 5990.
(273) Hruszkewycz, D. P.; Balcells, D.; Guard, L. M.; Hazari, N.; Tilset, M. *J. Am. Chem. Soc.* **2014**, *136*, 7300.
(274) Takahashi, Y.; Tsutsumi, K.; Nakagai, Y.; Morimoto, T.; Kakiuchi, K.; Ogoshi, S.; Kurosawa, H. *Organometallics* **2008**, *27*, 276.
(275) Murahashi, T.; Kurosawa, H. *J. Synth. Org. Chem. Jpn.* **2003**, *61*, 652.
(276) Murahashi, T.; Ogoshi, S.; Kurosawa, H. *Chem. Rec.* **2003**, *3*, 101.
(277) Murahashi, T.; Kurosawa, H. *Coordin. Chem. Rev.* **2002**, *231*, 207.
(278) Murahashi, T.; Mochizuki, E.; Kai, Y.; Kurosawa, H. *J. Am. Chem. Soc.* **1999**, *121*, 10660.
(279) Tatsumi, Y.; Naga, R.; Nakashima, H.; Murahashi, T.; Kurosawa, H. *Chem. Commun.* **2004**, 1430.
(280) Horiuchi, S.; Tachibana, Y.; Yamashita, M.; Yamamoto, K.; Masai, K.; Takase, K.; Matsutani, T.; Kawamata, S.; Kurashige, Y.; Yanai, T.; Murahashi, T. *Nat. Commun.* **2015**, *6*.
(281) Uberman, P. M.; Caira, M. R.; Martin, S. E. *Organometallics* **2013**, *32*, 3220.
(282) Yang, J.; Li, P.; Zhang, Y.; Wang, L. *Dalton Trans.* **2014**, *43*, 14114.
(283) Omondi, B.; Shaw, M. L.; Holzapfel, C. W. *J. Organomet. Chem.* **2011**, *696*, 3091.
(284) Atkins, P. J. S., D. F *Inorganic Chemistry*; 3 ed.; W. H. Freeman and CO: New York, 1999.
(285) Ma, B. W.; Li, J.; Djurovich, P. I.; Yousufuddin, M.; Bau, R.; Thompson, M. E. *J. Am. Chem. Soc.* **2005**, *127*, 28.
(286) Schilter, D.; Clegg, J. K.; Harding, M. M.; Rendina, L. M. *Dalton Trans.* **2010**, *39*, 239.
(287) Yam, V. W. W.; Wong, K. M. C.; Zhu, N. Y. *J. Am. Chem. Soc.* **2002**, *124*, 6506.
(288) Yu, C.; Wong, K. M. C.; Chan, K. H. Y.; Yam, V. W. W. *Angew. Chem. Int. Edit.* **2005**, *44*, 791.
(289) Cho, S.; Mara, M. W.; Wang, X.; Lockard, J. V.; Rachford, A. A.; Castellano, F. N.; Chen, L. X. *J. Phys. Chem. A* **2011**, *115*, 3990.
(290) Kozhevnikov, V. N.; Donnio, B.; Heinrich, B.; Bruce, D. W. *Chem. Commun.* **2014**, *50*, 14191.
(291) Aliprandi, A.; Mauro, M.; De Cola, L. *Nat Chem* **2015**, *advance online publication*.
(292) Vogler, A.; Kunkely, H. *Coordin. Chem. Rev.* **2000**, *208*, 321.
(293) Yamazaki, S. *Polyhedron* **1985**, *4*, 1915.
(294) Akoka, S.; Barantin, L.; Trierweiler, M. *Anal. Chem.* **1999**, *71*, 2554.
(295) Cavinato, G.; Vavasori, A.; Toniolo, L.; Dolmella, A. *Inorg. Chim. Acta* **2004**, *357*, 2737.
(296) Zeldin, M.; Mehta, P.; Vernon, W. D. *Inorg. Chem.* **1979**, *18*, 463.
(297) Crabtree, R. H.; Felkin, H.; Morris, G. E. *J. Organomet. Chem.* **1977**, *141*, 205.
(298) Xu, Y.; Mingos, M. P.; Brown, J. M. *Chem. Commun.* **2008**, 199.

(299) Tang, J. A.; Gruppi, F.; Fleysher, R.; Sodickson, D. K.; Canary, J. W.; Jerschow, A. *Chem. Commun.* **2011**, *47*, 958.
(300) P. G. T. Fogg, W. G. *Solubility of Gases in Liquids*; John Wiley & Sons: Chichester, 1990.
(301) Palit, C. M.; Graham, D. J.; Chen, C.-H.; Foxman, B. M.; Ozerov, O. V. *Chem. Commun.* **2014**, *50*, 12840.
(302) Brown, K. M.; Dennis, J. E. *Numer. Math.* **1972**, *18*, 289.
(303) Laidler, K. J. *Chemical Kinetics*; Second ed.; McGraw-Hill, 1976, 16.
(304) Shapley, J. R.; Schrock, R. R.; Osborn, J. A. *J. Am. Chem. Soc.* **1969**, *91*, 2816.
(305) Bernardi, A.; Femoni, C.; Iapalucci, M. C.; Longoni, G.; Zacchini, S. *Dalton Trans.* **2009**, 4245.
(306) Amssoms, K.; Oza, S. L.; Augustyns, K.; Yamani, A.; Lambeir, A. M.; Bal, G.; Van der Veken, P.; Fairlamb, A. H.; Haemers, A. *Bioorg. Med. Chem. Lett.* **2002**, *12*, 2703.
(307) Amssons, K.; Oza, S. L.; Ravaschino, E.; Yamani, A.; Lambeir, A. M.; Rajan, P.; Bal, G.; Rodriguez, J. B.; Fairlamb, A. H.; Augustyns, K.; Haemers, A. *Bioorg. Med. Chem. Lett.* **2002**, *12*, 2553.
(308) Burns, M. J.; Fairlamb, I. J. S.; Kapdi, A. R.; Sehnal, P.; Taylor, R. J. K. *Org. Lett.* **2007**, *9*, 5397.
(309) Miyaura, N.; Suzuki, A. *Chem. Rev.* **1995**, *95*, 2457.
(310) Mann, B. E.; Musco, A. *J. Chem. Soc. Dalton Trans.* **1975**, 1673.
(311) Fauvarque, J. F.; Pfluger, F.; Troupel, M. *J. Organomet. Chem.* **1981**, *208*, 419.
(312) Beeby, A.; Bettington, S.; Fairlamb, I. J. S.; Goeta, A. E.; Kapdi, A. R.; Niemela, E. H.; Thompson, A. L. *New J. Chem.* **2004**, *28*, 600.
(313) De Meijere, A.; Meyer, F. E. *Angew. Chem. Int. Edit.* **1994**, *33*, 2379.
(314) Hierso, J. C.; Fihri, A.; Amardeil, W.; Meunier, P.; Doucet, H.; Santelli, M.; Donnadieu, B. *Organometallics* **2003**, *22*, 4490.
(315) Lennox, A. J. J.; Lloyd-Jones, G. C. *Chem. Soc. Rev.* **2014**, *43*, 412.
(316) Mickel, S. J.; Sedelmeier, G. H.; Niederer, D.; Schuerch, F.; Seger, M.; Schreiner, K.; Daeffler, R.; Osmani, A.; Bixel, D.; Loiseleur, O.; Cercus, J.; Stettler, H.; Schaer, K.; Gamboni, R.; Bach, A.; Chen, G. P.; Chen, W. C.; Geng, P.; Lee, G. T.; Loeser, E.; McKenna, J.; Kinder, F. R.; Konigsberger, K.; Prasad, K.; Ramsey, T. M.; Reel, N.; Repic, O.; Rogers, L.; Shieh, W. C.; Wang, R. M.; Waykole, L.; Xue, S.; Florence, G.; Paterson, I. *Org. Process Res. Dev.* **2004**, *8*, 113.
(317) Fairlamb, I. J. S.; Marrison, L. R.; Dickinson, J. M.; Lu, F. J.; Schmidt, J. P. *Bioorg. Med. Chem.* **2004**, *12*, 4285.
(318) Wolfe, J. P.; Singer, R. A.; Yang, B. H.; Buchwald, S. L. *J. Am. Chem. Soc.* **1999**, *121*, 9550.
(319) Amatore, C.; Le Duc, G.; Jutand, A. *Chem-Eur. J.* **2013**, *19*, 10082.
(320) Amatore, C.; Jutand, A.; Le Duc, G. *Chem-Eur. J.* **2012**, *18*, 6616.
(321) Sicre, C.; Alonso-Gomez, J. L.; Cid, M. M. *Tetrahedron* **2006**, *62*, 11063.
(322) Daniels, C. J.; McLean, M. A.; Schulte, R. F.; Robb, F. J.; Gill, A. B.; McGlashan, N.; Graves, M. J.; Schwaiger, M.; Lomas, D. J.; Brindle, K. M.; Gallagher, F. A. *NMR Biomed.* **2016**, *29*, 387.
(323) Marco-Rius, I.; Tayler, M. C. D.; Kettunen, M. I.; Larkin, T. J.; Timm, K. N.; Serrao, E. M.; Rodrigues, T. B.; Pileio, G.; Ardenkjaer-Larsen, J. H.; Levitt, M. H.; Brindle, K. M. *NMR Biomed.* **2013**, *26*, 1696.
(324) Theis, T.; Ortiz, G. X., Jr.; Logan, A. W. J.; Claytor, K. E.; Feng, Y.; Huhn, W. P.; Blum, V.; Malcolmson, S. J.; Chekmenev, E. Y.; Wang, Q.; Warren, W. S. *Sci. Adv.* **2016**, *2*, e1501438.

(325) Purwanto; Deshpande, R. M.; Chaudhari, R. V.; Delmas, H. *J. Chem. Eng. Data* **1996**, *41*, 1414.
(326) Appleby, K. M.; Mewis, R. E.; Olaru, A. M.; Green, G. G. R.; Fairlamb, I. J. S.; Duckett, S. B. *Chem. Sci.* **2015**, *6*, 3981.
(327) Stigler, S. M. *Ann. Stat.* **1981**, *9*, 465.
(328) Lasdon, L. S.; Waren, A. D.; Jain, A.; Ratner, M. *ACM Trans. Math. Softw.* **1978**, *4*, 34.
(329) Wider, G.; Dreier, L. *J. Am. Chem. Soc.* **2006**, *128*, 2571.
(330) Dolomanov, O. V.; Bourhis, L. J.; Gildea, R. J.; Howard, J. A. K.; Puschmann, H. *J. Appl. Crystallogr.* **2009**, *42*, 339.
(331) Sheldrick, G. M. *Acta Crystallogr. A* **2008**, *64*, 112.
(332) Hennig, J.; Nauerth, A.; Friedburg, H. *Magnet. Reson. Med.* **1986**, *3*, 823.
(333) Brumbaugh, J. S.; Sen, A. *J. Am. Chem. Soc.* **1988**, *110*, 803.
(334) Stang, P. J.; Cao, D. H.; Saito, S.; Arif, A. M. *J. Am. Chem. Soc.* **1995**, *117*, 6273.
(335) Bushnell, G. W.; Hunter, R. G.; McFarland, J. J.; Dixon, K. R. *Can. J. Chem.* **1972**, *50*, 3694.
(336) Malpass, J. R.; Hemmings, D. A.; Wallis, A. L.; Fletcher, S. R.; Patel, S. *J. Chem. Soc. Perkin. Trans. 1* **2001**, 1044.
(337) Shah, P.; Dolores Santana, M.; Garcia, J.; Luis Serrano, J.; Naik, M.; Pednekar, S.; Kapdi, A. R. *Tetrahedron* **2013**, *69*, 1446.
(338) Fraccarollo, D.; Bertani, R.; Mozzon, M.; Belluco, U.; Michelin, R. A. *Inorg. Chim. Acta* **1992**, *201*, 15.